Resistive Gaseous Detectors

Resistive Gaseous Detectors

Designs, Performance, and Perspectives

Marcello Abbrescia, Vladimir Peskov, and Paulo Fonte

WILEY-VCH

Authors

Prof. Marcello Abbrescia
Department of Physics
University of Bari
and Sezione INFN
70126 Bari
Italy

Prof. Paulo Fonte
Polytechnic Institute of Coimbra
Coimbra Institute of Engineering
Rua Pedro Nunes
3030-199 Coimbra
Portugal

and

Laboratory of Instrumentation and
Experimental Particle Physics (LIP)
Physics Department
University of Coimbra
3004-516 Coimbra
Portugal

Prof. Vladimir Peskov
CERN
PH-UAI
581/R-015
1211 Geneva 23
Switzerland

Cover Images: (Background image) © teekid/Gettyimages;
(Illustration) © Wiley

Library of Congress Card No.: applied for

British Library Cataloguing-in-Publication Data
A catalogue record for this book is available from the British Library.

Bibliographic information published by the Deutsche Nationalbibliothek
The Deutsche Nationalbibliothek lists this publication in the Deutsche Nationalbibliografie; detailed bibliographic data are available on the Internet at <http://dnb.d-nb.de>.

Print ISBN: 978-3-527-34076-7
ePDF ISBN: 978-3-527-69872-1
ePub ISBN: 978-3-527-69870-7
Mobi ISBN: 978-3-527-69871-4
oBook ISBN: 978-3-527-69869-1

Typesetting SPi Global, Chennai, India
Printing and Binding

Printed on acid-free paper

Contents

Preface

This book is devoted to those gaseous detectors of elementary particles that incorporate resistive electrodes, whose most well-established instance is the resistive plate chamber. These detectors have several unique and important practical features, such as good spark protection and excellent time resolution, even down to few tens of picoseconds.

There are numerous scientific publications on many different instances of resistive plate chamber designs, and their operation and performance, but there are still few review papers, especially books, summarizing their basic principles of operation, historical development, latest achievements, and their growing applications in various fields.

This book is intended to cover the matters mentioned above and integrate them with the available physical modelling. It was meant to target a wide auditorium, including beginners of the discipline. We hope that this is achieved by an approach where the subject is presented first in a simple way, and later on with a slow increase in complexity.

At the same time, we believe that it will be very useful for the scientific community, where there is an established body of knowledge to be summarized and critically evaluated.

Marcello Abbrescia
Vladimir Peskov
Paulo Fonte

Acknowledgments

The development and success of resistive plate chambers have benefited from the work of a huge community of scientists, engineers, technicians, and students, spread all over the world. We warmly thank all these top-level experts for day-by-day interactions and for sharing with us their experience, which provided a picture of the combined efforts of this community that we tried to accurately report in this book.

Special thanks to our colleagues and friends from the ALICE, ATLAS, and CMS experiments, and from the EEE project, with whom some of us collaborate very closely. It was a great experience!

Abbreviations

ABS	Absorption factors
ADC	Analog to digital converter
ALICE	A large ion collider experiment
ASIC	Application-specific integrated circuit
ATLAS	A Toroidal LHC Apparatus
CERN	Organisation Européenne pour la recherche nucléaire or European Organization for Nuclear Research
CMS	Compact muon solenoid
CNAF	Centro Nazionale Analisi Fotogrammi
CNC	Computer numerical controlled (machine)
DESY	Deutsches Elektronen-Synchrotron
GEM	Gas electron multiplier
HPTDC	High performance time to digital converter
HV	High voltage
LHC	Large Hadron Collider
MIP	Minimum ionizing particle
MPGC	Micropattern gaseous detectors
MRPC	Multi-gap resistive plate chamber
MSGC	Microstrip gas chamber
MWPC	Multiwire proportional chamber
PCB	Printed circuit board
PET	Polyethylene terephthalate
PET	Positron emission tomography
PM	Photomultiplier
PSC	Planar (Pestov) spark chambers
RICH	Ring Imaging Cherenkov
RPC	Resistive plate chamber
TDC	Time to digital converter
TTL	Transistor–transistor logic

Introduction

After the invention of avalanche/discharge gaseous detectors, so-called Geiger counters, which took place around 100 years ago, three major breakthroughs marked important milestones in this field. These were as follows:

- The invention of multiwire proportional chambers (MWPCs), for which Georges Charpak was awarded the Nobel Prize in 1992;
- The invention of resistive plate chambers (RPCs), at the beginning of the 1980s;
- The development of micropattern gaseous detectors (MPGDs), at the end of the 1990s, which are devices conceptually similar to multiwire chambers, but manufactured using microelectronic technologies.

In particular, RPCs, which are extensively covered in this book, are spark-protected position-sensitive detectors for charged particles, gamma photons, and neutrons, which feature at the same time excellent position – below 100 μm – and time – better than 50 ps – resolutions, and which, in addition, are robust, easy to build, and relatively inexpensive.

Nowadays, RPCs are in a blooming phase: they are successfully used in many experiments, including the ones at the Large Hadron Collider (LHC) at the European Organization for Nuclear Research (CERN) (the total area covered in these experiments being around 10 000 m^2), and in gigantic astrophysics experiments (the surface of the Astrophysical Radiation with Ground-based Observatory at YangBaJing (ARGO-YBJ) experiment was more than 7000 m^2). There are ambitious plans to use them for several LHC detector upgrades and in some new experiments, as well as in various more specific applications like time of flight-positron emission tomography (TOF-PET), homeland security, flame detection, and so on.

The aim of this book is to describe the main designs, performance, and applications of RPCs as well as highlight the main challenges the RPC community had to overcome and may face in the next decade.

We also review the recent, but fast and very promising, development of another type of resistive electrode gaseous detector: micropattern detectors having at least one of their electrodes made of resistive materials. These innovative detectors combine in one design the best features of RPCs (spark protection) and MPGDs (high granularity, high position resolution). These robust detectors will be used for the upgrade of the A Toroidal LHC Apparatus (ATLAS) and Compact Muon Solenoid (CMS) experiments and in some more practical applications, like, for instance, environmental monitoring.

Resistive Gaseous Detectors: Designs, Performance, and Perspectives, First Edition.
Marcello Abbrescia, Vladimir Peskov, and Paulo Fonte.

This book contains nine chapters.

The first chapter describes the principles of operation of gaseous detectors, their main designs, and some limits in their characteristics. One of them is a gain limit, which may lead to discharges. Then, the idea of discharge quenching and localization based on resistive electrodes is introduced; this idea opened up a new direction in detector development. Then a simplified model of spark quenching in RPCs is briefly described.

The second chapter is devoted to the history of gaseous detectors having parallel-plate electrodes. After considering the early designs made with metallic electrodes, and the associated problems related to discharge quenching, the early resistive gaseous detectors, originated from the pioneering works of Babykin and Parkhomchuk, are described. The first RPC prototype, with a 1-mm gap and operating at atmospheric pressure, is discussed. Then the famous Pestov spark counter, which allowed achieving an impressive time resolution around 50 ps, is highlighted. Some other detectors with resistive electrodes are mentioned as well: Iarocci tubes and resistive MWPCs.

In the third chapter, the focus is on the "classical" RPCs with Bakelite electrodes, developed by Santonico and Cardarelli in the early 1980s. Glass RPCs, well suited for low counting rate applications, are also mentioned. We describe their designs, construction features (including the method of treating the Bakelite electrodes' inner surfaces with linseed oil), as well as the physics behind their operation; this includes avalanche and streamer operation modes, detailed explanation of the spark quenching mechanisms, signal development, parameters determining efficiency and time resolution, choice of gases, nature of noise pulses, and dark current.

In Chapter 4 one of the modern designs – double-gap RPC – is introduced, which is a device used in many experiments, including at LHC. Double-gap RPCs operate in signal coincidence mode, allowing to achieve better performance, for instance, in terms of higher detection efficiency and time and spatial resolutions. Then we move on to describing the features of wide-gap RPCs. The main focus, however, is on the RPC multi-gap design, which marked an important breakthrough in this field, and on timing RPCs. We also report about some more advanced descriptions of the behavior of these devices, in particular for what concerns space-charge effects.

Applications of RPCs in high-energy physics experiments are described in Chapter 5. Probably, the most impressive examples are the LHC experiments, for their complexity and area covered. Smaller earlier scale experiments, such as L3 and BaBar at SLAC, are described as well. Timing RPCs used to perform particle identification in the TOF systems at the A Large Ion Collider Experiment (ALICE) and the High Acceptance Di-Electron Spectrometer (HADES) experiment are described. Applications of RPCs in astrophysics are also considered, like the ARGO-YBJ and the Extreme Energy Events projects. The ARGO-YBJ experiment, entirely implemented with RPCs, has been able to perform detailed studies on extensive air showers and on their anisotropy. The Extreme Energy Events (EEE) project has the potential to detect cosmic showers of much higher energy and features an unprecedented total observation area. In addition, it has also an important education component, since its RPC stations are installed

in high schools, where students have the opportunity to participate in the data taking of a real scientific experiment and get the feeling of true scientific research.

Chapter 6 is devoted to two of the most delicate issues in this field: materials and aging. There is a plethora of resistive materials that can, in principle, be used; but just a few of them have actual application. We discuss the reasons and the present understanding of their microscopic behavior. Factors which may affect the stability of operation, such as material resistivity and their degradation with time, counting rate, temperature variations, and relative associated issues, are considered in great detail. Aging was a problem spotted for the first time when these devices were used in large-scale experiments, and was to be solved before the next generation was to be put in place. We discuss the solutions adopted.

High counting rate is the main subject of Chapter 7. As resistive detectors are intrinsically rate limited, this is a factor to be considered for any implementation where some rate performance is required. Further improvements on rate capability are possible using electrodes made of materials with relatively low resistivity (10^8–10^{10} Ω cm). The recent efforts to develop small-gap RPCs having simultaneously high time and position resolutions are described as well. These impressive achievements open new perspectives for innovative RPC applications.

In Chapter 8, a new generation of gaseous detectors with resistive electrodes is introduced. These detectors are manufactured by means of microelectronic technologies capable of producing resistive and metallic patterned electrodes with small gaps between them. The unique feature of these detectors is their excellent spatial resolution, reaching in some designs the unprecedented value of 12 μm. The plans to use resistive MICRO-MEsh GAS chamber (MICROMEGAS) for the LHC upgrade, together with other detectors, are discussed.

Finally, in Chapter 9, applications of RPC beyond high-energy physic and astrophysics experiments are considered. The attempts to implement them in some medical devices, for instance mammographic scanners and positron emission tomography (PET) devices, or for homeland security or environmental protection and in cryogenic time projection chambers (TPCs) are described.

This book summarizes the latest achievement in the field of gaseous detector with resistive electrodes. We hope it will be useful to graduates specializing in high-energy physics, astrophysics, medical physics, and radiation measurements in general; we also hope that it will suitable at different levels, starting from students and postgrads, to PhDs and beyond, researchers, lecturers, professors; finally, to engineers working in various industrial applications, like electronics and homeland security.

1

"Classical" Gaseous Detectors and Their Limits

Resistive gaseous detectors are a family of detectors of charged particles, energetic photons, and neutrons, whose active medium is a gas, and which are characterized by having at least one of the electrodes made of resistive materials, whose resistivity typically ranges in the 10^8–10^{12} Ω cm interval. The main advantage of these devices is that they are intrinsically spark protected, even if at the price of being counting rate limited. To appreciate in practice the importance of this feature, it will be useful to briefly review some main designs of traditional gaseous detectors that existed before the implementation of resistive electrodes, and the principles they operate upon.

1.1 Ionization Chambers

Historically, the first gaseous detector used in experimental measurements at the beginning of the last century was the so-called ionization chamber. This detector, depending on the experimental requirements, can have different geometries: planar, cylindrical, spherical, and so on. However, its principle of operation is independent of its geometry.

The drawings of a planar and a cylindrical ionization chamber are shown schematically in Figure 1.1. Ionization chambers consist of two metallic electrodes: anode and cathode, between which an adequate voltage difference is applied. Such detectors can operate filled with various gases (including air), typically at a pressure around 1 atm. They are still used today, even outside the field of high-energy physics, for instance, in smoke detectors, and in particular mostly for dosimetry applications (see Wikipedia, The Free Encyclopedia, 2017 and references therein, and Chapter 6 of Khan and Gibbon, 2014).

If an intense flux of ionizing radiation (either X-rays, or γ-rays or charged particles, which produce in the gas a certain number of ion-electron pairs) impinges in the region between the electrodes, the resulting current, measured as a function of the applied voltage, will look as schematically shown in Figure 1.2. At low voltages (roughly below 1 kV, depending on the specific geometry and gas used), it will grow until reaching a kind of saturation region – usually called

Resistive Gaseous Detectors: Designs, Performance, and Perspectives, First Edition.
Marcello Abbrescia, Vladimir Peskov, and Paulo Fonte.

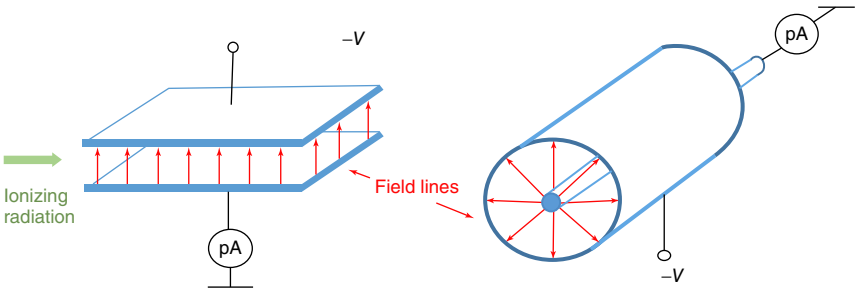

Figure 1.1 Schematic drawings of a planar and a cylindrical ionization chamber; "pA" stands pico-Amperometers, i.e. devices used to measure very small amounts of current.

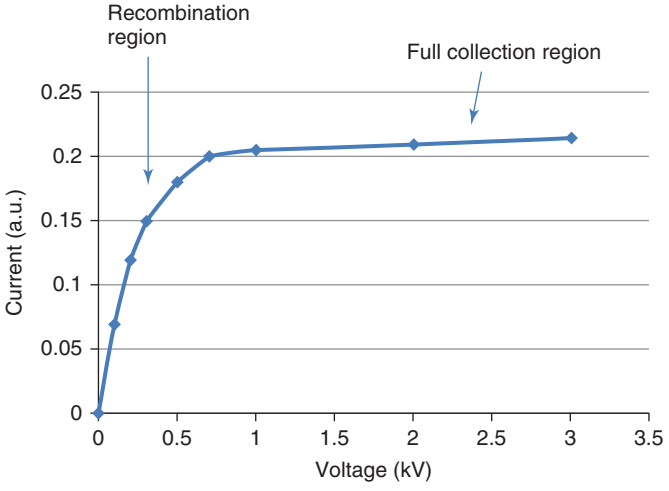

Figure 1.2 Typical current versus applied voltage curve, measured with an ionization chamber, when irradiated by a flux of photons or charged particles.

a "plateau." In this region, practically all primary electron-ion pairs produced by the impinging ionizing radiation are collected on the electrodes. At voltages below the plateau region, some electron-ion pairs recombine, and this is the reason why the collected current is lower than the saturated value.

The value of the current in the plateau region is given by

$$I = k_i \frac{W_{\text{dep}}}{W_{\text{i}}}, \tag{1.1}$$

where k_{i} is a coefficient W_{dep} is the energy deposited by the ionizing radiation inside the volume of the ionization chamber and W_{i} is the mean energy required for the creation of a single electron-ion pair. Note that W_{i} is higher than the ionization potential (typically twice more) because part of the energy deposited by the ionizing particles goes in other energy dissipating channels (excitation of atomic energy levels or excitation of molecular electronic, vibrational and rotational degrees of freedom, for instance) which do not produce ion/electron pairs in the gas.

In the case of X-rays, for instance:

$$W_{\text{dep}} = \int N_{\text{abs}}(\nu) E_{\text{v}} \mathrm{d}\nu \tag{1.2}$$

where $N_{\text{abs}}(\nu)$ is the number of photons with energy E_{v} absorbed in the detector unit volume and ν the frequency of the impinging radiation.

The capability of ionization chambers to detect radiation is determined by the sensitivity of the current meter used to measure the current flowing between the two electrodes; since this, at the beginning of the last century, was relatively low compared to the present standards, this kind of detectors could detect only relatively high intensity radiation, and not single photons or ionizing particles.

1.2 Single-Wire Counters Operated in Avalanche Mode

The first gaseous detector able to record individual photons and elementary particles was the avalanche counter, invented by Rutherford and Geiger (1908). This detector is schematically shown in Figure 1.3. It is a metallic cylinder (with a typical diameter of 2–3 cm) in the center of which a thin metallic wire with diameter

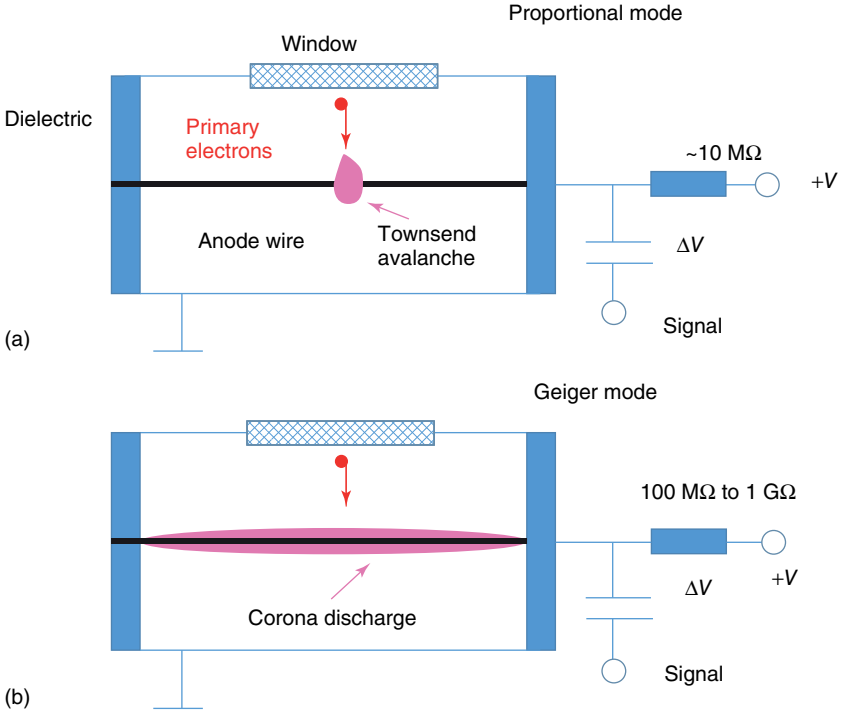

Figure 1.3 Schematic drawings of a single-wire cylindrical counter invented by Geiger and Rutherford in 1908. This detector is usually exploited either in a proportional mode (a) or in a so-called Geiger mode (b).

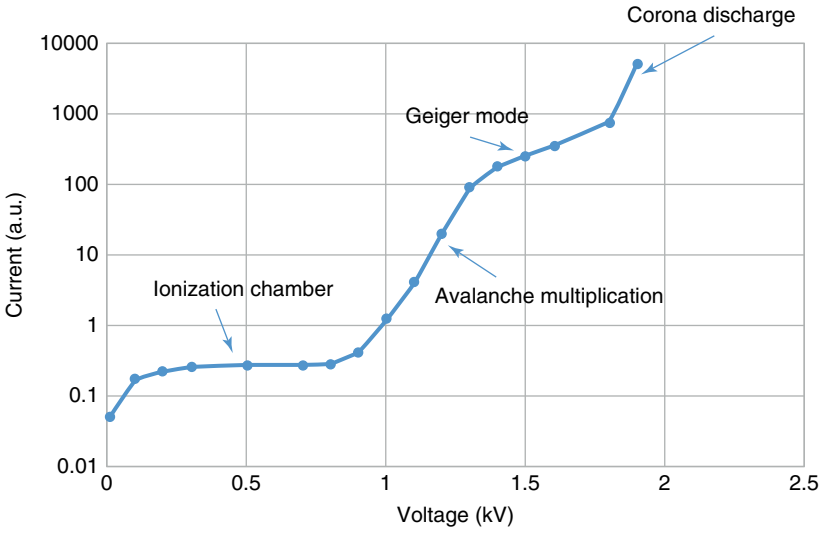

Figure 1.4 Typical voltage–current characteristics for a single-wire counter irradiated by photons or charged particles.

around 0.1 mm or below is stretched. A positive voltage is applied to the central wire while the cylinder is connected to the ground.

The typical voltage–current characteristic curve of this detector, when subject to an intense radiation source, is shown in Figure 1.4. Just like for the previous figure, the values of the voltages and currents are to be intended as order of magnitudes, as they strongly depend on the exact geometry of the detector and on the gas filling it. The figure should only be taken as a general illustration of the expected behavior of a cylindrical counter.

At low applied voltages, this detector operates just like a cylindrical ionization chamber (the relative region is marked as "Ionization chamber" in the figure). However, at sufficiently large voltages, a sharp rise of the current is seen – an indication of the beginning of electron avalanche multiplication.

1.3 Avalanche and Discharge Development in Uniform or Cylindrical Electric Fields

Electron avalanche multiplication in gases was first observed, and then carefully studied, by John Sealy Townsend between 1897 and 1901. This process starts at some critical value of E/n_A (E being the electric field strength and n_A the gas number density, that is, the number of molecules or atoms per cubic meter), which depends on the geometry of the gas-filled space in which this phenomenon takes place. A free electron, drifting in the gas under the influence of the electric field, experiences various types of collisions with the atoms and molecules surrounding it, which can roughly be classified into two categories: elastic and inelastic. During elastic collisions, the electron only changes the direction of its motion,

but it does not lose its kinetic energy. As a result, the electron, after traversing a zone characterized by a potential difference of ΔV, will gain a kinetic energy:

$$E_{\mathrm{k}} = |q_e|\Delta V, \tag{1.3}$$

where q_{e} is the elementary electric charge of the electron.

Inelastic collisions are relevant at elevated electric fields; the electron loses part of its kinetic energy, and this leads either to the excitation of various levels of atoms or molecules (electronic for atoms, rotational, vibrational, and electronic for molecules) or to their ionization. In the latter case, another free electron, additional to the previous, appears in the gas volume (see Figure 1.5).

In the simplest case of electric field E with parallel field lines directed along the x axis, the infinitesimal increase $\mathrm{d}n_{\mathrm{e}}$ of the number of free electrons n_{e} in an avalanche process can be described mathematically as

$$\mathrm{d}n_{\mathrm{e}} = \alpha n_{\mathrm{e}} \mathrm{d}x \tag{1.4}$$

where α is the so-called first Townsend coefficient, expressing the probability for an electron to generate additional ion-electron pairs per unit length, which depends on E; note that gaseous detector usually operate at constant pressure, so here we neglect the dependance on n_A. By integrating Equation (1.4), one obtains that

$$n_{\mathrm{e}} = \exp(\alpha d), \tag{1.5}$$

with d being the distance across which the avalanche develops (eventually limited mechanically by the electrodes, which define the gap width in the case of a detector with parallel plate geometry).

If n_0 primary electrons located at $x = 0$ initiate an avalanche, then the total number n_{e} of created electrons will be proportional to n_0 (every time in a detector, the output signal is proportional to the total number of primary electrons the term

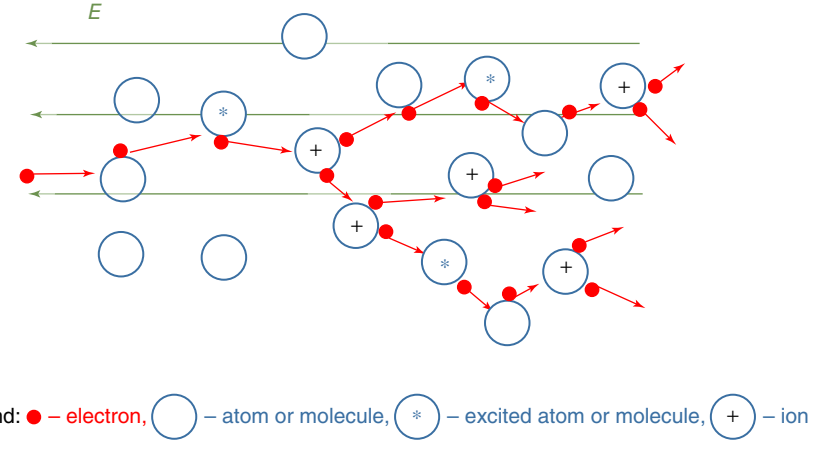

Figure 1.5 Schematics of the Townsend avalanche development in a gas: a free electron (coming from the left) drifting in an electric field intense enough experiences elastic and inelastic collisions with atoms and molecules, resulting in the creation of new free electrons, plus excited or ionized atomic or molecular species.

"proportional counter" is generally used):

$$n_e = n_0 \exp(\alpha d) \tag{1.6}$$

and the value

$$A = \exp(\alpha d) \tag{1.7}$$

is often called the multiplication factor or "gas gain," or simply "gain."

In the case of a nonuniform electric field in the gas, the gain has a more complicated form:

$$A = \exp\left(\int_a^b \alpha\{E(x)\}\mathrm{d}x\right) \tag{1.8}$$

which only in simple cases can be computed analytically and in most cases must be calculated numerically; in this case, a and b represent the coordinates of the initial and final point of the avalanche. For instance, for a single-wire counter, like the one described in Figure 1.3a;

$$A = \exp\left(\int_{r_a}^{r_c} \alpha(r)\mathrm{d}r\right), \tag{1.9}$$

where r_a and r_c are the radius of the anode and the cathode, respectively.

Note that electron drift velocity $v_-(E)$ in an electric field is much larger than the the ion drift velocity v_+, typically by a factor on the order of 1000. As a result, the avalanche consists of two parts: a fast "head" moving toward the anode, created by energetic electrons, and, remaining behind, a conical-shape "body" consisting in positive ions slowly drifting in the opposite direction.

The avalanche structure in the case of the parallel-plate geometry is shown in Figure 1.6 for two essential moments:

1) $t_- = d/v_-$, when the avalanche electrons reach the anode;
2) $t_+ = d/v_+$, when the last positive ions reach the cathode.

For resistive plate chambers (RPCs), which is an important subject of this book described in detail in Chapter 3, the electric fields used are on the order of 50–100 kV/cm, and therefore typical values for t_- are a few nanoseconds and for t_+ a few microseconds.

De-excitation of excited levels of atoms and molecules occurs via various channels. One of the most important among them in practice is ultraviolet (UV) photon emission which, due to the high energy of photons, can cause photoionization of the surrounding atoms and molecules, so that some secondary additional free electrons – called photoelectrons – can be created inside and outside the avalanche volumes (e.g., see Fonte *et al.*, 1991a), as also shown schematically in Figure 1.6a. This is sometimes also called an electron–photon feedback process.

One can introduce an overall probability γ_{ph} per avalanche electron to produce a new photoelectron. The total number n_{pe} of such secondary photoelectrons produced in an avalanche will be then:

$$n_{pe} = A n_0 \gamma_{ph}. \tag{1.10}$$

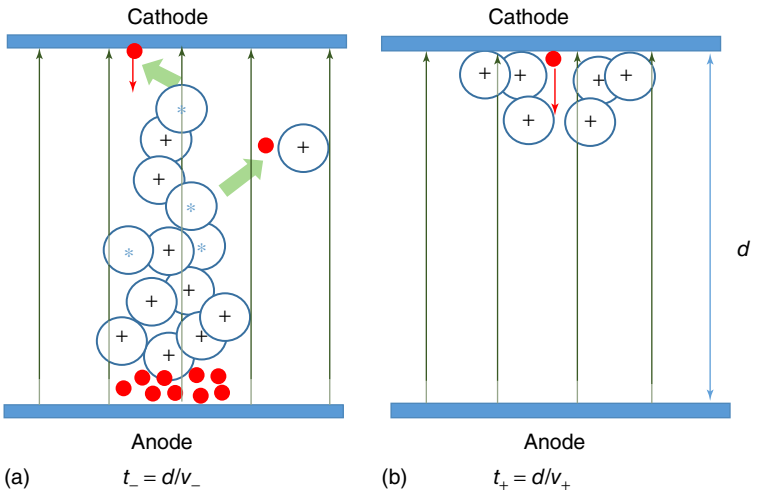

Figure 1.6 Schematic representation of the avalanche structure at two time intervals (a) $t_- = d/v_-$ showing also an electron created by gas self-photoionization; (b) $t_+ = d/v_+$, showing also a possible ion-ejected electron; $t = 0$ corresponds to the time when the avalanche was started by a single electron at the cathode. Small filled circles are electrons, open circles with a "+" sign in the center represent positive ions.

Note that the de-excitation of excited electronic levels leading to UV emission usually occurs quite rapidly, in a time much shorter than t_-.

The photoelectrons, being in a region where the electric field is not zero, may give rise to secondary avalanches as well; let us consider, in particular, the case when all photoelectrons are multiplied by the same gain A earlier defined. This happens in cylindrical wire counters when photoelectrons are created wherever in the gas volume or at the cathode, and in parallel plate chambers when all photoelectrons are created from – or very close – to the cathode. Even in this extreme case, if $A\gamma_{ph} \ll 1$ the photoelectron production process can be neglected, and the avalanche will be well localized in space (as it is represented in Figure 1.6a).

After the collection of all the avalanche electrons on the detector anode (which takes place around time t_-), ions still continue their slow drift and later on at some moment t_+ the last ones will reach the cathode (see Figure 1.6b).

As an ion approaches the cathode surface, it can be neutralized via electron tunneling from the cathode taking one of the electrons inside the conduction band of the material (Mc Daniel, 1964). Indicating with E_i the ion first ionization energy, and with φ the work function of the cathode (i.e., the energy needed to extract an electron from it), if $E_i > \varphi$ an excess in energy $E_{ex} = E_i - \varphi$ will result (see Figure 1.7). This can be transferred to another electron inside the cathode and, in the case of $E_{ex} > \varphi$ the electron can escape from it.

Overall, if the condition

$$E_i > 2\varphi \tag{1.11}$$

is met, a free electron can be emitted from the cathode as a result of ion recombination; the relative probability is indicated with γ_+ and it is sometimes called

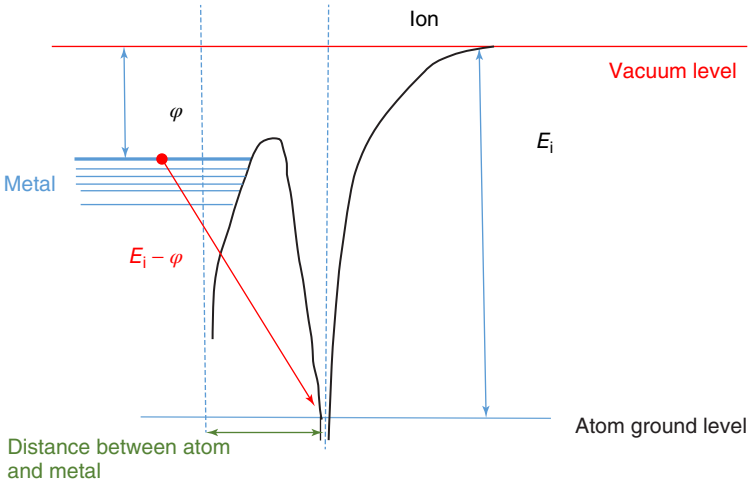

Figure 1.7 Schematic representation of the energy levels and tunneling effect of an ion approaching the metal electrode.

"second Townsend coefficient" (Davies and Evans, 1973). This electron emission initiates ion feedback.

In single-wire counters, when both $A\gamma_{ph}$ and $A\gamma_{+}$ are much less than unity, the amplitude S_d of the signals from the detector will be proportional to the primary ionization:

$$S_d = kAn_0, \tag{1.12}$$

where k is a proportionality coefficient depending on the actual induction process and electronics characteristics. The voltage interval where this behavior holds (between the "ionization chamber" region and the knee in "avalanche multiplication") is called the proportional region (see Figure 1.4).

In parallel plate chambers, as will be seen in detail in Chapter 3, even if this conditions is met, there is often no proportionality between the primary ionization and the output signal, since in this case the gain A depends strongly on the position inside the gas volume where the ion-electron pairs are created. For other detectors, like mesh detectors (for instance MICROMEGAS) which is described later on in this book, Equation (1.12) is still valid, provided that the drift volume and the amplification volume are separated.

The development of avalanches depends on their size. When this is sufficiently small, it can be safely assumed that the local electric field is almost entirely due to the external electric field (which, for instance, depends on electrode configuration, and applied voltage). However, it must be noted that the electric field inside an avalanche, generated by the spatial separation between the "head," negatively charged, and the "body" of the avalanche, positively charged, is opposite in direction with respect to the external field. For sufficiently large avalanches, this "space charge field" – as it is usually called – cannot be neglected anymore, and affects avalanche development. The appearance of space-charge effects is signaled in Figure 1.4 by the fact that the gas gain curve begins deviating from the

straight line (in a logarithmic scale). In single-wire counters, this is usually taken as the end of the proportional region.

Space-charge effects, briefly mentioned here, play a very important role in the operation of some resistive detectors; in particular, when a parallel-plate configuration with quite thin (order of a few hundred micrometers) gaps are used. This is discussed in detail later on, in particular in Chapter 4.

Increasing the applied voltage beyond the proportional region, in the interval labeled as "Geiger mode" in Figure 1.4, the amplitude of all pulses from the detector becomes almost equal to each other, independent of the primary ionization n_0.

Depending on the gas, in this region, or with another further gain increase, if either $A\gamma_{\mathrm{ph}}$ or $A\gamma_{+}$ starts approaching unity, secondary processes strongly affect the detector operation: each primary electron is accompanied by one or even more secondary avalanches called "successors." Finally, at $A\gamma_{\mathrm{ph}} = 1$ or $A\gamma_{+} = 1$ (whichever condition comes first), a continuous discharge appears (in the region marked in Figure 1.4 as "corona discharge").

Strictly speaking, Geiger mode is just an unstable corona discharge (Nappi and Peskov, 2013), so there is not a clear distinction between the two operation modes. In early designs, large resistors, 100 MΩ or larger, were always used in the electric circuits of single-wire counters, connected in series with the high-voltage power supply (as shown in Figure 1.3b). A corona current (which is typically a few microamperes) causes a significant voltage drop ΔV, of even a few hundred volts, on such resistors, consequently reducing the voltage across the detector and temporarily lowering the electric field in the gas; this, as a consequence, leads to the interruption of the corona discharge. In this counter, the output signal is taken measuring the voltage across the quenching resistor; therefore, a voltage drop ΔV of the magnitude mentioned would indicate the passage of an ionizing particle. At the beginning of the last century, when electronics was still at an initial stage of development, wire counters operating in Geiger mode offered the possibility of recording single charged particles or photons in a very simple way, without using amplifiers. This feature determined the tremendous success of the Geiger counters at that time.

It is interesting to note that although single-wire counters were not resistive detectors in the sense used in this book (where detectors in which resistive elements are embedded in their structure are mainly treated), they were the first in which the principle of discharge quenching with the help of resistive elements (the resistor put in series with the power supply) was implemented. As will be shown subsequently, the principle exploited in modern resistive detectors has many similarities with it.

Note also that later on it was discovered (Trost, 1937) that in some gas mixtures another mode of operation appears, in which the discharge is quenched not by the external resistor, but by intrinsic mechanisms, one of them being the strong space charge created by the corona discharge around the anode wire (see Nappi and Peskov, 2013 for more details).

Until the 1950s, Geiger and proportional counters were practically the only electronic detectors of elementary particles. When parallel-plate devices were also introduced, the details of avalanche development and feedback processes

were carefully studied in many gases and gas mixtures, both for cylindrical and parallel-plate geometry. Various methods were used, including the visualization of these phenomena with the help of Wilson cameras, which revealed many important peculiarities (see, for instance, Raether, 1964 and references therein).

It was observed that at low gas gains, the avalanche dynamic is quite similar for both cylindrical and parallel-plate geometries; however, at high gas gains, differences appear. In particular, in the case of the parallel-plate geometry, one of the two following modes of operation occurs (for more details, see Fonte *et al.*, 1991b):

1) A "fast" breakdown or
2) A "slow" breakdown.

1.3.1 Fast Breakdown

In most of the cases, at some critical total charge in the avalanche, a transition from primary avalanches to sparks was observed. Scrupulous studies, performed by Raether (e.g., see Raether, 1964) showed that for parallel-plate detectors this happens when

$$An_0 \gtrsim 10^8 \text{ electrons} \tag{1.13}$$

In this condition, often called the "Raether limit," the electric field generated close to the "head" of the avalanche by the space charge becomes comparable with the external applied field. Consequently, the field lines in the vicinity of the avalanche are bent toward the positive "body" of the avalanche, made primarily of ions (see Figure 1.8a). Due to this focusing effect, with a consequent increase of the field strength in this region, secondary avalanches initiated close to the volume of the primary avalanche start drifting toward the "body" while they are strongly multiplicated because of the enhanced electric field nearby. The ionic column thus grows quite rapidly toward the cathode, leading to the formation of

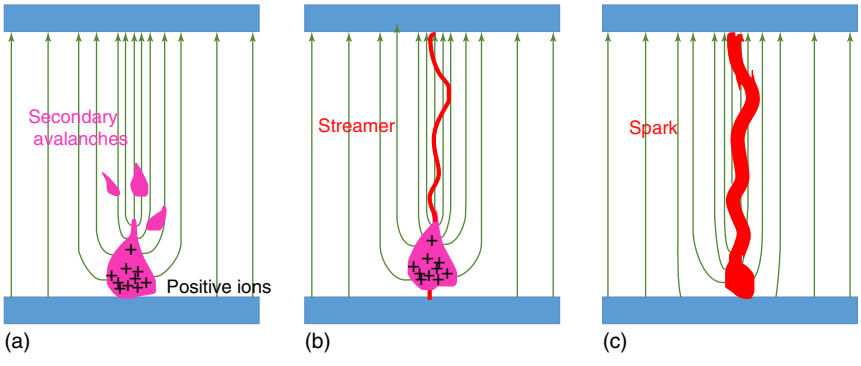

Figure 1.8 Three stages of spark development, when the total charge in the avalanche reaches the Raether limit: (a) field lines close to the avalanche experience a focusing effect and some secondary avalanches start moving toward the positive ions "body"; (b) a thin plasma filament – a streamer (or Kanal) – is formed; (c) when the streamer reaches the electrodes, a spark happens through the channel opened in this way.

a thin plasma channel, called streamer (or Kanal, or, sometimes, Kanal mechanism), schematically shown in Figure 1.8b. When the streamer touches the cathode, a powerful spark happens via this conductive channel (Figure 1.8c).

This process is called fast breakdown. Eventually, if no quenching mechanisms are in place, the spark will fully discharge the detector anode–cathode capacitance.

Note that if the voltage between the electrodes is further increased, the streamer may propagate not only to the cathode but to the anode as well; hence, the distinction of "cathode streamer" and "anode streamer."

It has been pointed out that photoelectrons produced via the mechanisms briefly outlined earlier in this chapter, play an important role in streamer development, and actually this is the common explanation for the streamer propagation mechanism (Raether, 1964). Nevertheless, this has been criticized (e.g., Kunhardt, 1980), on the grounds of whether the quantity and range of the relevant photons is adequate to sustain the streamer. Recent calculations (Capeillère *et al.*, 2008) have further clarified that for the mechanism to be effective the photon range must lie within some boundaries, which is hardly a good explanatory basis for an almost universal phenomenon in gases. A possible, more robust, explanation is that diffusion – a truly universal phenomenon – may be enough to populate the high-gain regions of the streamer (Ebert *et al.*, 1997). Vacuum ultraviolet (VUV in the following) and visible photons reaching the cathode can also create electrons via the photoelectric effect.

When the electric field is not uniform, in particular in the case of thick central wire detectors, where the field lines are radial in shape, an interesting phenomenon may happen. In this case, the streamer appears in the strong electric field close to the anode, and starts moving toward the cathode. However, when reaching a region of weak electric field far from the central wire, where multiplication processes are not so effective, it may suddenly stop propagating and decays without reaching the cathode (see Figure 1.9). This creates a fast, large-amplitude pulse current in the output readout circuit, but not a spark discharge (since there is no a conductive bridge between the cathode and the anode). This phenomenon is called "limited streamer mode" and this type of streamer is often called a "self-quenched streamer" (SQS). It typically appears

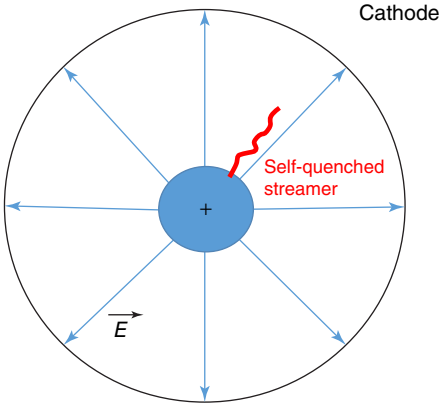

Figure 1.9 Schematic representation of a self-quenched streamer appearing in wire detectors having a certain ratio r_a/r_c.

in wire-type detectors characterized by a large ratio r_a/r_c. More details could be found in (Razin, 2001).

1.3.2 Slow Breakdown

Another type of breakdown, often called a "slow breakdown" (called so because it develops in a timescale of microseconds or even longer), also seldom appears in parallel-plate detectors, for example, when filled with very clean noble gases or when they are constructed with photocathodes having a high UV and visible photon sensitivity. In these cases, both γ_{ph} and γ_+ have exceptionally high values; therefore, the conditions $A\gamma_{ph} = 1$ or $A\gamma_+ = 1$ may be satisfied before the condition (1.13) $An_0 \gtrsim 10^8$. The slow breakdown develops via the generation of several or, sometimes, even up to dozens, secondary processes (Raether, 1964). Similarly to Geiger discharges, the region where the secondary avalanches appear rapidly expands in space; however, the final stage of this development strongly depends on the gas composition, pressure, and the detector geometry. In most of the cases, it also leads to a spark, however in some occasions could also be considered a kind of glow discharge.

1.4 Pulsed Spark and Streamer Detectors

There were early attempts to record radiation, also at the single particle level, with parallel-plate counters (e.g., see Keuffel, 1948); however, when using a constant applied voltage, their behavior was sometimes very unstable.

There were three main reasons for that:

1) If for some reason (e.g., due to the appearance of alpha particles, neutrons, or a cosmic shower) a large number of primary electrons was released in their volume, then the condition (1.13) $An_0 \gtrsim 10^8$ is verified, causing a spark breakdown.
2) Another problem was "after-pulses": a series of pulses following the primary avalanche, sometimes continuing for a long period of time.
3) Moreover, undesirable sparks often appeared due to the imperfection of electrode manufacturing: not well-rounded edges, micro-points or microinsertions (dust, etc) on the electrode surfaces.

A much more stable operation was achieved not using a constant applied high voltage, but using a pulsed (or triggered) mode of operation.

In this case, a relatively "low" constant voltage (on the order of a few kilovolts) was applied continuously to a parallel-plate detector, surrounded either by a scintillator-based triggering device (see Figure 1.10) or by an array of Geiger counters. When a charged particle crossed the scintillators (or Geiger counters) and, consequently the parallel-plate detector therein, a trigger signal was generated by the scintillators (or Geiger counters).

Using some kind of electronics, at this moment a short (on the order of microseconds) high-voltage pulse with an amplitude typically above HV = 10 kV (the exact value depending on the particular design and gas composition) was

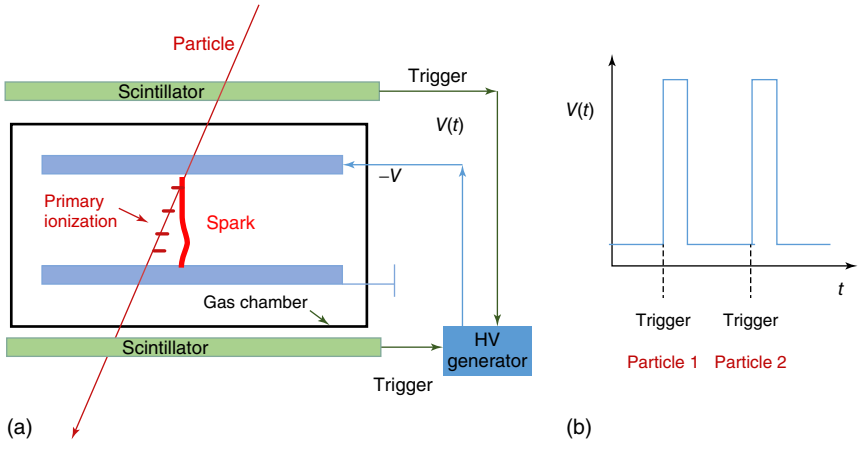

Figure 1.10 Simplified drawing of a spark counter, surrounded by scintillators and operating in a pulse mode.

applied to the electrodes of the parallel-plate detector. In this high electric field, the primary electrons created by the passing particle (and already kept apart from ions due to the low constant electric field) initiate Townsend avalanches which then rapidly transit to a spark. The position of the spark was recorded by photographic methods. To visualize the particle track, a stack of such parallel-plate detectors was used.

The low voltage between the pulsed HV was necessary to "clean up" the gap from undesirable ions appearing there for any reason: electron emission from electrodes, cosmic rays, natural radioactivity, residual ions from the previous sparks, and so on.

Until the 1970s, spark counters were one of the main detectors of charged particles, which allowed visualizing particle trajectories, and they successfully competed with emulsion films and cloud and bubble chambers.

In particular, the advantage of spark counters with respect to its competitors was their unprecedented fast response time (on the order of nanoseconds), which was quite important in high-energy and astrophysics experiments. However, due to their peculiar operation mode, spark counters had also serious drawbacks: relatively low operational rates, limited by the dead time (inactive in between HV pulses), which is typically about 0.01 s (e.g., see Gajon and Lksin, 1963); long readout time, on the order of milliseconds, imposed by the photographic or film readout techniques, so the data was only available offline; problems in recording several events happening at the same time; rather complicated designs.

A remarkable modification of the spark counter was the so-called streamer chamber. In these detectors, the duration of the HV pulse was only a few nanoseconds – which was remarkable at the time – and the (single) gap was relatively wide, on the order of centimeters. During this extremely short time interval, streamers started developing near the primary electrons created by the particle but remained too small in length to trigger sparks, producing at the same time sufficient light to make visible in three dimensions (3D) the trajectories of

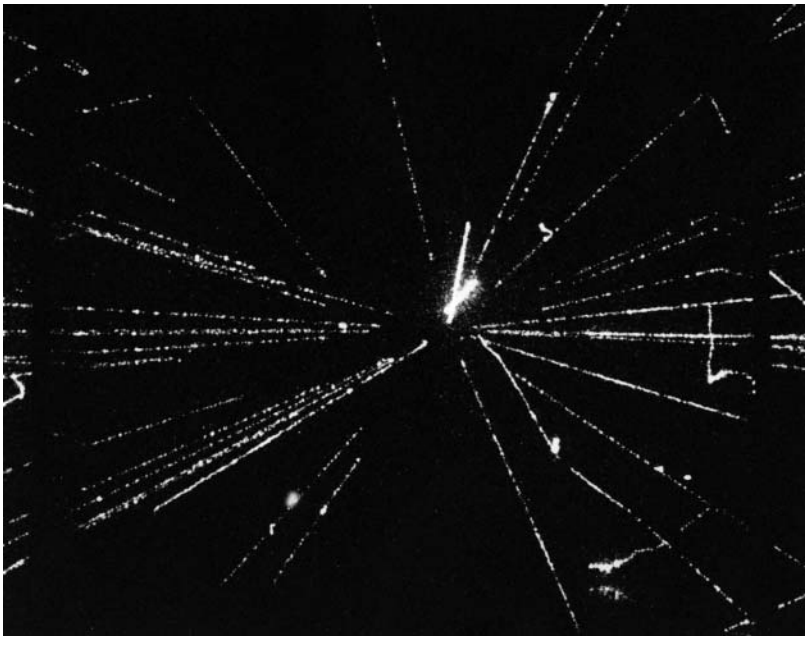

Figure 1.11 A proton–antiproton collision recorded using a streamer chamber at the UA5 experiment at CERN. (https://commons.wikimedia.org/wiki/File:CERN_UA5_-_ppbar_interaction_at_540GeV.jpg. Licenced under CC BY 3.0.)

the particles impinging on the device. A nice picture obtained with a streamer chamber is shown in Figure 1.11. Although these devices were able to detect multiple tracks, they remained too slow, due to the long "dead" time between pulses and the photographic readout technique used.

1.5 Multiwire Proportional Chambers

In 1968 G. Charpak invented a new avalanche gaseous detector, which he called the multiwire proportional chamber (MWPC) (Charpak *et al*., 1968). In contrast to spark and streamer chambers, it was a continuously operating device, thus self-triggering, with a fast electronic readout allowing to record events even at a high rate (even up to 10^5 Hz/wire), including multiple tracks. This detector is represented schematically in Figure 1.12a,b.

The first version of the MWPC (see Figure 1.12a) consisted of two parallel cathode planes with an array of thin parallel anode wires stretched in between, usually in the middle. Typically, the anode pitch, depending on the particular design, was in the 3–6 mm range, while the anode–cathode gap was around 5–8 mm. The charged particles crossing the MWPC would produce primary electrons in the gas volume, which will drift toward the anode wires. As they approach the anode at a distance typically around a few anode radius, where the electric field is more intense, the primary electrons give rise to Townsend avalanches developing close to the wires. The avalanches induce negative electronic signals on

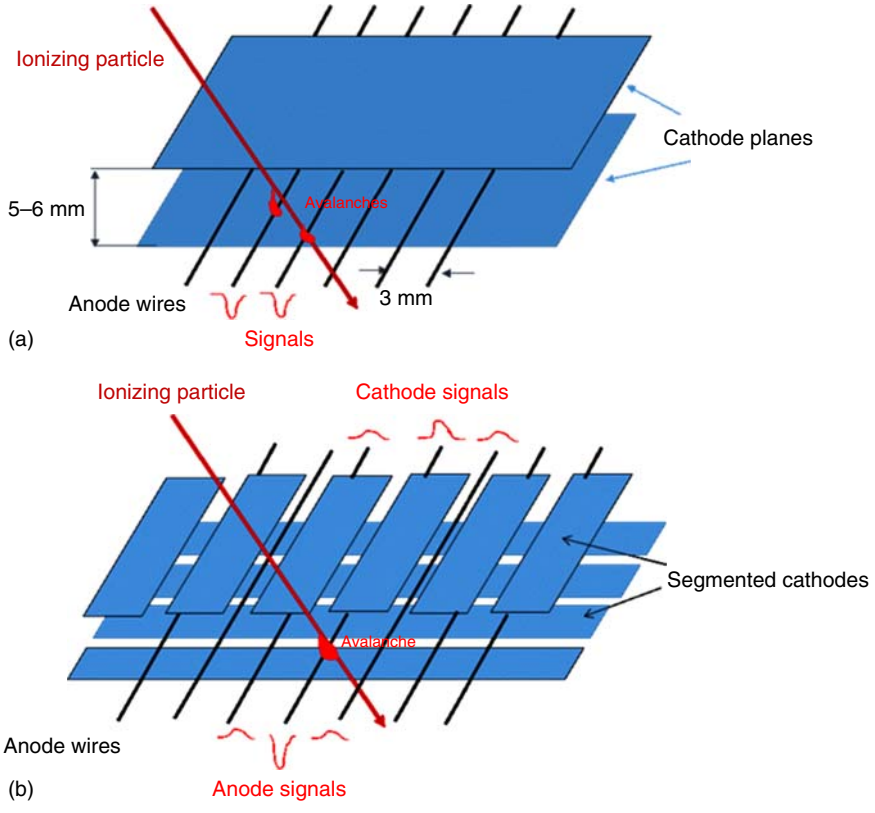

Figure 1.12 Schematics of a MWPC: (a) the first version of an MWPC with unsegmented cathode plane and (b) modern design of a bi-dimensionally sensitive MWPC, with cathodes segmented for isolation from each other's parts (strips, wires, etc.).

the anodic wires, where electrons are collected, and positive signals on the surrounding electrodes. Overall, this process is very similar to the one happening in single-wire counters, and in fact an MWPC can be considered as an array of single-wire counters, which share the gas volume and the cathode electrodes.

Originally, this detector could provide the coordinates of an impinging particle in one direction only: in fact, the signals were read out from the anode wires and one could just measure which wire was interested by the avalanche process. As a consequence, only the position of the avalanche in the direction perpendicular to the wires (and parallel to the cathodes) could be measured.

Later on, the signals induced on the other electrodes also started to be exploited, allowing to determine the position of the avalanches in two dimensions. One way of implementing this approach was to use cathodes segmented in strips, as shown in Figure 1.12b, and connecting each cathodic strip to its own readout circuit. Positive avalanche ions drifting toward the cathode induce signals on the closest strips and from the profile of the induced charges one can determine the avalanche position with an accuracy of about a few hundreds

micrometers (down to 14 μm in special cases Fischer *et al*., 1986), which is comparable to the earlier spark and streamer detectors.

Another advantage of MWPCs is that, in contrast to the spark and streamer chambers, they operate in proportional mode, and the output signal is proportional to the primary ionization n_0. Sparks rarely happen in well-designed MWPCs, but they may arise mainly due to construction defects such as sharp metallic edges, unprotected wire tips, dielectric insertions on the cathode or anodic wires, and so on. Various technical solutions were devised to protect the front-end electronics in the case of occasional sparks. For example, in the *R*ing *I*maging *CH*erenkov (RICH) detector of the ALICE (a large ion collider experiment) experiment at CERN (ALICE Collaboration, 2000), all anodic wires are connected to the HV supply via 10–100 MΩ resistors, whereas the signals are taken from the segmented cathode plane. In the event of undesirable sparks, the resistors will limit the discharge current just like it was done in the first Geiger counters (Figure 1.3).

In some particular gas mixtures and depending on particular conditions, it is possible to operate MWPCs in the Geiger or SQS modes (see, for example Peskov, 1979), and this has found some practical use (Bałanda *et al*., 2004).

Thanks to their excellent characteristics, MWPCs and their descendants (drift chambers, time projection chambers, etc.) rapidly replaced spark and streamer counters, as well as cloud and bubble chambers, in most high-energy physics experiments. Moreover, MWPCs filled with photosensitive vapors (Seguinot and Ypsilantis, 1977; Bogomolov *et al*., 1978) played a very important role in the development of RICH detectors (Seguinot and Ypsilantis, 1994). However, despite their tremendous success, MWPCs suffered from an essential drawback: a limited time resolution, on the order of microseconds. This derives from the fact that primary electrons can be released essentially anywhere in the detector volume and have to drift to the nearest anode wire, producing an avalanche there. The drift time is quite variable and the time jitter is almost equal to the maximum drift time.

1.6 A New Idea for Discharge Quenching and Localization

As the technology in particle physics detectors progressed, new high energy physics experiments demanded not only high spatial resolution and fast electronic readout but also better timing characteristics. An interest in parallel-plate geometry detectors, offering a minimal jitter and thus excellent timing, appeared again after the invention of the so-called continuous operation spark counters (Babykin *et al*., 1956; Parkhomchuk *et al*., 1971). A very practical and successful implementation of these concepts, later on, brought about the birth of the RPCs in the 1980s (Santonico and Cardarelli, 1981).

A simplified drawing of this innovative device, which is described in more detail in Chapter 3, is shown in Figure 1.13. At a first glance it resembles very much a spark counter, but with a fundamental difference: its electrodes are not made

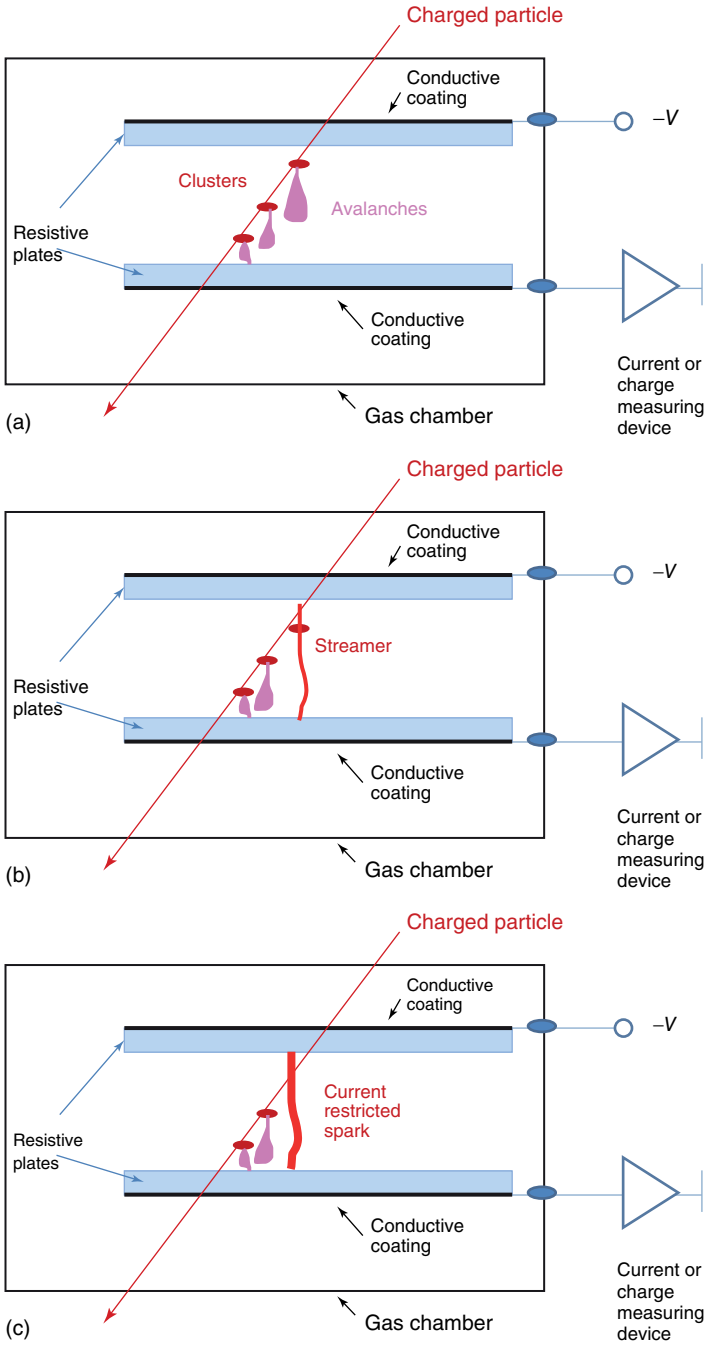

Figure 1.13 Schematic drawing of an RPC illustrating its design and operation principle: (a) creation of avalanches by primary electrons produced by ionizing charged particles crossing the detector; (b) if the total charge in the avalanche reaches the Raether limit, the avalanche transforms to a streamer; (c) when the streamer reaches the resistive electrodes, it causes a local discharge; nevertheless, the released energy in the spark is strongly limited by the resistance of the plates.

of metal, but of materials with a relatively high electrical resistivity, typically in the 10^{10}–10^{12} Ω cm range, made with 1–2 mm Bakelite or glass plates. The outer surfaces of these electrodes are coated with a conductive or semiconductive layer to allow a reliable connection with an external applied constant high voltage.

In the gap between the plates, filled with a suitable gas, a uniform electric field is generated by the HV connected to the electrode plates and, if the field is strong enough, the primary electrons produced by impinging ionizing particles give rise to Townsend avalanches. The first stage of avalanche development, before reaching the electrodes, is quite the same as in classical spark counters, and if the total charge in the avalanche approaches or overcomes the Rather limit, the avalanche transforms to a streamer. However, when the streamer touches the resistive electrodes, a quite new phenomenon takes place.

In contrast to metals, the resistive cathode plate is unable to feed the streamer with a high current density since, generally, high resistivity materials are not efficient electron emitters. Moreover, the anode plate is not an ideal dielectric, but rather a high resistivity layer, which, under the applied high voltage, becomes positively charged. Therefore , when an avalanche or a streamer reaches the anode surface, this gets locally discharged (see Figure 1.14). This causes a local reduction in the electric field intensity, drastically reducing the charge supporting processes.

Both phenomena contribute to the restriction of the discharge current, even if most probably the local partial discharging effect is dominant. This was clearly demonstrated with an RPC, whose cathode was metallic and whose anode resistive: the power dissipated in the discharge in this case was almost the same as in an RPC having both electrodes made of resistive material (T. Francke, private communication).

The role of the partial discharging effect, and the role of the resistive electrodes, can be better understood from Figure 1.15, which shows a simplified circuit model of an RPC. From a semi-quantitative point of view, an RPC has

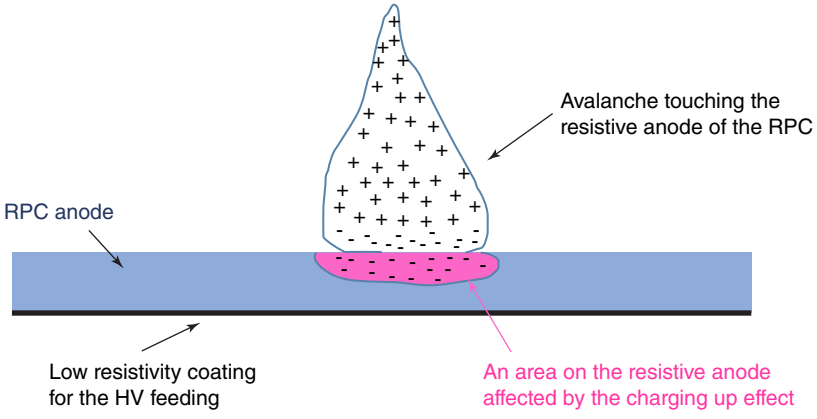

Figure 1.14 Schematic representation of the avalanche and the local partial anode discharging at the moment when the avalanche touches the dielectric anode.

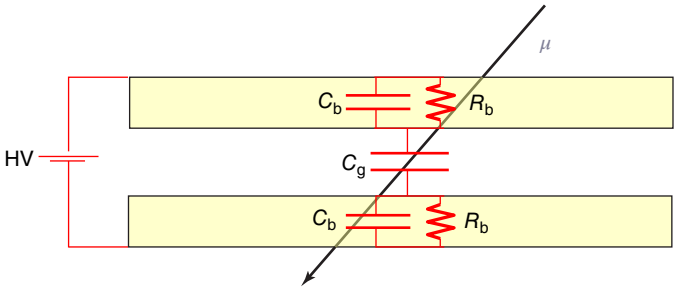

Figure 1.15 Simplified circuit for an RPC with resistive electrodes. C_b and C_g represent the capacitance of each electrode plate and of the gas gap, respectively; R_b represents the resistance of the electrode plates.

the structure of a capacitor, with two layers of dielectric material at its interior; moreover, the electrodes are made by resistive material, and this fact is taken into account considering their resistance R_b as shown in Figure 1.15. Basically, two situations can happen:

1) The gas is not ionized. In this "static" situation, the applied voltage HV is correspondingly transferred to the gas gap, and no current is flowing through the circuit.
2) The gas is crossed by an ionizing particle. In this case, the related discharge can be modeled as a current generator, which discharges the capacitor C_g (associated to the gas gap) in such a way that the voltage initially applied to the gas is transferred to the resistive electrodes (described by the capacity C_b and, as already pointed out, by the resistance R_b). The system comes back to the initial configuration following an exponential law, with a characteristic time constant τ given by

$$\tau = 2R_b\left(\frac{C_b}{2} + C_g\right) = 2\rho_b\frac{d}{S}\left(\frac{1}{2}\varepsilon_0\varepsilon_r\frac{S}{d} + \varepsilon_0\frac{S}{g}\right) = \rho_b\varepsilon_0\left(\varepsilon_r + 2\frac{d}{g}\right) \tag{1.14}$$

where ε_r is the relative dielectric constant of the electrode material, ρ_b its resistivity, ε_0 is the dielectric constant of the vacuum, g is the gas gap thickness, d is the thickness of the electrodes, and S is the electrode surface considered. Note that τ does not depend on the dimension S of the zone considered on the electrode. The spark quenching effect is stronger when C_b is small, so the thickness of the anode plate and its dielectric constant play an important role.

Equation (1.14) gives, for a value $\rho_b = 10^{11}$ Ω cm, a time constant τ around 10 ms, which has to be compared to the typical avalanche or discharge durations which are on the order of 10 ns $\ll \tau$. In this time interval, the electrodes behave as perfect dielectric materials; in other words, they are perfect insulators, and therefore the voltage across the gas gap is very low and the discharge inside the gas cannot be sustained. This is the auto quenching mechanism at the base of the operation of this detector. For the typical resistivities used in RPCs (see preceding text), the discharge current is reduced by orders of magnitudes when compared to spark counters with metallic electrodes.

In contrast to classical spark counters, where after the discharge the voltage drops in the entire gap, RPCs remain sensitive to incoming particles on the whole area unaffected by the local partial discharge effect (and the sensitivity drops only in the region of the given avalanche/streamer). This is why in early days this detector was often referred to as a continuously operating spark counter. After a time span a few times τ, the voltage on this small area is restored and the detector becomes again efficient in this area. Of course, the presence of resistive materials imposes some counting rate limitation owing to voltage drops across these.

In this simplified model of the RPC operation, the current leaks along the electrode surfaces as well as the influence of spacers, used to keep the electrode parallel, were not taken into account. These effects are considered later on in this book.

Summarizing, the unique features of RPCs are as follows:

1) It is a continuously operating detector (no need of pulsed HV for discharge quenching).
2) It has imaging capability, thanks also to its good spatial resolution (in some state-of-the-art designs 30–50 μm).
3) It has multi-hit capability, meaning that it can detect many events, even simultaneously.
4) It has a superior time resolution (in the most sophisticated configurations often below 50 ps);
5) Discharges in RPCs have limited energy and thus are not harmful – they do not destroy either the detector or the front-end electronics;
6) The size of the region affected by the charging up effect is relatively small, so the rest of the chamber remains active;
7) RPCs can be electronically read out, and this has many advantages compared to the optical recording, for example, in speed and image processing;
8) RPCs are relatively easy to build and they are suitable to cover large sensitive areas, in some experiments even up to thousands of square meters.

Later on in this book, we describe in more detail various RPC designs, the physics behind their operation, as well as the fast growing application of these devices.

References

ALICE Collaboration (2000) Time of Flight System. Technical Design Report, CERN/LHCC 2000-12, CERN, Geneva, Switzerland.

Babykin, M.V. *et al*. (1956) Plane-parallel spark counters for the measurement of small times; resolving time of spark counters. *Sov. J. At. Energy*, **4**, 627.

Bałanda, A. *et al*. (2004) The HADES pre-shower detector. *Nucl. Instrum. Methods Phys. Res., Sect. A*, **531**, 445–458.

Bogomolov, G. *et al*. (1978) Multiwire gas counters for coordinate measurements in the VUV region. *Instrum. Exp. Dent. Tech.*, **21**, 778–782.

Capeillère, J. *et al*. (2008) The finite volume method solution of the radiative transfer equation for photon transport in non-thermal gas discharges: application to the

calculation of photoionization in streamer discharges. *J. Phys. D: Appl. Phys.*, **41**, 234018, 13 pp.
Charpak, G. *et al*. (1968) The use of multiwire proportional counters to select and localize charged particles. *Nucl. Instrum. Methods*, **62**, 262.
Davies, A.J. and Evans, C.J. (1973) The Theory of Ionization Growth in Gases Under Pulsed and Static Conditions. CERN Yellow Report 73-10, CERN, Geneva, Switzerland.
Ebert, U., van Saarloos, W., and Caroli, C. (1997) Propagation and structure of planar streamer fronts. *Phys. Rev. E*, **55** (2), 1530–1549.
Fischer, J., Radeka, V., and Smith, G.C. (1986) X-ray position detection in the region of 6 μm RMS with wire proportional chambers. *Nucl. Instrum. Methods Phys. Res., Sect. A*, **252**, 239–245.
Fonte, P. *et al*. (1991a) VUV emission and breakdown in parallel-plate chambers. *Nucl. Instrum Methods Phys. Res., Sect. A*, **310**, 140–145.
Fonte, P. *et al*. (1991b) Feedback and breakdown in parallel-plate chambers. *Nucl. Instrum Methods Phys. Res., Sect. A*, **305**, 91–110.
Gajon, M.I. and Lksin, G.A. (1963) Spark detectors for charged particles. *Sov. Phys. Usp.*, **6**, 428.
Keuffel, J. (1948) Parallel-plate counters and the measurement of very small time intervals. *Phys. Rev.*, **73**, 531.
Khan, F.M. and Gibbon, J.P. (2014) *Khan's the Physics of Radiation Therapy*, Lippincott Williams & Wilkins/Wolters Kluwer.
Kunhardt, E.E. (1980) Electrical breakdown of gases: the prebreakdown stage. *IEEE Trans. Plasma Sci.*, **PS-8** (3), 130–138.
Mc Daniel, E.W. (1964) *Collision Phenomena in Ionized Gases*, John Wiley & Sons, Inc., New York.
Nappi, E. and Peskov, V. (2013) *Imaging Gaseous Detectors and their Applications*, Wiley-VCH Verlag GmbH & Co. KGaA.
Parkhomchuk, V.V. *et al*. (1971) A spark counter with large area. *Nucl. Instrum. Methods*, **93**, 269.
Peskov, V. (1979) Geiger counters of VUV and x-ray radiation with the spatial resolution of 0.3 mm. *Instruments and Experimental Techniques*, **22**, 1395–1400.
Raether, H. (1964) *Electron Avalanches and Breakdown in Gases*, Butterworths, London.
Razin, V.I. (2001) Self-quenched streamer operating mode of gas-discharge detectors (Review). *Instrum. Exp. Tech.*, **44** (4), 425–443.
Rutherford, E. and Geiger, H. (1908) An electrical method of counting the number of α particles from radioactive substances. *Proc. R. Soc. London, Ser. A*, **81** (546), 141–161.
Santonico, R. and Cardarelli, R. (1981) Development of resistive plate counters. *Nucl. Instrum. Methods Phys. Res.*, **187**, 377.
Seguinot, J. and Ypsilantis, T. (1977) Photo-ionization and Cherenkov ring imaging. *Nucl. Instrum. Methods*, **142**, 377–391.
Seguinot, J. and Ypsilantis, T. (1994) A historical survey of ring imaging counters. *Nucl. Instrum. Methods Phys. Res., Sect. A*, **343**, 1–29.
Trost, A. (1937) Über Zählrohre mit Dampfzusatz. *Z. Phys.*, **105**, 399.
Wikipedia, The Free Encyclopedia (2017) Ionization Chamber, https://en.wikipedia.org/wiki/Ionization_chamber (accessed 28 October 2017).

2

Historical Developments Leading to Modern Resistive Gaseous Detectors

2.1 Introduction: the Importance of the Parallel-Plate Geometry

As outlined in the previous chapter, the first gaseous detectors were based on a cylindrical geometry: the primary electrons created by the crossing ionizing particle were collected at a central wire and the avalanche processes occurred in the region immediately surrounding it. It has to be stressed again that this family of devices, whose original conception dates back to the beginning of 1900, is still extremely successful, and even used nowadays: at the Large Hadron Collider experiments – probably the most complex and advanced experiments for particle physics in operation – gaseous detectors based on a cylindrical geometry are still extensively used.

Even if in the previous chapter the two geometries, cylindrical and parallel plate, have been treated at the same level, from the historical point of view, detectors with a planar geometry were developed relatively late with respect to cylindrical ones. The need for developing gaseous detectors with a time resolution better than the one provided, for instance, by the Geiger–Muller detector (the prototype of central wire detectors) or the ones derived from it, was determinant to drive the introduction of planar detectors.

The first detectors of this kind were developed in the 1940s, and we review some of the various technological instances of this concept later on in this chapter, together with the further developments that lead to the devices used nowadays.

To understand why parallel-plate detectors could, in principle, provide a time resolution much better than the one characteristic of cylindrical devices, let us consider again and in more details the fact that the main difference between a central wire detector and one based on a planar geometry is that in the former the electric field decreases inversely with the distance from the central wire, while in the latter it is uniform. Since electron avalanche processes need the electric field to be intense enough (more than a few kilovolts per centimeter, intending this value as an order of magnitude, depending, for instance, on the gas mixture used), the consequence is that multiplication phenomena in a central wire gaseous detector can take place only at very small distances from the wire, where the electric field strength is above the multiplication threshold (see Figure 2.1). In a parallel-plate detector, in principle, the whole volume can

Resistive Gaseous Detectors: Designs, Performance, and Perspectives, First Edition.
Marcello Abbrescia, Vladimir Peskov, and Paulo Fonte.

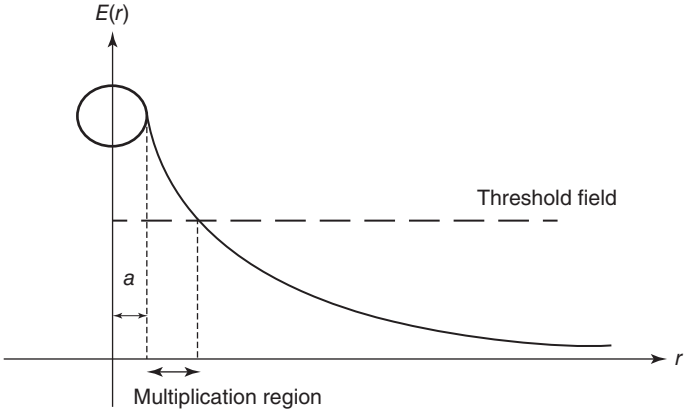

Figure 2.1 Schematic view of the electric field strength in a cylindrical detector, putting in evidence that just a part close to the central wire can host multiplication processes.

be available for multiplication, and, no region of the detector is privileged or disfavored for this process.

However, in both cases, primary ionization (i.e., the generation of one or more primary ion-electron pairs due to the passage of an ionizing particle or due to processes induced by photons or neutrons) can be produced at any point of the gas volume. This means that in a cylindrical detector, the primary electron(s) will have to drift for a variable time, depending on the position they were generated at, before reaching the region around the wire where they can start an avalanche, and give rise to a detectable signal, as shown in Figure 2.2a. The time between the creation of the primary electrons and the generation of the output

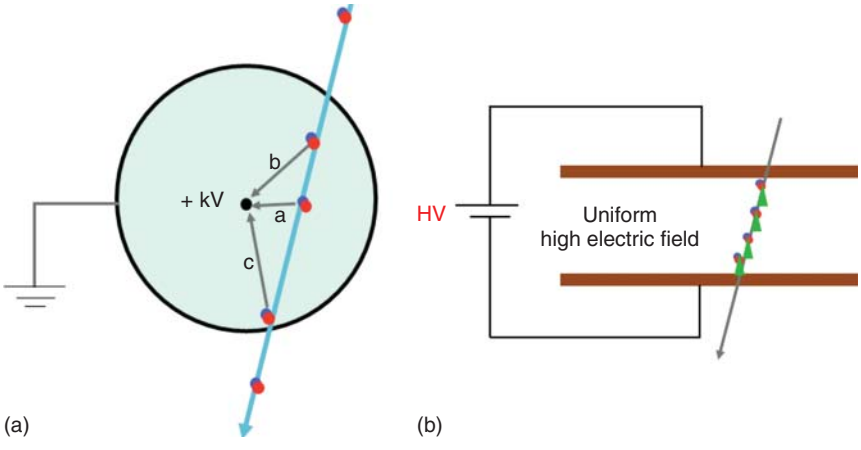

Figure 2.2 (a) Schematic view of a cylindrical detector, where the different distances to be covered by the drifting electrons toward the central multiplication region are in evidence. This is the most important limit to time resolution in this case. (b) in a parallel-plate detector, all electrons immediately start avalanching, and all the avalanches induce at the same time a signal on read-out electrodes, leading to a much better time resolution.

signal will be intrinsically affected by fluctuations, due to the fact that different primary electrons will have to travel different distances depending on where they were generated.

Electron drift velocity in gases heavily depends on the gas mixture used and, to some extent, on the applied electric field; just as an example, in gas mixtures made of Ar/C_4H_{10}, which are popular for multiwire proportional chambers (MWPCs), it can range around 3–5 cm/μs at the operating voltages normally used for these devices (see Figure 2.3). Given the fact that typical transversal dimension of central wire detectors are on the order of a few centimeters, this can easily lead to a time resolution of a few hundreds of nanoseconds, a limit that is not easy at all to overcome.

On the contrary, in planar geometry, a primary electron can give origin to an avalanche, immediately after it was generated (see Figure 2.2b), as the electrons do not have to drift toward the amplification region, since the whole gas volume is available for amplification (if the electric field is intense enough). In other words, in parallel-plate detectors, there is no separation between drift and multiplication region, and this drastically reduces the timing fluctuations described. Moreover, the resulting signal is the sum of the signals produced by the various avalanches, and this further reduces timing fluctuations.

As a consequence, planar detectors are the only ones in the family of gaseous detectors, up to now, to reach time resolutions for charged particles significantly better than 1 ns; the record in this field is held by the multigap resistive plate chamber (MRPC; described in detail in Chapter 4) with a time resolution which can reach 35 ps.

As outlined in Chapter 1, the drawback, however, is that in gaseous planar detectors, there are no simple quenching mechanisms, and a discharge initiated

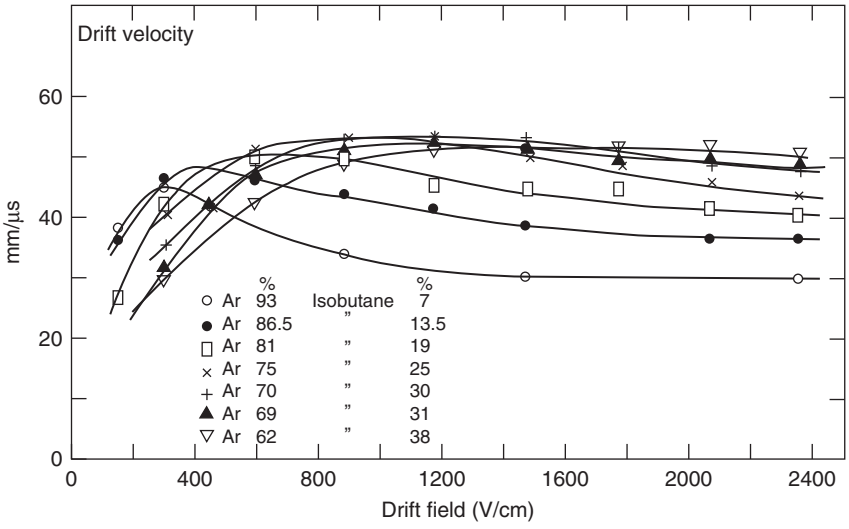

Figure 2.3 Electron drift velocity in argon-isobutane mixtures, at atmospheric pressure. (Breskin *et al*. 1974. Reproduced with permission of Elsevier.)

by the passage of an ionizing particle continues until the external operating voltage used to create the necessary electric field inside the gas is, somehow, removed. The electrodes used in the first detectors of this kind were metallic, and therefore an avalanche developing inside the gas will tend to transform into a spark thanks to the energy and charge present on the two electrodes. The first prototypes of these devices, difficult to build and necessarily provided with a sophisticated – in relation to the époque – electronics able to remove the operating voltage immediately after the passage of an ionizing particle, had a lifetime on the order of a few months. Unavoidably, the detector ended its lifetime with the formation, on one of the electrodes, of a point where a spark was continuously forming. That was the reason resistive electrodes were to be introduced.

2.2 First Parallel-Plate Counters

In 1948, J. W. Keuffel published the first results obtained with parallel-plate counters (PPCs) (Keuffel, 1948, 1949). The first prototype consisted in two molybdenum disks, separated by a 3.0 mm gap and with a 3.1 cm^2 area. Later on, Keuffel built counters made out of two copper plates (or steel coated with copper) kept at a 2.5-mm distance and with a 35 cm^2 area. Across the two electrodes, put at a potential difference variable between 1 and 3 kV, xylene vapors ($C_6H_{12}(CH_3)_2$) were flowed, at a partial pressure around 6 mmHg, plus Ar, for a total pressure of 0.5 atm (Figure 2.4).

These devices were operated in spark mode, with output pulses around 100 V (on a 50 Ω output impedance); the counter was characterized by a wide single counting plateau, ranging typically from around 0.9 up to 3.0 kV; the end of the counting region was marked by spurious counting, the ultimate amount of applied voltage permissible depending on the dead time imposed on the counter by a quench circuit. Efficiency, measured with cosmic rays, was on the order of 90% in the plateau region, and time resolution, called in the Figure "uncertainty in reaction time", from 18 ns up to 5 ns, depending on the applied high voltage (see Figure 2.5).

Even if from their simple structure this is not immediately evident, these were delicate devices, difficult to build, and a critical point was the electrode surface preparation. During construction, the surfaces were to be brushed with sandpaper, more and more fine grit. Immediately before the final assembly, they were to be washed with xylene, alcohol, and distilled water. Then the sealed tube containing the detector had to be put under high vacuum conditions, warmed up to 200°C. At this temperature, hydrogen was introduced in the tube in order to reduce possible oxides which could be present inside, then evacuated again at 10^{-5} mmHg or lower, cooled down and then filled with the active gas mixture. In order to have a working detector, it was necessary to introduce in the tube the xylene and only later on the argon (most probably to allow the formation of a layer of xylene on the cathode); the order and the accuracy in all these operations was essential to obtain working detectors.

Total working time of Keuffel PPCs was around a few months; each time the lifetime of the detector was interrupted with the formation of a point on the

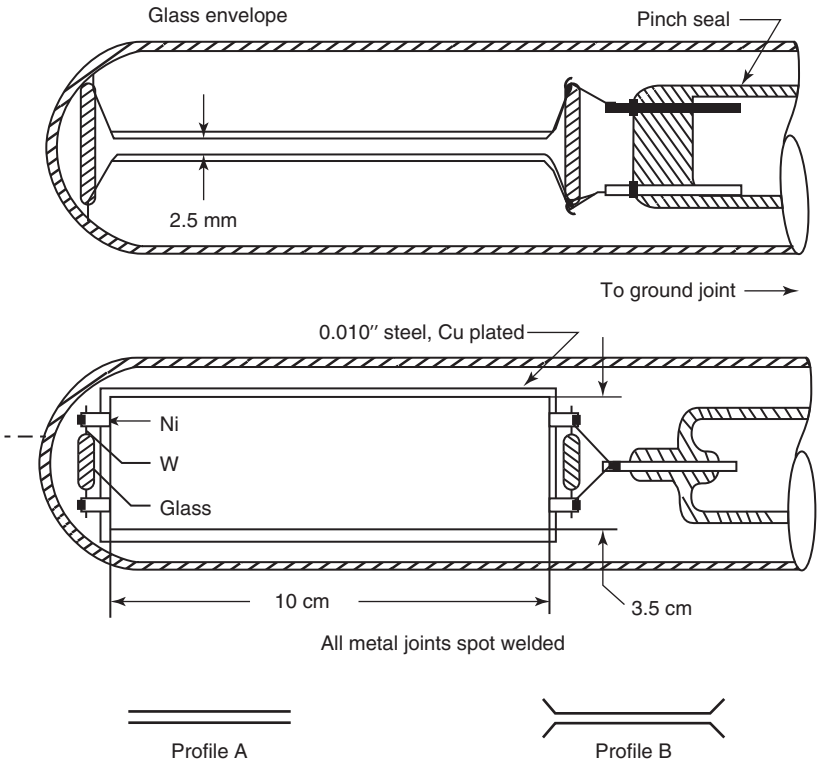

Figure 2.4 Layout of one of the original parallel-plate counters built by Keuffel. (Keuffel 1949. Reproduced with permission of American Institute of Physics.)

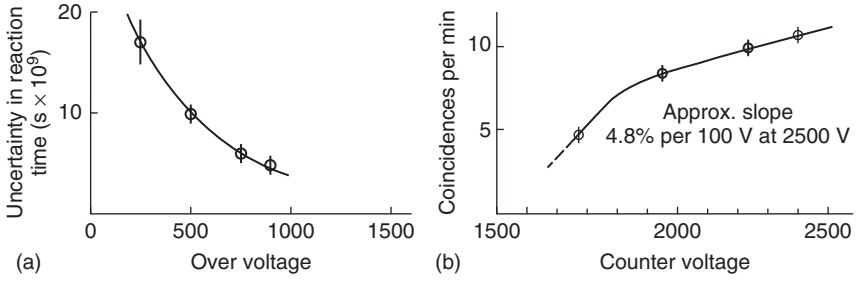

Figure 2.5 Time resolution (a) and coincidence rate (b) versus operating voltage of one of the first Keuffel PPCs; the term overvoltage refers here to the applied voltage in addition to the one needed to reach the spark detection threshold. (Keuffel 1949. Reproduced with permission of American Institute of Physics.)

electrodes where a spark was always originating. Sometimes the detector could be recuperated by taking it out from the glass container, swabbing it with xylene, and repeating the operation of warming up and filling with the gas.

The detector could not work without an external switching off circuit which removed the applied voltage for a period around 0.01–0.05 s after the passage of

an ionizing particle; in fact, after the passage of an ionizing particle, permanent discharge conditions took place, continuously fed by the charge on the metallic electrodes and the current flowing through them, added to the secondary photon emission from the electrodes. These mechanisms have been described in Chapter 1.

Of course, the fact that these detectors had to be switched off for a relatively long time after detecting an ionizing particle imposed a stringent limit of the maximum flux of particles that could be detected. In other words, these devices were severely rate limited.

It is interesting to note that in the use of these detectors the appearance of light emission concentrated in the region of the discharge between the electrodes had been already noted, foretelling the future of the optically readout spark counter (Bella *et al*., 1952).

Almost at the same time of Keuffel studies, Madansky and Pidd also produced analogous devices (Madansky and Pidd, 1949, 1950). In their detector, the anode was made of copper, while the cathode could be made in aluminum, gold, platinum, lead, and so on. In a variation, two copper foils, 3 mm thick, were stretched "like the leather of a drum" on a metallic frame of a few centimeter in diameter (see Figure 2.6). The distance between the electrodes was variable between 0.5 and 5 mm and was kept as constant as possible with the use of spacers made of insulating material between them. The authors explicitly stated that perfect parallelisms was essential to guarantee electric field uniformity (declared to be better than 0.2%) and, as a consequence, detector performance.

The gas mixture used was 90% Ar (as the active component) and 10% butane, and the authors carried out a systematic study of detector performance as a

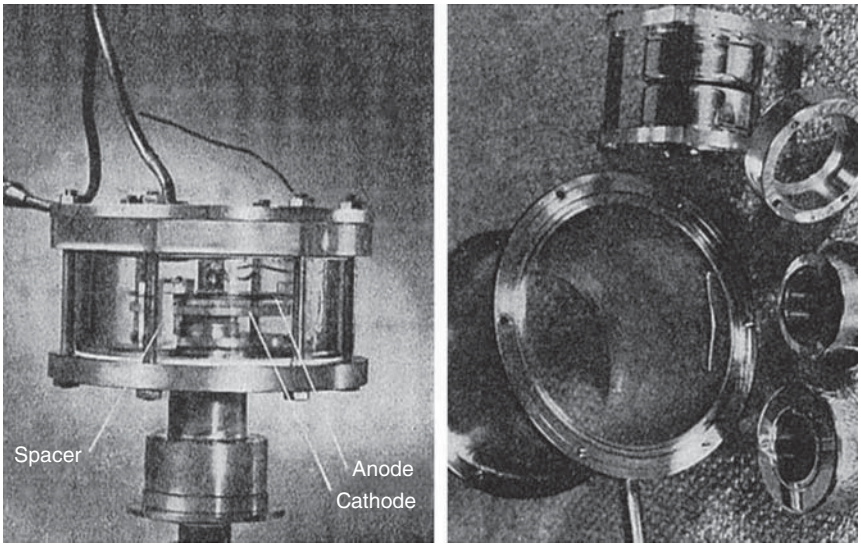

Figure 2.6 Two pictures of the Madansky and Pidd PPCs, taken from one of the original papers published in 1949. (Madansky and Pidd 1949. Reproduced with permission of American Physical Society (APS).)

function of the operating pressure (between 10 and 150 mmHg) and electrode distance. Output signals had an amplitude of a few hundred volts over a 50 Ω impedance, and the time it had to be switched off after a discharge had taken place varied between 0.1 and 0.001 s. Efficiency of β particles was better than 98% and time resolution was between 18 and 6 ns, depending on the operating voltage (see Figure 2.7).

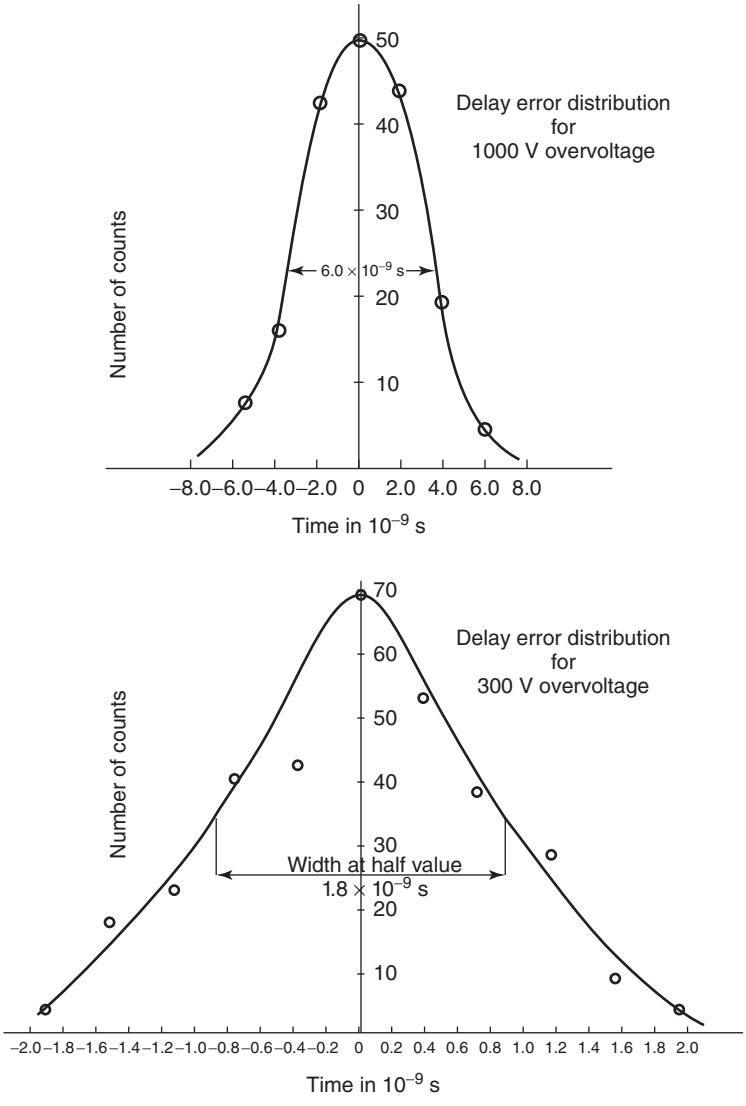

Figure 2.7 Timing distribution (called in the figure "Delay error distrubution", as it used at that times), at two values of the operating voltage, from one of the Madansky and Pidd Parallel-Plate Counters. The plot labeled with (a) refers to a higher value of the operating voltage, the one labeled with (b) to a lower operating voltage. (Madansky and Pidd 1950. Reproduced with permission of AIP Publishing LLC.)

2.3 Further Developments

During the 1950s many works were published on this field, both for what concerns the development of the detector itself, and for the electronics necessary for its rapid switch-off after the passage of an ionizing particle. Interesting works, for instance, were done by Franzinetti and Bella (Bella *et al*., 1952) and, for what concerns the control electronics, by Focardi *et al*. (1957).

Some interesting variations of the basic principle were developed. One of them is the flash chamber, developed in Pisa by the Conversi group, which exploits the fact that a discharge inside these devices is usually accompanied by the emission of visible photons. Basically, it consisted of a plane capacitor filled with a network of glass tubes, shown in Figure 2.8, around 1 cm in diameter, without any central wire, covered with black paper to shield them against external light, and filled with argon or neon at 0.5 atm (Conversi, 1982). A conceptual schematic is shown in Figure 2.8.

Again, this device could not be operated continuosly: A few hundred nanoseconds after the passage of an ionizing particle, a potential difference at the metallic electrodes corresponding to an electric field up to 10 kV/cm, of 2 μs duration was applied. In this way, a discharge accompanied by light emission was originated and the device could be optically read out. Using a large number of glass tubes, sometimes put perpendicularly to each other, it was made possible to visually detect, as a sequence of light flashes, the path of an ionizing particle crossing the apparatus, and to reconstruct it in three dimensions. A layout of one of the first implementations is reported in Figure 2.9.

With such a system, the first photographs of muon tracks or electromagnetic showers were done. One picture remained famous, relative to a double track event, probably originated by a e^+e^- pair produced by the conversion of a γ-ray in the detector itself (see Figure 2.10).

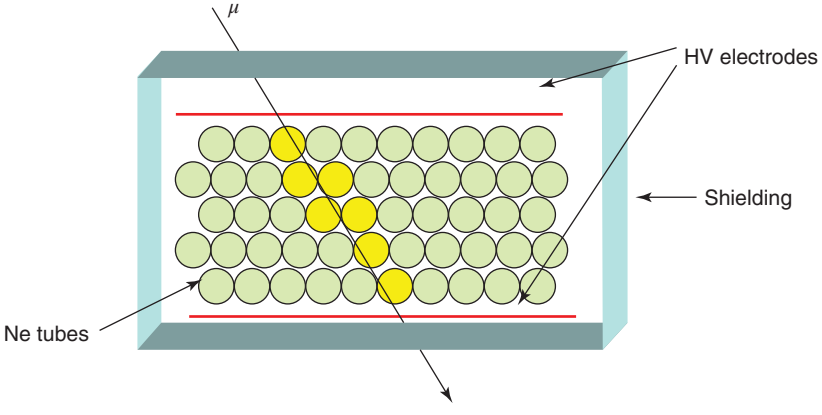

Figure 2.8 Sketch of the working principle of the flash chamber. The high voltage was applied to the external electrode, and the passage of an ionizing particle was observed by the light related to the small spark taking place inside the tubes filled with neon.

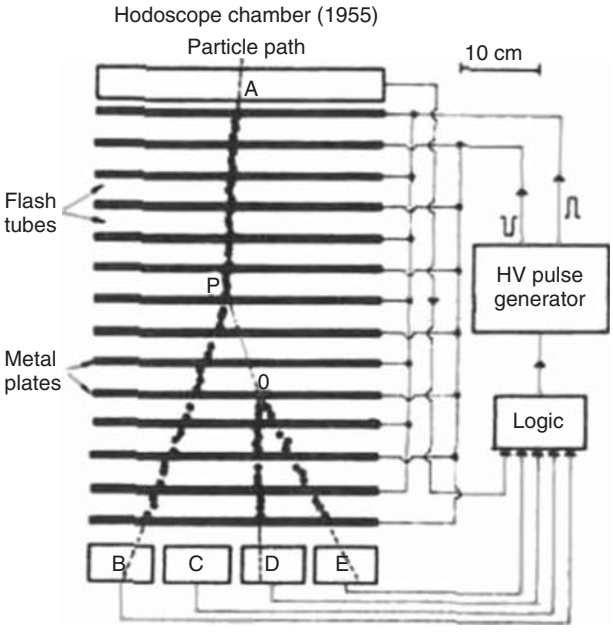

Figure 2.9 One of the original sketches of the first flash chamber. A high-voltage pulse generator was connected to the plates of a parallel-plate device. The gap – a few centimeters – between any pair of contiguous plates is filled with neon tubes (not shown in the figure). Tracks of ionizing particles are seen as sequences of flashes (black spots in the figure). (Conversi 1982. Reprinted with permission of CERN.)

Apart from the intrinsic beauty of the idea, and the beautiful results obtained, according to Conversi, these studies were at the origin of the development of spark chambers, which played such an important role in high-energy particle detection.

Later, however, some researchers studied (see (Raether, 1964) and reference therein) and tried to exploit in some practical devices (e.g., see Charpak *et al*., 1978) avalanche mode of operation in parallel-plate detectors (usually called parallel-plate avalanche counters, PPACs). The high voltage applied to these detectors is constant, continuous in time, and is sufficiently low, so that avalanches do not reach the Raether limit (see Chapter 1) and therefore they do not transit to sparks (Fonte *et al*., 1991). The signals from the avalanche detector are correspondingly small, but important advantages are that it can operate at much higher counting rates, than spark counters, and can also handle many events simultaneously. Note that the electrodes used were metallic, sometimes solid and sometimes in the form of meshes.

2.4 The First RPC Prototypes

As previously outlined, probably the first "precursor" for the invention of planar spark counters (PSCs) with resistive electrodes has to be found in the work by

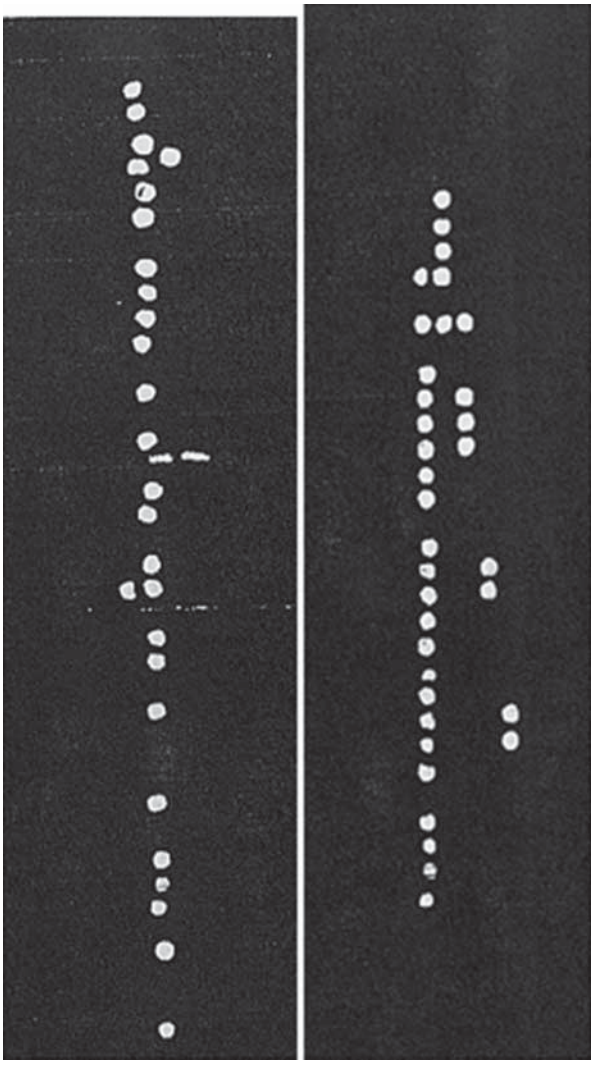

Figure 2.10 Two of the first pictures of cosmic ray events recorded in 1955 by triggering a flash chamber; a single-track event due to a muon (left) and a two-track event, presumably due to an e^+e^- pair from the interaction of a γ-ray in one of the chamber plates. (Conversi 1982. Reprinted with permission of CERN.)

Babykin *et al*. (1956). These authors experimented with PPCs, one electrode of which was segmented in metallic pads connected to a resistive load. The idea was to localize the spark and to record its position electronically thanks to the quenching mechanisms briefly described at the end of the previous chapter.

However, it is generally accepted that the first planar detectors with resistive electrodes[1] were developed by the Novosibirsk group (see Parkhomchuk *et al*., 1971); their device is schematically shown in Figure 2.11.

It had a copper cathode and the anode made of a special glass developed by Yu. Pestov; in the first tests, two samples were used with resistivity 2×10^8 and 4×10^9 Ω cm, respectively, and with an active area of 600 cm^2. The glass

1 Which in time became known as "Pestov counters."

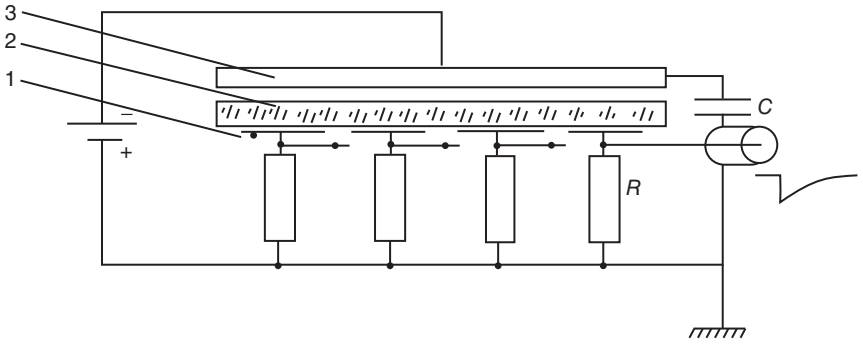

Figure 2.11 Schematics of the first design of the RPC constructed and tested by Parkhomchuk *et al*.; the various materials indicated in the figure are 1 – conductive layer, 2 – semiconductive glass, 3 – copper cathode. (Parkhomchuk *et al*. 1971. Reproduced with permission of Elsevier.)

contained iron ions Fe^+, which, according to the authors, allowed electronic conduction, leading them to refer to it as "semiconductive." Later on, this technology was transferred to the Schott Company, which produced pieces with size around 10×10 cm^2 or slightly larger.

The outer surface of the glass was coated with a conductive layer. The gap between electrodes was 1 mm. The gas mixture was 55% Ar + 30% ether vapor +10% air + 5% divinyl vapor at a total pressure of 1 atm. The passing particles triggered a spark, the energy of which was limited by the glass resistivity; the signal was taken from the conductive layer. The high-voltage recovery time after the sparks were 0.3 and 3 ms for the first and second samples of glass, respectively. In spite of the fact that signals from this detector were orders of magnitude smaller than in the case of classical spark counters with metallic electrodes, the time resolution of such a detector was better than 1 ns (see Figure 2.12).

Due to the internal quenching mechanism offered by the resistive anode, the detector did not require the use of a pulsed high voltage, and this was an important breakthrough which allowed large-area detectors, relatively easy to build at low cost. Moreover, differently from Keuffel chambers, these detectors, as described in the previous Chapter, remained insensitive after the passage of an ionizing particle only in the zone immediately nearby; the discharge and the corresponding dead zone were localized, while the rest of the counter remained fully sensitive.

2.5 Pestov's Planar Spark Chambers

The device described in the previous paragraph was the first parallel-plate detector with resistive electrodes and actually was the first prototype of modern RPCs. Shortly later, however, another design attracted even more attention from the researchers; it had three important modifications:

1) The gap between the electrodes was reduced to 0.1 mm.
2) The detector operated in gas mixtures mainly done by argon and/or neon.
3) The gas pressure was increased to several atmospheres.

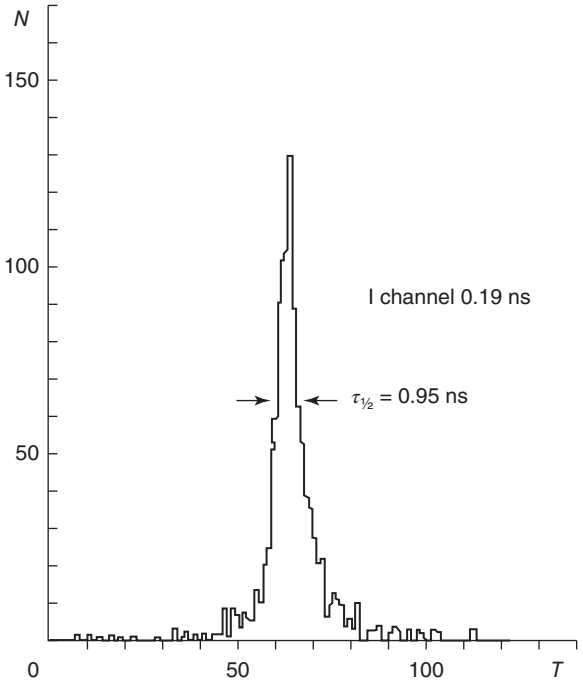

Figure 2.12 Histogram of the time distribution measured with two RPCs arranged as a cosmic ray telescope. (Parkhomchuk *et al*. 1971. Reproduced with permission of Elsevier.)

These modifications allowed reaching a time resolution of about 100 ps, which, at the time, was very impressive, specially taking into consideration the status of development of wideband electronics (Pestov, 1982).

Two plane electrodes were mounted parallel to each other at a distance of, typically, 100 μm, with a precision in the spacing about 1–5% (Atwood *et al*., 1983). The small gap between electrodes imposed high requirements on the surface quality (flatness, roughness), on the spacers and how they were fixed. A potential difference corresponding to an electric field on the order of 2×10^4 V/cm was applied to the electrodes.

The cathode was made of ordinary glass, where a thin copper layer had been previously laid on. The anode was built using the special glass developed by Yu. Pestov, whose volume resistivity was in the 10^9–10^{10} Ω cm range, already used also by Parkhomchuk and described in the corresponding section. Electrode dimensions in the given detector were typically around a few hundred square centimeters (up to 30×30 cm^2) (see Figures 2.13 and 2.14).

Between the two electrodes was flowed an adequate gas mixture at a pressure of 10 atm, composed of Ar or Ne as the main elements, plus organic gases to ensure a high absorption in the UV region beyond 225 nm. A standard mixture was 70% (in volume) of Ar, 16.5% of isobutene, 3.3% of ethylene, 1.3% butadiene, 7.4% hydrogen, and 1.5% diethyl ether (from Badura *et al*., 1996).

The passage of an ionizing particle gave rise to a discharge between the two electrodes; nevertheless, the high resistivity imposed a limit on the total charge available for the discharge, while supposedly the high photon absorption coefficient of the gas mixture prevented the UV photons produced in the process to

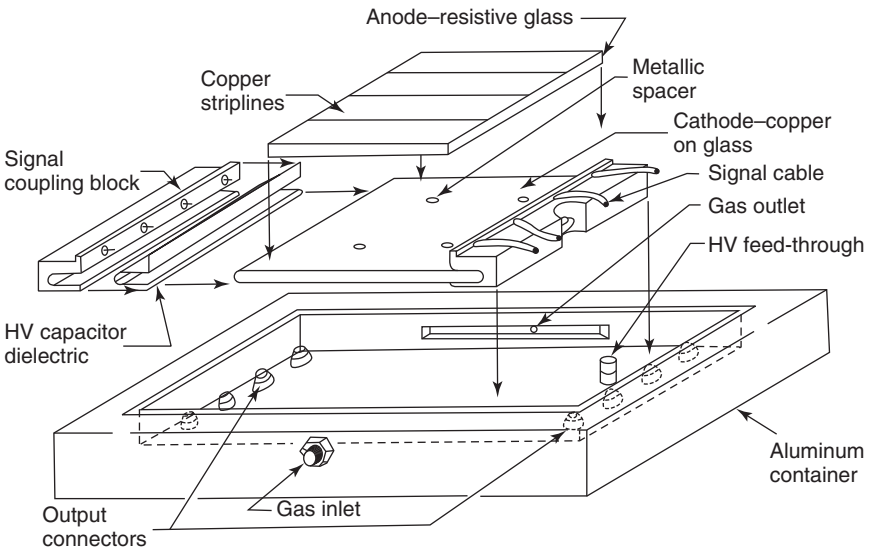

Figure 2.13 Exploded view of a Pestov counter. (Atwood *et al*. 1983. Reproduced with permission of Elsevier.)

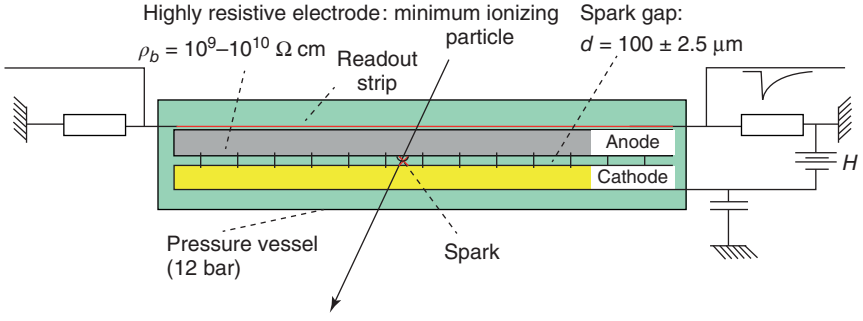

Figure 2.14 Transversal view of a Pestov detector. (Badura *et al*. 1996. Reproduced with permission of Elsevier.)

propagate and provoke secondary avalanches. Therefore, a spark made inactive a region of the detector with dimensions on the order of 1 mm^2, whose exact dimension depended on the distance between the two electrodes, the operating voltage, and the gas pressure. The time needed to charge up again the depleted region of the resistive electrode depended on the glass resistivity, as seen in Chapter 1.

Signal readout was performed by means of long copper strips 10 mm wide glued on the back of the anode; the signal produced by a discharge after the passage of an ionizing particle was typically of a few volts on a 50 Ω impedance, with a rise time less than 1 ns, and a typical duration of around 5 ns.

As already pointed out, an interesting characteristics of PSCs was their excellent time resolution (Figure 2.15), whose best published value was 24 ps, obtained with a 0.1-mm gap thickness at 14 atm (Fedotovich *et al*., 1978).

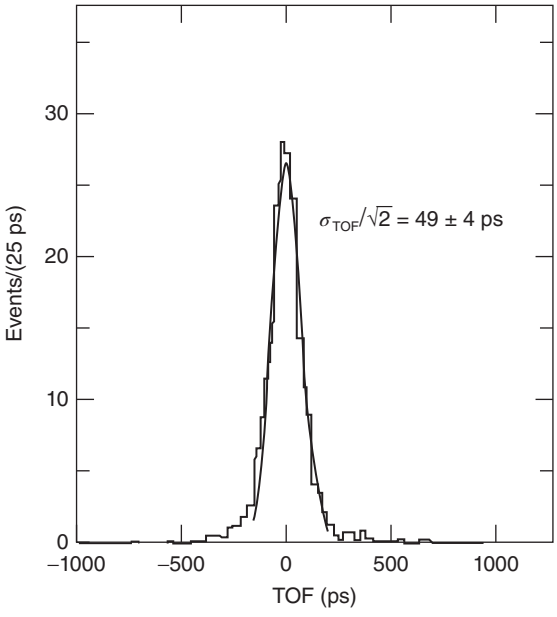

Figure 2.15 Distribution of the time of flight between two identical Pestov counters for cosmic ray triggers. The solid line is a Gaussian fit, allowing to infer a time resolution of the single counter around 50 ps. (Atwood *et al*. 1983. Reproduced with permission of Elsevier.)

Under these conditions, longitudinal space resolution, as measured by the time difference between the two ends of the strips was around 0.2 mm, while in the other coordinate it was essentially determined by the strip width.

PSCs needed an accurate preparation of the surfaces, before they could be used. The electrodes, in fact, had to be polished thoroughly with cerium oxide and cleaned and deionized water. The interference patterns observed on the thin water layer on the electrode surface was used to spot possible imperfections of the surfaces.

Once prepared, inserted in the container, and brought to the operating pressure, such detectors had to undergo a conditioning period before they could be used. During a whole week, the operating voltage was slowly increased while the detector was subjected to radiation; the detector had to accumulate something like 10^6 sparks/cm^2 to form a thin layer of polymer which, according to Pestov's observations, greatly improved the detector performance.

After a first phase of R&D these detectors were used in physics experiments. Despite their extraordinary time resolution, however, they were used only in few cases, for instance, for the measure of the π form factor at the accumulation ring VEPP-2, at Novosibirsk (Atwood *et al*., 1983), in 1975–1982, and then at the NA49 experiment at CERN (see Figure 2.16). This was mainly due to the complexity of this device imposed by the necessity to operate them at pressures much higher than atmospheric, and the long process of preparation of the electrode surfaces. In 1986–1991, the R&D work was continued within the SLAC-Novosibirsk collaboration and later in the framework of the PesTOF collaboration (Schmidt, 1999).

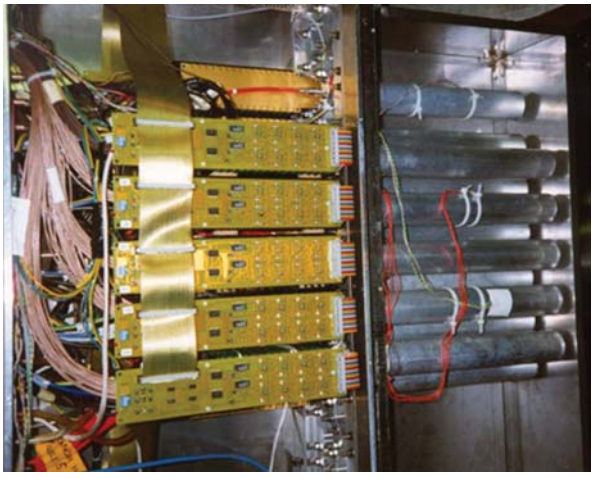

Figure 2.16 A stack of 14 PSCs at the NA49 experiment at CERN. (Schmidt 1999. Reproduced with permission of Elsevier.)

2.6 Wire-Type Detectors with Resistive Cathodes

At the beginning of the 1980s, wire detectors with resistive cathodes became very popular. However, in this case, the role of the resistive materials was not one of a discharge quencher, as one can at first guess; on the contrary, resistive materials were used rather for signal pickup purposes: resistive layers, in contrast to metallic ones, do not screen the signals (or at least they do screen them only partially) produced by the drifting ions and electrons. This allowed the use of metallic readout strips, typically attached to the outer surface on the resistive cathode. By the way, note that the same concept is still used: the fact that a resistive layer is transparent to induced signals is exploited in modern RPCs to obtain the position information.

Probably the most remarkable example of this type of detector is the "Iarocci tube" (Iarocci, 1983). It is a rectangular plastic box (with a typical cross section size 1×1 cm^2 and a length up to few meters, with the inner walls coated with a resistive layer (graphite based) serving as a cathode. A 100–200 μm-thick anode wire is stretched along the axis. Due to the relatively large diameter of this wire, the detector operates in the limited streamer mode, described earlier. Ionizing particles trigger short-range streamers, which do not reach the cathode. These streamers induce large signals on the readout strips placed on the outer surface of the detector which are used to determine their position.

These tubes were successfully used in several experiments like CHARM, NUSEX, UA1, ALEPH, DELPHI, OPAL, and so on and a total of more than 600 000 individual modules are esteemed to have been produced.

As another example, we will mention a thin-gap cathode strip MWPC, developed for the ATLAS experiment at LHC (Majewski, 1983). In this detector, the readout cathode strips are placed at a distance of only 1 mm from the anode wire planes to ensure that the induced signal distribution on the strips would

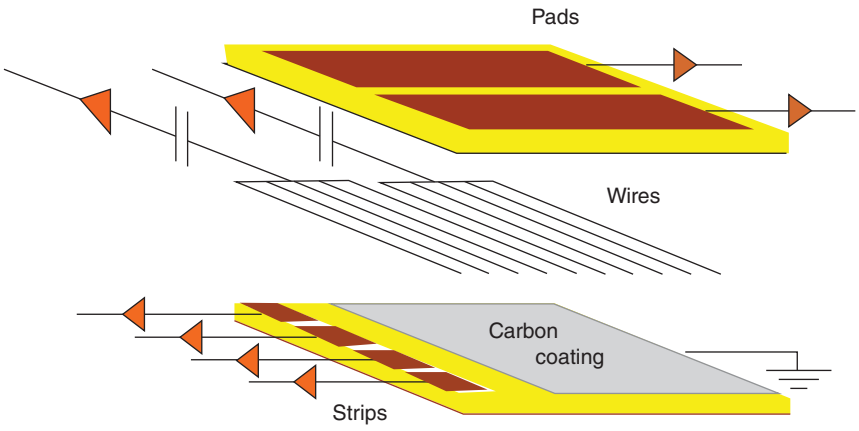

Figure 2.17 Schematic view of the MWPC with resistive cathode. (Amram *et al*. 2011. Reproduced with permission of Elsevier.)

keep a narrow profile (see Figure 2.17). However, the metallic readout strips create a strongly nonuniform electric field which often causes breakdowns. To solve this problem, the inner surface of the cathode is coated with a resistive layer, so that the field in this region is made more uniform. This approach also helps suppress the photon feedback caused by this discharge propagation, by temporary locally desensitizing the detector around the original streamer due to the charging up effect (see Majewski, 1983)).

These two examples show that resistive electrodes and materials may have more functionalities than just simple discharge quenching.

References

Amram, N. *et al*. (2011) Position resolution and efficiency measurements with large scale thin gap chambers for the super LHC. *Nucl. Instrum. Methods Phys. Res., Sect. A*, **628**, 177.

Atwood, W.B. *et al*. (1983) A test of planar spark counters at the PEP storage rings. *Nucl. Instrum. Methods Phys. Res.*, **206** (1–2), 99–106.

Babykin, M.V. *et al*. (1956) Plane-parallel spark counters for the measurement of small times. *Sov. J. At. Energy*, **4**, 487.

Badura, E. *et al*. (1996) Status of the Pestov spark counter development for the ALICE experiment. *Nucl. Instrum. Methods Phys. Res., Sect. A*, **379**, 468–471.

Bella, F. *et al*. (1952) On spark counters. *Il Nuovo Cimento*, **10** (9), 1338–1340.

Breskin, A. *et al*. (1974) Further results on the operation of high-accuracy drift chambers. *Nucl. Instrum. Methods*, **119**, 9–28.

Charpak, G. *et al*. (1978) The multistep avalanche chamber: a new high ate, high accuracy gaseous detectors. *Phys. Lett.*, **78B** (4), 523.

Conversi, M. (1982) The development of the flash and spark chambers in the 1950s. *J. Phys. Colloq.*, **43** (C8), C8-91–C8-99.

Fedotovich, G.V. *et al*. (1978) Spark Counter with a Localized Discharge, http://plasmapanel.grid.umich.edu/articles/articlelist.html (accessed 10 October 2017).
Focardi, S. *et al*. (1957) Metodi di comando rapido dei rivelatori di tracce. *Il Nuovo Cimento*, **5** (1), 275–282.
Fonte, P. *et al*. (1991) Feedback and breakdown in parallel-plate chambers. *Nucl. Instrum. Methods Phys. Res., Sect. A*, **305**, 91–110.
Iarocci, E. (1983) Plastic streamer tubes and their applications in high energy physics. *Nucl. Instrum. Methods Phys. Res.*, **217**, 30–42.
Keuffel, J.W. (1948) Parallel-plate counters and the measurement of very small time intervals. *Phys. Rev.*, **73**, 531.
Keuffel, J.W. (1949) Parallel-plate counters. *Rev. Sci. Instrum.*, **20**, 202. doi: 10.1063/1.1741489.
Madansky, L. and Pidd, R.W. (1949) Some properties of the parallel plate spark counter I. *Phys. Rev.*, **75**, 1175.
Madansky, L. and Pidd, R.W. (1950) Some properties of the parallel plate spark counter II. *Rev. Sci. Instrum.*, **21**, 407.
Majewski, S. (1983) A thin multiwire chamber operating in the high multiplication mode. *Nucl. Instrum. Methods Phys. Res.*, **217**, 265.
Parkhomchuk, V.V. *et al*. (1971) A spark counter with large area. *Nucl. Instrum. Methods*, **93**, 269–270.
Pestov, Y.N. (1982) Status and future developments of spark counters with a localized discharge. *Nucl. Instrum. Methods Phys. Res.*, **196** (1), 45–47.
Raether, H. (1964) *Electron Avalanches and Breakdowns in Gases*, Butterworths, London.
Schmidt, H.R. (1999) Pestov spark counters: work principle and applications. *Nucl. Phys. B (Proc. Suppl.)*, **78** (1–3), 372–380.

3

Basics of Resistive Plate Chambers

3.1 Introduction

In this chapter, the earliest version of the resistive plate chambers (RPCs) – single-gap RPC – is considered in detail. As is often done in physics, it is quite useful to start from the simplest experimental situations in order to understand more complex ones. Here, we will do the same, using this simplest device to study the basic phenomena occurring in an RPC, such as its operation modes and the avalanche-to-streamer transition; in this simple case, some formulae about the main processes taking place therein and their main characteristics, like signal development, induced charge, time resolution, and so on, can be written in a closed form, and this provides a deeper understanding of how this device operates. The material presented in this chapter also constitutes the necessary background for examining and understanding more complicated RPC designs, like double or multigap RPCs, timing RPCs, high-rate and high-position resolution RPCs, which are illustrated in the following chapters.

3.2 Santonico and Cardarelli's RPCs

At the beginning of the 1980s, Rinaldo Santonico and Roberto Cardarelli built in Rome the first prototypes of the modern RPCs, using phenolic laminate compressed at high pressure; they operated at atmospheric pressure and did not require processes to prepare the electrodes as long and complex as those necessary for the Pestov counters (Santonico *et al*., 1981).

These authors creatively put in place all together the basic idea of the modern RPCs:

- Planar geometry (with the consequent advantages of time resolution);
- Use of resistive materials for the electrodes (which allowed detector self-quenching and no need for a pulsed operation mode and high-voltage (HV) removal after the passage of an ionizing particle and the subsequent discharge);
- Application of the HV to the electrodes via a signal-transparent resistive layer; and, moreover,
- The idea to produce detectors that are easy to build, in order to make them suitable to cover large surfaces.

Resistive Gaseous Detectors: Designs, Performance, and Perspectives, First Edition.
Marcello Abbrescia, Vladimir Peskov, and Paulo Fonte.

The new material used for the electrode plates, Bakelite resin, was a phenolic resin formed from a condensation reaction of phenol with formaldehyde. Bakelite resin is often used for the creation of phenolic sheet materials. A phenolic sheet is a hard, dense material obtained by applying heat and pressure to layers of paper or glass cloth impregnated with phenolic resin. Cellulose paper, cotton fabrics, synthetic yarn fabrics, and glass fabrics are all possible materials used in lamination. When heat and pressure are applied, polymerization transforms the layers into a thermosetting industrial laminated plastic. Bakelite phenolic sheets can be produced using various additives to meet diverse mechanical, electrical, and thermal requirements. Some of these high-pressure laminates (HPLs) were used to build the first prototypes of Santonico and Cardarelli's RPCs.

Note that quite often, even if the terminology is not completely appropriate, in modern RPC parlance, the material used to build these RPCs is referred to simply as "Bakelite," and these devices as Bakelite RPCs; for the sake of simplicity, in this book, we use the term Bakelite in this acceptation.

The layout of the original RPC prototype is shown in Figure 3.1, and explained more schematically in Figure 3.2. To the two 2-mm-thick parallel Bakelite electrode plates, characterized by a resistivity in the 10^{10}–10^{12} Ω cm range, a voltage difference of 7–10 kV (depending on the gas mixture used) was applied, which created a uniform electric field in the region in between (usually called gas gap, 2-mm thick as well in this prototype).

The two Bakelite electrodes were laterally sealed by a frame of polyvinyl chloride (PVC), which is a good insulator. The distance between the two plates was guaranteed to be constant, even in the innermost region, using a network of button-like spacers (100 per square meter) built with a precision better than around 0.01 mm and glued to the planes. A structure sufficiently rigid is produced, where a gas mixture – the active medium of the detector – is flowed through four holes on opposing sides of the PVC frame. An exploded view of a single-gap RPC is shown in Figure 3.3.

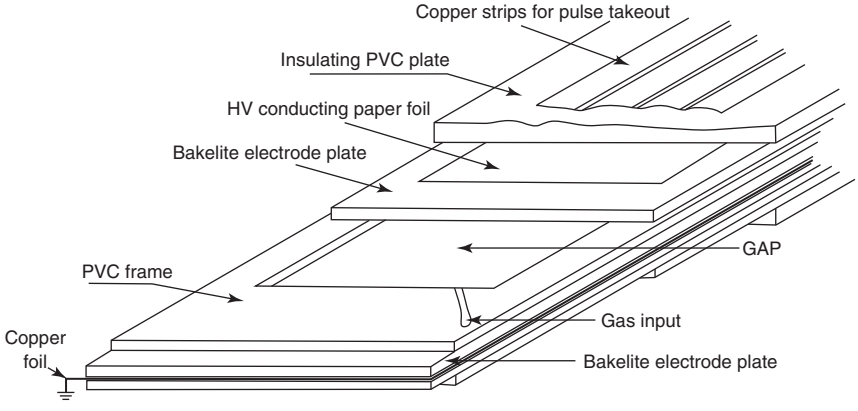

Figure 3.1 Layout of original Santonico and Cardarelli's RPC. (Santonico *et al*. 1981. Reproduced with permission of Elsevier.) The first prototype originally consisted of two identical counters rigidly superimposed one on the other, with the same copper foil as common ground plate; in this sense, it resembled quite closely the double-gap design that is described in detail in Chapter 4.

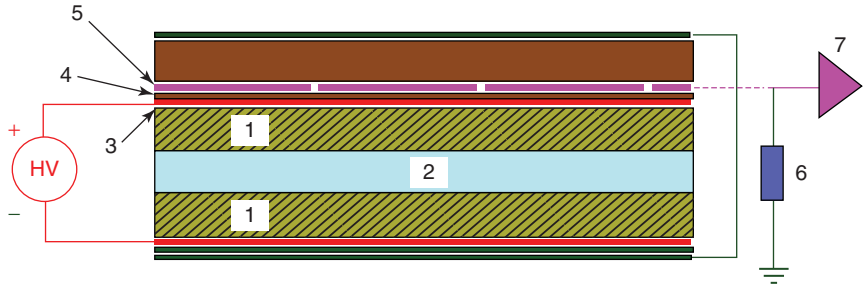

Figure 3.2 Schematics of Santonico and Cardarelli's RPC. (1) Bakelite electrodes (2 mm), (2) gas gap (2 mm), (3) HV electrodes (200 μm of graphite), (4) Mylar insulator (50 μm), (5) readout strips, (6) resistor, and (7) readout electronics.

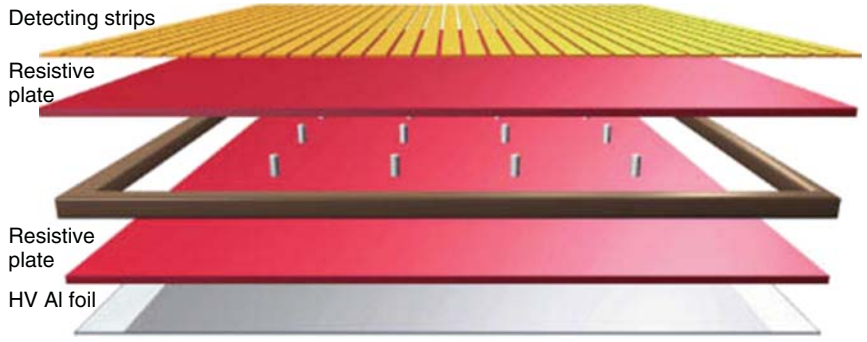

Figure 3.3 An exploded view of a resistive plate chamber. (http://cms.web.cern.ch/news/resistive-plate-chambers. Reprinted with permission of CERN.)

The planes of Bakelite facing the gas have, unavoidably, local nonuniformities at the microscopic level. Any small protruding point in the electrode surface would provoke a much more intense local field, increasing the probability of local discharges. A better smoothness of the surface was therefore achieved by coating the inner surfaces with a paint made with linseed oil diluted in pentane; the painting was applied by filling the assembled detectors with the oil mixture, and then emptying by putting them in vertical position (see Figure 3.4). This procedure assures a significant reduction in the "dark" counting rate (see paragraph 3.8), that is, the detector counting rate when no external radiation is impinging on the detector (Abbrescia *et al.*, 1997a).

Originally, the gas mixture used was typically composed of argon, butane, and some kind of chlorofluorocarbon (generally simply called "Freon," which actually is a commercial name used to indicate an entire class of gases), at atmospheric pressure. Generally, argon in percentages between 60% and 70% (in volume) was used, plus 30–40% of butane and a low (3–5) percentage of CF_3Br. In this case, argon, characterized by an elevated specific ionization (about 26.4 eV/electron-ion pair), constituted the "active part" of the gas mixture. Of course, changing the composition of the gas mixture implied a change in the operating voltage of the detector.

Electric field in the gas gap was created, in the first prototypes, by applying on the external side of one of the two Bakelite electrodes, a copper foil, 50 μm thick;

(a) (b)

Figure 3.4 Part of the linseed-oil-coating facility used at the CMS Korean construction site; (a) the lifting device of the oil tank and (b) frame holding the gas gaps vertically during the oil-coating process. (Ahn *et al*. 2005. Reproduced with permission of Elsevier.)

the other Bakelite electrode was connected to the HV, on its outer side as well, using a layer of conductive paper. Later on, copper and conductive paper were not used anymore, and the Bakelite sheets were coated with thin layers of a conductive painting, typically containing graphite, characterized by a surface resistivity in the 200–300 kΩ/□ range, and connected, one to the HV, the other to the ground. In more recent models, a narrow region around the spacers is removed from the graphite electrodes, to provide better spacer insulation. Moreover, to ensure insulation between the HV electrodes and the readout strips, a 0.2–0.3-mm-thick layer of mylar or polyethylene is used, glued on the graphite layer.

Performance of the first prototypes of RPCs were very promising; efficiency reaching almost 100% and time resolution around 1 ns for cosmic rays triggered with scintillators above and below the RPC under test, are shown in Figure 3.5.

Note that these devices, when switched on for the first time, are characterized by elevated values of current and counting rate; these values decrease, often by one or 2 orders of magnitudes, by keeping the detector on, during a time span which can range from a few days to a couple of weeks. This operation is often referred to with the word "conditioning," (note, that similar conditioning procedure was applied in first RPCs, developed by Pestov group (see Chapter 2)). Sometimes conditioning it is performed by filling the gas gap with pure argon, since it has been observed that this gives faster and more effective results. Most probably, the progressive decrease of current and counting rate is due to dirt or

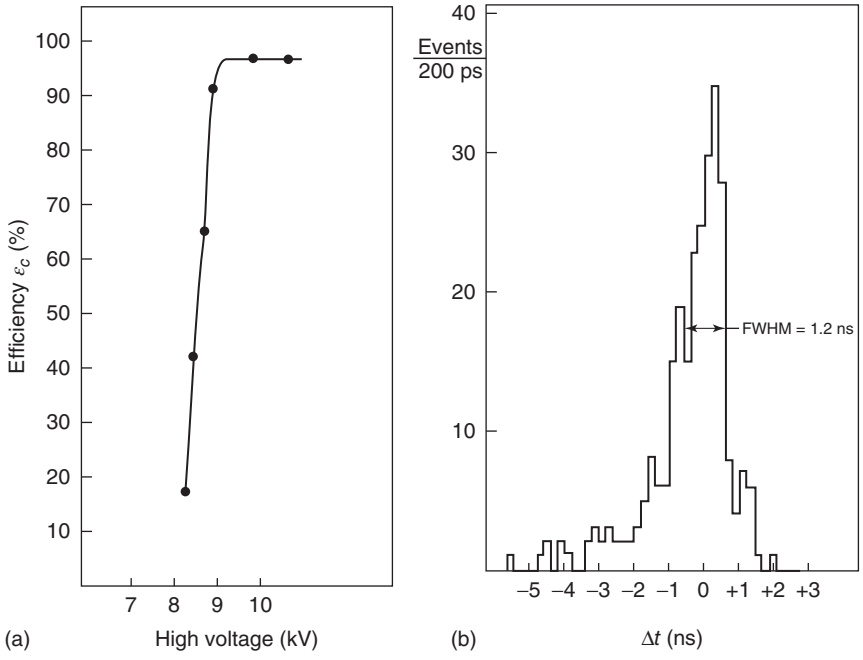

Figure 3.5 Efficiency (a) and time resolution (b) for one of the first prototypes of RPCs. (Santonico *et al*. 1981. Reproduced with permission of Elsevier.) In both cases, the trigger was provided by a set of scintillators above and under the RPC under test; the time resolution plot includes the time jitter given by the scintillators.

small particles of dust inside the gap, which at the beginning constitute localized discharge spots and thereafter are gradually etched by discharges. Also, glass RPCs, described later on in this chapter, show a similar behavior and generally need to be conditioned.

Signal readout can be performed on one or on both sides of the detector. The readout electrodes are independent of the HV and can have any desired shape and dimension. One of the most common solutions is the following: aluminum or copper strips, typically a few centimeters wide are used on one side, and on the other side an aluminum foil. As an alternative, using two sets of strips, one perpendicular to the other, glued on the opposite sides of the RPC, one can measure at the same time the two Cartesian coordinates of the ionizing particle impinging point. Another common configuration consists in the use of a network of rectangular readout electrodes (usually called "pads"), typically a few centimeters in dimension.

For mechanical rigidity, the whole detector sometimes is wrapped with additional protective layers of material, e.g. propylene or PVC sheets covered with aluminium foils. Since Bakelite-impregnated material can be produced, in principle, with arbitrary dimension, RPC detector dimensions can be arbitrary, too; the first prototype was produced using Bakelite sheets $103 \times 22 \times 0.3$ cm^3, from which an active area of 85×13 cm^2 was obtained. Nowadays it is quite common to use Bakelite sheets 1–2 m^2 in dimension, with an active area basically

of the same size. Often, one or more detector units are enclosed in a metallic frame to guarantee rigidity and ease of transportation of the whole structure.

As described in Chapter 1, when the gas contained in an RPC is crossed by an ionizing particle, a certain number of primary ion-electron pairs are formed which give rise to a small discharge between the two electrodes, provided that the applied electric field is intense enough. As already pointed out, the discharge generated remains confined in the zone immediately close to the primary ionization and does not extend to the whole sensitive detector volume. This is due to the high electrode resistivity and to the properties of the gas mixture used. In particular, the authors (Cardarelli *et al*., 1988) pointed out that the discharge is limited by three main mechanisms:

1) Decrease of the electric field on the electrodes around the discharge zone, due to the neutralization of the charges on them and their high resistivity;
2) Absorption of the UV photons produced in the streamer phase, thanks to the high UV absorption coefficient of the isobutane contained in the gas mixture, which prevents the formation of secondary discharges due to photoelectrons;
3) Capture of the electrons in the discharge region, thanks to the high Freon electronegativity (see below).

Here, a few words about points 2 and 3 deserve to be said. A molecular gas or a gas mixture which is characterized by a high-absorption UV coefficient (like the isobutane previously cited), is said to have quenching properties, since it reduces the probability of the feedback processes mentioned in Chapter 1. Using quenching mixtures in gaseous detectors is generally considered an advantage, since it helps keeping discharges contained in a zone spatially limited.

Moreover, an electron drifting in gas under the effect of a strong applied electric field, in addition to provoking avalanche ionization, as seen in Chapter 1, can also undergo interactions with the atoms and molecules of the gas and form negative ions with some of them, for example oxygen or freon. The class of molecules and atoms which are likely to form negative ions are named "electronegative". This process is called "attachment" and its result is reducing the number of free electrons in the gas. If electron multiplication is also taking place, this is basically a concurrent process, reducing the total net gain. An attachment coefficient can be introduced, here indicated with η, which gives the probability (per unit length) for an electron to undergo attachment. In this case, the variation dn_e in the number of n_e free electrons in dx is simply given by

$$dn_e = (\alpha - \eta)\ n_e dx \tag{3.1}$$

where α, already introduced in Chapter 1, is the first Townsend coefficient.

$$\alpha^* = \alpha - \eta \tag{3.2}$$

is also called the effective first Townsend coefficient.

It was immediately clear that the choice of the gas mixture was crucial for a correct operation of these devices. Given the gas mixture used, containing a relevant fraction of argon, and the applied voltage (even up to 10 kV or more), the signals developed in these devices were big enough to be fed to standard discriminators, without any need of pre-amplification. Signals produced were typically a few tens

of nanoseconds in duration, and characterized by a voltage amplitude (on a 50 Ω readout impedance) of a few hundreds of millivolts, corresponding to integrated charge on the order of 100 pC. RPCs operated under these conditions were said to operate in "streamer" mode.

Note that in the currently used RPC parlance, the term streamer is generally used not only to indicate the processes described earlier in Chapter 1 (also called Kanal or Kanal mechanism), but also mostly the mild discharges (i.e., the complex phenomena that take place after a streamer has established a positive column between anode and cathode) that, strictly speaking, follow the streamer if the electric field is intense enough.

For instance, when RPCs are said to be operated in streamer mode, this usually just means that they are operated at such voltages that the signals are large enough not to be compatible anymore with the presence of avalanches only in the gas. In this book, we stick to this widespread custom; when we (seldom) need to distinguish the two things, we make it quite clear from the context, or using the terms "discharges" or "mild sparks" or similar, to strictly indicate the latter. For a more detailed description of these processes in RPCs, see Section 3.4.

The value of the charge generated per avalanche is crucial to determine the maximum frequency at which these devices can reveal particles without a sensible efficiency reduction. As a matter of fact, the charge flowing in the gas must be supplied by the current, necessarily limited, crossing the two resistive electrodes. A small value of avalanche charge allows to keep this current low and the efficiency high. This issue is studied in detail later on, in relation to the RPC rate capability.

Readout is based on signal induction on readout electrodes by the electric charges moving in the gas gap; the induction is made possible by the fact that the resistive electrodes and the graphite paint are basically transparent to the rapid signals induced, thanks to their high resistivity. If, in place of graphite paint, a metallic electrode were to be used, the signals would be shielded and it would not be possible to perform position measurements with external readout strips. A systematic study of the charge induced on 6-mm strips showed that this is localized in a region on the order of 1 cm^2 around the discharge point.

Readout strips can be freely dimensioned according to the requirements of the experiment these devices are used for; sometimes, in this kind of RPC, they are dimensioned so that their nominal impedance is around 50 Ω. A long aluminum or copper strip can be considered as a transmission line; this means that the induced signal is practically not integrated and therefore the voltage variations at the end of the strips are proportional, moment by moment, to the discharge amplitude in the gas.

On the contrary, a pad can be approximated by a concentrated capacity. For instance, 30×30 cm^2 pads connected with an electronics characterized by an input impedance on the order of 100 Ω implies a time constant on the order of 100 ns which, being an order of magnitude larger than the signal rise time, leads to integration phenomena, degrading the time characteristics of the signal. This imposes a limit on the maximum dimensions for these electrodes in the case of RPCs used for timing or triggering applications. In general, the dimensions of the readout electrodes mostly determine the spatial resolution achievable with these devices.

Note that while most RPC implementations are read out by centimeter-scale wide strips that provide some modest avalanche localization capability by identification of the hit strip, some applications, mostly in muon tomography or biomedicine (which will be described in more detail in Chapters 7 and 9) require a much better position measurement on both coordinates. These matters are further developed in section 3.5.5.

3.3 Glass RPCs

From the original design, dating to the beginning of 1980s, a number of improvements have taken place in this type of detectors. For this reason, the further focus in this chapter is on some later generations of single-gap RPCs made of different materials and having new design features.

For instance, RPCs made with melamine and cellulose electrodes were tested, but without any noticeable improvements in their performance (Crotty *et al*., 1993); note also that Bakelite sheets are often produced with a thin layer of melamine on top, to obtain a smoother surface. These attempts demonstrated that, in principle, many different resistive materials can be used in RPC design and construction.

More success came from the implementation of electrodes made of common glass (not different from the one commonly used for windows) (Bencivenni *et al*., 1994). These RPCs offer better mechanical rigidity; moreover, since their surface is usually smoother than Bakelite at the microscopic level, the linseed oil coating is no longer necessary. This, at the time, was an important point, since it was not well known what could happen to the linseed oil coating in the long run. RPCs with electrodes made of glass remain quite popular and are used in some high-energy physics experiments till today.

An example of a state-of-the-art glass RPC is the one developed by one Italian group in the framework of the MONOLITH project (Gustavino *et al*., 2001a). It made use of commercially available materials with high-quality surfaces, and the simple assembling procedures allowed the realization of large sensitive planes at low cost. The glass RPC used had a pair of commercial float glass electrodes 243 mm wide, 1.85 mm thick, and up to 2 m long. The volume resistivity at room temperature of this glass is around 10^{12} Ω cm, suitable for operation in streamer mode in low particle rate environments. A uniform time resolution of about 1 ns can be achieved even on a large-scale production, because the spacers used in the construction (see Figure 3.6) permit a gap precision better than 0.5%, slightly worse with respect to Bakelite RPCs. Moreover, the detector spacers were designed and arranged in a special way to ensure a uniform and steady gas flow, which is usually a problem in large gaseous detectors. Some design features can be seen in Figures 3.7 and 3.8.

Figure 3.8 shows one of the injection molded spacers. The spacers were clamped to the glass with the sticks inserted between the electrodes (see Figures 3.7 and 3.8), not using any kind of glue, which was an important simplification in the construction procedures. The shape of the stick was knurled to prevent possible discharge between the plates.

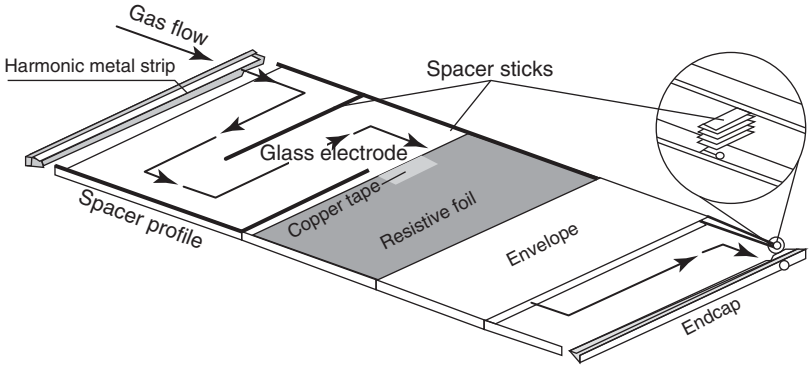

Figure 3.6 Sketch of a glass RPC. (Gustavino *et al*. 2001a. Reproduced with permission of Elsevier.)

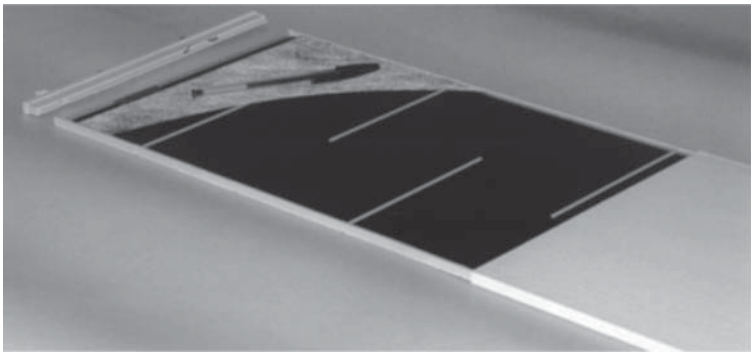

Figure 3.7 Photograph of a glass RPC. (Gustavino *et al*. 2001a. Reproduced with permission of Elsevier.)

A 140 μm-thick carbon-polyethylene adhesive foil was applied to the external surfaces of the glass electrodes to provide the HV supply (note that in Figure 3.7 the foil on the upper electrode has been partially "removed" to show the spacers inserted between the glass plates). The surface resistivity of the foil was about 10 MΩ/sq. After assembling, the glass plates with the spacers were inserted in an extruded envelope with 1.5-mm thick walls. The external cross section of the envelope is 250×9 mm^2. Figure 3.9 shows four assembled together glass RPCs placed on one readout plane.

Readout consisted of flat cables glued to a printed circuit board (PCB) fiberglass sheet. The width of the pickup strips, around 1 cm, was determined by the granularity needed in the experiment; in this case, eight flat cable conductors were connected together and to each channel.

Compared to Bakelite RPCs, glass RPCs are sometimes considered to be more suitable for large-scale production because of their simplicity, which implies an important reduction in the manpower necessary for their construction. For instance, an important production of around 150 glass RPCs was recently

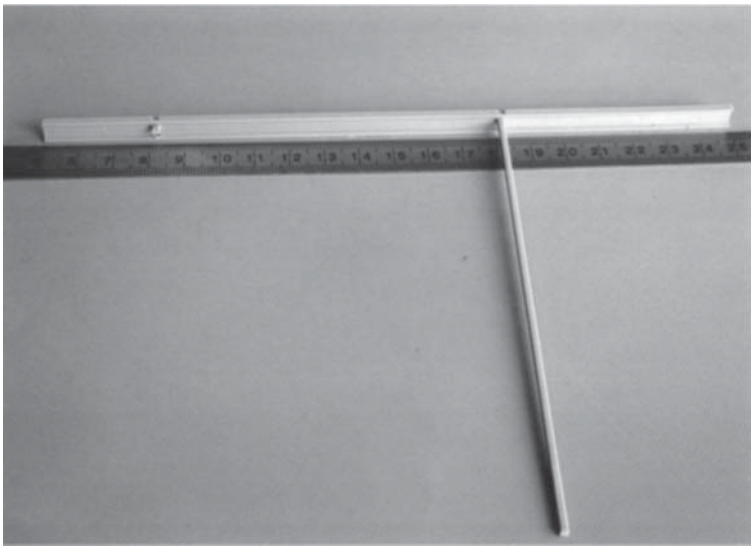

Figure 3.8 Photograph of a special shaped spacer placed between the glass electrodes and providing a channel for the gas to flow back and forth across the total area of the detector, as shown in Figure 3.6. Each such spacer consists of two sticks, 2 mm and 150 mm long, respectively, that are orthogonal to the 200-mm-long support structure. (Gustavino *et al*. 2001a. Reproduced with permission of Elsevier.)

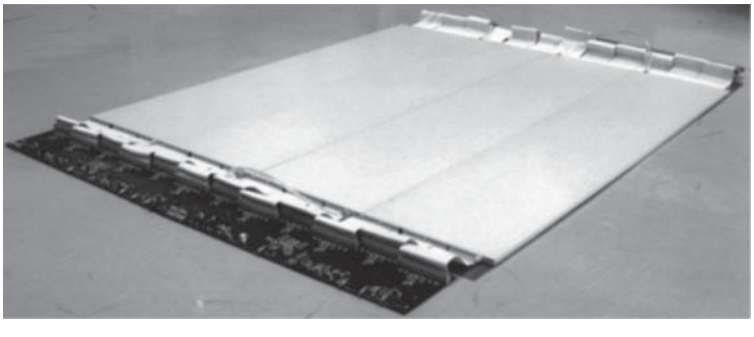

Figure 3.9 Photograph of four glass RPCs coupled to a readout plane based on flat cables.

performed by high-school teams of teachers and students, in the framework of the Extreme Energy Events experiment (Abbrescia *et al*., 2013).

Indeed, the glass electrodes do not need the inner surface treatment with linseed oil, and the graphite coating is often replaced by an adhesive foil, the spacers are assembled without gluing, and the HV contacts are realized without soldering. Another advantage is the use of an envelope for the gas containment instead of a glued frame between the electrodes, which could reduce the occurrence of gas leakages.

Glass RPCs, due to their relative high resistivity and thus limited rate capability, were used basically in cosmic ray experiments, like, for instance, the OPERA experiment (Candela *et al*., 2007), but found important applications in accelerators too, where the rate requirements were not so compelling like, for instance, at BELLE (Abashian *et al*., 2000).

3.4 Avalanche and Streamer Modes

3.4.1 Streamer Mode

In Chapter 1 we qualitatively described the avalanche-to-streamer transition. This phenomenon was studied in detail by many authors and the basic results are summarized in a famous book by Raether (1964). As already pointed out, one of the main conclusions is that sparks appear when the total charge in the avalanche is close or exceeds 10^8 electrons (the so-called Raether limit). Oscillograms of the signals from a parallel plate chamber with metallic electrodes during the avalanche-spark transition in methylal are shown in Figure 3.10, taken from his book.

In Figure 3.10, one can clearly see a first pulse related to the primary avalanche (called "precursor"), followed, after some delay time τ_b, by a much more intense signal, a current rapidly growing – which is related to the streamer almost

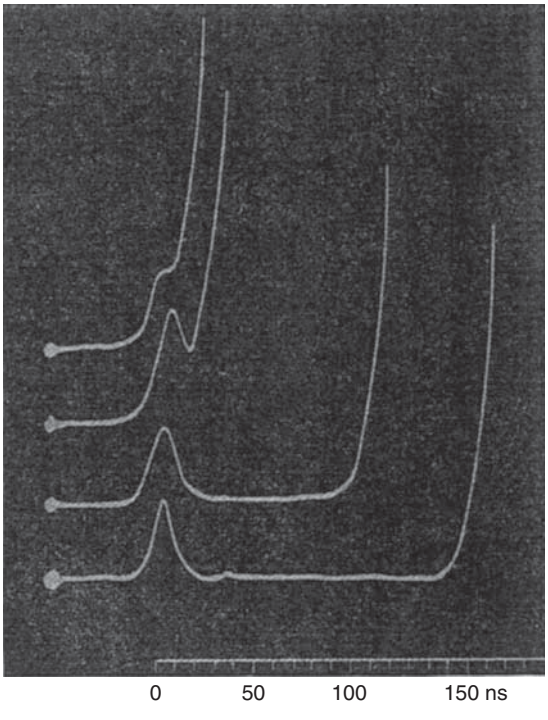

Figure 3.10 Oscillograms of the current related to a static breakdown in methylal at various voltages (increasing from the lowest to upper curves) in a metallic parallel plate chamber. (Raether 1964. Reprinted with permission of CERN.)

immediately transforming to sparks. The very same behavior was observed in many other gas mixtures in non-pulsed gaseous detectors (like parallel plate avalanche chambers (PPACs); for more details, see Fonte *et al.* (1991a), indicating that this is a quite general sequence of processes. The time τ_b reduces as the voltage is increased (which, in the case of the Figure 3.10, happens from the bottom to the top), so that at some voltage the avalanche pulse is hardly separated from the rising edge of the streamer (see, for instance, the upper curve in Figure 3.10).

Later studies demonstrated that streamers transit to sparks via several fast intermediate discharge stages: from a glow discharge to a dense plasma channel as shown schematically in Figure 3.11a (from Haydon, 1973). In the case of a

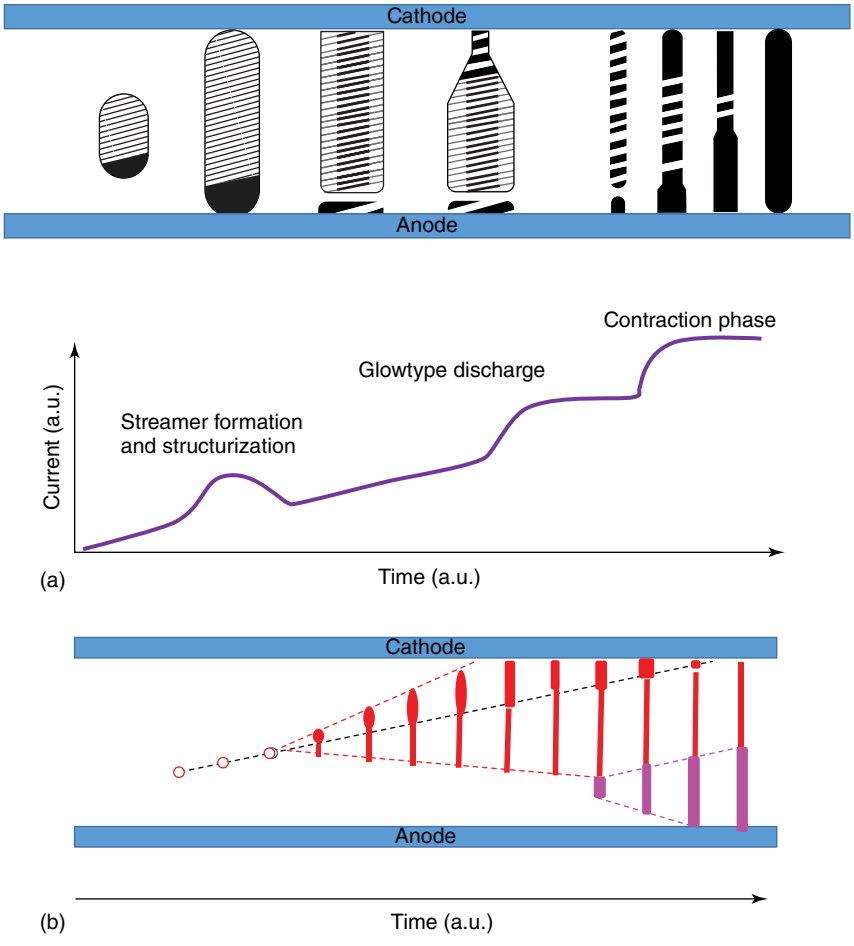

Figure 3.11 Schematic of streamer development: (a) various intermediate stages and corresponding current versus time during the streamer to the spark transition and (b) streamer contraction effects appearing with further overvoltage increase. The horizontal axis is time. Several authors made attempts to calculate the dynamic of the avalanche-to-spark transition (see, e.g., Fonte, 1996 and references therein), which is a complex process and cannot be easily modeled. (Adapted from Fonte 1996.)

large enough overvoltage, as was mentioned in Chapter 1, the streamer starts propagating simultaneously in both directions: toward the anode and toward the cathode.

According to a generally accepted terminology, by "overvoltage" we mean here the voltage above the maximum DC voltage at which the gap is still stable. This is also relevant for poorly quenched gas mixtures (where UV photon absorption is not so relevant), which undergo breakdown via the feedback mechanism (as described in Chapter 1): through a generation of secondary avalanches.

Let us now pass on to some considerations about what is known on avalanche-to-discharge transition in the case of the RPCs. This transition process has been studied in several works. As an example, some results taken from Cardarelli *et al*. (1996) are shown in Figure 3.12. Similar to Figure 3.10, two signals can be observed: the first produced by a primary avalanche and the second appearing after some delay (decreasing when increasing the applied voltage), corresponding to the discharge triggered by the streamer. As can be seen, at the larger values of the applied voltage the avalanche almost merges with the subsequent streamer, so that they cannot be distinguished one from the other anymore (Figure 3.12c).

The authors of the publication refer to this RPC operation mode as "streamer mode," using a terminology quite common in the RPC community. As already pointed out, this terminology cannot be considered as completely precise: the streamer reaching the resistive cathode is not self-quenched, and, on the contrary, it causes a low current discharge. Systematic tests of various resistive cathodes of RPCs performed with XCounter AB Sweden (in which one of the authors of this book, Vladimir Peskov, participated) reveal that in most of the cases the discharge current is limited by the resistivity of the cathode material, proving that the streamer initiates a short living low current discharge. The power dissipated by such a discharge depends also on the gas mixture. For example, in mixtures with electronegative gases (reminder: gases that tend to capture free electrons in the gas mixture) the discharge in the RPC typically has a lower current compared to other mixtures.

One can expect that in RPCs, in a way very similar to what happens in parallel-plate chambers with metallic electrodes, the transition from avalanche to streamer takes place when the avalanche size has reached (or overcome) the Raether limit. Indeed, this was confirmed by studies performed in Cardarelli *et al*. (1996). Their results related to these studies are shown in Figure 3.13.

For any recorded waveform, the authors evaluated the charge induced on the readout electrode by integrating the amplitude profile of the current measured on the same electrode with respect to time. As can be seen from Figure 3.13, at voltages around 9.2 kV corresponding to an induced fast charge in the avalanche about 1 pC (around 10^7 electrons), the curve for the precursor charge signal (lower curve) exhibits a clear knee and its slope becomes lower. Above this critical charge, streamer signals appear (upper curve). Note that the exact value of the transition from avalanche to streamers depends on several parameters: the width of the avalanche gap, gas composition, and so on. Note also that the 1 pC value refers to the charge induced on the readout electrodes, which is typically a factor 5–20 times less than the total electron charge impinging on the anode (which,

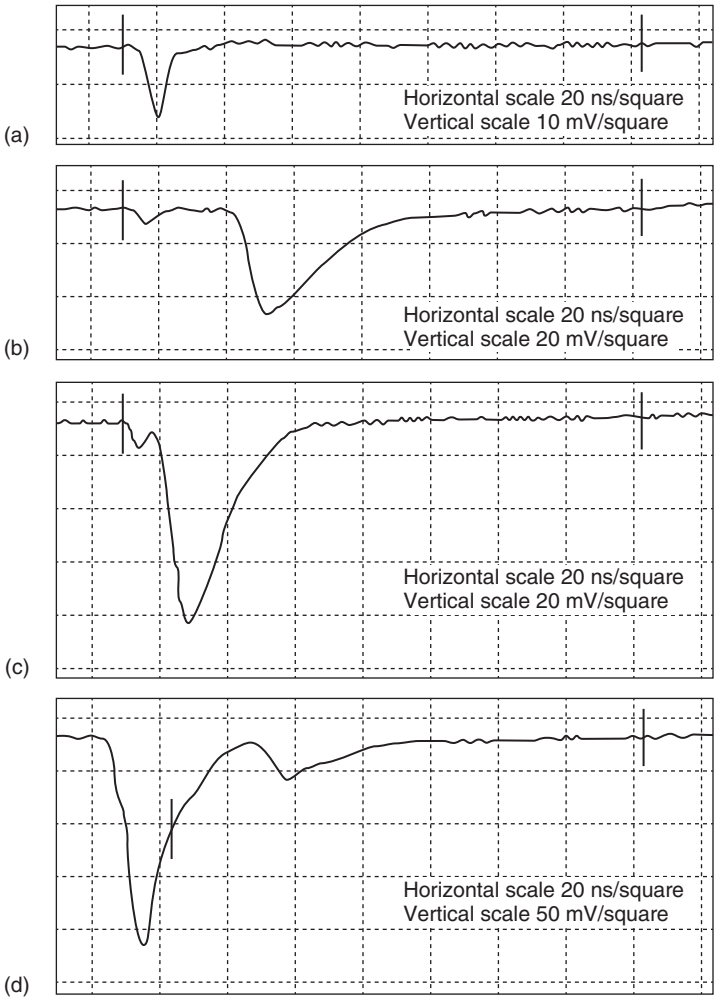

Figure 3.12 Signal waveforms recorded with an RPC operating in Ar/*n*-C_4H_{10}/$C_2H_2F_4$ (10/7/83 in volume) at gradually increasing operating voltages: (a) 9.4 kV, (b) 9.6 kV, (c) 10.2 kV, and (d) 14.0 kV. In panel (c) also, the secondary discharge, delayed about 50 ns with respect to the primary avalanche and the primary discharge, is visible. This is one of the first observations of this behavior in RPCs. (from Cardarelli *et al*. 1996. Reproduced with permission of Elsevier.)

therefore, is very close to the 10^8 electrons of the Raether limit). This relation between induced charge and charge contained in the avalanche is demonstrated in Section 3.5.

At this time, it is relevant to better clarify what an integrated fast signal is. A typical charge signal from an RPC as a function of time is shown in Figure 3.14. It has two components: a fast one (3–20 ns wide for gas gaps from 0.3 to 2 mm) related to the collection of the avalanche electrons and a slow one, lasting up to several microseconds, induced by the movement of the avalanche positive ions toward the cathode. In RPCs, to profit from its excellent timing characteristics,

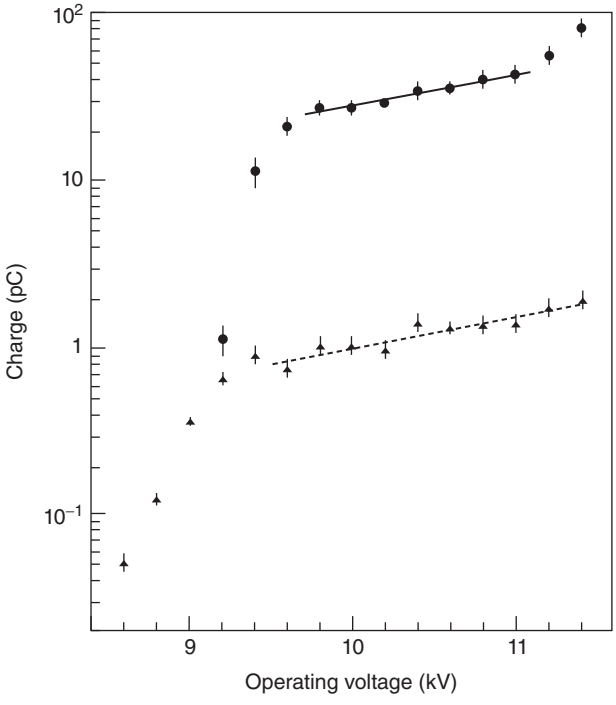

Figure 3.13 Integrated precursor charge signal (lower curve) as a function of the voltage for the RPC having a 2-mm gap between electrodes and operating in Ar/*n*-C_4H_{10}/$C_2H_2F_4$ (in ratios 10/7/83 in volume). Up to 9.2 kV signal amplitude has an exponentially growth; then, above 9.2 kV, a strong signal saturation is visible, presumably due to the space-charge effect (see Section 4.4). At the same time, discharges accompanying the streamer development appeared (upper curve). (from Cardarelli *et al*. 1996. Reproduced with permission of Elsevier.)

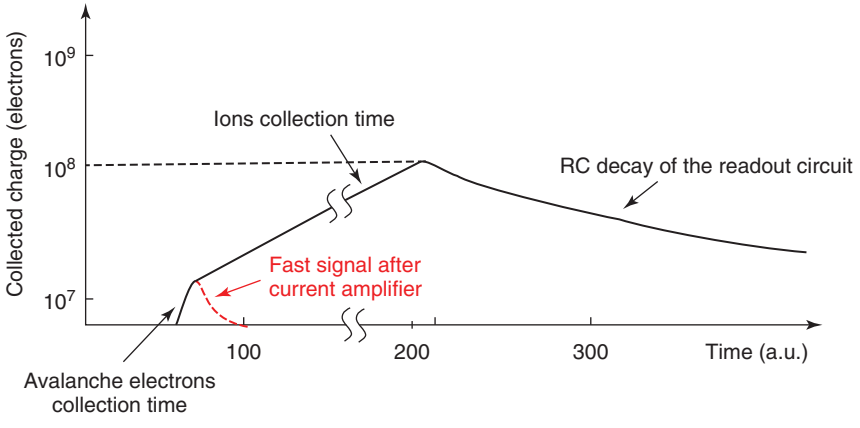

Figure 3.14 Schematic representation of a charge signal from an RPC as a function of time. Two signal components, fast and slow, are clearly seen. With a current amplifier, the fast component is usually recorded. The integrated charge in the fast component contains only 5–20% of the total signal charge. This qualitative picture refers to the case of the RC time constant of the readout circuit, much larger than the ion collection time.

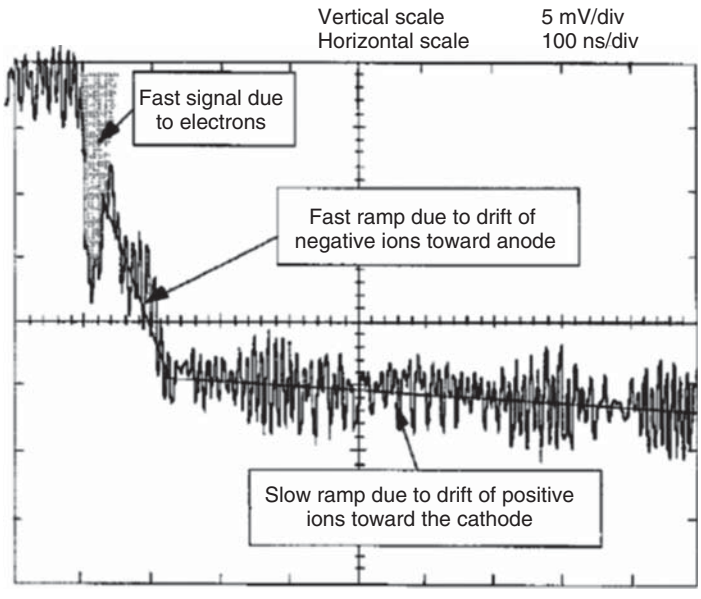

Figure 3.15 RPC signal on expanded time scale. (Cerron Zeballos *et al*. 1997. Reproduced with permission of Elsevier.) The authors of the work attribute the first fast signal to the movement of the electrons, the fast ramp to the movement of the negative ions, and the slow ramp (almost flat on this time scale) to the drift of the positive ions. Note that this waveform refers to RPCs operated in avalanche mode, which will be explained in more detail in Section 3.4.2.

usually the fast signal is recorded with the help of an appropriate current amplifier. As can be seen from Figure 3.14, the integrated charge of the fast electron signal at the moment when the transition to a streamer occurs is around 10^7 electrons. Moreover, in the figure, it is in evidence that the fast component is typically from 5% to 20% of the total signal charge. Hence, the transition to streamer happens at a total charge of about 10^8 electrons, which is close to the Raether limit.

Note that, in principle, also the negative ions formed in the avalanche induce a signal on readout electrodes; however, this is quite difficult to be observed in practice. Authors of the work (Cerron Zeballos *et al*., 1997) speculate that under some conditions they can distinguish in the slow signal component the motion of negative ions from the motion of positive ions (see Figure 3.15).

3.4.2 Avalanche Mode

Sometime after the invention of RPCs, some interest in operating these devices in avalanche mode arose, related mainly to the issue of increasing their rate capability in order to use them at the Large Hadron Collider experiments which, at the time, were at the design phase. Operating RPCs in avalanche mode had the advantage of reducing the charge traveling inside the gas gap, which is a direct benefit for increasing the rate capability. The drawback was that, being the relative signals

smaller, they required pre-amplification (and therefore a more sophisticated front end electronics) before subsequent processing.

Several independent publications on this subject appeared almost at the same time and we review them following the chronology of their submissions to the publisher. In Cardarelli *et al*. (1993) it was observed that electronegative components, such as some kind of Freon, added in large fractions to the RPC gas mixture, had an effect of reducing the size of the signal induced on the readout strips (see Figure 3.16).

This is not astonishing if one remembers that Freon is an electronegative gas and therefore some avalanche electrons can be captured by the Freon components forming slow drifting electronegative ions (see Figure 3.17). This effect reduces the amount of free electrons in the gas (for a detailed explanation, see Doroud *et al*., 2009).

A nice experimental demonstration of the electron capture effect and how the electron capture affects the amplitude of the signal fast component of the signal was done in the work by Cerron Zeballos *et al.*, (1995). Signals recorded with a charge-sensitive amplifier are shown from an RPC flushed in sequence with mixtures containing different amount of electronegative components are shown in Figure 3.18. In the upper plot, the gas has no Freon additives. As it was explained

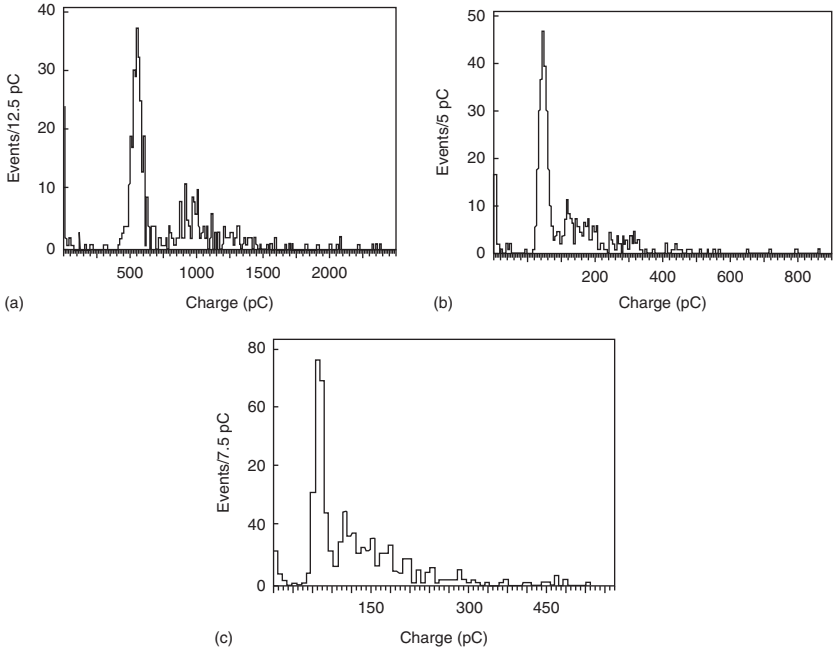

Figure 3.16 Cosmic rays signal charge distributions, for different amounts of CF_3Br (commercially known as Freon 13B1): (a) 0%, (b) 4%, and (c) 8% – added to an Ar/isobutane mixture (60/40 in volume). The operating voltages in these measurements were 7.2, 7.2, and 7.8 kV, respectively. (Cardarelli *et al*. 1993. Reproduced with permission of Elsevier.)

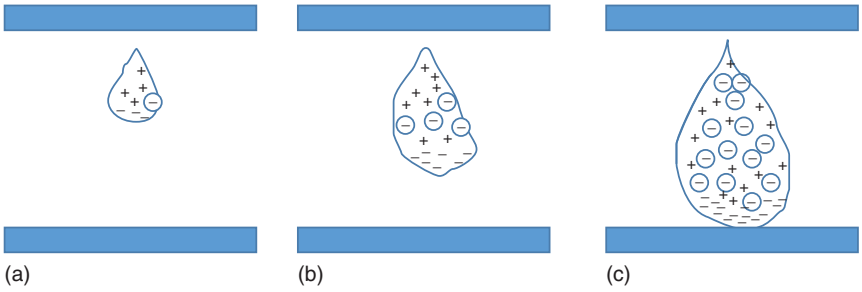

Figure 3.17 Schematics of the avalanche structure in electronegative gas mixtures for three specific moments: (a) the avalanche has just started its development, some electrons are captured and form electronegative molecules (circles with negative sign inside), (b) a medium-size avalanche is formed, and (c) the avalanche head reaches the anode: a signal fast component is determined by the motion of electrons, whereas negative ions contribute to the slow signal.

earlier (see Figure 3.14), the first signal (a step) is generated by the movement of avalanche electrons, whereas the slow ramp is due to the drift of the positive ion cloud. The oscillogram in the middle corresponds to the case when the gas mixture contains CF_4, which is not as electronegative as are other Freons. The fast step becomes slightly smaller. The low sweep is for the gas containing 10% of Freon (CCl_2F_2). The fast step can no longer be observed. It can be seen therefore that the ratio of the fast to the slow component of the signal is essentially different if Freon is part of the gas mixture. One should note, however, that the ratio fast to slow component depends on several factors (see again Cerron Zeballos *et al*., 1997; Doroud *et al*., 2009).

In later publications (see, e.g., Cardarelli *et al*., 2012) Cardarelli *et al*. refer to Figure 3.16 as the first observation of the avalanche mode, although, strictly speaking, it was not clearly stated in that particular paper.

Pure avalanche mode of the RPC operation was reported in three works, all submitted in September 1993 (Anderson *et al*., 1994; Crotty *et al*., 1994; Duerdoth *et al*., 1994). As an example, in Figure 3.19 a typical signal from an RPC, not followed by the discharge and thus operated in "pure" avalanche mode, is presented.

Of course, when the voltage was increased, the appearance of mild discharges following the primary avalanche was observed, indicating the end of the pure avalanche mode (see Figure 3.20).

As mentioned, similar results, but obtained in other gases and with different designs of RPCs, were obtained in parallel works (Duerdoth *et al*., 1994; Crotty *et al*., 1994).

Pulse amplitudes for pure avalanche mode and for "streamer" mode are shown in Figure 3.21. The avalanche pulses reached a maximum charge corresponding to the charge required to trigger the transition to a streamer. It can be seen that, contrary to what is observed for the proportional pulses, the charge of the streamer pulses at a given voltage is strongly dependent on the fraction of Freon in the mixture. In all concentrations, the total charge of the streamers continues to grow

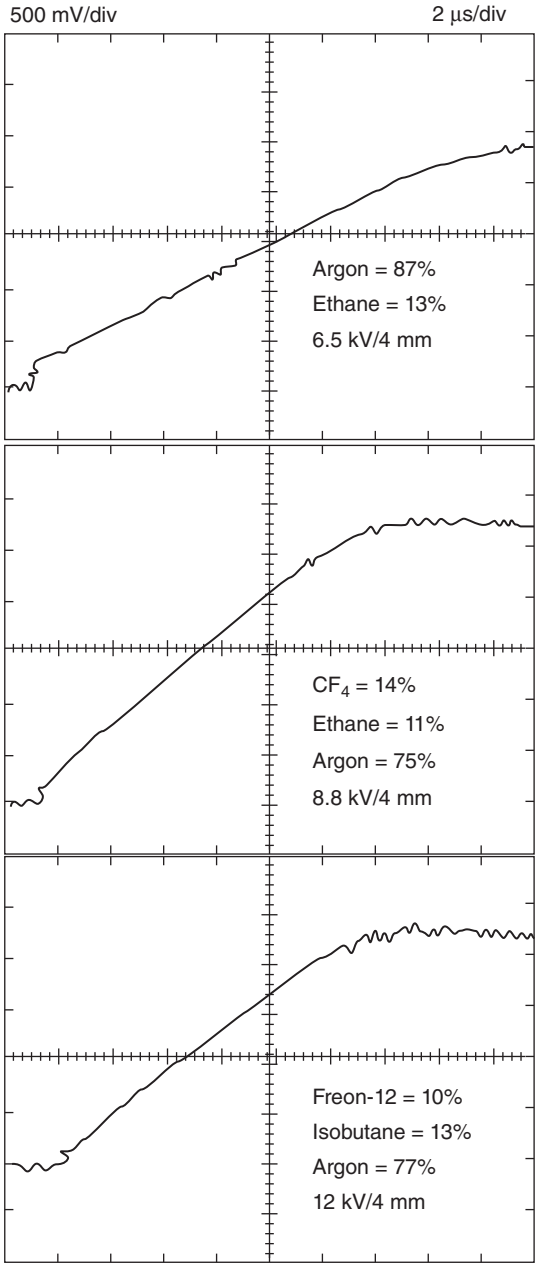

Figure 3.18 Signal oscillograms from a single-gap RPC (4-mm gap) observed with a charge-sensitive amplifier in gas mixtures containing various concentration of electronegative components; the amount and type of the Freon used is indicated in the insertions. (Cerron Zeballos 1995. Reproduced with permission of Elsevier.)

with the applied voltage; the authors of the paper (Duerdoth *et al*., 1994) attribute it, partially, to the increasing amount of after-pulses, that is, secondary discharges following the first.

As mentioned earlier, one of the main advantages of the avalanche mode is that it allows reaching higher rate capability, that is, RPCs operated in this way can efficiently detect ionizing particles even when the flux is relatively high, as can be

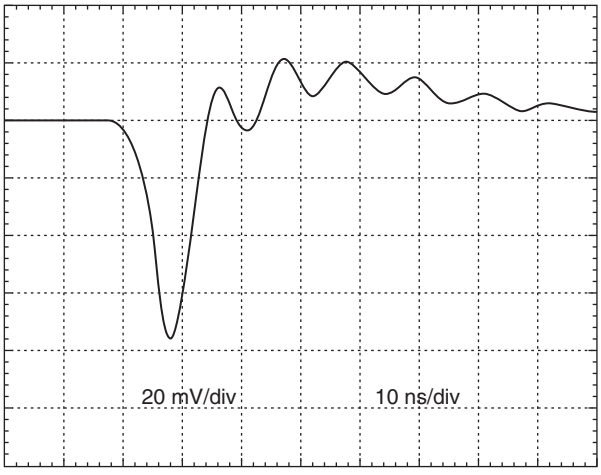

Figure 3.19 Typical signal recorded with a fast Ortec amplifier from the RPC operated in pure avalanche mode in Ar + 10% isobutene at a total pressure of 1 atm. (Anderson *et al*. 1994. Reproduced with permission of Elsevier.)

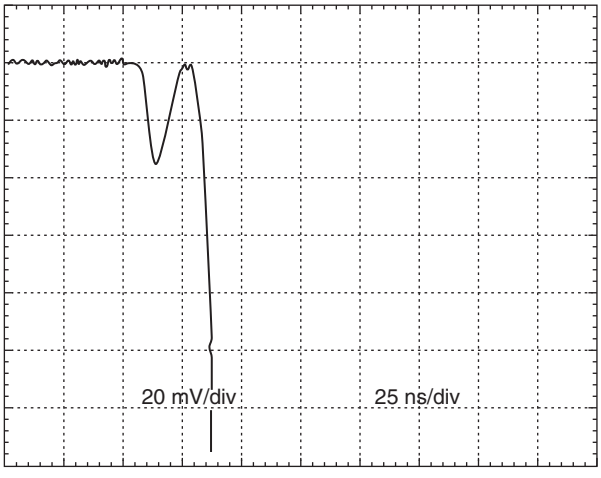

Figure 3.20 Typical oscillogram of the signal recorded at elevated voltage when one can observe a primary avalanche followed by a mild discharge (often called a "streamer"). (Anderson *et al*. 1994. Reproduced with permission of Elsevier.)

clearly seen from Figure 3.22. For this reason nowadays, most RPCs are exploited in avalanche mode; this issue is discussed in detail later on in this book.

3.5 Signal Development

3.5.1 Signal Formation

In the following, some simplified analytical calculations suitable to understand in more detail what happens in an RPC at a fundamental level and how the relative

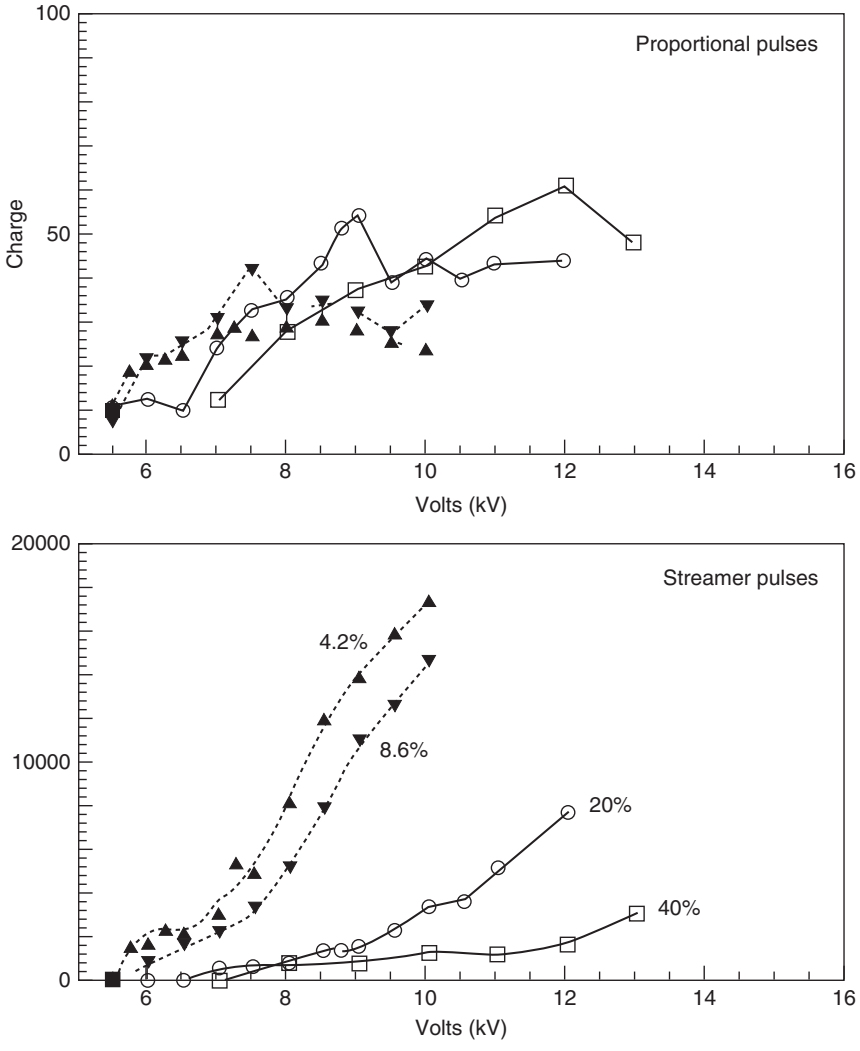

Figure 3.21 Total charge (in arbitrary units) versus the applied voltage applied to an RPC for two cases: pure avalanche mode (marked in the figure as "proportional pulses") and for the "streamer" operational mode (marked in the figure as "streamer pulses"). Gas mixtures were argon/isobutane (with constant ratio of 60/40) based, with the addition of Freon content varied from 4% to 40%. (Duerdoth *et al*. 1994. Reproduced with permission of Elsevier.)

signal develops and is induced on readout electrodes are reported. These calculations, although simple in principle, are not trivial, and in fact about 10 years passed since RPC invention before the basic formulas were written down and the first conclusions drawn. One of the most simple and general approaches, which starts from the basic processes taking place in the gas, to end up with the modeling of RPC performance and the prediction on how it depends on its constructive parameters is described in Abbrescia *et al*. (1999a). Another nice paper which basically exploits the same approach is Riegler *et al*. (2003). We believe that

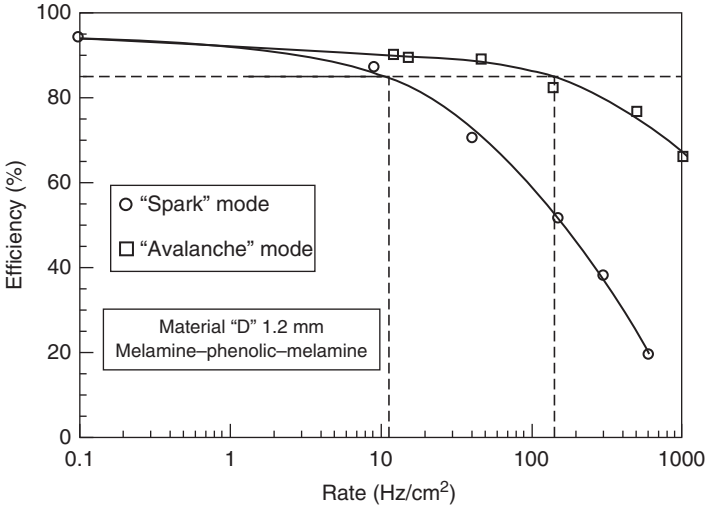

Figure 3.22 RPC efficiency versus the counting rate for avalanche and spark modes. The gas mixture is 81% Ar, 13% isobutane, 6% Freon-12. (Crotty *et al*. 1994. Reproduced with permission of Elsevier.)

following the underlying ideas of this approach can give interesting insights into how RPCs work and allow understanding them at a deeper level.

As usual, let us start considering a single-gap RPC whose gas gap is traversed by an ionizing particle, which generates n_{cl} ion-electron clusters along its path. For "cluster" here, we intend a primary ion-electron pair, directly generated by the impinging particle, plus the additional pairs that can be generated by the primary electron in case it has enough kinetic energy to further ionize the atoms or molecules in the gas mixture. Note that the number of clusters n_{cl} following the passage of an ionizing particle, of course, is not fixed, but its actual value changes from event to event according to a certain probability distribution. We say that n_{cl} is a stochastic variable; it depends linearly on the gas thickness g crossed by the particle.

Values for the average value of the number of clusters per unit length, which here will be indicated with λ, have been measured experimentally for many gases and can be found in the literature; in case of gas mixtures, the value for λ is the weighted average of the ones corresponding to the gas mixture components (and the weights are the gas fractions). Note that dedicated software exists, like, for instance, HEED that can be used to compute or retrieve this, and other relevant gas quantities (for details, look at Smirnov, 1994).

In the gas mixtures used for RPCs, λ depends significantly on the gas mixture used. For instance, in argon and isobutane typical accepted values are 2.5 and 9 clusters/mm, respectively. For the gas mixture used at two of the LHC experiments, ATLAS (a toroidal LHC apparatus) and CMS (compact muon solenoid), made out of $C_2H_2F_4/iC_2H_{10}/SF_6$ in 95/4.7/0.3 proportions, a value around 5.5 clusters/mm, giving rise to 11 ion/electron pairs, on the average, in the 2-mm gas gap of the RPCs, has been used for a long time (and still it is).

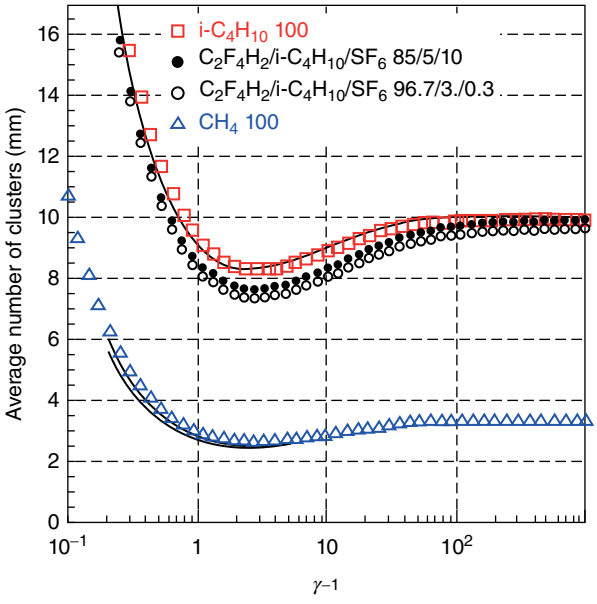

Figure 3.23 Average number of cluster/mm for different gases as a function of the particle energy, as simulated by HEED. (Riegler *et al*. 2004. Reproduced with permission of Elsevier.)

Note that later on it was found out that HEED simulations would point to a value slightly higher, around 7 clusters/mm (see Figure 3.23), and this would help explain some of the features observed, even if some debate is still ongoing.

λ depends, in general, on the energy of the impinging particle. Here, for the sake of simplicity, we will suppose that the energy lost by the particle crossing the gas gap (which typically is on the order of hundreds of electron volts) is negligible with respect to its kinetic energy; this is quite a common case; for instance, this assumption is generally true in most cosmic ray experiments, or the muon systems of the LHC experiments. In this case, we can safely assume that the kinetic and total energy of the impinging particle, and consequently the primary ion/electron pair density λ (i.e., average the number of primary ion-electron clusters per unit length) is constant throughout the particle path in the gas gap.

In case the particle is crossing the RPC gas gap not perpendicularly, we will also define $\lambda_{\text{eff}} = \frac{\lambda}{\cos\varphi}$, where φ is the azimuthal angle of the track of the incident particle ($0 \leq \varphi < \pi/2$), and which will be used in the following.

Given these assumptions, the probability P_{cl} that k ion/electron clusters are generated in the gas gap (whose width is indicated with g) by an ionizing particle can be computed by simple binomial statistics; the following result is obtained (Poisson's distribution):

$$P_{\text{cl}}(n_{\text{cl}} = k) = \frac{(g\lambda_{\text{eff}})^k}{k!} e^{-g\lambda_{\text{eff}}} \tag{3.3}$$

As expected, the average value of this probability distribution is simply $g\,\lambda_{\text{eff}}$, that is, simply the average number of cluster per unit length multiplied by the track length.

Moreover, the probability $P(n_{cl} = 0)$ that not one single cluster is generated in the gas gap by the passage of an ionizing particle is easily computed from the above mentioned formula by putting $n_{cl} = 0$, and is given by

$$P_{cl}(n_{cl} = 0) = e^{-g\lambda_{eff}} \tag{3.4}$$

Equation 3.4 is important since it expresses the intrinsic inefficiency of a gaseous detector, and its value imposes limits on the thickness of the gas layers used if one wants to build a detector with a reasonable efficiency. Just as an example, by assuming $\lambda = 5.5$ cluster/mm, and a gas gap thickness $g = 0.2$ mm, Equation 3.4 would result in an intrinsic inefficiency around 11%. These very simple considerations, therefore, give an immediate hint on how to design these kinds of particle detectors, and why certain values are used as typical dimension (for instance, gap thickness on the order of 1–2 mm).

Let us now consider the dimensions of the clusters, in terms of the number of ion/electron pairs contained in each cluster. The number of free electrons in a cluster (and, of course, the number of ions) follows a probability distribution that has been experimentally measured for very few gases (Ar, CO_2, some hydrocarbons, etc.) (Fischle *et al*., 1991) (see Figure 3.24). Of course, it depends on the average energy deposited in the interaction, and on the fluctuations around this average energy. Generally, the secondary electrons in the cluster are quite close in space to the primary electron. In the cases where the primary electron is quite energetic (these are also commonly called "*delta rays*"), the number of electrons in the cluster can be correspondingly high, reaching even 100 or more, and the electrons can be scattered over large distances. However, these are rare cases.

It has been found that a reasonable approximation for the experimentally observed cluster size distributions (and the ones computed by a complex modeling of the energy deposited and the atomic or molecular levels) is provided

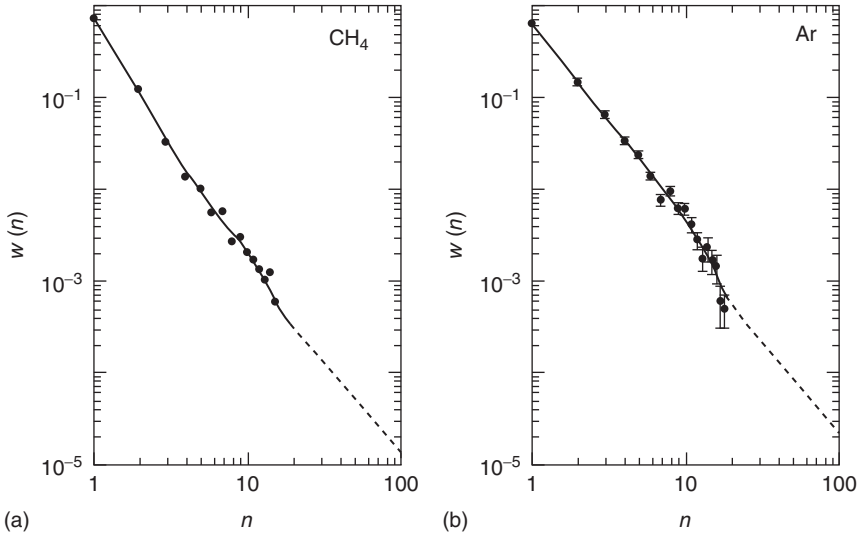

Figure 3.24 Experimental ionization cluster size for (a) methane and (b) argon. (Fischle *et al*. 1991. Reproduced with permission of Elsevier.)

by a simple $1/n^2$ law, which is often used as a reasonable approximation. Also, interesting theoretical studies about cluster size have been performed, like the one, for argon, reported in Lapique and Piuz (1980).

Let us now pass on and consider how the primary clusters are spatially distributed in the gas gap crossed by the ionizing particle. Let us denote with x_0^j the initial position of the jth cluster and let us consider the probability $P_{\mathrm{cl}}(x_0^j)$ of finding the jth cluster generated at a distance x from the cathode (usually, the convention, that we will follow here too, is to label the cluster generated closest to the cathode as the first ($j=1$), so $x=0$ corresponds to the position of the cathode surface facing the gas). This probability can be computed using Poisson statistics, which provides the following result:

$$P_{\mathrm{cl}}^j(x_0^j = x) = \frac{j\lambda_{\mathrm{eff}}}{(j-1)!}(x\lambda_{\mathrm{eff}})^{j-1}e^{-x\lambda_{\mathrm{eff}}} \quad 0 < x < g \tag{3.5}$$

Even if this formula could appear complex, the cluster's initial position distributions are quite simple and intuitive; for instance, the first cluster initial position, obtained by placing $j=1$ in Equation 3.5 follows a decreasing exponential distribution:

$$P_{\mathrm{cl}}^1(x_0^1 = x) = \lambda_{\mathrm{eff}}e^{-x\lambda_{\mathrm{eff}}} \quad 0 < x < g \tag{3.6}$$

and the average distance of the first cluster from the cathode is $\langle x_0^1 \rangle = 1/\lambda_{\mathrm{eff}}$, as expected.

The second cluster position will be distributed according to

$$P_{\mathrm{cl}}^2(x_0^2 = x) = x\lambda_{\mathrm{eff}}^2e^{-x\lambda_{\mathrm{eff}}} \quad 0 < x < g \tag{3.7}$$

which is characterized by a broad (Gaussian-like) peak and whose average value is $\langle x_0^2 \rangle = 2/\lambda_{\mathrm{eff}}$ with respect to the cathode, and so on.

Let us now consider the effect of a uniform electric field in the gas gap, due to an applied external voltage: the free electrons will start drifting toward the anode, while the ions will move toward the cathode. Since ion mobility in gases is usually about 3 orders of magnitude less than electron mobility, their average velocity will be about a factor 1000 less; therefore, for the moment we focus our attention on the signal induced by the electrons.

As already pointed out, if the electric field is intense enough, the electrons contained in the cluster will acquire enough kinetic energy to start avalanching. The simplest model of an avalanche is a pure exponential development (derived assuming a probability of producing secondary ionizations constant throughout the electron drift path). In this case, the charge contained in the avalanches at a certain position x (with respect to the cathode) will be given by

$$q(x) = \sum_{j=1}^{n_{\mathrm{cl}}} q_{\mathrm{e}}n_0^j M_j e^{\alpha^*(x-x_0^j)} \quad x_0^{n_{\mathrm{cl}}} < x \leq g \tag{3.8}$$

where n_0^j is the number of primary electrons contained in the jth cluster, α^* is the effective first Townsend coefficient (i.e., the first Townsend coefficient α minus the attachment coefficient η), q_{e} is the elementary electron charge and the meaning of M_j is explained just below. Note that this formula is only valid rigorously in

the region comprised in between the last cluster (the farthest from the cathode) and the anode, and in fact it is generally used to compute the avalanches charge when they impinge on the anode, that is, for $x = g$.

Another way to express Formula 3.8 is by rewriting it in terms of the time elapsed from the passage of the impinging particle (assumed to take place at $t = 0$) as

$$q(t) = \sum_{j=1}^{n_{\mathrm{cl}}} q_{\mathrm{e}} n_0^j M_j e^{\alpha^* v_{\mathrm{d}} t} = q_{\mathrm{e}} e^{\alpha^* v_{\mathrm{d}} t} \sum_{j=1}^{n_{\mathrm{cl}}} n_0^j M_j \quad 0 < t \leq \frac{g - x_0^{n_{\mathrm{cl}}}}{v_{\mathrm{d}}} \tag{3.9}$$

where we exploited the fact that the distance covered by the electrons in the gap after $t = 0$ is proportional to the module of the electron drift velocity v_{d}. In case $t > \frac{g - x_0^{n_{\mathrm{cl}}}}{v_{\mathrm{d}}}$ (which represents the time when the cluster closest to the anode arrives on its surface), one or more of the clusters have already impinged onto the anode, and therefore just the contribution of the clusters actually drifting in the gap at that time t should be taken into consideration. Formulas 3.8 and 3.9 are fundamental for further considerations, in particular for understanding charge spectra and efficiency in RPCs, and will be extensively used later on.

Deviations from this simple law will be considered later on, when effects related to space charge and avalanche saturation will be examined. The Townsend coefficient has been experimentally measured for many gases, also the ones interesting for RPCs (Colucci *et al.*, 1994) (see Figure 3.25), and can also be computed by means of dedicated software (Biagi, 1994) (see Figure 3.26).

In Formulas 3.8 and 3.9 M_j is introduced to take into account stochastic fluctuations in the avalanche processes; it being a statistical process, one has to expect deviations from the simple exponential growth. In a simplified model, valid for low values of the reduced electric field E/p (where p is gas pressure), the probability that n_e electrons are contained in the avalanche after a path length

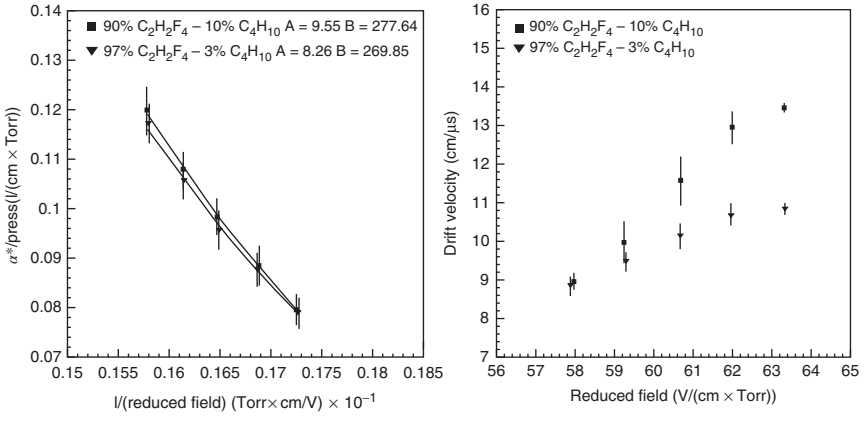

Figure 3.25 (a) Effective first Townsend coefficient and (b) drift velocity for a gas mixture containing $C_2H_2F_4$. (Colucci *et al.* 1994. Reproduced with permission of Elsevier.)

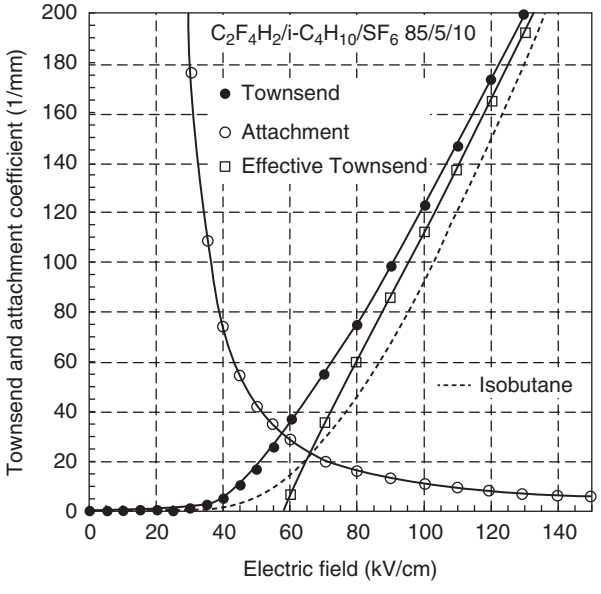

Figure 3.26 Townsend, attachment and effective Townsend coefficients at $p = 1$ atm, as computed by the IMONTE (Biagi, 1994) program. (Riegler *et al*. 2004. Reproduced with permission of Elsevier.)

$l = g - x_0$ is given by Furry's law:

$$P_{\mathrm{F}}(n_e) = \frac{1}{N} \exp\left(-\frac{n_e}{N}\right) \tag{3.10}$$

where $N = e^{\alpha^*(g-x_0)}$. This result, obtained long ago, at first glance is surprising since, according to this distribution, the most probable number of electrons in an avalanche is just 1, no matter the average gain. However, again, the significant value is its average value which, due to the fact that a decreasing exponential distribution, like the one in the previous equation, is characterized by a quite long tail toward high values, is still N.

Furry's law was extensively used for avalanches in drift tubes or multiwire proportional chambers (MWPCs); however, a typical operating voltage for an RPC is on the order of 10 kV on a 2-mm gap (the actual value depending on the gas mixture used). This has the consequence that the electric field in an RPC is much higher than the ones used in MWPCs, unless for the regions very close to the wires.

It has been demonstrated that in such cases of high values of E/p, a Polya distribution must be used in place of Furry's law. This is generally expressed by

$$P_{\mathrm{P}}(n_e) = \left[\frac{n_e}{N}(1+\theta)\right]^{\theta} \exp\left[-\frac{n_e}{N}(1+\theta)\right] \tag{3.11}$$

where the symbols have the same meaning as in Formula 3.10. θ is a parameter which is not easy to determine either by theoretical considerations or experimental measurements. Quite often a value around 0.5 is assumed. In case of a Polya

distribution, note that the most probable value is no longer one, and depends on the value chosen for θ. A nice overview of the different theoretical models and comparison with experimental data is reported in Genz (1973).

The factor M_j in Formula 3.6 or 3.7 are random numbers extracted from a Polya distribution; since this has an average value of N, they are renormalized by dividing them by N itself. In this procedure, we assume that the avalanches grow independently from each other.

At this point all the basic information about the development of the avalanches in the gas gap of an RPC has been given. However, what we are really interested in is not the avalanche size itself, but the signal that the avalanches induce on the readout electrodes. Note, in fact, that in an RPC (as well as in many other detectors) the signal does not derive from the actual electrons impinging on the anode or readout electrodes, but by their movement while they are still drifting in the gas gap.

The signal induced on the readout electrodes (being them strips or pads) is generally computed by using the Shockley–Ramo theorem (Shockley, 1938) and (Ramo, 1939), usually expressed with the help of the concept of the "weighting field" $\boldsymbol{E}_\mathbf{w}$. To compute this $\boldsymbol{E}_\mathbf{w}$ the readout electrode has to be (ideally) put at a "weighting potential" $V_w = 1$, while all the others at 0 (see Figure 3.27). The resulting field – calculated just as if we were computing an electrostatic field in these particular conditions – is the weighting field $\boldsymbol{E}_\mathbf{w}$ we are looking for (relative to the weighting potential V_w). The theorem states that the current induced on the readout electrode by a charge q has the following simple expression:

$$i_{\text{ind}} = q\boldsymbol{v}_\mathbf{d} \cdot \boldsymbol{E}_\mathbf{w} \tag{3.12}$$

where $\boldsymbol{v}_\mathbf{d}$ is its drift velocity. Note that, rigorously speaking, $\boldsymbol{E}_\mathbf{w}$ is given the dimensions of an inverse of a length, while V_w is a pure number, in order for Formula 3.12 to be dimensionally correct; here bold symbols are used to indicate vectors. The Shockley–Ramo theorem can be derived from the Green's reciprocity theorem, well known in electrostatics.

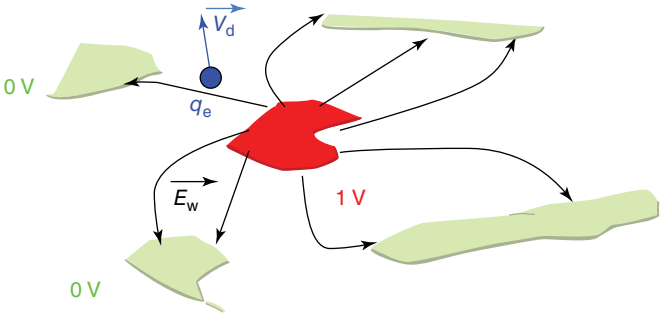

Figure 3.27 Conceptual sketch of how to compute the weighting field of the Ramo–Shockley theorem; the dark gray electrode is the readout (conceptually put at 1), the light gray ones are all the others (put at 0). The resulting field – computed like we were computing a standard electric field given these contour conditions – is the weighting field, that has to be scalarly multiplied with the charge drift velocity to compute the induced signal.

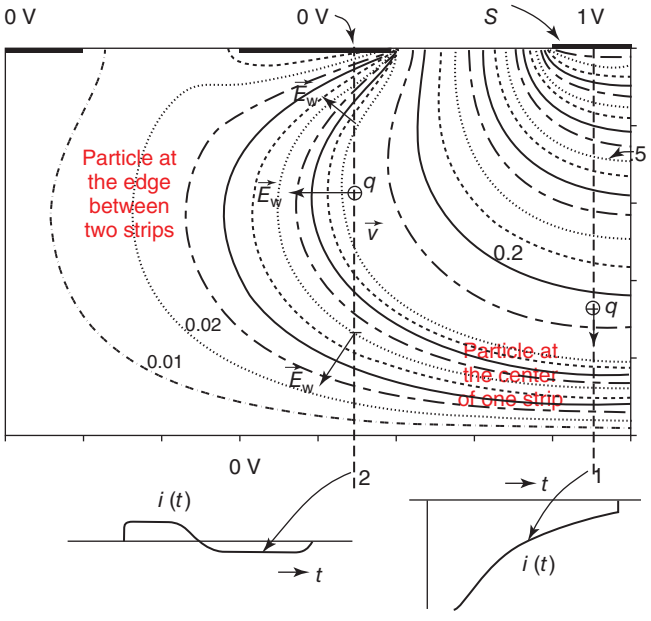

Figure 3.28 Equipotential lines for the weighting field for a parallel plate detector with readout strips. A charge moving close to the center of one strip perpendicularly to the electrodes (case 1 in the figure) experiences a field which is essentially parallel to its drift velocity, and therefore the induced signal on the readout strip *S* does not change sign. A charge moving in between two strips (case 2 in the figure) will experience in some regions a weighting field, making an acute angle with its drift velocity; and in some other regions an obtuse one, leading to an induced signal on the readout strip *S* of changing polarity.

In an RPC, $\boldsymbol{v_d}$ has a quite simple expression, being the electron drift velocity essentially perpendicular to the electrode plates and approximately constant. $\boldsymbol{E_w}$ can also be simplified if we consider that strip or pad dimensions are typically characterized by dimensions (on the centimeter order) much larger than typical gap dimensions (millimeter or lower). In these cases, for most of the volume in the gas gap, the edge effects on $\boldsymbol{E_w}$ between two adjacent strips or pads can be neglected, and $\boldsymbol{E_w}$ can be safely assumed uniform and, again, perpendicular to the electrodes (see Figure 3.28).

In this case, the module of the weighting field can be expressed as

$$E_w = \frac{\varepsilon_r}{\varepsilon_r g + 2d} = \frac{1}{g + 2d/\varepsilon_r} \tag{3.13}$$

and correspondingly the voltage drop ΔV_w from the cathode to the anode as

$$\Delta V_w = \frac{\varepsilon_r g}{\varepsilon_r g + 2d} = \frac{g}{g + 2d/\varepsilon_r} \tag{3.14}$$

where d is the electrode plate thickness and ε_r is the electrode relative dielectric permittivity. Here the electrode plate is considered to behave as a pure dielectric; this is true during a the time scale of few nanoseconds, characteristics of signal developments in RPCs. It is no more true when considering longer processes

like, for instance, electrode charging up after a discharge has taken place, which typically happens in a several milliseconds time duration.

Within these simplified assumptions, the current $i_{\text{ind}}(t)$ induced by the avalanches in the gas gap on the external pickup electrodes can be written as

$$i_{\text{ind}}(t) = \boldsymbol{v_d} \cdot \boldsymbol{E_w} \; q_e e^{\alpha^* v_d t} \sum_{j=1}^{n_{\text{cl}}} n_0^j M_j \tag{3.15}$$

This formula is quite useful, since $i_{\text{ind}}(t)$ contains basically most of the information coming out from an RPC. The charge q_{ind} induced on the external pickup electrodes can be computed by direct integration of the previous Formula 3.15, and is given by

$$q_{\text{ind}} = \frac{\varepsilon_r g}{\varepsilon_r g + 2d} \frac{q_e}{\alpha^* g} \sum_{j=1}^{n_{\text{cl}}} n_0^j M_j [e^{\alpha^*(g - x_0^j)} - 1] \tag{3.16}$$

In the next paragraphs we focus on what can be deduced, starting from these Formulas 3.15 and 3.16, about the charge distribution, efficiency, and time resolution, which are three fundamental aspects of RPC performance.

3.5.2 Charge Distribution

One of the most interesting things that can be computed following the approach described in the previous paragraph is the charge distribution that an ionizing particle crossing the gas gap on an RPC is expected to produce on an external readout electrode. There are sophisticated calculations starting from Equation 3.16 which predict the shape of such a distribution; however, since in Equation 3.16 many stochastic variables are present, in many cases, a Monte Carlo approach is followed.

As a starting point, the charge distributions for single-gap RPCs, characterized by a gap width of 2 and 9 mm, respectively, are reported in Figure 3.29 as computed by means of Monte Carlo techniques applied to Equation 3.16 (see Abbrescia *et al.*, 1999a for details). These correspond to two cases relevant from the historical point of view, since, at the beginning of 1990s, some debate was taking place regarding the best gap thickness to choose in single-gap RPCs; 2 mm corresponds to what was at the time considered a "narrow-gap" RPC, while 9 mm to what was generally labeled as a "wide-gap" RPC (which is discussed more in detail in Chapter 4). For this particular simulation, λ was assumed to be 5.5 clusters/mm in both cases, and the product $\alpha^* g = 9$; this product is roughly related to the gain in the gas gap.

The two sets of distributions differ significantly: in the narrow-gap case, the curves tend to diverge for $q_{\text{ind}} \to 0$; while in the wide-gap case, they tend to vanish. In other words, even if the average induced charge is roughly the same, the number of events characterized by small charge is greater in narrow gap with respect to wide gap RPCs. There is also an excess of events in the right tail of the distribution, counterbalanced by less events in the central part (with respect to the 9 mm). On the contrary, the curves for the wide-gap case vanish for charges close to zero.

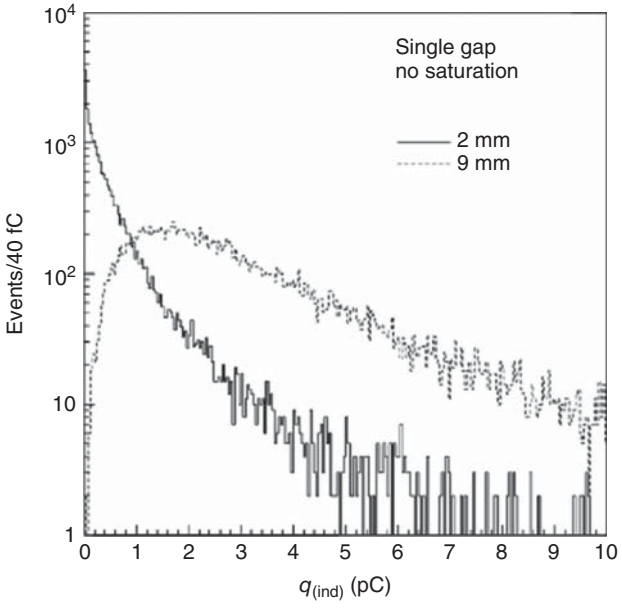

Figure 3.29 Simulated spectra of the induced charge, for a 2-mm single-gap RPC, compared to the same spectra but for a 9-mm single-gap RPC. (Abbrescia *et al*. 2001. Reproduced with permission of Elsevier.)

Essentially, the events with a charge less than certain electronic thresholds are the ones which are bound not to be detected, confused with the "electronic" noise (where we indicate with this term all the fluctuations around the baseline amplifier output voltage, due to multiple reasons). This implies that the shape of the charge distribution close to zero is fundamental to predict the efficiency the device will be able to reach given certain operating conditions.

As already pointed out, some hints about the basic features of RPC charge spectra can be obtained by means of analytical calculations, performed under simplifying assumptions.

As a simplifying approach, let us neglect the fluctuations in the number of electrons n_0^j contained in each cluster and in the gas gain, assuming both to be constant and equal to their average values. In this case, the charge q_{ind} induced by the drift of the jth cluster toward the anode is an analytical function of the initial cluster position x_0^j. Associated with x_0^j there is its probability distribution function (p.d.f.) $P^j_{q_{\text{ind}}}$, so the problem is reduced to compute the probability distribution of a function depending on a stochastic variable. This can be done applying directly the results of probability theory (see Abbrescia *et al.*, 1999a), and the final result is

$$P^j_{q_{\text{ind}}}(y) = R_j \left| \log\left(\frac{q_{\text{ind}}}{B_j}\right)^{j-1} q_{\text{ind}}^{\left(\frac{\lambda}{\alpha^*}-1\right)} \right| \tag{3.17}$$

where $B_j = \frac{q_e M_j n_0^j \Delta V_w}{\alpha^* g} e^{\alpha^* g}$, R_j is an appropriate renormalization constant, and y is the dumb variable used for the probability distribution just computed (see Abbrescia *et al.*, 1999a).

In the case $j = 1$ (the cluster closest to the cathode, which gives rise to most of the induced charge, given the fact that the corresponding avalanche has a longer path to cover towards the anode) the above formula reduces to

$$P(q_{\text{ind}} = q) = S_n q^{\frac{\lambda}{\alpha^*}-1} \tag{3.18}$$

where in the last expression the new renormalization constant S_n has absorbed all not-interesting factors, which are constant for a given operating voltage and gas used. It is interesting to note that the charge distribution depends just on the λ/α^* ratio, so that there are three cases of interest:

1) $(\lambda/\alpha^*) < 1$; in this case, the resulting distribution is strictly decreasing, and diverges for $q_{\text{ind}} \to 0$: this is the typical situation of a narrow-gap RPC.
2) $(\lambda/\alpha^*) \approx 1$; in this particular case, $P(q)$ is constant.
3) $(\lambda/\alpha^*) > 1$; in this case, the resulting distribution is strictly increasing, and starts at 0 for $q_{\text{ind}} = 0$: this is typical of a wide-gap RPC where, thanks to the large value of gap width g, α^* can be set conveniently low.

The fact that the ratio λ/α^* determines the shape of the charge distribution is not surprising: the two processes active in competition in the gap are cluster generation (ruled by $e^{-\lambda x}$, for the first cluster), and avalanche multiplication (ruled by $e^{\alpha^*(g-x_0^j)}$). A larger width of active gas is present in wide gaps, and this leads to higher efficiency. For instance, in a 2-mm gap, for a given threshold, the useful gas length to produce a visible signal is, roughly, 1.8 mm (depending on α^*), so that only 200 μm (or much less if α^* is small) are available to start one ionization process. In wide gaps, the useful gas length is a bit larger, since, though operating at smaller α^*, there are still a few millimeters left to produce ionizations. More considerations about wide-gap RPC are developed in Chapter 4.

Finally, note that the sum reported in Formula 3.16 can even be computed analytically taking into account the distribution of n_{cl} and x_0^j, yielding approximately a gamma distribution for the avalanche charge produced from a single ionizing particle (for details, see Fonte, 2013).

As already pointed out, when the gain in the gap is large enough, deviations from the simple exponential growth appear; these are due to the so-called space-charge effects, that is, distortions of the electric field experienced by the electrons in the avalanche due to the field generated by the ions and electrons of the avalanche itself. This is examined in detail later on in this book.

However even if all the results reported exclude space-charge effect, anyhow, notably, for unclear reasons, there is experimental evidence that the charge distribution in the presence of space-charge effects still follows a gamma distribution but with smaller variance Kornakov (2013) and Fonte (2013).

3.5.3 Efficiency

RPC efficiency can be computed by looking at the charge distribution close to zero, that is, counting the fraction of events which are under a certain electronic threshold.

As a start, and for the sake of simplicity, let us consider from Equation 3.16 just the contribution from only one cluster – in particular, the closest to the cathode;

in this case, the charge induced on an external pickup electrode has a simplified expression and is given by

$$q^1_{\text{ind}} = \frac{q_e}{\alpha^* g}\Delta V_w n^1_0 M_1 [e^{\alpha^*(g-x_0)} - 1] \tag{3.19}$$

For an event to be revealed – that is, distinguished with respect to the intrinsic noise of the system – its induced charge q^1_{ind} has to be greater than a certain electronic threshold q_{thr}, characteristic of the readout electronics (and higher than the system electronic noise). Only these events will account for the efficiency of the detector. Inverting Equation 3.19 we obtain that in order to satisfy this condition, the cluster we are considering has to be originated at a distance from the cathode less than:

$$x^1_0 < g - \frac{1}{\alpha^*} \ln\left(\frac{q_{\text{thr}}}{A_1} + 1\right) \tag{3.20}$$

where

$$A_1 = \frac{q_e \Delta V_w M_1 n^1_0}{\alpha^* g} \tag{3.21}$$

Recalling that the first cluster position x^1_0 is distributed according to a decreasing exponential, the probability that the above mentioned condition is satisfied is given by the integral of $P(x^1_0)$ between 0 and $g - \frac{1}{\alpha^*} \ln\left(\frac{q_{\text{thr}}}{A_1} + 1\right)$ This is, within these approximations, the efficiency of the chamber:

$$\varepsilon_c = 1 - e^{-\lambda\left[g - \frac{1}{\alpha^*}\ln\left(\frac{q_{\text{thr}}}{A_1}+1\right)\right]} \tag{3.22}$$

There are possible refinements to this formula (which was first reported in (Abbrescia *et al*., 1999b); for instance, one can consider that, given the statistic of cluster distribution, the first cluster is created at an average distance of $1/\lambda$ from the cathode, the second at $2/\lambda$, and so on. This implies that each cluster induced a charge, on the average, which is a factor $e^{-\alpha^*/\lambda}$ with respect to the previous one. A 2-mm single-gap RPC is typically operated at $\alpha^* \sim 9\,\text{mm}^{-1}$ and therefore the ratio $q^{2\text{nd}}_{\text{ind}}/q^{1\text{st}}_{\text{ind}} = 0.2$, $q^{3\text{rd}}_{\text{ind}}/q^{1\text{st}}_{\text{ind}} = 0.04$, and so on. A simple approximation to include the fact that not just the first cluster is contributing to the efficiency can be done assuming that the total induced charge is roughly a factor ∼1.25 greater than the one resulting from Equation 3.19 (i.e., the factor A in the expression must be multiplied by 1.25). An example of the results is shown in Figure 3.30.

A similar approach is also reported in Riegler *et al*. (2003), where the underlying idea is that the RPC is considered to be efficient if the first cluster creates an avalanche that exceeds the threshold, or the first cluster happens to be attached and the second cluster exceeds the threshold, or the first and second clusters are attached and the third exceeds the threshold, and so on. In addition, it is assumed that the clusters contain only one electron and avalanche fluctuations are neglected. In this case, a closed expression for the efficiency can be computed, and the result is

$$\varepsilon_c = 1 - e^{-(1-\eta/\alpha)g\lambda}\left[1 + \Delta V_w \frac{\alpha - \eta}{q_e} q_{\text{thr}}\right]^{\lambda/\alpha} \tag{3.23}$$

with the meaning for the symbols already used.

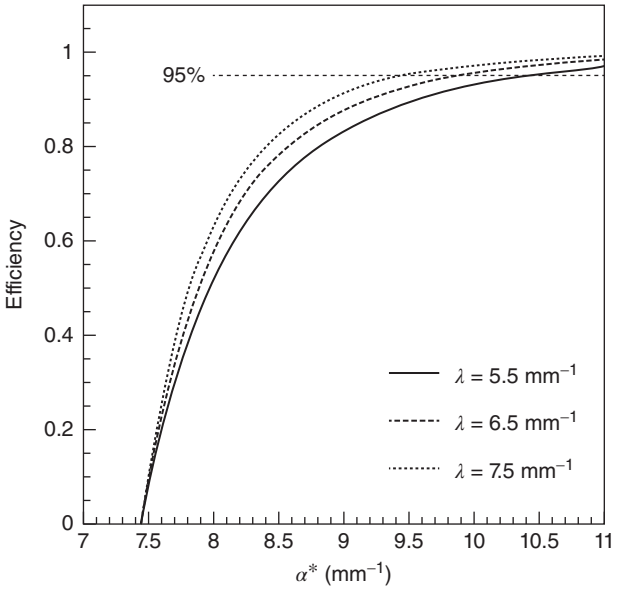

Figure 3.30 Simulated single-gap RPC efficiency versus the effective first Townsend coefficient for three values of the average number of clusters λ generated by the passage of an ionizing particle. (Abbrescia *et al*. 1999b. Reproduced with permission of Elsevier.)

3.5.4 Time Resolution

Time resolution can be computed using these formulas as well. A useful simplified approach is reported in Riegler *et al*. (2003). The idea is to start considering the signal – this time in terms of induced current – of a single primary electron somewhere in the RPC gas gap:

$$i_{\text{ind}}(t) = I_s e^{\alpha^* v_d t} \tag{3.24}$$

where I_s is the signal current amplitude, different from event to event, exponentially distributed around some average amplitude. The time t where the signal crosses a certain threshold I_{thr} is then given by

$$t = \frac{1}{\alpha^* v_d} \ln \frac{I_{\text{thr}}}{I_s} \tag{3.25}$$

By inverting this expression, and making the corresponding computations, one can obtain that the fluctuations on the crossing time t, that is, the RPC time resolution, is given by the simple formula:

$$\sigma_t = \frac{1.28}{\alpha^* v_d} \tag{3.26}$$

We therefore expect the intrinsic time resolution, on a first approximation, to depend only on the drift velocity and the effective Townsend coefficient and not on the threshold. This is also confirmed by a full Monte Carlo simulation, like the one whose results are reported in Figure 3.31. For a 2-mm RPC, the

above mentioned formula gives $\sigma_t \approx 1$ ns, while for a small gap, timing RPC, which is described in Chapter 4, it gives $\sigma_t \approx 50$ ps, in good agreement with experimental data. Intrinsic time resolution of RPCs is therefore dominated by the magnitudes of the effective Townsend coefficient and the drift velocity and is to the first order independent of the primary ionization parameters.

Later on, more refined approaches were developed by several authors, culminating in a very comprehensive treatment by Riegler (2009). Theoretical timing distributions were derived under simplified but useful conditions, including all intrinsic physical effects except the space charge effect (which is considered in detail in Chapter 4). Although the basic scaling mentioned remains valid, the timing variance is demonstrated to be a decreasing function of the variable $n_{av} = \frac{\alpha^*}{\alpha}\lambda g = \frac{\alpha^*}{\alpha} n_{cl}$, which is the average number of initiated avalanches, differing from n_{cl} in that there is a correction for the probability that the primary electron will be captured by the electronegativity in the gas. Therefore, some dependency on other parameters, for instance, λ, also holds. The value 1.28 mentioned holds in the limit $n_{av} \to 0$ (i.e., the case for a single primary electron, with negligible probability of a second one). The asymptotic behavior of the timing standard deviation is $\sim 1/\sqrt{n_{av}}$. Note, finally, that adding multiple gaps – that is, in the case of multi-gap RPC, introduced and described in detail in Chapter 4 – there will be, on the average, λg sub-avalanches in each of the N_g gaps. Since the signals coming from each gap sum up on the readout electrodes, this is basically equivalent to scaling λ proportionally to the number of gaps.

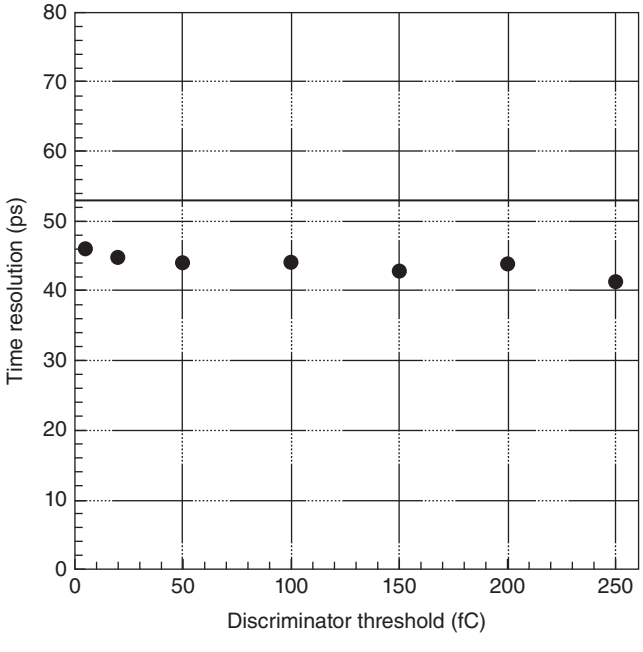

Figure 3.31 Full Monte Carlo simulation of time resolution versus electronic threshold, for a 300 μm RPC operated at 3 kV. The full line represent the value of the time resolution as computed from Formula 3.26 (Riegler *et al*. 2003. Reproduced with permission of Elsevier.)

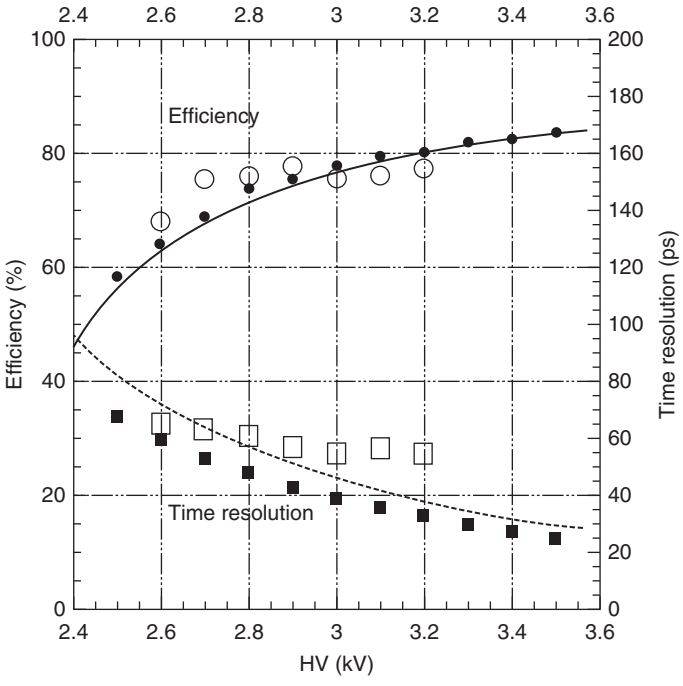

Figure 3.32 Simulated efficiency and time resolution, for a single-gap 300 μm RPC operated at 3 kV. (Riegler *et al*. 2003. Reproduced with permission of Elsevier.) Open points are experimental data, closed circles results from a full Monte Carlo simulation based on the principles described in the previous paragraphs. Also, the results from Equations 3.23 and 3.26 are overlaid.

These cited formulas, both for efficiency and time resolution, are extensively used to compute the expected performance of an RPC given its construction parameters, and they give results comparable to the experimental data (see, for instance, Figure 3.32), providing a useful tool to understand RPC detector physics and predict its performance.

3.5.5 Position Resolution

While most RPC implementations are read out by centimeter-scale wide strips that provide some modest avalanche localization capability (to be called here, for convenience, position resolution) by identification of the hit strip, applications (mostly) in muon tomography or biomedicine require a much better position measurement on both coordinates.

The main approach concerns the measurement of the induced charges in strip electrodes pitched on the millimeter range, attempting to recover the avalanche position from the observed charge profile, which is a historic method in gaseous detectors. It is possible to place the strips in perpendicular directions on each side of the chamber, achieving an, in principle, identical resolution on both coordinates of the (single) chamber plane. This symmetry is a capability of RPCs/PPCs that is unmatched by any other gaseous detector.

Although the distribution of the induced charges over any electrode shape can be calculated with some ease (see Chapter 4), there were also dedicated measurements of the charge distribution in strips (Narita 2010, 2012; Qite Li, 2012), addressing the corresponding position resolution.

The charge interpolation method when applied to RPCs with millimeter-scale strip pitch yielded position resolutions approaching 100 μm in one dimension under beam conditions (Aielli *et al.*, 2014). An alternative method, digital readout of very finely spaced strips, has shown resolution of 50 μm in a small prototype illuminated by collimated X-rays (Crotty *et al.*, 2003).

Chambers dedicated to muon tomography (see Chapter 9) demonstrated a bidimensional resolution better than 0.5 mm over the whole 1.06 m^2 active area, which was effective in identifying heavy materials (Baesso *et al.*, 2014). Another, 1.15 m^2, prototype has shown a resolution of 0.272 mm in a single spot illuminated by collimated X-rays.

The combination of accurate timing (see Section 4.6) and bidimensional position resolution has been also explored.

It is inherent in timing RPCs for time-of-flight (TOF) applications read out by strip electrodes (the alternative is by small pads as in HARP and ALICE TOF) that some bidimensional position resolution is available, determined transversally by the width of the readout strips and longitudinally by the measurement of the time difference of the signal propagation between both chamber ends. This is a function of the timing accuracy of the readout electronics for the measurement of the specific signal shape generated, but it is independent of the particle's TOF. This has been used in FOPI (Kiš *et al.*, 2011) and HADES (see Section 5.6). In the case of FOPI, a strip pitch of 2.5 mm yielded a transversal resolution better than 1.7 mm along with 1.53 cm in the longitudinal dimension.

A more specialized approach attempts to use thin strips in mutually perpendicular dimensions and charge interpolation, while keeping the signal propagation qualities required for good timing. In small areas (64 cm^2), simultaneous bidimensional position resolution well below 100 μm and timing resolution around 80 ps has been demonstrated by tracking cosmic rays over a large fraction of the active area (Blanco *et al.*, 2012) (see further description in Section 7.7). An ongoing related development in meter-square areas has reached 1.33 mm along with 150 ps by tracking cosmic rays over the entire active area of the detector (Assis *et al.*, 2016). Local resolutions of 250 μm and 65 ps have been demonstrated on a multichamber setup with an active area of 0.65 m^2 (Shi *et al.*, 2014).

3.6 Choice of Gas Mixtures

3.6.1 Main Requirements for RPC Gas Mixtures

The choice of the gas mixture for an RPC is, in general, a difficult task. This is not surprising, since the gas, in a certain sense, is the "core" of a gaseous detector, as are RPCs. In particular, RPCs require for efficient operation the use of gas mixtures with a somewhat demanding combination of characteristics:

A) High density of primary ion-electron clusters, to assure high detection efficiency; this depends on the particle energy deposition (that can be computed using the Bethe–Bloch formula), the average atomic number, density, and specific ionization potential of the gas mixture used;
B) Relevant "quenching" properties, that is, it should be characterized by low photon emission and/or transmission, to reduce the photon feedback phenomena;
C) Being electronegative, to reduce the transversal side of the discharges and improve its localization;
D) Possibly, it should not be dangerous for human health.

In addition, desirable characteristics include the following:

1) The chemistry processes which take place during electron multiplication should have reasonable limits in the production of the following species:
   a) Aggressive chemicals such as hydrofluoric acid, which may attack the chamber and gas system components;
   b) Polymerization materials, which may form depositions of extraneous material on the plates.
2) The gas mixture should be eco-friendly. This implies that it should be characterized by a negligible ozone depletion power (ODP) and low global warming potential (GWP) when flushed to the atmosphere, in order to reduce, respectively, damage to the ozone layer or the greenhouse effect, as it has been prescribed, for instance, by the European Community and the regulations of other countries, following the Kyoto Protocol.

Different gas and gas mixtures have been tested in the past in the attempt to achieve these goals. When using RPCs operated in avalanche mode, conditions A to C are currently met using mixtures of tetrafluoroethane ($C_2H_2F_4$), a gas widely used in refrigerating plants, commercially known as R134a with density 4.25 kg/m^3, in combination with sulfur hexafluoride (SF_6), a strongly electronegative gas used for industrial electrical insulation and, sometimes, butane (C_4H_{10}). The main component is always tetrafluorethane (even up to more than 90%) with a few percentages in volume of the other components.

Long-term observations also reveal that Bakelite RPCs require the enrichment of the mixture with an amount of water vapor (typically from 30% to 50% of relative humidity) in order to keep the conductivity of the plates stable in time. In fact, recently produced Bakelite contains a certain percentage of water, and keeping one of the electrode surfaces in contact with a perfect anhydrous gas would make it dry, with the consequence that its resistivity would increase in time (Carboni *et al*., 2004). The fact that glass RPCs do not require this care is generally considered an advantage. More details can be found in Chapter 6.

Condition 1 concerns what is usually called "aging," that is, the progressive deterioration of the detector performance with time, in particular in terms of an efficiency decrease and an increase in the dark current. This was sometimes put in relation with the production of hydrofluoric acid during the multiplication processes, mostly in streamers, taking place in RPCs. This phenomenon is reviewed in Chapter 6.

There have been studies about the production of hydrofluoric acid (HF, also called fluoridric acid) in Bakelite RPCs, being now believed that this is an aggressive agent that must be minimized. HF, in fact, can attack the electrodes themselves, or other components of the system, like the gas pipes and connectors. The most practical way to achieve this is by reducing as much as possible the streamer component during RPC operation, and removing the HF produced by keeping a high gas flow. In big experiments, due to the huge amount of gas used, the gas cannot be thrown out and must be recirculated, and this implies that it must be filtered in order to remove the pollutants produced, and in particular HF (Band *et al.*, 2008; Abbrescia *et al.*, 2006). Some authors also observed damage in glass RPCs when a mixture containing both Freon and vapor is used (Kubo *et al.*, 2003).

Characteristic 1b has been investigated as well and there are indications of Teflon-like material deposition on the electrodes (Gramacho *et al.*, 2009). Practical effects include the observation of a severe rise of dark current and lowering of the efficiency in a glass streamer-mode RPC system (Kubo *et al.*, 2003), while, on the other hand, no aging effects have been reported on glass RPCs operated in avalanche mode, even if some HF production must take place there as well.

About characteristic 2, the first Freon used in RPCs, namely, CF_3Br, was highly harmful to the ozone layer and it was soon prohibited back in the 1990s, together with other gases having the same characteristic. Its replacement, tetrafluoroethane, was used in increasing fraction in RPCs in order to operate them in avalanche mode. $C_2H_2F_4$ is ozone friendly but, on the other hand, it is characterized by a GWP around 1430 (the reference being carbon dioxide $GWP(CO_2) = 1$). Regulations from the European Community derived from the adoption of the Kyoto Protocol, prohibit for many applications the use of gas mixtures with a $GWP > 150$. One should note that scientific laboratories are explicitly excluded from this prohibition; nevertheless, many laboratories, and in particular CERN, are pushing the collaborations of the experiments working there to look for possible replacements.

The search for a new RPC gas mixture to be used in the near future is quite complicated, and is still ongoing, due to the many possible candidates, many possible gas mixtures and different percentages that could, in principle, be used. One possible idea, proposed time ago by one of the authors of this book (Marcello Abbrescia), consists in finding a molecule as similar as possible to $C_2H_2F_4$ but characterized by an acceptable GWP. Of course, this is not sufficient to assure that the new gas would be suitable for RPC operation, and the corresponding tests to assure that RPCs filled with this mixture provide the necessary efficiency, time resolution, rate capability, and aging tolerance, are needed. On the other hand, the criteria proposed seem to be quite reasonable to spot a possible candidate in the huge amount of possibilities (Abbrescia *et al.*, 2016).

Among the possible candidates spotted using this method, there is tetrafluoropropane, $C_3H_4F_4$; the two molecules, essentially, differ by one carbon and one hydrogen atom. Tetrafluoropropane comes in two allotropic forms, commercially indicated as HFO-1234yf and HFO-1234ze, which both satisfy the requirement about their GWP, being $GWP(\text{HFO-1234yf}) = 4$, and $GWP(\text{HFO-1234ze}) = 6$.

However, one of them, HFO-1234yf, is reported to be mildly flammable, and cannot be used in large-scale experiments. Both gases are quite expensive at the moment (around 10 times the cost of R-134a), but it must be stressed that once R-134a is phased out, HFO-1234ze is one of the most interesting candidates to replace it, and this could produce a decrease in its price in the coming years. Tests on mixtures obtained by gradually replacing tetrafluoroethane are ongoing, and show promising results (Benussi *et al*., 2014; Cardarelli *et al*., 2014).

3.6.2 Quenching Gas Mixtures

3.6.2.1 General Information

Gas mixtures, in which secondary processes are fully or strongly supressed (so that γ_{ph} and γ_{+} are very small) are called "quenchers". This fundamental characteristic of the gas mixtures concerns the avoidance of photoionization, either in the electrodes or in the gas itself. If $F_{av}(\nu)$ is the photon emission spectrum of the avalanche, then, in a simple case (for instance, neglecting any angular dependences, etc.), the number of photons which reach the cathode will be proportional to:

$$N_{phc}\alpha \int F_{av}(\nu)\exp\{-\sigma\ (\nu)N_{mol}g\}\ \mathrm{d}\nu. \tag{3.27}$$

In this formula, the last member describes photoabsorption: $\sigma(\nu)$ is the photon absorption cross section as a function of its frequency ν, N_{mol} is the number of molecules per unit volume (also called number density), and g is the distance to the cathode from the photon production location. In some cases, for example, a single-wire counter, this formula is quite accurate. In the case of RPCs, to be rigorous, one should integrate on the surface of the cathode in elements ds, and consider the solid angle from the avalanche to ds. For this geometry, mainly the cathode surface close to the avalanche contributes to the production of secondary electrons. The number of photoelectrons created from the cathode will be proportional to:

$$N_{ec} \propto \int F_{av}(\nu)\exp\{-\sigma(\nu)N_{mol}g\}Q_c(\nu)\ \mathrm{d}\nu \tag{3.28}$$

where $Q_c(\nu)$ is the cathode quantum efficiency. Recall that the quantum efficiency is usually defined as the number of photoelectrons created per incident photon. Note that, contrary to metallic cathodes, where $Q_c(\nu)$ is quite stable with time, in the case of dielectric cathodes $Q_c(\nu)$ has very strong variations, perhaps due to the charging up effect.

However, in the case of both metallic and semiconductive electrodes (for instance, CsI, GaAs, etc.), the quantum efficiencies sharply increase with the frequency ν, so mainly ultraviolet (UV) and vacuum ultraviolet (VUV) photons, (that by definition are photons with wavelength roughly between 50 and 300 nm), contribute to photoelectron production. It is possible, or even likely, that the same happens for glass and other dielectric materials, even if some definitive measurements about that still have to be performed.

VUV photons, emitted by the avalanche, can, in principle, also ionize the surrounding gas. The number of photons absorbed N_{phg} in the gas is proportional to:

$$N_{\mathrm{phg}} \propto \int F_{\mathrm{av}}(\nu)[1 - \exp\{-\sigma(\nu)N_{\mathrm{mol}}g\}]\,\mathrm{d}\nu, \tag{3.29}$$

with the same meaning for the symbols as used in the Formulas 3.27 and 3.28. Correspondingly, the number of photoelectrons N_{eg} created in the gas is:

$$N_{\mathrm{eg}} \propto \int F_{\mathrm{av}}(\nu)[1 - \exp\{-\sigma(\nu)N_{\mathrm{mol}}g\}]Q_{\mathrm{g}}(\nu)\,\mathrm{d}\nu, \tag{3.30}$$

where $Q_{\mathrm{g}}(\nu)$ is the gas quantum efficiency for the photoionization process.

As was mentioned, one can, in principle, optimize the gas mixtures in such a way that avalanche UV emission is strongly diminished. Some gases like isobutane are not only strong UV absorbers but also practically do not emit VUV photons. Moreover, using electronegative gases, like, for example, some kind of Freon, have the effect of capturing some of the photoelectrons, thereby reducing the probability (γ_{ph} and γ_{+}) of triggering subsequent secondary avalanches.

It should be also noted that the processes of de-excitation by photoemission are in competition with non-radiative processes, such as collisional de-excitations. Large molecules with broad rotational/vibrational energy bands are especially apt for this purpose, that is, photoemission quenching. It has been shown quite directly that Argon dimer emission can be efficiently suppressed by a small fraction of a complex molecule (Fonte *et al*., 1991b).

Therefore, there are several ways to reduce photon feedback, and it can be assumed that, except for mixtures suited for photodetectors which must be themselves UV transparent, in most cases it is possible to sufficiently suppress photon feedback. This is also demonstrated by the fact that for many detectors operated in avalanche mode, successor avalanches are rare.

However, in the case of streamers and especially if followed by a discharge, a drastic change happens. Both of them are plasma filaments and the emission is determined by the plasma conditions, that is, the temperature, electron density, and so on. As a rule, any plasma has strong emission in the UV and VUV region of spectra. Therefore, adding UV absorbing gases, and electronegative components, and increasing the gas pressure or the gap width are the ways to reduce the number of photons capable of causing the photon feedback.

Let us now discuss ion feedback. This effect is rather well understood in the case of metallic cathodes (see, e.g., Nappi and Peskov, 2013): as was outlined in Chapter 1, it consists in the fact that, if the ionization potential of an ion $E_{\mathrm{i}} > 2\varphi$ (where φ is the extraction energy from the cathode), a free electron can be emitted from the cathode, with a probability γ_{+}, as a result of ion recombination. An experimental study of $\gamma_{+} = \gamma_{+}(E_{\mathrm{i}}, E)$ in the case of gaseous detectors (and particularly single-wire counters) is reported in the papers (Peskov, 1976, 1977). It was demonstrated that in all gases under investigation the values of γ_{+} linearly increase with E_{i} and depend also on the gas composition and the value of E/p.

$$\gamma_{+} = k_{\mathrm{gas}}\ (E/p)\ (E_{\mathrm{i}} - 2\varphi), \tag{3.31}$$

where E is the electric field close to the cathode and p is the gas pressure, and k_{gas} is a coefficient depending on E/p ratio (being in addition $k_{gas}(E/p) \ll k_{vac}$). Therefore, gases with small ionization potentials are especially attractive.

Unfortunately, in the case of dielectric cathodes, very little is known about the way how ions interact with their surface.

3.6.2.2 Historical Review about Gas Mixtures for Inhibiting Photon Feedback

Let us now examine which gas mixtures were found to be most suitable for the RPCs, during the process of their development.

In the pioneering works of the Novosibirsk group who developed the first prototypes of RPCs with metallic cathodes, the focus was on searching for gases with high atomic weight and strongly absorbing VUV in order to suppress photon feedback. For example, in (Parkhomchuk *et al*., 1971) the RPC, having a gap of 1 mm, was filled with a gas mixture 55% Ar + 30% ether + 10% air + 5% divinyl at a total pressure of 1 atm. Later on, to improve time resolution, this group started reducing the RPC gas gap thickness, operating at 12 atm pressure. In this case, the gas mixture was also carefully optimized to absorb UV radiation of avalanches in the widest possible spectral-band interval (see Figure 3.33).

These authors (Pestov, 1988) evaluated the contribution of photo effect for various metallic cathodes. Discharge localization was chosen as a qualitative criterion. The discharge localization was estimated from the mean pulse height of the charge from the narrow gap high-pressure RPC.

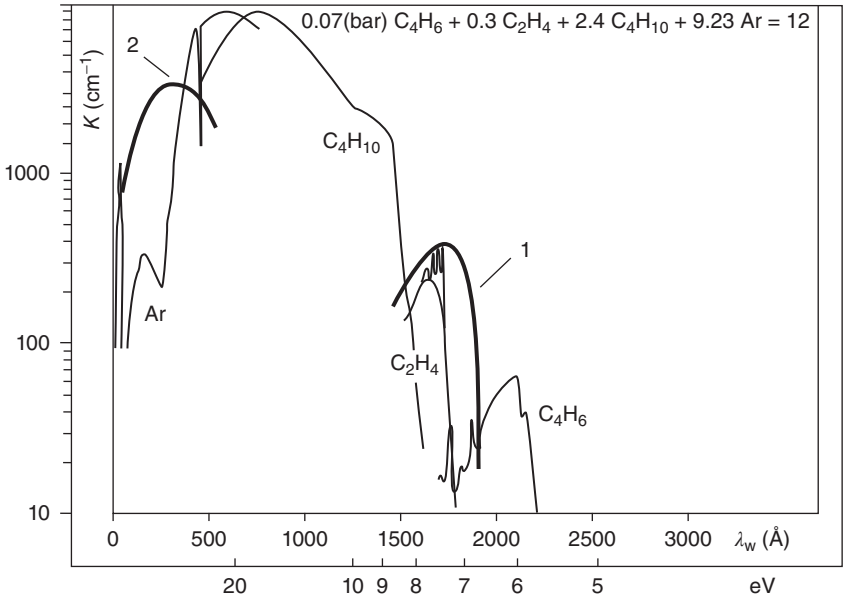

Figure 3.33 Linear absorption coefficient for the components of the gas mixture used in high-pressure Pestov counters (corresponding to their quantity). The curves 1 and 2 correspond to propylene (C_3H_6) and neon, respectively. (Pestov *et al*. 2000. Reproduced with permission of Elsevier.)

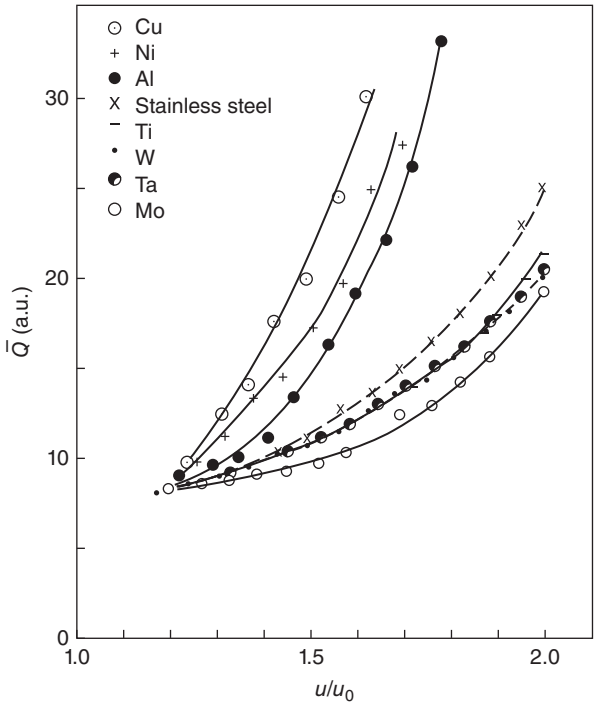

Figure 3.34 The mean charge of the signal from the narrow-gap high-pressure RPC as a function of overvoltage just after the assembly of the detector for different cathode materials. (Pestov 1988. Reproduced with permission of Elsevier.)

It was assumed that when photon feedback appears, the secondary pulses/streamers are unresolved in time (due to the extremely fast timing) and thus are integrated with a primary pulse, giving an artificial rise of its amplitude. Figure 3.34 shows the mean charge dependence on the overvoltage, where the overvoltage is the ratio of the operating voltage with respect to the threshold one. These curves were obtained just after the detector assembly and reflected the cathode quantum efficiency for the spark emission in the same standard gas mixture. As can be seen, the effective quantum efficiency for different cathode materials decreased in the following order: Cu, Ni, Al, and so on.

Recall that Pestov counters, before operation, were usually treated by continuous discharges caused by a γ-ray source, to achieve, by means of this so-called burning-in treatment, a stable operation. During the burning-in period, a polymeric film deposited on the cathode surface had the effect of changing its characteristics. As a result, after such a treatment, counters made out with different cathode materials were characterized by the same mean pulse charge (see Figure 3.35).

In the case of the first prototype of Santonico and Cardarelli's RPCs, the gas used was Ar + 50% butane; its choice also was dictated by the same ideas as in the case of Pestov counters, that is, to suppress the UV radiation. The authors believed that after a discharge caused by the ionizing radiation the efficiency of

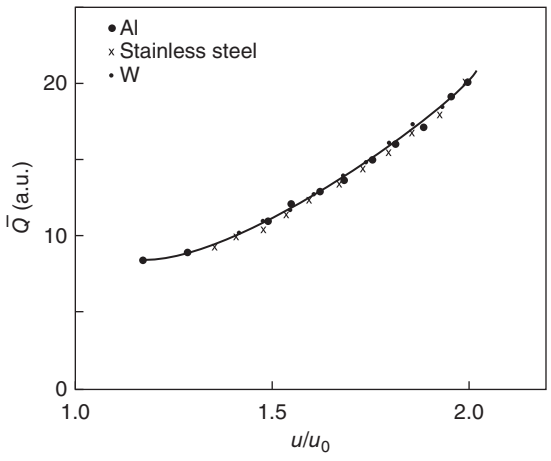

Figure 3.35 The mean charge of signals from Pestov RPC as a function of the overvoltage after the burning-in period for aluminum, stainless steel, and tungsten cathodes. (Pestov 1988. Reproduced with permission of Elsevier.)

the discharge-affected area significantly dropped. On the other hand, due to the UV absorbing component of the gas, the photons produced by the discharge are not allowed to propagate in the gas too far away, thus reducing the possibility of originating secondary discharges in other points of the detector.

In one of their successive works (Cardarelli *et al*., 1988), Santonico's team investigated RPCs operated in the above mentioned gas mixtures of argon and isobutane in different fractions, but containing also a small percentage of some kind of Freon, initially CF_3Br, which due to its electron affinity had the effect of capturing a large number of avalanche-free electrons. As already pointed out, note that Freon is a generic commercial name, which actually covers many different fluorinated gases; different kinds of Freon have been used in RPCs in different periods.

In fact, electron affinity changes the avalanche development and streamer formation for the following reasons:

1) Electronegative gases, basically, reduce the effective Townsend coefficient (see Formulas 3.1 and 3.2), requiring a higher voltage for the same signal induced. Moreover, according to some authors, it has the effect of stretching the useful operational voltage interval: the voltage interval where an acceptable efficiency value (say, 90–95%) is combined with a reduced streamer contamination (typically less than 10%) is generally called "useful plateau." Later on, it was found out that SF_6 is particularly useful to keep the avalanche and streamer stages well separated, that is, it allows to operate RPCs in avalanche mode with a quite reduced streamer contamination (see Camarri *et al*., 1998 and Figure 3.36), and in fact now SF_6 is an essential component of the gas mixtures standardly used in experiments employing RPCs.
2) Electronegative ions move as slowly as the positive ions; and since their drift velocity is orders of magnitude less than the electron drift velocity, at the time scale of avalanches and streamers, the ions are practically immobile. Therefore, the positive and negative ions are superimposed in space and the net charge density is the difference in number densities (see Figure 3.17).

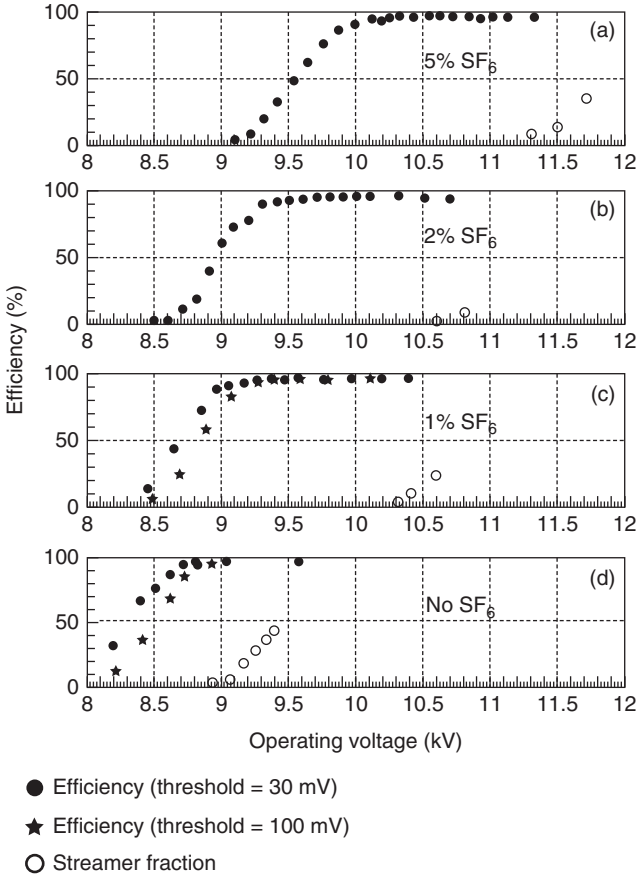

Figure 3.36 Detection efficiency and streamer probability versus operating voltage for (a) 5%, (b) 2%, (c) 1% SF_6 concentrations, and (d) no SF_6. The "useful plateaus," as was defined in the text, clearly increase with increasing fractions of SF_6, hinting at a good separation between the avalanche and streamer phases. The rest of the mixture is $C_2H_2F_4/C_4H_{10}$ in 97/3 relative fraction. (Camarri *et al*. 1998. Reproduced with permission of Elsevier.)

Note that when using gases with complex molecules (like, but not only, some electronegative gases), it happens that, when the streamer reaches the cathode, the subsequent plasma discharge is accompanied by complicated processes such as molecule dissociation, creation of molecular fragments, attachment, and detachment.

As was mentioned earlier, the avalanche mode offers higher rate capability, so after the work by Cardarelli *et al*. (1988) the gases with electronegative additives became very popular. For example, the RPCs in the LHC experiment are flushed with the cited gas mixture consisting of 94.7% $C_2H_2F_4$; 5% iC_4H_{10}; and 0.3% SF_6.

One search for new gas mixtures was carried out by one of the authors of this book (see Abbrescia *et al*., 2012), who studied the possibility of adding Helium to the gas mixture as a "space holder" gas (in the author's words), that is, a gas

that behaves roughly like vacuum, thus effectively reducing the gas density and consequently the necessary operating field (a fact that is generally considered to be advantageous, in a purely technical basis). The effect is quite similar to operating RPCs at a reduced pressure. Effects of temperature and pressure on RPC operation have been studied extensively and are outlined later on in this book. For the remaining part of the mixture, the presence of the standard components was respected.

Authors of the work (Lopes *et al*., 2012) compared Freon-containing gas mixtures with pure isobutene gas and demonstrated that some compromises can be found in terms of a reduced plateau, higher presence of streamers, and the subsequent degradation of time resolution. However, operation at 90–95% efficiency with resolutions in the range 90–110 ps under SF_6-free gas mixtures has been convincingly demonstrated.

Certainly, any gas aiming at replacing the present gas mixture will require a new cycle of systematic studies to demonstrate, for example, the necessary aging properties. For instance, the new gas should ensure low aging for future experiments expecting to deal, over their operating life, with transported charges up to $1-3$ C/cm^2 (Zhu, 2012; Wang *et al*., 2010, 2012).

3.6.2.3 Some Considerations on Delayed Afterpulses

Earlier, we considered gases mainly from the point of view of photo processes. As it can be inferred from the studies presented in Inoue (1997) and Pestov (1988), photo processes can be responsible for secondary streamers. However, many authors observed after-pulses delayed with respect to the primary pulse on timescales exceeding the electron drift time by orders of magnitude. An attempt to shed light on this phenomenon was done in the work by Iacobaeus *et al*. (2002).

These studies were performed with a glass RPC described in Gustavino *et al*. (2001b) for detecting cosmic rays. The gas mixture was Ar/Isobutane/Freon (R134) used in the ratio 48/4/48.

Figure 3.37 shows the appearance of clustered spurious pulses from an RPC. The upper trace of the oscillogram shows the pulse from the photomultiplier tube coupled to a scintillator (triggered on muons in coincidence with another other scintillator). The lower trace shows a pulse due to a muon (directly measured on the 50 Ω input of the oscilloscope) from the RPC and, in addition, also after-pulses appearing at an increasing applied voltage. The amplitudes of these after-pulses are very randomly distributed and may be considerably larger than the muon pulses. Note that many other authors have observed these after-pulses (Abe *et al*., 2000). The common explanation to the origin of the after-pulses is that they are due to a photo effect caused by a primary avalanche or a streamer inside the detector (Abe *et al*., 2000). However, observations show that grouped spurious pulses have a sporadic delay that sometimes can be very long, and this would exclude the explanation based on the photo effect. By the comparison of the pulse-height spectra of the spurious pulses with those produced by single photo electrons (measured with detectors operating in proportional mode), one can conclude that the spurious pulses, depending on conditions, may contain between a few up to a few thousands of electrons (Gustavino *et al*., 2001b).

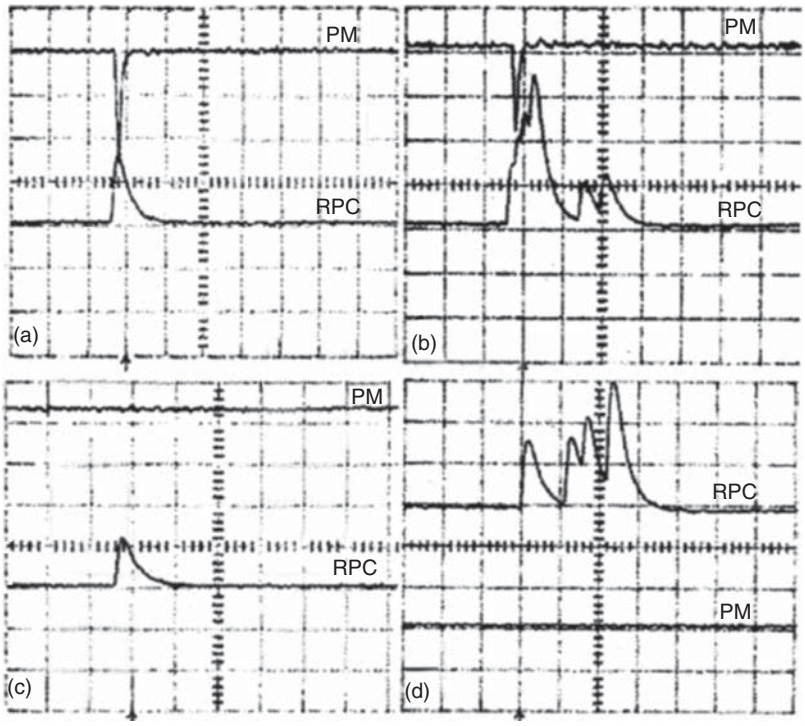

Figure 3.37 The oscillograms (a) and (b) show signals measured in coincidence with cosmic muons and (c) and (d) noise signals from the RPC. Various voltages were applied to the RPC in the different measurements, (a) and (c) were at $V = 7:6$ kV and (b) and (d) at $V = 8:75$ kV. The oscilloscope sensitivity was set to 5 mV/div for the photomultiplier (PM) signal and 100 mV/div for the RPC. The horizontal scale was set to 0.2 s/div. A gas mixture made out of Ar/isobutane/Freon (R134a) was used, in the ratio 48/4/48. (Iacobaeus *et al*. 2002. Reproduced with permission of Nuclear Science, IEEE Transactions.)

Since the amplitudes of these pulses correspond to a large number of electrons presumably created at the cathode surface (immediately or in a short time interval), one can speculate that their possible origin could be an explosive type of emission from the cathode surface. Indeed, a generally accepted explanation of the Malter effect is a charging up of dielectric films on the metallic cathode surface, by positive ions. If the dielectric film is thin enough, the electric field generated may be intense enough to cause a field emission. A classical field emission takes place with an emission in the form of single electrons.

Relatively recent studies of breakdown mechanisms in high vacuum (Latham, 1995) reveal, however, that the field emission could rather be in the form of bursted electron emission, the so-called explosive field emission. These emissions originate at some points on the metallic cathode, where there are sharp tips or, even more important, microscopic dielectric insertions. The theory of this effect is based on the fact that dielectric insertions are not ideal dielectrics and contain a system of low-energy electron states, due to impurities, crystal defects, and so on. In a high electric field, electrons from the cathode are able

to tunnel to the dielectric insertion where they accumulate. After some critical concentration, they suddenly emit to the vacuum in the form of jets of electrons. It looks like a similar phenomenon may occur in gaseous detectors.

3.7 Current in RPCs

Current in RPCs is generally considered to be composed of two components. When the applied voltage and, as a consequence, the electric field across the gas gap, are relatively low, multiplication processes in the gas are negligible. Under these conditions, the gas resistance being quite high, the current measured across the two RPC electrodes derives from the current flowing through the resistive electrodes and then through the spacers, the seal around the chamber, and/or, in general, any point of contact between the resistive anode and cathode. It shows an approximately linear ohmic behavior and, in principle, the relation between the applied ΔV_{app}, the current measured I should be given by

$$\Delta V_{\text{app}} = IR \tag{3.32}$$

where R is the total resistance of the device (i.e., a combination of the resistance of the resistive electrodes, the spacers, the seal, etc.).

In principle, by plotting I measured at different values of ΔV_{app} one could infer, by the slope of the resulting straight line fitting the data, the value of R in Formula 3.32. Note, however, that it is not easy to discern, by applying this method, which component of the chamber mostly contributes to the resistance measured in an RPC. Using the second Ohm's law, it is possible to demonstrate that most of the contribution derives from the spacers and the seal, and that the one coming from the resistive electrodes accounts just for 10–20% of the total; this is because of the much larger surfaces (more than hundred times more) involved in the latter case.

However, one is generally not interested in R, but rather in the electrode resistivity, which plays, as we see in the following, a quite important role in the RPC rate capability and, in general, to spot any premature sign of detector aging.

A solution widely adopted to measure electrode resistivity consists in filling these devices with pure argon, which is characterized by a sufficiently high Townsend coefficient even when the applied electric field is relatively low (around 1–2 kV applied on a 2-mm gap, for instance). Under these conditions, the gas conductivity is no longer negligible, a discharge appears and a kind of short circuit is created between the resistive anode and cathode, bypassing any contribution to the total resistance observed due to the spacers and the seal. Therefore, by measuring I versus ΔV_{app} one can have a clear hint of the resistance due to the electrodes alone, and, from that, of their resistivity. Moreover, this method probes the whole electrode area and is sensitive to possible localized defects which manifest as early discharge onsets or current spikes.

In many gas mixtures after the first ohmic phase, the current I is no longer linearly proportional to ΔV_{app}. Multiplication processes become important, and one would expect an approximately exponential behavior, or, anyhow, a much rapid raise with respect to the linear proportionality characteristic of the ohmic

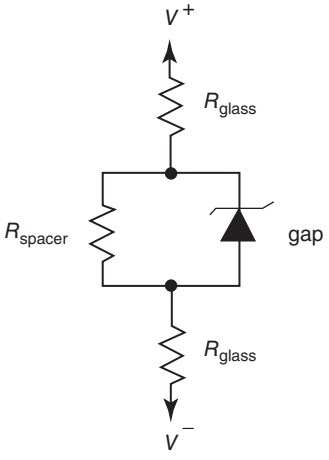

Figure 3.38 Equivalent circuit often used to describe the current in an RPC in steady conditions; in this particular case, glass electrodes are considered. At low voltages, the multiplication processes in the gas are negligible and, therefore, $R_{gap} \approx \infty$ and $dV/dI = 2\,R_{glass} + R_{spacer}$. At high voltages, $R_{gap} \approx 0$ and $dV/dI = 2\,R_{glass}$.

region. Sometimes, an equivalent circuit to describe the current behavior, in steady conditions, as a function of the operating voltage in an RPC is used. This is reported in Figure 3.38, where the diode mimics the role of the gas, which, at voltages low enough, is an almost perfect insulator.

Many factors contribute to determine the amount of the current measured in this region; for instance, it strongly depends on the gas mixture used and whether we operate the device in avalanche or streamer mode. It also depends on the environmental conditions, like temperature and pressure, as pointed out in the last section of this chapter. Examples of the current behavior, putting in evidence the transition between the ohmic region and the subsequent one, are reported in Figure 3.39, for the case of a single-gap 2-mm Bakelite RPC operated

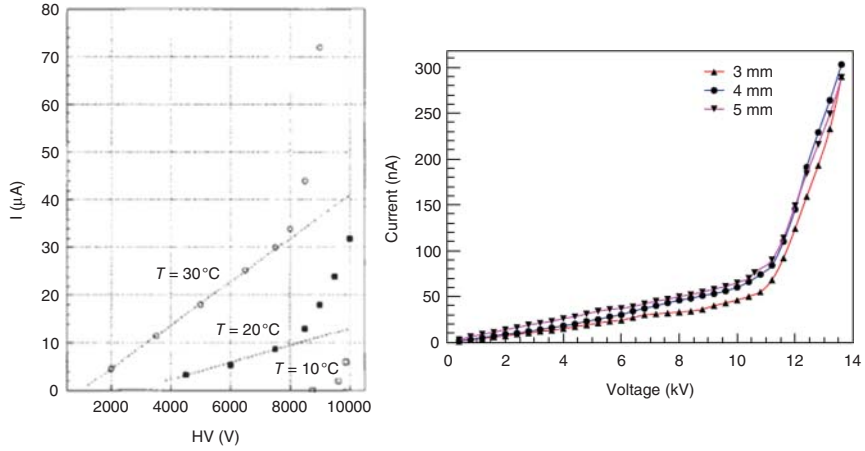

Figure 3.39 Current measured in an RPC versus the applied voltage, (a) for a single-gap 2-mm Bakelite RPC operated in streamer mode, at different temperatures. (Abbrescia *et al*. 1995. Reproduced with permission of Elsevier.) (b) For a single-gap 2-mm glass RPC with different electrode thicknesses operated in avalanche mode. (Sadiq *et al*. 2016. Reproduced with permission of IOP.)

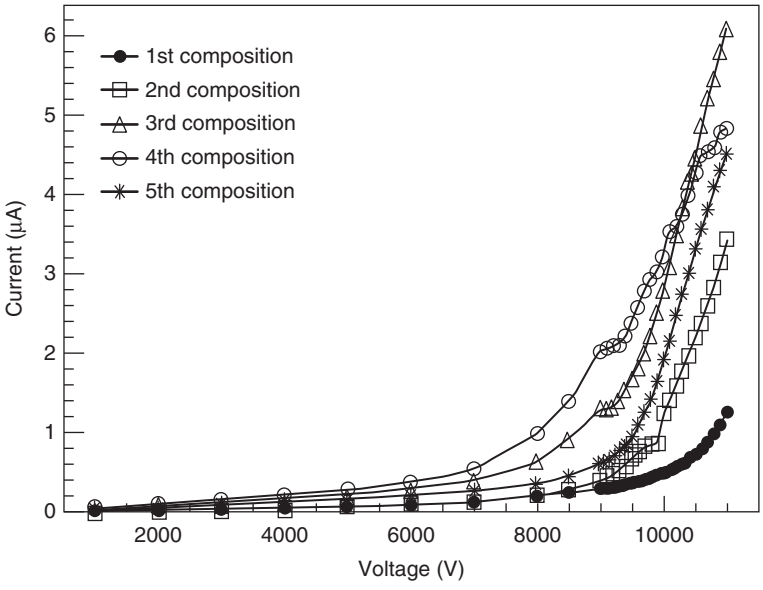

Figure 3.40 Current versus voltage characteristics for the different gas compositions, reported in Table 3.1. (Manisha *et al*. 2016. Reproduced with permission of Elsevier.)

Table 3.1 Different compositions of the gas mixtures (using R134A, SF_6, Ar, C_4H_{10}) used for the RPC characterization to obtain the data reported in Figure 3.40.

S. No.	Freon (R134A) (%)	Isobutane (C_4H_{10}) (%)	SF_6 (%)	Argon (Ar) (%)
1st composition	95.2	4.5	0.3	—
2nd composition	95.5	4.5	—	—
3rd composition	100	—	—	—
4th composition	—	—	—	100
5th composition	62	8	—	30

Manisha *et al*. 2016. Reproduced with permission of Elsevier.

in streamer mode, at different temperatures, (Abbrescia *et al*., 1995), and for a single-gap 2-mm glass RPC with different electrode thicknesses operated in avalanche mode (Sadiq *et al*., 2016). The current measured with an RPC filled with different gas mixtures, taken from Manisha *et al*. (2016), is reported in Figure 3.40.

The plots reported in Figures 3.39 and 3.40 were measured using cosmics. Generally speaking, the current measured across the electrodes of an RPC at a given voltage and in the presence only of cosmic and natural radioactivity background is referred to as "dark" current.

When multiplication processes are no longer negligible, and given stable operating conditions, the amount of current flowing in an RPC depends also on the flux of particles impinging on it. In this case, we do not speak anymore of "dark"

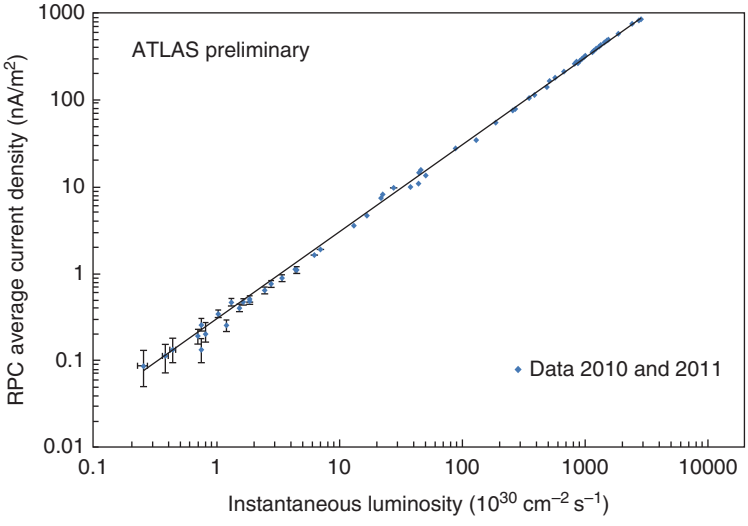

Figure 3.41 RPC average current density (pedestal subtracted) as a function of the instantaneous luminosity at beam dump, for the ATLAS muon system. The measurements include both 2010 and 2011 data. (Aielli *et al*. 2013. http://iopscience.iop.org/article/10.1088/1748-0221/8/02/P02020/meta. Licensed Under CC BY 3.0.)

current. If the charge developing in each amplification process is supposed to be, on the average, constant, the current measured can be used as an estimate of the particle flux. However, to obtain accurate results, one should take care to subtract from the total current the ohmic component, usually by extrapolating its value measured at lower voltages to the actual device operating voltage. Again, this is a procedure quite often used in large experiments (see Figure 3.41).

Note that, at high rate, the applied voltage ΔV_{app} might not coincide any more with the voltage drop ΔV_{gap} across the gas gap. This is due to the fact that at increasing current, the voltage drop across the electrode plates ΔV_{el} (related to their total resistance) is no longer negligible. Of course, it must always be

$$\Delta V_{\text{app}} = \Delta V_{\text{el}} + \Delta V_{\text{gap}} \tag{3.33}$$

This, which at first might seem trivial, has important consequences. Let us consider an RPC fully efficient at rate close to zero, which is subject to an increasing particle flux. As the rate increases and ΔV_{app} is kept constant, ΔV_{gap} decreases, since the voltage drop across the resistive electrode becomes more and more relevant. Since the amplification processes in the gas gap depend on ΔV_{gap}, the detector gain will progressively decrease as well, until a not negligible fraction of events will generate signals under the electronic threshold, that is, the detector loses efficiency. This leads to an important limitation in the maximum efficiency RPCs can have when exposed to an intense flux of particles, that is, what is generally called a limitation in their rate capability. To convert this simple qualitative picture to a quantitative one, one has to take into consideration also pulse fluctuations. An attempt for a more complete picture and relative calculations is done later on in this book.

At large experiments, for practical reasons related, for instance, to detector and readout electronics heating, it is also important to keep the overall power consumption – which is related to the current drawn via RPC – at reasonable levels. For instance, at CMS, the limit is around 3 W/m^2.

In general, it has been found that the degradation processes in RPCs due, for instance, to the production of aggressive chemical compounds taking place in the avalanche and streamers inside the gas gap, are roughly proportional to the amount of current integrated during the detector lifetime, that is, the total charge. This is not surprising, since the total charge is a direct measure of the number of ionizations taking place, and thus somehow related to the number of molecules that can be broken and produce chemical species not present in the gas mixture originally flowed in the detector. Therefore, there is a general trend in keeping the current in RPCs as low as possible (compatibly with operation at reasonable efficiency), to limit aging processes. Note, however, that, at constant integrated current (or charge), possible damage depends also on the materials chosen for the detector and the gas system, the exact gas mixture used (in particular if it contains water vapor or not), and some other factors.

Finally, of course, one should mention that much deeper studies on the current in RPCs, on a fundamental point of view, can be performed. For instance, a nice and detailed model can be found in Ammosov *et al*. (1997), where not only the current flowing in the electrodes bulk is considered but the current along the surfaces as well.

3.8 Dark Counting Rate

It is well known that practically all gaseous detectors at elevated voltages exhibit spurious pulses which are not directly connected (or at least are not coincident in time) to the cosmic radiation or natural radioactivity. These are generally referred to as dark (because they occur even in absence of any impinging radiation) or "noise" pulses.

Usually, their rate rapidly increases with voltage. Results of some recent studies can be found in Iacobaeus *et al*. (2002). The origin of these pulses is not well understood and it may change from detector to detector. In the case of a single-wire counter or a parallel-plate chamber with metallic electrodes operating in avalanche mode, possible explanations of these pulses are the following:

1) Various current leaks in the electrically "weak" regions of the detector, mainly in the dielectric structure supporting the anode–cathode electrodes;
2) Electron emission from dielectric insertions (oxide layer, dust, etc.) on the cathode;
3) Combination of the two effects mentioned.

In the first case, the leaked current quite often has a sporadic nature and can manifest itself via pulses. It can be strongly reduced by means of carefully designed dielectric interfaces between the anode wire and the cathode cylinder.

For example, rectangular grooves on the dielectric surface efficiently prevent the current from leaking along the dielectric surface (Iacobaeus *et al*., 2002).

The second phenomenon is a kind of Malter effect already mentioned. More detailed studies reveal, however, (see, for instance, Fonte *et al*., 1999; Ivaniouchenkov *et al*., 1998) that in addition to the single-electron emission the metallic surfaces, during and even shortly after positive ion bombardment, emit not only single electrons, but rather sporadic bursts of electrons (another designation used is "explosive field emission" Iacobaeus *et al*., 2002). Note that, in practice, dielectric micro-layers on the metallic surfaces always exist and they are oxidation films, dielectric insertions after surface treatment, various microparticles, and so on. Therefore, after any avalanche in the detector caused, for example, by natural radiation, there could be such emission from the cathode which in some cases may last for up to 10–20 min and will be a reason for spurious pulses not coinciding in time with the primary avalanche.

RPCs also show noise pulses, as reported in Figure 3.42. Imaging of their positions performed by one of us (Paulo Fonte, unpublished results) with a position-sensitive RPC show that they are, in first approximation, uniformly distributed along the cathode surface, but usually do not appear near the surface of spacers. Note that cosmic muon mapping with RPC also show that the sensitivity near spacers is much smaller than elsewhere, indicating that the electric field drops in these regions, as expected. Therefore, one can rule out that the origin of the noise pulses in the current leak along the spacers.

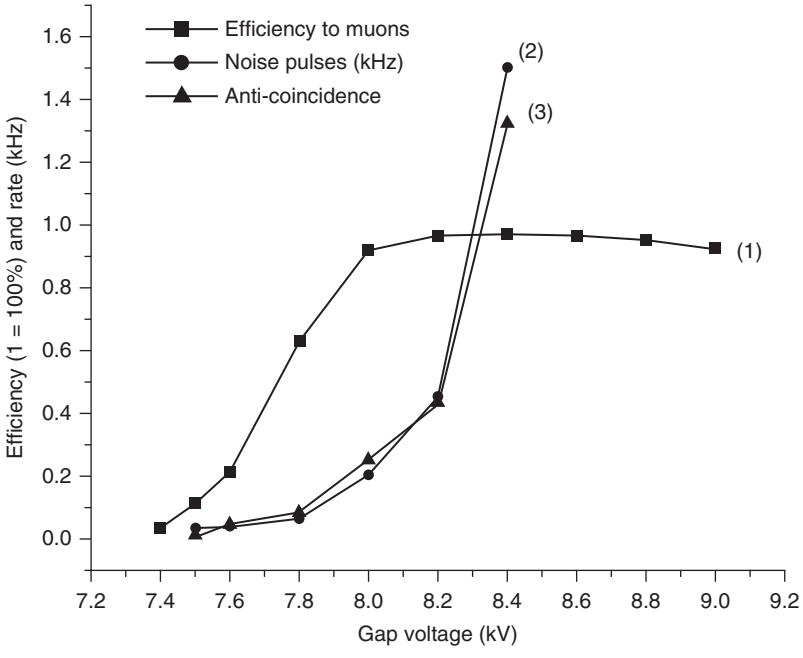

Figure 3.42 The efficiency (1) and the rate of noise pulses (2), (3) versus the voltage applied on the RPC; (2) and (3) correspond to measurements done in coincidence and anticoincidence with the signals from the scintillators, respectively. (Adapted from Gustavino *et al*. 2001b.)

What is the origin of the noise pulses then? Authors of (Iacobaeus *et al*., 2002) speculate that they appear due to the Malter-type effect: electron extraction (and electron jets) from the cathode, the surface of which is charged up by positive ions. Of course, the presence of micro-points or irregularities on the electrodes plays an important role here. It is interesting to note that the rate of noise pulses depends on the intensity of the external radiation. In the work of Iacobaeus *et al*. (2002), the RPC, and for comparison the parallel plate avalanche counter (PPAC) with metallic electrodes, were irradiated by a strong X-ray flux, producing locally a counting rate up to 10^5 Hz/mm^2. Figure 3.43 shows the rate of spurious pulses after the beam was blocked. One can see that both detectors show a clear decrease in time of the noise pulse rate, in a time span which may reach even about 6 min.

In Manisha *et al*. (2016), an attempt was made to investigate if the rate of noise pulses depended on the gas mixture composition. Four different gas mixtures were tested, as well as pure argon (see Table 3.1). However, no clear link between the counting rate and the gas was observed.

Finally, it must be noted that when an RPC is subject to a not negligible flux of impinging particles, the total counting rate will be, of course, the sum of the noise and the particle counting rates. Therefore, in application like muon triggering (or vetoing against them), it is quite important that the noise should be much less than the particle counting rate, not to cause accidental coincidences and triggers. Conversely, if the noise counting rate is negligible with respect to the particle counting rate, this, in principle, can be used as a direct estimate of the flux of impinging particles (see Figure 3.44).

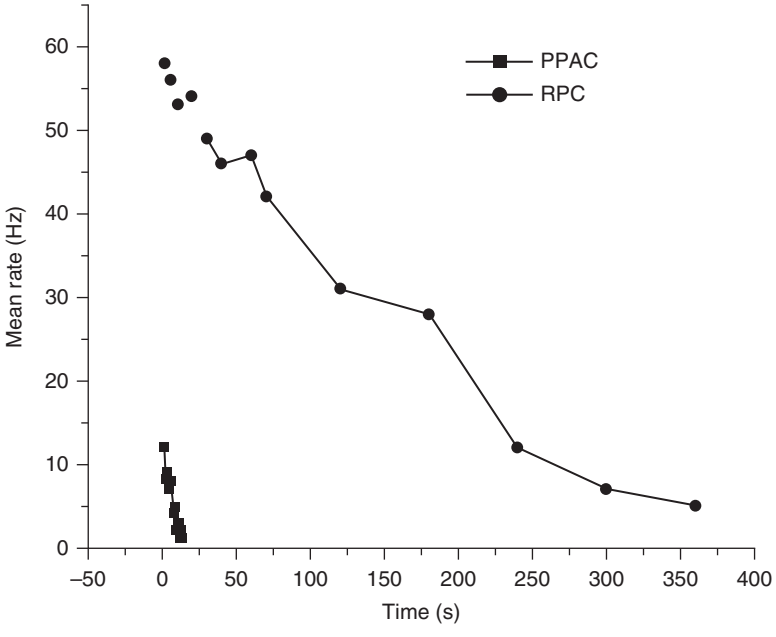

Figure 3.43 The rate of the after-pulses for the parallel-plate chambers working in avalanche mode (Cu electrodes) and RPC (made with undoped Si), also working in avalanche mode. (Iacobaeus *et al*. 2002. Reproduced with permission of Nuclear Science, IEEE Transactions.)

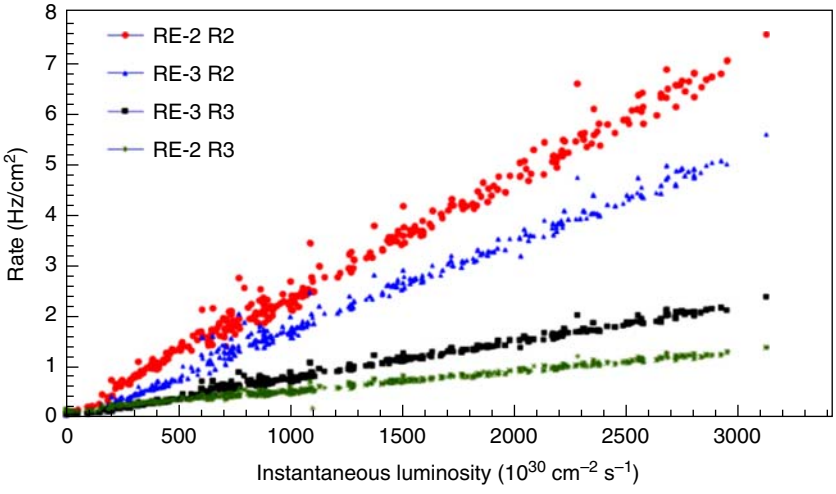

Figure 3.44 RPC counting rate as function of instantaneous LHC luminosity, for the endcap stations 2 and 3 of the negative disk 2 and 3 of the muon systems of the CMS experiment; a very clear relation between the flux of impinging particles (proportional to the accelerator instantaneous luminosity) and the detector counting rate can be seen. (Paolucci *et al*. 2013. Reproduced with permission of Nuclear Science, IEEE Transactions.)

3.9 Effects of Temperature and Pressure

There is an important amount of experimental data showing that temperature and pressure affect the RPC operation in a relevant way. As a first point, temperature has a direct effect on the resistivity of the electrode materials. Both for Bakelite and glass, it is generally believed that increasing their temperature implies lowering the plates' resistivity. For Bakelite, there are nice direct verifications of this trend, reported, for instance, in Arnaldi *et al*. (2000) and shown in Figure 3.45; Bakelite resistivity decreases even by an order of magnitude for a temperature increase of about 20°C. Of course, if electrode resistivity varies, this has a consequence on the ohmic component of the current drawn by these devices, as can be seen from Figure 3.39.

As for float glass, an exponential effect of an order of magnitude resistivity decrease for a temperature increase of 25°C was measured and its direct effect on the chamber's rate capability demonstrated by C. Gustavino *et al*. (2004). This phenomenon appears to be common and of identical strength in this type of glasses (González-Díaz D. *et al.*, 2005) and cannot be overlooked as a practical tool to tune glass RPC's rate capability.

Moreover, both the temperature T and the pressure p of the gas contained inside the chambers have a direct relationship with the gas density ρ_g. Generally speaking, gas parameters (in particular, drift and multiplication parameters) depend on the E/ρ_g ratio, and therefore any change in T and/or p, affecting ρ_g, will affect the gas parameters too. Keeping the ratio E/ρ_g constant as much as possible is the method generally pursued to keep RPC performance constant against

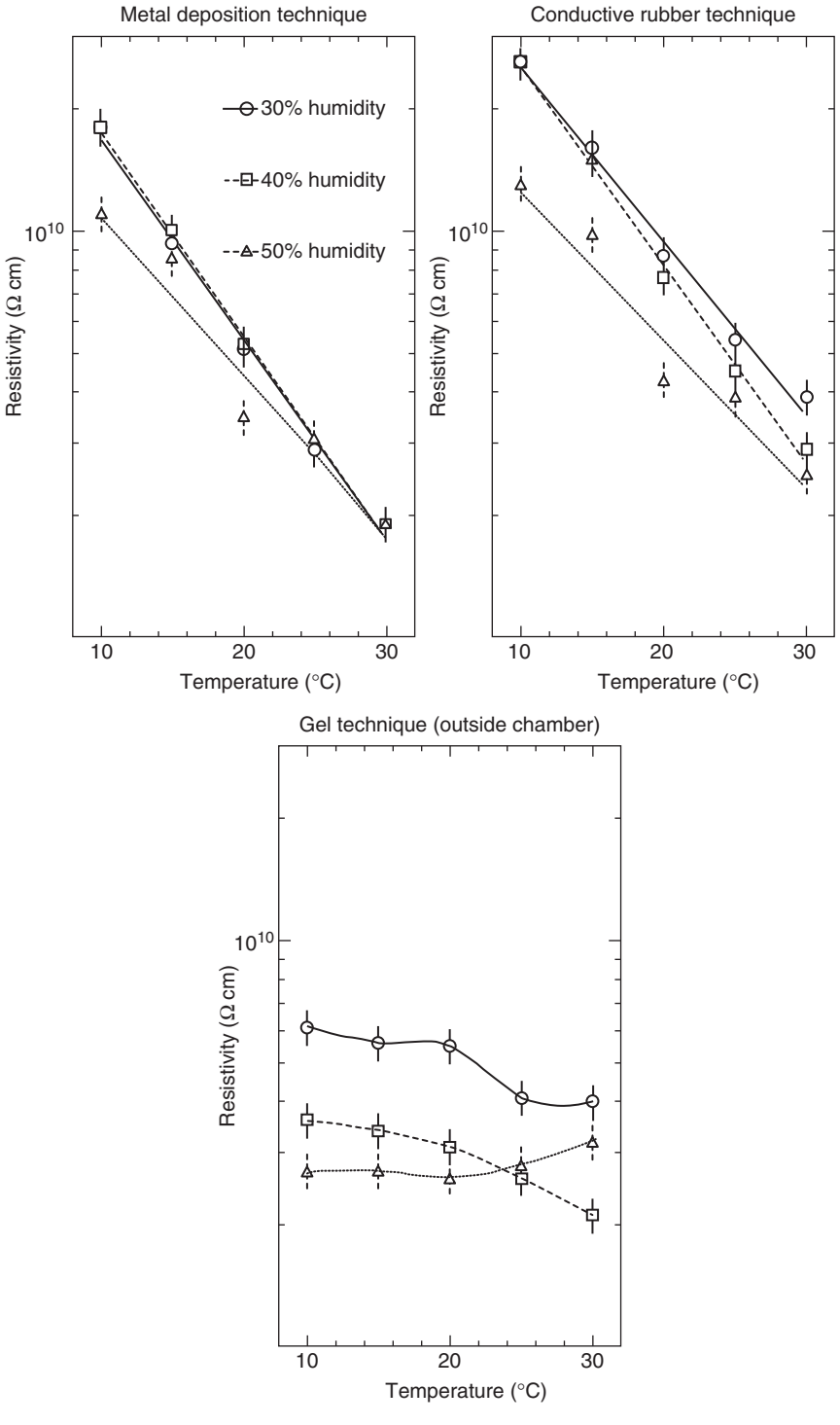

Figure 3.45 Resistivity of phenolic Bakelite versus temperature, measured with three different methods. (Arnaldi *et al*., 2000. Reproduced with permission of Elsevier.) The authors report similar results for melaminic Bakelite, too.

changes in environmental conditions. This is essential in the operation of large experiments, as will be seen in following.

In general, when operating RPCs at varying temperatures, one observes changes in the current drawn, counting rate of noise pulses, efficiency, and time resolution. In this case, both electrode resistivity and gas density are changing, and therefore, one has to take into account all these phenomena acting together, whose effects sometimes it is not easy to disentangle.

Dark current and noise rate versus the operating voltage, taken at different temperatures, for the Bakelite RPCs developed in the framework of the ARGO-YBJ experiment are reported in Figure 3.46. Usually an increase in temperature has the effect of increasing both current and counting rate, even at a constant operating voltage. Similar results are reported for multi-gap RPCs fabricated in glass (described in detail in Chapter 4), which are reported in Figure 3.47. As temperature increases, Bakelite or glass resistivity decreases, and this leads to an increased ohmic current. Moreover, a temperature increase, presuming that pressure remains more or less stable at the atmospheric value, implies a reduced gas density, and therefore an increased E/ρ_g ratio. Therefore, RPCs operate at an increased value of the effective first Townsend coefficient (which, as already pointed out, depends on the E/ρ_g ratio), with a subsequent drift of the operating point, just as if the applied voltage was increased by the same relative amount.

Pressure increase will shift the RPC operating point in the direction opposite to a temperature increase.

When comparing data from the very same RPC, but taken at different T and p values, generally the concept of "effective voltage" ΔV_{eff} is introduced, defined as

$$\Delta V_{\text{eff}} = \Delta V_{\text{app}} \frac{T}{T_0} \frac{p_0}{p} \tag{3.34}$$

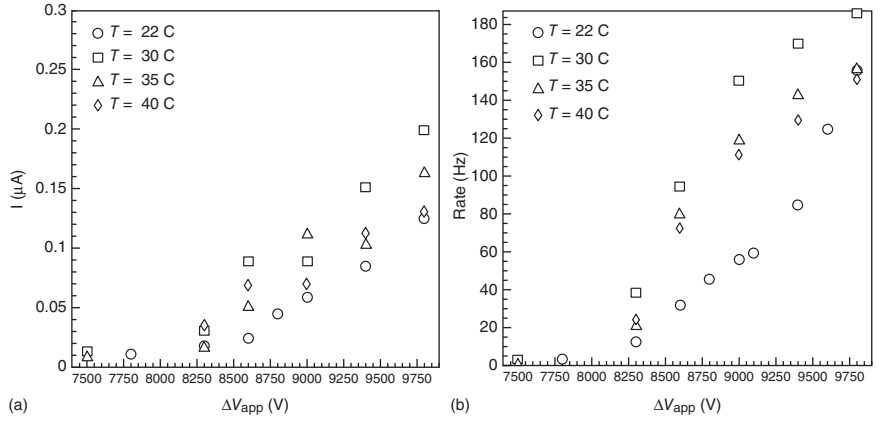

Figure 3.46 Dark current (a) and counting rate (b) versus ΔV_{app}, measured at different temperatures, for single-gap Bakelite RPCs, tested in the framework of the R&D for the ARGO-YBJ experiment. (De Vincenzi *et al.* 2003. Reproduced with permission of Elsevier.)

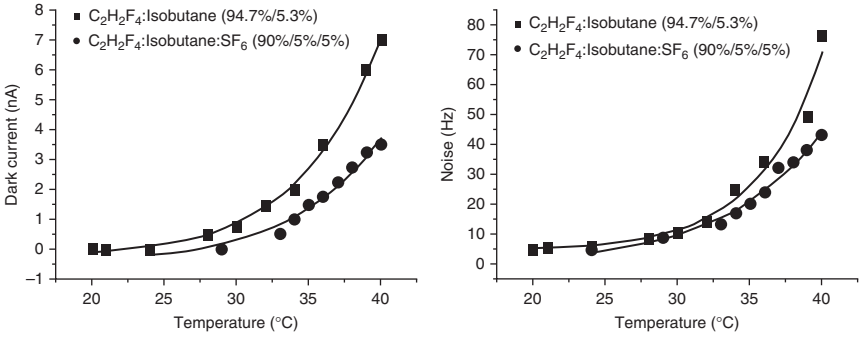

Figure 3.47 (a) Dark current (i.e., the current measured with the chamber just exposed to the natural background and without any specific irradiation). (b) Noise rate versus temperature, for two different gas mixtures, filling multi-gap RPCs, described in Chapter 4. (Zhao *et al*. 2005. Reproduced with permission of Elsevier.)

where p and T are the actual values of temperature and pressure (changing, with time), p_0 and T_0 are some reference values for temperature and pressure chosen appropriately (often, but not always, $p_0 = 1013$ mbar and $T_0 = 273$ K), and ΔV_{app} is the high voltage applied across the RPC (Abbrescia *et al*., 1995).

In principle, if the assumption that keeping the gas density ρ_g constant would maintain gas parameters stable, data collected at different T and p values and plotted versus ΔV_{eff} (and not ΔV_{app}) would refer to same values of the E/ρ_g ratio. A nice verification of this fact is reported in Figure 3.48 for temperature, and in

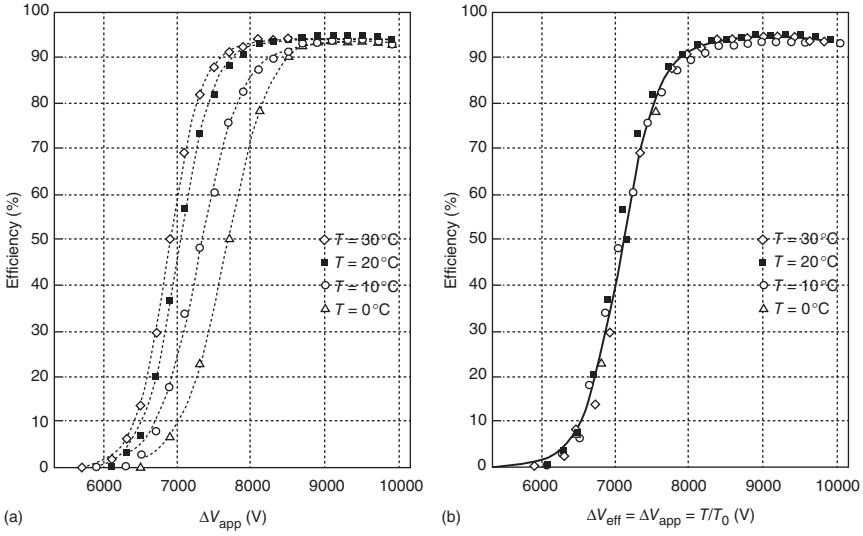

Figure 3.48 (a) Efficiency for a single-gap RPC operated in streamer mode versus ΔV_{app}, at different temperatures. (b) The same as in (a) but with efficiency plotted versus ΔV_{eff}, showing that, in this case, the curves roughly collapse in a single one. (Abbrescia *et al*. 1995. Reproduced with permission of Elsevier.)

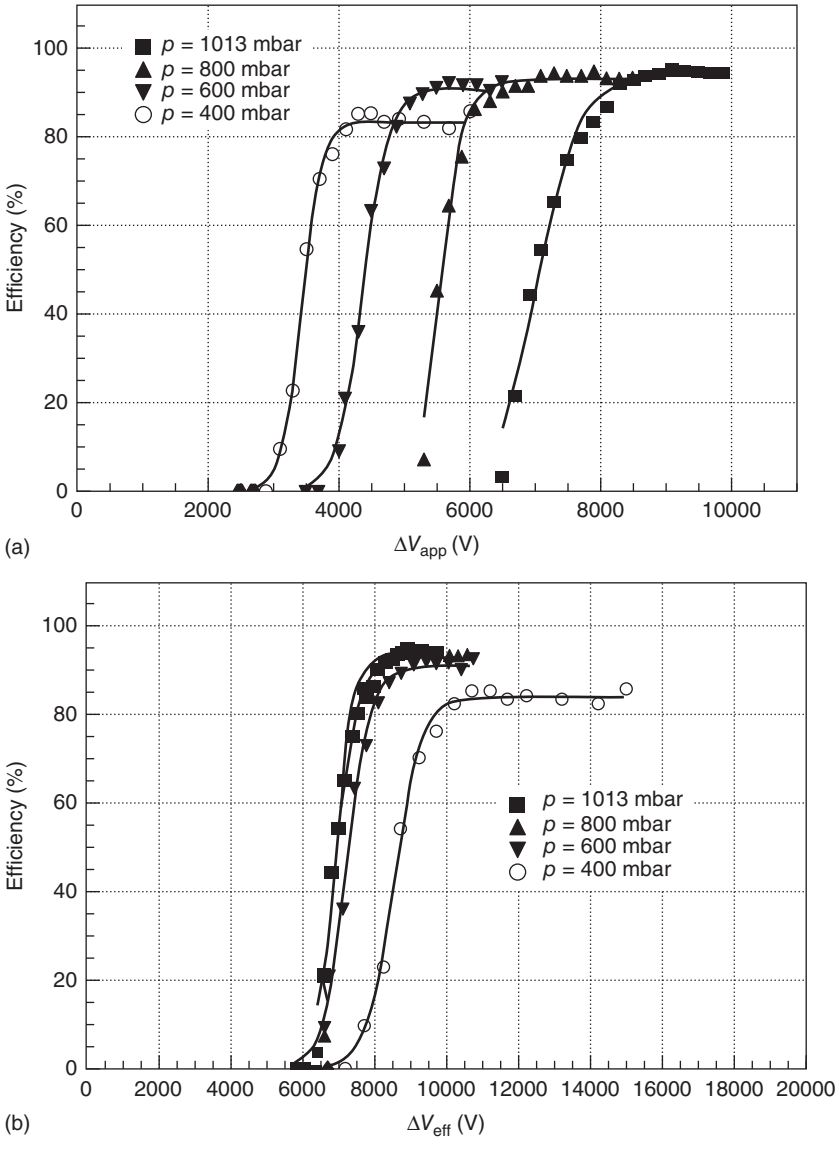

Figure 3.49 (a) Efficiency versus ΔV_{app} for a single-gap RPC operated in streamer mode, at different pressure; (b) the same as in (a) but plotted versus ΔV_{eff}, showing, for pressure above 600 mbar, that the curves merge in a single one. (Abbrescia *et al*. 1997b. Reproduced with permission of Elsevier.)

Figure 3.49 for pressure; efficiency curves collected in different condition collapse in a single one when plotted versus ΔV_{eff}.

Note that this rule is valid if the variations considered in T and p are not too large. For instance, from Figure 3.49 it is clear that data collected at 400 mbar deviate from the others; in this particular case, this is related to a reduced number

of primary ion-electron pairs, put in evidence also by the fact the relative efficiency curve has a lower plateau with respect to the others.

Nevertheless, it has become standard procedure to keep the ΔV_{eff} value as much constant as possible, in particular at large experiments. For the experiments at the Large Hadron Collider, being the underground caverns where the detectors are installed essentially thermostatic, the most important correction is the one related to the environmental pressure variations, which reflect on the pressure inside the chambers. Nevertheless, this turns out to be essential; during a 1-year time span, pressure variations around 40–50 mbar are common, and these have a 4–5% effect on ΔV_{eff}, which means a few hundred volts variation in absolute terms (given that RPC at ATLAS and CMS operate around 10 kV), which is not negligible at all. An example of the importance of this procedure is reported in Figure 3.50. Note that also in this case, it has been found that some refinement to the simple rule reported in Formula 3.34 can be done (Aielli *et al*., 2013) and (Abbrescia, 2013) and has been effectively implemented.

One should also note that other environmental parameters can influence RPC performance. For instance, for some time, anhydrous gas mixtures were used for RPCs. Since Bakelite, at production, contains a certain amount of water, putting it in contact with completely anhydrous gas mixtures would have the effect of drying it up. This, in turn, is generally believed to increase its resistivity; a nice verification of this point is reported in Figure 3.51, which also shows that the process seems to be, at least partially, reversible. Another study, performed for many materials, in addition to Bakelite, is reported in Crotty *et al*. (1995) and Figure 3.52.

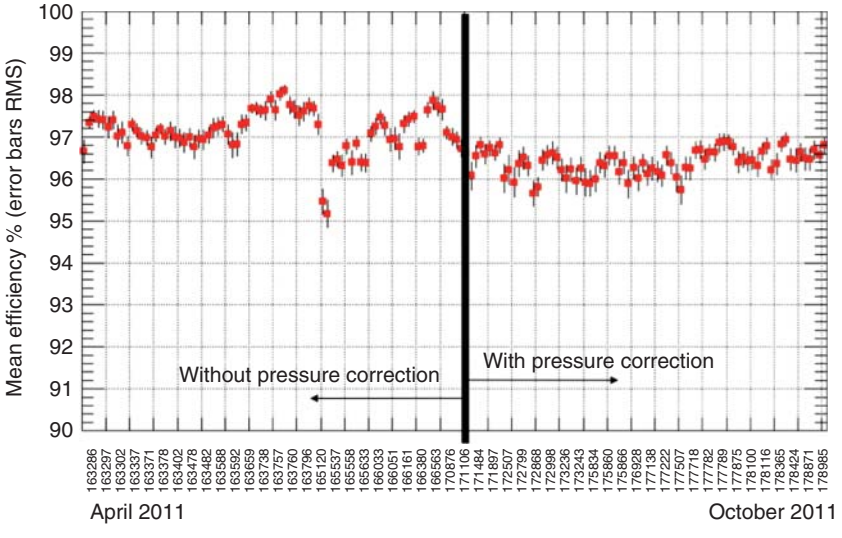

Figure 3.50 Average efficiency of the RPCs in the CMS muon systems versus time. Periods with and without automatic correction of the HV working point with atmospheric pressure are shown. (Paolucci *et al*. 2013. http://iopscience.iop.org/article/10.1088/1748-0221/8/04/P04005/meta. Licensed Under CC BY 3.0.)

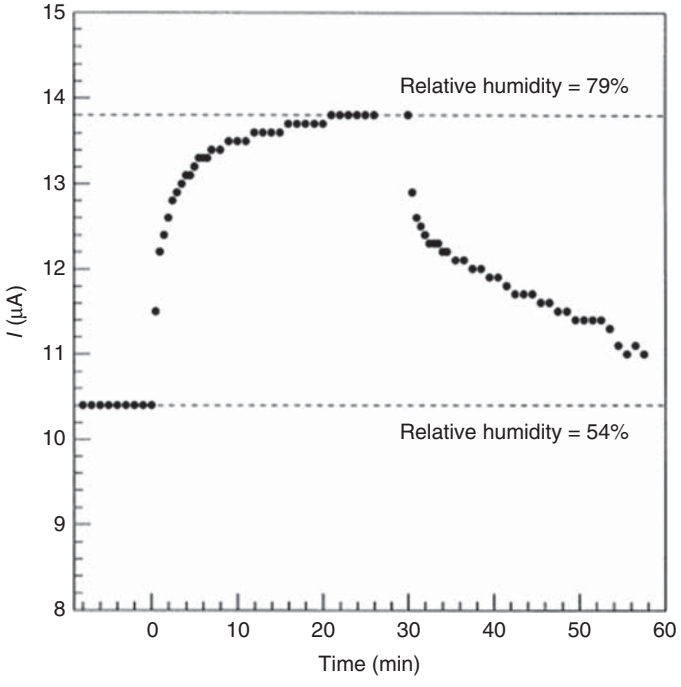

Figure 3.51 Variation in the "dark" current drawn by an RPC versus time going from lower to higher humidity conditions and vice versa. (Ahn *et al*. 2000. Reproduced with permission of Elsevier.) Higher current, in this case, is a hint of a reduced resistivity.

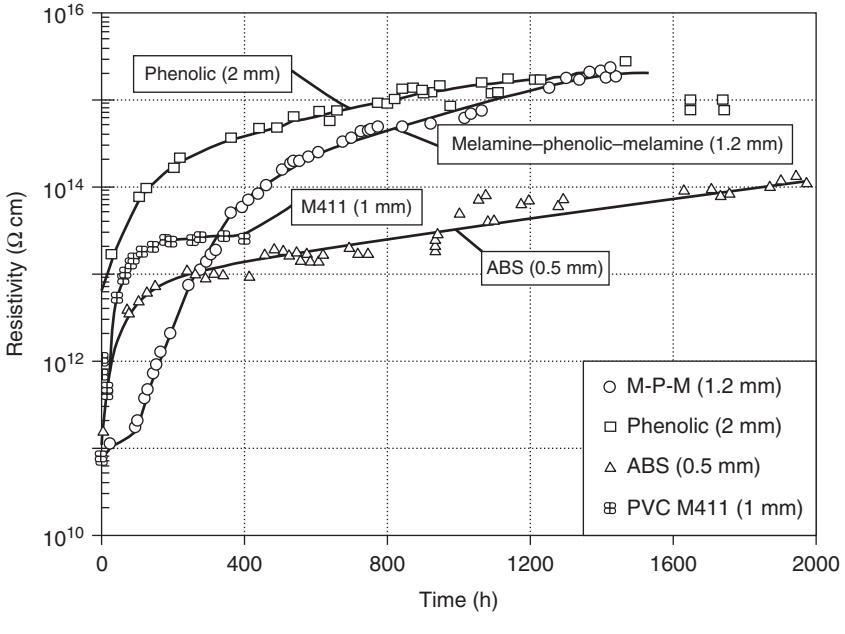

Figure 3.52 Resistivity of various plastic materials used for RPC construction over time, when left in a dry atmosphere. (Crotty *et al*. 1995. Reproduced with permission of Elsevier.)

Of course, a significant change in Bakelite resistivity might imply a change in the operating point and rate capability of this device (as will be seen in the following); this is the reason why nowadays the gas mixtures used for Bakelite RPCs are usually added with water vapor to reach a relative humidity in the 30–50% range. Gas mixture humidification, even if it keeps Bakelite resistivity stable in time, has an important drawback: Water vapor is generally believed to play a relevant role in hydrofluoric acid production, which sometimes can take place during avalanche and streamer processes in the gas gap, and, therefore, in the subsequent detector aging processes. Even if there is some evidence of this fact, some debate on this issue is still going on and a definite conclusion is still to be drawn.

Of course, the use of water vapour is not necessary for glass RPCs.

References

Abashian, A. *et al*. (2000) The K_L/μ detector subsystem for the BELLE experiment at the KEK B-factory. *Nucl. Instrum. Methods Phys. Res., Sect. A*, **449**, 112–124.

Abbrescia, M. (2013) Operation, performance and upgrade of the CMS resistive plate chamber system at LHC. *Nucl. Instrum. Methods Phys. Res., Sect. A*, **732**, 195–198.

Abbrescia, M. *et al*. (1995) Resistive plate chambers performances at cosmic ray fluxes. *Nucl. Instrum. Methods Phys. Res., Sect. A*, **359**, 603–609.

Abbrescia, M. *et al*. (1997a) Effect of the linseed oil surface treatment on the performance of resistive plate chambers. *Nucl. Instrum. Methods Phys. Res., Sect. A*, **394**, 13–20.

Abbrescia, M. *et al*. (1997b) Resistive plate chambers performances at low pressure. *Nucl. Instrum. Methods Phys. Res., Sect. A*, **394**, 341–348.

Abbrescia, M. *et al*. (1999a) The simulation of resistive plate chambers in avalanche mode: charge spectra and efficiency. *Nucl. Instrum. Methods Phys. Res., Sect. A*, **431**, 413–427.

Abbrescia, M. *et al*. (1999b) Progresses in the simulation of resistive plate chambers in avalanche mode. *Nucl. Phys. B (Proc. Suppl.)*, **78**, 459–464.

Abbrescia, M. *et al*. (2001) The resistive plate chambers for CMS and their simulation. *Nucl. Instrum. Methods Phys. Res., Sect. A*, **471**, 55–59.

Abbrescia, M. *et al*. (2006) HF production in CMS-resistive plate chambers. *Nucl. Phys. B (Proc. Suppl.)*, **158**, 30–34.

Abbrescia, M. *et al*. (2012) New gas mixtures for resistive plate chambers operated in avalanche mode. *Nucl. Instrum. Methods Phys. Res., Sect. A*, **661**, 190.

Abbrescia, M. *et al*. (2013) The EEE experiment project: status and first physics results. *Eur. Phys. J. Plus*, **128**, 62.

Abbrescia, M. *et al*. (2016) Eco-friendly gas mixtures for Resistive Plate Chambers based on tetrafluoropropene and Helium, *JINST*, **11**, P08019.

Abe, K. *et al*. (2000) Performance of glass RPC operated in streamer mode with SF_6 gas mixture. *Nucl. Instrum. Methods*, **455** (2), 397–404.

Ahn, S.H. *et al*. (2000) Temperature and humidity dependence of bulk resistivity of Bakelite for resistive plate chambers in CMS. *Nucl. Instrum. Methods Phys. Res., Sect. A*, **451**, 582–587.

Ahn, S.H. *et al*. (2005) Effects of linseed oil treatment on the forward resistive plate chamber for compact muon solenoid in the high-eta region. *J. Korean Phys. Soc.*, **46**, 1325–1335.

Aielli, G. *et al*. (2013) Performance, operation and detector studies with the ATLAS resistive plate chambers. *JINST*, **8**, P02020.

Aielli, G. *et al*. (2014) The RPC space resolution with the charge centroid method. *JINST*, **9**, C09030.

Ammosov, V. *et al*. (1997) Electric field and currents in resistive plate chambers. *Nucl. Instrum. Methods Phys. Res., Sect. A*, **401**, 217–228.

Anderson, B.E. *et al*. (1994) High counting rate resistive plate chamber. *Nucl. Instrum. Methods Phys. Res., Sect. A*, **348**, 324–328.

Arnaldi, R. *et al*. (2000) Influence of temperature and humidity on Bakelite resistivity. *Nucl. Instrum. Methods Phys. Res., Sect. A*, **456**, 140–142.

Assis, P. *et al*. (2016) A large area TOF-tracker device based on multi-gap resistive plate chambers. *JINST*, **11**, C10002.

Baesso, P., Cussans, D., Thomay, C., and Velthuis, J. (2014) Toward a RPC-based muon tomography system for cargo containers. *JINST*, **9**, C10041.

Band, H. *et al*. (2008) Study of HF Production in BaBar Resistive Plate Chambers. *Nucl. Instrum. Meth.*, **A594**, 33–38, SLAC-PUB-12854.

Bencivenni, G. *et al*. (1994) A modular design for glass spark counter. *Nucl. Instrum. Methods Phys. Res., Sect. A*, **345**, 456–460.

Benussi, L. *et al*. (2014) A Study of HFO-1234ze (1,3,3,3-Tetrafluoropropene) as an Eco-Friendly Replacement in RPC Detectors. INFN report INFN-14-14/LNF, SIDS–Pubblicazioni, Laboratori Nazionali di Frascati, Frascati (RM), Italy.

Biagi, S. (1994) IMONTE program to compute gas transport parameters.

Blanco, A. *et al*. (2012) TOFtracker: gaseous detector with bidimensional tracking and time-of-flight capabilities. *JINST*, **7**, P11012.

Camarri, P. *et al*. (1998) Streamer suppression with SF_6 in RPCs operated in avalanche mode. *Nucl. Instrum. Methods Phys. Res., Sect. A*, **414**, 317–324.

Candela, A. *et al*. (2007) Glass resistive plate chambers in the OPERA experiment. *Nucl. Instrum. Methods Phys. Res., Sect. A*, **581**, 206–208.

Carboni, G. *et al*. (2004) Final results from an extensive aging test of Bakelite resistive plate chambers. *Nucl. Instrum. Methods Phys. Res., Sect. A*, **533**, 107–111.

Cardarelli, R. *et al*. (1988) Progress in resistive plate counters. *Nucl. Instrum. Methods Phys. Res., Sect. A*, **263**, 20–25.

Cardarelli, R. *et al*. (1993) Performance of a resistive plate chamber operated with pure CF_3Br. *Nucl. Instrum. Methods Phys. Res., Sect. A*, **333**, 399–403.

Cardarelli, R. *et al*. (1996) Avalanche and streamer mode operation of resistive plate chambers. *Nucl. Instrum. Methods Phys. Res., Sect. A*, **382**, 470–474.

Cardarelli, R. *et al*. (2012) RPC performance vs. front-end electronics. *Nucl. Instrum. Methods Phys. Res., Sect. A*, **661**, S198–S200.

Cardarelli, R. *et al*. (2014) New RPC gas mixtures for large area apparatuses. *JINST*, **9**, C11003.

Cerron Zeballos, E. *et al*. (1995) High rate resistive plate chambers. *Nucl. Instrum. Methods Phys. Res., Sect. A*, **367**, 388–393.

Cerron Zeballos, E. *et al*. (1997) Pure avalanche mode operation of a 2 mm gap resistive plate chamber. *Nucl. Instrum. Methods Phys. Res., Sect. A*, **396**, 93–102.

Colucci, A. *et al*. (1994) Measurement of drift velocity and amplification coefficient in $C_2H_2F_4$-isobutane mixtures for avalanche-operated resistive plate counters. *Nucl. Instrum. Methods Phys. Res., Sect. A*, **425**, 84–91.

Crotty, I. *et al*. (1993) Investigation of resistive parallel plate chambers. *Nucl. Instrum. Methods Phys. Res., Sect. A*, **329**, 133–139.

Crotty, I. *et al*. (1994) The non-spark mode and high rate operation of resistive parallel plate chambers. *Nucl. Instrum. Methods Phys. Res., Sect. A*, **337**, 370–381.

Crotty, I. *et al*. (1995) The wide gap resistive plate chamber. *Nucl. Instrum. Methods Phys. Res., Sect. A*, **360**, 512–520.

Crotty, I. *et al*. (2003) High-rate, high-position resolution microgap RPCs for X-ray imaging applications. *Nucl. Instrum. Methods Phys. Res., Sect. A*, **505**, 203.

De Vincenzi, M. *et al*. (2003) Study of the performance of standard RPC chambers as a function of Bakelite temperature. *Nucl. Instrum. Methods Phys. Res., Sect. A*, **508**, 94–97.

Doroud, K. *et al*. (2009) Recombination: an important effect in multigap resistive plate chambers. *Nucl. Instrum. Methods Phys. Res., Sect. A*, **610**, 649.

Duerdoth, I. *et al*. (1994) The transition from proportional to streamer mode in a resistive plate chamber. *Nucl. Instrum. Methods Phys. Res., Sect. A*, **348**, 303–306.

Fischle, H. *et al*. (1991) Experimental determination of ionization cluster size distribution in counting gases. *Nucl. Instrum. Methods Phys. Res., Sect. A*, **301**, 202–214.

Fonte, P. (1996) A model of breakdown in parallel-plate detectors. *IEEE Trans. Nucl. Sci.*, **43**, 2135–2140.

Fonte, P. (2013) Analytical calculation of the charge spectrum generated by ionizing particles in resistive plate chambers at low gas *gain*. *JINST*, **8**, P04017. doi: 10.1088/1748-0221/8/04/P04017.

Fonte, P. *et al*. (1991a) Feedback and break-down in parallel plate chambers. *Nucl. Instrum. Methods Phys. Res., Sect. A*, **305**, 91–110.

Fonte, P. *et al*. (1991b) VUV emission and breakdown in parallel-plate chambers. *Nucl. Instrum. Methods Phys. Res., Sect. A*, **310**, 143–145.

Fonte, P. *et al*. (1999) The fundamental limitations of high-rate gaseous detectors. *IEEE Trans. Nucl. Sci*, **46**, 321–325.

Genz, H. (1973) Single electron detection in proportional gas counters. *Nucl. Instrum. Methods*, **112**, 83–90.

González-Díaz, D. *et al.* (2005) The effect of temperature on the rate capability of glass timing RPCs, *Nucl. Instrum. Methods Phys. Res., Sect. A*, **555**, 72–79.

Gramacho, S. *et al*. (2009) A long-run study of aging in glass timing RPCs with analysis of the deposited material. *Nucl. Instrum. Methods Phys. Res., Sect. A*, **602**, 775–779.

Gustavino, C. *et al*. (2001a) A glass resistive plate chamber for large experiments. *Nucl. Instrum. Methods Phys. Res., Sect. A*, **457**, 558–563.

Gustavino, C. *et al*. (2001b) Some studies of MONOLITH RPCs, MONOLITH Internal Rep., June 2001.
Gustavino C. *et al*. (2004) Performance of glass RPC operated in avalanche mode, *Nucl. Instrum. Methods Phys. Res., Sect A*, **527**, 471–477.
Haydon, S.C. (1973) in *Electrical Breakdown of Gases* (ed. J.A. Rees), MacMillan, London.
Iacobaeus, C. *et al*. (2002) Sporadic electron jets from cathodes–the main breakdown-triggering mechanism in gaseous detectors. *IEEE Trans. Nucl. Sci.*, **49**, 1622.
Inoue, Y. (1997) Observation of light from resistive plate chambers. *Nucl. Instrum. Methods Phys. Res., Sect. A*, **A394**, 65–73.
Ivaniouchenkov, I. *et al*. (1998) The high-rate behaviour of parallel mesh chambers. *Trans. Nucl. Sci.*, **45**, 258.
Kiš, M. *et al*. (2011) A multi-strip multi-gap RPC barrel for time-of-flight measurements. *Nucl. Instrum. Methods Phys. Res., Sect. A*, **646**, 27–34.
Kornakov, G. (2013) New advances and developments on the RPC TOF Wall of the HADES experiment at GSI. PhD thesis, http://hdl.handle.net/10347/7281 (accessed 25 October 2017).
Kubo, T. *et al*. (2003) Study of the effect of water vapor on a glass RPC with and without freon. *Nucl. Instrum. Methods Phys. Res., Sect. A*, **509**, 50–55.
Lapique, F. and Piuz, F. (1980) Simulation of the measurement by primary cluster counting of the energy lost by a relativistic ionizing particle in argon. *Nucl. Instrum. Methods*, **175**, 297–318.
Latham, R. (1995) *High Voltage Vacuum Insulation*, Academic Press, New York.
Lopes, L. *et al*. (2012) Systematic study of gas mixtures for timing RPC. *Nucl. Instrum. Methods Phys. Res., Sect. A*, **661**, S194–S197.
Manisha *et al*. (2016) Development and Characterization of Single Gap Glass RPC, https://arxiv.org/ftp/arxiv/papers/1603/1603.01719.pdf (accessed 25 October 2017).
Nappi, E. and Peskov, V. (2013) *Imaging Gaseous Detectors and their Applications*, Wiley-VCH Verlag GmbH. ISBN: 978-3-527-40898-6.
Narita, S. *et al.* (2010) Measurements of induced charge profile in RPC with Submilli-strips. *IEEE Trans. Nucl. Sci.*, **57**, 2210–2214.
Narita, S., Hoshi, Y., Neichi, K., and Yamaguchi, A. (2012) Induced charge profile in glass RPC operated in avalanche mode. *Nuclear Science Symposium and Medical Imaging Conference (NSS/MIC)*. IEEE. doi: 10.1109/NSSMIC.2012.6551287.
Paolucci, P. *et al*. (2013) CMS resistive plate chambers overview, from the present system to the upgrade phase I. *JINST*, **8**, P04005.
Parkhomchuk, V.V. *et al*. (1971) A spark counter with large area. *Nucl. Instrum. Methods*, **93** (2), 269–270.
Peskov, V. (1976) Secondary processes in a gas counter I. *Sov. Phys. Tech. Phys.*, **20** (6), 791.
Peskov, V. (1977) Secondary processes in gas-filled counters II. *Sov. Phys. Tech. Phys.*, **22** (3), 335.
Pestov, Y. (1988) The status of spark counters with a localized discharge. *Nucl. Instrum. Methods Phys. Res., Sect. A*, **265**, 150–156.

Pestov, Y. *et al*. (2000) Timing performance of spark counters and photon feedback. *Nucl. Instrum. Methods Phys. Res., Sect. A*, **456**, 11–15.

Qite Li *et al*. (2012) Study of spatial resolution properties of a glass RPC. *Nucl. Instrum. Methods Phys. Res., Sect A*, **663**, 22–25.

Raether, H. (1964) *Electron Avalanches and Breakdown in Gases*, Butterworths, London.

Ramo, S. (1939) Currents induced by electron motion. *Proc. IRE*, **27** (9), 584–585. doi: 10.1109/JRPROC.1939.228757.

Riegler, W. (2009) Time response functions and avalanche fluctuations in resistive plate chambers. *Nucl. Instrum. Methods Phys. Res., Sect. A*, **602**, 377.

Riegler, W. *et al*. (2003) Detector physics and simulation of resistive plate chambers. *Nucl. Instrum. Methods Phys. Res., Sect. A*, **500**, 144–152.

Riegler, W. *et al*. (2004) The physics of resistive plate chambers. *Nucl. Instrum. Methods Phys. Res., Sect. A*, **518**, 86–90.

Sadiq, J. *et al*. (2016) Effect of glass thickness variations on the performance of RPC detectors. *JINST*, **11**, C10003.

Santonico, R. *et al*. (1981) Development of resistive plate counters. *Nucl. Instrum. Methods Phys. Res.*, **187**, 377.

Shi, L. *et al*. (2014) A high time and spatial resolution MRPC designed for muon tomography. *JINST*, **9**, C12038.

Shockley, W. (1938) Currents to conductors induced by a moving point charge. *J. Appl. Phys.*, **9** (10), 635. doi: 10.1063/1.1710367.

Smirnov, I. (1994) HEED, Program to Compute Energy Loss of Fast Particles in Gases, Version 1.01, CERN.

Wang, J. *et al*. (2010) Development of multi-gap resistive plate chambers with low-resistive silicate glass electrodes for operation at high particle fluxes and large transported charges. *Nucl. Instrum. Methods Phys. Res., Sect. A*, **621**, 151.

Wang, Y. *et al*. (2012) PoS(RPC2012)014]

Zhao, Y.E. *et al*. (2005) Effects of temperature on the multi-gap resistive plate chamber operation. *Nucl. Instrum. Methods Phys. Res., Sect. A*, **547**, 334–341.

Zhu, J. (2012) PoS(RPC2012)062.

4

Further Developments in Resistive Plate Chambers

4.1 Double Gap RPCs

The single-gap resistive plate chambers (RPCs), as described in the original paper by Santonico and Cardarelli (1981), gave rise to a plethora of further developments in this field, using this module as a starting point and changing its geometrical parameters or simply the number of modules used.

For instance, it was clear from the beginning that the performances achieved could be improved using two single-gap RPC modules arranged in such a way as to induce their signals on the very same set of readout electrodes; this was called the "double-gap" configuration, typically realized with readout strips embedded between two gaps, as shown in Figure 4.1. An ionizing particle crossing this device would normally produce ion-electron pairs in both gaps; and, with the appropriate configuration for the electric fields, the signals induced by the avalanches in the two gaps would be practically simultaneous and add up on the central readout electrodes. This, of course, would increase the efficiency of the device; even considering the two single gaps to be just in a logical OR (i.e., we assume that we detect a signal on the central readout strips if the avalanches drifting in either one of the two gaps induce a signal), its efficiency ε_{tot} would be given by[1]

$$\varepsilon_{\text{tot}} = \varepsilon_1 + \varepsilon_2 - \varepsilon_1\varepsilon_2 \tag{4.1}$$

Note that, as a matter of fact, Formula 4.1 is just the simplest approximation for ε_{tot}; the overall efficiency is, in general, higher than the one given by the previous formula. The reason is that the signal on the central readout electrodes is not just the digital sum of the signals from the two gaps, but it is the analog sum, that is, the two signals add their instantaneous values; the total amplitude can pass the threshold, and therefore the signal is detected, even if both signals from both gaps are under threshold.

We also would expect the time resolution of a double-gap RPC to be at least a factor $1/\sqrt{2}$ better than the time resolution of a single-gap RPC, given the same configuration in terms of geometry, gas used, and electric field applied. This derives from the fact that having two independent signals related to the same

1 Because the total inefficiency is the probability that both chambers are inefficient, that is: $(1-\varepsilon_{\text{tot}}) = (1-\varepsilon_1)(1-\varepsilon_2)$.

Resistive Gaseous Detectors: Designs, Performance, and Perspectives, First Edition.
Marcello Abbrescia, Vladimir Peskov, and Paulo Fonte.

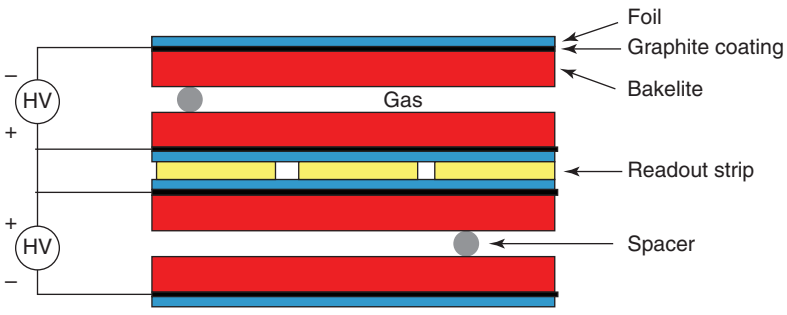

Figure 4.1 Schematic layout of a double-gap RPC; note that the voltage is applied in a such a way that the electrons produced in both gaps move toward the central readout strips; under these conditions, both induced signals have the same polarity. Note also that the spacers are usually staggered in the two gaps, so that the zone corresponding to a spacer would be characterized by a lower efficiency (since just one gap is active there) but would not be completely inactive. (From http://www.pd.infn.it/~zotto/beauty97/rpc.html.)

impinging particles, the fastest determines the threshold crossing time measured with the detector. Again, the total signal being the analog sum, and not just the OR of the two signals, the actual overall time resolution is usually slightly better than this value. As expected, double-gap RPCs perform better with respect to

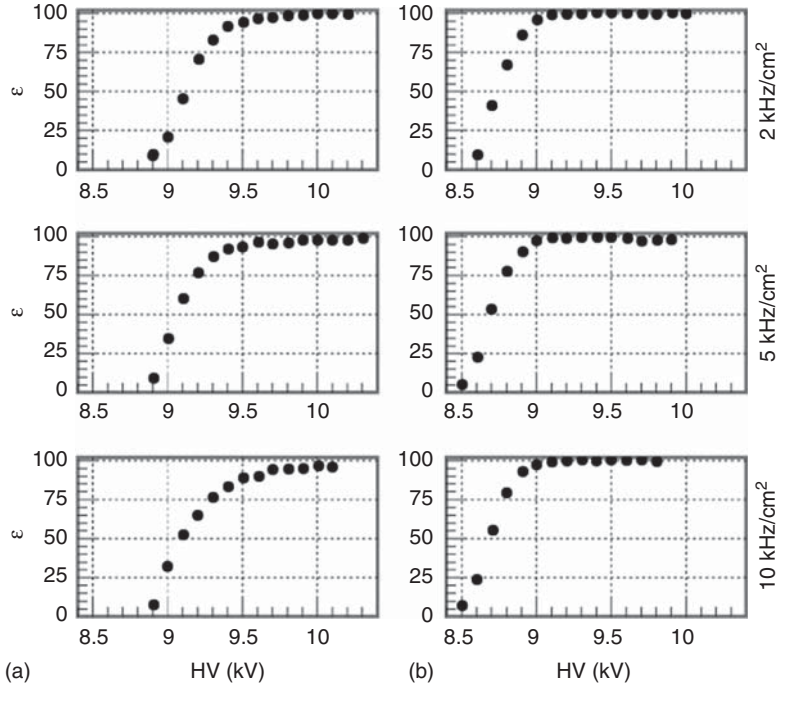

Figure 4.2 Efficiency curves for single-gap RPC (a) and double-gap RPC (b) at various beam intensities, as measured in the framework of the R&D for the RPCs proposed for the LHCb experiment at LHC. (Adinolfi *et al*. 2000. Reproduced with permission of Elsevier.) Higher efficiency at lower voltage is reached in the case of double-gap RPCs with respect to single-gap RPCs.

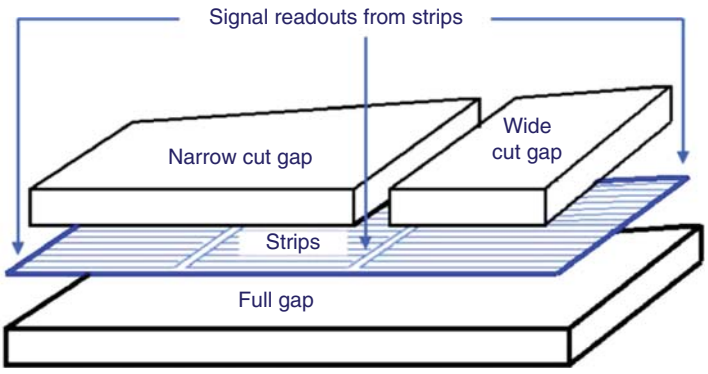

Figure 4.3 Layout of a double-gap RPC built for the endcaps of the muon systems of the CMS experiment. The top layer is divided into two gas gaps (conventionally called in CMS experiment "narrow" and "wide") to allow for signal readout from the segmented strips placed between the two layers. (Park *et al*. 2005. Reproduced with permission of Elsevier.)

single-gap RPCs also at high rate, given the same conditions and characteristics of the basic modules (see, for instance, (Adinolfi *et al*., 2000) and Figure 4.2).

Due to these remarkable characteristics, and the intrinsic reliability (if one of the two gaps, for some reason, does not produce acceptable signals the other one can still provide an acceptable performance), the double-gap configuration was chosen in the mid 1990s for several high-energy physics experiments, one remarkable example being the L3 experiment at large electron positron (LEP) (Aloisio *et al*., 1996). Later on, the most relevant implementation was on the muon system of the Compact Muon Solenoid (CMS) experiment at the Large Hadron Collider (LHC) at CERN (European Organization for Nuclear Research; see Figure 4.3). Here, an overall surface of about 2000 m^2 is covered with double-gap RPCs, with a total of about 150 000 readout channels; this (and other systems implemented with RPCs) is described in more detail in Chapter 5.

4.2 Wide-Gap RPCs

Other interesting studies on RPCs were performed in the beginning of the 1990s, in an attempt to find the optimal configuration for this device. The reason for these studies, in particular, was related to the fact that, in the beginning of 1990s, the use of RPCs in cosmic-ray experiments was well established, but there was a general feeling that additional R&D was needed before these detectors – which at the time were relatively recent – could be judged suitable to be used at experiments mounted at high-luminosity accelerators; indeed, this was the period when the design of the detectors, at that time "a long way to go" LHC experiments, began. The main issue, in particular, was related to the RPC rate capability, that is, their ability to remain efficient even at high fluxes of impinging particles, which is discussed in detail later on in this book.

The most natural parameter that, potentially, could be changed and optimized, was the gap width, originally set in the Santonico and Cardarelli's RPCs to 2 mm. As it was outlined in Chapter 3, RPCs were originally thought to be operated in streamer mode, which produces a drifting charge inside the gas gap typically

from 10 to 20 times higher than when operating the RPC in avalanche mode. Large pulses have the advantage to render the front-end amplifiers unnecessary, but have the inconvenience that the large current flowing in the electrodes significantly reduces the effective voltage applied to the gas, leading to a limited rate capability; in addition, an increased time walk, frequent after-pulses in addition to the principal signal, and, in general, accelerated aging processes are drawbacks of this operating mode.

Also, when operating RPCs in avalanche mode (lowering the applied voltage and reducing the gain in the gas, and using amplifiers in the front-end electronics) one has to take care of what is generally called the "streamer probability," that is, the percentage of times that the number of electrons in an avalanche reaches the Raether limit and the avalanche transforms itself into a streamer, would not be too high. This is because, when using amplifiers at the front end, streamers are particularly harmful, since a streamer, due its large signal amplitude, would generally trigger also the channels close to the one corresponding to the position of the impinging particle, leading to the appearance of clusters of neighboring strips firing all at the same time and eventually spoiling the detector spatial resolution.

The first attempts to overcome this problem were done in the group led by M.C.S. Williams at CERN (Crotty *et al*., 1995), where "wide"-gap RPCs were proposed. The statistics of electron production in an RPC gas gap, and how the avalanche and induction processes can be modeled, have been described in Chapter 3; those calculations can be used to comprehend rigorously the line of reasoning outlined in the following. Here, to understand why increasing the gas gap size could be considered an advantage, we will just remember that in an RPC the final charge of the avalanches depends significantly on the distance from the anode where the corresponding primary ion-electron pairs were created. If one primary ion-electron pair is created too close to the anode, it may happen that there will be not enough space for it to grow large enough to induce a detectable signal on the readout electrodes. Let us indicate by A the gain of an electron traversing the whole gas gap, on the average given by

$$A = e^{\alpha^* g} \tag{4.2}$$

where α^*, as usual, is the effective first Townsend coefficient, and g is the gas gap width. An electron produced at a distance x from the anode will then have an average gain A':

$$A(x)' = e^{\alpha^* x} = e^{\alpha^* g \frac{x}{g}} = A^{\left(\frac{x}{g}\right)} \tag{4.3}$$

To fix our ideas, let us consider now a 2-mm RPC, filled with a certain gas mixture, equipped with a readout electronics characterized by a threshold that, to be passed, needs an avalanche with a size corresponding, say, to a 10^5 gain. Using Poisson statistics and supposing that, for instance, the number of clusters per millimeter generated by an ionizing particle is around 3 mm^{-1}, typical of the argon-based gas mixtures that were used at the time, one finds that there is a 5% probability that an ionizing particle will not produce any pair in the 1 mm closest to the cathode. Since we want to operate our detector close to 100% efficiency, we most probably want to get an efficiency higher than 95%, that all the primary pairs produced in the remaining part of the gap should be detected; this means that the gain in the remaining 1 mm should be close to the 10^5 value cited before.

Under these conditions, if an impinging particle happens to produce a primary electron immediately close to the cathode, this will traverse the full 2-mm gap and experience a gain A of around 10^{10}, giving rise to an avalanche much larger than the Raether limit, and very likely transforming into a streamer. Therefore, the device, if arranged to detect particles with high efficiency will produce sometimes small and, sometimes, large signals. This is usually expressed by saying that the dynamic range of the induced signals in RPCs is large (ranging on several orders of magnitude), which, by the way, is an important difference with respect to central wire detectors.

This is a problem that has to be overcome in practice; as it was already pointed out, one issue in operating RPCs in avalanche mode is that it is desirable for them to work at full efficiency but at the same time with a reduced "streamer probability" (as was defined earlier). In this respect, the concept of "useful plateau," usually defined as the region in the efficiency versus applied voltage curve where efficiency is higher than 95% and streamer probability lower than 10%, is often used. Streamers, in practice, are often detected by looking at those events where a certain number of neighboring strips are fired at the same time. For a safe operation, the useful plateau has to be at least a few hundred volts wide. Under certain conditions, the useful plateau is narrow or does not even exist. In general, the choice of detector configuration, gas mixtures, and readout electronics plays a crucial role here (see Figure 4.4).

Let us now consider what happens when increasing the gap to, for instance, 8 mm; in this case, there will be still 1 mm of the gap needed to produce the necessary ion-electron primary pair to guarantee an efficiency of at least 95%, but 7 mm more in the gap will remain available for the avalanche process. If a gain $A' = 10^5$ over $x = 7$ mm is set, from Formula 4.3 we can deduce that this implies a gain $A = 5.2 \times 10^5$ for an electron traversing the whole gap; in other words, the ratio between the maximum and minimum signals is strongly reduced. In this particular case, increasing the gap from 2 to 8 mm guarantees a reduction in the dynamic range from 10^5 to around 5, with a corresponding reduction, at the same efficiency value, of the expected streamer probability.

These considerations found a nice experimental confirmation. In Figure 4.5, for instance, the charge induced on readout electrodes in the cases of 2- and 8-mm RPCs are reported (Cerron Zeballos *et al*., 1996a). The charge distribution corresponding to the 2-mm gap RPC is characterized by a much longer tail toward the right, with a prominent peak of "streamer" pulses, confirming, at least from a qualitative point of view, what was deduced from the considerations exposed earlier.

As expected, wide-gap RPCs are easier to operate, are characterized by a wider useful plateau (see Figure 4.6) and show a remarkable rate capability (see Figure 4.7). However, they have the important drawback of a worse time resolution with respect to narrow-gap RPCs. Let us remember that in an RPC the time resolution depends on electron drift velocity v_d and on the effective first Townsend coefficient α^* (see Formula 3.26). The fact that the total gain A in both narrow- and wide-gap RPCs must roughly be the same (limited by the gain-dependent streamer probability) leads to the fact that wide-gap RPCs are operated at lower electric fields, with a corresponding reduction in α^* (and, to a lesser extent, in v_d) and a worsening in time resolution (see Figure 4.8). In other

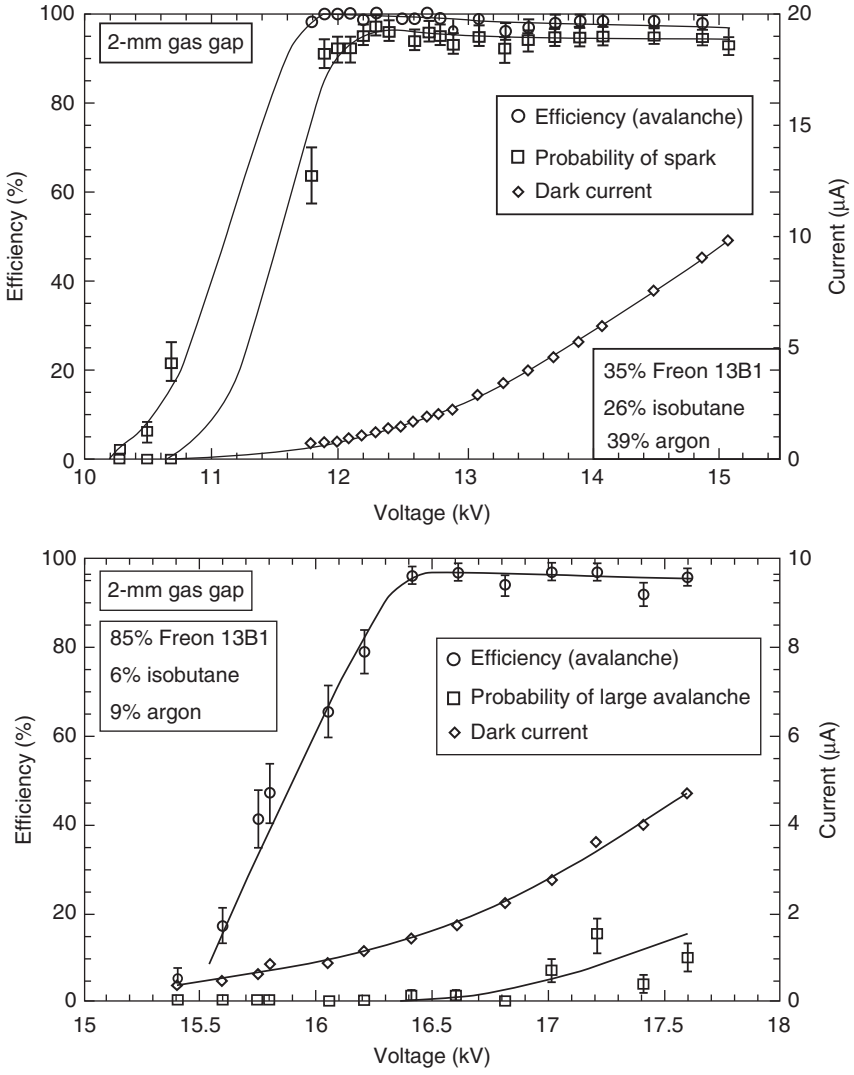

Figure 4.4 Efficiency plateau of a single-gap 2-mm RPC, filled with two different gas mixtures, and increasing the percentage of Freon 13B1. Also, the streamer probability and current are shown. It is evident how the choice of the correct gas mixture is crucial to obtain high efficiency while keeping streamer probability at acceptable levels. (Cerron Zeballos *et al*. 1996a. Reproduced with permission of Elsevier.)

words (Cerron Zeballos *et al*., 1996a), in a wide-gap chamber the avalanches have to drift over several millimeters of space, and this leads to an increased signal rise time. This led to the fact that other solutions, different from wide-gap RPCs, were investigated, like the multi-gap RPCs.

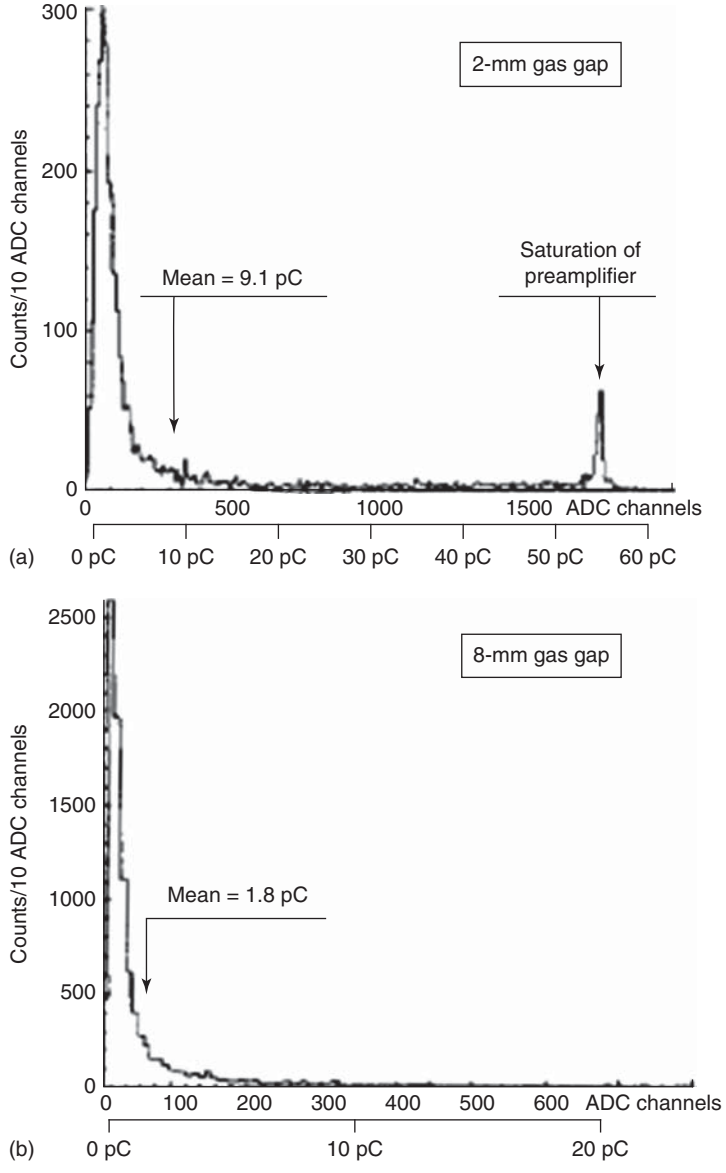

Figure 4.5 Induced charge distributions for (a) a 2-mm and an 8-mm (b) RPC, exposed to a particle flux of 100 Hz/cm^2. (Cerron Zeballos *et al*. 1996a. Reproduced with permission of Elsevier.)

4.3 The Multi-gap RPCs

Multi-gap RPCs (often indicated as MRPCs) were first proposed in 1996 in the group led by M.C.S. Williams (Cerron Zeballos *et al*., 1996b), and, in a sense, they

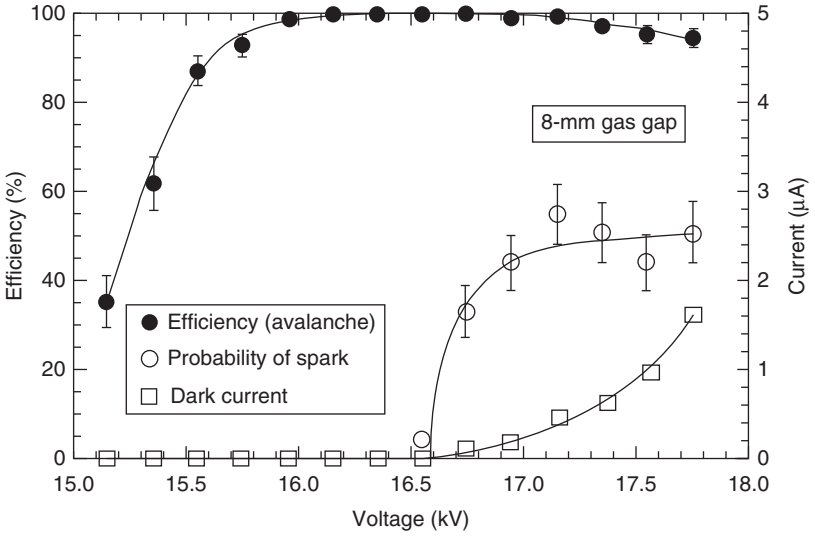

Figure 4.6 Efficiency plateau measured with cosmic rays for a single-gap RPC very similar to the one whose measures are reported in Figure 4.4, but with an 8-mm gas gap, and filled with a Ar/CO_2/DME 42/39/19 gas mixture. Also, the streamer probability and current are shown. (Cerron Zeballos *et al*. 1996a. Reproduced with permission of Elsevier.)

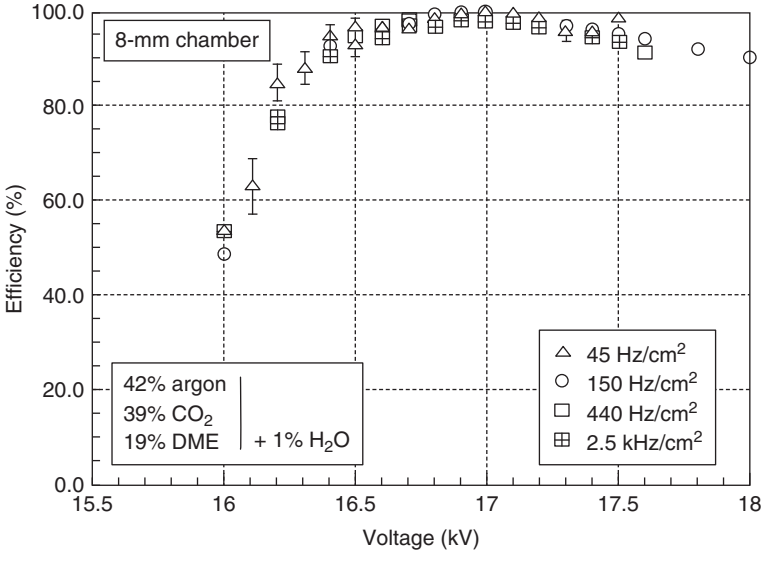

Figure 4.7 Efficiency plateau for an 8-mm RPC, at four different values of the particle flux. (Cerron Zeballos *et al*. 1996a. Reproduced with permission of Elsevier.)

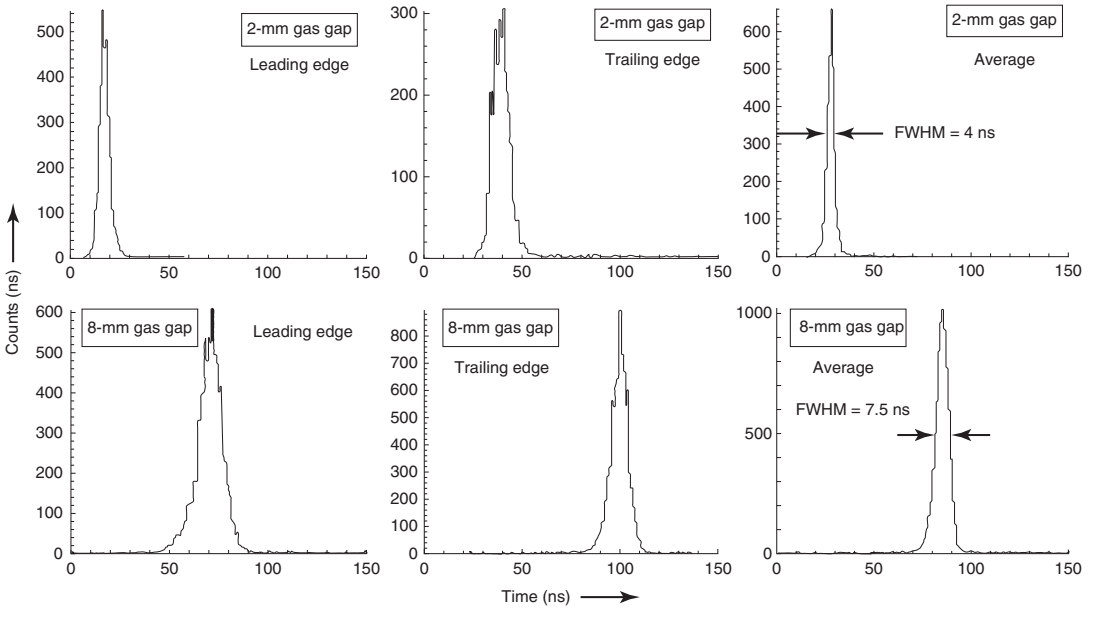

Figure 4.8 Time distributions corresponding to the leading edge, trailing edge, and the average between leading and trailing edges for two RPCs, one (upper plots) with a 2-mm gas gap, the other (lower plots) with an 8-mm gas gap. In both cases, the data were taken at the "knee" of the efficiency plateau, at a particle flux of 100 Hz/cm^2. The distributions corresponding to the 2-mm RPC are much narrower and earlier in time. (Cerron Zeballos *et al*. 1996a. Reproduced with permission of Elsevier.)

were the evolution of the double-gap concept, successfully getting together the advantages (for instance, in terms of rate capability and a smaller charge dynamic range) of the wide-gap RPCs – previously studied by the same group – with the possibility of obtaining an improved time resolution.

Essentially, the idea was to divide the gas gap where the primary ionization takes place in smaller slices. This is practically performed using not just one or two gaps, but a whole stack of resistive electrodes, with just the two outermost ones connected to the high voltage, while the internal ones are left electrically floating (see Figures 4.9 and 4.10).

It is fundamental to note that even if the internal plates are left electrically floating, they get the right voltage by themselves (as is shown, for an applied voltage of 10 kV, in Figure 4.9), and there is no need to add any connection within the frame to apply a voltage to these inner resistive plates. Under static conditions this is due to simple electrostatics, given the fact that these plates are in a strong electric field and given the symmetry of the system. Under dynamic conditions, moreover, there is a feedback mechanism that tends to keep the electrodes at the right potential and dictates equal current in all gap gaps. Basically, if, for any reason, the voltage on one resistive plate deviates, this will cause an increase in the electric field in one sub-gap and a decrease in another; in the gap with the higher field, larger avalanches, compared to the other sub-gap, will be produced. Larger avalanches imply an increased flow of electrons and positive ions in one gap (i.e., an increased current in one gap), bringing more charge on one of the resistive electrodes of the neighboring gap. This will change the potential of both electrodes and, in the end, has the effect to restore the correct field and gain in both gaps (Cerron Zeballos *et al*., 1996b).

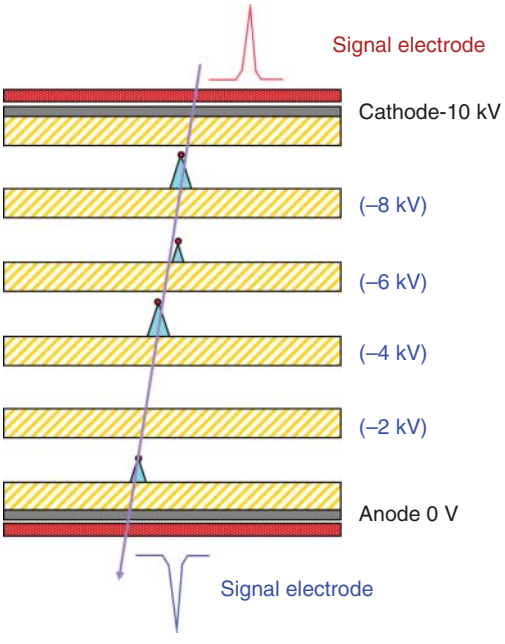

Figure 4.9 Conceptual layout of a multi-gap resistive plate chamber (sometimes indicated as MRPC). The detector consists of a stack of resistive electrodes, and an impinging particle can create primary ion-electron pairs in any of the gas gaps. (From Shao *et al*. 2006.)

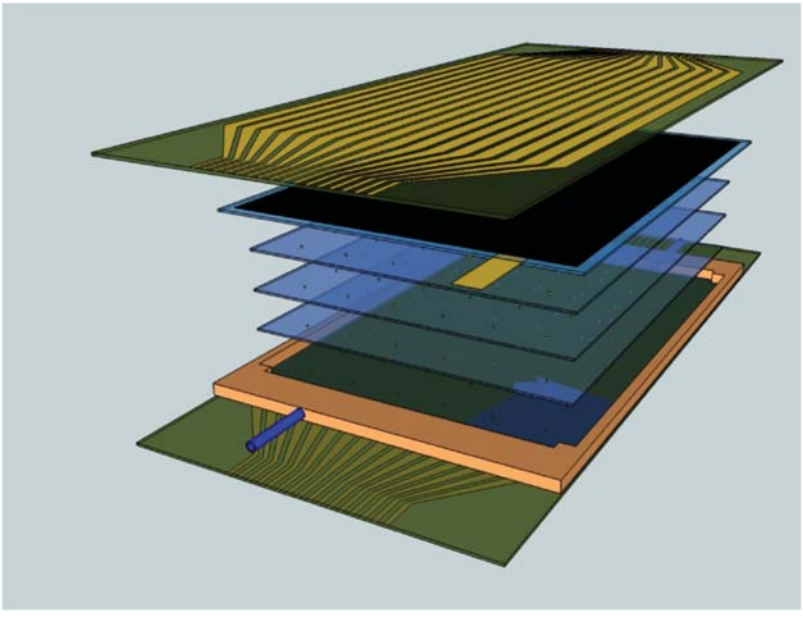

Figure 4.10 Conceptual exploded view of a multi-gap RPC. The internal layers (light gray), the outermost electrodes (in dark gray) connected to the high voltage, the readout strips (positioned onto the outer electrodes), and the gas inlet can be seen (https://project-aqua.web.cern.ch/project-aqua/rpcpet.html).

Gap spacing in MRPCs is typically much smaller than in standard RPCs, ranging around a few hundred micrometers per gap; for instance, in the time-of-flight (TOF) system of the ALICE experiment, it is 250 μm (see Figure 4.11), while in the MRPCs used for the Extreme Energy Events project it is 320 μm. Usually, five or more gaps are used, and this assures that an adequate number of primary ion-electron pairs are generated each time an ionizing particle crosses the device.

Most of the MRPCs have been produced using electrodes made of float glass, with glass easily available on the market, and typically used for other purposes, like common glass for windows, with a typical resistivity of a few times 10^{12} Ω cm, significantly higher than the characteristic resistivity of RPCs made with Bakelite (around 10^{10}–10^{11} Ω cm). The glass plates are often kept parallel using insulating rods of the appropriate diameter stretched between the plates (commonly fishing lines are used; see Figure 4.12). The two outermost plates are painted with a graphite paint to make their outer surfaces conductive and easily connect them to the high voltage power supply.

Even if the most widespread MRPCs are made using glass electrodes, note that, more recently, also MRPCs made with phenolic resins (i.e., Bakelite) have been produced, and they show quite encouraging results (Lee *et al*., 2012).

Basically, the operating principle of an MRPC is similar to standard RPCs. When an ionizing particle impinges on the detector it produces primary ion-electron pairs in the gas gaps (usually more than one); when the appropriate potential difference is applied to the stack of resistive electrodes, the electrons

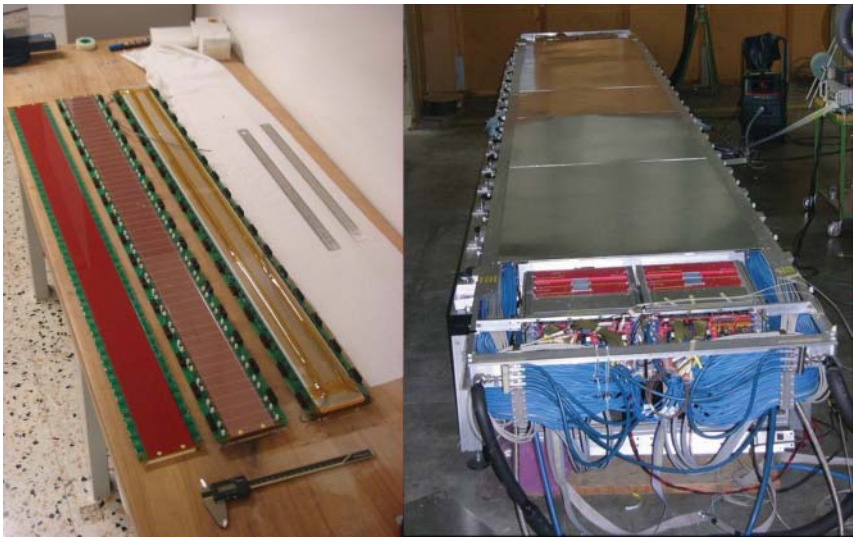

(a) (b)

Figure 4.11 (a) A multi-gap RPC developed for the time-of-flight system of the ALICE experiment during its assembly phase; (b) one of the super modules for the same system completed (photographs from the ALICE-TOF Bologna group website: http://www.bo.infn.it/alice-tof-hw/public/TOFphotos/TOFphotos_INDEX.html).

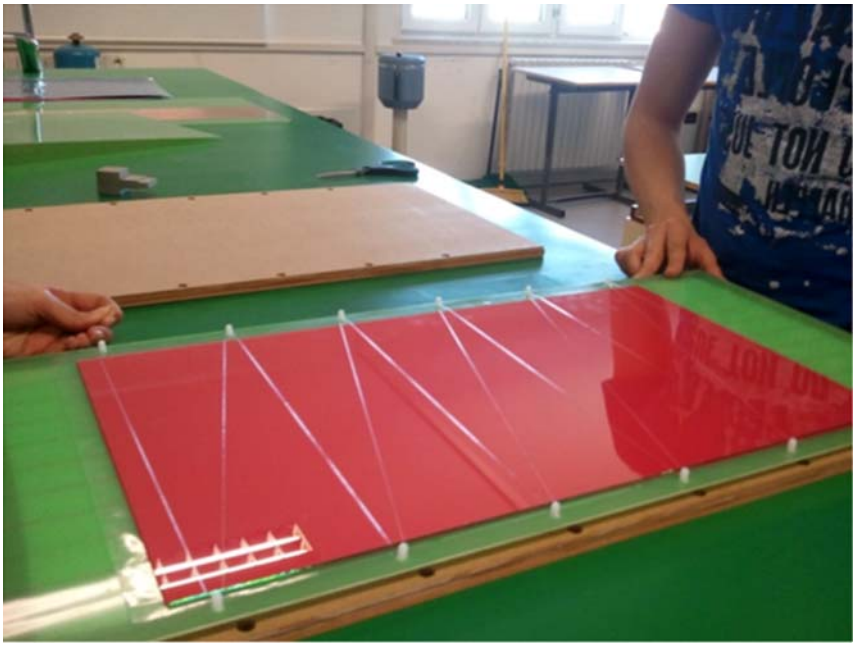

Figure 4.12 Fishing lines stretched and used to keep to electrodes on an MRPC at the right distance. (From Garritano *et al*. 2015.)

produced in the gaps drift toward the anode and, if the electric field is intense enough, give rise to a corresponding number of avalanches. Their movement induces a signal on the external pickup electrodes, which are pads or strips positioned close to the outermost glass plates, and usually separated from the conductive graphite coating with an insulating layer. Since the various avalanches are generated practically at the same time, the relative signals are summed up on the readout electrodes; therefore, even if the signal related to a single avalanche is small (i.e., lower than the electronic threshold), their sum may pass the threshold.

Note that, in general, the signal induced on readout electrodes by a moving charge depends on the distance across which the charge has moved; this is clearly seen by applying the Ramo theorem, already cited in Chapter 3. Therefore, one would expect that in narrow-gap RPCs the signal induced per gap would be lower with respect to wide-gap RPCs, given the same avalanche size.

Indeed, in a multi-gap structure, the weighting field factor used to compute the induced charge and reported in Equation 3.14 has to be modified to take into account the different geometry; it can be computed using the same procedure already outlined, which in this case yields:

$$\Delta V_{\mathrm{w}} = \frac{\varepsilon_{\mathrm{r}} g}{N_{\mathrm{g}} \varepsilon_{\mathrm{r}} g + (N_{\mathrm{g}} + 1) d} \tag{4.4}$$

where N_{g} is the number of gaps, and the other symbols have the usual meaning, that is, g is the gap width, d the electrode thickness, and ε_{r} its relative dielectric permittivity.

Note that in a multi-gap configuration, the readout electrodes are positioned on one side of the gap stack, while in the double gap they are positioned in the middle, and this has consequences on the amount of the induced charge in the different cases, as can be seen from Figure 4.13.

If, for instance, we consider in the three cases a charge of 1 pC drifting in each gap, in the limit of infinitely thin resistive electrodes (i.e., we put $d = 0$ in Equation 4.4), the induced charge q_{ind} will be 1 pC in the single-gap case, 2 pC in the double-gap case, and 1 pC again for the multi-gap case (independent on N_{g} in this approximation). This is often expressed by saying that in MRPCs the charge drifting in each gap contributes for a factor $1/N_{\mathrm{g}}$ to the induced charge. Moreover, in practice, the finite thickness d of the resistive electrodes with respect to the gap width g must also be taken into account, which further reduces the induced charge.

The first prototype of MRPC (Cerron Zeballos *et al.*, 1996b) had three gaps, each 3 mm wide, and its performance was compared to a 9-mm "wide"-gap RPC, made essentially of the same materials.

As has been pointed out previously in this chapter, not the whole gas gap is "active" in an RPC, in the sense that at least one primary ion-electron pair has to be produced close enough to the cathode so that the corresponding avalanche can grow large enough to produce a detectable signal. A region of about 1–1.5 mm from the cathode(s) is generally needed, to assure the necessary number of primary ion-electron pairs, the exact value depending on the gas mixture used. In a MRPC, this region is actually divided among the various gaps (see Figure 4.14), and the authors infer, following a line of reasoning very similar

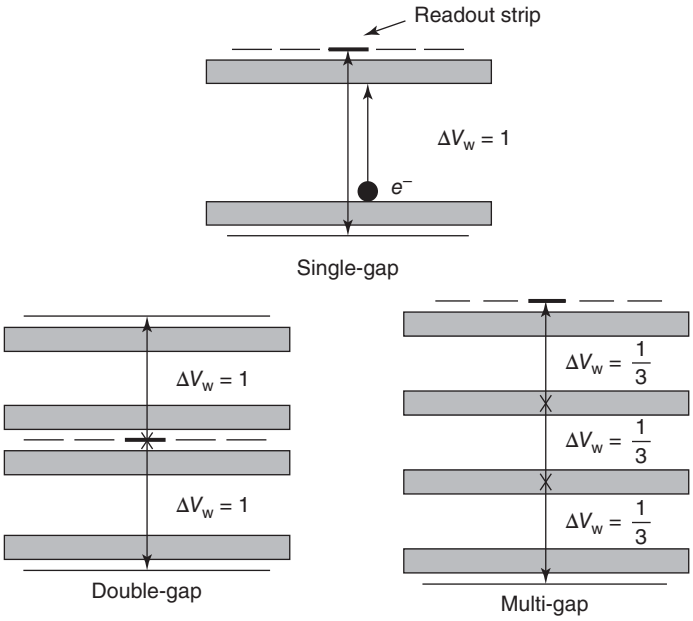

Figure 4.13 Conceptual layouts of a single-, a double-, and a multi-gap RPC, used to easily visualize the values of ΔV_w in the different cases. (Abbrescia *et al*. 1999a. Reproduced with permission of Elsevier.)

to the one already reported for the wide-gap RPCs, that the signal's dynamic range in the two cases (wide-gap and multi-gap) is basically the same and in the 10–20 range.

However, in a multi-gap, the distance available for the avalanches to develop and to induce a signal on the readout electrodes is smaller with respect to an RPC with a single gap with the same total gap thickness (in this particular case, a factor 3). The last point can be also inferred from Equation 4.4, where the number of gaps N_g appears at the denominator. This implies that, in order for the avalanches produced in one gap of a MRPC to give rise to above-threshold signals, an increased value of the effective first Townsend coefficient must be used; in this particular case, the authors compute a factor around 2 more, and concerns were at the time expressed whether a gas suitable to provide a wide efficiency plateau could be found. Nevertheless, at the cost of using quaternary gas mixtures, encouraging results were found (see Figure 4.15).

Later on, more prototypes of MRPCs were constructed. For instance, in Cerron Zeballos *et al*. (1997a), the authors describe three 24×24 cm^2 MRPCs, one made with two gaps of 4 mm each, one with three gaps of 3 mm each, and one with four gaps of 2 mm each, using 0.8-mm melamine-phenolic-melamine foils for the inner electrically floating planes, and melamine-phenolic foils, with the melamine surfaces facing the gas, for the outer planes. The performance, in particular in terms of time resolution, appeared from the very beginning much improved when using many gaps of reduced thickness, as can be seen from Figure 4.16.

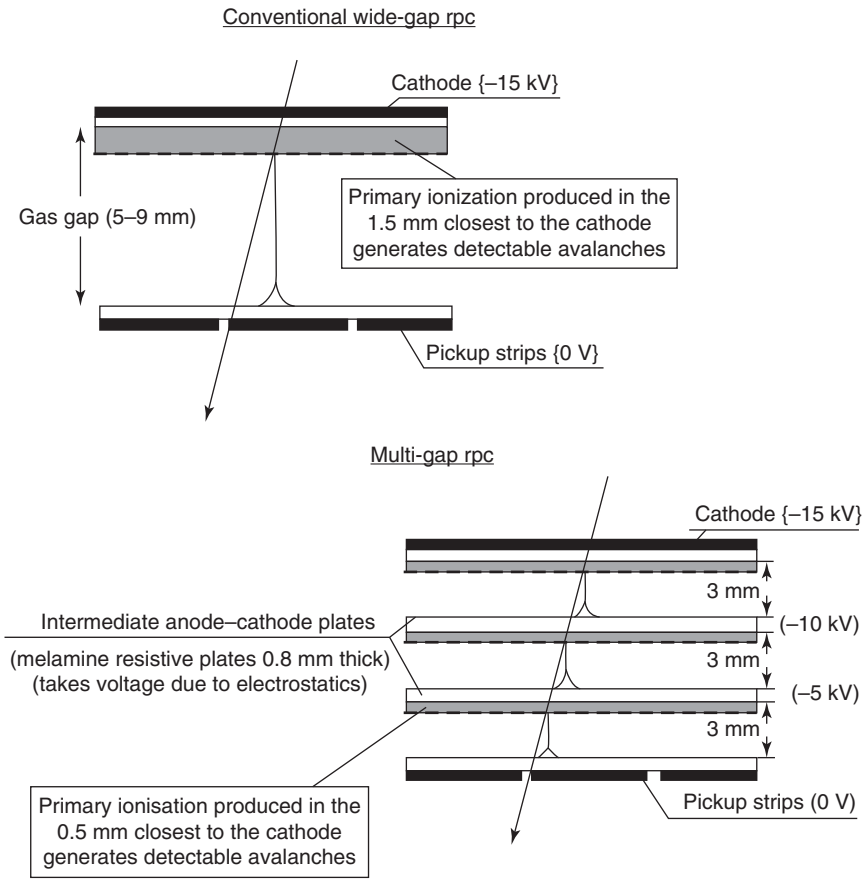

Figure 4.14 Schematic diagram and principle of operation of a multi-gap RPC compared to a conventional 9-mm RPC. (Cerron Zeballos *et al*. 1996b. Reproduced with permission of Elsevier.) The region(s) where primary ionization has to take place is put in evidence in the two cases.

This feature was further developed when these devices were proposed as instruments for accurate timing measurements, for instance to measure the TOF of the collision products at the LHC experiments. This development took place within the R&D efforts for the ALICE TOF detector (ALICE Collaboration 2000) and it was reached by introducing sub-millimetre size gas gaps defined by mechanically accurate glass electrodes in a multigap construction (Fonte, P., Smirnitski, A., and Williams, M.C.S. (2000), Akindinov, A. *et al*. (2000), Akindinov, A. *et al*. (2001)), reaching a time resolution below 50 ps (Fonte, P et al. (2000)). More details about these and other developments are given in Section 4.6.

It is important to state, for the moment, that the operation of RPCs, and most prominently timing RPCs, depends on a nonproportional behavior of the avalanche. At a certain point, avalanche growth ceases to be exponential and proceeds at a much lower multiplication rate due to the so-called space-charge effects (Fonte, 2002). This reduces the final size of the avalanches, allowing these

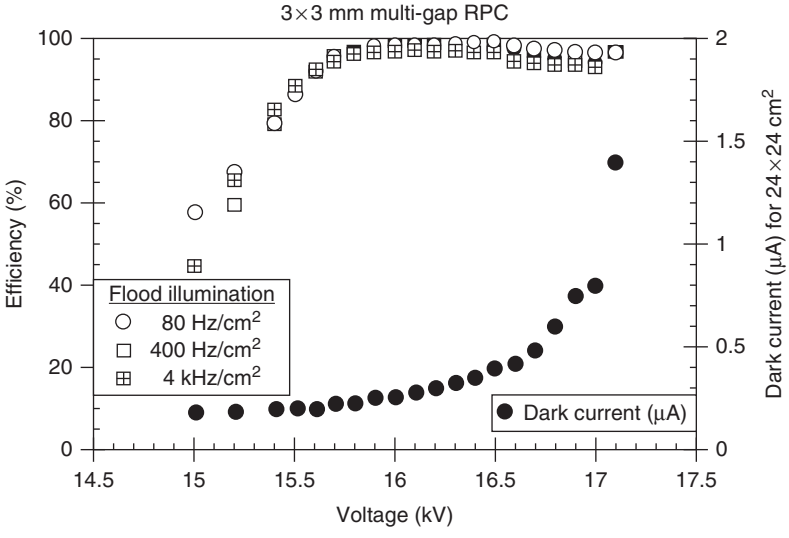

Figure 4.15 Efficiency and current versus operating voltage for the first multi-gap RPC, for various intensities of impinging flux. The gas mixture used was $Ar/CO_2/C_4F_{10}$/DME in 86/8.5/0.5/5 relative proportions. (Cerron Zeballos *et al*. 1996b. Reproduced with permission of Elsevier.)

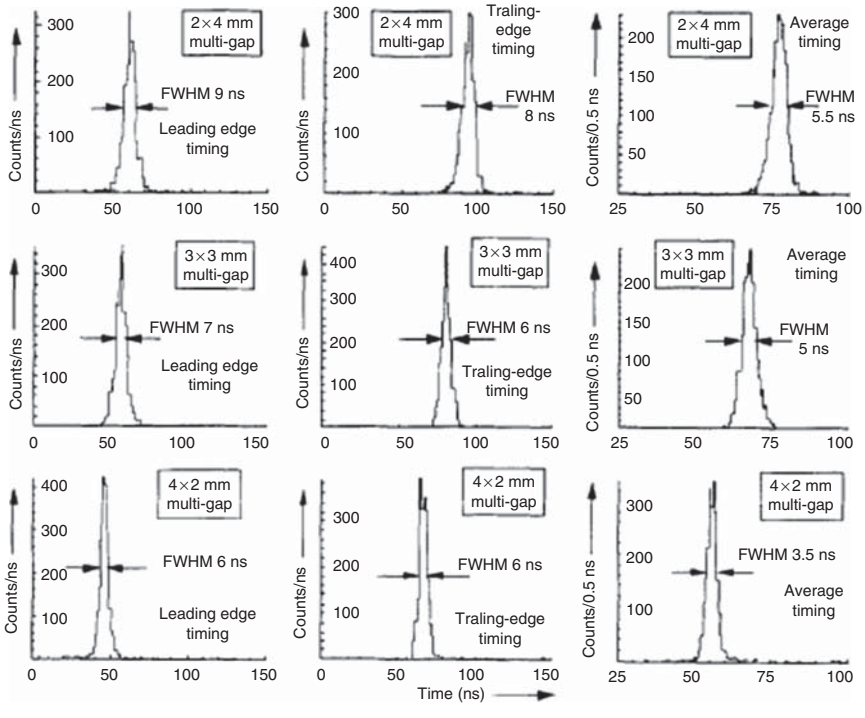

Figure 4.16 Time spectra for the 2×4, 3×3, and 4×2 mm multi-gap RPCs exposed to a 100 Hz/cm^2 flux of impinging particles. (Cerron Zeballos *et al*. 1997a. Reproduced with permission of Elsevier.) In the first and the last case, the same total thickness of gas is used, but the time resolution is definitely better when using many narrow gaps.

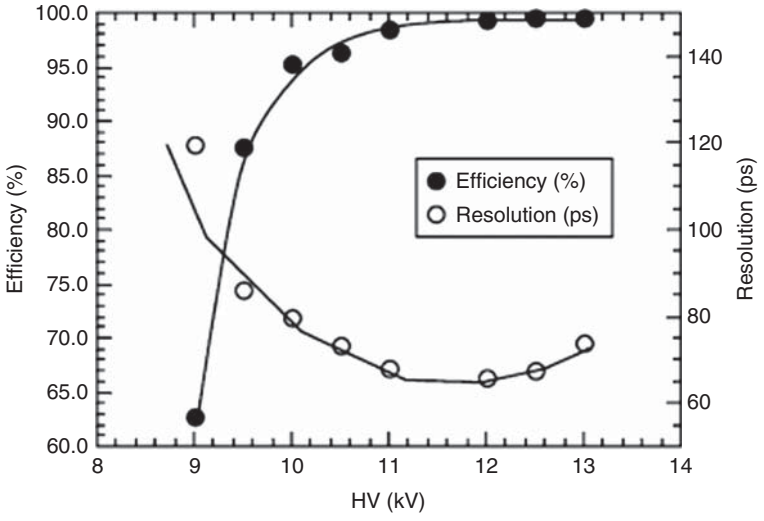

Figure 4.17 Efficiency and time resolution of a MRPC made with five gaps each 220 μm thick. (Akindinov *et al*. 2000. Reproduced with permission of Elsevier.)

devices to be successfully operated. The reduced size of the avalanches implies a reduced probability of streamer formation; of course if the avalanche exceeds the Raether limit they will nevertheless transform into streamers. This point is examined in more detail in the next sections.

4.4 "Space-Charge" Effects

After some experience operating RPCs was gained, and the relative experimental results reviewed in a critical way, it became progressively clear that the assumption that the avalanches grow in the gas gap following a pure exponential law was too simplistic. In fact, it was clear from the amplitude of the signals observed that the number of electrons contained in the avalanches was generally quite close to the Raether limit, even when front-end preamplifiers were used and the devices operated in avalanche mode. Anyhow, these effects became more and more evident when RPCs with narrow gaps (few hundred micrometers) were progressively developed and studied in detail (see Fonte *et al.*, 2002). Some help to interpret the results came, of course, also from the first modeling of the behavior of these detectors, as described in Chapter 3, and extended to multi-gap or narrow-gap configurations.

What basically happens is that the electronic and ionic charge clouds that compose the avalanche during its progression are partially overlapped in space (see Figure 4.18), generating their own electric field: this is called the space-charge field. This field is superimposed on the applied field, reducing it in the region between the electron and ion clouds and reinforcing it upstream and downstream. It is clear that the line integral of the electrical field between the

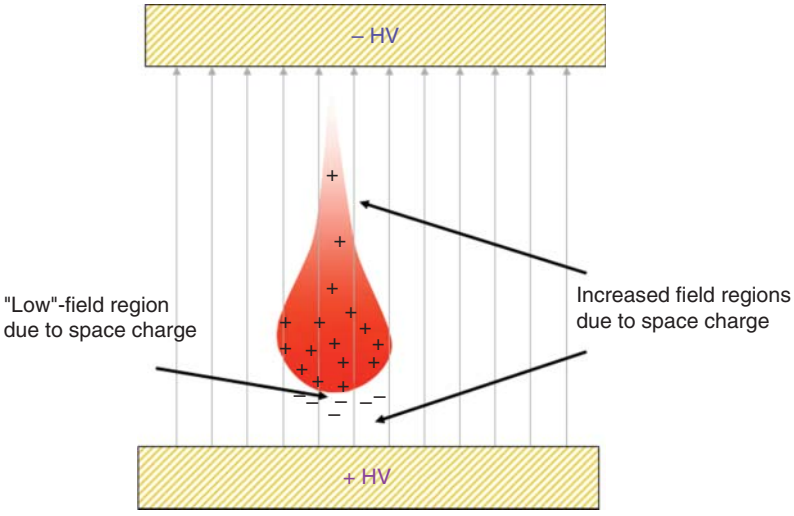

Figure 4.18 Conceptual view of an avalanche, with the regions where the electric field is significantly different from the applied field due to the space-charge effects put in evidence.

field-defining electrodes held at constant potential difference must not change, so the space-charge field must in some places be contrary and in others favorable to the applied field.

The region of reduced electric field between the electron and ion clouds is felt by a substantial part of the electrons, which undergo a multiplication rate that is reduced with respect to the unperturbed case. The overall effect is that the total avalanche gain in that situation is smaller than it would be in the absence of this effect: the space-charge effect. In RPCs with thin gaps (on the order of a few hundreds of micrometers), the gain reduction may reach several orders of magnitude: a fundamental effect for the successful operation of timing RPCs (for more details, see later on in this chapter). A more detailed discussion on the space-charge effect is given in section 4.6.

The space-charge effects in RPCs have been modeled empirically and this is described in Section 4.5. Within the practical operating range, the various models seem to be essentially equivalent (Mangiarotti *et al.*, 2006).

In the high-gain regions upstream and downstream from the avalanche, there are regions of increased electric field where enhanced multiplication may take place if any free electrons are present there. Eventually a self-sustained process called "streamer" will form in such regions. The streamer grows rapidly toward the electrodes, eventually bridging them, creating a "canal" from which a spark forms (see Chapter 1). A very useful overview of such matters can be found in Rees (1973).

For completeness, it should be mentioned that, in addition to streamer breakdown, there is a form of breakdown that depends on the extraction of electrons from the cathode by the avalanche photons or ions and their posterior amplification in the gas gap, generating positive feedback (see Chapter 1 for details). Such breakdown mechanism is characterized by a series of successor avalanches that follow the initial one, the series eventually diverging. Empirical observation of

avalanches in RPCs seems to indicate that the gas mixtures used very effectively suppress this mechanism.

4.5 Review of Analytical Models of RPC Behavior

There are various ways to mathematically model charge saturation in RPCs. One approach, described in Abbrescia *et al.* (1999b), allows to immediately grasp an idea of the effect of saturation on the signals and charge spectra.

Basically, the idea for including saturation effects in a simulation consists in letting an avalanche grow exponentially until it reaches a size corresponding to a certain charge q_{sat}; then, in a crude approximation, the avalanche stops its growth and just drifts toward the anode.

In this case, expression (3.16) has to be modified to take into account the two different phases: exponential growth and drift. Let us define the saturation length x^j_{sat} as

$$x^j_{\text{sat}} = x^j_0 + \frac{1}{\alpha^*} \log\left(\frac{q_{\text{sat}}}{q_e n^j_0}\right) \tag{4.5}$$

obtained computing the distance an avalanche has to travel to grow up to the saturation charge q_{sat}. Here, as usual, x^j_0 is the distance, measured from the cathode, where a certain primary ion-electron cluster (j) is produced, n^j_0 is the number of electrons contained, and α^* is the effective first Townsend coefficient. Then, if $x^j_{\text{sat}} < g$ (g being the gap thickness), the charge induced by this cluster is given by

$$q_{\text{ind}} = \frac{q_{\text{e}}}{\eta g} \Delta V_{\text{w}} n^j_0 M_j \left[e^{\eta(x_{\text{sat}} - x^j_0)} - 1\right] + M_j \Delta V_{\text{w}} \frac{g - x^j_{\text{sat}}}{g} q_{\text{sat}} \tag{4.6}$$

where M_j is the factor taking into account avalanche growth fluctuations and ΔV_{w} is the weighting field voltage drop across the gap. Even if the approximation is very simple, the agreement with charge spectra experimentally measured is impressive. A comparison between this model and experimental data taken from Camarri *et al.* (1998), referring to a single-gap RPC, is shown in Figure 4.19; in this case, parameters for the gas are taken from Colucci *et al.* (1999). From Equation 3.16 one would expect a monotonically decreasing distribution, like the one shown in the first panel of the same figure. But when saturation effects are taken into account, a broad peak appears, more and more evident, and shifts to the right, as the operating voltage increases. This is exactly the behavior observed experimentally.

As R&D on technical aspects of RPCs progressed, a deeper comprehension on different features of their behavior was also gained. A relevant part of the effort was devoted to RPC modeling; often, models were developed to describe a specific issue, and later on they evolved into a more comprehensive description of these devices. We now give a fast review of some of the main progress made in this field, which continue up to the present day, recommending the reader to revert to the original references for more details.

One point that is not to be underestimated is that RPCs are geometrically simple but structurally complex, involving:

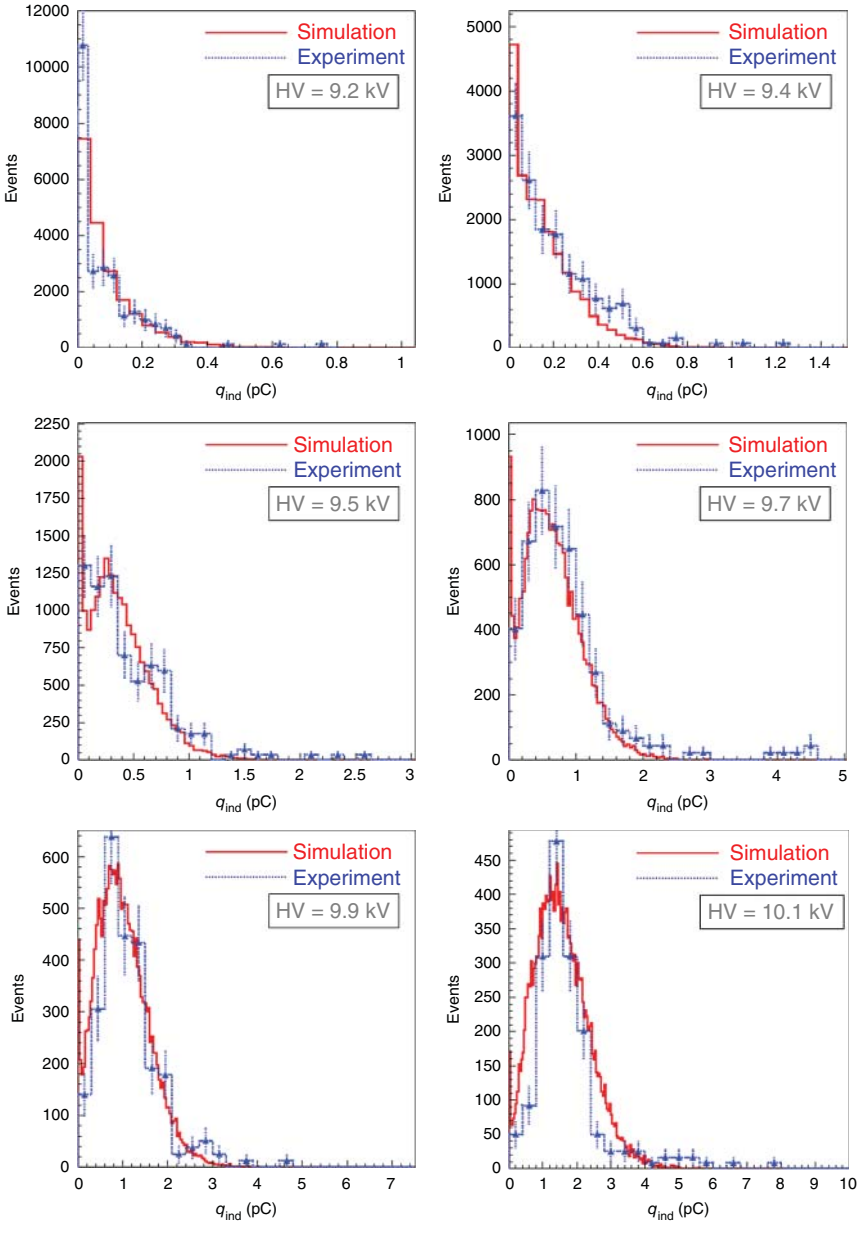

Figure 4.19 Comparison between simulated and experimental charge distributions for a single-gap RPC filled with a tetrafluoroethane gas mixture. (Abbrescia 2003. Reproduced with permission of Elsevier.)

1) Electron avalanches deeply affected by their space charge;
2) Highly variable currents flowing through resistive materials;
3) Electrical induction through materials with varied electrical properties;
4) Propagation of fast signals in multiconductor transmission lines (MTLs).

Moreover, modeling is complicated by the various timescales involved:

1) The electrical relaxation time of the resistive electrodes, on the order of milliseconds to seconds for common materials, affecting the gap voltage;
2) The electrical relaxation time of the high-voltage distribution layers and the drift time of the avalanche ions, on the scale of microseconds, affecting the signal induction process and the gap voltage;
3) The development time of avalanches and streamers, on the scale of nanoseconds, with sub-processes (e.g., electron–atom collision rates) at smaller scales.

In principle, all scales are relevant for the observable quantities (statistical distributions, etc.), which renders very difficult a first-principles, microscopic approach. However, the geometrical simplicity of RPCs has allowed to address analytically many deterministic and stochastic processes, but a general framework (analytical or Monte Carlo) for integrating all phenomena at the different timescales is missing.

In the following sections, we describe some of the most straightforward analytical results concerning these matters. Of course, such matters can be also tackled by Monte Carlo simulations, and the reader is referred to such works (e.g., Abbrescia, 2004; Lippmann and Riegler, 2004; Riegler *et al*., 2003 and references therein).

4.5.1 Electron Avalanches Deeply Affected by Space Charge

Concerning the modeling of avalanches under the space-charge regime, several empirical models were proposed. The general behavior is that for small voltages the progression is exponential as in a Townsend avalanche, but as the charges get larger the space-charge effect linearizes the curve.

The most simple and popular model (e.g., Carboni *et al*., 2003) concerns just the linearization in two segments of the avalanche charge n_e (as defined in Equation 3.1) versus the voltage applied to the gas gap, ΔV_{gap} (Equation 3.33), as exemplified in Figure 4.20. The first segment, at zero charge, describes the Townsend part (mostly invisible in practical terms) up to a threshold voltage ΔV_0 and the second segment approaches the space-charge regime with slope k_s.

$$n_e = \begin{cases} 0, & \Delta V_{gap} < \Delta V_0 \\ k_s(\Delta V_{gap} - HV_0), & \Delta V_{gap} > \Delta V_0 \end{cases} \tag{4.7}$$

A slightly more fundamental approach involves the modification of α^* in Equation 3.1, a "perturbated α"[2] (α^*_{per}), to be a decreasing function of n_e: $\alpha^*_{per}(n_e)$. From Raether (1964).

$$\begin{aligned} \alpha^*_{per} &= \alpha^* & n_e &\le n_{e,sat} \\ \alpha^*_{per} &= \alpha^*(1 - B_s \ln(n_e/n_{e,sat})) & n_e &> n_{e,sat} \end{aligned}, \tag{4.8}$$

2 That is, α^* but perturbed by the space-charge field

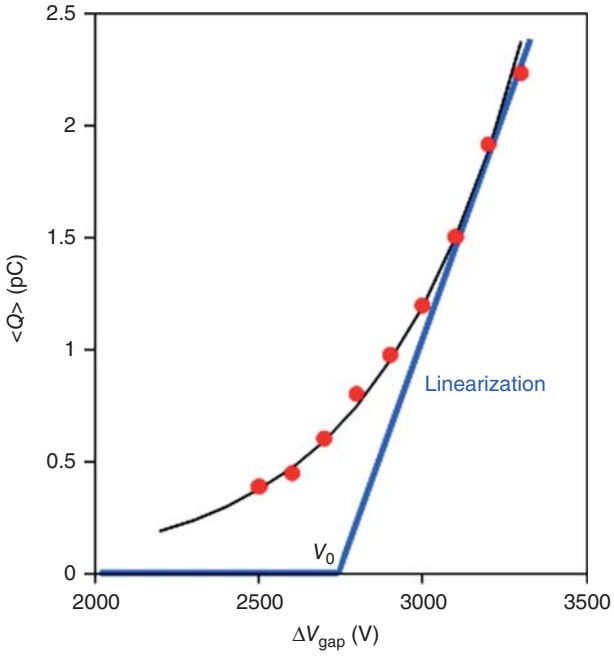

Figure 4.20 Example of the experimental function charge versus applied voltage for a single 0.3-mm gas gap RPC and its linearizing approach (thick line) with $\Delta V_0 = 2865$ V and $\kappa = 5.4$ fC/V. The black line is just to guide the eye.

where $n_{e,\,sat}$ is a parameter indicating the "saturation" level of n_e that separates the proportional from the space-charge regimes and B_s is a dimensionless shape parameter related to the sharpness of the transition. From Aielli *et al.* (2001)

$$\alpha^*_{per} = \alpha^*(1 - n_e/n_{e,sat}); \tag{4.9}$$

from Fonte (2002, 2013b)

$$\alpha^*_{per} = \frac{\alpha^*}{1 + (n_e/n_{e,sat})^{B_s}}. \tag{4.10}$$

In Figure 4.21, a comparison between these functions is shown.
The solutions are, respectively,

$$\begin{aligned} n_e &= n_0 e^{\alpha^* x} && x \le x_{sat} = \ln(N_{e,sat}/n_0)/\alpha^* \\ n_e &= n_{e,sat} \exp\left[\frac{1 - e^{-B_s\alpha^*(x - x_{sat})}}{B_s}\right] && x > x_{sat}, \end{aligned} \tag{4.11}$$

$$n_e = n_0 + n_{e,sat} \ln\left(\frac{1 + B_s e^{\alpha^* x}}{1 + B_s}\right), \tag{4.12}$$

$$n_e = n_{e,sat} \sqrt[B]{W(ue^{u+B_s\alpha^*})}, \quad u = (n_0/n_{e,sat})^{B_s} \tag{4.13}$$

(with $W(ye^y) = y$ being Lambert's function) of which a comparison is depicted in Figure 4.22. It can be perceived that models 4.12 and 4.13 provide a smooth transition between the exponential and linear behaviors, qualitatively matching the observations, while model 4.11 describes a fully saturated behavior.

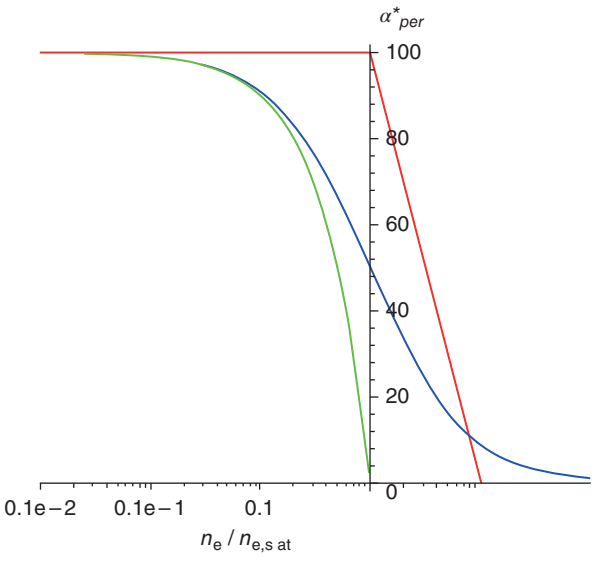

Figure 4.21 Comparison between the functions 4.8, 4.9, 4.10 represented, respectively, in the figure by the rightmost, leftmost and intermediate lines.

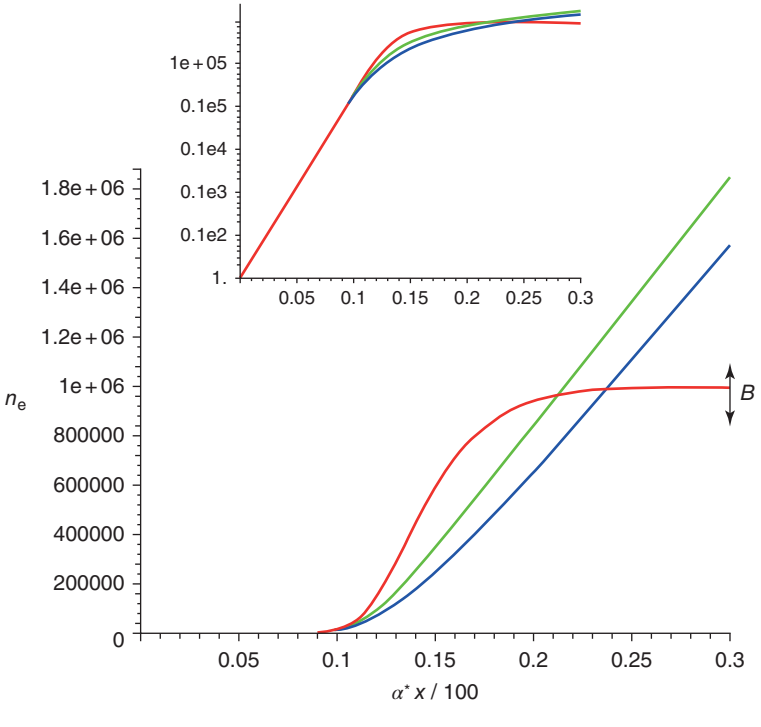

Figure 4.22 Comparison between the solutions of the different space-charge models, (4.11), (4.12), (4.13) respectively in the medium-gray, black and light gray lines. The inset in semilog scale evidences the transition from exponential to linear behavior. The arrow means that the *B* parameter controls the saturation charge.

4.5.2 Highly Variable Currents Flowing through Resistive Materials

The flow of variable currents through the resistive electrodes may be understood as the nearly instantaneous deposition of the avalanche-generated charges on the surface of the resistive electrodes and its subsequent cancellation by the electrical relaxation of the material. This process is illustrated in Figure 4.23 for a single charge.

The time-dependent solution for this situation is known (Lippmann *et al.*, 2006) and consists of two parts: one corresponding to two infinite half-spaces plus a complicated correction due to the presence of the electrodes, which is merely indicated in Equation 4.14 and is a function of $e^{-t/\tau}$:

$$\Delta\vec{E}_g \cdot \hat{x} = \overbrace{\frac{q}{2\pi(\varepsilon+\varepsilon_0)} \frac{x e^{-t/\tau_1}}{(\rho^2+x^2)^{\frac{3}{2}}}}^{\text{infinitely thick layers}} + \text{contribution from the metalic electrodes}(e^{-t/\tau(k)})$$
$$\tau_1 = \frac{\varepsilon+\varepsilon_0}{\sigma}; \tau_2 = \frac{d\varepsilon}{g\sigma} + \frac{\varepsilon_0}{\sigma}; \tau(k) \subset [\tau_1, \tau_2], \tag{4.14}$$

where $\Delta\overline{E_g} \cdot \overline{x}$ is the component of the perturbation electric field perpendicular to the electrodes, x is the coordinate along this direction and ρ the one parallel to the electrodes, σ and ε are, respectively, the conductivity and the electrical permittivity of the resistive material. Both components decay exponentially in time with a bounded set of characteristic times, as indicated in Equation 4.14. In glass, for typical values of the material parameters, these times lie around 1 s.

Solutions for an extensive set of other useful situations are given in Riegler (2016).

On any point in the gas gap, there will be a superimposition of such disturbances originated at random times and locations. The average value of the disturbance $\langle \Delta E_g \rangle$ may be understood as simply an ohmic voltage drop of the average gap current density across the resistive element, to be subtracted to the applied voltage

$$\langle \Delta\vec{E}_g \rangle = \langle j \rangle / \sigma \tag{4.15}$$

where $\langle j \rangle$ is the average gap-generated current density.

This constitutes a shot-noise process with variance given by Campbell's theorem, which can be written in our case (González-Díaz *et al.*, 2006)

$$\mathbb{V}(\Delta E_g) = \frac{1}{2} \frac{\langle \Delta E_g \rangle^2}{N_{\text{pert}}} \left(1 + \frac{\mathbb{V}(Q)}{\langle Q \rangle^2}\right) \propto \overline{\phi}$$
$$N_{\text{pert}} = A_{\text{pert}} \phi \tau \tag{4.16}$$

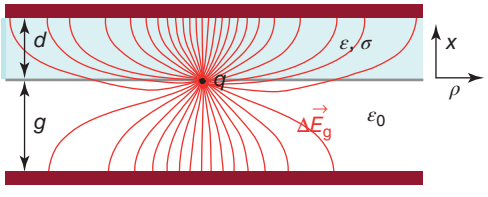

Figure 4.23 Depiction of the electric field perturbation in the gas gap, ΔE_g, produced by a single charge deposited in the surface of the resistive electrode.

where Q is the deposited charge per shot, $\langle \Delta Eg \rangle$ is the average field perturbation, N_{pert} is the average number of shots that contribute to the perturbation, A_{pert} is an indicative area around the relevant point for which the perturbation is possible, ϕ is the average particle flow density, τ is the characteristic relaxation time, and $\mathbb{V}(\,)$ denotes the variance of a given stochastic variable. It turns out that the variance is proportional to the particle flow density.

Such matters have been as well tackled by Monte Carlo, with compatible results (Lippmann *et al*., 2006).

4.5.3 Electrical Induction through Materials with Varied Electrical Properties

A sophisticated theory of signal induction exists (Riegler, 2004) for a very general situation: arbitrary charge movements in a medium of non-homogeneous properties, which induce voltages in electrodes interconnected by arbitrary linear networks.

When the conductivity of the materials can be neglected, the situation is purely electrostatic and can be handled in terms of Ramo's theorem (as already described in Chapter 3) or by direct calculation of the variation of the charge densities induced in the electrode surfaces by the movement of the charges in the gas gap.

When conductivity must be taken into account, the fundamental idea is that replacing $\varepsilon \to \varepsilon + \sigma/u$ in the electrostatic solution of the problem (e.g., Equation 4.14) and inverting the Laplace transform from the frequency domain (u, where u is the complex frequency) to the time domain provides the impulse response for which the electrostatic solution is a Dirac $\delta(t)$ impulse. Other situations can be handled by superposition (convolution). Such matters have been recently much developed for application in several situations of interest (Riegler, 2016).

Departures from the electrostatic situation can be observed when the charge movements or the electronics response are longer than the relaxation time of the materials. This includes differentiation of the signal and lateral signal spread. For typical (glass or phenolic electrodes) RPCs, the plates have a negligible effect, but the medium resistivity layers used to apply the high voltage may have an impact. An example is shown in Figure 4.24.

The plot shows the reduced induced surface charge density ς' as a function of the reduced time for different values of the radial coordinate when a charge crosses the gap in a time equal to the relaxation time of the resistive layer at $x = 0$. Note that the induced current density is proportional to the slope of the curves.

It can be seen that close to the charge's flight path the induced charge first rises and then falls, causing a (differentiation-like) change of sign in the induced current density and lateral spreading of the charge. For sufficiently long reduced times, the induced charge becomes equal over the whole electrode.

4.5.4 Propagation of Fast Signals in Multiconductor Transmission Lines

Very often the readout of RPCs is made by a series of parallel strip-like electrodes placed on one face of the chamber with a ground plane on the other face. This is

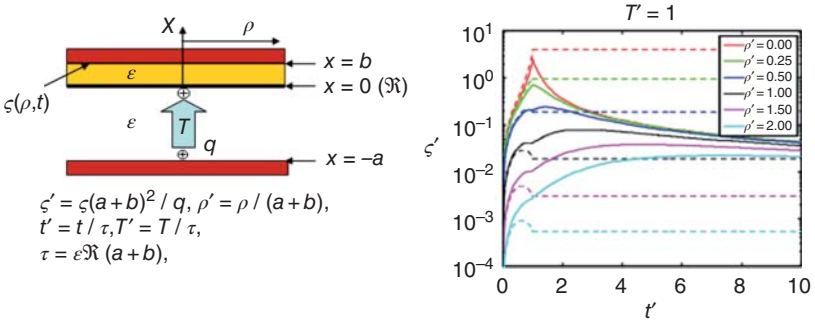

Figure 4.24 Example of calculation of the time evolution of the reduced induced charge density $\varsigma'(\rho, t)$ on the $z = b$ electrode through the thin resistive layer at $z = 0$ by a charge that crosses the gap in a time $T = \tau$. (Fonte 2013a, reproduced with permission) The plot is done in the reduced variables indicated, where $\mathfrak{R}$ is the surface resistivity of the intermediate layer. For comparison, the dashed lines correspond to the electrostatic case with $\mathfrak{R} = 0$.

particularly important in timing RPCs, for which the average of the time measured in both ends of the strips is independent of the avalanche position.

Such a set of long conductors in mutual presence is known as a multiconductor transmission line, on which the conductors couple via their mutual capacitances and inductances. (Note that in here we do not mean the phenomenon of induced charge sharing between the strips when the avalanche occurs close to their separation line, but an electrical transformer-like coupling.) An exact theory exists for the general case (e.g., Djordjević and Sarkar, 1987) and it was adapted to RPCs (Riegler and Burgarth, 2002), having been observed a generally good match with measurements in RPCs (Gonzalez-Diaz *et al.*, 2011).

The principal quantities relevant for the problem are represented in Figure 4.25. The N strips have self and mutual capacitances (C, C', C'', etc.) and inductances (L, L', L'', etc.), eventually have series resistance R and parallel conductance G and

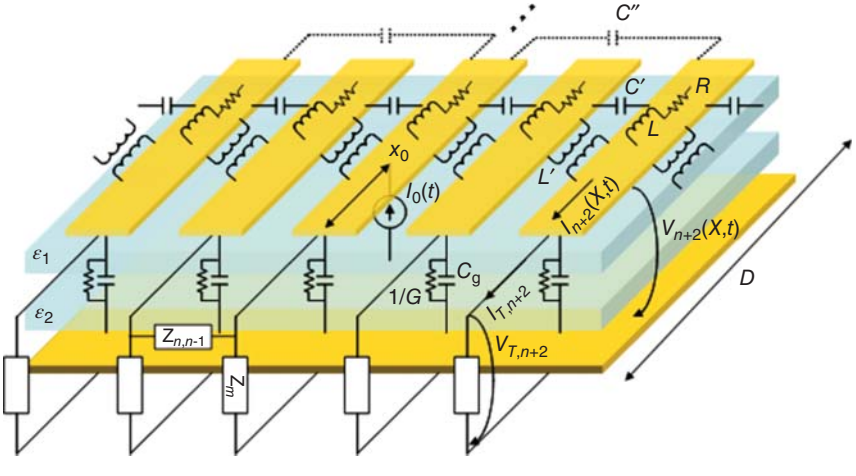

Figure 4.25 Representation of the problem and of the principal basic quantities. The resistance between the strips is neglected.

are terminated by an arbitrary passive network on both ends. In RPCs, the current $I_0(t)$ is injected in a single strip at position x_0, while the strips have total length D. Other situations can be handled by superimposition. Voltage and current waves propagate in both directions, appearing at the terminations the voltages $V_{\mathrm{T},n}$ and being reflected there.

In general, the following phenomena emerge:

1) Capacitive-inductive coupling between strips, causing crosstalk;
2) Formation of fixed propagation modes, each with a different velocity w_{m};
3) The injected signal is expressed a unique linear combination of modes and the differential velocity of the modes leads to their decoherence (or modal dispersion), causing broadening of the signal and extra crosstalk.

The general theory only admits numerical solutions, which obscure the statement of the general features of the phenomenon. Instructive analytical expressions can be obtained for the case of a reduced number of strips (2 or 5 Gonzalez-Diaz *et al*., 2011) or postulating weak coupling between the electrodes (Fonte, 2013b), which for a spread-out conductor system such as an RPC is reasonable and supported by observations (Gonzalez-Diaz *et al*., 2011).

The problem can be formulated only in terms of the self and mutual capacities between the electrodes ($C, C', C'', \ldots$), forming the capacity matrix and on the same quantities with the dielectrics removed ($C_0, C_0', C_0'', \ldots$), from which the inductances can be calculated (because $c^2 = 1/(LC_0)$). Therefore, neglecting the material's change of permittivity with frequency, only electrostatic calculations are needed to state the line properties.

In the weak-coupling approximation, the C'' and higher cross-couplings are second order and can be neglected, and the system properties depend only on the quantities

$$\upsilon = C'/C, \quad \upsilon_0 = C_0'/C_0 \tag{4.17}$$

The modal velocity spectrum is contained within

$$|w_{\mathrm{m}} - \langle w \rangle| \leq \Delta w = \underbrace{\frac{1}{\sqrt{LC}}}_{\langle w \rangle} |\upsilon - \upsilon_0| \tag{4.18}$$

which can be nullified if there is "compensation," $|\upsilon - \upsilon_0| = 0$, achievable via a criterious arrangement of the electrodes and dielectrics (Gonzalez-Diaz *et al*., 2011). Calculations for realistic cases show that modal dispersion, $1/\Delta w$, can reach up to 1 ns/m, which for timing RPCs is very significative.

The inductocapacitive next-neighbor crosstalk is given by

$$\frac{V_{\mathrm{T},n+1}}{V_{\mathrm{T},n}} = \frac{R_{\mathrm{T}}}{Z_{\mathrm{c}} + R_{\mathrm{T}}} \frac{\upsilon + \upsilon_0}{2} \tag{4.19}$$

where R_{T} is the value of the (all equal) termination resistors and $Z_{\mathrm{c}} = \sqrt{L/C}$ is the strip's characteristic impedance. To this fundamental crosstalk is added the extra crosstalk from modal decoherence, as exemplified in Figure 4.26. In this figure, the capacitive-like effect of small losses in the glass is also exemplified.

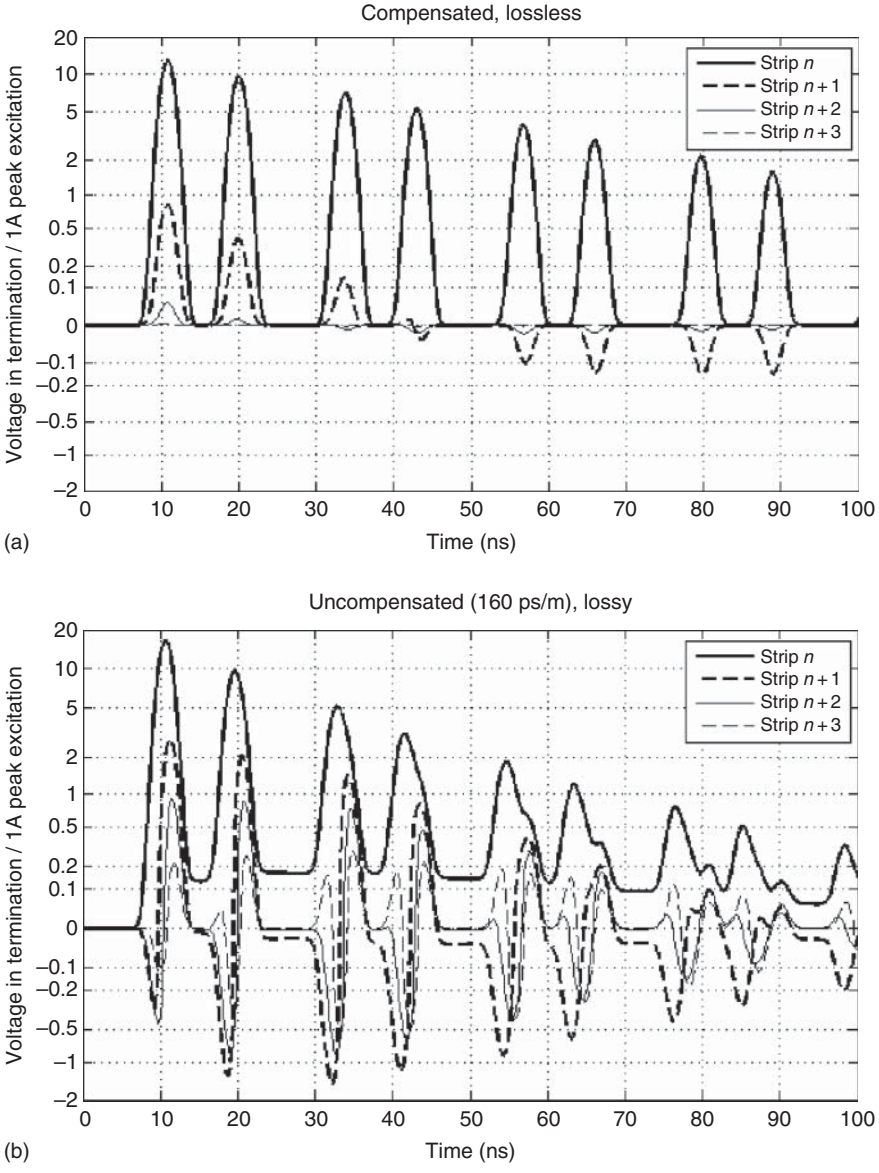

Figure 4.26 Example of calculation of the signals visible in one end of a multi-strip RPC (Fonte, 2013b) up to the third neighbour, comparing the compensated, lossless (a) and uncompensated, loss (b) cases. The first pulse is the direct signal and the subsequent pulses its reflections. Note the strongly nonlinear vertical scale.

4.6 Timing RPCs

Now we will concentrate on RPCs specifically conceived to yield a time resolution much better than the nanosecond scale. The motivation for the development of RPCs with time resolution on the practical range for TOF measurements (below

100 ps) arose in the framework of the R&D efforts for the TOF detector of the ALICE experiment, as the large area required, more than 100 m^2, was impossible to cover using the standard technology of plastic scintillator bar readout by photomultipliers.

Following earlier work on thin-gap PPCs, which reached 200 ps resolution (ALICE collaboration, 2000), this goal was achieved in reliable and efficient detectors by strongly reducing the width of the gas gaps in four-gap symmetric multi-gap RPCs (Akindinov *et al*., 2001; Fonte *et al*., 2000,b).

Initially this was attributed to the fact that by dividing a certain gas layer in many sub-gaps, the jitter due to the drift of the electrons in each gap was reduced. This is a qualitative explanation which could somehow be misleading. As a matter of fact, since the electric field is uniform everywhere in the gas, each electron grows into an avalanche regardless of its position, and the amplitude of the instantaneous induced signal will just depend on the time elapsed since the primary ionization, and on the statistical fluctuations, both in the avalanche initial number of electrons and in its growth (see Equation 3.15). This implies that, at a certain time, all drifting avalanches contribute for the same average amount to the induced signal; therefore, the abovementioned statistical fluctuations will be the main sources of time jitter (see Figure 4.27). Another way to clarify this point is to observe that the signals are induced when the avalanches are still drifting in the gap, and not when they arrive at the anode.

Many investigations were performed (see, for instance, Riegler *et al*., 2003; Lippmann and Riegler, 2004 and references therein) in order to clarify the physical mechanism by which this performance is achieved. The main actor was found to be the reduction of the gas gap by an order of magnitude (from millimeters to tenths of a millimeter), which dramatically increases the space-charge effect (Fonte and Peskov, 2002) and has several important positive consequences (see illustration in Figure 4.27):

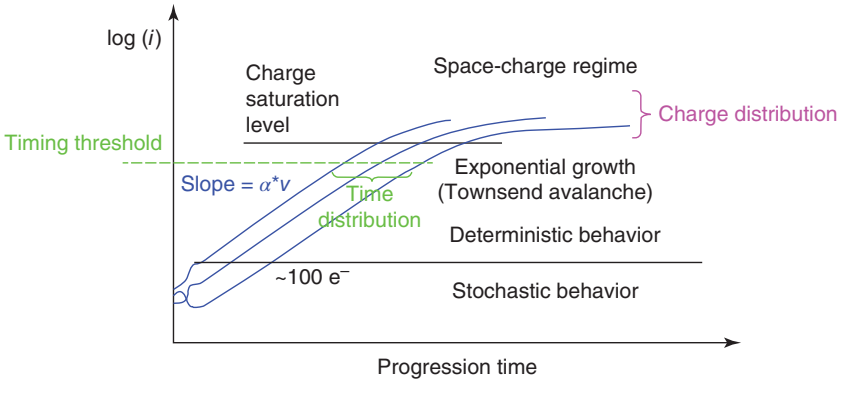

Figure 4.27 Qualitative representation of the different phases of the avalanche, as they are currently understood, and the origin of the observable time and charge distributions. The initial current grows exponentially in time until the discriminating level is reached. The time delay is independent of the position occupied by the initial charges, being the observed timing jitter dependent on the avalanche and cluster statistics (stochastic behavior) and, inversely, on the current growth (ionization) rate $\alpha^* v_d$.

1) In the first stages of the avalanche, the ones most relevant for the time resolution (time is typically measured when the avalanche is still relatively small), α^* can be large, being reduced afterwards by the space-charge effect and keeping the avalanche within a reasonable final size (a few picocoulomb). Therefore, the ionization rate $\alpha^* v_d$ in Equation 3.26, which determines the basic timing scale, is considerably increased. A secondary benefit is the very large electric field in the narrow gap that somewhat increases the drift velocity (see, for instance de Urquijo *et al*., 2009).
2) As the avalanche is strongly saturated, all primary charges initiating avalanches in approximatelly the half-gap closer to the cathode are almost equally amplified. This allows about half of the gas gap to be sensitive to any primary charge there deposited, in contrast with a proportional operation where the gas gain exponentially depends on the distance from the primary charge to the anode (see also discussion in section 4.2). This feature allows a reasonable efficiency per gap for minimum ionizing particles (MIPs) (75% for a single 0.3-mm gas gap Fonte and Peskov, 2002). The full efficiency is achieved by using several gaps, normally in a multi-gap architecture. This also somewhat improves the intrinsic time resolution (see Chapter 3), as dramatically demonstrated in An *et al*. (2008).

Note in Figure 4.27 the evident inverse relationship between the current growth slope – the ionization rate – and the width of the time distribution. It is a matter of debate whether the timing threshold should be considered as being within the Townsend region or in the space-charge region.

An approximate formula for the time resolution for single-gap RPCs can be computed, and this was reported in Equation 3.26. By following a generalized approach, but using basically the same arguments as the ones used for Equation 3.26, one can deduce that in multi-gap RPCs the time standard deviation, σ_t, can be asymptotically (for a large number of primary charges) approximated by

$$\sigma_t = \frac{1}{\sqrt{N_g \lambda g}} \frac{U}{\alpha^* v_d} = \sqrt{\frac{g}{N_g \lambda}} \frac{U}{(\alpha^* g) v_d} \tag{4.20}$$

where N_g represents the number of gas gaps and, as usual, g their size, λ is the number of clusters per unit length, α^* the effective first Townsend coefficient, v_d the electron drift velocity, and U is a factor of order 1 that accounts for the avalanche statistics, and for the fact that not all primary ionizations contribute equally (Gonzalez-Diaz *et al*., 2017).

The first formulation indicates that, not unexpectedly, the time resolution is inversely proportional to the square root of the total number of primary charges created in the gas gaps ($N_g \lambda g$), which is typical of a counting-like error, and, as pointed out before, inversely on the ionization rate $\alpha^* v_d$.

This formulation seems to imply that lowering g would increase σ_t. However, in practice, g and α^* are not independent variables. Their product, $\alpha^* g$, is the natural logarithm of the gas gain for an avalanche started at the cathode, which is limited by the onset of streamers and therefore has a limited maximum value. This is reflected on the second formulation of Equation 4.20, which evidences a more

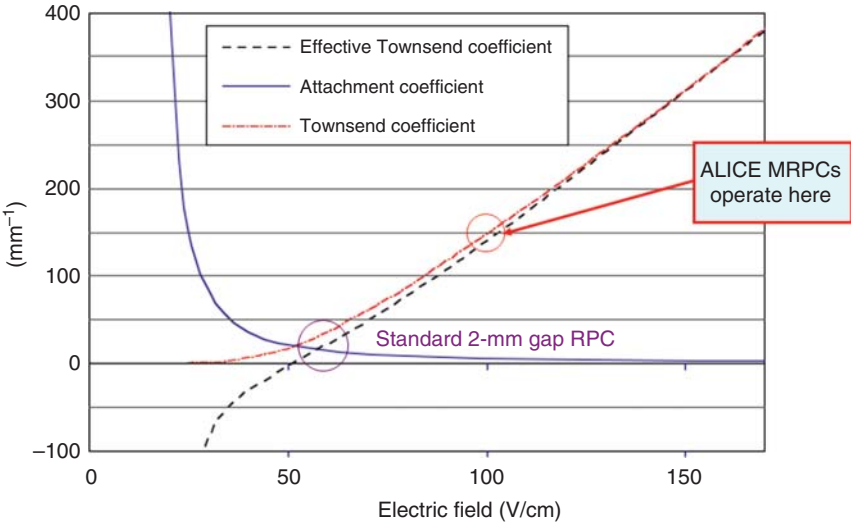

Figure 4.28 First Townsend coefficient, attachment coefficient, and effective first Townsend coefficient, as computed by the MAGBOLTZ simulation program, for a gas mixture $C_2H_2F_4/SF_6/i\text{-}C_4H_{10}$ 90/5/5 in relative fractions. (Williams 2016. Courtesy of M. C. S. Williams.)

correct dependence on g. Aditionally, as stated before, the space-charge effect, very strong for small g, allows for a large initial value of $\alpha^* g$ (see also Figure 4.28) that is later reduced, keeping the avalanche size on reasonable values.

In practice, the achievement of optimum time resolutions requires the correction of the measured time by the avalanche charge, as a considerable correlation has been observed. This correlation may be just caused by the bandwidth limitations of the readout electronics or it may have a deeper physical origin, so far not identified.

The ionization rate close to the time-discriminating threshold level in timing RPCs has been measured to be on the order of 9×10^9 s^{-1} (Blanco *et al.*, 2001) which, in an exponentially growing signal, translates to a signal bandwidth close to 1.5 GHz. The readout of such signals via striplines readout in both ends (Pestov-counter-like) with the intention of measuring an accurate edge time poses special problems of crosstalk and dispersion (Gonzalez-Diaz *et al.*, 2011).

In Figure 4.27 are qualitatively depicted the different phases of the avalanche starting from a single ionization cluster, as it is currently understood, along with the origin of the observable time and charge distributions. As normally the avalanches start from a random location within the gas gap, their total progression time is quite variable.

From the same figure it can be also appreciated that a standard constant-fraction discriminator, based on the detection of the crossing point between a signal and its delayed and amplified version, will not work on exponentially growing signals, as these operations only cause, viewed in log-scale, parallel shifts of the curves without generating any crossing point.

It has been established experimentally that resolutions down to 60 ps are possible in 0.3-mm single-gap RPCs (Blanco *et al.*, 2003), however with an

efficiency of only 75% for 3.5 GeV/c negative pions. It is suggested by modeling that for a large number of gas gaps the time resolution should be (asymptotically) improved inversely to the square root of the number of gas gaps (see Equation 4.20). A time resolution of 20 ps (the standing record) was measured between two identical symmetric RPCs each with 12 + 12 160 μm wide gaps in an almost parallel and monoenergetic beam of high-energy pions (Figure 4.29) (An *et al*., 2008).

The response of timing RPC to highly ionizing particles (Ayyad *et al*., 2012; Cabanelas *et al*., 2009; Casarejos *et al*., 2012; Machado *et al*., 2015), neutrons (Blanco *et al*., 2015), and gamma photons (Lopes *et al*., 2007) has been also studied.

A currently favored configuration is the symmetric multi-strip multi-gap timing RPC (Blanco *et al*., 2001; Petrovici *et al*., 2003). The wide strips (on the

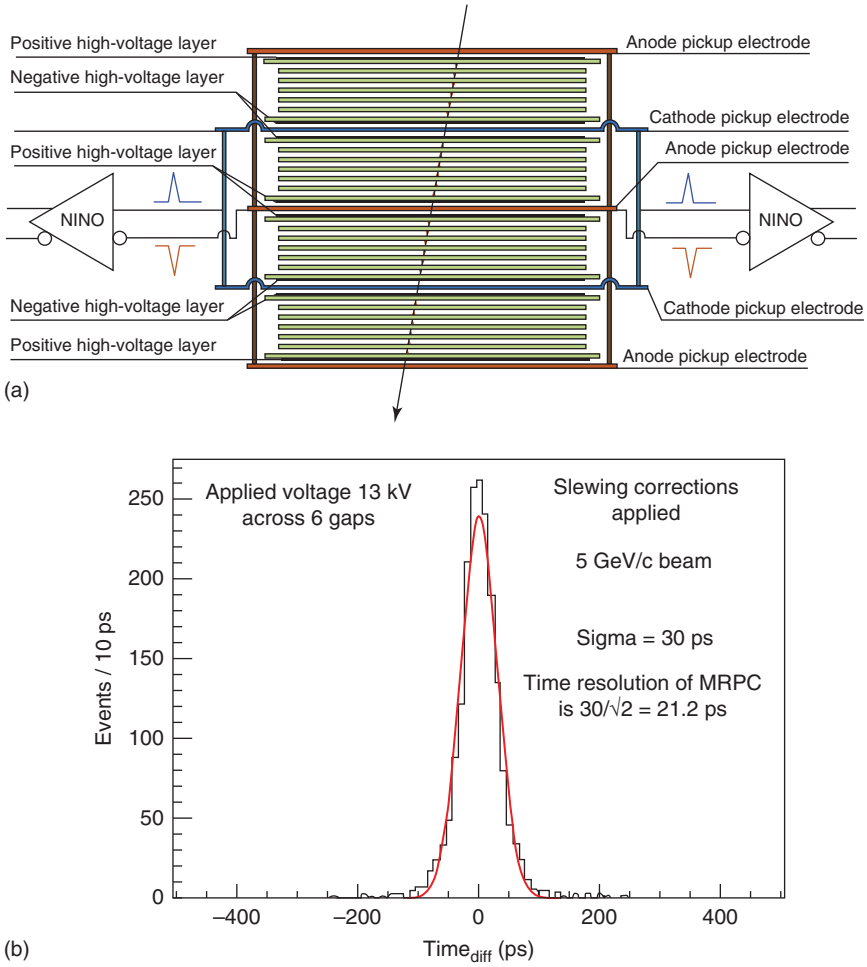

Figure 4.29 (a) Structure of one of the 20 ps RPC. (An *et al*. 2008. Reproduced with permission of Elsevier.) and (b) the corresponding time resolution plot.

order of a few centimeters) are matched to the (generally modest) position resolution requirements in the direction transversal to the strips. The strips are read out on both ends by fast (timing-capable) amplifiers and the time difference between them determines a longitudinal position with an accuracy equally on the order of a few centimeters. Because this geometry allows covering large areas with (centimeter level) bidimensional position resolution and state-of-the-art timing resolution while reading out only the strip ends, it is pursued by many groups. Details may be found in the following references, which correspond to recent works of the main groups in the field (Abbrescia *et al*., 2008; Babkin *et al*., 2016; Deppner *et al*., 2016; Petriş *et al*., 2016; Shi, 2014; Tomida, 2016; Wang *et al*., 2016a,b), and references therein. However, the multi-hit capability (correct timing response to almost simultaneous hits in close-by strips) of this type of detector remains to be solidly established (Wang *et al*., 2010). A tested safe (but work-intensive) alternative is the use of individually shielded RPC cells (Belver *et al*., 2009).

The combination of accurate timing and bidimensional position resolution has been also explored, as discussed in section 3.5.5.

4.7 The Importance of Front-End Electronics for Operation in Streamer and Avalanche Modes

Most RPCs operating in streamer mode generate large signals, even up to 1 nC, much larger than those generated by multi-wire proportional chambers (MWPCs). However, rate capability considerations, which will be examined in detail in Chapter 7, soon advised to reduce this amount, either by reducing the streamer charge by a judicious addition of SF_6 to the mixture (Arnaldi *et al*., 2000) or by working in avalanche mode (Camarri *et al*., 1998; Koreshev *et al*., 2000). The advent of timing RPCs, requiring sub-millimeter gas gaps, further reduced the amount of available signal.

In streamer mode, little or no front-end amplification was required, with the chamber electrodes often connecting directly to logic gates (see Table 4.1). But in avalanche mode proper amplifiers are required, with special bandwidth requirements in the case of timing RPCs. The solutions devised are many, tailored to specific needs. Naturally, with the constant evolution of electronic technology new solutions have been continuously proposed.

In Table 4.1, we try to summarize the main characteristics of the front-end amplifiers and integrated solutions employed for the major RPC applications, along with some interesting prototypes.

4.8 Attempts to Increase Sensitivity via Secondary Electron Emission

Among the many interesting studies performed in the 1990s to further improve RPC performance, we now mention the use of secondary electron emitters,

Table 4.1 Summary of the characteristics of front-end electronic systems used in RPCs at recent experiments and some relevant prototyping efforts.

Experiment/ collaboration	Technology/ chip name	Topology	*Q* gain (V/pC)	Gain[a)]	Bandwidth or rise time[b)]	Input equivalent noise	Zin (Ω)	Power/ ch (mW)	Testbench time resolution	References
Streamer mode										
ALICE-muon	0.8 μm BiCMOS 8 ch ASIC "ADULT"	Dual threshold comparator		700	Few ns	100 μV		90		Royer *et al.* (2000), Arnaldi *et al.* (2005)
ALICE-muon	0.35 μm CMOS 8 ch ASIC "FEERIC"	I-amp + comparator	0.33	25	130 kHz	2 mV or 6 fC	50	60	<400 ps@ >100 fC	Manen *et al.* (2013)
ARGO	See ATLAS	V-amp + comparator with input attenuator								Aielli *et al.* (2001)
BaBar	Discrete BJT	Under-biased cascode amp. Fixed 70 mV threshold								Cavallo *et al.* (1996, 1998)
Belle	MAX908CPD	Comparator			12 ns			3.5		Abashian *et al.* (2000)
Daya Bay, BESIII muon	CMP401GS	Quad comparator			Few nanoseconds			42		Ablikim (2009), Yang *et al.* (2010)
OPERA (trigger + veto)	SN75LVDS386 16 ch LVDS line receiver	Comparator			0.8 ns	Few mV	100 k	10		Balsamo *et al.* (2012)

Avalanche mode										
ATLAS	0.5 μm GaAs MESFET 8-ch ASIC	V-amp + 3-level comparator with input transformer		1500	50–150 MHz	50 mV/ 1500 = 33 μV	2000	22		Giannini *et al.* (1999)
CALICE	0.35 μm SiGe 64 ch ASIC "HARDROC"	I-amp + 3-level comparators (1 : 10 : 100) + aux charge output	≤2		15–25 ns		"Low"			Dulucq *et al.* (2010)
CALICE	0.25 μm CMOS 64 ch ASIC "DCAL"									Adams *et al.* (2016)
CMS, PHENIX	0.8 μm BiCMOS 8 ch ASIC	I-amp + comparator	0.5			1.7 fC	15	45		Abbrescia *et al.* (2000)
INO	0.35 μm CMOS ASIC "ANUSPARSH"	Differential I-amp + comparator		6 V/mA	"Low"			45	72 ps	Chandratre *et al.* (2015)
Timing										
ALICE TOF STAR BESIII TOF EEE	0.25 μm CMOS 8 ch ASIC "NINO"	Differential V-amp with cascode inputs + comparator	1.8		1 ns	<0.8 fC	40–75	30	70 ps @100 fC 20 ps @ >200 fC	Anghinolfi *et al.* (2004)
FOPI	Discrete MMIC, 4 ch card	2 gain stages + comparator		400	1 GHz	20 μV	50	1850	7 ps @ >5 mV	Ciobanu *et al.* (2007)
HADES	Discrete MMIC, 4 ch card	1 gain stage + comparator		60	2 GHz	300 μV	50	500	40 ps @ 40 fC; 17 ps @ >100 fC	Belver *et al.* (2010)

(Continued)

Table 4.1 (Continued)

Experiment/ collaboration	Technology/ chip name	Topology	*Q* gain (V/pC)	Gain[a)]	Bandwidth or rise time[b)]	Input equivalent noise	Zin (Ω)	Power/ ch (mW)	Testbench time resolution	References
HARP	Discrete BJT 8 ch	8-ch summing preamp	0.1		≤1 ns	<10 fC	30	350/8	<25 ps @ 200 fC	Ammosov *et al.* (2007)
LEPS	Discrete MMIC 8 ch card	2 gain stages + comparator		200	2 GHz					Tomida *et al.* (2014)
Prototypes										
	Discrete MMIC	2-stage V-amp		40	2.5 GHz	3.2 fC	50		<10 ps @ >100 fC	Blanco *et al.* (2001)
	MAX3664	Transimpedance amp		6000	590 MHz	55 nA	0 (virtual ground)	1200		Llope (2008)
	0.18 μm CMOS ASIC "PADI"	Differential V-amp with cascode inputs + comparator		60	180 MHz	32 μV	48–58	30	<10 ps @ >10 mV	Ciobanu *et al.* (2008, 2012)
	Discrete Si—Ge BJT	2 gain stages	2–6		30–100 MHz 100–300 ps	0.08 fC	50–200	2		Cardarelli *et al.* (2013)

a) Of the input stage in case of integrated comparators
b) Note that for a perfectly rectangular input signal a risetime of 1ns corresponds to a bandwidth of ~300MHz.

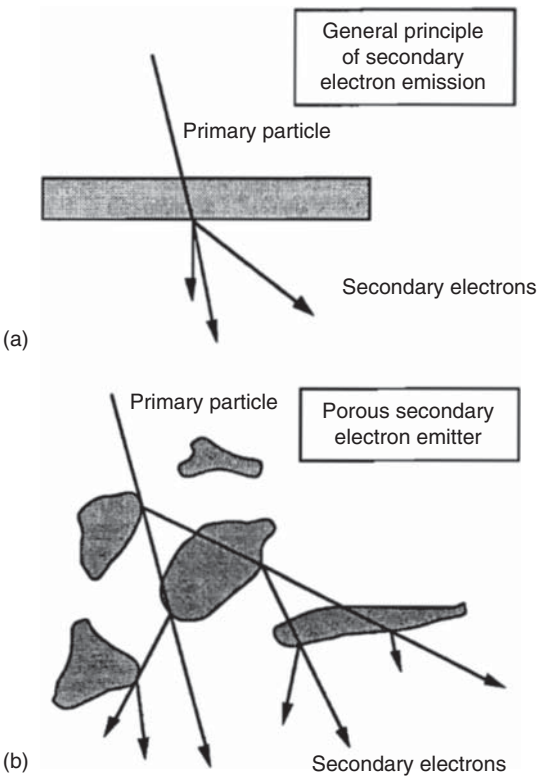

Figure 4.30 (a) Illustration of the general principle of secondary electron emission and (b) schematic representation of the enhancement of secondary electron emission when using porous surfaces. (Cerron Zeballos 1996. Reprinted with the permission of CERN.)

coupled with the microstrip readout technique. The former allowed to improve detection efficiency for ionizing particles and, as a consequence, to widen the variety of gases which can be used, including nonflammable gas mixtures, the latter allowed to reach an impressive spatial resolution even down to a few tens of micrometers.

Charged particles passing through RPC electrodes can create secondary electrons and δ-electrons. These electrons have typical kinetic energy ranging from a few to one hundred electron-volts and, therefore, those produced in the vicinity of the surface may escape into the gas, as schematically shown in Figure 4.30a.

The escape mechanism for these electrons is very similar to the emission of photoelectrons in the case of photoelectric effect; this is the reason why, as a rule, good photocathodes are also good secondary electron emitters. Therefore, in order to enhance the effect of secondary electron emission, a layer of photoemissive material can be used to cover an RPC cathode. It is known that some of the best secondary electron emitters are alkali-halides, such as CsI, KCl, and others.

Another important point to consider is the structure of the secondary electron emitters. Porous structures, for example, provide a much better yield, since there are many independent surfaces from which the secondary electrons can escape. At very high voltages these electrons may even create secondary electrons, so

some sort of multiplication is possible, as shown in Figure 4.30b (see, for a further description of this effect, Gavalian *et al*., 1994).

The first tests on RPCs whose electrodes were combined with CsI secondary electron emitters are reported in Anderson *et al*. (1994).

As expected, it was demonstrated that beta particles passing through an RPC can create several additional electrons from a CsI layer. Since, in parallel-plate geometry, the gas gain depends exponentially on the distance of the primary electrons from the anode, the electrons emitted from the cathode will give rise to the biggest avalanches. For this reason, they can provide important contributions to RPC efficiency and time resolution. As a consequence, one can not only use a wider variety of gases, but, in some cases, obtain better values of the time resolution, with the same geometrical configuration. Another important advantage of CsI-coated RPCs is almost zero parallax, meaning that they are almost insensitive to the inclination of the tracks, which sometimes could be a problem, in particular when using large gaps.

Systematic studies of wide- and narrow-gap RPCs combined with secondary electron emitters were performed and reported in Cerron Zeballos (1996), Crotty *et al*. (1996), and Cerron Zeballos *et al*. (1997a). In addition to planar and porous CsI cathodes, some other emitters, known to be good photocathodes, were tested: SbCs, di(ethylferrocenil)mercury (DEFM in the following), TiO_2, metalorganic compounds and even TEA (triethylamine), and TMAE (terakis(dimethylamino)ethylene) liquid layers. In the latter case, the cathode was cooled to ensure proper condensation (for details, see Francke *et al*., 2016).

Although the best results were obtained in laboratory with a SbCs emitter (Cerron Zeballos *et al*., 1997a), in practice layers of porous CsI or polycrystalline DEFM (see Figure 4.31) are much preferable: SbC is not only difficult to manufacture on a large scale but its yield also degrades extremely rapidly in non-clean gases. The clearest secondary electron emission effect was observed in helium gas mixtures containing low concentrations of quenchers, for instance He + 10% ethane, where the contribution from the primary electrons created by particles in the gas is minimum. As an illustration, pulse-height spectra, obtained under various conditions, are presented in Figures 4.32–4.34.

In both cases, when the electrode was not covered with a secondary electron emitter, the pulse–height spectra were identical for positive or negative polarities of the high voltage across the gap (Figure 4.32). On the contrary, when one of the electrodes (the cathode) was covered with an emitter, a clear difference appeared in the pulse-height spectra, when recorded at different polarities (Figures 4.33 and 4.34). This is a direct proof of the appearance of secondary electrons originated from the emitters.

The shape of the pulse-height spectra, of course, depends on the applied voltage. The authors of the publications mentioned that, depending on the actual conditions, between 1 and 3 secondary electrons per incident particle were ejected from the emitters. This number was estimated by comparing the average value of a given pulse-height spectrum with the mean of a single-electron spectrum obtained with ultraviolet light. The net result was that, using a secondary electron emitter, the detection efficiency in narrow-gap RPCs was increased with respect

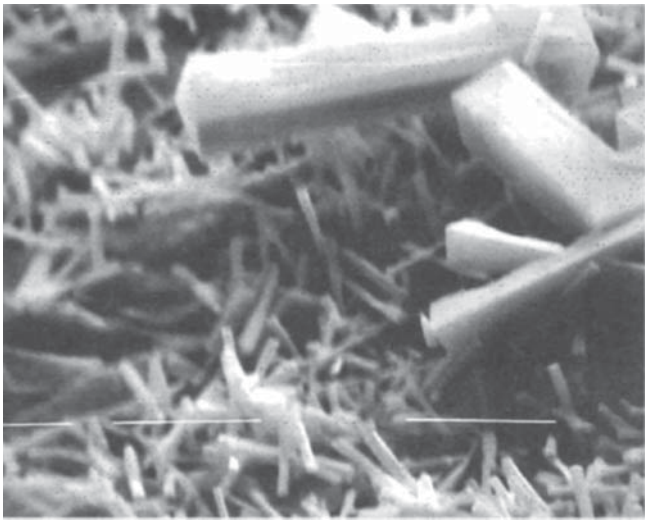

Figure 4.31 Photograph of a layer of di(ethylferrocenil)mercury, taken with 2500 magnification. The white lines are 10 μm in length. (Cerron Zeballos 1996. Reprinted with the permission of CERN.)

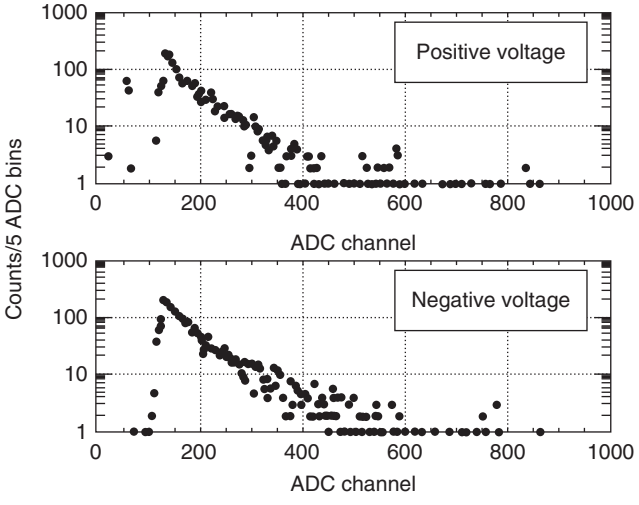

Figure 4.32 Pulse-height distributions for positive and negative applied voltages to the ungrounded electrode (the other one was connected to the charge-sensitive amplifier) when none of them was coated with any secondary electron emitters. Partial pressure of isobutane in a mixture with He was 9.8 Torr. (Cerron Zeballos 1996. Reprinted with the permission of CERN.)

to standard RPC; for instance, in Figure 4.35, efficiency is seen to be increased of a factor around 2 in the threshold range corresponding to 10^4 to 2×10^5 electrons.

In the same series of works Cerron Zeballos (1996), Crotty *et al.* (1996), and Cerron Zeballos *et al.* (1997b), the first attempt to achieve a high-position resolution with a standard 8-mm wide-gap RPC with electrodes made of melamine,

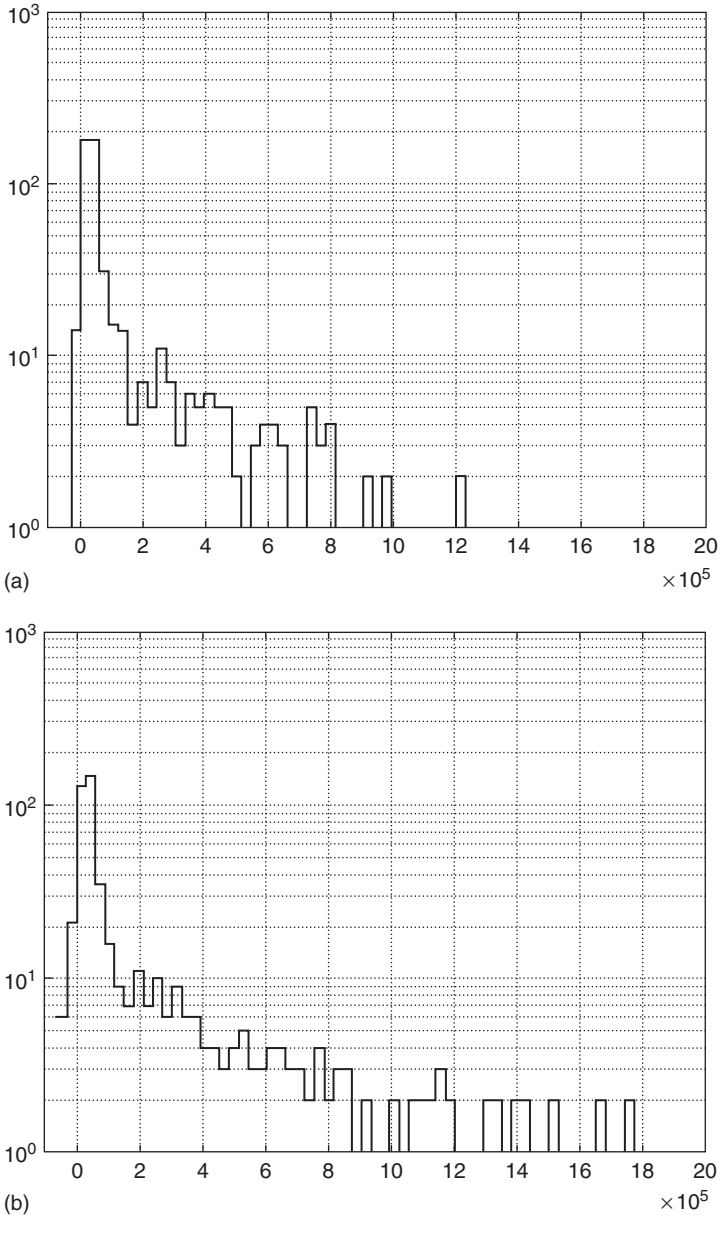

Figure 4.33 (a,b) Typical pulse-height spectrum of signals produced by one spill of beam particles at two polarities of the voltage applied across a narrow-gap (0.1 mm) RPC one electrode of which was coated with a CsI layer. The gas mixture was He + 18% C_4H_{10}. X scale is calibrated in number of electrons. (Fonte *et al*. 2000. Reproduced with permission of Elsevier.)

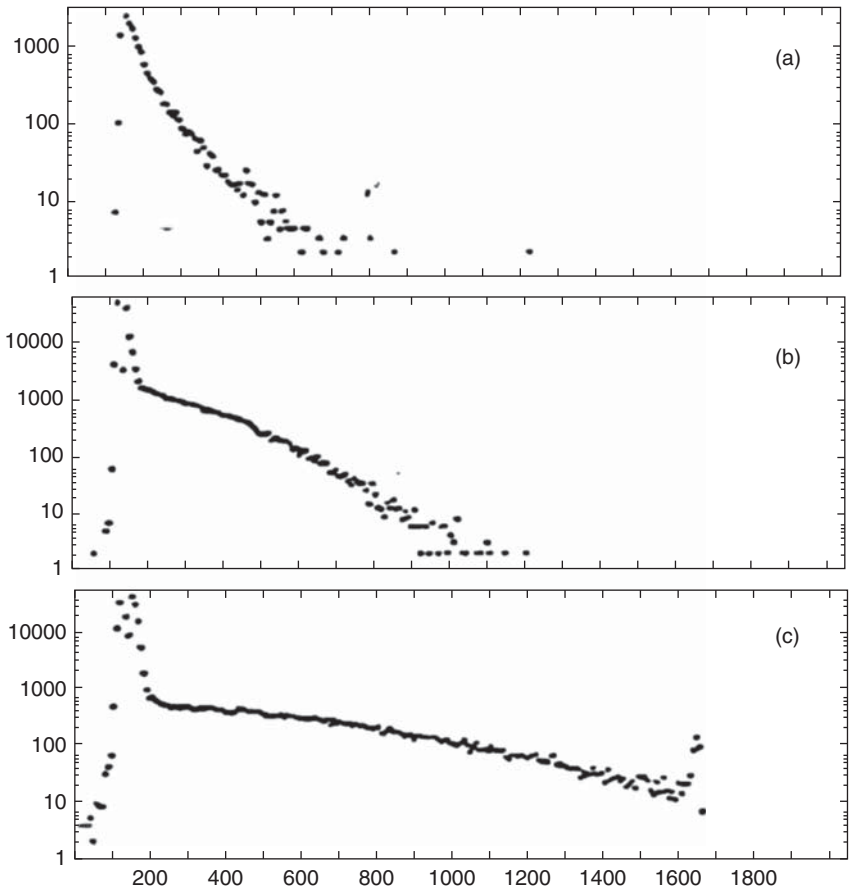

Figure 4.34 Pulse-height distributions obtained with a 5-mm wide-gap RPC filled with a He+ 7% ethane gas mixture, with a DEFM secondary electron emitter, at 6.5 kV applied voltage; (a) single-electron spectrum obtained with a lamp, (b) and (c) with two opposite polarities of the electric field inside the gas gap. The numbers on the X-axis are the pulse-height analyzer channel number. (From Crotty *et al*. 1996.)

0.9 mm thick, was performed. In this case, the anode of the RPC was equipped with thin readout strips, 280 μm wide placed on a 380 μm pitch. The cathode was a single-pad electrode, attached via a 1 MΩ resistor to the high-voltage power supply. The spatial resolution was first evaluated with a pion beam at the T9 test facility located at the CERN PS East Hall, and then later on in the laboratory with a collimated X-ray source. In both cases, comparable results were achieved.

As an example, the width of the centroid distribution measured with an X-ray gun is presented in Figure 4.36. As can be seen, the full-width at half maximum (FWHM) of this distribution is 115 μm. Note, however, that this width has contributions from the many factors other than the intrinsic detector spatial resolution: the collimator width (100 μm), the beam divergence (20 μm), and the electronic

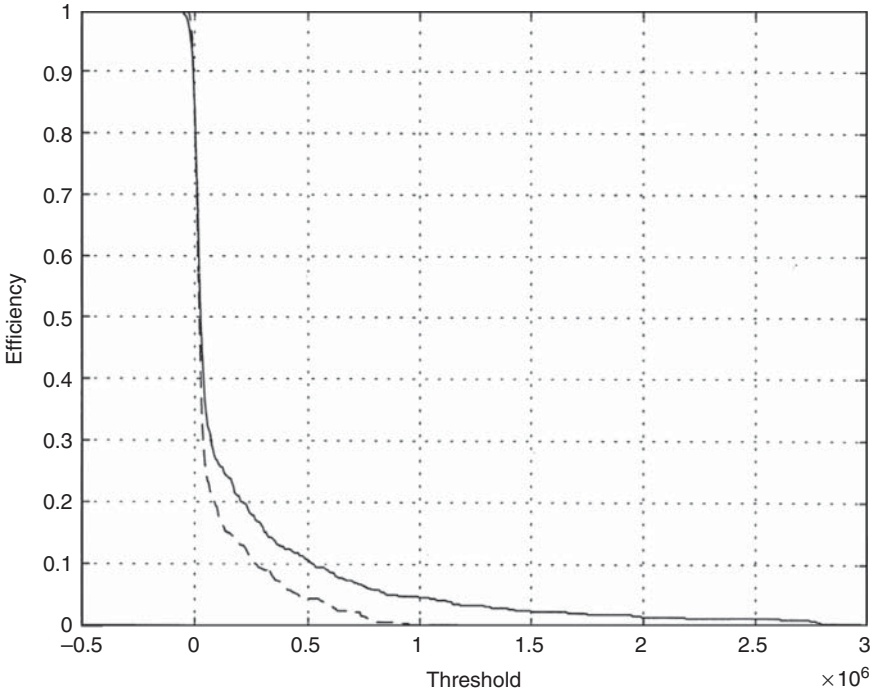

Figure 4.35 Efficiency of an RPC (whose gap width was 0.1 mm) covered with an inner electrode surface covered with a layer of CsI converter (solid line) versus electronic threshold (in "number of electrons in the avalanche" units). For comparison, efficiency due to the interaction of the beam particles with the gas alone is presented (dashed line). The gas mixture used was $C_2H_2F_6 + 5\%\ C_4H_{10} + 10\%\ SF_6$. (Fonte *et al*. 2000. Reproduced with permission of Elsevier.)

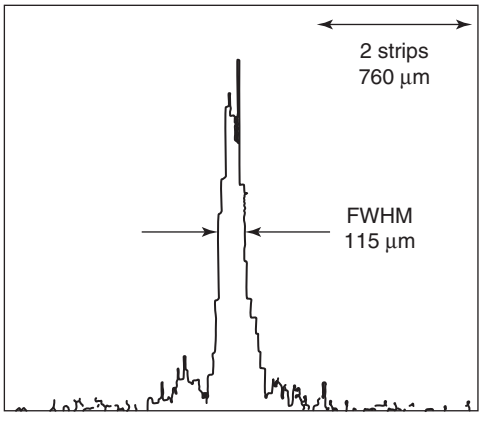

Figure 4.36 Spatial resolution for RPC equipped with 280 μm wide strips (on a 380 μm strip pitch), measured using an X-ray generator. The scale of the X-axis is indicated in the right upper corner of the figure. (Cerron Zeballos *et al*. 1997b. Reproduced with permission of Elsevier.)

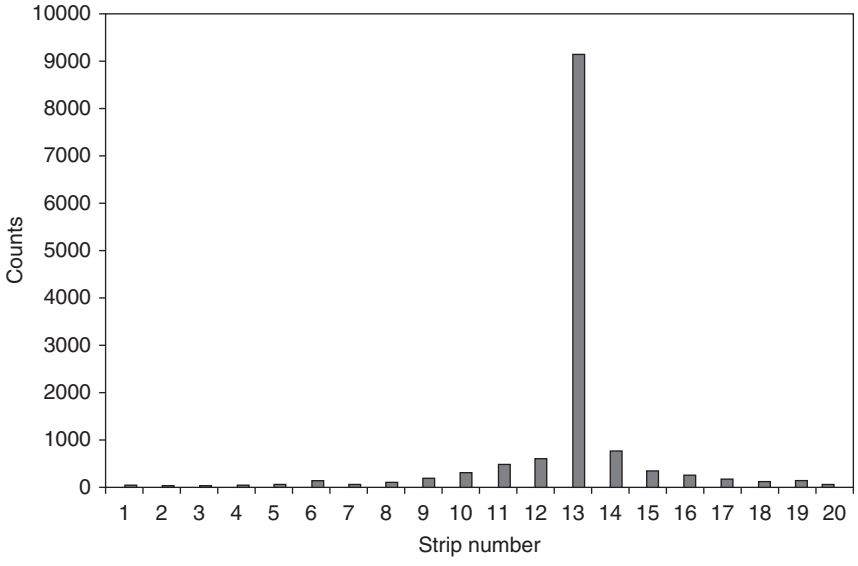

Figure 4.37 Counting rate from the cathodic strips of a microgap (0.1 mm) RPC, when irradiated with a collimated (30 μm) 25 keV X-ray beam. In these particular measurements, the beam was aligned along the strip #13, and the gas mixture used was Xe + 40% Kr + 20% CO_2. (Fonte *et al*. 2000. Reproduced with permission of Elsevier.)

noise (22 μm). If one subtracts these contributions in quadrature, then the intrinsic chamber spatial resolution (related to the dimensions of the avalanche in the gap and the area on the strip array where this induces detectable signals) can be estimated to be around 48 μm FWHM.

Later on, an even better spatial resolution was achieved, with a microgap (0.1-mm thick gap) RPC having a cathode covered with a CsI porous layer around 5 μm thick. The anode was made of a particular type of glass, called Desag glass, and covered with 30 μm pitch anodic chromium strips. Each strip was connected to a charge-sensitive amplifier and, for position measurements, a collimated X-ray beam was used, hitting the cathode at a very small angle, while the number of counts from all strips was measured. Depending on the position of the X-ray beam, a maximum counting rate was measured from one or two adjacent strips. The counting rate distribution across the strips (shown in Figure 4.37) demonstrated that under these conditions a position resolution better than 30 μm could be achieved. Note that this was obtained in a simple strip-by-strip counting mode, without the use of any additional signal treatment (for example, centroiding). This good position resolution was possible because there was no intermediate drift space between the converter and the amplification region. Efficiency for 20 keV X-rays was a few % in a gas mixture of Xe + 40% Kr + 20% CO_2. It was also observed that the same position resolution (~30 μm) could be achieved (for the same beam geometry) even without the secondary electron converter; in this case, however, the efficiency was correspondingly lower.

References

Abashian, A. *et al*. (2000) The K(L)/mu detector subsystem for the BELLE experiment at the KEK B-factory. *Nucl. Instrum. Methods Phys. Res., Sect. A*, **449**, 112–124.

Abbrescia, M. (2003) The dynamic behaviour of resistive plate chambers. Talk Given for the VII Workshop on Resistive Plate Chambers and Related Detectors, Clermont-Ferrand.

Abbrescia, M. (2004) The dynamic behaviour of resistive plate chambers. *Nucl. Instrum. Methods Phys. Res., Sect. A*, **533**, 7.

Abbrescia, M. *et al*. (1999a) The simulation of resistive plate chambers in avalanche mode: charge spectra and efficiency. *Nucl. Instrum. Methods Phys. Res., Sect. A*, **431**, 413–427.

Abbrescia, M. *et al*. (1999b) Progresses in the simulation of resistive plate chambers in avalanche mode. *Nucl. Phys. B (Proc. Suppl.)*, **78**, 459–446.

Abbrescia, M. *et al*. (2000) New developments on front-end electronics for the CMS resistive plate chambers. *Nucl. Instrum. Methods Phys. Res., Sect. A*, **456**, 143–149.

Abbrescia, M. *et al*. (2008) Performance of a six gap MRPC built for large area coverage. *Nucl. Instrum. Methods Phys. Res., Sect. A*, **593**, 3.

Ablikim, M. (2009) The BESIII collaboration, Design and Construction of the BESIII Detector, arXiv:0911.4960.

Adams, C. *et al*. (2016) Design, Construction and Testing of the Digital Hadron Calorimeter (DHCAL) Electronics, arXiv:1603.01654v1.

Adinolfi, M. *et al*. (2000) Performance of low-resistivity single and dual-gap RPCs for LHCb. *Nucl. Instrum. Methods Phys. Res., Sect. A*, **456**, 95–98.

Aielli, G. *et al*. (2001) A systematic study of the ARGO experiment front-end electronics. Proceedings of ICRC 2001, p. 2862.

Akindinov, A. *et al*. (2000) The multigap resistive plate chamber as a time-of-flight detector. *Nucl. Instrum. Methods Phys. Res., Sect. A*, **456**, 16–22.

Akindinov, A. *et al*. (2001) A four-gap glass-RPC time of flight array with 90 ps time resolution, ALICE note ALICE-PUB-99-34. *IEEE Trans. Nucl. Sci.*, **48**, 1658–1663. doi: 10.1109/23.960353.

ALICE collaboration (2000) ALICE time-of-flight system (TOF): technical design Report. Alice-TDR-8; CERN-LHCC-2000-012.

Aloisio, A. *et al*. (1996) The RPC trigger system of the F/B muon spectrometer at the L3 experiment. *Nucl. Instrum. Methods Phys. Res., Sect. A*, **379**, 552–554.

Ammosov, V. *et al*. (2007) The HARP resistive plate chambers: characteristics and physics performance. *Nucl. Instrum. Methods Phys. Res., Sect. A*, **578**, 119–138.

An, S. *et al*. (2008) A 20ps timing device — a multigap resistive plate chamber with 24 gas gaps. *Nucl. Instrum. Methods Phys. Res., Sect. A*, **594**, 39–43.

Anderson, D.F. *et al*. (1994) High counting rate resistive-plate chamber. *Nucl. Instrum. Methods Phys. Res., Sect. A*, **348**, 324.

Anghinolfi, F., Jarron, P., Krummenacher, F., Usenko, E., and Williams, M.C.S. (2004) NINO: an ultrafast low-power front-end amplifier discriminator for the time-of-flight detector in the ALICE experiment. *IEEE Trans. Nucl. Sci.*, **51** (5).

Arnaldi, R. *et al*. (2000) Study of the resistive plate chambers for the ALICE Dimuon arm. *Nucl. Instrum. Methods Phys. Res., Sect. A*, **456**, 73–76.

Arnaldi, R. *et al*. (2005) Front-end electronics for the RPCs of the ALICE Dimuon trigger. *IEEE Trans. Nucl. Sci.*, **52** (4).

Assis, P. *et al*. (2016) A large area TOF-tracker device based on multi-gap Resistive Plate Chambers. *JINST*, **11**, C10002.

Ayyad, Y. *et al*. (2012) First results with RPC prototypes for the detection of relativistic heavy-ions at the R3B experiment. *Nucl. Instrum. Methods Phys. Res., Sect. A*, **661**, 141.

Babkin, V.A. *et al*. (2016) Development of the MRPC for the TOF system of the MultiPurpose Detector. *JINST*, **11**, C06007.

Balsamo, E. *et al*. (2012) The OPERA RPCs front end electronics; a novel application of LVDS line receiver as low cost discriminator. *JINST*, **7**, P11007.

Belver, D. *et al*. (2009) The HADES RPC inner TOF wall. *Nucl. Instrum. Methods Phys. Res., Sect. A*, **602**, 687–690.

Belver, D. *et al*. (2010) Performance of the low-jitter high-gain/bandwidth front-end electronics of the HADES tRPC wall. *IEEE Trans. Nucl. Sci.*, **57** (5), 2848–2856.

Blanco, A., Carolino, N., Fonte, P., and Gobbi, A. (2001) A new front-end electronics chain for timing RPCs. *IEEE Trans. Nucl. Sci.*, **48** (4), 1249.

Blanco, A. *et al*. (2003) Single-gap timing RPCs with bidimensional position-sensitive readout for very accurate TOF systems. *Nucl. Instrum. Methods Phys. Res., Sect. A*, **508**, 70–74.

Blanco, A. *et al*. (2015) Performance of timing resistive plate chambers with relativistic neutrons from 300 to 1500 MeV. *JINST*, **10**, C02034.

Cabanelas, P. *et al*. (2009) Performances of 4-gap timing RPCs for relativistic ions in the range Z=1–6. *JINST*, **4**, P11007.

Camarri, P., Cardarelli, R., Di Ciaccio, A., and Santonico, R. (1998) Streamer suppression with SF6 in RPC's operated in avalanche mode. *Nucl. Instrum. Methods Phys. Res., Sect. A*, **414**, 317–324.

Carboni, G. *et al*. (2003) A model for RPC detectors operating at high rate. *Nucl. Instrum. Methods Phys. Res., Sect. A*, **498**, 135.

Cardarelli, R. *et al*. (2013) Performance of RPCs and diamond detectors using a new very fast low noise preamplifier. *JINST*, **8**, P01003.

Casarejos, E. *et al*. (2012) Detection efficiency of relativistic heavy-ions with resistive-plate chambers. *Nucl. Instrum. Methods Phys. Res., Sect. A*, **674**, 39.

Cavallo, N. *et al*. (1996) Front-End Card Design for the RPC Detector at BaBar. INFN/TC-96/22.

Cavallo, N. *et al*. (1998) Electronics design of the front-end for the RPC Muon detector at BaBar. *Nucl. Phys. B (Proc. Suppl.)*, **61B**, 545–550.

Cerron Zeballos, E. (1996) New developments on RPC: secondary electron emission and microstrip readout. Proceedings of 3rd International Workshop on Resistive Chambers and Related Detectors. Scientifica Acta, vol. **XI**, p. 45.

Cerron Zeballos, E. *et al*. (1996a) A comparison of the narrow gap and wide gap resistive plate chamber. *Nucl. Instrum. Methods Phys. Res., Sect. A*, **373**, 35–42.

Cerron Zeballos, E. *et al*. (1996b) A new type of resistive plate chamber: the multigap RPC. *Nucl. Instrum. Methods Phys. Res., Sect. A*, **374**, 132–136.

Cerron Zeballos, E. *et al*. (1997a) Latest results from the multigap resistive plate chamber. *Nucl. Instrum. Methods Phys. Res., Sect. A*, **392**, 145–149.

Cerron Zeballos, E. *et al*. (1997b) Resistive plate chambers with secondary electron emitters and microstrip readout. *Nucl. Instrum. Methods Phys. Res., Sect. A*, **392**, 150.

Cerron Zeballos, E. *et al*. (1999) A very large multigap resistive plate chamber. *Nucl. Instrum. Methods Phys. Res., Sect. A*, **434**, 362.

Chandratre, V. B. *et al*., ANUSPARSH-II frontend ASIC for avalanche mode of RPC detector using regulated cascode trans-impedance amplifier, *Proc. DAE-BRNS Symp. Nucl. Phys.* **60** (2015), http://www.sympnp.org/proceedings/60/G13.pdf (accessed 21 November 2017).

Ciobanu, M. *et al*. (2007) A front-end electronics card comprising a high gain/high bandwidth amplifier and a fast discriminator for time-of-flight measurements. *IEEE Trans. Nucl. Sci.*, **54** (4), 1201.

Ciobanu, M. *et al*. (2008) PADI, a fast preamplifier – discriminator for time-of-flight measurements. IEEE Nuclear Science Symposium Conference Record, N30-18 (2008) 2018–2024.

Ciobanu, M. *et al*. (2012) PADI-6 and PADI-7, new ASIC prototypes for CBM ToF. GSI Scientific Report 2012 PHN-SIS18-ACC-35, https://repository.gsi.de/record/52186/files/PHN-SIS18-ACC-35.pdf (accessed 28 October 2017).

Colucci, A. *et al*. (1999) Measurement of drift velocity and amplification coefficient in $C_2H_2F_4$–isobutane mixtures for avalanche-operated resistive-plate counters. *Nucl. Instrum. Methods Phys. Res., Sect. A*, **425**, 84–91.

Crotty, I. *et al*. (1995) The wide gap resistive plate chamber. *Nucl. Instrum. Methods Phys. Res., Sect. A*, **360**, 512–520.

Crotty, I. *et al*. (1996) A new resistive plate chamber with secondary electron emitters and two dimensional MIicrostrip readout. IEEE Nuclear Science Symposium. Conference Record, vol. **1**, p. 362.

de Urquijo, J. *et al*. (2009) Electron swarm coefficients in 1,1,1,2 tetrafluoroethane (R134a) and its mixtures with Ar. *Eur. Phys. J. D*, **51** (2), 241–245.

Deppner, I. *et al*. (2016) Performance studies of MRPC prototypes for CBM. *JINST*, **11**, C10006.

Djordjević, A.R. and Sarkar, T.K. (1987) Analysis of time response of lossy multiconductor transmission line networks. *IEEE Trans. Microwave Theory Tech.*, **35** (10), 898–908.

Dulucq, F. *et al*. (2010) HARDROC: readout chip for CALICE/EUDET digital hadronic calorimeter. Nuclear Science Symposium Conference Record (NSS/MIC), IEEE. doi: 10.1109/NSSMIC.2010.5874060.

Fonte, P. (2002) Applications and new developments in resistive plate chambers. *IEEE Trans. Nucl. Sci.*, **49** (3), 881–887.

Fonte, P. (2013a) Survey of physical modelling in resistive plate chambers. *JINST*, **8**. doi: 10.1088/1748-0221/8/11/p11001.

Fonte, P. (2013b) Frequency-domain formulation of signal propagation in multistrip resistive plate chambers and its low-loss, weak-coupling analytical approximation. *JINST*, **8**, P08007.

Fonte, P., Ferreira Marques, R., Pinhão, J., Carolino, N., and Policarpo, A. (2000) High resolution RPCs for large TOF systems. *Nucl. Instrum. Methods Phys. Res., Sect. A*, **449**, 295. doi: 10.1016/S0168-9002(99)01299-1.

Fonte, P. and Peskov, V. (2002) High-resolution TOF With RPCs. *Nucl. Instrum. Methods Phys. Res., Sect. A*, **477**, 17–22.

Fonte, P., Smirnitski, A., and Williams, M.C.S. (2000) A new high-resolution time-of-flight technology. *Nucl. Instrum. Methods Phys. Res., Sect. A*, **443**, 201–204. doi: 10.1016/S0168-9002(99)01008-6.

Fonte, P. *et al*. (2000) Micro-gap parallel-plate chambers with porous secondary electron emitters. *Nucl. Instrum. Methods Phys. Res., Sect. A*, **454**, 260.

Francke, T. *et al*. (2016) *Position-Sensitive Gaseous Photomultipliers: Research and Applications*, IGI Global, USA.

Garritano, L. *et al*. (2015) An educational activity: building a MRPC, world. *J. Chem. Educ.*, **3** (6), 150–159. doi: 10.12691/wjce-3-6-4.

Gavalian, V.G. *et al*. (1994) Multiwire particle detectors based on porous dielectric layers. *Nucl. Instrum. Methods Phys. Res., Sect. A*, **350**, 244.

Giannini, F., Limiti, E., Orengo, G., and Cardarelli, R. (1999) An 8 channel GaAs IC front-end discriminator for RPC detectors. *Nucl. Instrum. Methods Phys. Res., Sect. A*, **432**, 440–449.

Gonzalez-Diaz, D., Chen, H.S., and Wang, Y. (2011) Signal coupling and signal integrity in multi-strip resistive plate chambers used for timing applications. *Nucl. Instrum. Methods Phys. Res., Sect. A*, **648**, 52.

González-Díaz, D. *et al*. (2006) An analytical description of rate effects in timing RPCs. *Nucl. Phys. B (Proc. Suppl.)*, **158**, 111.

D. Gonzalez-Diaz *et al*., Detectors and Concepts for sub-100 ps timing with gaseous detectors, 2017 **JINST 12** C03029.

Kiš, M. *et al*. (2011) A multi-strip multi-gap RPC barrel for time-of-flight measurements. *Nucl. Instrum. Methods Phys. Res., Sect. A*, **646**, 27–34.

Koreshev, V., Ammosov, V., Ivanilov, A., Sviridov, Y., Zaets, V., and Semak, A. (2000) Operation of narrow gap RPC with tetrafluoroethane based mixtures. *Nucl. Instrum. Methods Phys. Res., Sect. A*, **456**, 46–49.

Lee, K.S. *et al*. (2012) Tests of multigap RPCs for high-η triggers in CMS. *JINST*, **7**, P10009.

Lippmann, C. and Riegler, W. (2004) Space charge effects in resistive plate chambers. *Nucl. Instrum. Methods Phys. Res., Sect. A*, **517**, 54.

Lippmann, C., Riegler, W., and Kalweit, A. (2006) Rate effects in resistive plate chambers. *Nucl. Phys. (Proc. Suppl.)*, **158**, 127.

Llope, W.J. (2008) Simple front-end electronics for multigap resistive plate chambers. *Nucl. Instrum. Methods Phys. Res., Sect. A*, **596**, 430–433.

Lopes, L. *et al*. (2007) Accurate timing of gamma photons with high-rate resistive plate chambers. *Nucl. Instrum. Methods Phys. Res., Sect. A*, **573**, 4.

Machado, J. *et al*. (2015) Performance of timing Resistive Plate Chambers with protons from 200 to 800 MeV. *JINST*, **10**, C01043.

Manen, S. *et al*. (2013) FEERIC, a very-front-end ASIC for the ALICE Muon trigger resistive plate chambers. Nuclear Science Symposium and Medical Imaging Conference (NSS/MIC), IEEE. doi: 10.1109/NSSMIC.2013.6829539.

Mangiarotti, A. *et al*. (2006) On the deterministic and stochastic solutions of space charge models and their impact on high resolution timing. *Nucl. Phys. B (Proc. Suppl.)*, **158**, 118–122. doi: 10.1016/j.nuclphysbps.2006.07.024.

Park, S. *et al*. (2005) Production of gas gaps for the forward RPCs of the CMS experiment. *Nucl. Instrum. Methods Phys. Res., Sect. A*, **550**, 551–558.

Petriş, M. *et al*. (2016) Time and position resolution of high granularity, high counting rate MRPC for the inner zone of the CBM-TOF wall. *JINST*, **11**, C09009.

Petrovici, M. *et al*. (2003) Multistrip multigap symmetric RPC. *Nucl. Instrum. Methods Phys. Res., Sect. A*, **508**, 75–78.

Raether, H. (1964) *Electron Avalanches and Breakdowns in Gases*, Butterworths, London.

Rees, J.A. (ed.) (1973) *Electrical Breadown of Gases*, The MacMillan Press, Ltd., London.

Riegler, W. (2004) Extended theorems for signal induction in particle detectors VCI 2004. *Nucl. Instrum. Methods Phys. Res., Sect. A*, **535**, 287–293.

Riegler, W. (2016) Electric fields, weighting fields, signals and charge diffusion in detectors including resistive materials. *JINST*, **11**, P11002.

Riegler, W. and Burgarth, D. (2002) Signal propagation, termination, crosstalk and losses in resistive plate chambers. *Nucl. Instrum. Methods Phys. Res., Sect. A*, **481**, 130–143.

Riegler, W., Lippmann, C., and Veenhof, R. (2003) Detector physics and simulation of resistive plate chambers. *Nucl. Instrum. Methods Phys. Res., Sect. A*, **500**, 144–162. doi: 10.1016/S0168-9002(03)00337-1.

Royer, L., Böhner, G., and Lecoq, J. (2000) A Front-End ASIC for the Dimuon Arm Trigger of the ALICE Experiment. CERN-ALI-2000-015; CERN-ALICE-PUB-2000-015.

Santonico, R. and Cardarelli, R. (1981) Development of resistive plate counters. *Nucl. Instrum. Methods Phys. Res.*, **187**, 377.

Shao, M. *et al*. (2006) Simulation study on the operation of a multi-gap resistive plate chamber. *Meas. Sci. Technol.*, **17**, 123–127.

Shi, L. (2014) A high time and spatial resolution MRPC designed for muon tomography. *JINST*, **9**, C12038.

Tomida, N. (2016) Performance of TOF-RPC for the BGOegg experiment. *et al.*, *JINST*, **11**, C11037.

Tomida, N. *et al*. (2014) Large strip RPCs for the LEPS2 TOF system. *Nucl. Instrum. Methods Phys. Res., Sect. A*, **766**, 283–287.

Wang, X.Z. *et al*. (2016a) The upgrade system of BESIII ETOF with MRPC technology. *JINST*, **11**, C08009.

Wang, Y. *et al*. (2010) Crosstalk research of long strip timing RPC. Nuclear Science Symposium Conference Record (NSS/MIC), 2010 IEEE. doi: 10.1109/NSSMIC.2010.5873868.

Wang, Y. *et al*. (2016b) Development and test of a real-size MRPC for CBM-TOF. *JINST*, **11**, C08007.
Williams, M.C.S. (2016) The multi gap RPC: why do they work so well. Talk Given at the XIII Workshop on Resistive Plate Chambers and Related Detectors, Gent.
Yang, H. *et al*. (2010) Towards an efficient prototype of a RPC detector readout system for the Daya bay neutrino experiment. *IEEE Trans. Nucl. Sci.*, **57** (4), 2371–2375.

5

Resistive Plate Chambers in High Energy Physics Experiments

In this chapter we review some experimental apparatus which have been or are using resistive plate chambers (RPCs). Of course, this is not an exhaustive review: we limit ourselves to some specific cases which, in our opinion, are particularly significant, either from the historical point of view, or because of the results obtained, or because of their technological relevance. We will not mention, if not *en passant*, the many important breakthroughs in terms of physics measurements, which were made possible by these devices; on the contrary, we concentrate on what was new or on what was learned from the detector point of view.

5.1 Early Experiments Using RPCs

RPCs were successfully employed since the beginning of the 1990s in many high-energy physics experiments, due to their remarkable characteristics in terms of high efficiency joined with an order of nanosecond time resolution. Historically, the firsts were NADIR (Neutron Antineutron Doublet Investigation by Reactor), FENICE (http://www.lnf.infn.it/esperimenti/fenice.html), E771 (at Fermi National Accelerator Laboratory), WA92 (fixed target experiment at CERN), and MINI (Abbrescia *et al.*, 1993). All these experiments used RPCs very similar to the ones originally developed by Santonico and Cardarelli, that is, they were 2-mm gas gap RPCs with electrodes made of Bakelite, operated in streamer mode. Let us recall that this operation mode did not require sophisticated front-end electronics, and therefore these detectors were relatively easy to operate, easy to build, and inexpensive enough to cover large surfaces.

NADIR was installed at the 250 kW nuclear reactor TRIGA MARK II at the Pavia University, in Italy, and was conceived to search for possible neutron–antineutron oscillations (Bressi *et al*., 1987). Neutrons from the nuclear reactor were impinging on a series of 130 μm grafoil (amorphous carbon) sheets. Since the annihilation of possible anti-neutrons on the target could have been hidden by signals produced by cosmic rays traversing the apparatus, double-gap RPCs divided into 41.6×0.5 m^2 modules (see Figures 5.1 and 5.2) were used to build a veto system all around the system, with a total surface of 120 m^2. The RPCs were operated in mixture made of Ar/iso-butane/Freon 113 (which

Resistive Gaseous Detectors: Designs, Performance, and Perspectives, First Edition.
Marcello Abbrescia, Vladimir Peskov, and Paulo Fonte.

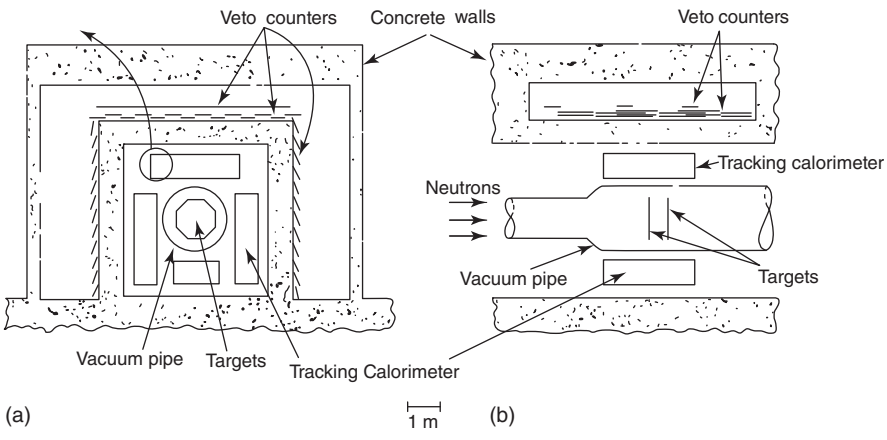

Figure 5.1 Transversal (a) and longitudinal (b) cross section of the apparatus of the NADIR experiment; the veto system, implemented with resistive plate chambers, is in evidence. (Bressi *et al*. 1987. Reproduced with permission of Elsevier.)

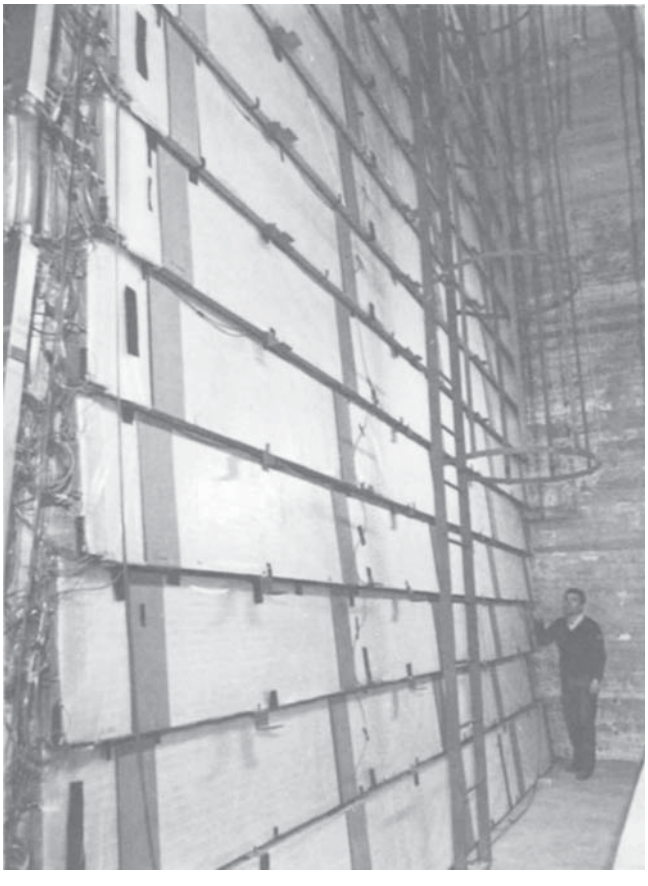

Figure 5.2 A side view of the veto counter system of the NADIR experiment. (Bressi *et al*. 1987. Reproduced with permission of Elsevier.)

is the commercial name of 1,1,2-triclorotrifluoroetano, whose brute formula is $ClCF_2CCl_2F$) in relative proportions 67/33/0.3 at an applied voltage around 8 kV.

The FENICE detector was installed at ADONE storage ring in Frascati (http://www.lnf.infn.it/acceleratori/adone/), an e^+e^- accumulator ring characterized by a center of mass. energy between 1.5 and 3.1 GeV and a luminosity around 10^{29} cm^{-2} s^{-1}. Built to measure the neutron electromagnetic form factor by means of the process $e^+e^- \rightarrow n\overline{n}$, it consisted of scintillators, limited streamer tubes, and iron converters. Again, RPCs were used as a veto against cosmic muons, with a total of about one hundred and fifty 2×1 m^2 modules operated in an Ar/iso-butane/Freon 69/30/1 gas mixture and an operating voltage around 8–9 kV.

RPCs were used for the first time to detect muons coming directly from particle interactions and not as a veto system in the E771 experiment; its muon system was made of three planes, each consisting of ten 2×1 m^2 RPC modules, superimposed at the edges to avoid inefficiencies due to dead zones (see Figures 5.3 and 5.4). The RPCs at the center had an "L" shape, to avoid being directly hit by the beam. Bakelite resistivity was around 10^{11} Ω cm, and the gas mixture was made of the usual components Ar/isobutene/Freon 13Bl 53/42/5, whose relative fractions were chosen after a careful study aimed to optimize the mixture. In this case, readout electrodes were pads, 6×6, 6×12, or 12×12 cm^2 in dimension, getting larger and larger when moving farther from the interaction point. Global efficiency of the system during the run was around 97% and time resolution in the 1 ns range.

From the historical point of view, E771 is of some importance since, for the first time in a working experiment, a decrease in efficiency and a worsening in time resolution was reported in connection with an increase of the flux of the particles impinging on the detectors. This is shown in Figure 5.5 for what concerns efficiency, and in Figure 5.6 for time resolution. In particular, efficiency was seen to decrease a few percentages with respect to its maximum value (measured at a low rate) when the particle flux reached around 10 Hz/cm^2. Also, the average response time was measured to be delayed a few nanoseconds, and time resolution was seen to change significantly. These were clear experimental evidences of the relation between RPC performance and particle rate, which is examined in more detail later on in this book.

The WA92 experiment, installed at the Omega spectrometer at the Super Proto Synchrotron at CERN, was designed to study the quark beauty hadroproduction using a 350 GeV/c π beam impinging on fixed targets (typically 2 mm of copper or tungsten). One of the signatures of beauty production contains a muon in the final state, and this was the reason WA92 was equipped with a high-acceptance muon hodoscope, made by two RPC planes behind iron and tungsten absorbers, at 14 and 16 m from the target, respectively (see Bacci *et al.*, 1993) and Figure 5.7). The hodoscope was made with 36 single-gap RPC modules, equipped with 3.1 pitch readout strips. Each plane, in turn, was made of three detector layers, two equipped with strips in the horizontal direction, the other in the vertical, so that to have a 3D reconstruction of the muon tracks. Gas mixture used was Ar/n-butane/Freon in 55/42/3 relative fraction, operating voltage around 3.5 kV/mm, average measured efficiency around 99%, time

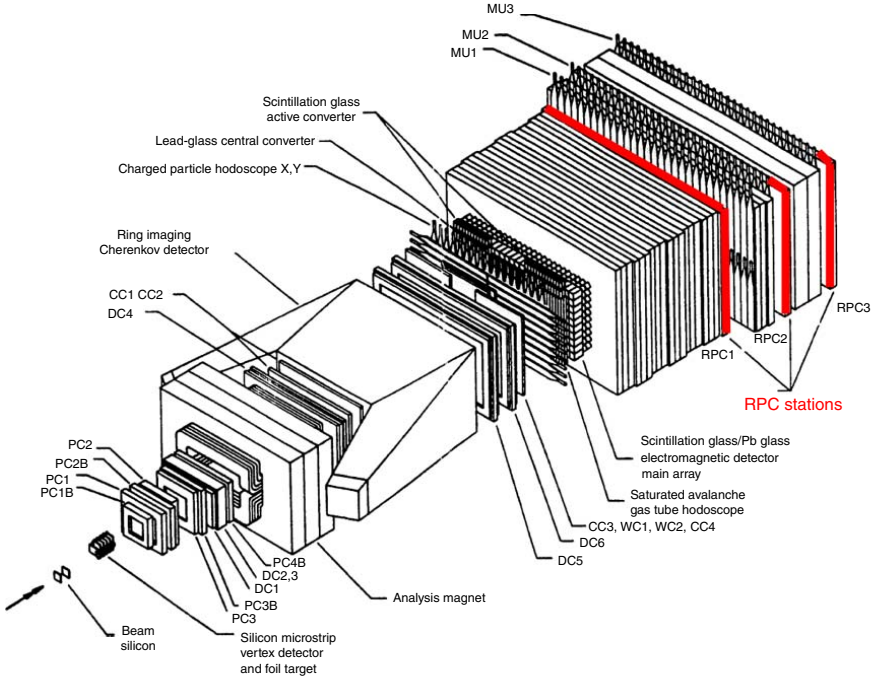

Figure 5.3 Layout of the E771 experiment with, in evidence, the three RPC stations used to detect and track muons from the interaction point. (Antoniazzi *et al*. 1992a. Reproduced with permission of Elsevier.)

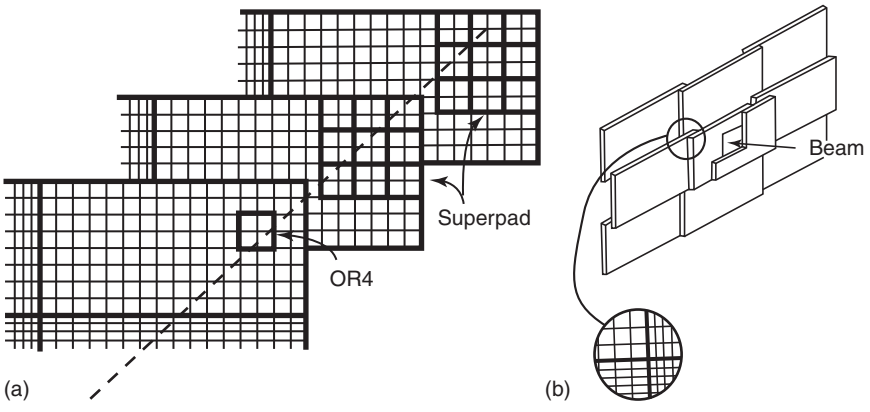

Figure 5.4 (a) Geometrical triple coincidence among three RPC planes in the E771 experiment and (b) RPC planes and pad structure. (Antoniazzi *et al*. 1992b. Reproduced with permission of Elsevier.)

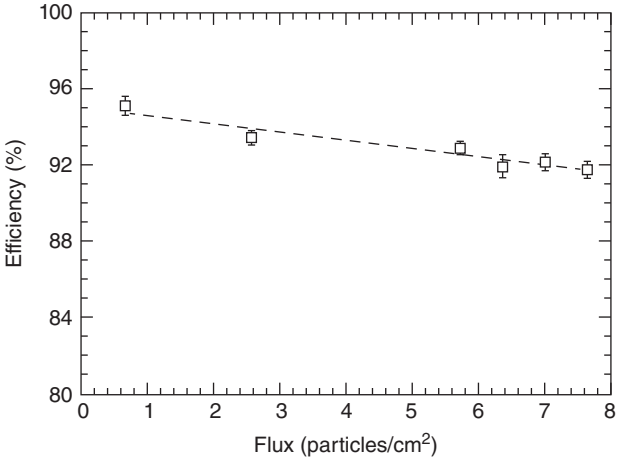

Figure 5.5 Muon detection efficiency versus particle rate, as measured at the E771 experiment; efficiency at low rate is not 100% because of geometrical inefficiencies. (Cataldi *et al*. 1994. Reproduced with permission of Elsevier.)

resolution a few nanoseconds, and spatial resolution around 1 cm, compatible with the strip pitch used. WA92 took data for about 15 days in 1991 and for 3 months in 1992, with a muon trigger rate around 700 Hz and a performance reported to be stable during the whole during data taking (see Figure 5.8).

MINI was the first little experiment completely implemented with RPCs (Abbrescia *et al*., 1993); it was designed for cosmic rays and detector studies at the same time. It was 11.35 m long, and it consisted of fourteen 4 m^2 chambers interleaved with nine 1-m-thick concrete absorbers (see Figure 5.9). Each chamber was made out of two 2×1 m^2 RPC modules equipped with 2-m-long and 3-cm-wide pickup strips (64 strips in total). In eight chambers

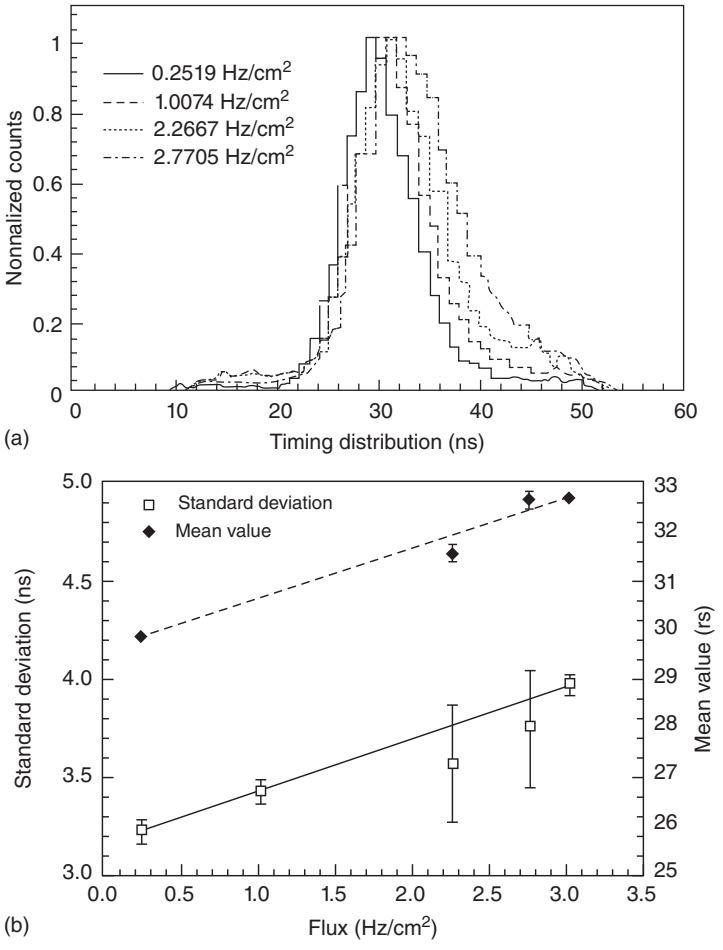

Figure 5.6 (a) Time distributions at different particle rates as measured in the E771 experiment and (b) mean and standard deviation of the time distributions versus particle flux. (Cataldi *et al*. 1994. Reproduced with permission of Elsevier.)

the strips were oriented horizontally, in the other six vertically, allowing a 3D reconstruction of the tracks of the impinging muons. The RPCs were operated in a gas mixture made of 58% argon, 40% butane, and 2% CF_3Br, using simple front-end electronics.

Some of the first studies about the effects of environmental conditions on RPC performance were performed at MINI; for this purpose, a large tank where temperature and pressure could be controlled was placed in front of it. Inside the tank a couple of test chambers were positioned, while the rest of the system could be used to select and track cosmic muons. Some of the results obtained have been already described in Chapter 3 (see also Abbrescia *et al*., 1995, 1997). At MINI, the concept of effective voltage $\Delta V_{\text{eff}} = \Delta V_{\text{app}} \frac{T}{T_0} \frac{p_0}{p}$ (where, as already mentioned in Chapter 3, ΔV_{app} is the applied voltage, T and p environmental temperature

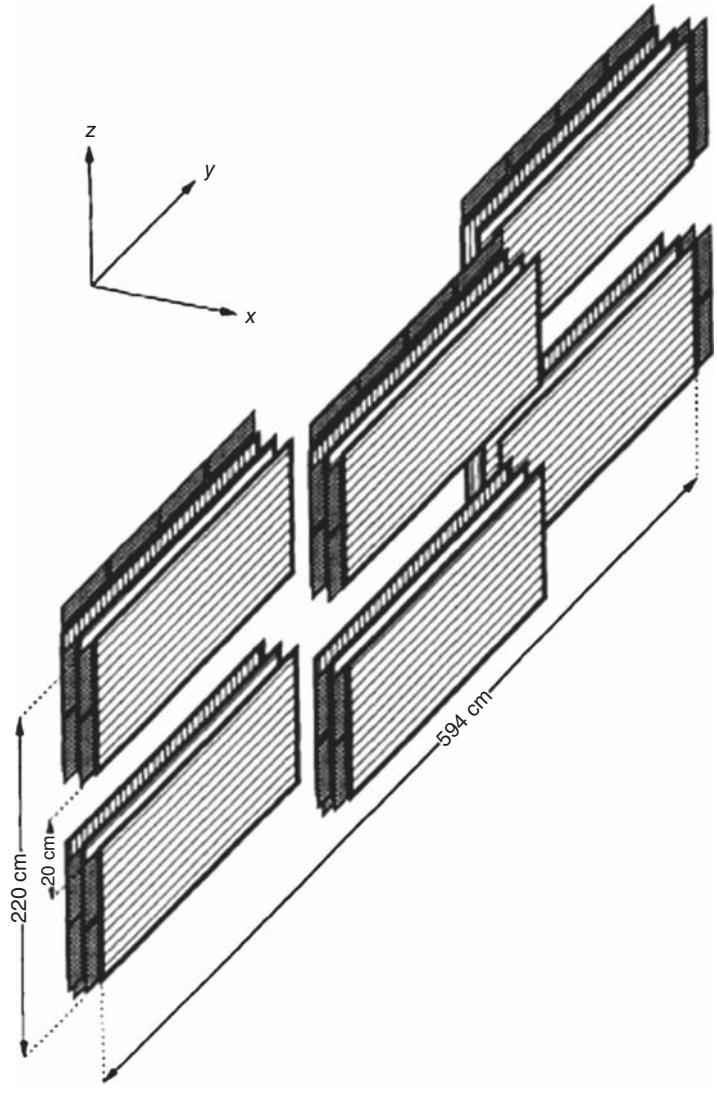

Figure 5.7 Schematic layout of one of the two hodoscope planes implemented with resistive plate chambers in the WA92 experiment. (Bacci *et al*. 1993. Reproduced with permission of Elsevier.)

and pressure, and T_0 and p_0 some reference temperature and pressure) was for the first time introduced and used. Studies on the local performance were performed, allowing to spot the small inefficiency zones corresponding to the spacers used to keep the two Bakelite plates at the desired distance and performing the first "muongraphies" (see Figure 5.10).

Finally, at MINI, efficiency curves were fitted with sigmoids for the first time, as proposed in Abbrescia *et al*., 1995. A sigmoid function is a mathematical function with an "S" shape, continuous and with all its derivatives continuous,

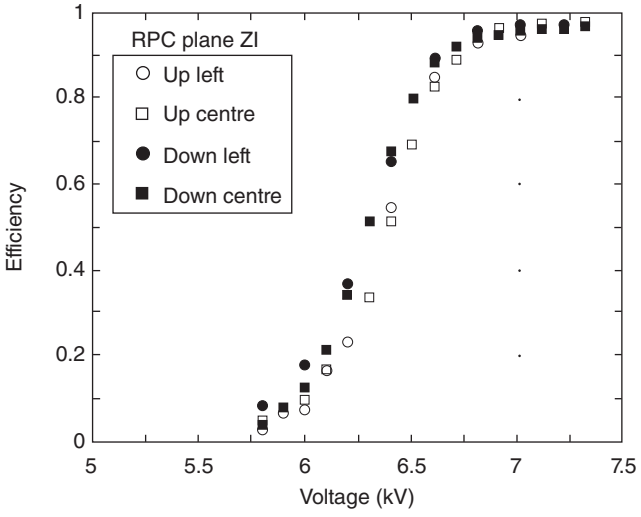

Figure 5.8 Efficiency versus operating voltage of some of the chambers installed in the RPC hodoscope of the WA92 experiment. (Bacci *et al*. 1993. Reproduced with permission of Elsevier.)

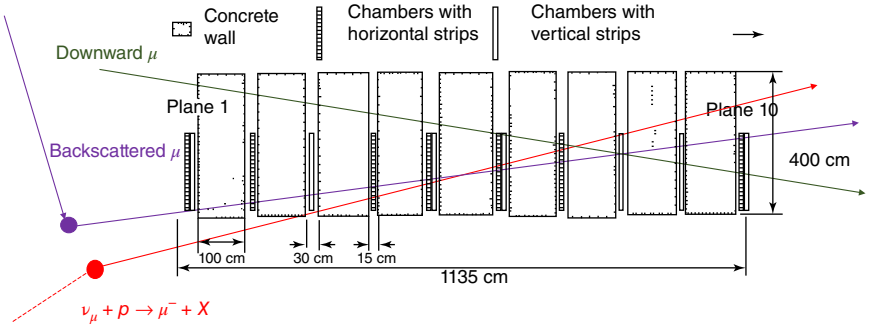

Figure 5.9 Schematic layout of the MINI apparatus. Due to its geometry, it could mostly detect particles close to the horizontal, which could be either downward muons, or muons undergoing backscattering in the ground immediately underneath the telescopes and emerging upward, or even muons deriving from neutrino interactions. (Abbrescia *et al*. 1993. Reproduced with permission of Elsevier.)

used in many different contexts. For fitting RPC efficiency curves, it was used in the following form:

$$\varepsilon = \frac{\varepsilon_{\max}}{1 + e^{-\lambda_s(\Delta V_{\text{eff}} - \Delta V_{50\%})}} \tag{5.1}$$

where ε is the efficiency measured at a certain value of the effective operating voltage ΔV_{eff}, $\varepsilon_{\max}$ is the asymptotic efficiency for $\Delta V_{\text{eff}} \rightarrow \infty$, the λ_s coefficient is proportional to the sigmoid slope at the inflection point, and the high-voltage value $\Delta V_{50\%}$ is the inflection point of the sigmoid, for which 50% of $\varepsilon_{\max}$ is reached. Formula (5.1) is particularly useful to fit experimental efficiency points, since the three parameters cited basically contain the most important

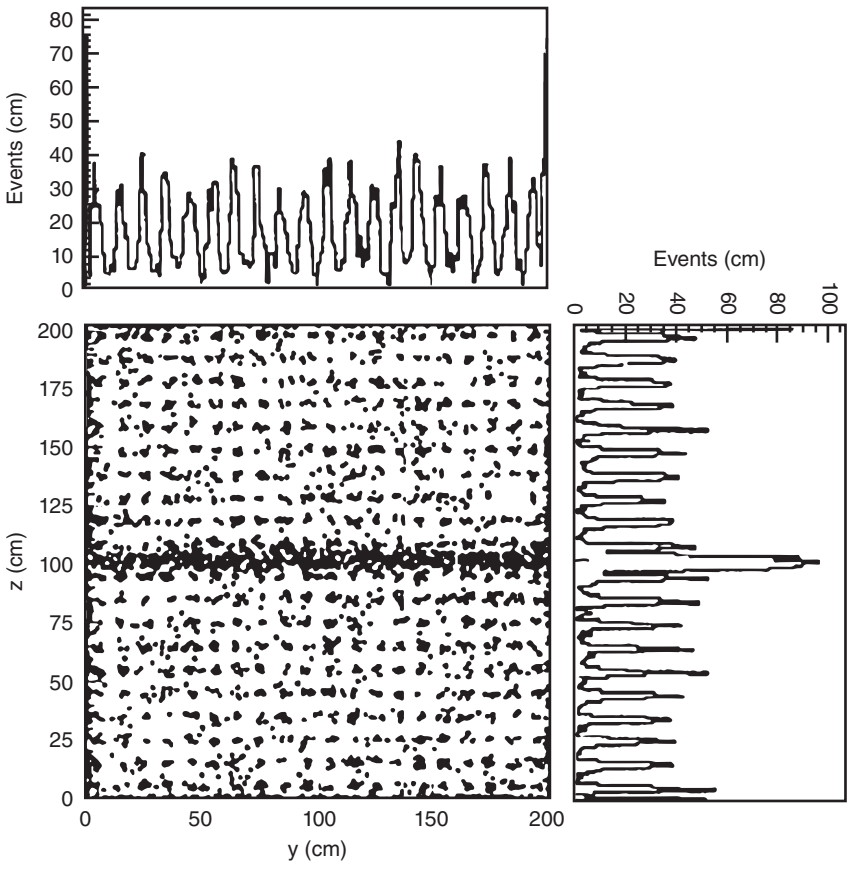

Figure 5.10 Scatter plot for crossing points in one of the chambers under test for muons not revealed in that chamber but selected and tracked by the MINI telescope. The position of the peaks in the two projections fits well with the lattice of the spacers the dark zone in the middle corresponds to the uncovered gap between two RPC modules. Plots of this kind were later referred to as "muongraphies" or "muon radiographies." (Abbrescia *et al*. 1995. Reproduced with permission of Elsevier.)

information about an efficiency curve, that is, its plateau value (estimated by means of $\varepsilon_{\max}$), the position of the efficiency curve itself ($\Delta V_{50\%}$), and its slope (related to λ_s). The use of sigmoids provides a uniform way to easily compare the performance of several chambers and to build the relative statistics; its use is widespread nowadays.

5.2 RPCs for the L3 Experiment at LEP

The encouraging results obtained using RPCs, briefly reviewed in the previous section, pushed physicists to employ them at the experiments which, at the time, were at the forefront of the research in high-energy physics. In particular, an RPC system was added to the forward–backward muon spectrometer of the L3, which was one of four large detectors experiment operating at the Large Electron

Positron (LEP) collider at CERN, in order to increase its angular coverage along the beam direction (Aloisio *et al*., 2000). The system was divided into two "octagonal rings" (forward and backward), made of 16 half-octants each, consisting of drift chambers, a toroidal magnet, and two RPCs layers, placed on the inner surfaces of the two outer drift chamber planes. The system was installed during 1994 (first half) and 1995 (second half). Each RPC layer was segmented in three counters of trapezoidal shape and different size, with an overlap among them to avoid dead areas (see Figure 5.11).

The total system consisted of 192 double-gap RPCs, covering a total area of more than 300 m^2 and operating in streamer mode. Gas mixture used was Ar/isobutane/CF_3Br 58/38/4 up to 1995, at the end of which it was changed, so that it was Ar/isobutane/tetrafluoroethane in 59/35/6 relative proportions since 1996. It was replaced by trifluoroborane (CF_3Br) and then replaced by tetrafluoroethane ($C_2H_2F_4$) since it is a gas potentially harmful to the ozone layer and had been prohibited. Chambers were read out with strip, 29 mm wide and with a 31-mm strip pitch, for a total of 6144 readout channel. Both sides of the readout electrodes were equipped with front-end electronic boards connected to 16 adjacent strips; signals were amplified, discriminated at around 60 mV, and converted and shaped in 200 ns transistor–transistor logic (TTL) differential outputs. The signals were opportunely grouped and sent to the relevant electronics for trigger purposes and for time measurements.

The performance of the RPC system at L3 was carefully studied during the data taking, monitoring the chamber current and counting rate, or measuring their efficiency by using di-muon tracks coming from Z decays and inclusive

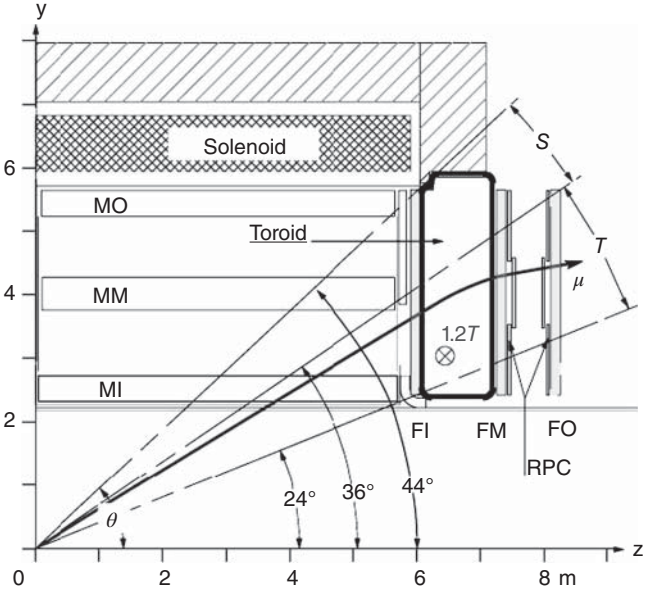

Figure 5.11 Cross section of the FB L3 muon spectrometer. Symbols MO, MM, MI stands for muon outer, medium and inner respectively) (Aloisio *et al*. 2000. Reproduced with permission of Elsevier.)

muon events for which a good track was reconstructed in the L3 central tracking detector and in the muon spectrometer. Since the system operated for about 7 years, this was an excellent opportunity to study the long-term performance of this device; as a matter of fact, it was the first time that RPC aging problems were considered and studied in detail.

Counting rate and current for the L3 RPC system are reported in Figure 5.12 for the 1994–2000 period, not showing dramatic changes in the time span considered. Space resolution, depicted in Figure 5.13, stayed around a value slightly higher than 10 mm, to be compared with the 31-mm strip pitch. Time resolution showed a slight increase, reaching about 3.5 ns after 7 years of operation.

The difficulties inherent to operating a large system for a long time became more evident when studying the efficiency behavior versus time, presented in Figure 5.14; a small loss, from 99.5% to 97%, was observed from 1994 to 1999, and a larger loss in 2000. The authors report that in the first year of operation all RPC chambers presented efficiency close to 100%, and that this quantity slowly moved

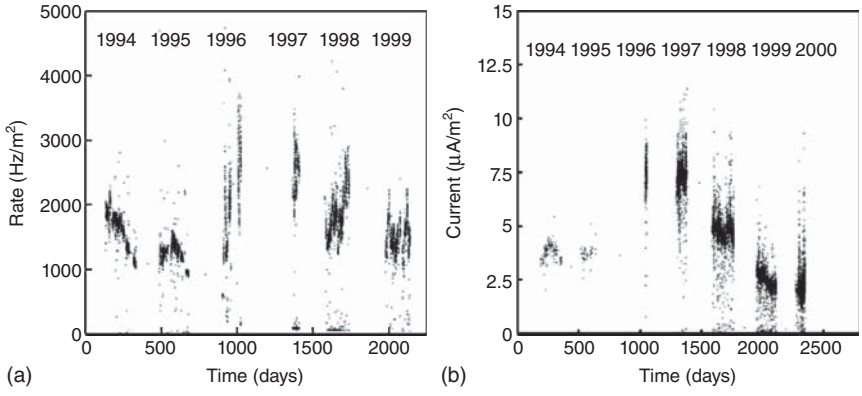

Figure 5.12 Counting rate (a) and current (b) for the L3 RPC system, since 1994 up to 2000. (Alviggi *et al*. 2003. Reproduced with permission of Elsevier.)

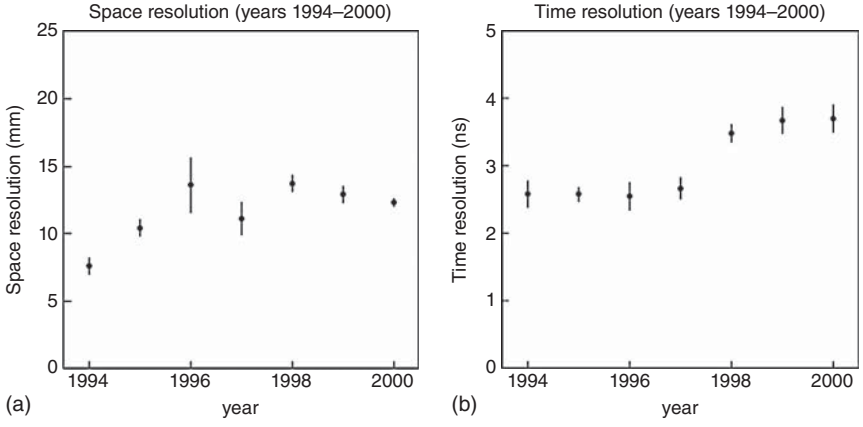

Figure 5.13 Space (a) and time (b) resolutions for the L3 RPC system, since 1994 up to 2000. (Alviggi *et al*. 2003. Reproduced with permission of Elsevier.)

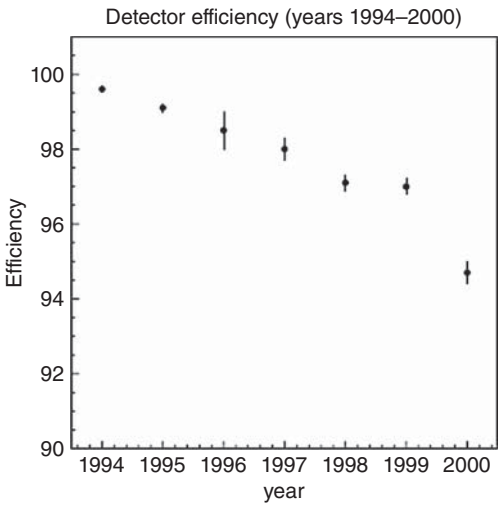

Figure 5.14 Global detector efficiency of the L3 RPC system, since 1994 up to 2000. (Alviggi *et al*. 2003. Reproduced with permission of Elsevier.)

toward lower efficiency values in the subsequent years. However, even in 2000, 75% of the chambers showed efficiency greater than 90%. Moreover, larger inefficiencies were concentrated in specific octants, and were due to the following:

1) Electronic failures, due to the LEP beam lost in the L3 detector and hitting the RPC chambers, generating high rate, and consequently large currents which damaged the front-end chips.
2) The change of the gas mixture in 1996, which caused an increase in the current absorbed; this led to a reduction in the operating voltage, causing a lower efficiency.
3) Gas leaks appearing in some chambers that could not be repaired immediately.

Overall, this could be considered good behavior for such a large system after so many years of operation and, moreover, no aging effects at the detector level were reported.

5.3 The Instrumented Flux Return of the BaBar Experiment

Probably the most significant, and also controversial, experience using RPCs in high-energy physics, before these were employed at Large Hadron Collider (LHC), was the one gained with the Instrumented Flux Return (IFR) of the BaBar (B/B-bar system of mesons) experiment, which operated at the PEP-II positron electron collider at the Stanford Linear Accelerator Center (SLAC) in California. This was due to fact that, for the first time, the importance of strict production and operation protocols, in order to assure good chamber quality and performance stability with time, was strikingly in evidence. As a matter of fact, aging effects, due to a combination of faulty construction procedures and operation, conditioned the performance of the system. Nevertheless, this was an important lesson learned, and the whole RPC community benefited from it.

In BaBar, RPCs were used as active detectors for muon identification and neutral hadron detection; they were positioned inside the gap between the iron plates used to return the magnetic flux of the experiment. The area covered by the RPC system was about 2000 m^2 for a total number of 774 planar RPCs and 32 cylindrical modules. The IFR, whose sketch is shown in Figure 5.15, was divided into a barrel and two endcaps. Each barrel sector was made of 19 RPC layers and 18 iron plates interleaved. A single IFR barrel layer was composed of three RPC modules of rectangular shape. In addition, a double layer of RPCs was inserted between the electromagnetic calorimetry and the coils (inner RPCs), for a total number of 374 modules in the barrel. The endcaps were composed of 18 RPC layers and 18 iron plates, with 432 modules in total that came in several sizes and shapes (trapezoidal, sometimes with circular cuts on a side to leave space for the beam pipe) for geometrical reasons.

In Babar, 2-mm single-gap RPCs, operated in streamer mode, were used; they were filled with a nonflammable gas mixture of argon, $C_2H_2F_4$, and isobutane whose proportions changed over time, but started with a mixture in the 48/48/4 ratio. They were produced at the General Tecnica Factory (close to Rome) between 1996 and 1997, which had been, and will be producing later on, Bakelite RPCs also for the other big experiments mentioned in this book. As usual, the inner surface of the Bakelite was varnished three times with a mixture of 70% linseed oil and 30% n-pentane, in order to make it smoother and to reduce accidental streamers from discharge points onto it.

The BaBar RPC system was a huge endeavor, almost a factor 10 larger in terms of covered surface with respect to the previous systems. RPC modules were to be shipped across the Atlantic; therefore, systematic tests on gas tightness, mechanical integrity (no broken spacers) dark current, single rate, and efficiencies were performed in Italy before departure and then repeated in the United States before installation.

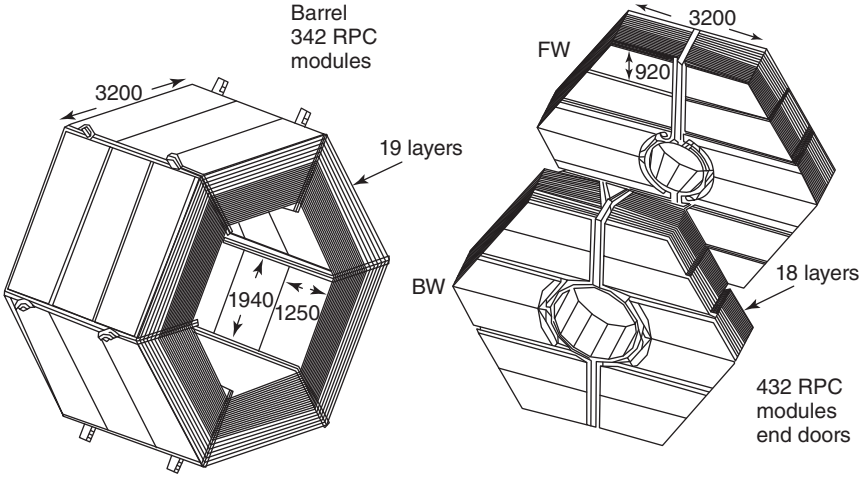

Figure 5.15 Overview of the RPC system of the Instrumented Flux Return of the BaBar experiment. (Anulli *et al*. 2002. Reproduced with permission of Elsevier.)

After installation, at the beginning of summer 1999, the temperature inside the experimental hall exceeded 30°C, and the chamber dark current started to increase at a point that it was decided to disconnect the chambers absorbing a current higher than 100 μA/m^2, and a cooling system was installed. However, even when the temperature returned to around 20°C and the chambers were connected again, dark current did not go back to the initial values, and detection efficiency soon started to decrease, as shown in Figure 5.16.

Moreover, the efficiency maps, similar to the muongraphies already described, showed strange patterns (one of them is shown in Figure 6.15 in Chapter 6, where aging issues are treated in deeper detail). Therefore, in order to identify the origin

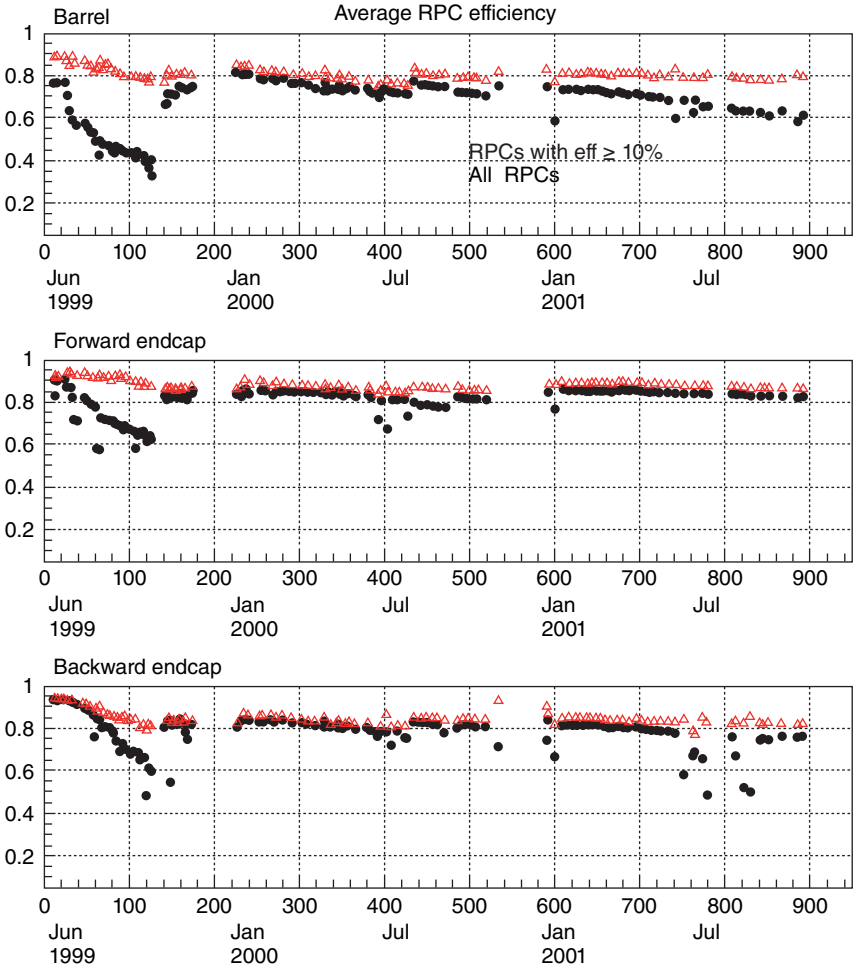

Figure 5.16 Efficiency history of RPCs. The dark markers represent the average efficiency of all BaBar RPCs including disconnected chambers. Empty markers represent the average efficiency of RPCs with efficiency greater than 10%. The evident recovery in efficiency around October 2000 is related installation of the cooling system. (Anulli *et al*. 2003. Reproduced with permission of Elsevier.)

of the problem, a long series of tests were performed: gas flow was increased in selected chambers, the front-end electronic threshold was reduced, weights were put over inefficient regions, and gas composition checked, but to no avail.

Finally, some damaged chambers were opened and thoroughly investigated; several drops of oil were found all over the Bakelite surface, with some of these droplets locally filling the gap and connecting the electrodes. In general, the oil was not polymerized and accumulated around the spacers and the frame. Of course, the short circuits created in this way locally reduced the electric field, with the relative consequences on current and efficiency; for a more detailed explanation of what happened, see Chapter 6.

Since the problem could not be solved in a simple way, in 2002 over two hundreds "second-generation" BaBar RPCs were installed, in the framework of the upgrade of the IFR. Even if the production of these RPCs took place at the same factory of the previous production, uttermost care was taken to keep the inner Bakelite surfaces as clean as possible and to ensure that the final linseed oil coating was thin and well polymerized (for instance, the varnishing with the linseed oil was done only once). New molded corner pieces were designed to replace the drilling method previously used for the gas inlets, and filters were added to purify the linseed oil, which was periodically analyzed. The new RPCs performed much better. For instance, the efficiency of some RPCs is reported in Figure 5.17, and shows good stability with time.

Anyhow, in some particular modules, exposed to the highest particle flux, aging effects again, manifesting themselves in terms of increased current and noise rate together with a reduced efficiency, were noticed as well (see Figure 5.18). Part of the efficiency decrease was attributed to the use of dry gas; it was observed that the initial gas mixture, with relative humidity (RH) close to 0%, was exhausted after passing through the RPC modules, with a RH = 20–30%, consistent with the removal of water from the Bakelite. The removal of water increased the Bakelite resistivity, lowering, as a consequence, RPC rate capability (for a detailed discussion of this point, read Chapter 7).

Detailed studies were performed to understand the correlations among dark current, noise rate, efficiency, and the position of each RPC module in the gas

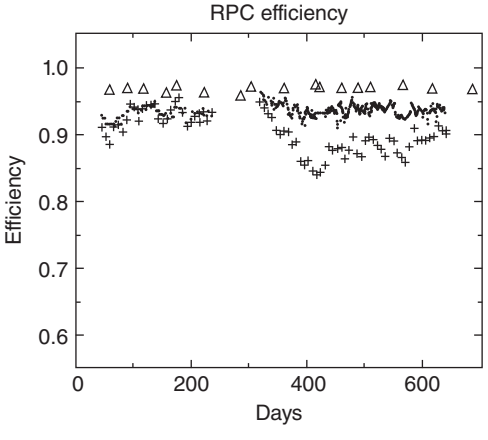

Figure 5.17 Average RPC efficiency, for endcup layers 1–12 of the BaBar IFR, measured with beam using μ-pairs (black points) and with cosmic rays (open triangles). The crosses show the efficiency of the fourth RPC in layer 1 of the west door. (Anulli *et al*. 2005. Reproduced with permission of Elsevier.)

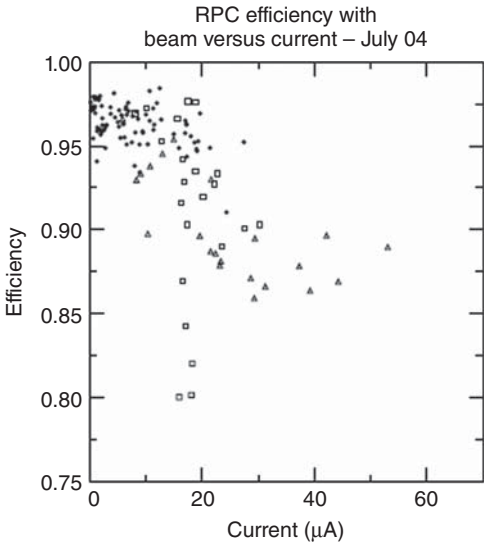

Figure 5.18 RPC efficiency (measured in July 2004) plotted against the current (both measured with beam) of the modules in layers 1–11. The solid circles and the open squares are modules in two different sets of positions of modules. In all cases a clear correlation between lower efficiency and higher currents can be seen. (Anulli *et al*. 2005. Reproduced with permission of Elsevier.)

circuit (Anulli *et al*., 2005). It was found, and this was the first strong experimental evidence, that one key player could be the production of hydrofluoric acid (HF) deriving from dissociation of tetrafluoroethane in streamers.

The RPC system of the BaBar experiment performed well up to the end of the data acquisition, thanks to the extreme care taken in its operation, and all the lessons learned from these detailed analysis. Many of the quality assurance improvements in RPC production made by the IFR group were later on adopted for the production of RPCs used by the LHC collaborations.

5.4 The ARGO-YBJ Detector

The ARGO-YBJ (Astrophysical Radiation with Ground-based Observatory at YangBaJing) experiment was installed at Yangbajing (China), on a high mountain, at about 4300 m above the sea level (see Figures 5.19 and 5.20). It was designed to detect the front of the extensive atmospheric showers (EASs) impinging onto the ground and originated by high-energy primaries of cosmic origin when entering the atmosphere. It has performed researches in the field of γ-ray astronomy (in particular, searches for point-like sources of energy above a few hundred GeV), very high energy γ-ray bursts, cosmic rays physics, Sun and heliosphere physics. It was the first large-scale detector completely implemented with RPCs, which were operated for many years in a hostile environment, characterized by low pressure and significant temperature excursions.

The detector was composed of a central region, 78×74 m^2 in dimension, fully paved with 1560 RPCs (2.80×1.25 m^2 each), surrounded by a "guard ring" made out of other 276 RPC modules, to increase the total sensitive area, so that the whole array covered a total surface of more 10 000 m^2, as shown in Figure 5.21. Producing this number of RPC modules was a challenge in itself,

Figure 5.19 Picture of the building hosting the ARGO-YBJ detector, at 4300 m a.s.l, against the landscape of the Himalayan mountains. (ARGO-YBJ 2000. The ARGO-YBJ offical web site: go.na.infn.it/.)

Figure 5.20 Picture of the experimental hall hosting the ARGO-YBJ detector. The carpet of RPCs is well in evidence. (Surdo and on behalf of the ARGO-YBJ Collaboration 2008. Reproduced with permission of Elsevier.)

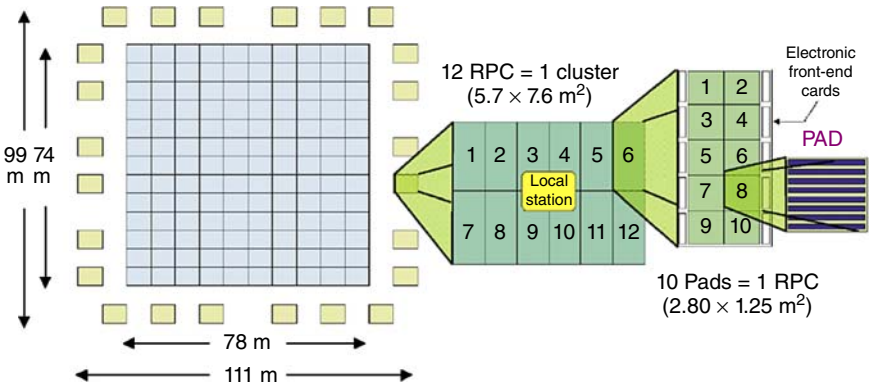

Figure 5.21 Schematic layout of the ARGO-YBJ detector, with details of the RPC readout segmentation. (Camarri 2009. Reproduced with permission of Elsevier.)

since this was the very first time a production on such a large scale was to be organized. Moreover, the RPCs used for ARGO-YBJ were produced in Italy and had to be transported over several thousands of kilometers to the experiment site, with the additional logistic problems deriving from the shipping across such a long distance. Fortunately, the whole process benefited from the lessons learned during the BaBar experience. In particular, improved techniques were used to ensure that the linseed oil coating of the Bakelite plates was completely dried up before operating the detectors, and strict procedures of quality control and quality assurance were put in place throughout all the production steps. This assured that the RPCs employed for ARGO-YBJ did not show any of the problems encountered in the RPC system of BaBar.

In ARGO-YBJ, RPCs were standard 2-mm Bakelite devices, equipped on one side with copper strips, whose signals were digitally read out and grouped in logical ORs of eight strips each, called "pads." On the other side of each gas volume, two copper "big pads" were used in order to collect the analog signal from the detector. The analog readout was put into operation in 2009; basically, it exploited the direct proportionality between the charge signal measured on the "big pads" and the number of charged particles impinging on the corresponding RPC module (see Figure 5.22). The charge readout was therefore used to measure the particle density and was particularly useful when reconstructing the front of the showers generated by very high-energy primaries, whose many particles impinging onto the detector had the effect of saturating the digital information from the strips. This technique had never been performed with RPCs before (Aielli *et al*., 2012a). For each event the location and timing of every detected particle was recorded, allowing the reconstruction of the lateral distribution and the arrival direction.

At ARGO-YBJ, RPCs were operated in a gas mixture of $C_2H_2F_4$/Ar/*i*-C_4H_{10} 75/15/10 and a voltage of 7.2 kV applied to the 2-mm gas gap. Temperature and pressure effects on RPC performance were particularly important, and detailed studies were performed about this issue. As an example, the correlation between detector current and temperature is depicted in Figure 5.23 (Camarri, 2009); similar studies, also on efficiency and time resolution, performed using a

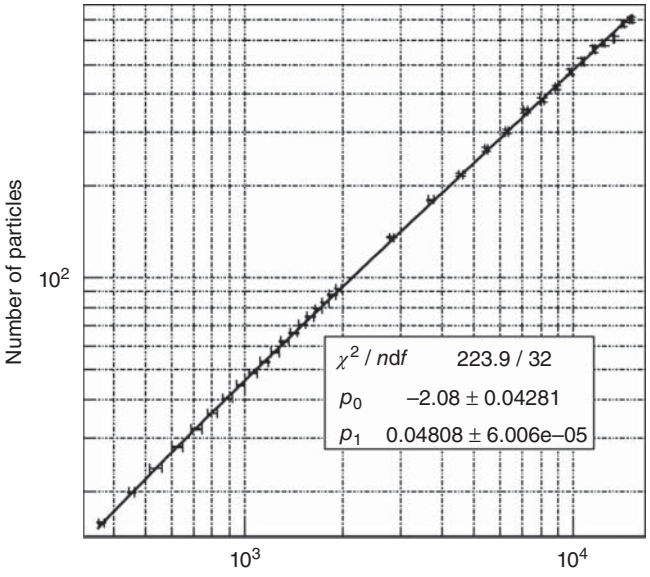

Figure 5.22 Number of charged particles versus RPC charge readout; a linear fit is superimposed. (Aielli *et al*. 2012a. Reproduced with permission of Elsevier.)

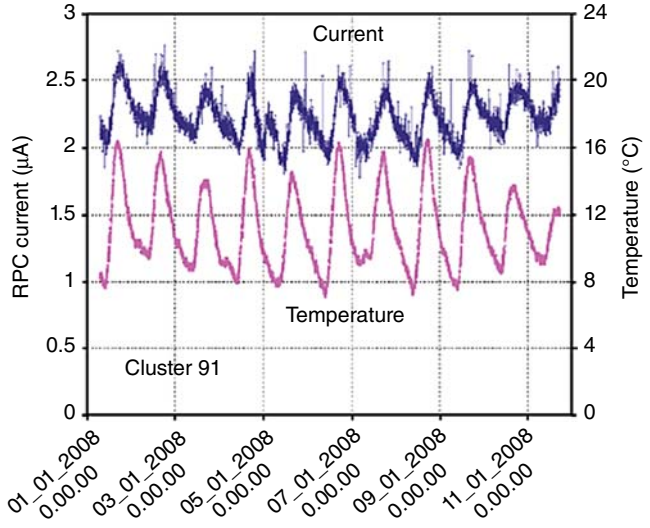

Figure 5.23 Current measured at one of the RPC clusters of the ARGO-YBJ experiment and temperature of the same cluster, for a time span of 10 days; a clear correlation can be seen. (Camarri 2009. Reproduced with permission of Elsevier)

dedicated RPC telescope hosted in the same hall of the ARGO-YBJ detector, are reported in Aielli *et al*. (2009). The effect of a reduction in pressure on the RPC working point, already discussed in Chapter 3, was also nicely confirmed, by comparing, for instance, RPC efficiency curves measured at sea level with the ones measured at the experimental hall, almost at half atmospheric pressure, as shown in Figure 5.24.

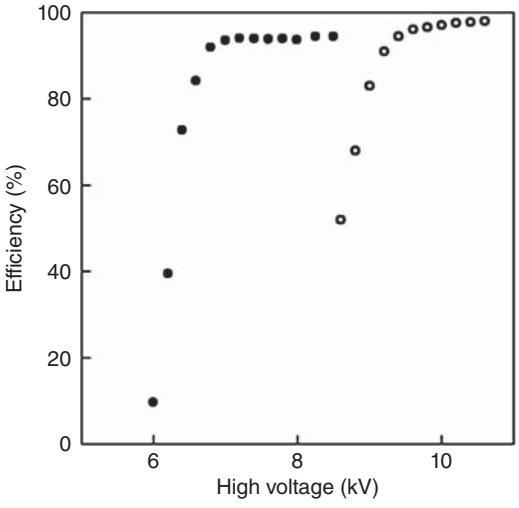

Figure 5.24 Efficiency versus high voltage for the RPCs of the ARGO-YBJ carpet, when measured at the experiment site (left) and at sea level (right); at low pressure a shift toward lower operating voltages is evident, while the reduction in the plateau efficiency is most likely due to a reduced number of ion-electron pairs. (Camarri 2009. Reproduced with permission of Elsevier.)

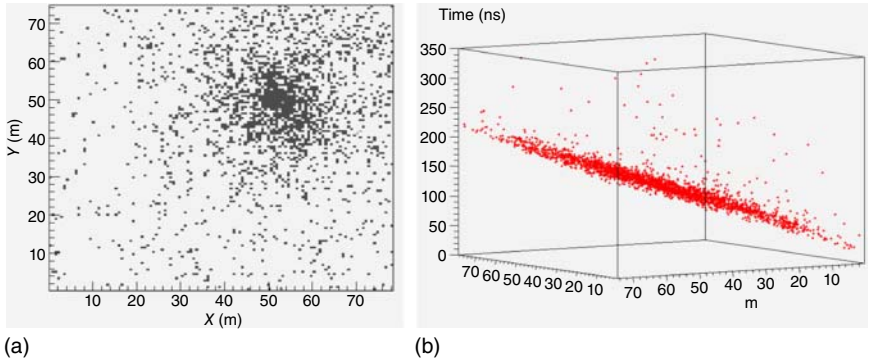

Figure 5.25 One of the events reconstructed with the ARGO-YBJ. (a) Space map of the hit pads on the central carpet (a small shower). (b) Space–time structure of the shower front. (Aielli *et al*. 2012b. Reproduced with permission of Elsevier.)

ARGO-YBJ started taking data with its complete layout in October 2007, and continued for many years almost uninterruptedly at a trigger rate of 3.6 kHz, with an around 90% duty cycle. Due to its peculiar structure, full coverage "pictures" of the showers fronts could be taken (see one of them in Figure 5.25); as a matter of fact, these were unprecedentedly detailed, and this allowed important progresses in the field of high-energy cosmic rays.

5.5 The "BIG" Experiments: ATLAS, ALICE, and CMS at LHC

After the experiences with BaBar and ARGO-YBJ, which involved large-scale detector production and detectors operated for many years, the next challenge for the RPC community, at the beginning of the 2000s, was to make them approved and be prepared to build the RPC systems foreseen for the experiments at the

LHC. In particular, the largest experiments, ATLAS (*A T*oroidal *L*HC *A*pparatu*S*) and CMS (Compact Muon Solenoid), were both designed with muon systems including RPCs as trigger (and, partly, tracking) detectors. It was a particularly delicate task, since effective muon triggering is essential for identifying the decay products of the long searched for Higgs boson, to be discovered in 2012. ALICE (A Large Ion Collider Experiment), in addition to muon triggering, envisaged also the use of multi-gap RPCs with order of hundred picosecond time resolution in the time of flight (TOF) system, for particle identification purposes.

The challenge, in the use of RPCs at the LHC experiments, consisted not only in the large areas to be covered but was also related to the conditions – particularly difficult – where they were to operate, in terms, for instance, of particle rate and integrated dose. As a first point, the necessary rate capability implied that these devices could not be operated in streamer mode, which had been demonstrated to be effective only up to fluxes of the 100 Hz/cm^2 order, whereas the fluxes at LHC were foreseen to be much higher.

Long tests devoted to demonstrate that RPCs operated in avalanche mode were able to stand the necessary particle rates were performed, in particular at the RD5 experimental facility, at CERN (Bohrer *et al*., 1992). As it has already been pointed out, this required the use of more sophisticated electronics, with adequate pre-amplifiers in the front end (which had to be designed as well); it implied also an accurate shielding of the detectors to avoid that environmental signals could be picked up by the readout strips, and accurate grounding of the whole system; both are simple in principle, but difficult to operatively achieve on large apparatus. It is also worth mentioning that RPCs were also considered for the muon system of another of the LHC experiments, namely LHCb, but they were eventually discarded because of the concern that they could not stand the high rate (much higher than CMS and ATLAS) characteristics of this experiment.

At RD5, the first experimental evidence that RPCs could reach a rate capability around, or more, than 1 kHz/cm^2 was established after long dedicated studies and careful tests (Bacci *et al*., 1995). The critical plot is reported in Figure 5.26, where the performance of a single-gap and a double-gap RPC is compared with an RPC operated in avalanche mode and exposed to the high-intensity beam of the CERN Super Proton Synchrotron. The improvement in rate capability was almost an order of magnitude, allowing the authors to conclude that RPCs were adequate for the muon trigger schemes presented in the ATLAS (ATLAS collaboration, 1992) and CMS (CMS collaboration, 1992) Letters of Intent.

Once the RPC rate capability was assessed and found to be satisfactory, also tests demonstrating that a stable performance could be maintained for several years, despite the harsh environment they should operate were performed, in particular at the Gamma Irradiation Facility, at CERN. Here chambers were irradiated using a ^{60}Co gamma-ray source, and the performance monitored across many years using the SPS muon beam (see, for instance, Arnaldi *et al*. (2000), Abbrescia *et al*. (2004)), and Aielli *et al*. (2006). These were particularly relevant in learning more about the aging processes in these detectors.

Thereafter, the construction phase of the huge number of RPCs needed for these experiments required several years to be completed, and all the necessary

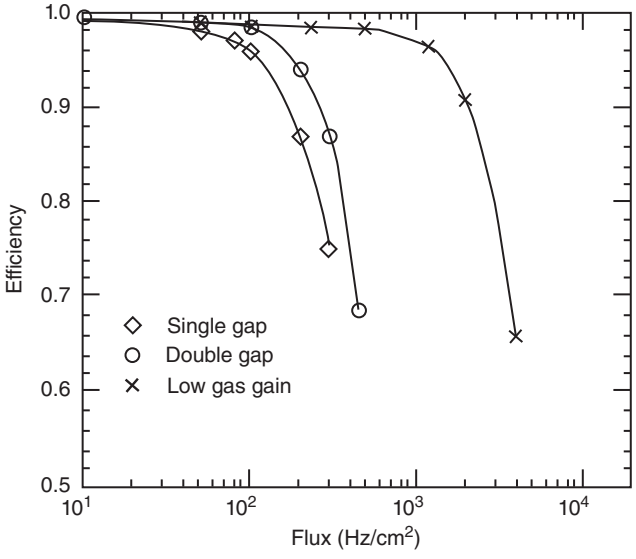

Figure 5.26 Detection efficiency as a function of the SPS beam flux for RPCs; a gas mixture containing 80% of CF_3Br and the rest of Ar/butane 60/40. Single- and double-gap RPCs operated in streamer mode are considered, and compared with an RPC operated in avalanche mode. (Bacci *et al*. 1995. Reproduced with permission of Elsevier.)

steps to ensure the highest quality were put in place. This resulted in the largest RPC systems operating nowadays.

5.5.1 ATLAS

The ATLAS RPC system is part of the Muon Spectrometer, characterized by a toroidal magnetic field, designed to trigger and measure the momentum of high-energy muons. In particular, the RPCs provide the first-level muon trigger and the measurement of the coordinate in the non-bending direction in the barrel region; they are complemented by monitored drift tubes (MDTs) to precisely measure the position in the bending plane. The system is arranged in three concentric layers of RPC "doublets" (two separate RPCs positioned one on top of the other), in which each RPC is read out with two sets of orthogonal strips with a pitch varying in the 23–35 mm range that provide the two coordinates of the hits (see Figure 5.27). Each layer is organized in 16 sectors along the azimuthal coordinate and, in order to facilitate the overlap between adjacent sectors, they come in different dimensions. Overall, there are 3714 RPC gas volumes, covering a total surface of about 4000 m^2. The basic ATLAS RPC module consists of a 2-mm Bakelite single-gap RPC, operated in avalanche mode and filled with a 94.7/5/0.3 $C_2H_2F_4/i\text{-}C_4H_{10}/SF_6$ gas mixture.

The ATLAS RPC performance has been thoroughly monitored during the years they have been operating at LHC, and various tools have been developed for this purpose, and many studies have been published. Most interesting quantities, like detector and trigger efficiency, timing information, and so on, are measured

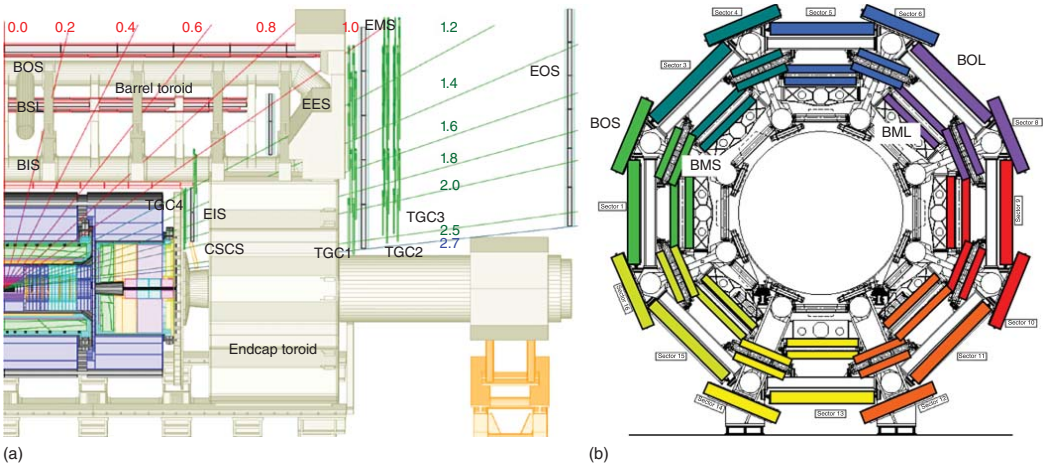

Figure 5.27 Views of the ATLAS experiment and the muon system: *y*–*z* plane (a) and *x*–*y* plane (b). The three RPC double layers (positioned around rectangulars in figure b) and the structure of small and large sectors are enhanced in the *x*–*y* view. (Aielli *et al*. 2013. http://iopscience.iop.org/article/10.1088/1748-0221/8/02/P02020/meta. Licensed under CC BY 3.0.)

offline, by making use of unbiased samples of muons identified by the inner detectors or the other muon chambers.

In general, the RPC system showed a remarkable stability and operated effectively being active in more than 99.9% of the ATLAS data taking, showing very good reliability. In Run 2, started in 2015 and foreseen to last up to 2018, the percentage of dead channels was around 3.5%, quite low for a system of such dimensions, and detector efficiency peaked at 98%, with a 1% inefficiency (from 2%) which can be accounted to the spacers (see Figure 5.28).

At LHC, RPC timing performance is basically exploited to assign the muons identified in the system to the right LHC bunch crossing; this takes place each 25 ns (each 50 ns during Run 1, the first period of data taking at LHC, from 2010 up to 2013) and therefore a few nanoseconds time resolution, typical of RPC with a 2-mm gap thickness, is more than enough for this task (see Figure 5.29).

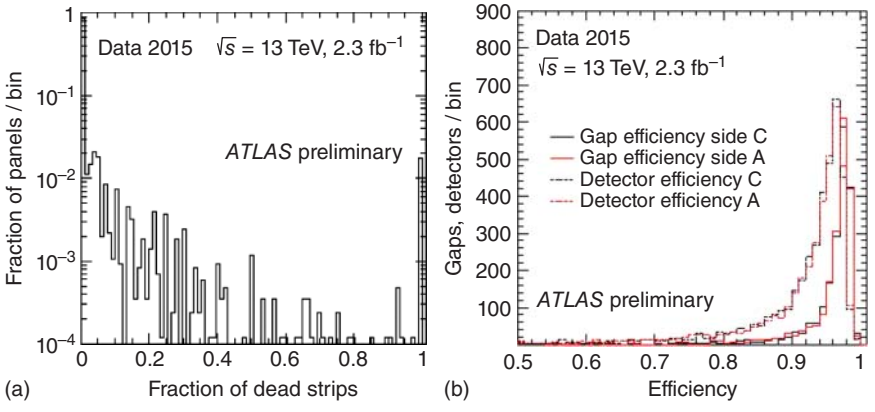

Figure 5.28 (a) Distribution of the fraction of "dead" strips; (b) ATLAS RPC efficiency; here, "gap efficiency" is defined by the presence of hits on at least one of the two strip panels reading the same RPC, while the "detector efficiency" is evaluated independently for each of the two readout strip panels. (From Corradi 2016.)

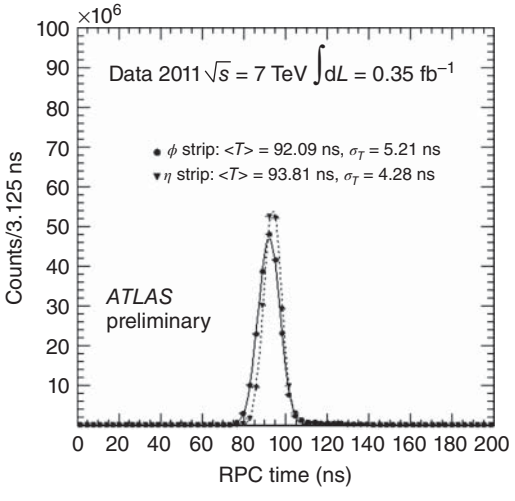

Figure 5.29 The hits time distribution for the ATLAS RPCs; in this case, off-line correction is applied and the time spread is dominated by the spread of signal propagation along the strips. (Aielli *et al*. 2013. http://iopscience.iop.org/article/10.1088/1748-0221/8/02/P02020/meta. Licensed under CC BY 3.0.)

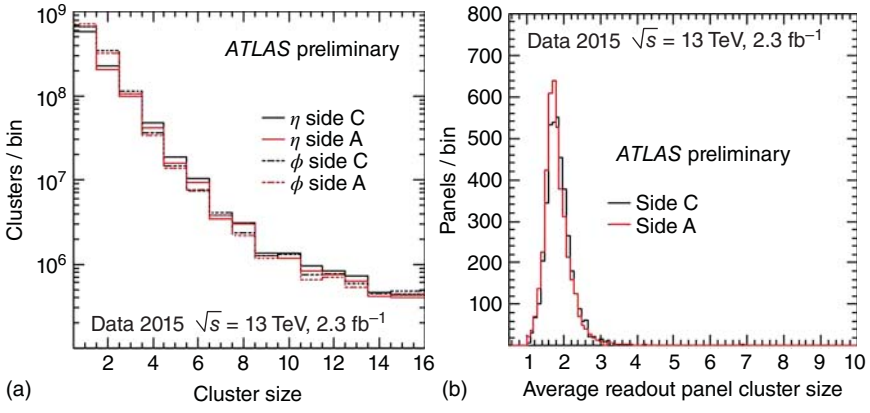

Figure 5.30 (a) Distribution of RPC cluster size and (b) distribution of average RPC cluster size. (Corradi 2016. http://iopscience.iop.org/article/10.1088/1748-0221/11/09/C09003/meta. Licensed under CC BY 3.0.)

The distribution of the cluster size (number of adjacent strips fired at the same time) and the average cluster size are shown in Figure 5.30 for 2015 data, being stable and consistent with the ones measured during Run 1. This is an important quantity: as a matter of fact, using sensitive front-end pre-amplifiers might have that drawback that, in the presence of electronic noise or particular intense signals, many strips could be fired together, spoiling the spatial resolution. Low cluster size is essential when some triggering and, even rough, tracking capability is required.

In collider experiments, trigger efficiency can be measured in many ways, a quite effective one being the use of reconstructed muons selected by independent triggers; one of these examples, for the ATLAS RPC system, is shown in Figure 5.31. Even if trigger efficiency reaches satisfactory values, spatial

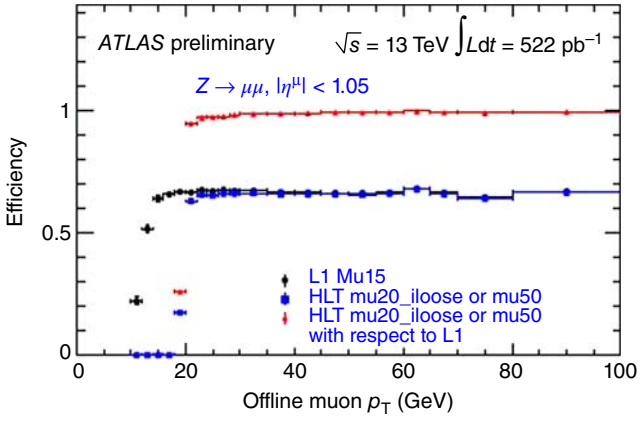

Figure 5.31 Efficiency × acceptance (acceptance roughly measures the region where the particles can be detected) of the ATLAS RPC barrel system as a function of the transverse momentum for reconstructed muon deriving from Z decays. (Corradi 2016. http://iopscience.iop.org/article/10.1088/1748-0221/11/09/C09003/meta. Licensed under CC BY 3.0.)

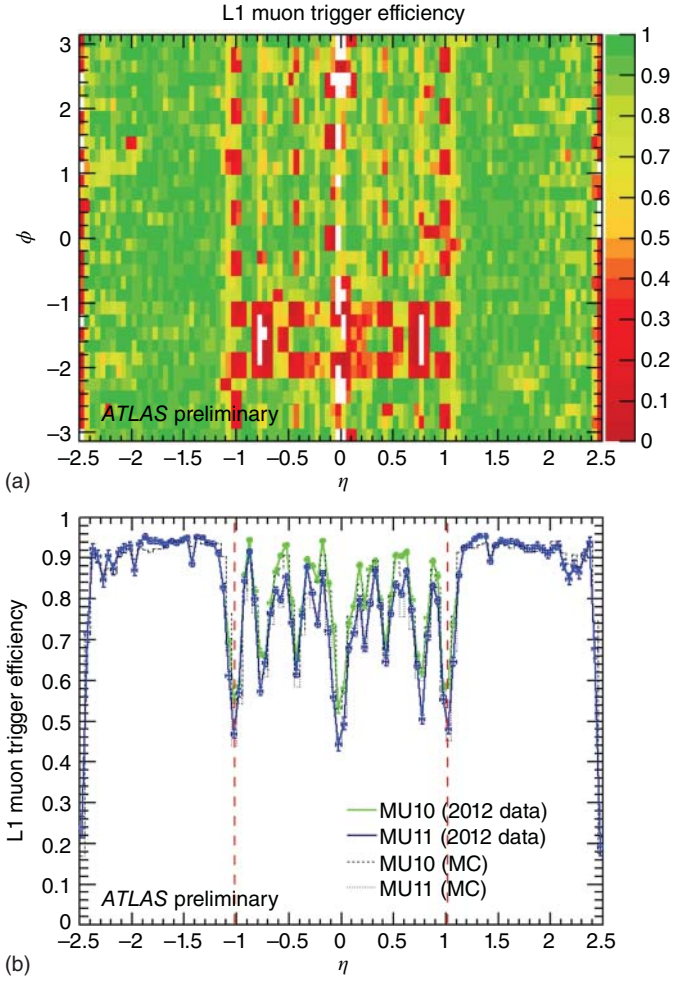

Figure 5.32 RPC trigger efficiency: (a) efficiency map of the L1 muon trigger for muons with transverse momentum >10 GeV and (b) efficiency as a function of pseudorapidity (which is a spatial coordinate describing the angle of a particle relative to the beam axis) for different trigger requirements. (Biondi 2015. Reprinted with permission of CERN.)

disuniformities are present, as seen in Figure 5.32. In ATLAS, in particular, these derive by some acceptance limitations in the lower part of the spectrometer because of the presence of structures to support the weight of the whole detector (the so-called feet) and of two elevator shafts for the access to calorimeters and to the inner part of the muon system. To overcome this problem, at least partially, a fourth layer of RPC chambers was installed in the "feet" region since the construction of ATLAS, which was put in operation during the long shutdown between Run 1 and 2 in 2012–2013. Moreover, additional chambers were also installed to cover the acceptance holes due to the elevator shaft and put in operation in 2017.

In ATLAS, the stabilization of the working point against temperature and pressure variations is performed using an empirical derivation of Formula (3.34), where the effective voltage ΔV_{eff} is given by

$$\Delta V_{\text{app}} = K_{\text{emp}} \Delta V_{\text{eff}} \tag{5.2}$$

and

$$K_{\text{emp}} = \left(1 + a_{\text{emp}} \frac{p - p_0}{p_0}\right)\left(1 - b_{\text{emp}} \frac{T - T_0}{T}\right) \tag{5.3}$$

and, as usual, p and T are the instantaneous values of pressure and temperature, p_0 and T_0 are two reference values, and ΔV_{app} is the applied voltage. a_{emp} and b_{emp} are parameters determined by means of dedicated tests and data analysis. About 300 temperature sensors are used, and the correction updated every few minutes to keep the system performance stable (Aielli *et al.*, 2013).

5.5.2 CMS

The design of the CMS muon system is described in detail in its Technical Design Report (CMS Collaboration, 1997). It is roughly cylindrical in shape, consisting of the barrel, the region at low pseudorapidity, divided into five "wheels," and of the endcaps, made of four disks each (see Figure 5.33). In CMS, RPCs are intended

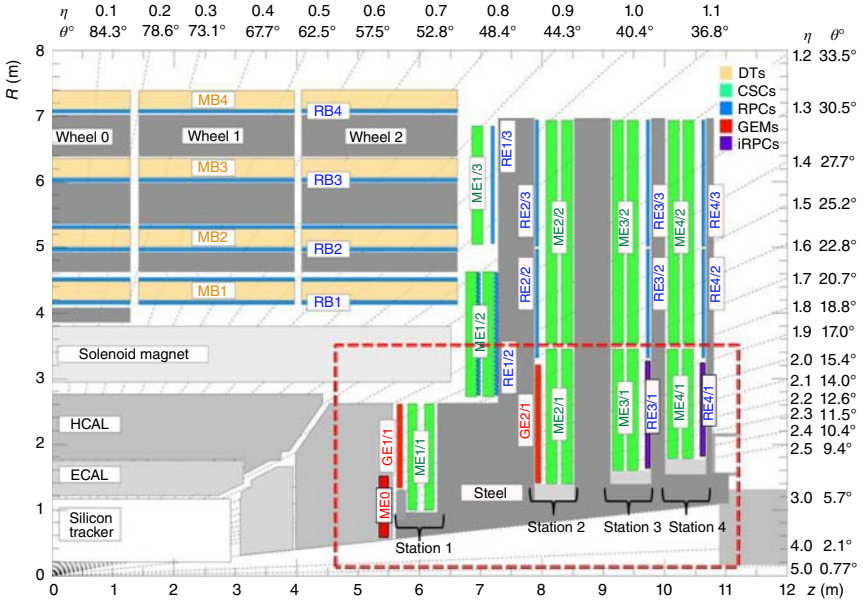

Figure 5.33 Schematic view of one quadrant of the CMS detector in the *R*–*z* plane. The *z*-axis is coincident with the beam axis, while *R* measures the distance from it. The RPC chambers are marked in light gray (they are in both the barrel and the endcaps of CMS, where they are labeled RB and RE, respectively) and they are coupled with DTs in the barrel, and CSCs in the endcaps (both in dark gray). The steel of the magnet return yoke is also shown. The region where new detectors are foreseen to be installed before the high luminosity phase of LHC is in evidence in the dashed box. (CMS Collaboration 2015. Reprinted with permission of CERN.)

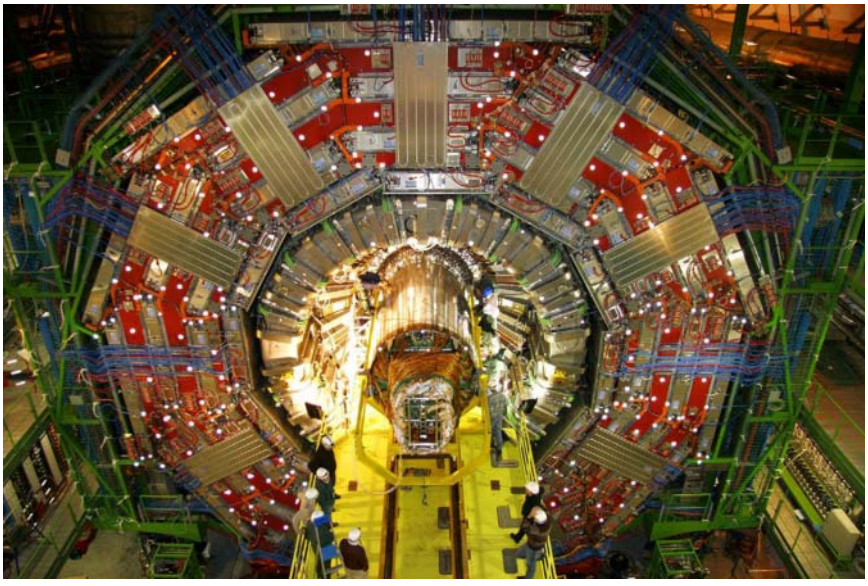

Figure 5.34 A front view of the CMS detector. The CMS barrel muon system is a 13-m-long cylinder divided into 5 wheels along the axes direction; each wheel is divided into 12 sectors, housing the muon stations in its iron gaps. In the barrel muons stations are composed by drift tubes and RPCs, which can be seen interleaved around magnet return yoke. (Colaleo *et al*. 2009. Reproduced with permission of Elsevier.)

mainly as trigger detectors, and they are complemented by drift tubes (DTs) in the barrel and cathode strip chambers (CSCs) in the endcaps for muon tracking purposes (see Figures 5.33 and 5.34). Each wheel is made up of four muon stations, which are a sandwich of one DT and one or two RPCs, placed in the CMS magnet return yoke. Each endcap disk is divided into three rings, where trapezoidal RPC chambers are used. Both in the barrel and endcap, the main unit of the RPC chamber is made by two gas gaps with a common readout plane of aluminum strips in the middle, filled with a $C_2H_2F_4/iC_4H_{10}/SF_6$ gas mixture, 95.2/4.5/0.3 in relative proportions and operated in avalanche mode. The RPC system installation began in 2004 and was completed in 2007, while the commissioning phase lasted up to 2008. The whole present system was not installed before the LHC start, and in fact the fourth endcap disks were instrumented with the last 144 RPC chambers during the long shutdown between Run 1 and 2.

In CMS, too, the RPC system has performed reliably up to the present date. For instance, during Run 1, in the 2010–2012 period, the contribution of the RPC system to the CMS downtime was below 1.5% (for further details, see Pugliese *et al*., 2014). In 2015 the total percentage of inactive channels was stable in the 2–2.5% range, the main source was noisy chambers being connected to faulty electronic boards or chambers with high/low voltage failures (see Figure 5.35). The chambers' intrinsic counting rate (noise pulses), reported in Figure 5.36, is measured before every proton fill, to immediately spot possible issues; even if some increasing trend can be noticed, in general it is around the 0.1 Hz/cm^2 order,

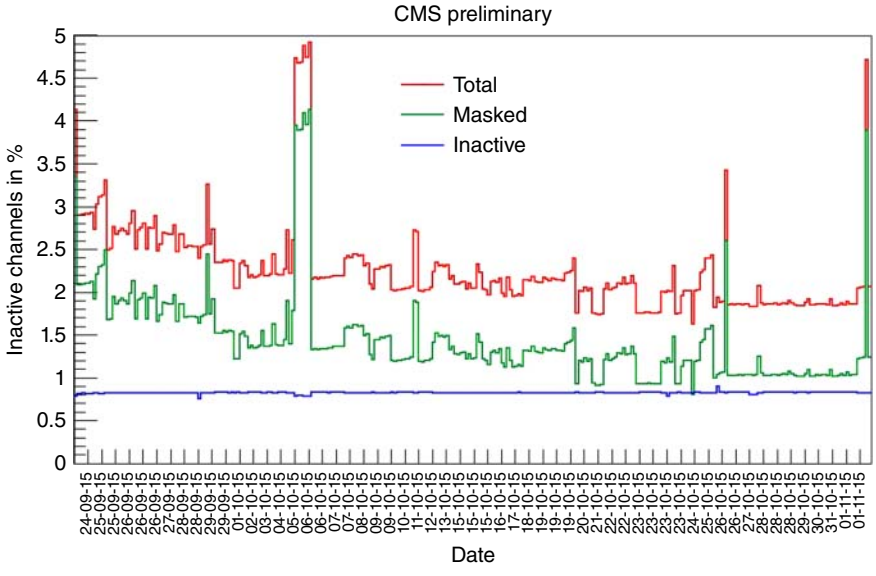

Figure 5.35 Percentage of inactive channels in the CMS RPC system, during 2015. Two contributions are considered: masked (i.e., voluntarily disconnected from the readout chain) strips, because connected to noisy chambers with faulty electronics, and inactive strips, connected to chambers with high- or low-voltage issues. (Pedraza 2016. Reproduced with permission of IOP Publishing.)

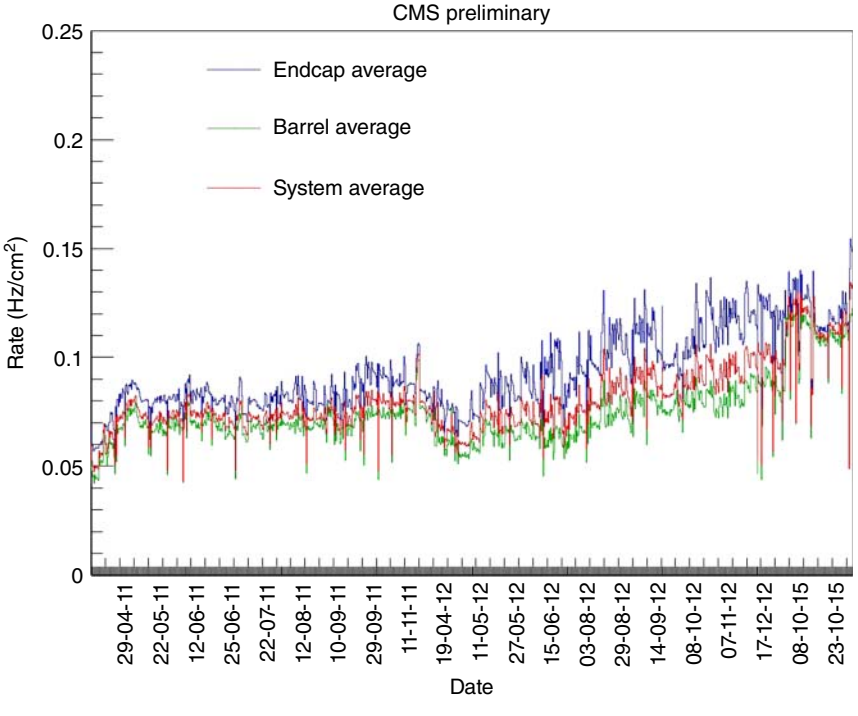

Figure 5.36 CMS RPC chambers intrinsic counting rate, measured before each proton fill, and divided for barrel and endcap. (Pedraza 2016. Reproduced with permission of IOP Publishing.)

assuring that no accidental coincidences can spoil the trigger performance (see Pedraza, 2016).

Particular care has been taken in measuring the local RPC chamber efficiency, setting up a data stream dedicated for this purpose. Efficiency is generally computed by extrapolating a muon track segment revealed in a nearby DT or CSC and checking if an RPC hit is present in a fiducial area around the predicted intersection point onto the chamber under examination. Thanks to the large amount of data in the data stream, statistics is high enough to be sensitive to efficiency variations at a few percentage levels and the precision of the tracking system allows selecting cells on the order 1–2 cm^2 in dimensions where efficiency can be measured. This results in muongraphies, very similar to the ones obtained in the MINI experiment, one of which is reported in Figure 5.37. Typically, in chambers without relevant issues, the main source of inefficiency is the presence of the spacers, which are aligned in the gaps of the double-gap modules; moreover, some efficiency decrease can be noticed close to the gap all-around frame. In both cases, this effect can be attributed to the lower electric field in these regions.

Calibration of the working point is performed on a regular basis; chamber efficiency is measured as a function of the operating voltage, the experimental points are fitted with a sigmoid (see Formula (5.1)), and the optimum working point is defined as the voltage corresponding to the 95% of the maximum efficiency plus 100 V for the barrel and 150 V for the endcaps. In this way, chambers are operated at a voltage which guarantees efficiency close to maximum, without pushing this voltage too high. Examples of such measurements are shown in Figure 5.38, for measurements performed in a time span from 2011 up to 2015. Of course, possible variations of the operating voltage with time can be a premonitory sign of aging effects; this is depicted in Figure 5.39, where some variations can indeed be spotted but that, for the moment, do not represent any obvious sign of detector aging.

In CMS, corrections to the RPC operating voltage are done in real time, performing a procedure similar to the one already reported for ATLAS, but using

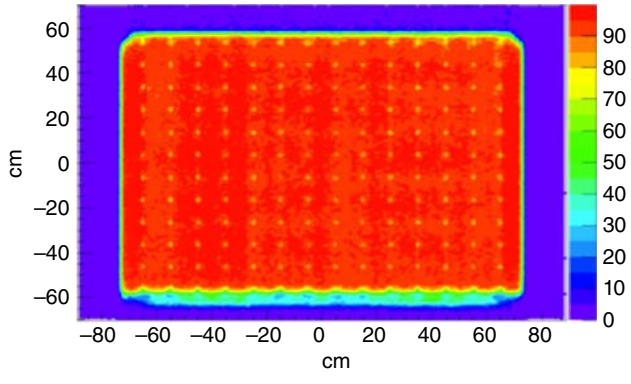

Figure 5.37 Two-dimensional efficiency of a CMS RPC barrel chamber, measured with a spatial resolution of about 2 cm^2. The effect of the spacers in the gaps and of the closing frame is clearly visible as a localized efficiency decrease. (Abbrescia 2013. Reproduced with permission of Elsevier.)

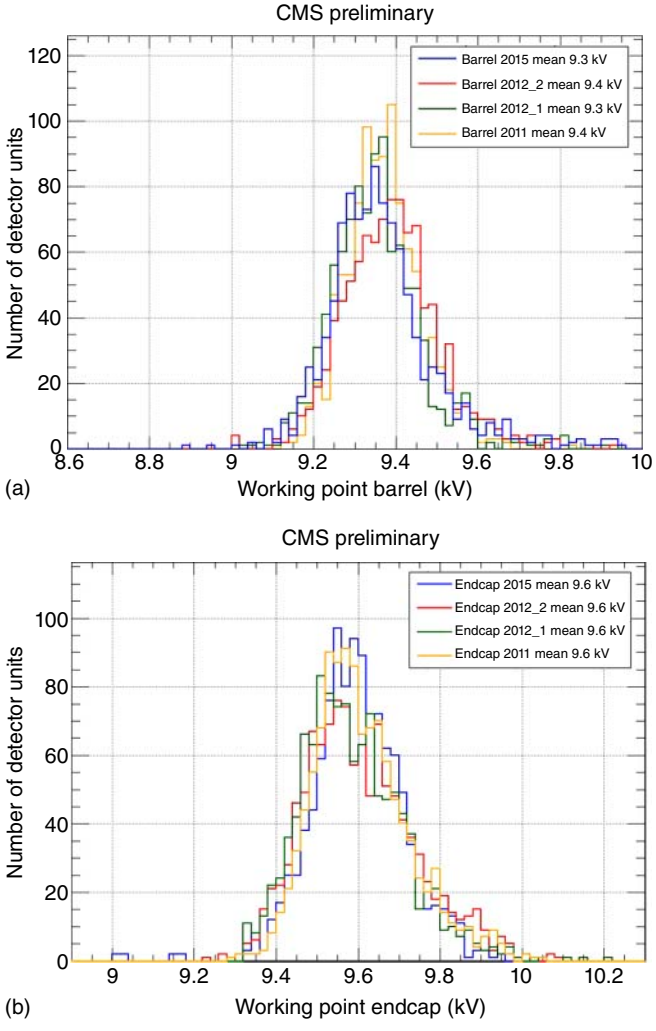

Figure 5.38 The CMS RPC operating voltage distributions for the barrel (a) and for the endcaps (b), as measured in four different campaigns, from 2011 up to 2015. Note that an around 300 V shift between barrel and endcap operating point is visisble this is generally attributed to slight differences in the construction process. (Pedraza 2016. Reproduced with permission of IOP Publishing.)

the following formula:

$$\Delta V_{\text{app}} = \Delta V_{\text{eff}} \left(1 - c_{\text{emp}} + c_{\text{emp}} \frac{p}{p_0}\right) \tag{5.4}$$

where c_{emp} is a free parameter computed by means of a fit to the data (for more details, see Abbrescia, 2013), generally put to 0.8, and the other symbols having the usual meaning already explained for Formulas (5.2) and (5.3). This proved to be an essential tool to guarantee a stable system operation; the effects of such a correction can be seen in Figure 5.40, where RPC efficiency, measured on a

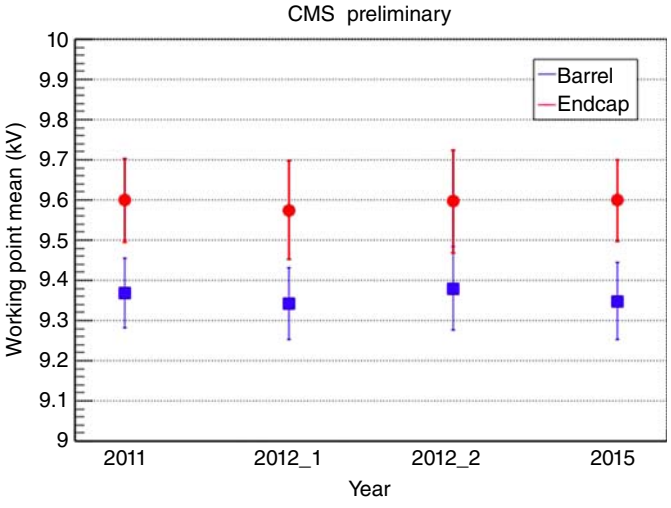

Figure 5.39 CMS RPC operating voltage through the years, for barrel and endcap chambers. (Pedraza 2016. Reproduced with permission of IOP Publishing.)

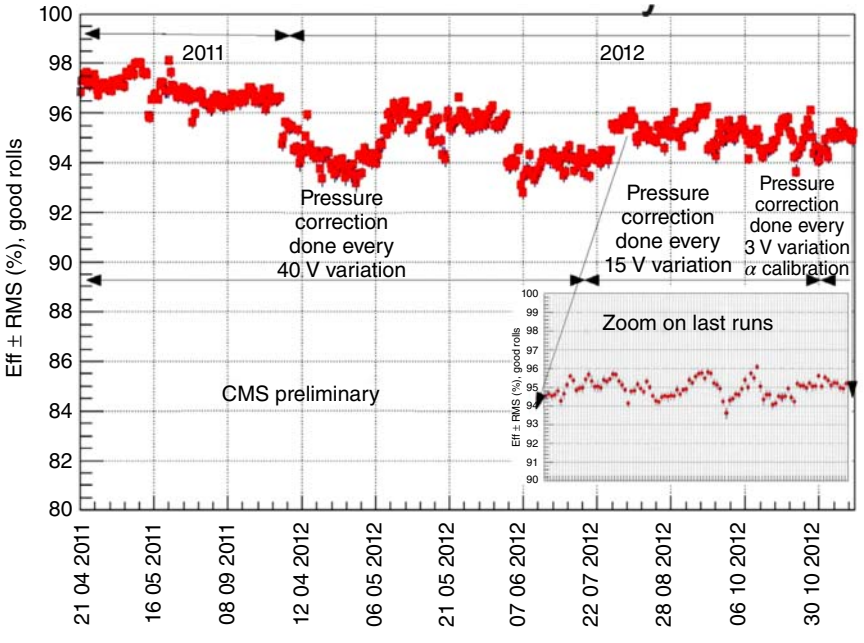

Figure 5.40 Average CMS RPC barrel efficiency, in the period starting from April 2011 until late 2012. Each point represents a run. A zoom of the last period when more and more refined algorithms for correcting the effects of the atmospheric pressure were applied is also reported; in particular, the period when Formula (5.4) was applied corresponds to the last few points to the right, where an improved stability with respect to earlier periods can be noted. (Abbrescia 2013. Reproduced with permission of Elsevier.)

run-by-run basis, is reported, and shows changes related to the environmental conditions, until this is applied.

5.5.3 Some Common Themes to ATLAS and CMS

For what concerns detector aging, none of the problems previously spotted, for instance, in BaBar, have been found, neither in ATLAS nor in CMS. Actually, the main concern for the present systems is the gas leak rate. In ATLAS, gas leaks are due to the breaking of the gas inlets/outlets of the RPC modules; approximately 400 inlets or outlets, out of 8000, developed leaks. In some cases, this implied that one or more RPCs had to be disconnected from the HV, resulting in the main source of failures during Run 1 and 2 (Corradi, 2016). In CMS, a similar problem occurred, but related to some T-shaped plastic connectors in the gas circuit, and located inside the chambers' metallic frame (where it is difficult to intervene), provoking analogous consequences. Even if various repair campaigns have been put in place, leaks are between 500 and 1000 l/h for each experiment, the actual value depending on the amount of chambers that were possible to extract and fix at the time.

In both ATLAS and CMS, due to the huge amount of gas needed, the mixture is recirculated after being purified by a sophisticated set of filters that removes any HF or other contamination potentially harmful to the system; in addition, some hundreds of liters per hour of fresh gas mixture are injected into the circuit. Even when comparing the gas leak rate with the total flow of the systems (in ATLAS, for instance, this is about 5000 l/h), this represents a relevant fraction of the fresh gas that is injected, and utmost efforts are made to reduce it. Moreover, the gas mixture used, as already pointed out, is potentially harmful because of its greenhouse effect and the replacement is still under study. Designing robust gas systems a precious lesson to be learned for the future.

5.5.4 ALICE

While both ATLAS and CMS are general purpose experiments, the ALICE experiment at the CERN LHC accelerator (ALICE Collaboration, 2008a) has been designed to specifically investigate the properties of the strongly interacting matter at very high temperatures and densities created in high-energy Pb–Pb collisions. Under these conditions, a new state of matter emerges: the quark-gluon plasma. This is thought to be the state of the universe in the first few microseconds after the Big Bang. A complementary program includes the study of lighter nuclei collisions.

The design of the ALICE detector is mostly determined by the extreme multiplicity of the high-energy ion collision events, up to a factor 1000 larger than in similar energy proton–proton collisions. A large dynamic range is required for momentum measurement, spanning more than three orders of magnitude from tens of MeV/c (collective effects at large length scales, good acceptance for resonance decays) to well over 100 GeV/c (jet physics). The set of detectors necessary to cope with these requirements are arranged in a central barrel-shaped region and in a complementary forward muon spectrometer. The central part is

immersed in a magnetic field of 0.5 T created by a solenoidal magnet. Within this field are placed the tracking detectors: Inner Tracker, based on silicon detectors, gaseous Time Projection Chamber, Transition Radiation Detector, and TOF.

Particle identification is an important part of the experiment. Charged particles in the intermediate momentum range are identified in ALICE by the TOF detector (Figure 5.41). The time measurement with the TOF, in conjunction with the momentum and track length measured by the tracking detectors, is used to calculate the particle mass. A time resolution of 100 ps will provide $3\sigma\pi/K$ separation up to 2.2 GeV/c and K/p separation up to 4 GeV/c.

The ALICE TOF is a large central barrel-like multi-gap RPC detector covering an area of 141 m^2, with an inner radius of 3.7 m and covering azimuthally the angles $\pm 45°$. The detector is segmented into 1593 symmetric (double stack) multi-gap RPC (MRPC) modules (see Figure 5.42), each with a total of 10 gas gaps of 250 μm width (see Figure 5.43 for details) and read out by 96 signal induction pads of 3.5×2.5 cm^2 (see Akindinov *et al*., 2009a). Therefore, the readout comprises 157 248 readout channels (pads). The chambers operate in a gas mixture of 90%/5%/5% $C_2H_2F_4$ (commercially known as R134a), *i*-C_4H_{10} and SF_6. The readout chain is based on the NINO integrated current amplifier and comparator (see Section 4.7 and Figure 5.44) and on the high performance time to digital converter (HPTDC) (Akindinov *et al*., 2004).

The intrinsic time resolution of the RPCs is close to 50 ps (Akindinov *et al*., 2009b) and the overall TOF system resolution is 80 ps (ALICE Collaboration, 2014) (Figure 5.45).

An example of the particle identification power provided by the TOF system in combination with the magnetic spectrometer is shown in Figure 5.46.

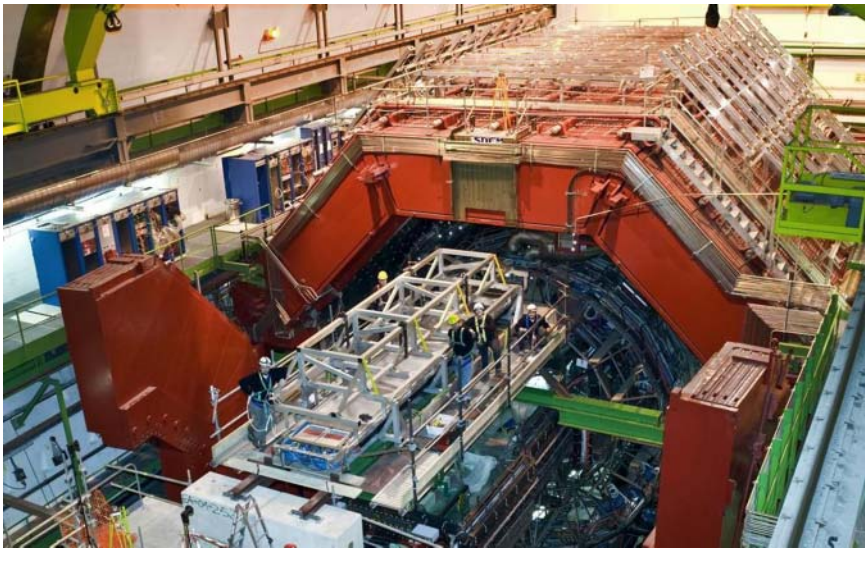

Figure 5.41 View of the ALICE time of flight detector during installation. The TOF detector has a cylindrical shape, covering polar angles between 45 degrees and 135 degrees over the full azimuth. It has a modular structure ; each of these sectors is divided into 5 modules along the beam direction. (ALICE Collaboration 2006. Reprinted with permission of CERN.)

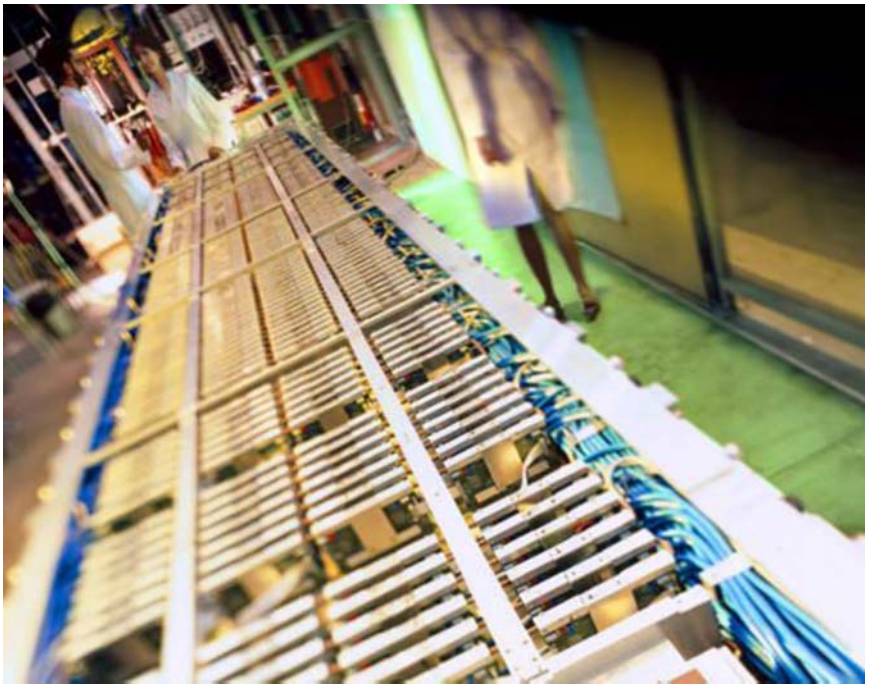

Figure 5.42 One of the ALICE TOF MRPC supermodules. (ALICE Collaboration 2008b. Reprinted with the permission of CERN.)

The trigger system of the forward muon spectrometer of ALICE (ALICE Collaboration, 2004) is equipped with 140 m^2 of single-gap RPCs operated in streamer mode (Arnaldi *et al*., 2002). The detector has shown very good stability (Figure 5.47) and the trigger performance is satisfactory (ALICE Collaboration, 2012).

5.6 The RPC-TOF System of the HADES Experiment

HADES (high-acceptance di-electron spectrometer) is a versatile detector for precise spectroscopy of e^+e^- pairs (di-electrons) and charged hadrons produced in proton, pion, and heavy-ion-induced reactions in a 1–3.5 GeV kinetic beam energy region. The main experimental goal is to investigate properties of dense nuclear matter created in the course of heavy ion collisions and ultimately learn about in-medium hadron properties (like masses, decay widths).

Its spectrometer is divided into six sectors surrounding the beam axis covering large angular acceptance between 16 and 88°. It comprises the following components: a diamond START detector, a ring maging Cherenkov (RICH), four sets of multiwire drift chambers (MDCs), a superconducting toroidal magnet, and a multiplicity/electron trigger array consisting of granular pre-shower detectors at forward angles and two TOF walls: a scintillator-based TOF wall and the RPC wall built from RPCs.

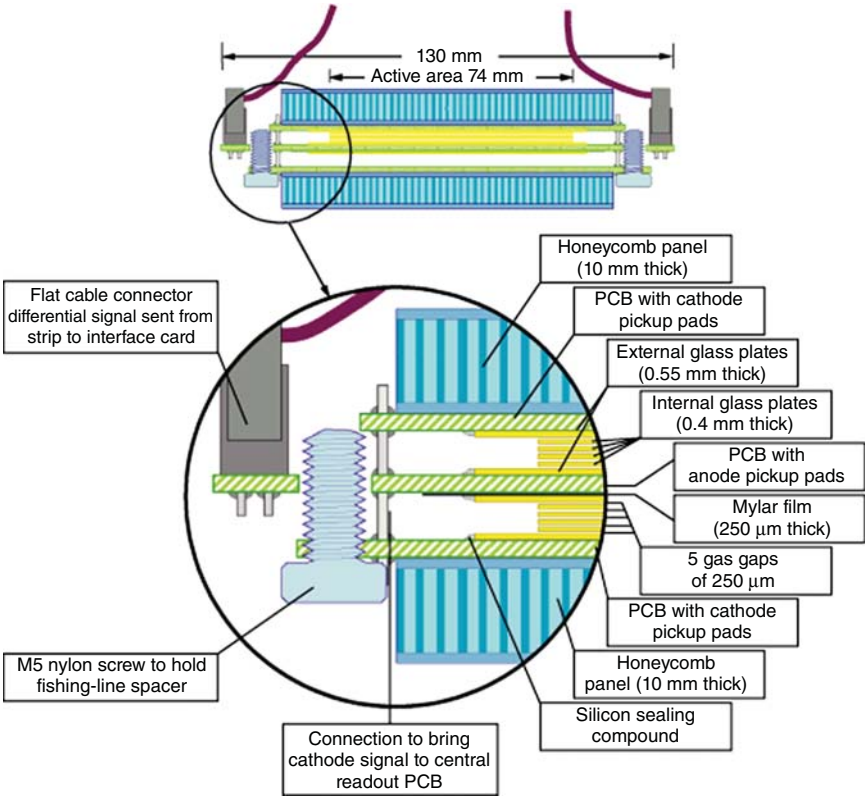

Figure 5.43 Cross-sectional drawing of the ALICE TOF MRPCs, detailing the many structural and functional elements. (ALICE Collaboration 2008b. Reprinted with the permission of CERN.)

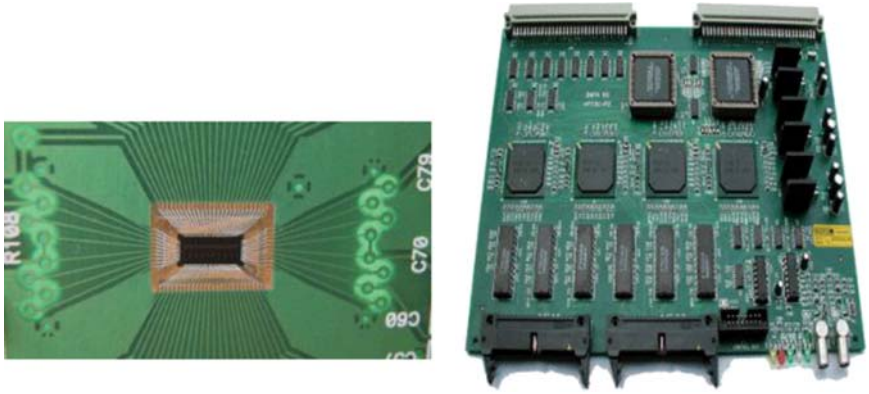

(a) (b)

Figure 5.44 The main components of the ALICE TOF data acquisition chain are (a) the NINO chip (see Section 4.7) and (b) the HPTDC time to digital converter (Akindinov *et al*., 2004). (ALICE Collaboration 2008b. Reprinted with the permission of CERN.)

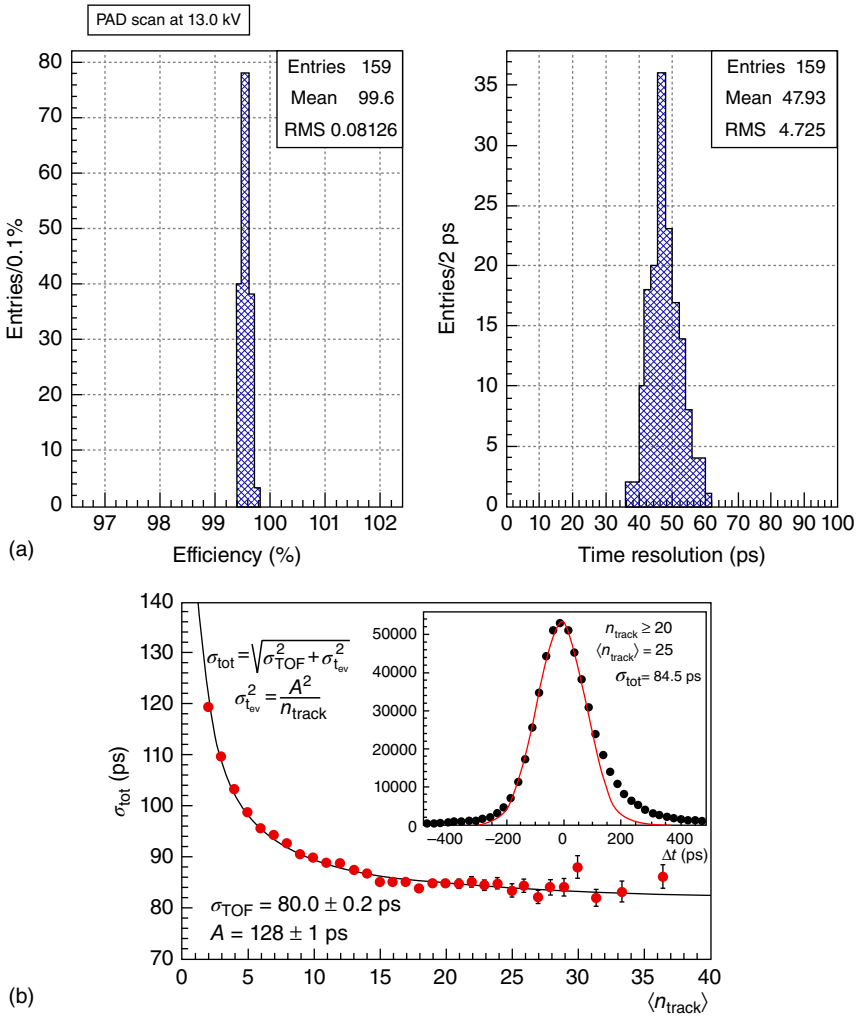

Figure 5.45 (a) Distribution of the measured efficiency and time resolution for 159 readout pads of the production chambers. (From Akindinov *et al*. 2009b. Reproduced with permission of Elsevier.) (b) The measured ALICE TOF system time resolution for pions with momentum close to 1 GeV/c, as a function of the number of tracks n_{track} used to define the event time; the inset shows the resolution for $n_{track} > 20$ (symbol A in the insertion represents a fitting parameter) (ALICE Collaboration 2014. Reproduced with permission of CERN.)

The RPC-TOF wall is divided into six sectors of trapezoidal shape covering a total area of about 8 m^2. It is composed of 1116 single-strip, four-gap, symmetric, timing RPCs "cells." Each cell is individually electrically shielded for robust multi-hit performance: a key characteristic of the design. The cells inside each sector are organized in two partially overlapping layers. Each layer is composed of 31 rows and 3 columns of cells, with widths ranging between 22 and 50 mm

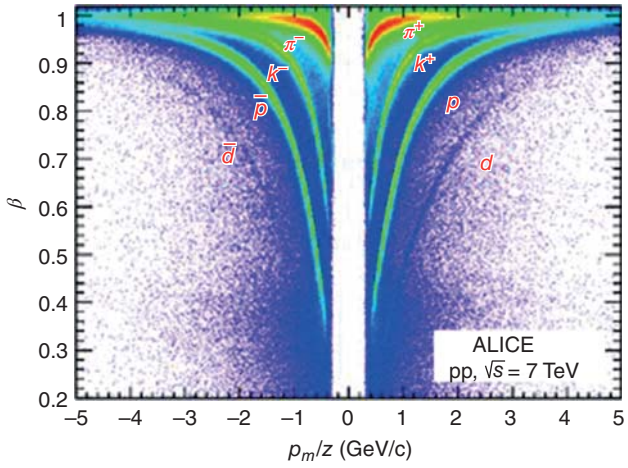

Figure 5.46 Particle velocity β measured by the TOF detector as a function of the rigidity p_m/z, where p_m is a particle momentum and z is the particle charge, for pseudorapidity <0.9. (Adam *et al*. 2015. https://link.springer.com/article/10.1140/epjc/s10052-015-3422-9. Licensed under CC BY 4.0.)

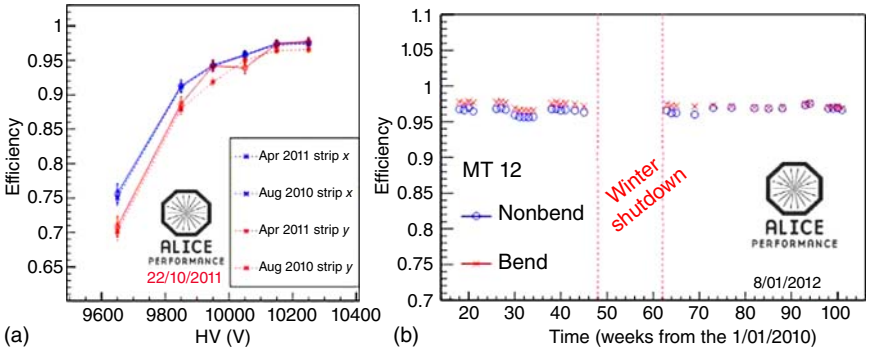

Figure 5.47 (a) Efficiency versus voltage curve for one RPC over a period of 8 months. (b) Average efficiency of one of the four detection planes as a function of time, corrected for temperature and pressure variations. (ALICE Collaboration 2012. Reprinted with the permission of CERN.)

and lengths between 120 and 520 mm. The cells are made of three aluminum electrodes and two glass (soda-lime) electrodes, all of 2 mm thickness. The four gaps are defined by polyether ether ketone (PEEK) monofilaments of 0.270 mm diameter. The ensemble is housed inside aluminum tubes (see Figure 5.48). A comprehensive description of the RPC-TOF wall can be found in Belver *et al.* (2009).

The detector shows an overall efficiency of 97% (Kornakov and for the HADES Collaboration, 2014) and a mean intrinsic time accuracy of around 66 ps (Figure 5.49) (Blanco *et al.*, 2012). The mean electron-track timing accuracy

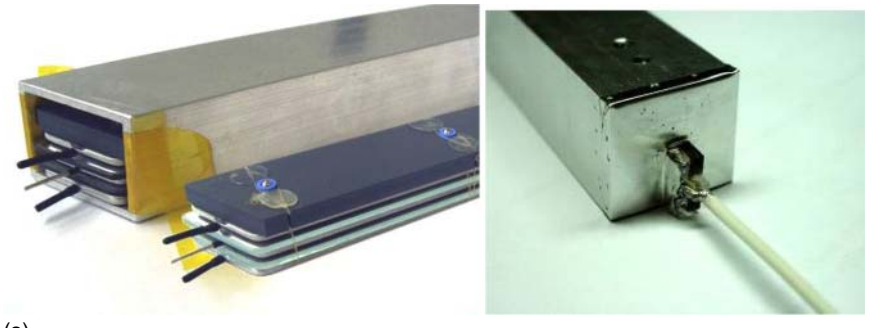

(a)

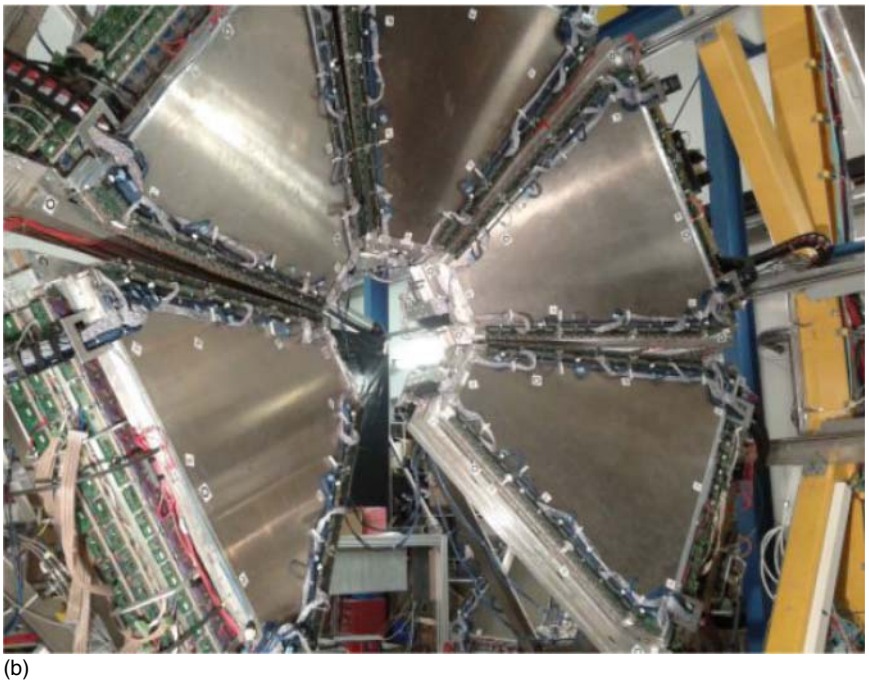

(b)

Figure 5.48 The HADES TOF wall detector is composed of fully shielded RPC "cells" (a) assembled in six sectors (b) with 186 variable-geometry cells each. (Blanco *et al*. 2012. http://iopscience.iop.org/article/10.1088/1748-0221/8/01/P01004/meta. Licensed under CC BY 3.0.)

is around 81 ps including contributions from the start and tracking systems. A worsening of resolution by only 10 ps at occupancies larger than 30% was measured in heavy ion collisions (see Figure 5.50), demonstrating a robust multi-hit performance (Kornakov and for the HADES Collaboration, 2014).

A typical particle identification plot is shown in Figure 5.51, evidencing the identification of a very rare sub-threshold production of K^-.

The RPC system provides some bi-dimensional position resolution determined transversally by the width of the RPC cells (variable from 2 to 5 cm) and longitudinally by the measurement of the time difference of the signal propagation

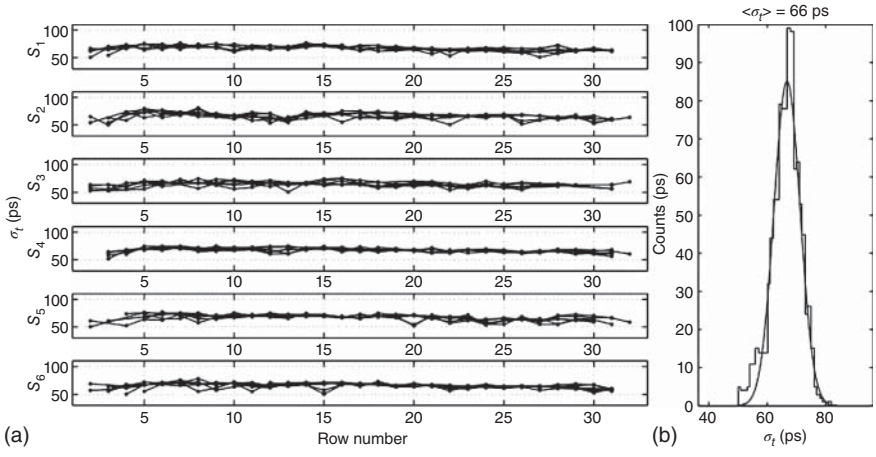

Figure 5.49 Intrinsic resolution of the RPC TOF wall for all overlapping cell pairs, between 50 and 80 ps (a) with average of 66 ps (b) for the charged fragments emanating from Au + Au collisions at $\sqrt{s} = 1.25$A GeV (Blanco *et al*. 2012. http://iopscience.iop.org/article/10.1088/1748-0221/8/01/P01004/meta. Licensed under CC BY 3.0.)

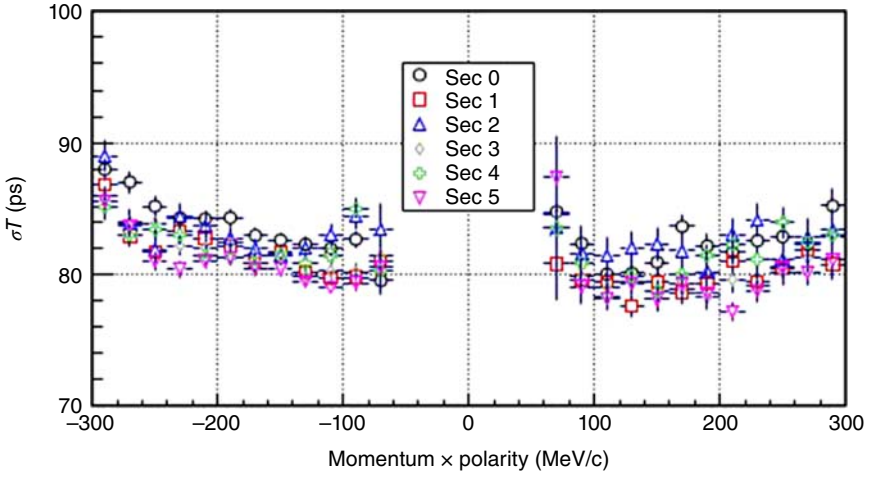

Figure 5.50 Timing accuracy for electrons and positrons as a function of momentum, including contributions from the start and tracking systems. (Kornakov and for the HADES Collaboration 2014. http://iopscience.iop.org/article/10.1088/1748-0221/9/11/C11015/meta. Licensed under CC BY 3.0.)

between both chamber ends. This is a function of the timing accuracy of the read-out electronics for the measurement of the specific signal shape generated, but it is independent of the particle's TOF. The results for the full wall can be seen in Figure 5.52, showing an average value of 7.6 mm for the position resolution (sigma).

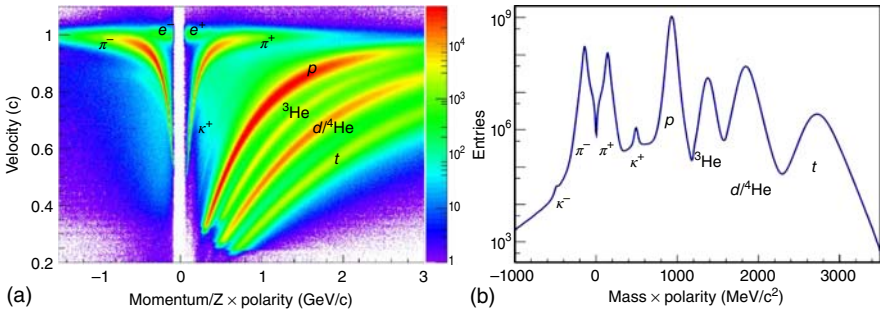

Figure 5.51 (a) Velocity/c as a function of the particle momentum times polarity. The different particle species are labeled. (b) Mass reconstructed from time of flight shows a very low background contamination, evidencing the identification of very rare sub-threshold produced K^-. (Kornakov and for the HADES Collaboration 2014. http://iopscience.iop.org/article/10.1088/1748-0221/9/11/C11015/meta. Licensed under CC BY 3.0.)

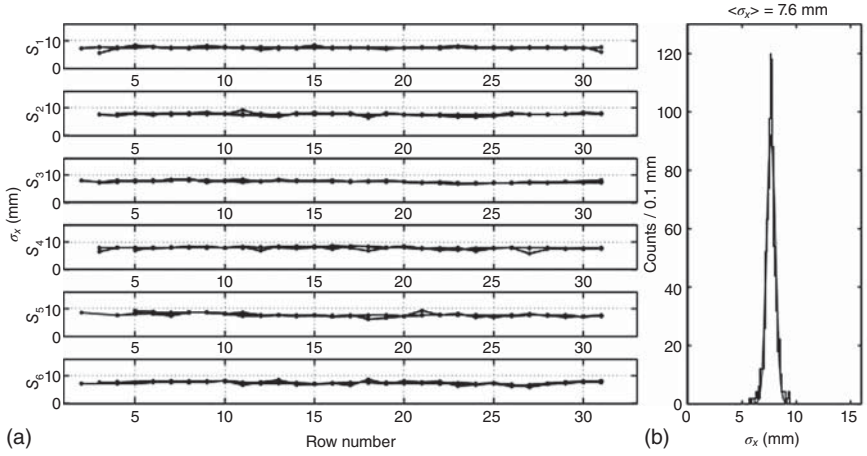

Figure 5.52 (a) Longitudinal position resolution (sigma) of the HADES TOF-wall for all cell pairs, sectors and rows, laying the values between 7.0 and 7.8 mm. (b) Distribution of the values, with an average of 7.6 mm. (Reproduced from Blanco *et al*. 2012.)

5.7 The Extreme Energy Events Experiment

The Extreme Energy Event experiment (EEE) is very peculiar. It was conceived around 2004 by its scientific leader, A. Zichichi, as an extensive air shower (EAS) array specifically devoted to study the highest energy part of the cosmic ray spectrum (more than 10^{18} eV), where intriguing issues are still open (Figure 5.53). It is implemented with glass multi-gap RPCs, very similar to the ones used for the ALICE TOF system and with similar performance.

The peculiarity of the EEE experiment is that the construction of the RPCs is performed at CERN by teams of high school students and teachers, under just a guidance of professional researchers from the EEE collaboration (see Figure 5.54). The chambers are then shipped to the home institutes, where they are assembled

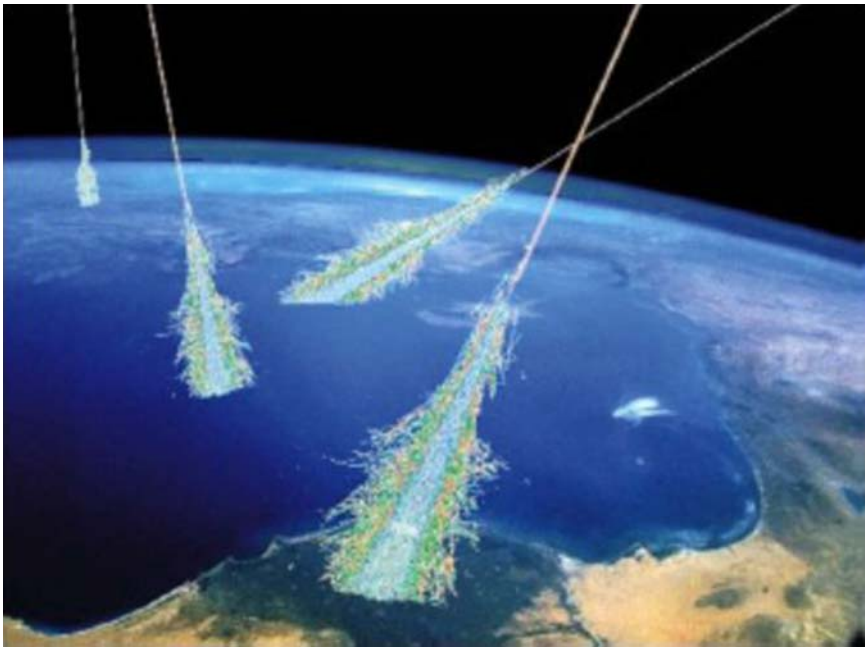

Figure 5.53 Artist's view of an extensive air shower developing in the atmosphere and impinging onto to the ground. When the energy of the primary particle is beyond 10^{16} eV, the shower footprint can be more than several kilometers in diameter.

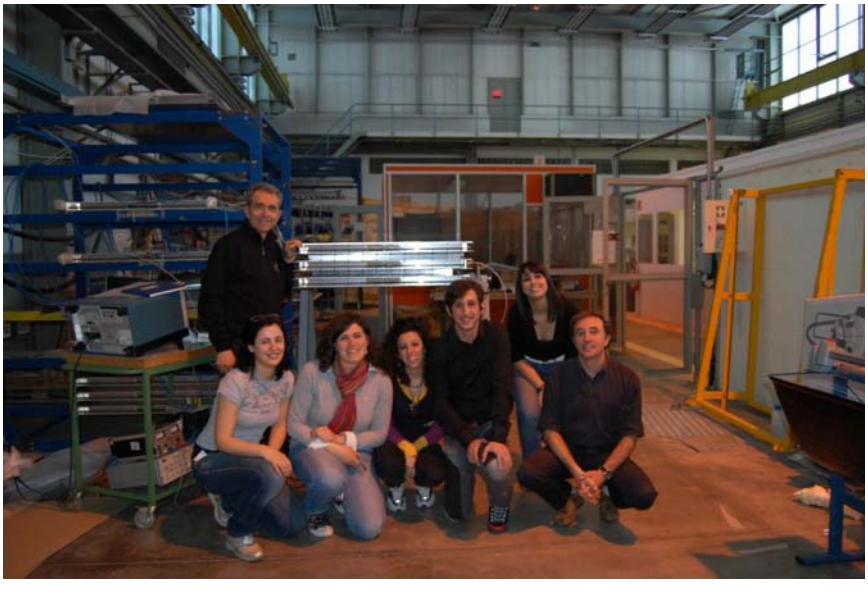

Figure 5.54 One of the teams taking part in the EEE experiment, this one in particular from the Instituto Staffa in Trinitapoli, posing in front of the chambers they have just completed, together with one of the authors of this book (Marcello Abbrescia). Collaboration between high schools students, teachers, and professional researchers is fundamental for the positive outcome of the EEE experiment. (Courtesy prof. Di Staso.)

in telescopes and operated there by school students and teachers. This makes the EEE project a unique tool for introducing high school students and teachers to research activities; as a matter of fact, the operation of the EEE network requires a strong and intense collaboration between high schools and research institutions.

At the end of 2016, the EEE network consists in 52 stations, 46 of which hosted in high schools, and the rest in local sections of the Istituto Nazionale di Fisica Nucleare (INFN), university physics departments and CERN. Additional schools might host an EEE telescope in the future and in the meantime take part in the monitoring of the present system and in the relative data analysis (see Figure 5.55).

Each EEE telescope consists in three glass multi-gap RPC chambers, each with six 300 μm gaps, filled with a gas mixture made out of $C_2H_2F_4/SF_6$ in 98/2 relative proportions, and operated in avalanche mode. The main differences with respect to the ALICE TOF chambers are their dimensions and the fact that they are single stack, with copper readout strips on just one side of the stack.

The EEE network operates as a whole, the stations being synchronized with each other at a few tens of nanosecond precision with a global positioning system

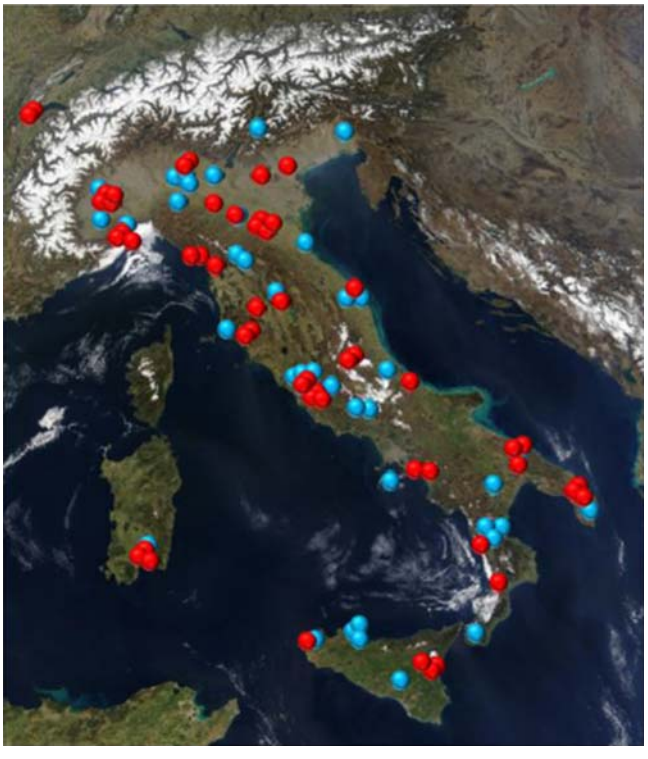

Figure 5.55 Map of the EEE network sites at the end of 2016: the dark gray points correspond to schools hosting a cosmic rays telescope, the light gray ones to schools taking part in the EEE project without hosting a detector but contributing to monitoring and data analysis. (La Rocca *et al*. 2016. http://iopscience.iop.org/article/10.1088/1748-0221/11/12/C12056/meta. Licensed under CC BY 3.0.)

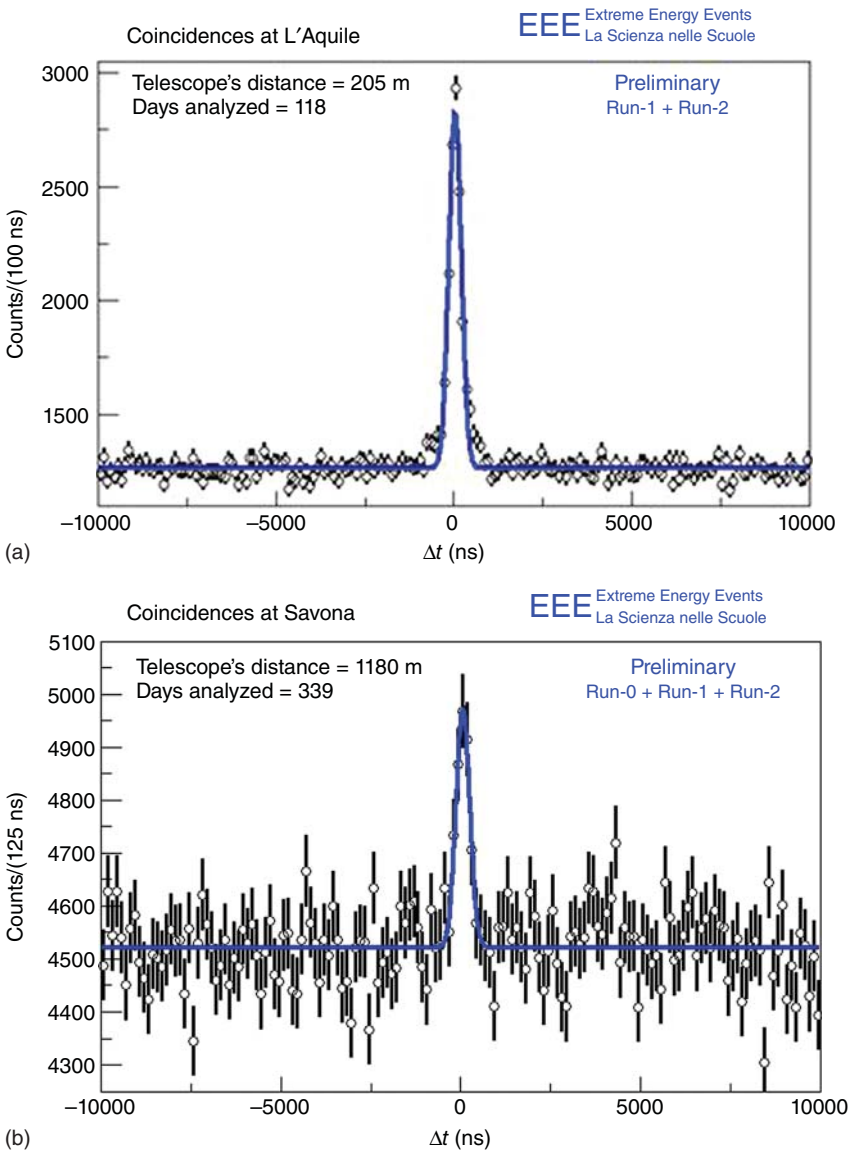

Figure 5.56 Time difference distribution for muon tracks as measured between two EEE telescopes located at (a) L'Aquila, about 200 m apart, and (b) at Savona, placed at a relative distance of 1.2 km. Events in the peak around zero correspond to track recorded in the two telescopes more or less at the same time, and are the signature for EAS impinging on the two telescopes. Note, that the telescopes at L'Aquila were involved and partially destroyed in the 2009 earthquake, and have been rebuilt and put into operation afterwards. (De Gruttola *et al*. 2016. Reproduced with permission of Elsevier.)

(GPS) system, and the relative data acquisition is performed through coordinated runs, during which the schools put effort into keeping their telescope running at the same time. The data are transferred at Centro Nazionale Analisi Fotogrammi (CNAF) (the biggest Italian facility for scientific computing) where they are reconstructed and made available for monitoring and analysis purposes. The first "pilot" coordinated run took place at the end of 2014, then two other runs took place, up to the end of May 2016, with more than 40 telescopes involved and a total of about 25 billion tracks collected and reconstructed; run 3 ended in summer 2017 and doubled the existing sample statistics.

In the EEE experiment, the signature of an EAS is provided by "coincidences," that is, muon tracks recorded in the EEE telescopes at almost the same time and roughly parallel, the largest the EAS energy, the biggest the telescopes relative distance. Examples of such events are shown in Figure 5.56; note that the peak is more evident with respect to the flat background of accidentals when the telescopes are closer, due to the fact that the cosmic rays spectrum is monotonically decreasing with energy.

The EEE telescopes are also able to monitor the local flux of the cosmic muons, and investigate its rapid variations at a few percentage precision; this makes them able to investigate interesting astrophysical phenomena, like the Forbush decreases, that is, the flux decreases related to solar phenomena such as solar flare followed by coronal mass emissions, that usually take place over a few hours. The Forbush decrease observed by a pair of EEE telescopes – actually the first to be ever detected in a school – is reported in Figure 5.57; it is compared and well in agreement with the cosmic neutron flux measured by one detector of the neutron monitor network, located in Oulu, Finland (see Abbrescia *et al*., 2011).

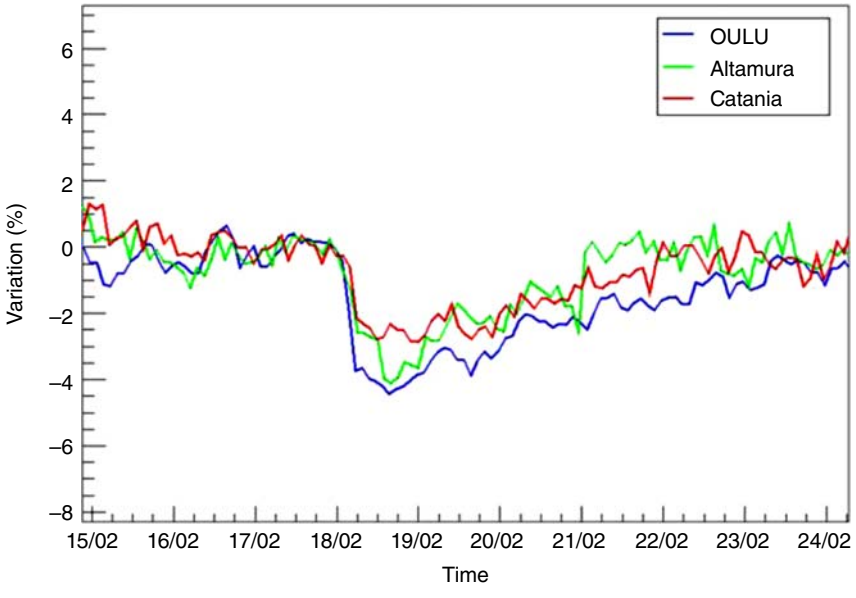

Figure 5.57 The first Forbush decrease observed in February 2011 by two EEE telescopes, located at Altamura and Catania, compared with the OULU neutron monitor data measured in the same time span. (Abbrescia *et al*. 2011. Reproduced with permission of Springer.)

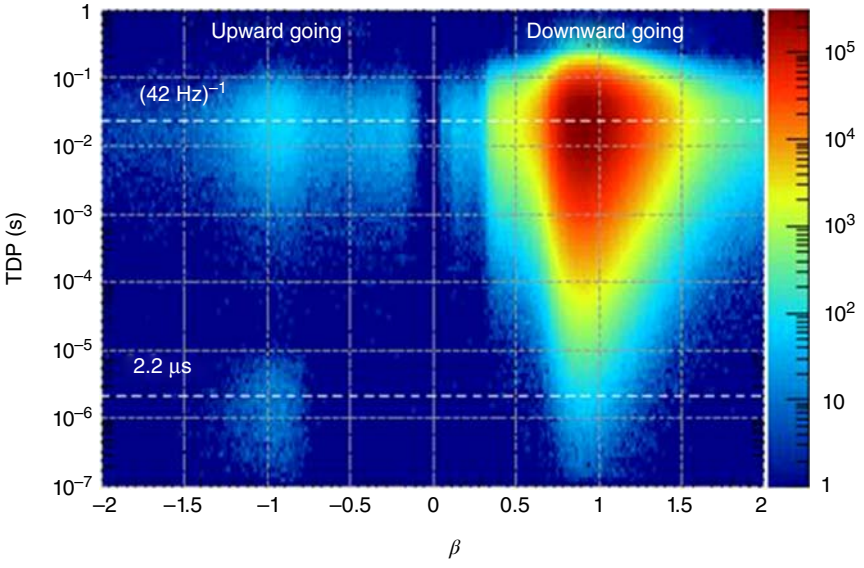

Figure 5.58 Distribution of the time difference with respect to the previous event versus their velocity β, for events detected in one telescope of the EEE network. Positive (negative) β values correspond to downward (upward)-going events. The events in the white spot coming after about 2.2 μs after the previous ones are interpreted as upward-going electrons from muon decay. (Abbrescia *et al*. 2016. Reproduced with permission of Elsevier.)

With the EEE network, other studies are performed, like searching for possible anisotropies in the angular distribution of the cosmic muons, or spotting the Moon shadow on them. Upward going muons are also quite interesting. A first step in this investigation was done when identifying a relevant fraction of the upward going events as relativistic upgoing electrons produced from the decay of downward-going muons stopping in the lowermost part of the telescope or in the ground immediately below it, confirming the excellent performance of the EEE detectors (see Figure 5.58).

As a matter of fact, the EEE experiment is, at the moment, the largest (in terms of chamber surface) experiment using multi-gap RPCs and is going to further expand in the coming years; the relative construction and operation endeavor is comparable, if not even larger, to the upgrades of the RPC systems of big LHC experiments. It is amazing, and quite significative, that it is carried on by teams involving high schools students too.

5.8 Other Experiments

As pointed out earlier on in the introduction to this chapter, it was not our intention to describe all experiments using RPCs, for the simple reason that they are too many. This testifies how effective these devices have been in the field of high-energy physics. Here, we will just report a list of other relevant experiments that have used RPCs, and the reader is invited to consult the references cited (and the references therein) for further details:

- BELLE (a particle physics experiment at the High Energy Accelerator Research Organisation (KEK), Japan), where 2000 m^2 of glass RPCs operating in streamer mode were used for detecting K_L and muons, and some hints of aging effects in this kind of devices were noticed (Yamaga *et al*., 2000).
- OPERA, designed to detect neutrino oscillations in the CERN Neutrinos to Gran Sasso (CNGS) beam, where something like 3000 m^2 of Bakelite RPCs were used and operated for many years in streamer mode in 24 layers of the muon spectrometer (Paoloni, 2014).
- BESIII (a particle physics experiment at the Beijing Electron–Positron Collider II), where RPCs were used in several layers of the muon counter, to cover a surface of around 1200 m^2 with RPCs operated in streamer mode and made with Chinese-produced Bakelite (at the time a novelty in this field) (Zhang *et al*., 2007).
- HARP (The High Acceptance Recoil Polarimeter), which was one of the first experiments using multi-gap RPCs similar to the ones developed for ALICE, but with a four-gap stack of glass plates, and a 300 μm gap thickness (Bogomilov *et al*., 2007).
- PHENIX (Pioneering High Energy Nuclear Interaction eXperiment), at the Relativistic Heavy Ion Collider (RHIC), which upgraded its muon spectrometers using RPCs quite similar to the one developed for the CMS endcaps (He, 2012).
- STAR (The Solenoidal Tracker at RHIC), where multi-gap RPCs with five 220 μm gas gaps were installed in 2009 as a 50 m^2 area TOF system (Llope, 2012).
- LEPS2, an experiment in subnuclear physics *via* photoproduction, where RPCs with a time resolution around 50 ps were developed for the TOF system (Tomida *et al*., 2012).
- FOPI, (4π) at the GSI heavy ion research center, where multi-gap RPCs, used in the upgraded barrel for particle identification, were read out by means of a peculiar multi-strip anode; hence the term MMRPCs (Kis *et al*., 2011).
- Daya Bay, a reactor neutrino experiment, where 1600 RPCs modules made with Bakelite cover about 2500 m^2 and are used as a veto against the background created by cosmic-ray muons (Liehua *et al*., 2011).
- BGOegg, where multi-gap glass RPCs are used in a TOF system to measure particle energy, and an around 60 ps time resolution is obtained (Tomida *et al*., 2016).

It is also worth mentioning that some experiments to be built in the near future also foresee an extensive use of RPCs; let us just mention:

- CBM (compressed barionic matter) at GSI, where MRCP will be used in an around 100 m^2 "wall" for TOF purposes (Herrmann *et al*., 2014).
- INO (India-based Neutrino Observatory), a big underground laboratory for non-accelerator high-energy physics (INO, 2016), where thousands of square meters of RPCs should be used as active elements in the iron calorimeter.
- SHIP, a fixed target facility at the CERN SPS, aimed to *S*earch for the *HI*dden *P*articles and tau neutrinos (SHIP, 2015), where both Bakelite and multi-gap timing RPCs are foreseen.

References

Abbrescia, M. (2013) Operation, performance and upgrade of the CMS resistive plate chamber system at LHC. *Nucl. Instrum. Methods Phys. Res., Sect. A*, **732**, 195–198.

Abbrescia, M. *et al*. (1993) A horizontal muon telescope implemented with resistive plate chambers. *Nucl. Instrum. Methods Phys. Res., Sect. A*, **336**, 322–329.

Abbrescia, M. *et al*. (1995) Resistive plate chambers performances at cosmic ray fluxes. *Nucl. Instrum. Methods Phys. Res., Sect. A*, **359**, 603–609.

Abbrescia, M. *et al*. (1997) Resistive plate chambers performances at low pressure. *Nucl. Instrum Methods Phys. Res., Sect. A*, **394**, 341–348.

Abbrescia, M. *et al*. (2004) Study of long-term performance of CMS RPC under irradiation at the CERN GIF. *Nucl .Instrum. Methods Phys. Res., Sect. A*, **533**, 102–110.

Abbrescia, M. *et al*. (2011) Observation of the February 2011 Forbush decrease by the EEE telescopes. *Europhys. J. Plus*, **126**, 61. doi: 10.1140/epjp/i2011-11061-5.

Abbrescia, M. *et al*. (2016) A study of upward going particles with the extreme energy events telescopes. *Nucl. Instrum. Methods Phys. Res., Sect. A*, **816**, 142–148.

Adam, J. *et al*. (2015) *Eur. Phys. J. C*, **75**, 226. doi: 10.1140/epjc/s10052-015-3422-9.

Aielli, G. *et al*. (2006) New results on ATLAS RPC's aging at CERN's GIF. *IEEE Trans. Nucl. Sci.*, **53** (2), 567–571.

Aielli, G. *et al*. (2009) Temperature effect on RPC performance in the ARGO-YBJ experiment. *Nucl. Instrum. Methods Phys. Res., Sect. A*, **608**, 246–250.

Aielli, G. *et al*. (2012a) Calibration of the RPC charge readout in the ARGO-YBJ experiment. *Nucl. Instrum. Methods Phys. Res., Sect. A*, **661**, S56–S59.

Aielli, G. *et al*. (2012b) Highlights from the ARGO-YBJ experiment. *Nucl. Instrum. Methods Phys. Res., Sect. A*, **661**, S50–S55.

Aielli, G. *et al*. (2013) Performance, operation and detector studies with the ATLAS resistive plate chambers. *JINST*, **8**, P02020.

Akindinov, A. *et al*. (2009a) The ALICE time-of-flight system: construction, assembly and quality tests. *Nuovo Cimento Soc. Ital. Fis., B*, **124**, 235–253. doi: 10.1393/ncb/i2009-10761-3.

Akindinov, A. *et al*. (2009b) Final test of the MRPC production for the ALICE TOF detector. *Nucl. Instrum. Methods Phys. Res., Sect. A*, **602**, 709–712.

Akindinov, A.V. *et al*. (2004) Design aspects and prototype test of a very precise TDC system implemented for the multigap RPC of the ALICE-TOF. *Nucl. Instrum. Methods Phys. Res., Sect. A*, **533**, 178–182.

ALICE Collaboration (2004) Muon Spectrometer Technical Design Report. ALICE-DOC-2004-004 v.1, https://edms.cern.ch/document/470838/1 (accessed 26 October 2017).

ALICE Collaboration (2006) https://cds.cern.ch/collection/ALICE%20Photos (accessed 26 October 2017).

ALICE Collaboration (2008a) The ALICE experiment at the CERN LHC. *JINST*, **3**, 1–245.

ALICE Collaboration (2008b) The ALICE public pages, http://aliceinfo.cern.ch/Public/en/Chapter2/Chap2_TOF.html (accessed 26 October 2017).

ALICE Collaboration (2012) Performance of the RPC-based ALICE muon trigger system at the LHC. *JINST*, **7**, T12002.
ALICE Collaboration (2014) Particle identification with the ALICE time-of-flight detector at the LHC. *Nucl. Instrum. Methods Phys. Res., Sect. A*, **766**, 288–291. doi: 10.1016/j.nima.2014.05.059.
Aloisio, A. *et al*. (2000) Long-term performance of the L3 RPC system. *Nucl. Instrum. Methods Phys. Res., Sect. A*, **456**, 113–116.
Alviggi, M. *et al*. (2003) Results on long-term performances and laboratory tests of the L3 RPC system at LEP. *Nucl. Instrum. Methods Phys. Res., Sect. A*, **515**, 328–334.
Antoniazzi, L. *et al*. (1992a) The TRIGA board for a fast muon trigger for E771. *Nucl. Instrum. Methods Phys. Res., Sect. A*, **314**, 563–571.
Antoniazzi, L. *et al*. (1992b) The E771 RPC detector. *Nucl. Instrum. Methods Phys. Res., Sect. A*, **315**, 92–94.
Anulli, F. *et al*. (2002) The BaBar instrumented flux return performance: lessons learned. *Nucl. Instrum. Methods Phys. Res., Sect. A*, **494**, 455–463.
Anulli, F. *et al*. (2003) Performances of RPCs in the BaBar experiment. *Nucl. Instrum. Methods Phys. Res., Sect. A*, **515**, 322–327.
Anulli, F. *et al*. (2005) Performance of second generation BABAR resistive plate chambers. *Nucl. Instrum. Methods Phys. Res., Sect. A*, **552**, 276–291.
ARGO-YBJ (2000) The ARGO-YBJ offical web site: http://argo.na.infn.it/.
Arnaldi, R. *et al*. (2000) Study of the resistive plate chambers for the ALICE Dimuon arm. *Nucl. Instrum. Methods Phys. Res., Sect. A*, **456**, 73–76.
Arnaldi, R. *et al*. (2002) Spatial resolution of RPC in streamer mode. *Nucl. Instrum. Methods Phys. Res., Sect. A*, **490**, 51.
ATLAS collaboration (1992) Letter of Intent for a General-Purpose p p Experiment at the Large Hadron Collider at CERN, CERN/LHCC/92-4, LHCC/1, 21 October 1992.
Bacci, C. *et al*. (1993) A hodoscope made of resistive plate chambers to identify muons in a fixed target beauty hadroproduction experiment. *Nucl. Instrum. Methods Phys. Res., Sect. A*, **324**, 83–92.
Bacci, C. *et al*. (1995) Test of a resistive plate chamber operating with low gas amplification at high intensity beams. *Nucl. Instrum. Methods Phys. Res., Sect. A*, **352**, 552–556.
Belver, D. *et al*. (2009) The HADES RPC inner TOF wall. *Nucl. Instrum. Methods Phys. Res., Sect. A*, **602**, 687.
Biondi, S. (2015) Upgrade of the ATLAS Muon Barrel Trigger for HL-LHC. Proceedings of Science (EPS-HEP2015), p. 289.
Blanco, A. *et al*. (2012) Performance of the HADES-TOF RPC wall in a Au + Au beam at 1.25 AGeV. *J.INST*, **8**, P01004.
Bogomilov, M. *et al*. (2007) Physics performance of the barrel RPC system of the HARP experiment. *IEEE Trans. Nucl. Sci.*, **54** (2), 342–353.
Bohrer, A. *et al*. (1992) Status Report of the RD5 experiment. CERN/DRDC/91-53.
Bressi, G. *et al*. (1987) An apparatus to search for free neutron-antineutron oscillations. *Nucl. Instrum. Methods Phys. Res., Sect. A*, **261** (3), 449–461.
Camarri, P. (2009) Operation and performance of RPCs in the ARGO-YBJ experiment. *Nucl. Instrum. Methods Phys. Res., Sect. A*, **602**, 668–673.

Cataldi, G. *et al*. (1994) Performance of the E771 RPC muon detector at Fermilab. *Nucl. Instrum. Methods Phys. Res., Sect. A*, **337**, 350–354.
CMS collaboration (1992) Letter of Intent by the CMS Collaboration for a General Purpose Detector at the LHC, CERN /LHCC 92-3, LHCC/I 1, 1 October 1992.
CMS Collaboration (1997) The muon project technical design report. CERN/LHCC 97–32, 15 December 1997.
CMS Collaboration (2015) Technical proposal for the phase-II upgrade of the compact Muon solenoid. CERN-LHCC-2015-10, LHCC-P-008, CMS-TDR-15-02, 1 June 2015, ISBN: 978–92–9083-417-5.
Colaleo, A. *et al*. (2009) The compact muon solenoid RPC barrel detector. *Nucl. Instrum. Methods Phys. Res., Sect. A*, **602**, 674–678.
Corradi, M. (2016) Performance of ATLAS RPC Level-1 muon trigger during the 2015 data taking. *JINST*, **11**, C09003.
De Gruttola, D. *et al*. (2016) A multigap resistive plate chambers array for the extreme energy events project. *Nucl. Part. Phys. Proc.*, **279–281**, 31–38.
He, X. (2012) PHENIX RPC R&D for the fast RPC muon trigger upgrade. *Nucl. Instrum. Methods Phys. Res., Sect. A*, **661**, S86–S89.
Herrmann, N. *et al*. (2014) Technical Design Report for the CBM Time of Flight System (TOF). GSI-2015-01999, GSI publisher, Darmstadt, Germany.
INO (2016) http://www.ino.tifr.res.in/ino/ (accessed 26 October 2017).
Kis, M. *et al*. (2011) A multi-strip multi-gap RPC barrel for time-of-flight measurements. *Nucl. Instrum. Methods Phys. Res., Sect. A*, **646**, 27–34.
Kornakov, G. and for the HADES Collaboration (2014) Time of flight measurement in heavy-ion collisions with the HADES RPC TOF wall. *JINST*, **9**, C11015. doi: 10.1088/1748-0221/9/11/C11015.
La Rocca, P. *et al*. (2016) The EEE project: a sparse array of telescopes for the measurement of cosmic ray muons. *JINST*, **11**, C12056.
Liehua, M. *et al*. (2011) The mass production and quality control of RPCs for the Daya bay experiment. *Nucl. Instrum. Methods Phys. Res., Sect. A*, **659**, 154–160.
Llope, W.J. (2012) Multigap RPCs in the STAR experiment at RHIC. *Nucl. Instrum. Methods Phys. Res., Sect. A*, **661**, S110–S113.
Paoloni, A. (2014) The OPERA RPC system. *JINST*, **9**, C10003.
Pedraza, I. (2016) First results of CMS RPC performance at 13 TeV. *JINST*, **11**, C12003.
Pugliese, G. *et al*. (2014) CMS RPC muon detector performance with 2010-2012 LHC data. *JINST*, **9**, C12016.
SHIP (2015) Technical Proposal: A Facility to Search for Hidden Particles (SHiP) at the CERN SPS, CERN-SPSC-2015-016 SPSC-P-350, 8 April 2015.
Surdo, A. and on behalf of the ARGO-YBJ Collaboration (2008) Talk given at the 21 European Cosmic Ray Symposium (ECRS 2008).
Tomida, N. *et al*. (2012) *High Time Resolution Resistive Plate Chambers for the LEPS2 Experiment*, SPring-8 Research Frontiers.
Tomida, N. *et al*. (2016) Performance of TOF-RPC for the BGOegg experiment. *JINST*, **11**, C11037.
Yamaga, M. *et al*. (2000) RPC systems for BELLE detector at KEKB. *Nucl. Instrum. Methods Phys. Res., Sect. A*, **456**, 109–112.
Zhang, J. *et al*. (2007) The design and mass production on resistive plate chambers for the BESIII experiment. *Nucl. Instrum. Methods Phys. Res., Sect. A*, **580**, 1250–1256.

6

Materials and Aging in Resistive Plate Chambers

In this chapter we speak about two issues which are probably among the less known in the field of resistive gaseous detectors, namely, materials and aging. The reason why the knowledge about the materials used for these devices and the aging processes related to operating them for an extended period of time is limited is due to the fact that their thorough understanding requires describing phenomena which are borderline between physics and chemistry. In addition, they are complex processes, where most probably there are multiple actors playing simultaneously important roles, whose reciprocate interplay is not negligible at all. Unfortunately, aging was only recognized to be a problem once resistive plate chambers (RPCs) had already been mounted and operated in large experiments, and this was an added difficulty for performing all the tests needed. Here, we report about the experiences gained by many authors who, for one reason or another, have been working in these fields, and we will try to provide a coherent picture of the various observations collected. Of course, when this is beyond our possibilities, we invite the reader to complete the picture, collecting additional data or providing a more detailed theoretical framework than the one presently available.

6.1 Materials

In the preceding chapters we have described some basic properties of the resistive materials used for various designs of RPCs. The main characteristics of RPCs used for some large experiments are presented in Table 6.1. As can be seen, the main materials used in these RPCs are glass and Bakelite. Let us discuss the known properties of these materials.

From the point of view of their macroscopic parameters, such as resistivity and temperature dependence, it is generally acknowledged that they are, in general, well measured. However, there is a lack of understanding of the microscopic picture of the charge-transfer processes in such materials. It is generally believed that avalanche or streamer charge deposited onto the RPC electrode surfaces is dissipated both through the volume of the electrodes and along their surfaces as well, and in minor amount via spacers and edges. Let us now consider separately the two main cases, electrodes made with glass or with Bakelite.

Resistive Gaseous Detectors: Designs, Performance, and Perspectives, First Edition.
Marcello Abbrescia, Vladimir Peskov, and Paulo Fonte.

Table 6.1 Summary of RPC operating conditions and used electrode materials in some experiments.

Experiment	Status	Electrode material and resistivity	Gas composition	Operation mode; charge/track	Particle rates and estimated accumulated charge
L3	Completed	Oiled Bakelite $\sim 2 \times 10^{11}\ \Omega$ cm	$Ar/iC_4H_{10}/C_2H_2F_4$ 59/35/6	Streamer	Comparable to cosmic rays
BaBar	Completed	Oiled Bakelite 10^{11}–$10^{12}\ \Omega$ cm	$Ar/iC_4H_{10}/C_2H_2F_4$ 48/48/4	Streamer $\sim 10^2$ pC	$\sim$10–20 Hz/cm^2 $\leq$10 C/cm^2
Belle	In progress	Float glass 10^{12}–$10^{13}\ \Omega$ cm	$Ar/iC_4H_{10}/C_2H_2F_4$ 30/8/62	Streamer	$\sim$10–20 Hz/cm^2
ALICE TOF	In progress	Soda-lime glass $\approx 10^{13}\ \Omega$ cm	$C_2H_2F_4$ / SF_6 93/7	Avalanche $\leq$10 pC	$\geq$7 Hz/cm^2
ALICE (trigger)	In progress	Oiled Bakelite $\sim 3 \times 10^{9}\ \Omega$ cm	$Ar/iC_4H_{10}/C_2H_2F_4/CF_4$ 49/40/10/1	Limited streamer	<100 Hz/cm^2 $\leq$0.2 C/cm^2
ATLAS	In progress	Oiled Bakelite $\sim 2 \times 10^{10}\ \Omega$ cm	$C_2H_2F_4/iC_4H_{10}/CF_6$ 96.7/3/0.3	Avalanche $\sim$30 pC	<100 Hz/cm^2 $\leq$0.3 C/cm^2
CMS	In progress	Oiled Bakelite $\sim 10^{10}\ \Omega$ cm	$C_2H_2F_4/iC_4H_{10}/CF_6$ 96/3.5/0.5	Avalanche $\sim$30 pC	<100 Hz/cm^2 $\leq$0.3 C/cm^2
ARGO-YBJ	In progress	Oiled Bakelite 10^{11}–$10^{12}\ \Omega$ cm	$C_2H_2F_4/Ar/iC_4H_{10}$ 75/15/10	Streamer	Cosmic rays
EEE	In progress	Soda-lime glass $\approx 10^{13}\ \Omega$ cm	$C_2H_2F_4/SF_6$ 98/2	Avalanche $\leq$10 pC	Cosmic rays

6.1.1 Glasses and Glass RPCs

The material used in the first RPC prototype was a Fe-doped glass (Parkhomchuk *et al*., 1971). Nowadays, the conductivity mechanism of glass is relatively well studied (see, e.g., Horst, 1990; Shelby, 1997).

A glass is a substance in which the molecular units have a disordered arrangement, but sufficient cohesion to ensure an overall strong mechanical rigidity. Materials of many different compositions may exist in this state; in other words, there is no one substance which is uniquely glass. The word "glass" is a generic term, so it is more appropriate to speak of "glasses" rather than "glass," just as we speak of "metals," "textiles," and "ceramics." Some hints about the nature of the glassy state are illustrated in Figures 6.1–6.5.

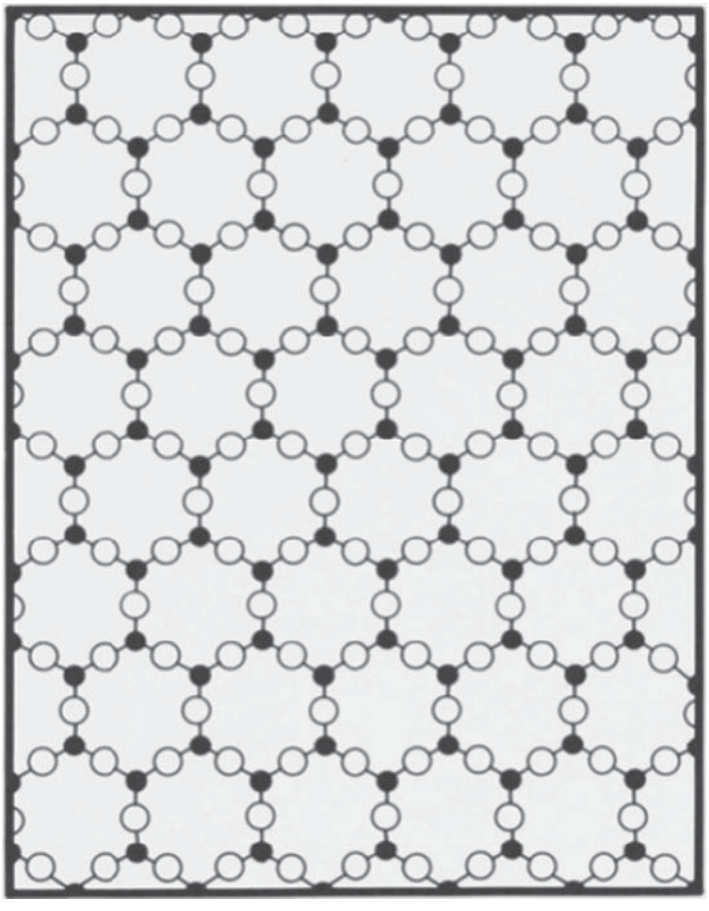

Figure 6.1 The schematics of quartz crystal in a two-dimensional representation of what is really a three-dimensional lattice. Black circles are silicon atoms, open circles are oxygen atoms. As can be seen, quartz is a truly crystalline substance. (From Brill 1962.)

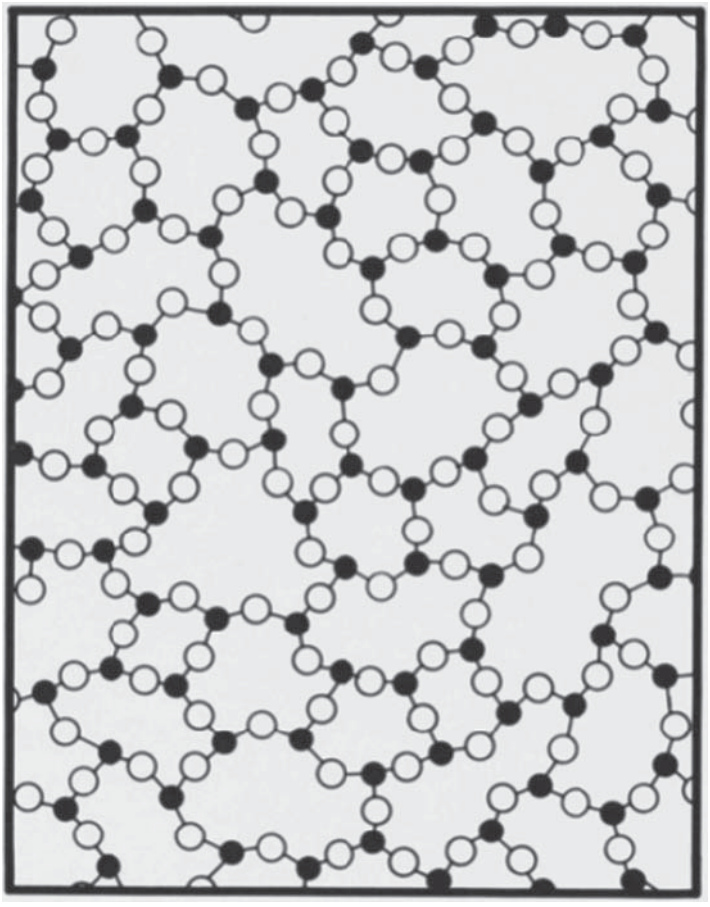

Figure 6.2 The structure of fused silica glass. As in the previous figure, the solid dots represent silicon atoms, while the open circles are oxygen atoms.

The two-dimensional approximation of the molecular structure of a crystal of quartz (namely silicon dioxide, SiO_2) is shown in Figure 6.1. Looking in three dimensions, each silicon atom is located at the center of a tetrahedron and is bound to four oxygen atoms located at the vertexes of the tetrahedron. The tetrahedra are arranged symmetrically in space so that each oxygen atom occupies a vertex for two different tetrahedra. Note that due to the limitations in drawing a two-dimensional representation of these 3D structures, Figure 6.1 (and the following) are somewhat deficient in oxygen atoms, as it would be required by the rules of chemical valency.

If a crystal of quartz is heated at high temperatures (let us say around 1500°C), the chemical bonds holding the atoms together are considerably weakened. Therefore, atoms in the glass, or small groups of atoms, collapse into a molten state which has a random, disordered structure. If then the melted quartz is cooled relatively quickly, some of the atoms may not get back into the crystalline structure, and the result is a glass structure of pure silica, as shown in Figure 6.2.

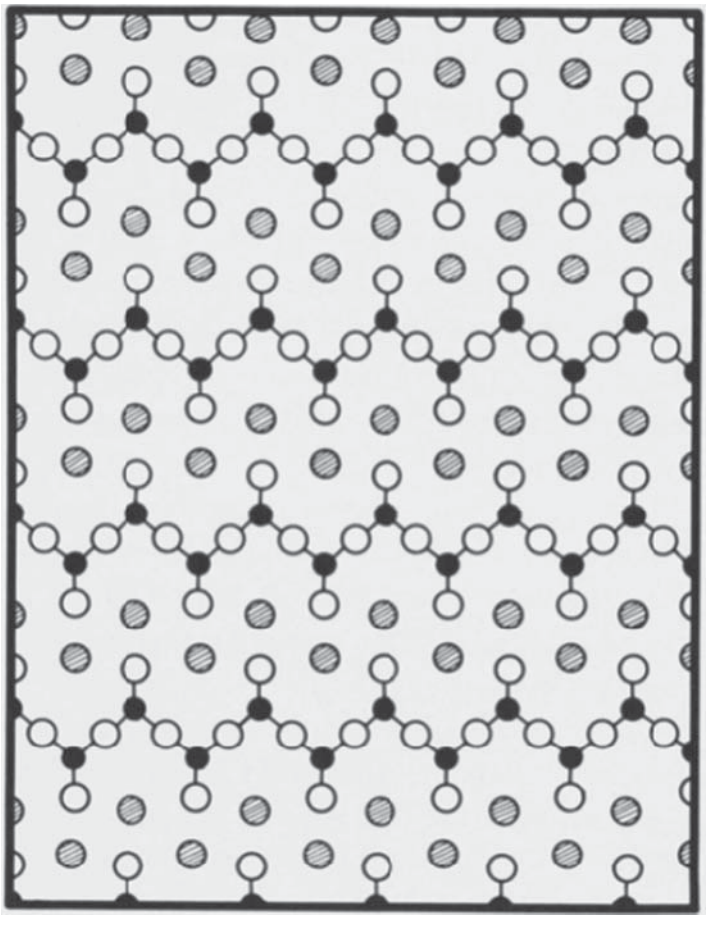

Figure 6.3 Two-dimensional representation of a perfect sodium disilicate crystal; cross-hatched circles represent sodium ions, open circles are oxygen atoms, and solid dots silicon atoms.

As another example, a two-dimensional image of a crystal lattice of sodium disilicate is shown in Figure 6.3. In this crystal, the cross-hatched circles represent sodium ions, which are interspersed in a regular manner between silicate chains. If this crystal is melted, it also collapses into the random structure of a liquid, and if cooled slowly its original crystalline structure can be restored. However, as in the previous case, relatively fast cooling will trap the atoms in a glassy structure such as that shown in Figure 6.4.

In the brief description of glasses given earlier, nothing was said about their chemical composition, because the number of possible compositions for glasses is quite large. As an illustration, the chemical structure of a typical Roman glass (i.e., a glass used nowadays for jewelry) is also reported in Figure 6.5, where one can notice the rich chemical variety of this glass. Chemical composition does, of course, greatly affect the physical and chemical properties of glasses, including their mechanisms for electrical conductivity.

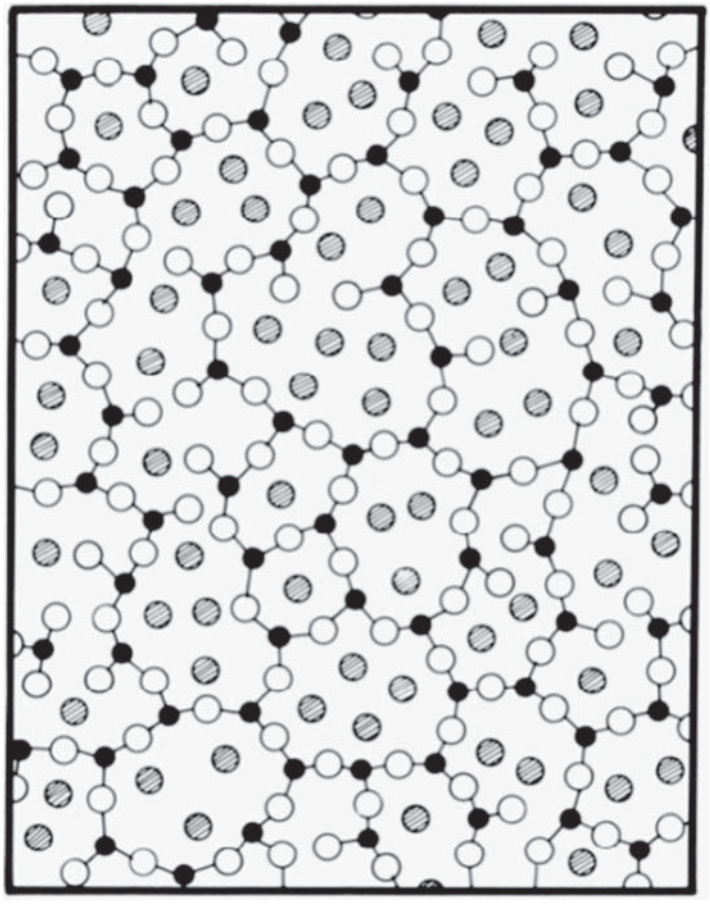

Figure 6.4 Schematic image of soda-silica glass, again cross-hatched circles represent sodium ions, open circles are oxygen atoms, and solid dots silicon atoms.

If a glass is warmed, some of the weaker chemical bonds may break and the glass begins to slightly soften. At some point, the structure collapses to an extent such that the positively charged cations (for instance, Na^+, K^+, Ca^{++}, Fe^{+++}) can break free and become mobile. This means that they can drift through the bulk of the softened glass.

According to Souquet *et al.* (2010), the magnitude of this conductivity, σ_{dc}, depends on the concentration of the charge carriers, n_{cat}, and their mobility, μ_{cat}:

$$\sigma_{dc} = n_{cat}\, q\, \mu_{cat} \tag{6.1}$$

where q is the electrical charge of the carriers.

The conductivity picture of glasses at room temperature is even more complicated and heavily depends on their composition. For example, the electrical conductivity of vitreous silica increases orders of magnitude when increasing the Na_2O content; in fact, it is generally believed that the electrical conduction in silicate glasses is mainly due to the displacement of monovalent cations (Na^+ and

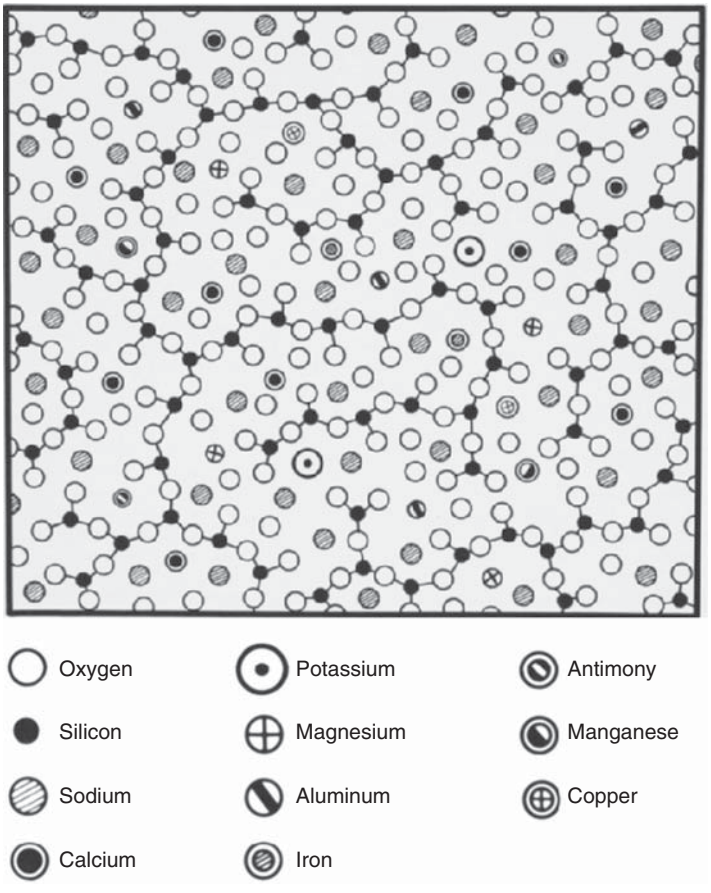

Figure 6.5 Roman glass structure.

other ions) through the glassy network under the influence of an external electric field (e.g., see Souquet *et al*., 2010; Braunger *et al*., 2012, 2014, and Morales *et al*., 2012).

At room temperature, the mobility of effective charge carriers is estimated to be close to 10^{-4} cm^2 s^{-1} V^{-1} for alkali disilicate glasses (Souquet *et al*., 2010), while the ratio between the number of effective charge carriers and the total number of alkali cations is estimated to be from 10^{-8} to 10^{-10}, comparable to the concentration of intrinsic defects in an ionic crystal or dissociated species from a weak electrolyte solution.

An attempt to schematically illustrate ion movements in an RPC is reported in Figure 6.6. Basically, the conducting ions (like, for instance Na^+) migrate through the bulk until they arrive onto the electrode surface; at the anode they are neutralized by the electrons coming from the avalanche in the gas, at the cathode they are neutralized by the current flowing through the conductive layer connected to the power supply. In both cases, some insulating layers and/or depletion zones are formed, causing electrode polarization.

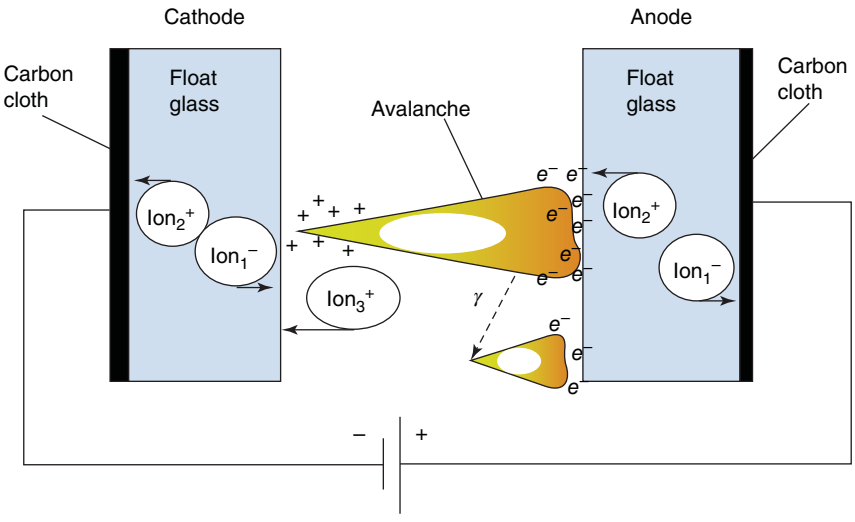

Figure 6.6 One of possible scenarios of ion movement in glass RPCs. (Va'vra 2003. Reproduced with permission of Elsevier.)

The evolution of resistivity with transferred charge for glass and some other materials at different temperatures is reported in Figure 6.7 (from Morales *et al*., 2012). Some materials show a resistivity roughly constant regardless of the transferred charge. In others (for instance, some glasses), resistivity suddenly increases when a certain charge value is reached; this is coherent with the model mentioned, since carriers that arrive at the electrode surfaces remain blocked there and do not participate anymore in the ion conduction process.

Note that many amorphous materials and some glasses at room and lower temperatures may have hopping conductivity mechanism (e.g., see Ezz Eldin *et al*., 1998; El-Desoky *et al*. 2003; Ashwajeet *et al*., 2015); in this case, conduction occurs by migration of charge carriers from one trap state to another at the vicinity of the Fermi level. Note that the states near the Fermi energy level originate from defects and impurities, and hence the conductivity varies with the trap density.

Although it seems like the role of the hopping mechanism is well established, there are speculations that some doped glasses may have n-type semiconductive properties; for instance, Pestov glass is believed to have some type of electron conductivity (Yu. Pestov, Private communication). To this family belongs also a low resistivity glass, the so-called Chinese, nicknamed this way since it was recently developed in China by a group with Tsinghua University (Wang, 2012a).

The main characteristics of these glass sheets are presented in Table 6.2. The temperature dependence of the resistivity for this glass is shown in Figure 6.8. Preliminary tests at Deutsches Elektronen-Synchrotron (DESY) showed a rate capability much higher than ordinary glass (see Figure 6.9); few such chambers were exposed for more than 1 year at the Gamma Irradiation Facility source (mentioned and described in more detail in Chapter 7) and their efficiency was monitored with cosmic rays in the presence of a high irradiation environment

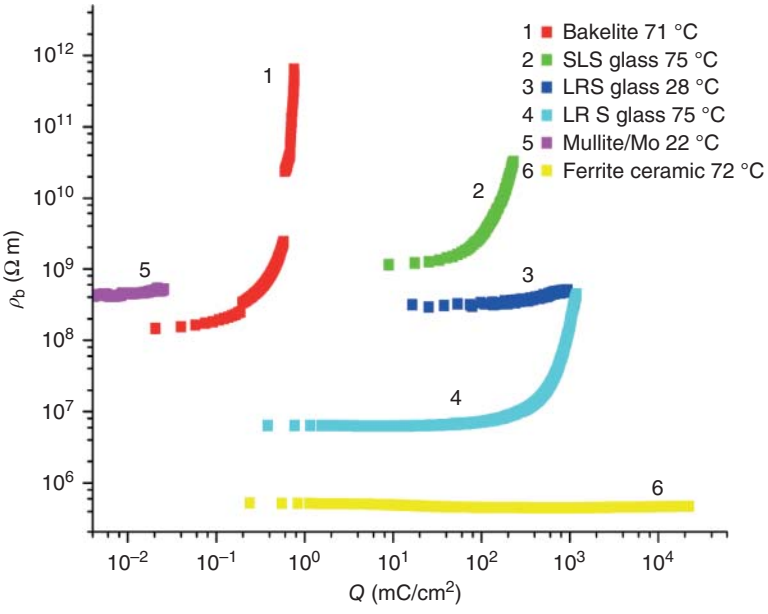

Figure 6.7 Resistivity versus transferred charge measured for glass and other materials at different temperatures. The symbols are: SLC glass, soda lime silicate glass, LRC, low resistive silicate glass (developed at Tsinghua University), mullite/Mo-mullite/molybdenum ceramic. Bakelite at 71°C (which cannot stand even 1 mC/cm^2 when there is no a gas moisture able to provide H^+ carriers) and ferrite ceramic at 72°C (which keeps a flat response even after having delivered 22 000 mC/cm^2) show the extreme behaviors. (Morales *et al*. 2012. https://www.researchgate.net/profile/Gustavo_Mata-Osoro/publication/237050954_Aging_and_conductivity_of_electrodes_for_high_rate_tRPCs_from_an_ion_conductivity_approach/links/02e7e51b0bcd899166000000.pdf. Licensed Under CC BY 3.0.)

Table 6.2 Specifications of the low-resistivity doped glass (J. Wang, private communication).

Maximum dimension	**50 cm × 50 cm**
Bulk resistivity	10^{10} Ω cm
Standard thickness	0.7 mm, 1.1 mm
Thickness uniformity	<20 μm (5 μm typical)
Surface roughness	<10 nm
Dielectric constant	7.5–9.5
DC measurement	Ohmic behavior stable up to 1 C/cm^2

Courtesy of Professor Yi Wang.

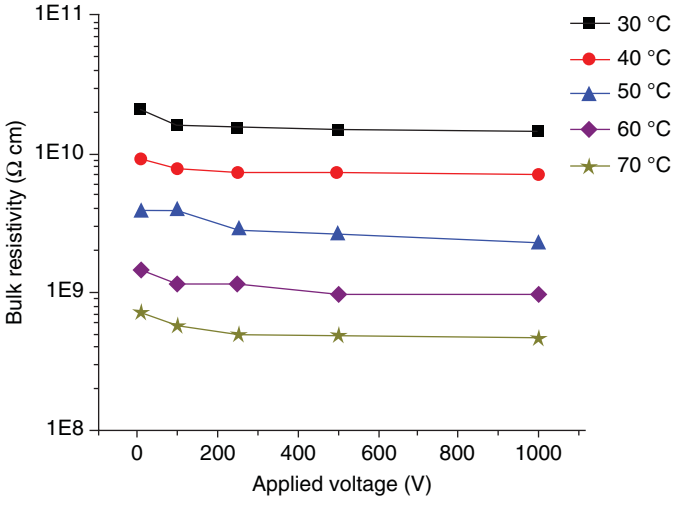

Figure 6.8 Bulk resistivity of low-resistivity glass as a function of applied voltage at various temperatures. (Wang *et al*. 2010. Reproduced with permission of Elsevier.)

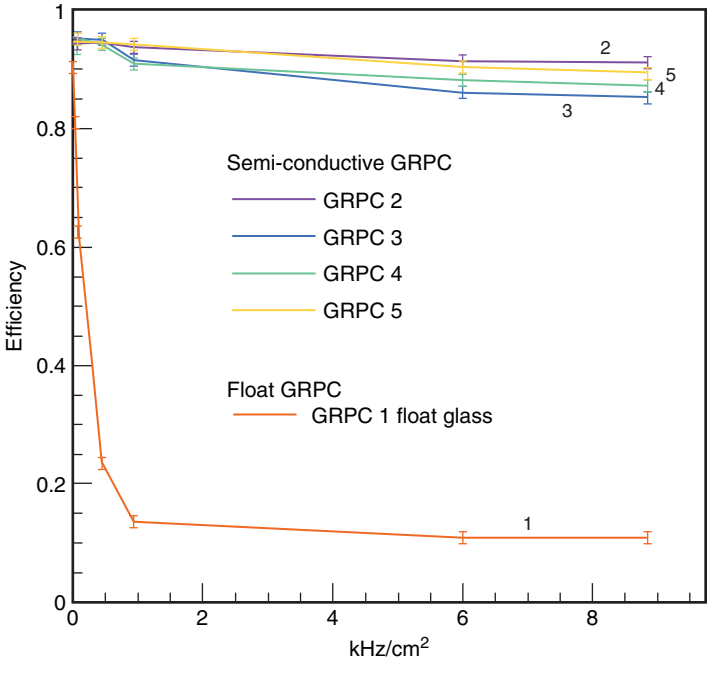

Figure 6.9 Efficiency versus particle rate for four low-resistivity glass RPC (marked on the drawing as GRPC2–GRPC.5 For comparison, data for the float glass RPC are presented as well. (Haddad *et al*. 2013. Reproduced with permission of Elsevier.)

($\sim 10^7$ γ/cm^2). Finally, the same detectors were also exposed to the PS T10 beam at CERN. Rate, high voltage, and threshold scans show that good efficiency, good precision, and reasonable time resolution can be achieved with such a detector. Glass RPCs made with this material are promising candidates to be used for several experiments, for example, compressed barionic matter time of flight (CBM TOF; e.g., see Depner *et al.*, 2014).

6.1.2 Bakelite

Bakelite, used for the construction of RPCs, is a multilayer paper structure impregnated with synthetic resin. When heat and pressure are applied, polymerization transforms this structure to a rigid phenolic sheet. Due to the complexity and nonuniformity of this material, very little is known about its conductivity mechanism. It is believed, however, that, in Bakelite, electric current is also due to ionic motion (e.g., see Morales *et al.*, 2012) and this is why a depletion effect was observed, as shown earlier in Figure 6.7. Moreover, in RPCs, the Bakelite is very often coated with a thin layer of linseed oil, making current flow a complicated process to describe, because both linseed oil and Bakelite are complex substances, with a chemical composition which is not even fixed. In such RPCs, the current flow most probably requires exchanges of charge carriers among different ion species in the gas, the linseed oil, and the Bakelite (see Figure 6.10); some considerations about this interesting, but still obscure, process are reported in Va'vra (2003).

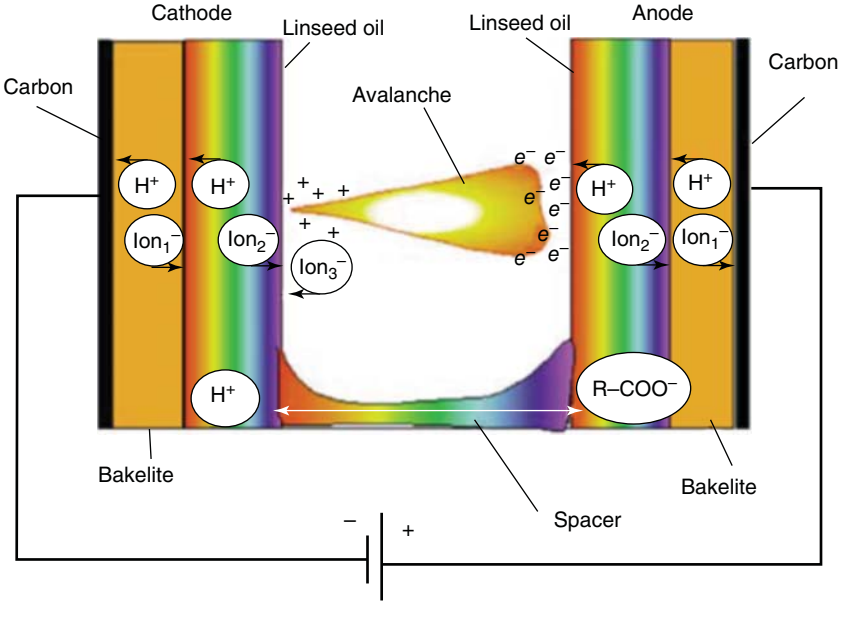

Figure 6.10 Model of charge transfer in oiled Bakelite RPC. (Va'vra 2003. Reproduced with permission of Elsevier. An ionic current in a Bakelite RPC whose electrodes are coated with linseed oil requires charge exchange among three different ions of the gas (marked as Ion_3), the linseed oil (Ion_2), and the Bakelite (Ion_1).

It is also believed that in the range of resistivity in which Bakelite RPCs operate (10^{10}–10^{12} Ω cm) water accumulated inside the Bakelite plays an important role. Of course, pure water is not conductive; however, when it contains some impurities, for example, when it is mixed with some acid species, it begins to conduct by means of ionic carriers. This was a hint to hypothesize that conduction in Bakelite electrodes may have an electrolytic nature. For sure, a variation in Bakelite water content has the effect of changing its resistivity, and this is the reason large experiments using Bakelite RPCs use gas mixtures with a relative humidity around 30–40%; this percentage was empirically determined for the first time during the tests performed at BaBar, by flowing a dry gas mixture in an RPC and measuring the relative water vapor content in the output gas. By the way, water content in a Bakelite sheet is not fixed, since water can get into (or out of) this material, even traversing the linseed oil layer onto it. Note that water content does not only influence the electrolytic composition of oil and phenolic/melamine compounds but could be the main charge transporter in Bakelite, which is characterized by a nonuniform structure, with microporous and random size micro/nanocapillaries.

It was suggested that Bakelite-containing water in high electric field can be represented by the equivalent model shown in Figure 6.11 (Va'vra, 2003). Phenolic-based electrolytes in the electric field can experience the following possible sequence of processes:

1) Phenol dissociation in $H^+ +$ benzene $- O^-$ ions.
2) Either the benzene–O^- ion delivers its charge to anode and benzene–O returns to the fluid, or benzene–O^- ion transfers its charge to OH^- ion via the reaction: benzene $- O^- + H_2O \rightarrow$ phenol $+ OH^-$.
3) Phenol returns into the cycle, and OH^- transfers its charge to the anode; H^+ ion delivers its charge to the cathode, where it forms an H_2 molecule and escapes.
4) In turn, the following processes happen: $2OH \rightarrow H_2O + 2O$, and $2O \rightarrow O_2$, which deliver oxygen close to the anode.

Linseed oil, especially when not fully polymerized, may also facilitate current conduction. It is an organic acid molecule schematically represented as $R - COOH$. In this case, the sequence of electrolytic processes suggested in (Va'Vra, 2003) is as follows:

1) $R - COOH$ dissociates into $H^+ + R - COO^-$.
2) $R - COO^-$ ions drift to the anode, are neutralized, and therefore deliver their charge to anode; then $R - COO$ returns to the fluid. Another possibility is that $R - COO^-$ ions transfer a charge to OH^- ions via $R - COO^- + H_2O \rightarrow COOH + OH^-$. $R - COOH$ returns into the cycle to the acid solution and OH^- transfers its charge to the anode.
3) H^+ ion delivers its charge to the cathode, where it forms an H_2 molecule and escapes as a gas.
4) $2OH \rightarrow H_2O + 2O$, and $2O \rightarrow O_2$, deliver oxygen near the anode (see Figure 6.11).

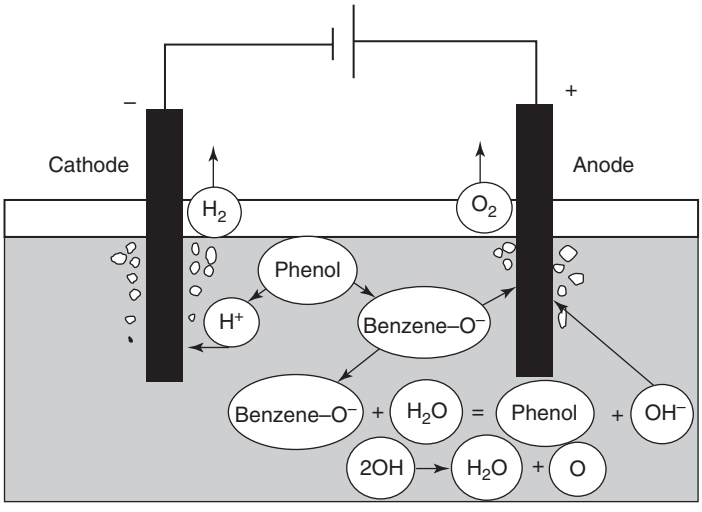

Figure 6.11 Equivalent model of the electrolytic process in the Bakelite. (Va'vra 2003. Reproduced with permission of Elsevier.

The important point of this model is that water strongly influences conductivity. If one removes water, $R-COO^-$ or OH^- will not transport any charge, and $R-COO$ will just deposit onto the anode, and it will not return $R-COOH$ into the cycle feeding the current; as a consequence, the current will slowly stop. Adding water back should restart the conduction. As a matter of fact, an increase of Bakelite resistivity when this material is progressively dried up has been experimentally observed several times.

Obviously, water content is not the only parameter allowing to tune the Bakelite electrical properties. An alternative way is to modify its manufacture technology. For example, an attempt was done to dope Bakelite, adding sodium ions into the epoxy resin during the production process (Dai *et al.*, 2014). The bulk resistivity of this Bakelite could be lowered down to $10^8\ \Omega\,\text{cm}$.

6.1.3 Methods to Measure Bakelite Resistivity

Generally speaking, Bakelite resistivity is less stable in time than glass resistivity. This is due to the fact that it is strongly influenced by external conditions, like environmental humidity, which can affect the water content of this material, or temperature (see Figure 6.12); moreover, these parameters can play a different role depending on the kind of surface treatment Bakelite undergoes during production, such as linseed oil or silicon coating.

For these reasons, resistivity of the RPC electrode plates needs careful consideration and monitoring; in already assembled RPCs, it can be monitored by filling them with argon and following the procedure described in Chapter 3. To measure Bakelite volume resistivity immediately after Bakelite manufacturing, one can use a widespread technique illustrated in Figure 6.13a,b. The Bakelite sheet

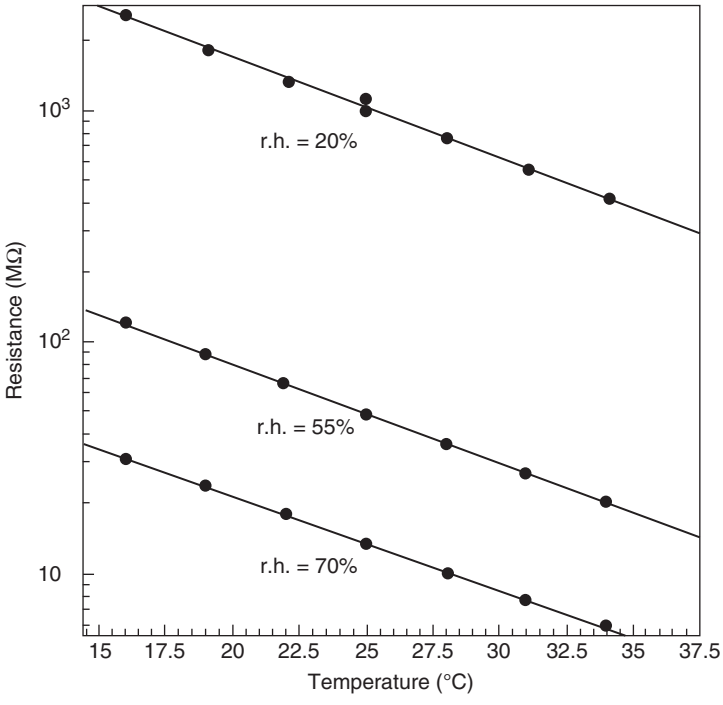

Figure 6.12 Resistance of Bakelite sheets, as a function of temperature, for three values of humidity. (Adapted from Bailey *et al*. 2008.)

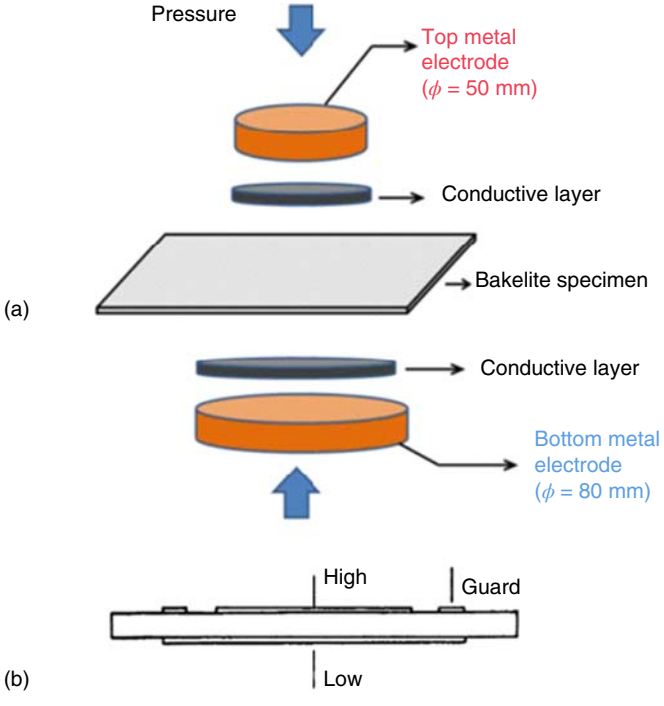

Figure 6.13 Schematics of the Bakelite volume resistivity measurement technique described in the text: (a) without a guard ring and (b) with a guard ring. (Adapted from Song *et al*. 2012.)

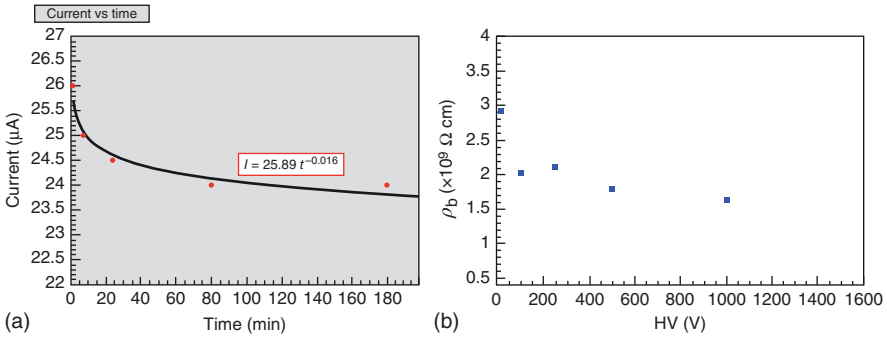

Figure 6.14 (a) Current versus time, measured during a test on Bakelite sheet resistivity. (b) Measured bulk resistivity at different applied voltages. (Adapted from Song *et al*. 2012.)

under test is squeezed between two metallic electrodes, as shown in Figure 6.13a, and the current is measured when a suitable voltage difference between the two electrodes, typically in the 100–1000 V range, is applied. The key point in this procedure is to ensure a good contact between metallic electrodes and the Bakelite surface; for this purpose, soft conductive layers (such as conductive rubber or conductive sponges) are used and a press machine, which can generate pressures up to around 10 atm, is employed to keep the test electrodes well in touch with the specimen. Examples of such measurements, taken from Song *et al*. (2012), are reported in Figure 6.14. Usually, measurements with conductive sponges provide lower resistivity values, which indicate that a better electric contact capability with the Bakelite specimen is established (Figure 6.15). Moreover, to minimize

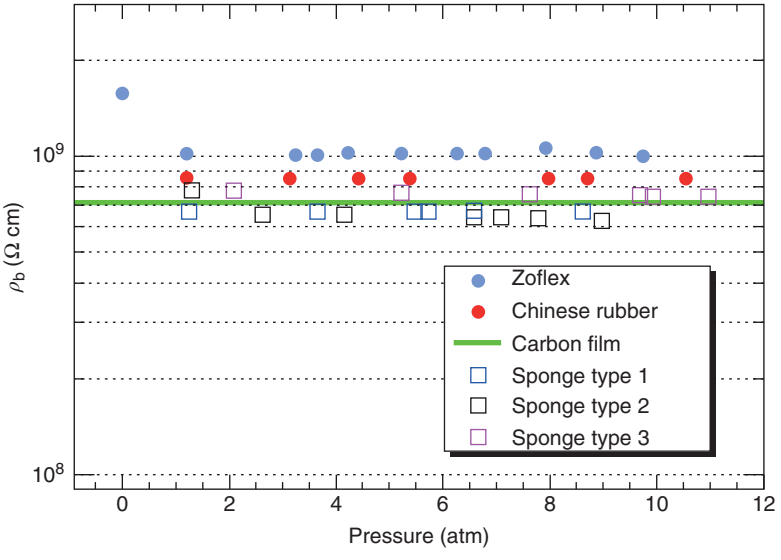

Figure 6.15 Bakelite resistivity versus applied pressure, measured with different kinds of conductive layers. Results are also compared with the ones obtained using carbon film electrodes. ZOFLEX is the commercial name of a conductive rubber. (Adapted from Song *et al*. 2012.)

a possible contribution from the surface current leaks, a guard electrode can be used (Figure 6.13b).

The procedure described is suitable to measure Bakelite bulk resistivity, but it is known that in Bakelite RPCs, the current flowing along the electrode surface plays a relevant role. It is therefore interesting to also measure surface resistivity, which refers to the resistance experienced by this kind of current. It also can be defined as the electrical resistance that exists between two parallel electrodes in contact through the surface.

The principle of the measurement technique used for surface resistivity is shown in Figure 6.16; in this case, the current between two parallel metallic strips attached to the surface and having a good mechanical and electrical contact with it, is measured. Surface resistivity ρ_s is therefore defined as.

$$\rho_s = (U/I_{sm})(D/L), \tag{6.2}$$

where U is the potential difference applied between the two electrodes, I_{sm} is the surface current measured, D is the length of the electrodes, and L their distance. The ratio L/D defines the number of squares covered by the measured area and thus in a general case ρ_s is expressed as ohm per square.

In practice, for simplicity, the electrodes usually are separated by a distance equal to the contact length of the said electrodes so that the four ends of the electrodes form a square; thus, the resistivity measured in this way directly gives the value in ohm per square.

Quite often, methods or geometries to minimize a possible contribution from the bulk current during surface resistivity measurements are used; for instance, in some cases, the bottom surface of the Bakelite under the test sheet is kept grounded. Examples of measures performed with this method are reported in Figure 6.17. Surface resistivity measures are difficult, since they can be affected not only by humidity and moisture on the sample surface but also by pollution and surface defects, or the presence of dielectric films onto it.

Finally, let us also mention that in the case of RPCs with readout strips used for position measurements, it is very important for the resistivity of the graphite coating used to deliver high voltage (HV) to be in the right range: it should be low enough to ensure uniform HV distribution and sufficiently high to be "transparent" for the avalanche-induced signal. Values between 0.1 and around 1 M Ω/sq seem to be optimum. A device often used to measure the surface resistivity of the

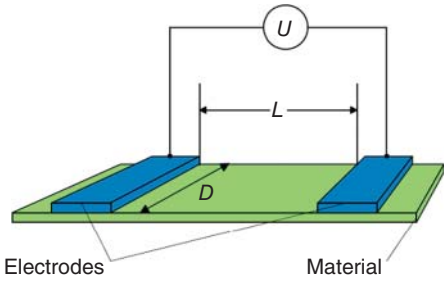

Figure 6.16 Methodology for Bakelite surface resistivity measurements. (Adapted from http://www.trekinc.com/pdf/1005_Resistivity_Resistance.pdf.)

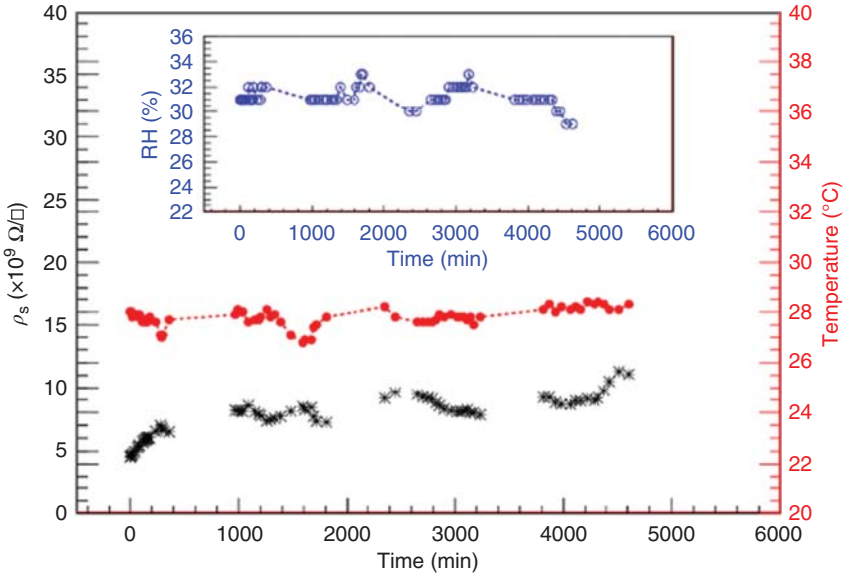

Figure 6.17 Evolution of the Bakelite surface resistivity in time, for two set of data taken at different temperatures; environmental relative humidity was kept around 30%. (Adapted from Song *et al*. 2012.)

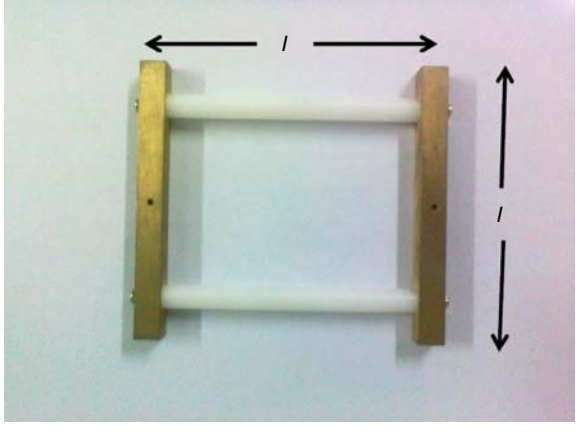

Figure 6.18 Photograph of a couple of simple brass electrodes used for the measurements of the surface resistivity of graphite layers on Bakelite or glass electrodes. (Neog *et al*. 2016. Reproduced with permission of Springer.)

graphite layer is shown in Figure 6.18. It consists of a jig with two metallic bars; ideally, the bars should have a V-shaped cross section and soft padded conducting edges at the bottom, which are placed on the surface under measurement.

Of course, these measures are relevant not only for Bakelite but for glass RPCs as well, since the way to apply the HV is basically the same in the two cases. Measures of surface resistivity of a graphite coating deposited on float glass, showing that some variations with time after drying can be observed, are reported in Figure 6.19 (Jaiswal *et al*., 2012).

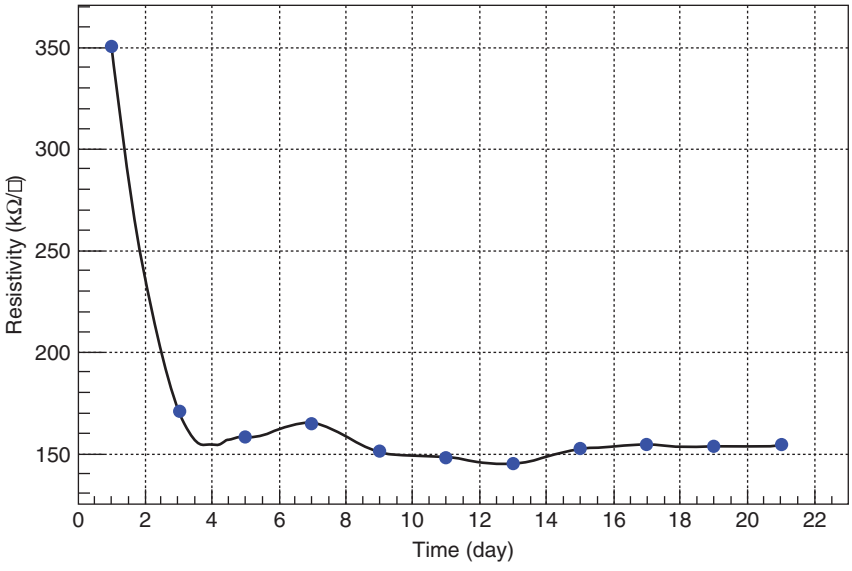

Figure 6.19 Variation of graphite layer surface resistance with time. (Jaiswal *et al*. 2012. Courtesy of Professor Venktesh Singh.)

6.1.4 Semiconductive Materials

Materials different from glass and Bakelite have also been tested as electrodes for RPCs; among these we can cite GaAs (e.g., see Francke *et al*., 2003) or ceramics (Lopes *et al*., 2006; Laso Garcia *et al*., 2016). GaAs is a classical semiconductor and its conductivity mechanism is well understood. Ceramics, on the other hand, are more complicated.

Ceramics are most often characterized by a crystalline molecular structure, but they may also contain a combination of glassy and crystalline phases (Moulson and Herbert, 2003). Most ceramic materials are dielectrics, but some of them, for example, ceramics based on ZnO, may possess semiconductive properties, in particular when they are appropriately doped.

As in most materials, conductivity in ceramics is of two types: electronic and ionic. In the first case, it is due to the passage of free electrons through the material. Although, in principle, in ceramics the ionic bonds holding the atoms together do not allow for free electrons, in some cases impurities of differing valence may be included in the material, and these impurities may act as donors or acceptors of electrons, just like in doped semiconductors. In other cases, transition metals or rare-earth elements of varying valency may be included; these impurities may act as centers for polarons, that is, "quasi particles" that create small regions of local polarization as they move from atom to atom. Electronically conductive ceramics are standardly used as resistors, electrodes, and heating elements (Hench and West, 1990).

Ionic conduction consists of the transit of ions (atoms of positive or negative charge) from one site to another via point defects called vacancies in the crystal lattice. In ceramics, at normal temperatures, very little ion hopping takes place,

because the atoms are at relatively low energy states. At elevated temperatures, however, vacancies become mobile, and certain ceramics exhibit what is known as fast ionic conduction. These ceramics are especially useful in fuel cells, batteries, and so on. Note that due to their semiconductive properties, some ceramics do not present any polarization effect even up to high values of transferred charge (see again Figure 6.7).

6.2 Aging Effects

Aging of gaseous detectors is generally defined as the degradation of their performance under prolonged exposure to ionizing radiation. It is a complex phenomenon that depends on many parameters. In the case of RPCs, for instance, aging depends on the materials used for the electrodes, on the gas composition (which may include tiny traces of badly controlled impurities), details of exposure to radiation, and many other factors, sometimes not well known.

Aging in RPCs usually manifests itself as an increase both in "dark" current and noise pulses; in the worst cases they both increase in time until the RPC cannot be brought up at the right operating voltage, or the noise counting rate is so high that it causes the chamber to continuously spark. Also, a progressive decrease in detection efficiency is observed. When these devices are opened, postmortem, sometimes one can observe in visual or microscopic inspection electrode erosion and/or traces of polymers deposited onto them.

Although the basic phenomenology of the aging process has been described in a huge number of publications, it is nevertheless still difficult to get a clear and complete picture of what happens at a more fundamental level. Many chemical processes probably occur simultaneously, and consequently, a quantitative description of aging effects, which would require as a minimum a detailed analysis of all gas-phase and gas-surface reaction products, is currently quite limited. At best, this can be described only qualitatively and some empirical systematic dependencies deduced and presented.

6.2.1 Aging in RPCs Operated in Streamer Mode

6.2.1.1 L3 and Belle

As already pointed out, the RPCs used for the first large-scale high-energy physics experiments, for instance, at L3 at the Large Electron Positron (LEP), did not show any relevant degradation in performance that could be attributed to the aging processes at the detector level. In fact, the main sources of the small loss of efficiency observed in the RPC systems of the L3 experiment were identified as some electronic channels failing, changes in the gas mixture, which was once done during operation, and gas leaks (see Chapter 5 and Alviggi *et al.*, 2003 for more details). Therefore, in the following, we concentrate on the aging processes driven by physics mechanisms occurring either in the gas, or inside the electrodes, or at the interface between gas and electrodes.

First, signs of RPC aging were observed later on in B-factory experiments, Belle and BaBar, which operated at much larger luminosity ($>3\times10^{33}$ cm^{-2} s^{-1})

compared to their predecessors at LEP, with a corresponding significant increase in the RPC counting rates compared with the previous accelerator or cosmic rays experiments. An important factor to be considered, by the way, was that Belle and BaBar RPCs were operated in streamer mode.

The Belle RPC electrodes were made of ordinary float glass, characterized by a resistivity around 10^{12} Ω cm or more. After an initial successful start with full efficiency, the RPCs started to deteriorate rapidly.

The Belle group had to stop operation and investigate the problem as soon as high currents were detected. It was the first time that, after massive investigation effort, they established that one of the potential reasons of RPC degradation was related to tetrafluoroethane $C_2H_2F_4$, which is the main component of current RPC gas mixtures and can produce hydrofluoric acid (HF) when streamer are produced. One popular belief, however not supported by compelling experimental evidence, was also that water vapor increases the processes related to the dissociation of tetrafluoroethane and HF acid production.

After several weeks of operation, with a gas mixture containing around 2000 ppm of H_2O the RPC dark current significantly increased and the efficiency correspondingly decreased (Abashian *et al*., 2000). Note that water vapors penetrated from ambient air via flexible polyolefin tubes used to deliver the gas to the RPCs. Of course, high current is a serious problem in RPCs, as was earlier explained. Increasing the applied voltage in an attempt to restore the efficiency did not help, since it merely resulted in increased dark current.

Later studies showed that the aging effects were due to the simultaneous etching of the glass by fluorine ions and deposition of avalanche products on the electrode surfaces. When the chambers were opened, both anode and cathode were found to be damaged; the anode surface had a high level of fluoride, while the cathode lacked sodium. The authors of (Sakai *et al.*, 2003; Kubo *et al.*, 2003) explained the symptoms of aged chambers by spontaneous field emission of electrons from local deposits/tips on the cathode surface.

In one test, the area with reduced efficiency was clearly located along the preferential path of the gas flow (Tonazzo, 2002). The radical solution adopted was to reduce the water concentration from 2000 ppm to less than 10 ppm by replacing polyolefin pipes with copper tubes. It was also observed that flushing the system with ammonia allowed to full recovery the damaged glass chambers (Kubo *et al*., 2003).

There are some speculations that the glass RPCs can suffer from long-term instabilities due to the migration of alkali ions under an intense electric field, which leads to a permanent increase in the surface resistivity (Va'vra, 2003). This phenomenon was observed in the case of MicroStrip Gas Chambers (a kind of micropattern gaseous detector, described in Chapter 8) made of ionic conductive D-263 glass and forced to choose for the substrate either an electron conductive or a diamond-coated glass (Bouclier *et al*., 1996).

6.2.1.2 Experience Gained in BaBar

The BaBar experience with RPCs has provided several important lessons to the "linseed-oiled Bakelite RPC" community. The timeline and a macroscopic

description of what happened have been already reported in Chapter 5; here, we will concentrate on the microscopic picture, trying to provide an interpretation on the basis of the underlying physical processes.

In BaBar, the RPC detector electrodes were made of Bakelite coated with a thin layer of linseed oil. As in other cases, after an initial rather successful operation, aging effects started to manifest themselves with a general performance deterioration: the chambers began to draw an increased current and lose efficiency (e.g., see Anulli *et al*., 2003). Actually, high temperature (around 35°C) lasting for several months during operation was considered as the main trigger for the degradation; anyhow this process continued, even after the temperature was lowered back to 24°C.

Later, scrupulous studies revealed the presence of linseed oil droplets on the inner surfaces of the RPCs. Basically, three sources of problems were identified:

1) Excess of linseed oil on the Bakelite surface, due to the poor coating quality, which was the source of the droplets; the droplets were not fully polymerized and appeared sticky when touched (see Figure 6.20)

   Note that BaBar RPCs were similar to the L3 ones, but with one small, important exception: the L3 electrode spacers and lateral supporting frame had simple straight surfaces; whereas in BaBar, they had been modified into a "mushroom-like" shape, in order to minimize leak currents. These new spacers, however, also acted as hidden storage cavities, trapping linseed not completely polymerized oil (see Figure 6.21).
2) Elevated temperature softening the oil film; as a consequence, oil changed viscosity and leaked from these hidden cavities into the chamber active volume. This resulted in gap thickness variations, and, in some cases, in the formation of stalagmites and even caused bridges between the two Bakelite electrodes, especially in the regions around the spacers and chamber edges. Moreover, it was found that the unpolymerized linseed oil coming from the BaBar RPC chambers showed a much lower volume resistivity ($\sim 2.1 \times 10^8\ \Omega\,\text{cm}$) compared to fresh linseed oil ($\sim 76.7 \times 10^8\ \Omega\,\text{cm}$) and to the Bakelite material ($\sim 2 \times 10^{11}\ \Omega\,\text{cm}$). Therefore, each gap-to-gap bridge represented a "short" circuit in the gap voltage (see Figure 6.22), causing local inefficiencies.

Figure 6.20 Photograph of the inner surface of one of the malfunctioning BaBar RPC electrodes. (From Lu 2005.)

Figure 6.21 A spacer taken from one of the BaBar RPC chambers; the accumulation of brown linseed oil on the bottom right (a dark spot in a black and white version of the photograph) of the spacer can be clearly seen; for the colour version see (Va'vra, 2012).

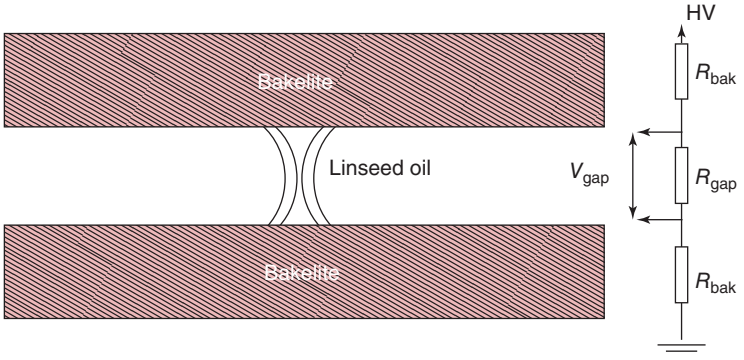

Figure 6.22 Schematic model of the inefficiency mechanism: linseed oil droplets connect the two Bakelite electrodes, reducing the electric field inside the gap. (Anulli *et al*. 2003. Reproduced with permission of Elsevier.)

It was also observed that there was an increase in Bakelite resistivity with time; this was due to the fact, as understood later, that no water vapor was added to the gas mixture, and the Bakelite progressively dried out. In fact, the efficiency close to the gas inlets in some RPCs was much worse than in other areas; this effect was attributed to the drying process close to the inlets being more effective.

The combined effects of an increased Bakelite resistivity and lower resistivity of the oil accumulated around spacers and edges was particularly harmful, causing large leak currents in these locations. Some examples of the measured inefficiency attributed to this effect are shown in Figure 6.23.

3) The intense electric field helped to pull the soft oil layer away from the Bakelite sheet (note that the electric force could be 70 times stronger than the gravity force!). The softened oil resulted also in formation of whiskers mainly onto the cathode (see Figure 6.24). Some authors speculated that these are related to high resistance regions in the bakelite and locally enhanced the Freon-based chemistry, possibly leading to more damage (Va'vra, 2012).

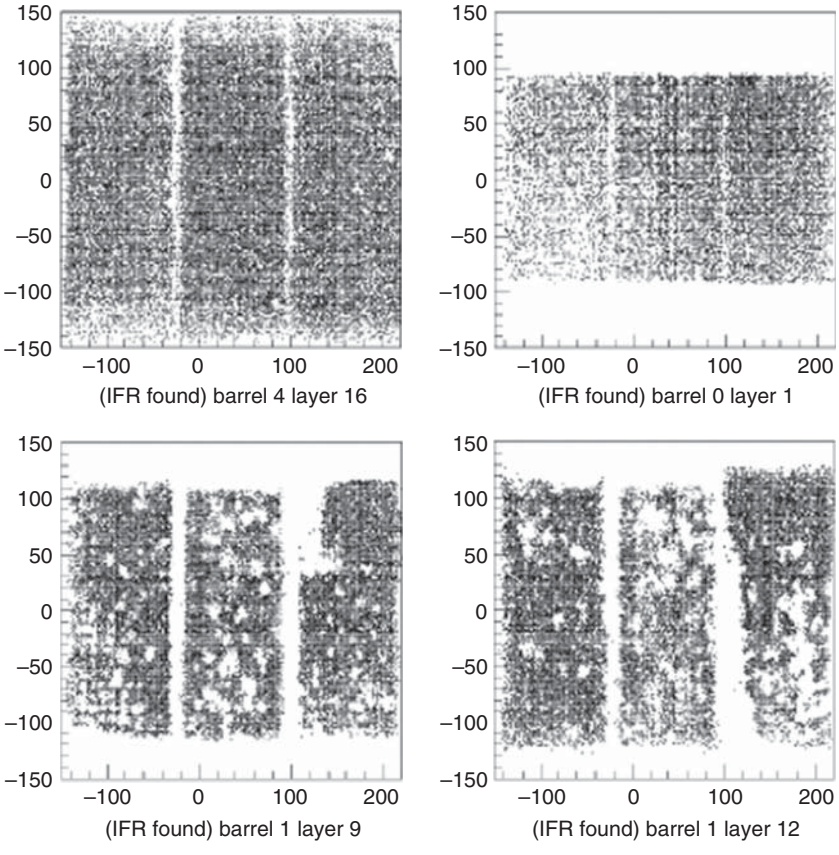

Figure 6.23 BaBar RPC efficiency map: the first histogram shows the efficiency map of a layer (composed of three RPCs) with high efficiency; in the other histograms, inefficiency patterns seem to start around the spacers and along the frame. (Anulli *et al*. 2003. Reproduced with permission of Elsevier.)

Figure 6.24 Whiskers formed onto the cathode of two BaBar RPC chambers. (From Va'vra 2012.)

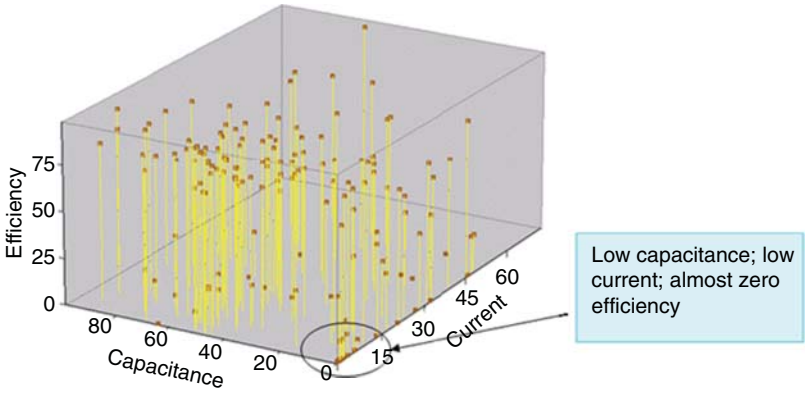

Figure 6.25 A 3D plot of the capacitance, efficiency, and dark current. In the corner of both low efficiency, and low dark current and low capacitance, a relevant number of RPCs are located. (From Lu 2005.)

Among other studies, the BaBar RPC group made capacitance measurements that revealed an unexpected fact: in a 3D plot for capacitance, efficiency, and dark current, a certain number of RPCs occupy the corner of both low efficiency, and low dark current and low capacitance (Figure 6.25).

That is fully opposite to any previous experience: usually, lower efficiency is a direct consequence of high dark current. Further studies discovered that the low capacitance is connected to a discontinuity on the graphite paint film; the original dark uniform graphite coating layer, located under the Mylar film, was found to have become light and semitransparent (see Figure 6.26).

After many initial troubles, all these problems were sorted out and solved by the BaBar community: new RPCs had a thinner linseed oil coating thoroughly polymerized before applying high voltage, the technology of graphite coating was improved, and the water vapors were added to the gas mixture to stabilize the effect of Bakelite drying.

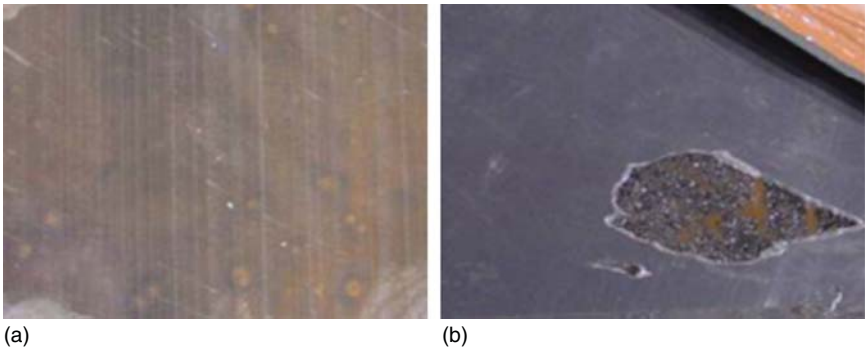

Figure 6.26 (a) The graphite film onto the anode of a dead BaBar RPC characterized by low dark current, low capacitance, and almost zero efficiency. It looks semitransparent, indicating graphite vanished. (b) The damaged region clearly put in evidence; an intact graphite layer should look dark and uniform. (From Lu 2005.)

6.2.2 Melamine and Bakelite RPCs without linseed oil treatment

After the experience with the BaBar RPCs, attempts were made to develop RPCs without oil coating. For example, various laboratory tests were performed with RPCs made of cellulose and melamine phenolic sheets (Crotty *et al*., 1993). We concentrate here on oilless Bakelite RPCs, since these were studied in more detail, and even used for the BES-III experiment.

The surfaces of the electrodes of these oilless RPCs are generally covered with a thin film of plastic, specifically conceived to reduce surface roughness. In the BES-III case, the film was 50 μm thick, and its resistivity could be customized to optimize RPC performance; in other words, this film played a role quite similar to the linseed oil coating, but it was integrated during fabrication into the structure of the Bakelite sheet. The surface quality of these laminates was reported to be superior to other Bakelite plates that have been used to construct RPCs elsewhere (e.g., see Lu, 2006). With these Bakelite sheets, more than 1300 m^2 of RPC chambers were produced and installed at the BES-III detector.

Initial tests show that prototype RPCs made by using resistive plates without the linseed oil treatment could achieve a performance level comparable to RPCs with the usual linseed-oil-treated Bakelite or resistive glass electrode RPCs (Xie *et al*., 2009). Nevertheless, later on, some aging effects were clearly observed in accelerated tests performed with a ^{60}Co source (Lu *et al*., 2012). For instance, the efficiency of three RPCs (numbered as RPC 1, RPC 3, and RPC 5) were measured during these tests, before and after 23 days of aging, and are shown in Figure 6.27. In particular, the equivalent dose for RPC 1 is roughly similar to the one foreseen to be integrated in 7.6 years of data taking at the experiment, and in this case serious aging has already shown up. Two other RPCs presented much less degradation, related to the fact that their equivalent absorbed dose was smaller.

During more "aggressive" tests, oil coated Bakelite electrodes and the oiless electrodes used in BES-III were exposed to HF vapors (Lu, 2009) and results were compared. As already mentioned in Chapter 5 and earlier in this chapter, some authors believe that HF is produced in the RPC gas by discharges due to the decomposition of $C_2H_2F_4$, the main component of most RPC gas mixtures, and a lot of measurements were performed to clarify this issue (see, for instance, Aielli *et al*., 2006; Abbrescia *et al*., 2008; Band *et al*., 2008). Others point out that just the presence of fluorine ions is detected in the RPC exhaust gas, which does not automatically imply that HF is produced. Recall that HF is a very aggressive acid and therefore could be expected to have the main role in damaging the RPC inner surfaces during operation.

As expected, the oil-less Bakelite surface was badly attacked by HF vapors, and some effects of this attack are shown in Figure 6.28. Moreover, a surface resistivity variation was also measured (see Figure 6.29); in particular, during the first hour of exposure, the surface resistivity dropped very rapidly by several orders of magnitudes.

This led to the conclusion that linseed oil coating is somehow effective to reduce the effects related to the attack of HF vapors, or any other attacking agent, whereas not oil-coated Bakelite sheets are generally considered not so robust against chemical agents.

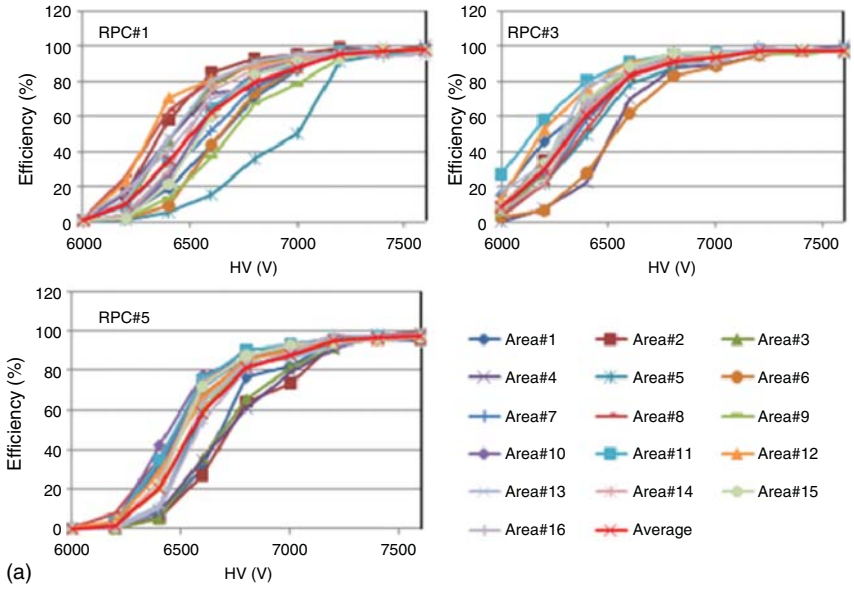

Figure 6.27 Efficiency measurements during accelerated aging tests for three RPCs manufactured without the usual linseed oil treatment, (a) at the beginning of the tests and (b) after 23 days. The efficiency was measured with cosmic rays in 16 monitoring areas (4×4 array) numbered correspondingly #1 to #16. In area #1 of RPC 1, serious aging has already shown up. The other three RPCs have much less degradation because their equivalent aging dose is smaller. (Lu *et al*. 2012. Reprinted with permission of CERN.)

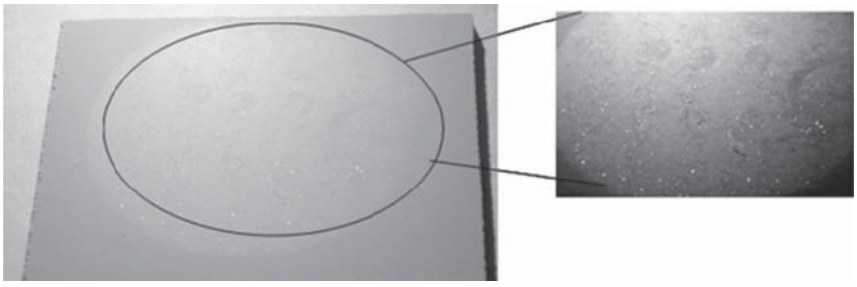

Figure 6.28 Photographs showing the HF corrosive action on the Bakelite used for the RPCs installed in the BES-III experiment. (Lu 2009. Reprinted with permission of CERN.)

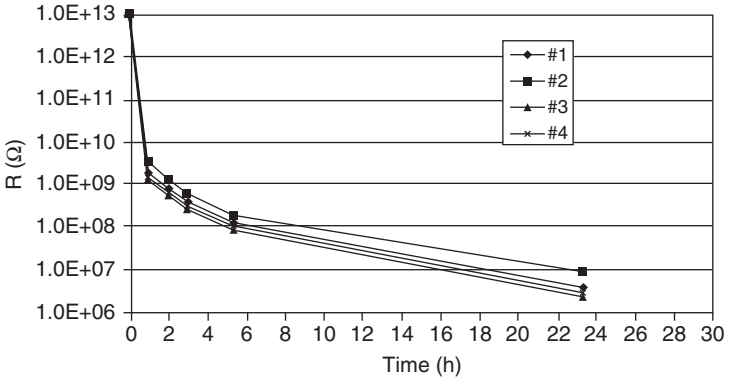

Figure 6.29 Surface resistivity variation of four BES-III Bakelite samples exposed to HF vapors. (Lu 2009. Reprinted with permission of CERN.)

6.3 Aging Studies of RPC Prototypes Operated in Avalanche Mode Designed for the LHC Experiments

Large Hadron Collider (LHC) imposed new challenges to the RPC community: in these experiments, RPCs with a total area of around 15 000 m^2 should work reliably and stably for many years at a counting rate much higher than in the BaBar environment. To meet these challenges, intense R&D efforts were launched by several teams, with the initial BaBar failure being a serious motivation for these studies. One of the outcomes of these studies was the decision to run ATLAS and CMS RPCs in avalanche mode. This allowed not only to improve their rate capability but also to reduce the aging effects, which at fixed working conditions (gas flow, temperature, humidity, etc.) are believed to be proportional, or more

than proportional, to the integrated operating current (and, in fact, integrated charge is a sort of "unit of measure" of how aged RPCs are). Among the main goals of these specific aging studies there were the following:

1) To investigate in more detail the degradation of the graphite coating which distributes the electric field on the Bakelite electrodes;
2) To evaluate the temperature effects, which, even for a high-quality oil coating, affect the electrode resistivity and may cause an increase in dark current and rate of noise pulses;
3) To investigate the effect of HF and other fragments on oil coating;
4) To study other possible changes in Bakelite electrodes due to various effects, such as drying, irradiation, and so on.

Most of these studies were successfully completed in the 2003–2006 period, that is, before the RPC installations took place. Various scrupulous investigations were performed: some of them were performed using cosmics, but the most relevant were accelerated tests where the detectors were irradiated using strong gamma rays or neutron sources able to create backgrounds much more intense than the LHC ones, which, in turn, led to much higher integrated charge. In this way, educated guesses about long-term detector performance could be extrapolated from tests performed during a shorter period of time.

Signs of degradation were observed in the case of ATLAS RPC prototypes at an integrated charge of around 0.4 C/cm^2, which corresponds to slightly more than 12 years of operation at LHC. In particular, a significant reduction of the RPC maximum rate capability was measured, from almost 2 kHz/cm^2 to a few hundred hertz per centimeter square (see Figure 6.30). This was attributed not only to an increase in Bakelite resistivity but mainly to the electrical degradation of the anodic graphite coating of the RPCs. Later on, with an improved graphite coating, it was possible to gain at least a factor of 2 in lifetime (e.g, see Aielli *et al*., 2003a). Analogous tests were performed for the CMS RPCs and these showed that, at least up to an accumulated charge 0.05 C/cm^2, no significant variation in electrode resistivity (Figure 6.31) and correspondingly in efficiency (Figure 6.32) was observed. In general, all these tests reassured the community that, once suitable precautions during chamber construction were taken, these devices could last the duration needed even under the harsh conditions at the LHC experiments.

Of course, a natural question arises about whether accelerated aging tests performed with very strong sources correctly predict the aging occurring with much weaker sources, but over a much longer period of time. There were a lot of disputes on this subject, and in fact one can envisage processes which do not only depend on the integrated charge but on the time elapsed since detector construction alone. However, experimental data accumulated later during the LHC operation (see Section 5.5) indicate that, at least in the case of RPCs, the accelerated tests gave quite reliable predictions, since no evident performance degradation has been spotted up to now.

Finally, let us mention ALICE Bakelite RPCs. Their total active area is smaller, about 150 m^2, compared with the ATLAS and CMS. The RPC electrodes are made of low-resistivity Bakelite (about $3 \times 10^9\ \Omega\,cm$) to achieve the desired

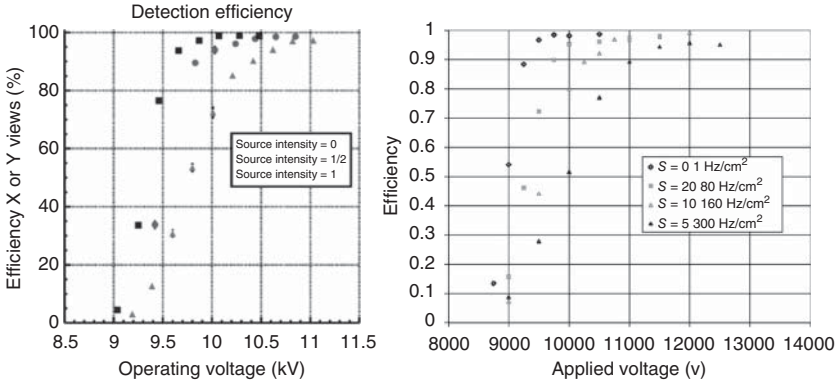

Figure 6.30 ATLAS RPC prototype efficiency versus applied voltage, at (a) an accumulated charge 0.1 C/cm^2 corresponding to 3 years of ATLAS operation and (b) at an accumulated charge 0.4 C/cm^2 corresponding to about 12 equivalent years of operation in ATLAS and then tested at the different rates indicated in the Figure. Remind that ATLAS RPCs are readout by two sets of strips perperdicular to each other (X and Y view). The source intensities in the plot at left are related to various background rates. The chambers were exposed first to a gamma ray source, to integrate the necessary dose and charge, and then efficiency was measured. (Aielli *et al*. 2002. Reproduced with permission of Elsevier.)

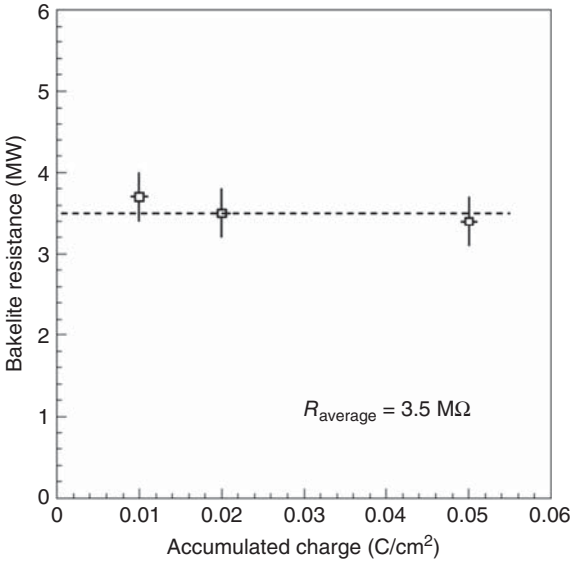

Figure 6.31 Bakelite resistance of CMS RPC prototypes as a function of the accumulated charge. (Abbrescia *et al*. 2003a. Reproduced with permission of Elsevier.)

rate capability in the heavy-ion collisions and also are coated with linseed oil to improve the smoothness of the electrode surface. The main difference in this case is related to the higher charge they operate (being in the middle between pure avalanche and streamer modes), and this, in principle, could cast some shadow on the lifetime of these devices. Nevertheless, extensive tests have shown that these RPCs show a quite stable performance up to about 50 mC/cm^2, as per the requirements for the 10-year operation program at LHC including a safety factor of 2 (Arnaldi *et al*., 2004).

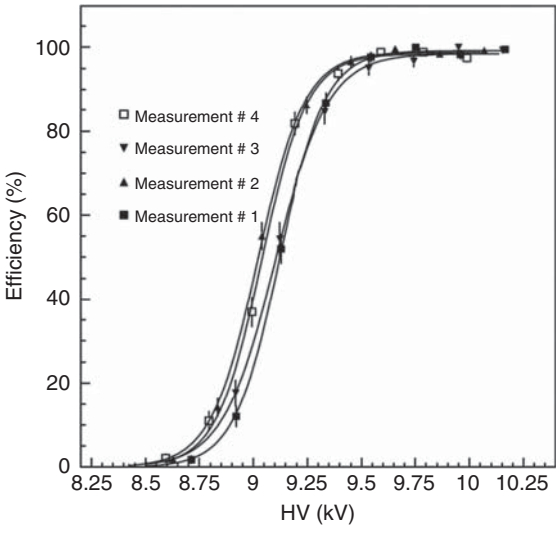

Figure 6.32 CMS RPC prototypes efficiency as a function of HV for four different measurements; in two cases, the RPCs had integrated around 0.05 C/cm^2. (Abbrescia *et al*. 2003a. Reproduced with permission of Elsevier.)

Aging factors corresponding to each measurement

Measurements #	Dose (Gy)	Charge (C/cm^2)	Fluence (γ/cm^2)
1	0	0	0
2	30	0.02	3×10^{12}
3	100	0.05	1×10^{13}
4	100	0.05	1×10^{13}

Note that all the aging tests described were performed using gamma sources. However, it was very clear from the beginning that in the LHC environment RPCs were foreseen to be exposed also to a high neutron background. In order to verify the safe operation of these detectors, neutron irradiation tests have also been carried out with RPCs at high neutron fluxes, integrating values of dose and fluence equivalent typically to 10 LHC-years (see, for instance, Abbrescia *et al*., 2003b). Before and after the irradiation, the performance of the detectors was studied with cosmic muons, showing no relevant aging effects. Moreover, no indication of damage or chemical changes was observed on the electrode surfaces, indicating that neutron radiation, in principle, should not be a source of particular damage for RPCs at LHC.

6.3.1 Temperature Effects

In order to reduce possible problems related to high environmental temperatures, a number of changes were implemented in view of the LHC experiments with respect to the production of RPCs for BaBar: the edge frames were made of polycarbonate and the same material was also used for the gap spacers. The linseed oil inner coating was made much thinner and great care was taken so that the oil was well polymerized. Also, the plate surfaces were improved using phenolic/melaminic polymer technology and smoother presses plates.

Anyhow, even for these RPCs, Bakelite resistivity shows a strong temperature dependence and decreases with increasing temperature. This is, of course, unavoidable, but should be taken into consideration since the temperature in RPC location in running experiments can be elevated due to the various reasons, for example, electronics dissipation power. This may cause the increase of the dark currents and the noise pulses rate and as a consequence a drop in the efficiency. Therefore, the RPC systems at LHC are always equipped with cooling systems for the front-end electronics.

In this framework, RPC operation (Aielli *et al*., 2003b) at a temperature interval 35 – 45°C has been carefully studied for high- and low-resistivity electrodes. Although, as expected, the counting rate and the operating current were shown to increase with temperature, an acceptable efficiency remains up to 45°C for high-resistivity (5×10^{11} Ω cm at room temperature), and up to 35°C for low-resistivity (4×10^{10} Ω cm at room temperature) electrode plates RPCs.

6.3.2 Effects of HF and Other Chemical Species

As already mentioned, in the presence of avalanches and/or streamers fluorine ionic and polar F-X components can be detected in RPC exhausted gas (Santonico, 2004). In particular, F^- radicals may be produced in connection with HF, which represents a possible cause for inner surface damaging due to its high chemical reactivity, especially if it is not efficiently removed by the gas flow and it remains for a not negligible time inside the chambers.

Furthermore, some authors believe that water not only may act as a catalyzer for HF production, but in addition HF may form a thin conductive layer on the inner surface of electrodes, increasing the ohmic component of the dark current. The HF may also harm the electrode surface damaging the polymerized oil layer.

Production of HF in RPCs has been studied in detail by several authors. One of the methods proposed was bubbling the exhaust gas from an RPC through a liquid solution known as total ionic strength adjusting buffer (TISAB), and measure the F^- ion concentration by means of an electrode probe. It is difficult to get an overall coherent picture from the results obtained, but, in general, it seems that F^- ions produced seem to be proportional to the RPC current, and that most of the F^- ions produced remain trapped inside the detector.

Of course, it is quite important to understand in detail the type of damage produced in these conditions. For these studies, generally Bakelite samples from RPCs with relatively high current are used. Typically, the visual inspection of their surface shows at least two different kinds of surface defects: “white point” (Figure 6.33a) and “orange point” (Figure 6.33b), which seem to point to different mechanisms of production and/or damage.

It is useful to analyze these spots (and compare them to undamaged Bakelite) by a powerful method called EDS, namely energy-dispersive X-ray spectrum. Basically, it relies on the excitation of well-defined atomic lines of the given atomic element using an external X-ray source. An example of such a spectrum is shown in Figure 6.34 for normal Bakelite.

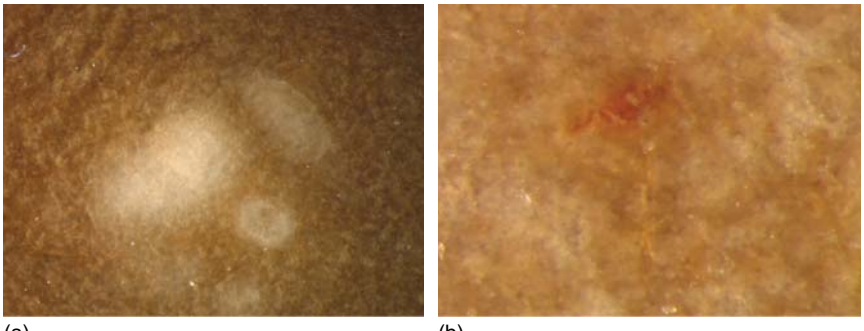

(a) (b)

Figure 6.33 Photographs of spots, appearing on the inner surfaces of oil-coated Bakelite electrodes presumably due to the chemical interaction with HF: (a) "white" spots (light gray) and (b) "orange" spots (dark gray in a black and white version of the photograph).

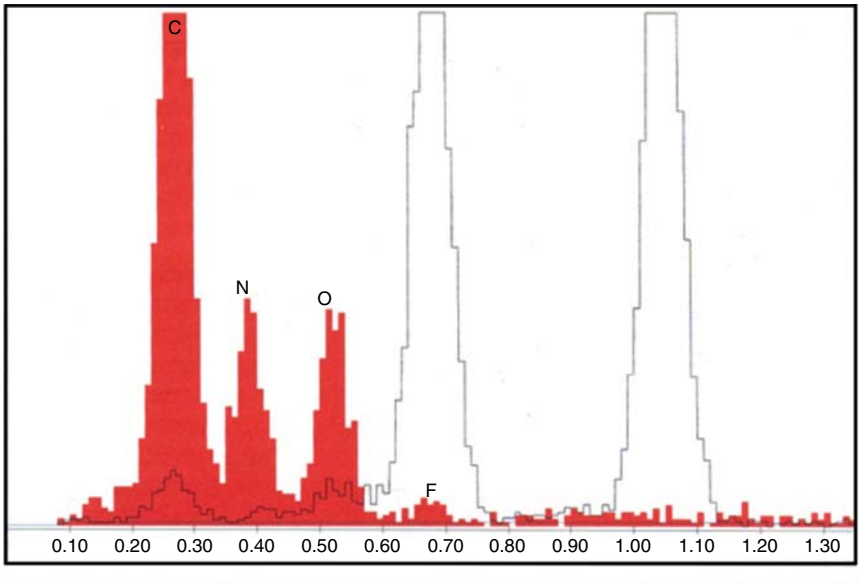

Element	Net intensity	Bkgd intensity	Intensity error	P/B
C K	9.88	0.06	3.20	164.67
N K	3.06	0.07	5.85	43.71
O K	3.28	0.08	5.65	41.00
F K	0.31	0.08	22.12	3.88

Figure 6.34 K_α X-ray EDS spectra for normal Bakelite surface (dark histograms) and from the mentioned spots (light histograms).

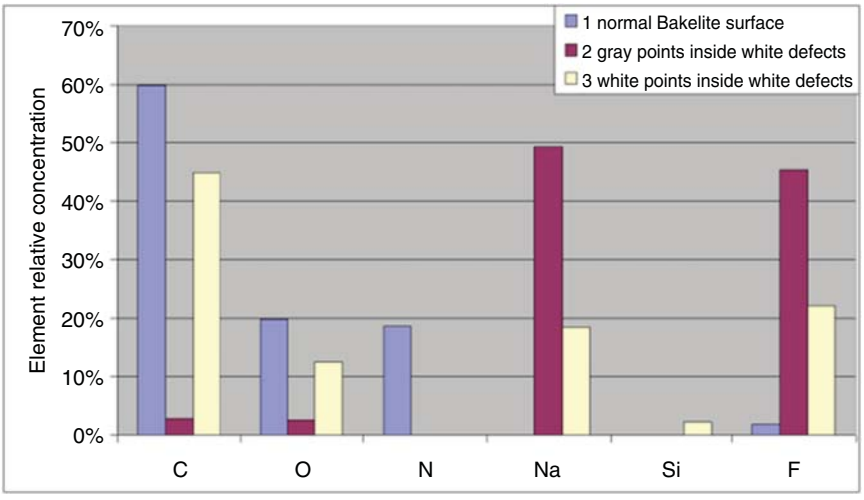

Figure 6.35 Elements relative concentration determined by the EDS method for normal Bakelite, white points and gray points inside white defects.

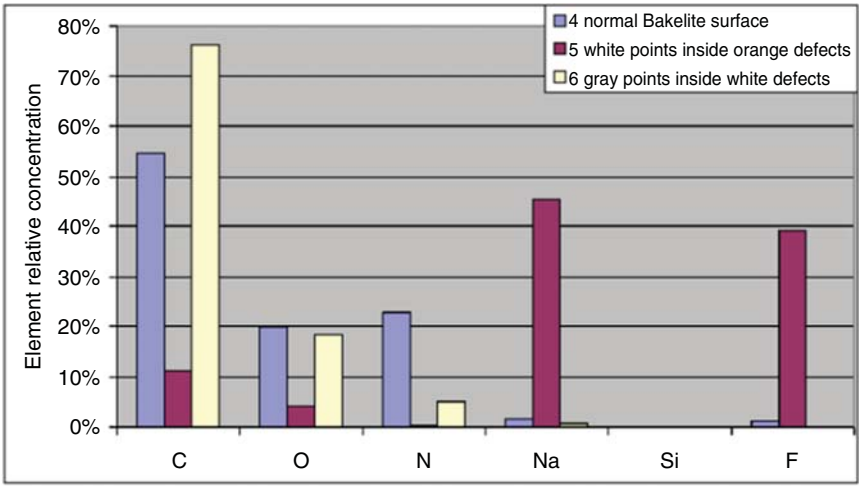

Figure 6.36 Elements relative concentration for normal Bakelite, white points located inside orange defects and gray points inside white defects.

Some results of such analysis, in terms or relative concentrations of the various chemical species, for standard Bakelite and the "white" and "orange" spots mentioned are presented in Figures 6.35 and 6.36. Though the interpretation of the results is difficult, in general, an elevated concentration of F (and Na) was recorded in all the different types of damaged regions.

Nevertheless, looking at it in perspective, one should also note that in spite of observed localized surface damaging appearing during the intense aging tests

performed in the laboratory, up to the moment, RPCs installed at the LHC experiments have demonstrated an overall good performance with no evident sign of aging degradation.

6.3.3 Other Possible Changes in Bakelite Electrodes

During the R&D phase of the LHC experiments, there was a reasonable worry that the electrical property of Bakelite might change with time, due to several other factors, for example, drying, inner charge polarization effect under the electric field, changes in conductivity due to the ionizing radiation, and so on. Some particular mechanisms were considered in Va'vra (2003).

In practice, however, it turned out that the major effect, which causes the resistivity changes, is the water evaporation from Bakelite, enhanced both by the current flowing in the electrodes and by the flux of dry gas in the chamber (e.g., see Carboni *et al*., 2004). To stabilize this effect, water vapors are added into the gas mixture used for the RPCs at LHC, and this procedure has demonstrated to be quite effective to stabilize Bakelite electrical characteristics.

6.3.4 Closed-Loop Gas Systems for LHC RPCs

One of the interesting features of the RPC systems of the experiments operating at LHC is that they use closed-loop recirculation gas systems. This is due to the facts that the gas mixture used is relatively expensive (around 60 €/m^3), the total gas volume is about several tens of cubic meters, and it is necessary to maintain a gas flow in the chambers on the order of 1 volume exchange per hour. Of course, this system has to be capable of efficiently removing any undesirable impurities, since several studies indicate a clear correlation between RPC performance and the quality of the gas mixture (see Capeans *et al*., 2011; Abbrescia *et al*., 2004).

Typically, the current drawn by the chambers can rapidly rise if the amount of pollutants in the mixture increases beyond a certain value. Furthermore, as was already mentioned, in the high radiation environment at LHC many different chemically reactive impurities are created in the RPC gas, mainly hydrocarbons, HF, F^-, Freon-type molecules, and other chemical species and they are potentially dangerous for the detector materials and even the gas system itself. The appearance of such impurities in the RPC exhaust gas, spotted using chromatographic techniques, is shown in Figure 6.37.

Therefore, the implementation of these systems requires special purifiers, combined with careful online monitoring of the gas system quality. To optimize them, one prototype was built and its operation and efficiency was checked with devoted tests with RPCs installed at CERN. After some tuning of the purifiers, the performances of these heavily irradiated RPCs showed to be unaffected in the long term, once that sufficiently low concentrations of impurities were achieved: after corrections for changes due to environmental conditions (current fluctuations induced by pressure and temperature variations), the currents drawn by the RPCs connected to the optimized closed-loop gas system proved to be very stable over the entire test period (e.g., see Altuntas *et al*., 2012).

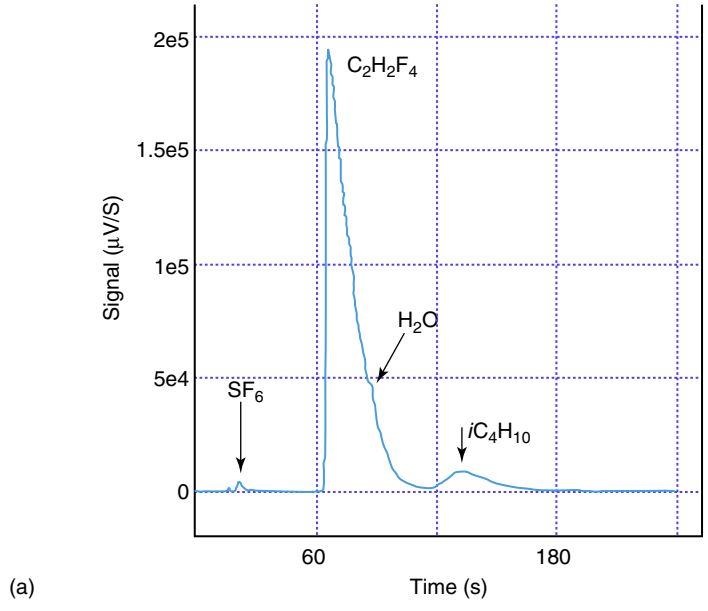

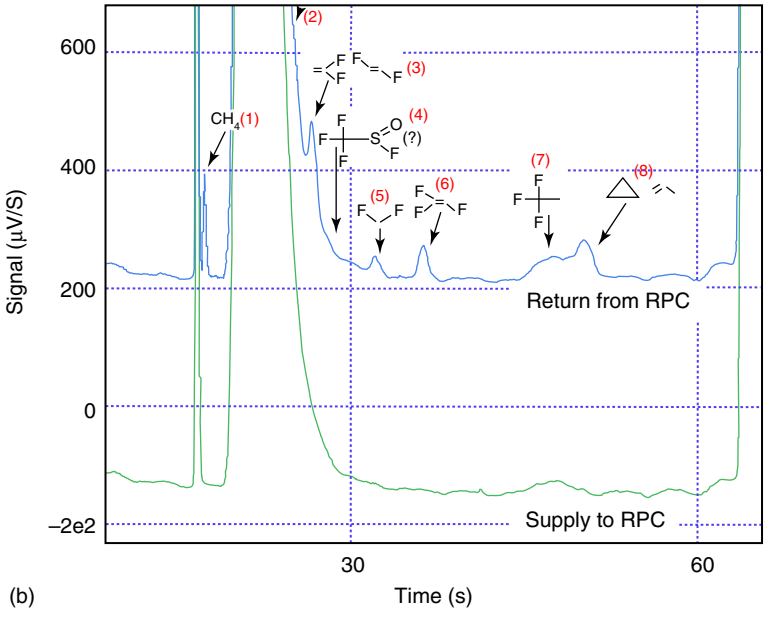

Figure 6.37 (a) Gas chromatogram of the gas mixture as it enters the RPCs. The chromatogram has been obtained using a PoraPlotU column. The main components of the RPC gas mixture are visible. (b) Zoomed area of the chromatograms of the clean gas supply and the returned mixture of irradiated RPC detectors, where pollutants show up. (Altuntas *et al*. 2012. Reprinted with permission of CERN.)

6.4 Aging Studies on Multi-Gap RPCs

Aging was, of course, also one of the main concerns for the long-term operation of multi-gap timing glass RPCs, and therefore systematic studies of possible aging effects were carried out and reported in several publications. For example, in Akindinov *et al*. (2004) and Alici *et al*. (2007), the main characteristics of RPCs, such as efficiency and time resolution, were measured with a particle beam, before and after their exposure to the gamma ray source of the CERN Gamma Irradiation Facility (GIF; see Figure 6.38). No relevant effects were observed even up to an accumulated charge around 24 mC/cm^2.

Other long-term aging studies were also performed in Gramacho *et al*. (2009). Timing RPCs, 0.3 mm gas gaps, were irradiated for 790 days of continuous operation at 300 Hz/cm^2, corresponding to an accumulated charge of more than 20 mC/cm^2. The chambers were kept under a continuous flow of 85% $C_2H_2F_4 + 10\%\ SF_6 + 5\%$ iso-C_4H_{10}, and no evidence of any systematic increase of dark current was found, even if a visual inspection revealed the existence of bluish deposits over the glass electrodes (Figure 6.39).

An interesting study aimed at the identification of the deposit components was performed by liquid extraction with organic solvents and subsequent analysis of these liquids by a gas chromatograph combined with a mass spectrometer. Since a relatively large amount of deposited material was needed for this type of analysis, also an "accelerated aging" was performed, during 1 week, changing the corresponding conditions: the environmental temperature was increased up to 50° C, the gap width was reduced to 120 μm, and the RPCs were operated in streamer (discharge) mode. These tests were made either in pure $C_2H_2F_4$ or in 90% $C_2H_2F_4 + 10\%\ SF_6$ gas mixture.

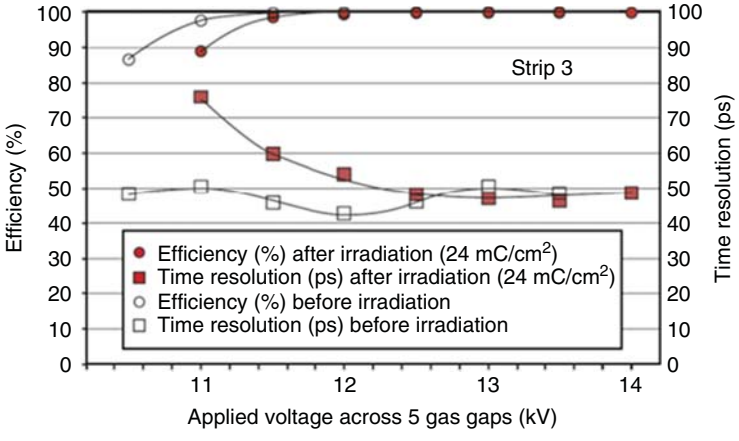

Figure 6.38 Efficiency (top) and time resolution (bottom) of an RPC before and after exposure at the CERN Gamma Irradiation Facility. The performance of the RPC before irradiation was measured using a gas mixture of 90% $C_2F_4H_2$, 5% SF_6, 5% iso-C_4H_{10}; after the irradiation, the mixture used was 93% $C_2F_4H_2$ and 7% SF_6. These "before" and "after" measurements were taken about 1 year apart. (Alici *et al*. 2007. Reproduced with permission of Elsevier.)

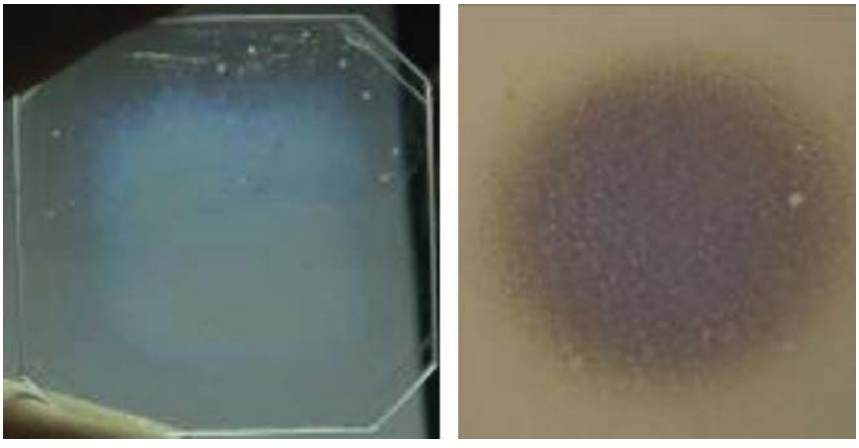

(a) (b)

Figure 6.39 (a) The deposits found on a glass cathode. The deposits were uniformly distributed over the entire active surface; some dots with higher amount of deposit could also be identified. (b) This photograph is a 60 times enlargement of one of these dots. (Gramacho *et al*. 2009. Reproduced with permission of Elsevier.)

The mass spectrum obtained for each of the peaks of the chromatogram gave information about the molecular mass of the compounds (M^+) and about the group of atoms that were present in the molecule. The interpretation of the mass spectrum is shown in Figure 6.40, where m is the mass of the compounds and z is the molecular ion charge. The identified species were mainly oligomers of tetrafluoroethylene.

In Wang *et al*. (2012b), aging studies were extended up to an accumulated charge of 50 mC/cm^2 and no degradation in RPC performance was observed. According to estimations, presented in Akindinov *et al*. (2004), this corresponds to 16 years of the ALICE-TOF RPC operation under LHC conditions.

Further chemical analysis of the outgoing gas from multi-gap resistive plate chambers (MRPCs) during tests mimicking the conditions at LHC and using gas chromatography measured concentration of fluorine under the limit of detection (Alici, 2012). It has been hypothesized that the reduced charge produced inside MRPCs and the fact that this detector is operated in pure avalanche mode with a very small gap distance (where avalanches are limited in size due to space-charge effects and streamers, if any, are small) leads also to a strong suppression of HF production by dissociation of gas molecules. Moreover, no water vapor is used in the gas mixtures employed for glass RPCs and since water vapor is generally believed to act as a catalyst for HF production, this could be an added reason for a reduced HF production in these devices.

As an overall conclusion to the material presented in this chapter, one can say that there is limited knowledge about the processes taking place in the dielectric materials used for the RPC construction and in the gas as well. Electro-chemical phenomena, for sure, play an important role and sometimes details can totally change the outcome. Nevertheless, the huge empirical experience accumulated

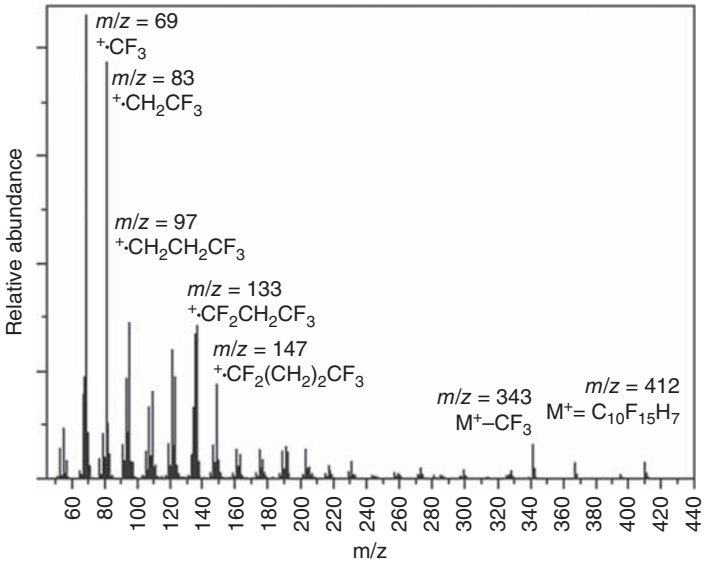

Figure 6.40 Mass spectrum, obtained from each of the peaks of the chromatogram, following the procedure outlined in the text. It gives information about the molecular mass. of the compound (M^+) and about the group of atoms that are present in the molecules. Peaks with $m/z = 69$, 83, 97, 133 and 147 corresponding to fragments CF_3^+, $CF_3CH_2^+$, $CF_3CH_2CH_2^+$ and $CF_3CH_2CF_2^+$ and $CF_3CH_2CF_2CH_2^+$ (or $CF_3CH_2CH_2CF_2^+$) were identified, as well as the M^+ peak with $m/z = 412$ and the molecular peak losing a CF_3 group ($m/z = 343$). (Gramacho *et al*. 2009. Reproduced with permission of Elsevier.)

by researches shows that, if the proper precautions are taken, these devices can be operated over extended periods without significant performance degradation.

References

Abashian, A. *et al*. (2000) The KL/μ detector subsystem for the BELLE experiment at the KEK B-factory, *Nucl. Instrum. Methods Phys. Res., Sect. A*, **449**, 112.

Abbrescia, M. *et al*. (2003a) Aging study for resistive plate chambers of the CMS muon trigger detector, *Nucl. Instrum. Methods Phys. Res., Sect. A*, **515**, 342.

Abbrescia, M. *et al*. (2003b) Neutron irradiation of RPCs for the CMS experiment, *Nucl. Instrum. Methods Phys. Res., Sect. A*, **508**, 120.

Abbrescia, M. *et al*. (2004) Study of long-term performance of CMS RPC under irradiation at the CERN GIF, *Nucl. Instrum. Methods Phys. Res., Sect. A*, **533**, 102.

Abbrescia, M. *et al*. (2008) Results about HF production and bakelite analysis for the CMS Resistive Plate Chambers, *Nucl. Instrum. Methods Phys. Res., Sect. A*, **594**, 140, 147.

Aielli, G. *et al*. (2002) RPC ageing studies, *Nucl. Instrum. Methods Phys. Res., Sect. A*, **478**, 271.

Aielli, G. *et al*. (2003a) Further advances in aging studies for RPCs, *Nucl. Instrum. Methods Phys. Res., Sect. A*, **515**, 335.

Aielli, G. *et al*. (2003b) RPC operation at high temperature, *Nucl. Instrum. Methods Phys. Res., Sect. A*, **508**, 44.
Aielli, G. *et al*. (2006) Fluoride production in RPCs operated with F-compound gases, *Nucl. Phys. B (Proc. Suppl.)*, **158**, 143–148.
Akindinov, A.V. *et al*. (2004) Study of gas mixtures and ageing of the multigap resistive plate chamber used for the Alice TOF, *Nucl. Instrum. Methods Phys. Res., Sect. A*, **533**, 93.
Alici, A. (2012) Status and performance of the ALICE MRPC-based Time-Of-Flight detector, *JINST*, **7**, P10024.
Alici, A. *et al*. (2007) Aging and rate effects of the Multigap RPC studied at the Gamma Irradiation Facility at CERN, *Nucl. Instrum. Methods Phys. Res., Sect. A*, **579**, 979.
Altuntas, E. *et al*. (2012) Long-term study of optimal gas purifiers for the RPC systems at LHC, PH-EP-Techn Note 2012-001, 13/01/2012.
Alviggi, M. *et al*. (2003) Results on long-term performances and laboratory tests of the L3 RPC system at LEP, *Nucl. Instrum. Methods Phys. Res., Sect. A*, **515**, 328.
Anulli, F. *et al*. (2003) Performances of RPCs in the BaBar experiment, *Nucl. Instrum. Methods Phys. Res., Sect. A*, **515**, 322.
Arnaldi, R. *et al*. (2004) Aging tests and chemical analysis of Resistive Plate Chambers for the trigger of the ALICE dimuon arm, *Nucl. Instrum. Methods Phys. Res., Sect. A*, **533**, 112.
Ashwajeet, J.S. *et al*. (2015) Electrical conduction in Borophosphate glasses doped with CoO and Li_2O, *Res. J. Mater. Sci.*, **3** (4), 1–6.
Bailey, P. *et al*. (2008) Quality Assurance Tests on Bakelite Produced for Station 3, Station 1 Prototype, and Station 1 RPCs of the PHENIX Forward Upgrade, unpublished report.
Band, H.R. *et al*. (2008) Study of HF production in BaBar Resistive Plate Chambers, *Nucl. Instrum. Methods Phys. Res., Sect. A*, **594**, 33–38.
Bouclier, R. *et al*. (1996) Ageing of microstrip gas chambers: problems and solutions, *Nucl. Instrum. Methods Phys. Res., Sect. A*, **381**, 289.
Braunger, M.L. *et al*. (2012) Electrical conductivity of silicate glasses with tetravalent cations substituting Si, *J. Non-Cryst. Solids*, **358**, 2855–2861.
Braunger, M.L. *et al*. (2014) Electrical conductivity of Ag-Na ion exchanged soda-lime glass, *Solid State Ionics*, **265**, 55–60.
Brill, R.H. (1962) A Note on the Scientist's Definition of Glass, *J. Glass Stud.*, **4**, 127.
Capeans, M. *et al*. (2011) Long term validation of the optimal filters configuration for the Resistive Plate Chambers gas system at the Large Hadron Collider experiments, Proceedings IEEE NSS7MIC, p. 1775.
Carboni, G. *et al*. (2004) Final results from an extensive ageing test of bakelite Resistive Plate Chambers, *Nucl. Instrum. Methods Phys. Res., Sect. A*, **533**, 107.
Crotty, I. *et al*. (1993) Investigation of resistive parallel plate chambers, *Nucl. Instrum. Methods Phys. Res., Sect. A*, **329**, 133.
Dai, T. *et al*. (2014) Low resistance bakelite RPC study for high rate working capability, *JINST*, **9**, C11013.
Deppner, I. *et al*. (2014) Report at the 11 Workshop on Resistive plate chambers, Frascati, http://agenda.infn.it/conferenceTimeTable.py?confId=3950 (accessed 30

October 2017); Deppner I. *et al* (2014) The CBM Time-of-Flight wall – a conceptual design, JINST 9 C10014.
El-Desoky, M.M. *et al*. (2003) DC conductivity and hopping mechanism in V_2O_5-B_2O_3-BaO glasses, *Phys. Status Solidi A*, **195** (2), 422–428.
Ezz Eldin, F.M. *et al*. (1998) Electrical conductivity of some alkali silicate glasses, *Mater. Chem. Phys.*, **52**, 175–179.
Francke, T. *et al*. (2003) Potential of RPCs for tracking, *Nucl. Instrum. Methods*, 83.
Gramacho, S. *et al*. (2009) A long-run study of aging in glass timing RPCs with analysis of the deposited material, *Nucl. Instrum. Methods Phys. Res., Sect. A*, **602**, 775.
Haddad, Y. *et al*. (2013) High rate resistive plate chamber for LHC detector upgrades, *Nucl. Instrum. Methods Phys. Res., Sect. A*, **718**, 424–426.
Hench, L.L. and West, J.K. (1990) *Principles of Electronic Ceramics*, John Wiley & Sons, Inc., New York.
Horst, S. (1990) *Glass Nature, Structure and Properties*, Springer, New York.
Jaiswal, M.K. *et al*. (2012) Study of Surface Resistivity of Resistive Plate Chamber Detectors, *Proc. DAE Symp. Nucl. Phys.*, **57**, 968.
Kubo, T. *et al*. (2003) Study of the effect of water vapor on a glass RPC with and without freon, *Nucl. Instrum. Methods Phys. Res., Sect. A*, **508**, 50.
Laso Garcia, A. *et al*. (2016) High-rate timing resistive plate chambers with ceramic electrodes, *Nucl. Instrum. Methods Phys. Res., Sect. A*, **818**, 45.
Lopes, L. *et al*. (2006) *Nucl. Phys. B (Proc. Suppl.)*, **158**, 66–70.
Lu, C. (2005) RPC Experience: Belle, BaBar and BESIII, http://www.slac.stanford.edu/econf/C0508141/proc/pres/ALCPG1001_TALK.PDF (accessed 30 October 2017).
Lu, C. (2006) RPC Experience: Belle, BaBar and BESIII, SLAC-pub-11744 March 2006, http://www.slac.stanford.edu/cgi-wrap/getdoc/slac-pub-11744.pdf (accessed 30 October 2017).
Lu, C. (2009) RPC electrode material study, *Nucl. Instrum. Methods Phys. Res., Sect. A*, **602**, 761.
Lu, C. *et al*. (2012) Aging study for the BESIII-type RPC, *Nucl. Instrum. Methods Phys. Res., Sect. A*, **661**, S226.
Morales, M. *et al*. (2012) Aging and Conductivity of Electrodes for High Rate tRPCs from An Ion Conductivity Approach POS (RPC 2012) 024.
Moulson, A.J. and Herbert, J.M. (2003) *Electroceramics: Materials, Properties*, 2nd edn, John Wiley & Sons, Inc.
Neog, H. *et al*. (2016) Building of a Bakelite resistive plate chamber prototype, in *XXI DAE-BRNS High Energy Physics Symposium. Springer Proceedings in Physics*, vol. **174** (ed. B. Bhuyan), Springer, Cham.
Parkhomchuk, V.V. *et al*. (1971) A spark counter with large area, *Nucl. Instrum. Methods*, **93**, 269.
Sakai, H. *et al*. (2003) Study of the effect of water vapor on a resistive plate chamber with glass electrodes, *Nucl. Instrum. Methods Phys. Res., Sect. A*, **484**, 153.
Santonico, R. (2004) RPC understanding and future perspectives, *Nucl. Instrum. Methods Phys. Res., Sect. A*, **533**, 1.
Shelby, J.E. (1997) *Introduction to Glass Science and Technology*, The Royal Society of Chemistry, Cambridge, UK.

Song, H. *et al*. (2012) Development of 1mm low resistivity bakelite plate for thin-gap RPC detector. Presented at the XI workshop on Resistive Plate Chambers and Related Detectors (RPC 2012 Workshop) @ Frascati, Italy February 7, 2012.

Souquet, J.-L. *et al*. (2010) Charge carrier concentration and mobility in alkali silicates, *J. Chem. Phys.*, **132**, 034704.

Tonazzo, A. (2002) Ageing measurements on glass RPCs. Conference Record, 2002 IEEE NSS Symposium, vol. **1**, 2002, pp. 605–609.

Va'vra, J. (2003) Physics and chemistry of aging – early developments, *Nucl. Instrum. Methods Phys. Res., Sect. A*, **515**, 1–14.

Va'vra, J. (2012) Some comments about possible problems of well-made RPCs and remediation of the old RPCs, BaBar Muon Detector Workshop, November 14, 2002, https://www.slac.stanford.edu/BFROOT/www/Detector/IFR/IfrUpgradeReview2002/021114Workshop/07.Vavra.RPCProblems.pdf (accessed 30 October 2017).

Wang, J. (2012a) Conceptual design of the CBM TOF wall with real size high rate MRPC modules based on the newly developed Chinese doped glass, Talk given during. The 11 Workshop on Resistive Plate Chambers and Related Detectors, Frascati, 2012 (see also https://pos.sissa.it/159/015/).

Wang, J. *et al*. (2010) Development of multi-gap resistive plate chambers with low-resistive silicate glass electrodes for operation at high particle fluxes and large transported charges, *Nucl. Instrum. Methods Phys. Res., Sect. A*, **621**, 151–156.

Wang, Y. *et al*. (2012b) Aging test of a real-size high rate MRPC for CBM-TOF wall, *JINST*, **7**, P110117.

Xie, Y. *et al*. (2009) First results of the RPC commissioning at BESIII, *Nucl. Instrum. Methods Phys. Res., Sect. A*, **599**, 20.

7

Advanced Designs: High-Rate, High-Spatial Resolution Resistive Plate Chambers

In this chapter we speak about some issues related to rate capability, which has been–and is presently-one of the hot topics in the resistive plate chambers (RPCs) community, and which needs to be tackled by a deep understanding of the physics processes involved and specific technological solutions. In addition, we also speak about RPCs built to obtain sub-millimeter spatial resolution, which is another topic recently getting more and more relevant, in particular with a view of possible applications outside the field of high-energy physics.

7.1 The Issue of Rate Capability

Resistive gaseous detectors are, in general, intrinsically rate limited. This drawback is related to the use of resistive materials which, on the other side, guarantees the important advantage of spark protection, typical of this detector species.

What basically happens has been already outlined: when an avalanche subsequent to the passage of an ionizing particle reaches one or both resistive electrodes, it neutralizes part of the surface polarization charge, consequently reducing the local electric field in the gas. Only a limited part of the electrodes is discharged in relation with the passage of an ionizing particle (and subsequent avalanches or streamers), while the rest remains basically untouched.

The time needed for the electrodes to be charged up again by an external supply depends on the time constant of the detector, that is, the product of its equivalent resistance and capacitance (see, for instance, Figure 1.15 or Figure 7.7). While the detector capacitance depends on its geometry, its equivalent resistance derives from the resistivity of the specific materials used, which, in principle, can span over several orders of magnitude: for instance, glass used to build RPCs may have a resistivity between 10^{10} and 10^{13} Ω cm. Therefore, with the same detector layout, one can face time constants ranging over several decades.

If another ionizing particle happens to cross the detector and enters the gas where the previous one has just passed, an electric field lower than the usual will be found, and this might be not strong enough to give rise to multiplication processes; in this case, the particle will go virtually undetected. From a macroscopic point of view, we expect that, as a consequence, the efficiency of a resistive

Resistive Gaseous Detectors: Designs, Performance, and Perspectives, First Edition.
Marcello Abbrescia, Vladimir Peskov, and Paulo Fonte.

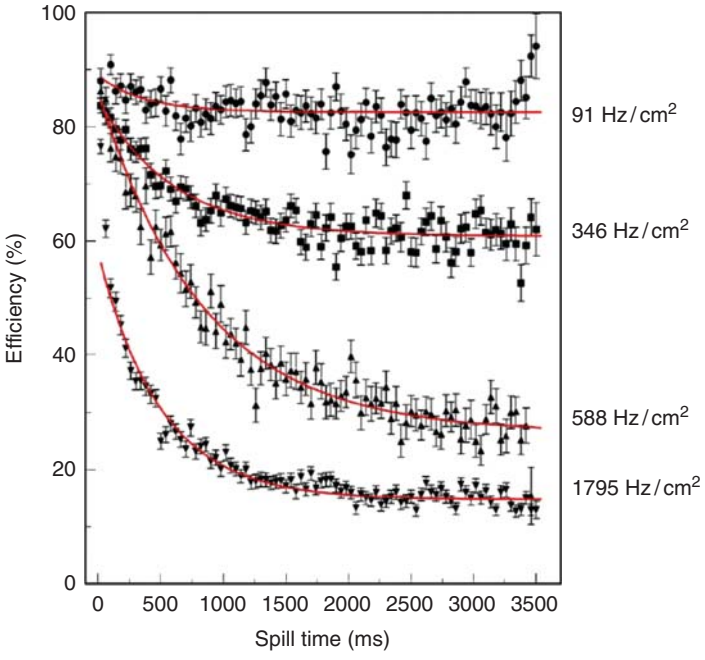

Figure 7.1 Minimum ionizing particle (MIP) detection efficiency as a function of spill time for various beam intensities. The curves are fits to the data using the sum of an exponential and a constant. Chamber were operated in avalanche mode. (From Bilki *et al*. 2009.)

gaseous detector will progressively deteriorate as the rate of impinging particles exceeds a certain value.

This effect is well known, and, for instance, it has been experimentally observed for RPCs in the very first years of 1990s. A more recent, but very nice, observation of this effect is reported in Figure 7.1, obtained with a glass 20×20 cm^2 RPC prototype (Bilki *et al*., 2009); here, the efficiency for ionizing particles is reported, as a function of time during a beam spill, for various beam intensities. Average efficiency is clearly seen to be decreasing as flux increases and, moreover, some time to reach the steady condition is needed, pointing out that this is an electrode discharge process that needs, in this particular case, almost 1 s to fully develop.

Usually, an estimate of the rate capability is performed by starting from a suitable value of the operating voltage, with the detector efficiency in plateau, and increasing the particle flux until efficiency becomes lower than, say, 90%, while keeping the applied voltage constant. The value of this flux is taken as the rate capability estimate (see all the remaining figures in this section).

At the beginning of the 1990s, rate limitation was a serious obstacle to the use of RPCs for experiments at high luminosity accelerators. Therefore, even if a limited rate capability is a common feature of all resistive gaseous detectors, in the following we concentrate on RPCs, since many studies have been performed to overcome this problem.

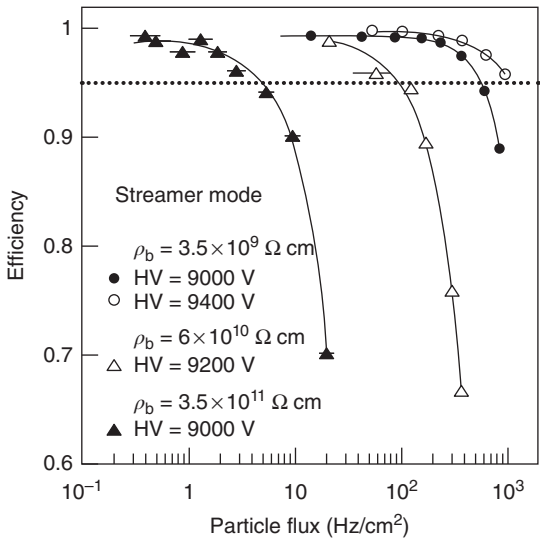

Figure 7.2 Efficiency versus incident flux for Bakelite RPC prototypes of different resistivity, operated in streamer mode; decreasing the resistivity results in a rate capability increase. (Arnaldi *et al*. 2000. Reproduced with permission of Elsevier.)

Rate capability, of course, is expected to be lower when the detector time constant is larger. Therefore, a natural way to tune rate capability is to use materials with different resistivity; an example of this is shown in Figure 7.2. Many studies about this point have been and are still being carried out (see Affatigato *et al*., 2015 and Figure 7.3 for a recent study); a more detailed discussion about this issue is done later on in this chapter.

The operating mode plays an important role in determining rate capability of a resistive gaseous detector. When streamers are developed in the gas, the amount of charge carried onto the electrode surfaces can arrive up to several hundreds of picocoulomb, much higher than operating the same devices in avalanche mode. This has the consequence to cause a more relevant reduction of the local electric field, and to discharge larger portions of the electrodes. Therefore, devices operated in streamer mode are expected to show a much lower rate capability than the same devices operated in avalanche more.

As a matter of fact, the RPCs operated in streamer mode used at the beginning of the 1990s were characterized by a rate capability around 100 Hz/cm^2, at best, generally not enough for operation in many parts of the muon systems of the experiments designed for the Large Hadron Collider (LHC) (see again Figure 7.2, which refers to RPCs operated in streamer mode). As it was mentioned in the previous Chapter, this problem was overcome using the same devices but operated in avalanche mode. In fact, the RPCs now in the muon systems of A Toroidal LHC Apparatus (ATLAS), A Large Ion Collider Experiment (ALICE) and Compact Muon Solenoid (CMS) bear a strong resemblance, from the detector point of views to the ones described in the original papers by Santonico and Cardarelli (1981) and Cardarelli *et al*. (1988). The price to pay is transferring part of the needed amplification from the gas to the front-end electronics, which has to be sufficiently sensitive and sophisticated. The importance of this step, and the more

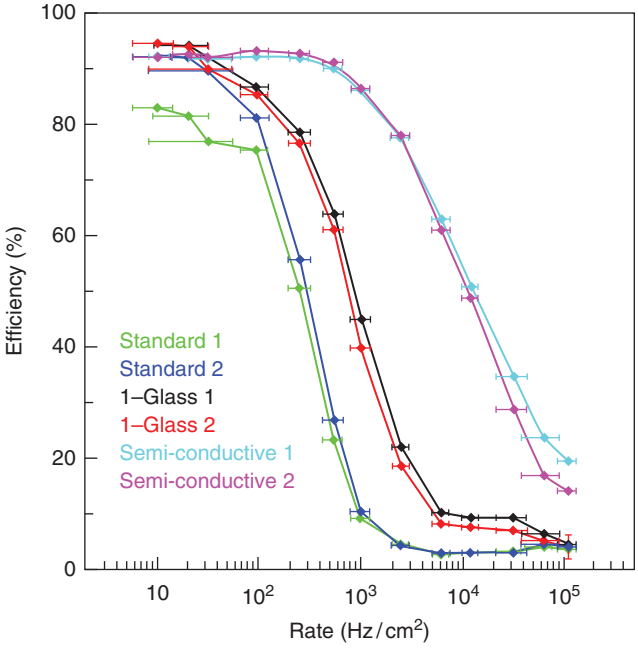

Figure 7.3 Rate capability of various glass RPC prototypes, characterized by different electrode resistivity; "Standard 1" and "Standard 2" refer to two prototypes with two electrodes made from soda-lime float glass plates 1.1 mm thick; "1-Glass" refer to two prototypes with one electrode made from the same glass, and the gas volume delimited on the other side by anode readout board. the highest rate capability is achieved with a kind of "semi-conductive" glass from Schott Glass Technologies Inc., model S8900. (Affatigato *et al*. 2015. Reproduced with permission of IOP Publishing.)

advances electronics that had to be developed, have been described in Section 4.7 of this book. An interesting study about rate capability in streamer and avalanche mode is reported in Crotty *et al*. (1994); one of the most significant results, taken from this paper, has already been shown in Figure 3.22 of this book. Similar results are reported in Figure 7.4, where rate capability of RPCs almost identical to the ones of Figure 7.2 is shown, but when operated in avalanche mode.

An important point to stress is that rate capability of RPCs is found to be different, even order of magnitudes, when it is measured using a point-like irradiation of the detector (as it happens with a collimated particle beam) with respect to when it is measured using uniform irradiation. Basically, this is due to the fact that, in order to charge up again a portion of the resistive electrodes which has been discharged by an avalanche or streamer, electric currents must flow, coming either from the graphite layers (connected to the power supply) through the electrodes or from other zones of the electrodes which are still charged; typically, this second kind of current flows at the surface of the resistive electrodes.

In the case of point-like irradiation, indeed, both these currents can occur at the same time. But when the detector is uniformly irradiated, all points onto the same

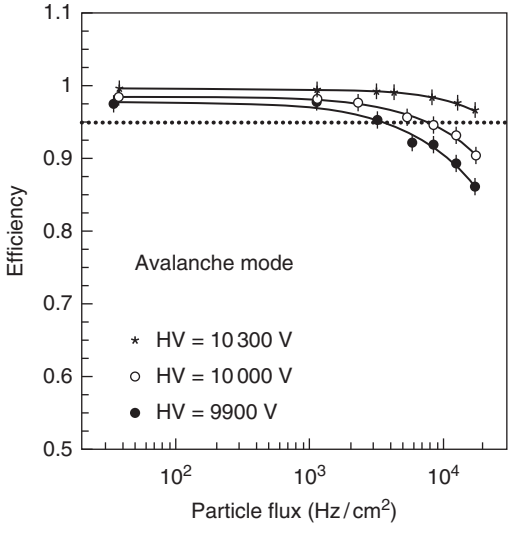

Figure 7.4 Efficiency versus the local particle flux, for RPCs very similar to the ones in Figure 7.2, but operated in avalanche mode; the rate capability increase is evident. (Arnaldi *et al*. 2000. Reproduced with permission of Elsevier.)

resistive electrode surface are on the average at the same potential, (since they are all discharged more or less of the same amount), and this strongly reduces the occurrence of surface currents. This recharging process is not as effective as in the first case, with a consequent reduction in rate capability. The amount of the reduction depends on the ratio between bulk and surface resistivity, and it is not easy to estimate. Nevertheless, several experimental confirmations of this effect have been found, one of them shown in Figure 7.5, taken from Crotty *et al*. (1994).

This is the reason why most reliable rate capability measurements are performed where an uniform detector irradiation is available. One common choice in the 1990s and 2000s was the already mentioned Gamma Irradiation Facility (GIF) at CERN where detectors could be simultaneously exposed to the photons from a ^{137}Cs source and to high-energy particles from the X5 beam line in SPS West Area (see Agosteo *et al*., 2000). Suitable filters in front of the ^{137}Cs source were used to modulate the photon flux impinging on the detectors under study, creating different rate conditions (see Figure 7.6). Detector performance was studied by means of its response to the particles from the beam. A new version of GIF, called GIF++, located at the CERN H4 beam line and equipped with a more intense source, is in operation since 2014, and here the detectors for the high-luminosity phase of LHC are currently tested.

7.2 The "Static" Model of RPCs at High Rate

One approach to understand in a more quantitative way what happens in RPCs at high rate has been described in Santonico (2014), and successfully applied in real conditions (Carboni *et al*., 2003).

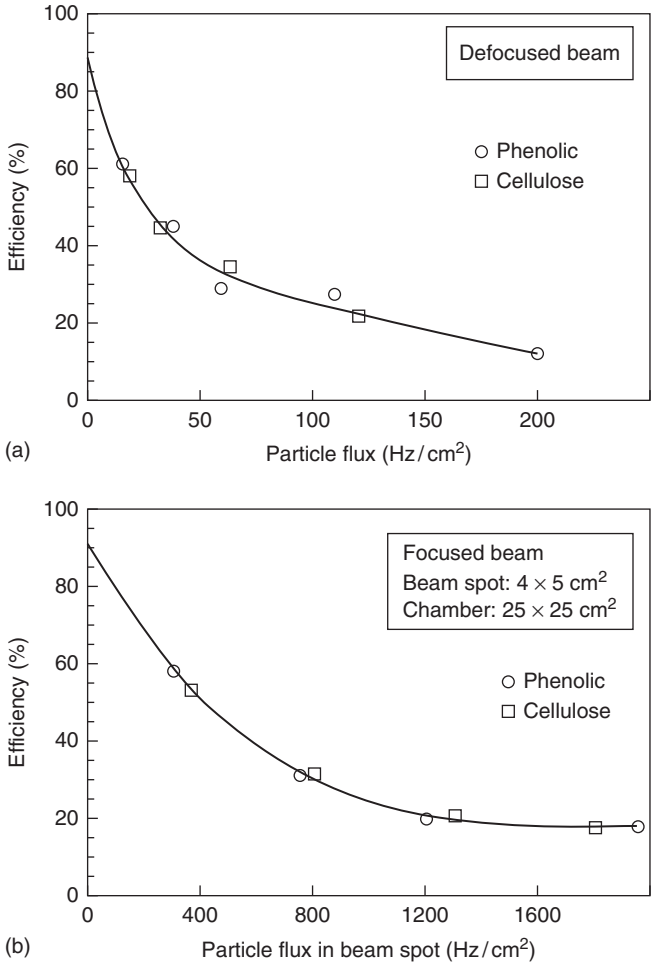

Figure 7.5 Efficiency versus particle flux for the same 25×25 cm^2 RPC but measured in two different conditions: (a) using a focused beam, with a 4×5 cm^2 beam spot and (b) using a defocused beam, and achieving almost a uniform beam irradiation on the whole chamber. In this particular case, almost an order of magnitude difference in rate capability between point-like irradiation with respect to uniform irradiation is measured. (Crotty *et al*. 1993. Reproduced with permission of Elsevier.)

Basically, the approach is not to consider all the complex processes outlined, but take into account just the ohmic drop ΔV_{el} due to the current I which is flowing through the electrodes.

The voltage ΔV_{gap} across the gas gap is given by $\Delta V_{\mathrm{gap}} = \Delta V_{\mathrm{appl}} - \Delta V_{\mathrm{el}}$, where ΔV_{el}, in explicit form, can put as

$$\Delta V_{\mathrm{el}} = R_{\mathrm{b}}\, I = \rho_{\mathrm{b}} \frac{2d}{S} \Phi\, S \langle q_{\mathrm{aval}} \rangle = 2\, \rho_{\mathrm{b}}\, d\, \Phi \langle q_{\mathrm{aval}} \rangle \tag{7.1}$$

where R_{b} is the electrode resistance, ρ_{b} is the resistivity of the electrodes material, d is the thickness of each plate (here we consider the simplest case, i.e., single gap

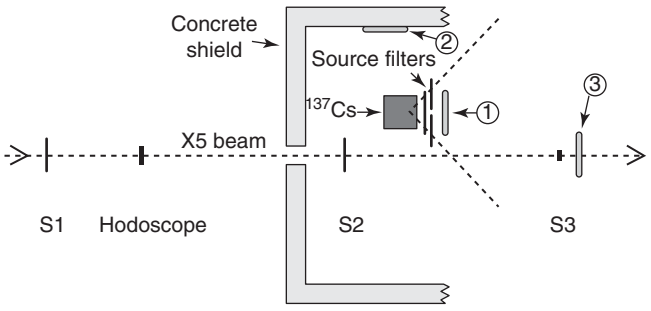

Figure 7.6 Schematic view of the GIF at CERN, where detectors could be uniformly irradiated with the photons from a ^{137}Ce source and their performance measured with the particles from the X5 beam line. (Carboni *et al*. 2003. Reproduced with permission of Elsevier.)

RPCs), S their surface, Φ the flux of impinging particles (in Hz/cm^2), and $\langle q_{\text{aval}} \rangle$ the average charge in the gas gap related to the avalanche (or streamer) processes associated to the impinging particles.

Under static conditions, ΔV_{appl} roughly equals ΔV_{gap}; at high rate, on the contrary, ΔV_{el} may be no more negligible with respect to ΔV_{appl} and, since the amplification processes depend on ΔV_{gap}, this can be significantly reduced, hence an efficiency decrease.

This approach, usually called "static" in the sense clarified earlier, is quite simple from the conceptual point of view, but has the disadvantage that it is not possible to directly compute RPC rate capability. One has to measure the efficiency curve at low rate, then compute ΔV_{gap} at the desired rate by using the abovementioned formula, and infer the efficiency at that rate from the efficiency measured at low rate at the same ΔV_{gap} just computed, taking into account that ΔV_{appl} could be, in principle, quite different at low and high rate. Basically, ΔV_{gap} is the driving parameter, so that plotting the efficiency curves taken at different rates, versus ΔV_{gap} (and not ΔV_{appl}), should make them coincide all.

The process is utterly complicated by the fact that I and R_{b} are not a priori known, and must be measured somehow; while I can be directly measured on the power supply, R_{b} must be inferred from other measures. One way to measure R_{b} is by a fit to the linear part of the drawn as a function of the operating voltage.

The efficiency curves measured for a 50×50 cm^2 RPC built in the framework of the activities related to the aging studies of the muon system of the LHCb experiment at different rates are shown in Figure 7.7. They are plotted as a function of the applied voltage ΔV_{appl} and they show the characteristic behavior expected in these cases: efficiency plateaus are lower and lower with increasing rate, showing a limited rate capability. Moreover, the efficiency curves, when plotted versus ΔV_{appl}, progressively shift toward the right, indicating that ΔV_{gap} starts becoming significantly lower than ΔV_{appl}, due to the ohmic drop through the electrodes. On the other hand, when the same experimental data are plotted versus ΔV_{gap}, computed with the procedure outlined, all curves coalesce in a single one.

Unfortunately, using this model it is not possible a priori (i.e., without measurements) to infer direct limits on the rate capability of a certain device. Anyhow, for sure it can be used to make deductions on how rate capability can be, in general,

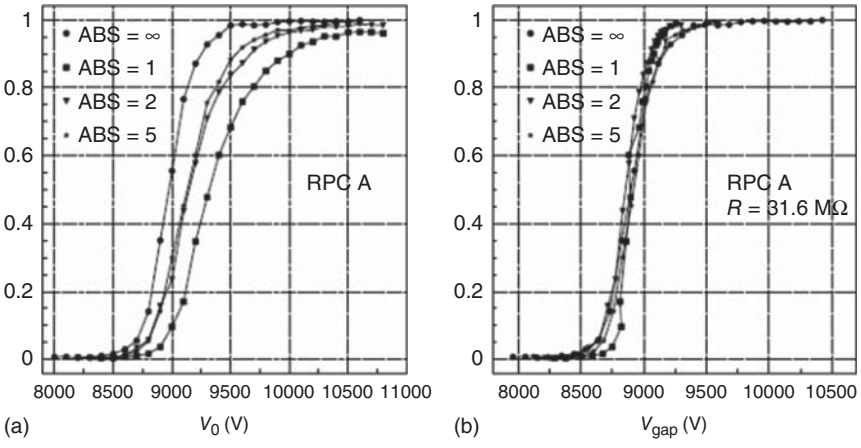

Figure 7.7 (a) Efficiency versus ΔV_{appl} for a 50×50 m^2 RPC, filled with a $C_2H_2F_4/C_4H_{10}/SF_6$ mixture in 95/4/1 proportions, measured at different rates. In this case, the measure was performed at CERN GIF, with the irradiation provided by photons coming from a ^{137}Cs source. The absorption factors (ABS) indicated in the figure refer to the filters placed in front of the source; higher ABS corresponds to a lower photon flux. (b) The same data but plotted versus $\Delta V_{gap} = \Delta V_{appl} - R\,I$ using the value of R determined by a fit of the I versus ΔV_{appl} current plot. (Carboni *et al*. 2003. Reproduced with permission of Elsevier.)

increased. If, given a certain flux of impinging particles, ΔV_{el} has to be kept as low as possible, the possibilities evidenced by Eq. (2.1) are to reduce either the electrode resistivity ρ, or their thickness d, or the average induced charge $\langle q_{aval} \rangle$, or whatever combination of these factors.

Of course, reducing electrode resistivity within some reasonable limits is the most obvious way to increase rate capability. Both for Bakelite and glass, resistivity ranges over various orders of magnitude, depending on the specific materials used and the manufacturing procedure. Bakelite used at the CERN LHC experiments is characterized by a resistivity slightly higher than 10^{10} Ω cm, and, in principle, it is possible to reduce this value by a factor 5–10 with minor changes in the production techniques. As a matter of fact, this is one of the paths currently followed in the framework of the upgrade of the muon systems of the ATLAS and CMS experiment, where RPCs with a rate capability around 2 kHz/cm^2 are required. For what concerns glass, new types of low-resistivity glasses are an interesting field of investigations, and some studies on this subject have been cited in Chapter 6.

Moreover, electrode thickness for the Bakelite RPCs used at the LHC experiments is 2 mm, which, for future chambers, could be, in principle, reduced down to around 1 mm (beyond which probably issues related mechanical rigidity could come into play), providing up to a factor 2 reduction for ΔV_{el}, with a subsequent increase (not easy to evaluate) in rate capability. Note that reducing electrode thickness beyond a certain value would imply a reduction of quenching properties due to local capacitance increase (see Figure 1.15). Other geometrical factors, like, for instance, gap thickness, seem not to play any role at all, since they do not appear in Eq. (7.1); this is not completely true, as we see later on in this chapter.

Finally, a reduction of $\langle q_{\text{aval}} \rangle$ is also a way to increase RPC rate capability. However, since a smaller $\langle q_{\text{aval}} \rangle$ also means smaller induced charge on readout electrodes $\langle q_{\text{ind}} \rangle$, which therefore could become at some point lower than the readout electronic threshold $\langle q_{\text{thr}} \rangle$. This has to be associated with a redesign of the front-end electronics, in a way much similar to what was done in the 1990s, when, passing from the streamer to the avalanche operation mode, part of the gain was transferred from the gas to the front-end electronics. It is quite an effective approach, however, since it reduces also issues related to detector aging, typically proportional to the charge integrated during the detector lifetime, and in fact this is another path that will be likely pursued for the upgrade of some of the muon systems at the LHC experiments.

7.3 The "Dynamic" Model of RPCs at High Rate

What really happens in an RPC at high rate is, of course, much more complicated than what was previously described. To have an idea, the evolution in time of $\Delta V_{\text{gap}}(t)$ in an RPC is plotted in Figure 7.8; in the same plot also the values corresponding to ΔV_{appl} and ΔV_{gap} computed using the static model are reported, for comparison. The picture shows sudden variations of $\Delta V_{\text{gap}}(t)$, and interesting

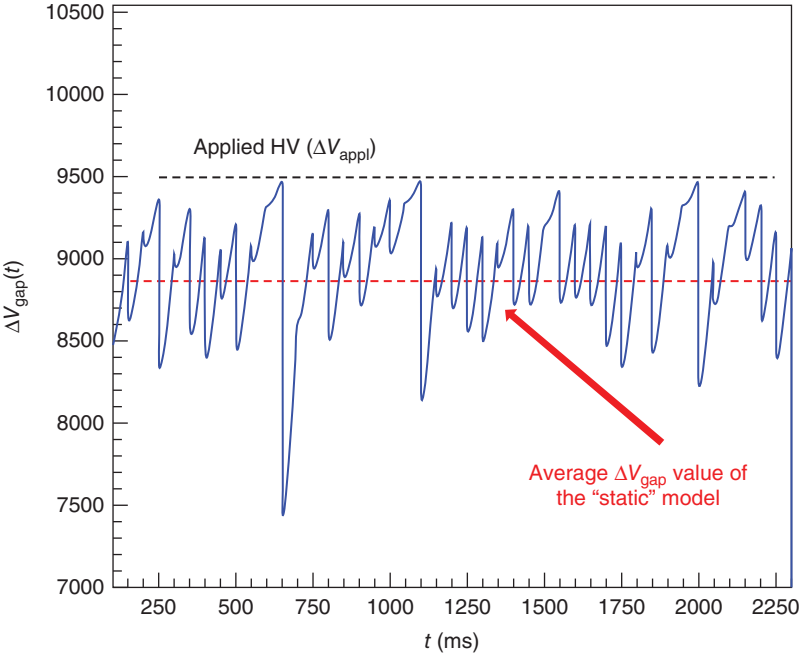

Figure 7.8 The evolution in time of $\Delta V_{\text{gap}}(t)$, that is, the instantaneous voltage drop between the two RPC electrode plates. In this particular case, the rate of particles impinging was simulated to be 20 Hz; since the area of the considered cell was 1 mm^2, this corresponds to, roughly, 2 kHz/cm^2. (Abbrescia 2016. Reproduced with permission of IOP Publishing.)

correlations between the amplitude of subsequent signals, all aspects which are completely lost when performing the drastic averages typical of the static model.

If a deeper understanding of what really happens in an RPC at high rate is to be achieved, one has to start using the basic equations describing the physics processes taking place in these devices, that is: primary ion-electron pair generation, electron migration and avalanching, and the corresponding signal induction on readout electrodes, that we already described in Chapters 3 and 4. In particular, one has to refer to the charge contained in an avalanche as computed by means of Eqs. 3.8 and 3.9, modified by the effects of space charge which can be quantitatively described in a simple way by the approximations summarized in Eqs. 4.6 and 4.7.

We can again use the simple circuit shown in Figure 1.15 to model the zone on the electrodes around an avalanche; note that now this circuit represents just a small portion with area S_a of the plates, in correspondence of the footprint of the avalanche disk as it touches the anode. At the start, the voltage across the gap ΔV_{gap} is equal to the applied external one ΔV_{appl} and the charge q_{el} on C_g is given by

$$q_{\text{el}} = \varepsilon_0 \frac{S_a}{g} \Delta V_{\text{gap}} \tag{7.2}$$

where g, as usual, is the gap thickness.

In relation with the passage of an ionizing particle, C_g is partially discharged, and the actual voltage across the gap is reduced proportionally to the total charge q_{aval} contained in the avalanches impinging onto the Bakelite plates:

$$\Delta V_{\text{gap}} = \frac{g}{\varepsilon_0} \frac{q_{\text{el}} - q_{\text{aval}}}{S_a} \tag{7.3}$$

Then Cg is charged up again by the external power supply to the asymptotic value ΔV_{appl}, with an exponential behavior characterized by an "electrode time constant," which is the same as already cited in Chapter 1, given by

$$\tau = 2R_{\text{b}} \left(\frac{C_b}{2} + C_g \right) = \rho_{\text{b}}\, \varepsilon_0 \left(\varepsilon_r + 2\frac{d}{g} \right) \tag{7.4}$$

where ε_r represents the electrode-relative dielectric constant, and the rest of the symbols have been already defined. Note that τ is independent of cell dimension, while q_{el} is not.

A subsequent avalanche develops according to the conditions found at the actual moment of its creation, among which the time delay from the passage of the previous particle and, consequently, the effective ΔV_{gap}. All these processes are difficult to model analytically, but can be conveniently simulated, using techniques similar to the ones used in Chapters 3 and 4.

The "effective" ΔV_{eff}, that is the value of $\Delta V_{\text{gap}}(t)$at the start of each avalanche computed in this way, is shown in Figure 7.9 for various values of the frequency of impinging particles. It can be noted that the average ΔV_{eff} reduces as the particle flux increases, as the ohmic model correctly foresees; however, its distribution spreads more and more, and this could not be possibly foreseen by a simple ohmic model. In other words, the avalanches at high rate develop in a lower average

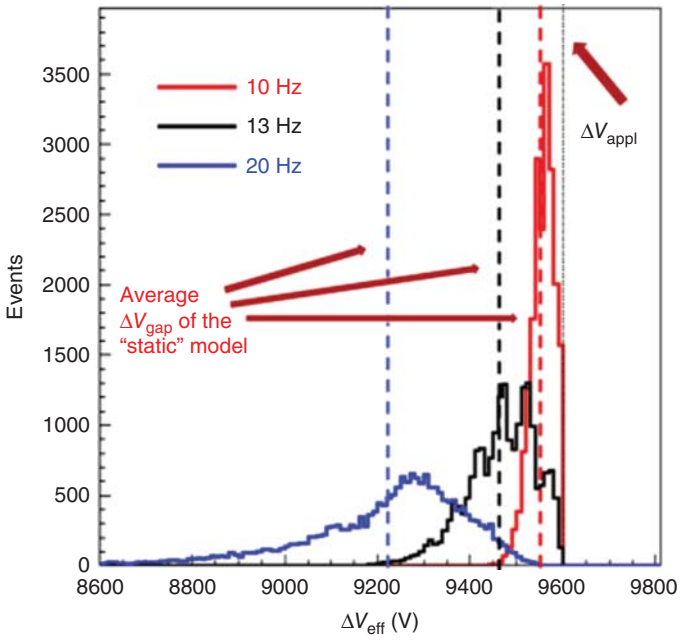

Figure 7.9 The "effective" ΔV_{eff} as defined in the text, for various values of the rate of impinging particles. (Abbrescia 2016. Reproduced with permission of IOP Publishing.)

electric field (with a correspondingly lower gain), but in addition the fluctuations on such a gain increase as the rate increases.

Simulated efficiency versus operating voltage, for single-gap RPCs operated with a $C_2H_2F_4$-based gas mixture, is presented in Figure 7.10; two values for the rate of incident particles are shown, 2 Hz/cm^2, characteristics of "cosmic rays" experiments, and 1.5 kHz/cm^2. Superimposed also two experimental curves, taken from Aielli *et al.* (2002), are reported. The two set of curves put in evidence the peculiar behavior of RPCs, the efficiency plateau is reached at higher and higher values of the operating voltage as the particle rate increases. Moreover, at high rate, the efficiency value at plateau is lower (Abbrescia, 2004).

Simulated efficiency versus rate, at a fixed operating voltage, is plotted in Figure 7.11. Also, a curve of experimental efficiency, taken from Bacci *et al.* (1995), is shown for comparison. Efficiency remains constant until the delay between subsequent incident particles is no more negligible with respect to electrode time constant τ. The average effective electric field inside the gap decreases rapidly. Note that the simulated curve, in order to reasonably reproduce data, has been obtained using a resistivity a factor twice with respect to the declared one. This might point out either the need to improve the model used or the need for a better accuracy in Bakelite resistivity measurements.

Efficiency at fixed ΔV_{appl} versus rate is shown in Figure 7.12 as well, but in this case the two calculated curves refer to avalanche and streamer events. For the streamer curve, q_{aval} has been multiplied by a factor 10 in order to simulate

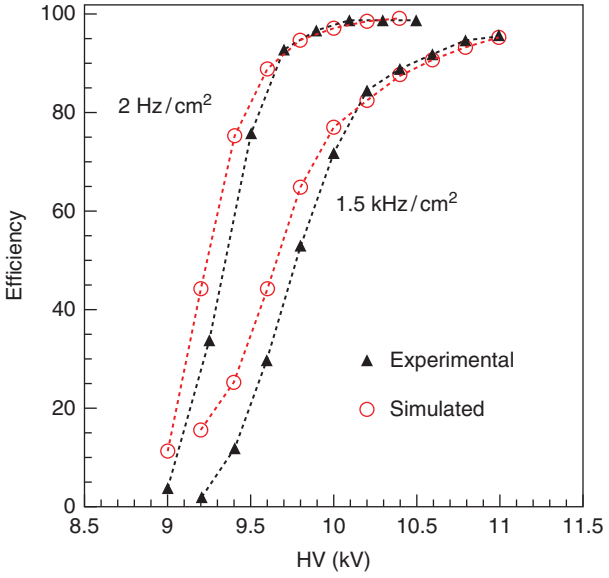

Figure 7.10 Efficiency versus operating voltage, for a single-gap RPC, at 2 Hz/cm^2 and 1.5 kHz/cm^2, experimental and simulated. (Abbrescia 2004. Reproduced with permission of Elsevier.)

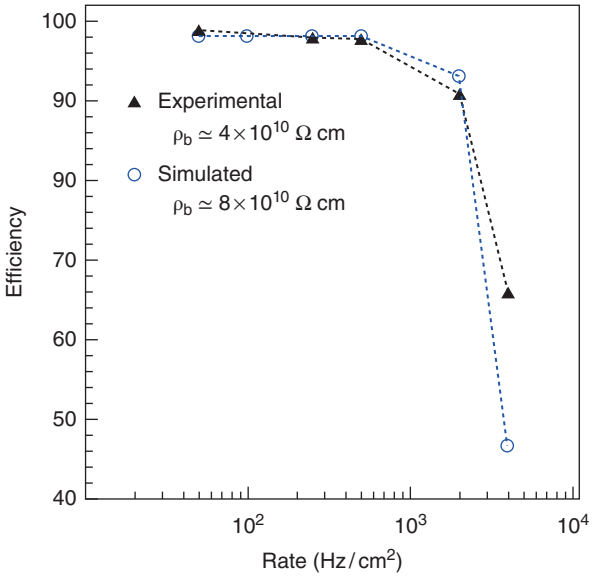

Figure 7.11 Efficiency versus rate of impinging particle, at fixed operating voltage, simulated and experimental. (Abbrescia 2004. Reproduced with permission of Elsevier.)

avalanches beyond the Raether limit, transforming into streamers. This has a relevant effect on rate capability, which is predicted to decrease to values around few hundreds hertz per square centimeter. On the same figure, experimental points taken from Arnaldi *et al*. (2000) are superimposed, and they fit nicely with the predictions. This is a direct indication of how an increase of rate capability

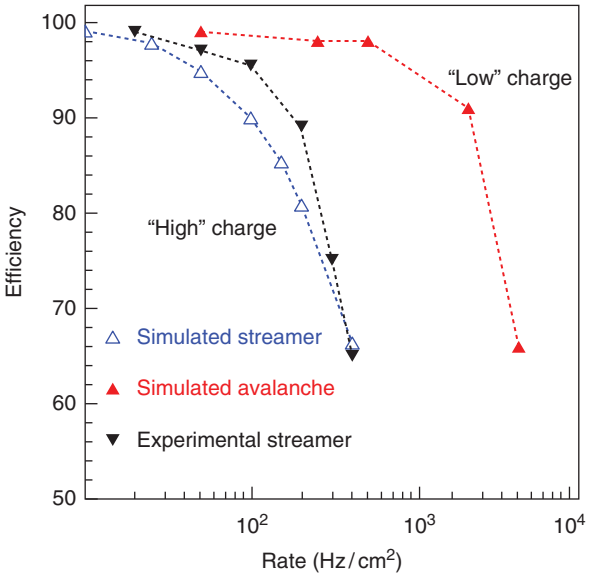

Figure 7.12 Efficiency versus rate of impinging particles, at fixed operated voltage, in the cases of avalanche and streamers, with an induced charge 10 times higher. Experimental points taken from (Arnaldi *et al.*, 2000) are also superimposed. (Abbrescia 2016. Reproduced with permission of IOP Publishing.)

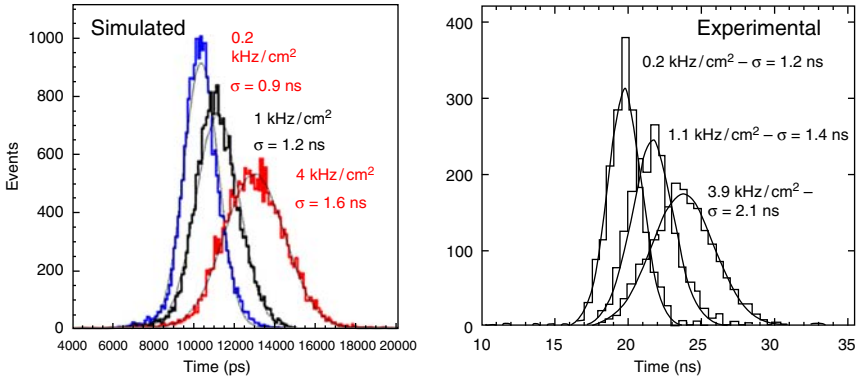

Figure 7.13 Simulated (a) and experimental (b) time distributions, for different values of the rate of impinging particles. (a) was taken from (Abbrescia 2004. Reproduced with permission of Elservier) and (b) from (Bacci *et al.* 1995. Reproduced with permission of Elsevier). Time zero in (a) correponds to the passage of the simulated particle while in (b) to the trigger.

can be also achieved by further reducing q_{aval}, as it was said a few times earlier (Abbrescia, 2016).

Simulated time distributions are reported in Figure 7.13, for three values of the rate of incident particles, chosen to reproduce similar curves, but obtained experimentally, see Bacci *et al.* (1995). At high rate, time distributions are shifted toward higher delays, mainly due to the electron drift velocity (Colucci *et al.*, 1999) diminishing with particle rate. High-rate time distributions show a degrading resolution (that can be noted by the fact that the distributions plotted in Figure 7.13 get wider and wider), due to ΔV_{eff} reductng and rapidly varying with time. Moreover and not surprisingly, simulated time resolution

are narrower with respect to experimental ones since no instrumental effect are taken into consideration.

Finally, let us note that some consideration about rate capability can be also derived from Formula 3.14, relative to the weighting field. Of course, a change in the detector configuration affecting ΔV_w would also affect rate capability, since it would change the induced charge q_{ind} given the same value of q_{aval}. Therefore, contrary to what can be predicted using the simple ohmic model, one can deduce that changing gap thickness g, by keeping all the rest unchanged does have an effect on rate capability. For instance, reducing g, q_{ind} will be lowered as well and consequently the rate capability. On the contrary, rate capability is in general improved if the ratio d/g is kept as low as possible.

7.4 The Upgrade of the Muon Systems of ATLAS and CMS

Some of the principles outlined will probably find implementation for the upgrade of the muon systems of the ATLAS and CMS experiments at LHC. This upgrade is necessary by the decision to prolong the operational lifetime of LHC RPCs during the so-called high luminosity phase of Large Hadron Collider (HL-LHC). LHC experiments were originally planned to operate for 10 years at a 10^{34} cm^{-2}s^{-1} design instantaneous luminosity, to integrate 500 fb^{-1} in total. The HL-LHC phase foresees an instantaneous luminosity around 5×10^{34} cm^{-2}s^{-1} with a corresponding integrated luminosity of about 300 fb^{-1}/year, and it is expected to last for a further 10 years at least.

Operating in these new harsh conditions will represent a major challenge for ATLAS and CMS. Therefore, both collaborations are putting considerable efforts to study the optimal strategy to cope with them. Muon systems, tracking and caloriments will be upgraded. The plans of ATLAS and CMS in this respect are outlined in upgrade official documents (see, respectively, ATLAS collaboration (2015) and CMS collaboration (2015).

For what concerns the ATLAS RPC system, a new layer of RPC chambers will be installed in the inner barrel stations of the muon spectrometer which, will increase the system redundancy, recover the overall efficiency of the trigger system if the efficiency in the old chambers is reduced, and close the present holes in the acceptance (see Figures 7.14 and 7.15). Here the rate capability needed, estimated by means of simulations, is likely to be around a couple of kHz/cm^2, with some safety factors included-.

In particular, it is proposed to use a triplet of new chambers with gas gap width of 1 mm (compared to 2 mm of the current RPCs) and with new high-sensitivity front-end electronics. This is based on SiGe technology and would assure noise much lower than 1000 electrons; some prototypes have already been produced and are currently under test (Cardarelli *et al*., 2013). A plot demonstrating these chambers rate capability is reported in Figure 7.16.

For what concerns the RPCs in CMS, whose requirements in term of rate capability are similar to those of ATLAS, several solutions are being currently investigated, which foresee the use of lower resistivity electrodes (made in Bakelite or

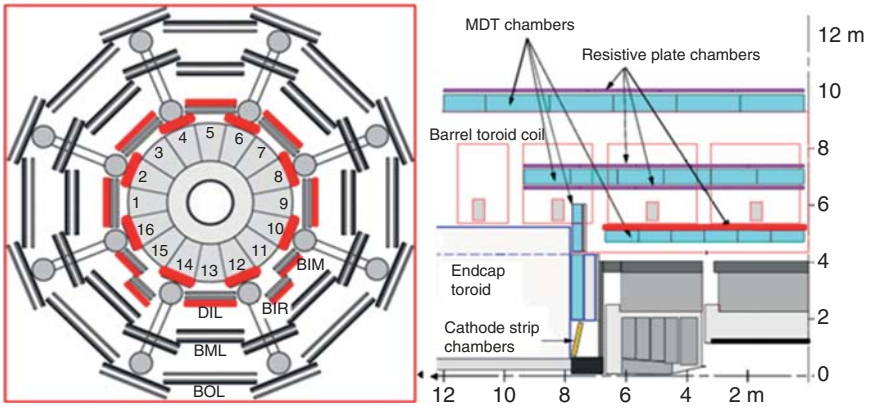

Figure 7.14 The proposed upgrade for the RPC system of the ATLAS experiment; the new RPC layer is shown in the two projections. (Vari and On behalf of the ATLAS collaboration 2015. Reprinted with permission of CERN.)

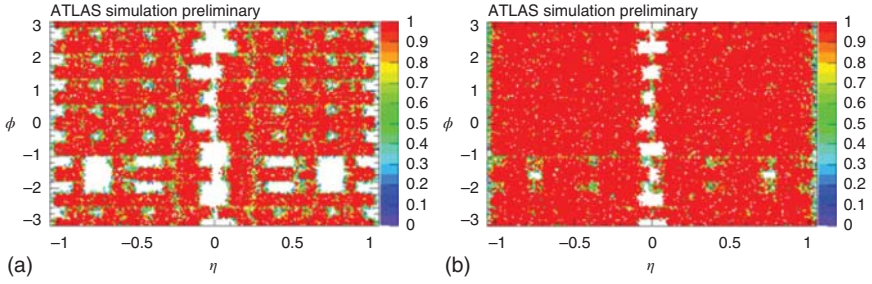

Figure 7.15 ATLAS muon trigger simulated acceptance for (a) the present configuration of the RPC system and (b) including the additional RPC layer proposed for the upgrade. (Biondi 2015. Reprinted with permission of CERN.)

glass), different geometries with respect to the standard 2-mm double-gap RPCs currently used, and more performant electronics.

A Bakelite RPC, developed at Korea Detector Laboratory (KODEL) for this purpose is shown in Figure 7.17; its structure is peculiar, being a hybrid between a double- and a multi-gap configuration, where readout strips are sandwiched between two gas gaps on each side (Lee, 2014). Its geometry, enhancing the charge induction on the readout strips, allows reaching rate capabilities around few thousands of hertz per square centimeter, as shown in the same figure.

Other tests have been performed using single-gap RPCs made with the low ($\approx 10^{10}$ Ω cm) resistivity glass developed at Tsinghua University already cited in Chapter 6 (Wang *et al.*, 2008). Rate capability of these devices measured at GIF++ with a gamma irradiation on the whole chamber are shown in Figure 7.18, and compared to the one of an RPC made of standard float glass, showing a relevant improvement in rate.

Finally, a more standard solution considered in CMS consists in keeping the double-gap geometry as it is (maybe reducing electrode and/or gap thickness) but

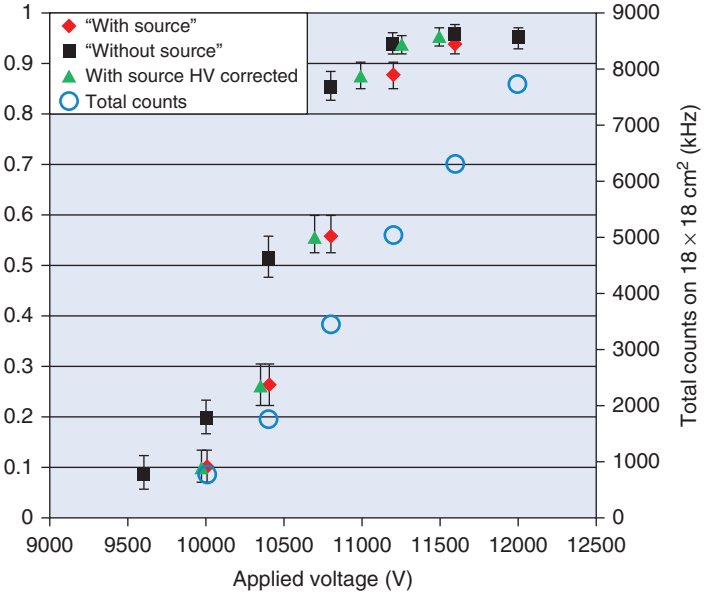

Figure 7.16 Efficiency as a function of applied voltage for a 1 + 1 mm doublet RPC equipped with a fast charge preamplifier. The efficiency curve is shown with and without irradiation with an X-ray source, corresponding to a hit rate of approximately 12 kHz/cm^2. The triangles represent the efficiency "with source" as a function of the actual voltage applied to the gas gap, after correction for the ohmic drop on the resistive plates. The chamber counting rate (noise counting rate + pulses from X-ray photons) is also shown. (ATLAS collaboration 2015. Reprinted with permission of CERN.)

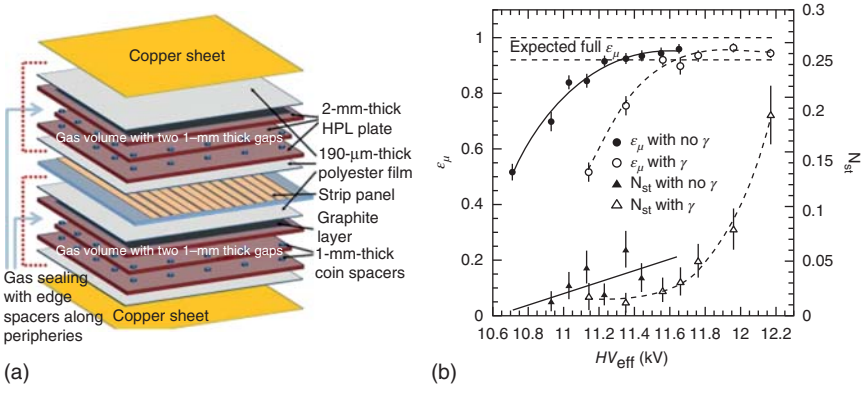

Figure 7.17 (a) View of the RPC prototype developed at KODEL University. (b) Efficiency plateau and cluster size (average number of strips fired in correspondance to an event) as function of operating voltage without irradiation (solid symbols) when fully irradiated at around 3 kHz/cm^2 (open symbols). (From Fagot *et al*., 2016.)

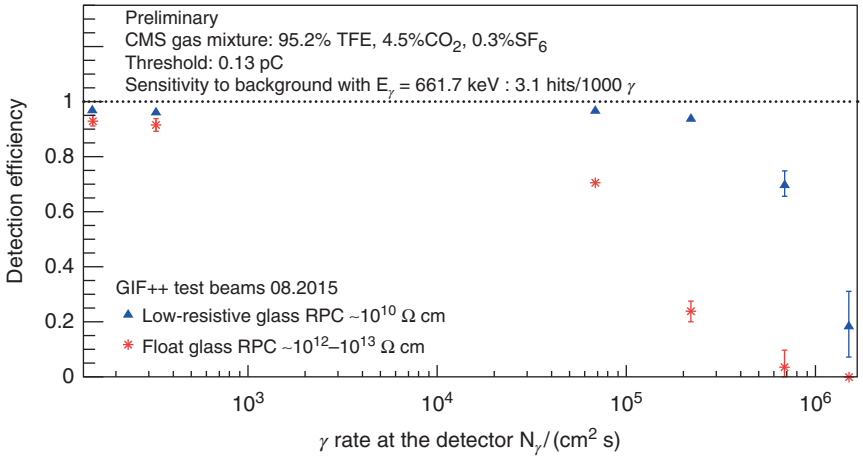

Figure 7.18 Efficiency of a Tsinghua glass RPC as function of the rate of impinging particles compared with a standard float glass RPC; since γ are used, which have an order of 1% probability to be converted, the counting rate is around 100 less than the one reported on the *x*-axis. (From Lagarde *et al*., 2016.)

using an enhanced electronics, based on the PETITROC (or similar) integrated circuit developed by the OMEGA group (Fleury *et al*., 2014). All these solutions seem to satisfy the requirements to be safely operated during the HL-LHC phase.

7.5 Special High Rate RPCs

Now, we perform a comparison among RPCs and parallel-plate chambers operated in avalanche mode (parallel-plate avalanche chambers, PPACs), with metallic electrodes; this is of some relevance, since PPACs represent, in a sense, the maximum limit in rate capability that could theoretically be reached with RPCs.

While in RPCs the first hints of rate limitation can be observed even at a few tens of hertz per square centimeter (depending on the materials, the operation mode and the configuration chosen, of course), PPACs show a different behavior, and counting rates up at least to 10^5–10^6 Hz/mm^2 can be reached without any decrease of the pulse height; this has suggested their use as specific high-rate detectors (see Fonte *et al*., 1998).

Some features of PPAC are illustrated in Figure 7.19. For a given fixed voltage across the electrodes, gas gain as a function of the counting rate in a PPAC remains constant; the horizontal arrows in the figure represent that gain, which stays constant up to a certain rate value. The maximum achievable gain, in turns, depends on the chosen gain, and it is represented with the open circles in the same figure. When this rate is reached, breakdown takes place repeatedly and if it is even slightly overcome, breakdown frequency will sharply increase.

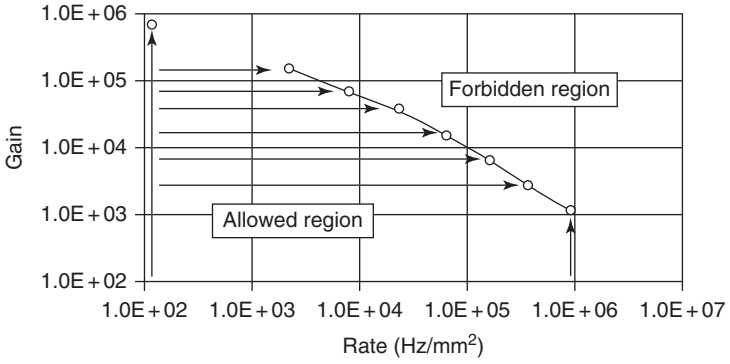

Figure 7.19 Gain (shown as arrows) versus counting rate for a parallel-plate avalanche chamber with metallic electrodes, measured using a ^{55}Fe source. The top electrode was a mesh combined with a drift region, very similar to the configuration shown in Figure 7.20, but with metallic anode. At each voltage across the PPAC gap, the signal amplitude does not change with rate, as explained in the text, even if at some critical rate breakdowns appears. The curve with circles represent the maximum achievable gain versus rate. (Adapted from Fonte *et al*., 1998.)

The physics behind these effects was studied in several works and summarized, for instance, in Peskov *et al*. (2009). In particular, it was shown that two main physics mechanisms contribute to the breakdowns in PPACs at high rates:

1) Avalanches overlapping in time and space,
2) Sporadic electron jets from cathode.

Let discuss these effects, at least shortly, since they lead to gain versus rate limitations at a fundamental level, which are valid for many gaseous detector, and not just for resistive ones (see Ivaniouchenkov *et al*., 1999).

Calculations show that when avalanches statistically overlap, and the probability of this increases with the counting rate, the total charge in the overlapped region can, for a short moment, reach the Raether limit, whereas the size of each individual avalanche is below the Raether limit (Peskov *et al*., 2009). This causes breakdown at a critical rate which depends, of course on the average avalanche size.

The appearance of sporadic electron jets emitted from the cathode was already discussed in Chapter 1. This an interesting, and not a completely understood, effect, contributing to breakdowns not only in gaseous detectors but even in the case of vacuum high voltage devices. According to Lalham (1995), in practice any, even extremely clean metallic surface, contains various types of dielectric insertions on the surface, like oxidation layers, microparticles, and so on. In the presence of very intense electric fields, electrons from the metal cathode can tunnel through these thin dielectric layers/ insertions and accumulate there. Then at a certain moment spontaneous emission from these layer takes place in the form of a burst, or even several bursts in sequence. The number of emitted electrons per jet can be quite high. In Fonte *et al*. (1999b), an attempt was done to explain, via this mechanism, high-amplitude pulses appearing in gaseous detectors just before the breakdown, when they are operated at high counting rates.

It was assumed that when the total charge in the avalanches created by these jets exceeds the Raether limit, breakdown happens even if the average size of the avalanches produced by the external radiation is much below the Raether limit.

These are the two main effects that intrinsically limit rate capability in PPACs, and even in micropattern detectors with metallic electrodes (see Chapter 8); this limit, of course, is much higher than in the case of RPCs and has a different nature (Fonte *et al*., 1998, 1999a,b; Ivaniouchenkov *et al*., 1999).

In principle, it could be very attractive, to combine the spark resistance of RPCs with the large counting rate capability of metallic chambers. Therefore, electrode resistivity optimization appeared from the beginning an effective way to achieve this task, even when the mathematics behind was not clear yet: a compromise should be anyhow reached, since resistivity should be low enough to reduce the effect of the voltage drop across the gap, but at the same time have a sufficient value to retain the advantage of spark protection restricting discharge current.

Here, we report about studies specifically devoted to develop RPCs able to stand rate capabilities much higher than the ones, on the order of the 1 kHz/cm^2, cited up to now in connection, for instance, with the experiments at LHC. Most often, these studies involve the use of materials different from Bakelite or glass, which constitute the bulk of the RPCs currently used.

Interesting steps in this direction were done with a custom-made medium resistivity material (a mixture of Araldite epoxy and MOLIN, ball-point pen black ink that yields a black rubber-like material), whose resistivity can be controlled in the 2×10^7 to 3×10^{12} Ω cm range, allowing for a large flexibility in the chamber counting characteristics, built using the hybrid configuration shown in Figure 7.20 (Fonte *et al*., 1999c). The detector was constituted by a drift region followed by an amplifying gap. The drift region was 15-mm thick and defined by two metallic meshes. The amplifying gap, 3.5-mm wide, was delimited by the lower drift mesh (cathode) and by a resistive plate (anode). Most tests were performed, creating primary charges by means of a collimated X-ray

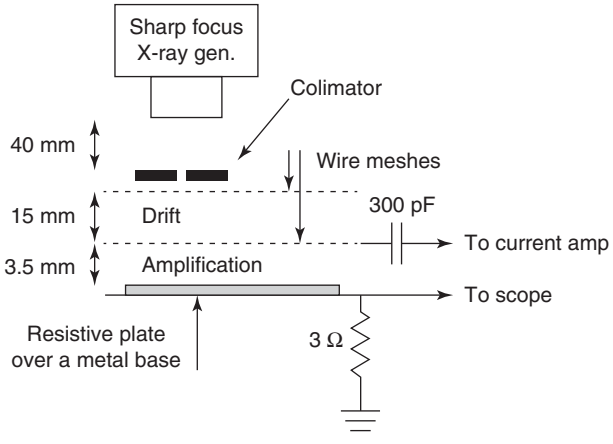

Figure 7.20 Schematic representation of the high counting rate hybrid prototype described in the text, whose main feature is the presence of drift and amplification zones, separated with metallic meshes. (Fonte *et al*. 1999c. Reproduced with permission of Elsevier.)

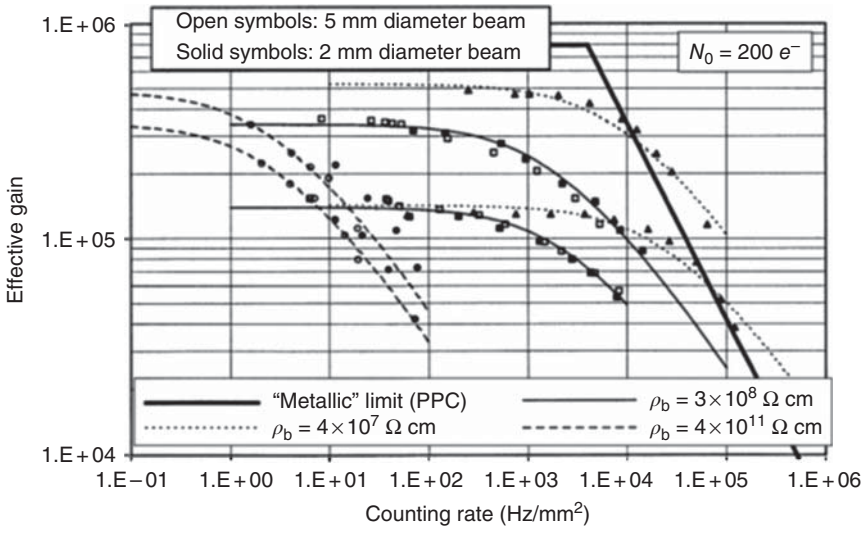

Figure 7.21 Gain-rate characteristics of the detector shown in Figure 7.20, for several values of the anode plate resistivity and beam diameters of 2 and 5 mm. With the lower resistivity material, counting rates up to 10^5 Hz/mm^2 were achieved, at gains between 10^4 and 10^5. The thin lines are drawn according to the model that the origin of the rate-gain dependence is that it is caused by a reduction of the effective gap electric field due to the ohmic voltage drop across the anode plate when crossed by the avalanche currents. The thick solid line marks the intrinsic counting rate limitations of a similarly built all-metallic PPAC. (Fonte *et al*. 1999c. Reproduced with permission of Elsevier.)

beam produced by a sharp-focus (0.1 mm) X-ray tube equipped with a Fe anode. The tube produces bremsstrahlung photons, whose energy distribution peaked at 5.5 keV, with a maximum energy around 10 keV. The beam was delimited by a collimator with selectable openings, 2 and 5 mm in diameter.

Some results obtained with this prototype are shown in Figure 7.21. A gain reduction was observed above a certain rate threshold, indicating the limit in rate capability of the device. The rate was different for each material sample (and each resistivity), but seemed to be relatively unaffected by the operating voltage or by the beam diameter. For the lowest anode resistivity studied, counting rates up to 10^5 Hz/mm^2 were achieved at gains between 10^4 and 10^5. This value is actually even slightly above the intrinsic rate-gain limitations that were found in similarly built metallic PPACs.

Work in this direction was continued by several groups Crotty *et al*. (2003), Francke *et al*. (2003), and Iacobaeus *et al*. (2003), which focused on tests of various commercially available low-resistivity materials. Results obtained fully confirmed the main conclusions of works Fonte *et al*. (1999c) in which it was shown that low-resistivity RPC under certain conditions can approach or even reach the rate limit of metallic PPAC.

As an example, the gain versus rate curves for low-resistivity narrow gap (0.3–0.5 mm) RPCs made of GaAs and Si are presented in Figure 7.22, as well as the maximum achievable gain for a metallic PPAC. One can see that at gains above 10^4, counting rates up to 10^5 Hz/mm^2 can be reached. In principle, one

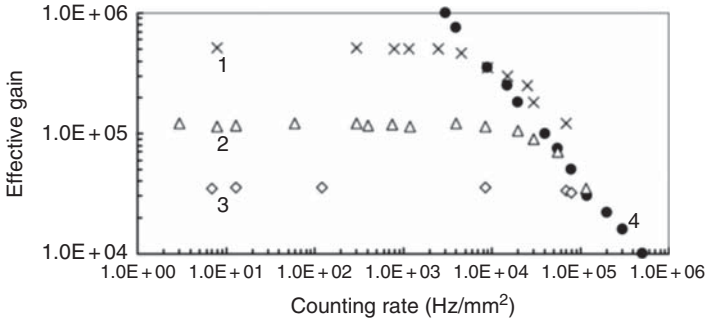

Figure 7.22 Gain versus rate for RPCs made of various low-resistivity materials: (1) $\rho_b = 3 \times 10^8\ \Omega$ cm; (2) $\rho = 4 \times 10^7\ \Omega$ cm; (3) $\rho_b = 3 \times 10^4\ \Omega$ cm (GaAs and Si); and (4) maximum achievable gain versus rate for a metallic PPAC. Measurements were performed with an X-ray beam. (Francke *et al*. 2003. Reproduced with permission of Elsevier.)

can operate these counters at much higher gains but at the expense of a lower achievable rate.

It was found that the breakdown characteristics of a "medium"-resistivity RPC is very different from a metallic PPAC or a high resistivity RPC. In particular, in the 10^7–$10^8\ \Omega$ cm resistivity range, a new phenomenon, a continuous glow discharge, may appear (Francke *et al*., 2003). Recall that there are various types of gaseous stationary discharges: corona discharges, arcs, and glow discharges. Each of them has a specific voltage versus current characteristics and also different values of typical currents: in the corona discharge, the typical order of magnitude is around 1 μA, in the glow discharge 1–100 mA, and in arcs several A or more. These borders are not very sharp, and of course depend on the gas composition and pressure. At 1 atm in some gases glow discharge current may approach Ampers (Karabadzhak and Peskov, 1987). Probably, this is the main reason glow discharge in RPCs is observed only in some specific electrode resistivity range, where the current stays within the interval mentioned.

From the point of view of possible electronics damage, glow discharge can be in some cases even more dangerous than sparks, because it is continuous. To identify the conditions at which sparks or glow discharges occur in RPCs, studies were performed with a wide range of electrode resistivities, using various gas mixtures, with quencher concentrations lower than 20%. The results of such measurements are summarized in Figure 7.23. As it can be seen, sparks appear at electrodes resistivity ρ_b either below $10^3\ \Omega$ cm or greater than $10^8\ \Omega$ cm. In the resistivity interval 10^3–10^8 mainly a glow discharge happens.

It was also found that the duration of the glow discharge can be decreased to a fraction of milliseconds or even fully suppressed using highly quenched mixtures, for example, using a 20–25% concentration of ethane in argon. Note, for comparison, that in the sparking region, highly quenched mixtures do not have any effect (Fonte *et al*., 1991).

In Lopes *et al*. (2006) and Laso Garcia *et al*. (2016), narrow-gap (250 − 300 μm) ceramic RPCs were investigated. In contrast to the studies just presented, where a single-gap low-resistivity RPC was used, this group studied the characteristics

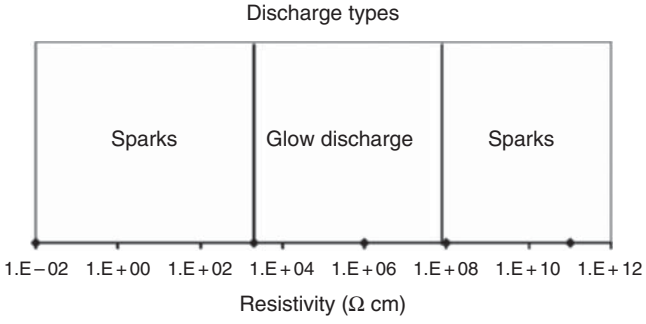

Figure 7.23 Types of discharges in RPCs with various electrode resistivities. "Sparks" at high resistivity" are actually current limited discharges, which are generally called by the RPC community as streamers (as already outlined in Chapter 3). Francke *et al*. 2003. Reproduced with permission of Elsevier.)

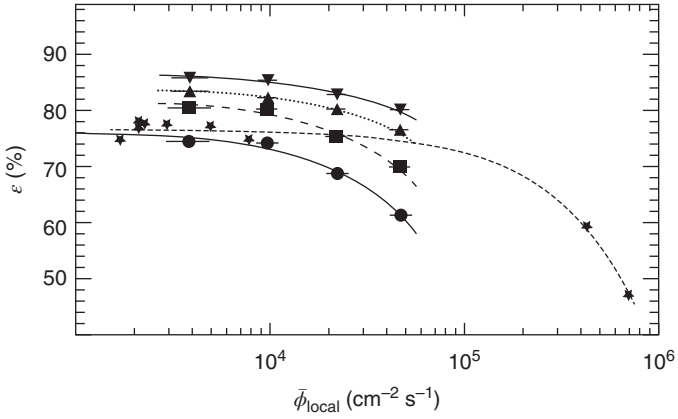

Figure 7.24 Efficiency as a function of the impinging particle flux for a multi-gap ceramic RPC with a 9×10^9 Ω cm bulk resistivity. The legends are ⋆ for proton beam and the electric field in the gap $E_{gap} = 95$ kV/cm; electron beam: for $E_{gap} = 92$ kV/cm, ■ for $E_{gap} = 94$ kV/cm, ▲ for $E_{gap} = 96$ kV/cm, ▼ for $E_{gap} = 98$ kV/cm. (Laso Garcia *et al*. 2016. Reproduced with permission of Elsevier.)

of multi-gap (4–6 gaps) RPCs. Ceramic bulk resistivity ρ could be tuned, during the manufacturing process, between 10^7 and 10^{13} Ω cm. The authors in particular focused to measure the efficiency of multi-gap RPC at various particle fluxes and applied voltage and electrode bulk resistivity, and the relative results are summarized in Figures 7.24 and 7.25.

The rate capability of a ceramic RPC was compared to RPCs made of semiconductive and float glass in Naumann *et al*. (2011) (see Figure 7.26); as expected, authors report that rate capability of ceramics exceeds that of float glass by more than 2 orders of magnitudes.

There are some other recent works in which attempts were done to achieve high rate operation with low-resistivity electrodes (Petrovici *et al*., 2012; Lei Xia, 2014; Dai *et al*., 2014). For example, in Petrovici *et al*. (2012) the rate limit at which

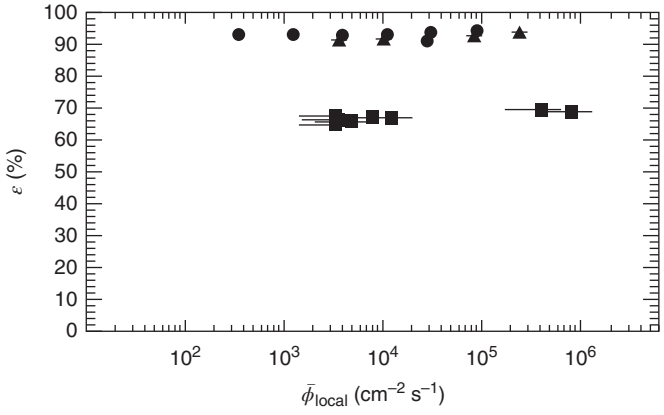

Figure 7.25 Efficiency as a function of particle flux, using electron and proton beams, measured with a multi-gap RPC having electrode resistivity of 9×10^9 Ω cm. $E_{gap} = 100$ kV/cm is represented by ●, $E_{gap} = 106$ kV/cm by ▲ for electron beams. For proton beams, ■ corresponds to $E_{gap} = 100$ kV/cm. (Laso Garcia *et al*. 2016. Reproduced with permission of Elsevier.)

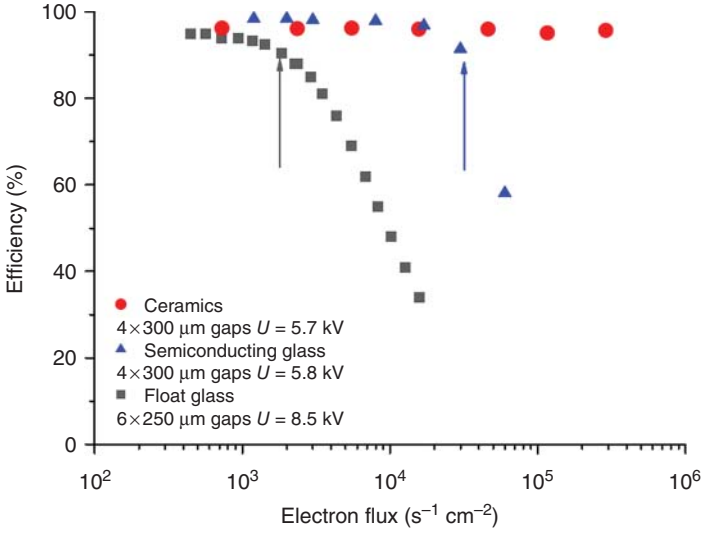

Figure 7.26 Efficiency of RPCs with different electrode materials (ceramics, semiconductive, and float glass) as a function of the particle flux; results were obtained using an electron beam. (Naumann *et al*. 2011. Reproduced with permission of Elsevier.)

the detection efficiency dropped around 10% was ≈10^5 Hz/cm^2; in this case, the electrodes of their multigap RPC were made of Pestov glass.

To have an approximate overall idea of the results obtained in this field, an RPC "world map" of rate capability is shown in Figure 7.27 (replotted with a modification from Gonzalez-Diaz, 2006). High resistive materials like silica glass show, in general, a lower rate capability. Sometimes these material are heated

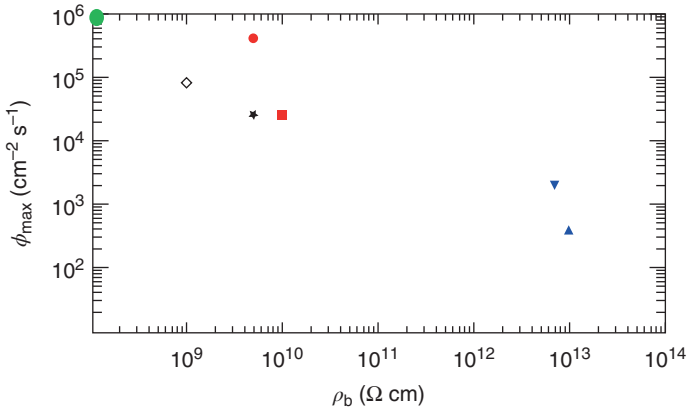

Figure 7.27 "World map" of RPC rate capabilities. (Replotted with a modification from Gonzalez-Diaz 2006.) The maximum flux, at which the efficiency drops by 10%, is plotted against the material bulk resistivity. The red circle and the red square are for ceramics, the upper triangle is for warmed silica glass, the lower triangle is for silica glass (Gonzalez-Diaz *et al*., 2005), the star is for semiconductor-doped glass (Wang *et al*., 2010), and the cross is for low-resistivity ceramic. The green point indicates the rate capability of an RPC with a GaAs or for ceramic cathode (Naumann *et al*., 2011).

up, so that their resistivity is somehow reduced and a moderately higher rate capability can be achieved. For low resistive materials, like semiconductor-doped glass or ceramics, much higher rate capabilities can be reached. Moreover, the 10^6 Hz/cm^2 frontier seems to be at reach for the prototypes described in Fonte *et al*. (1999c), Crotty *et al*. (2003), Iacobaeus *et al*. (2003), Francke *et al*. (2003, 2004), and Lopes *et al*. (2004).

7.5.1 High-Rate, High-Position Resolution RPCs

Another interesting development consists in low-resistivity RPCs, which are read out with a microstrip readout (already cited at the end of Chapter 4), allowing, in principle, to achieve with the same device very high counting rates and excellent position resolution.

The first feature simplifies the determination of the particles coordinate at their high fluxes.

Studies in this direction are described in Crotty *et al*. (2003), Iacobaeus *et al*. (2003), Francke *et al*. (2003, 2004), where microstrips were placed inside the gas gap onto the anode plate. These studies were performed in parallel with the ones already described at the end of Chapter 4, with the difference that a CsI layer was not always used.

Having the strips located inside the gas gap has the advantage that the region of the induced charge is narrower with respect to that having the strips outside. This not only improves spatial resolution but also allows a higher rate capability, since more particles impinging simultaneously in the same region can be detected separately.

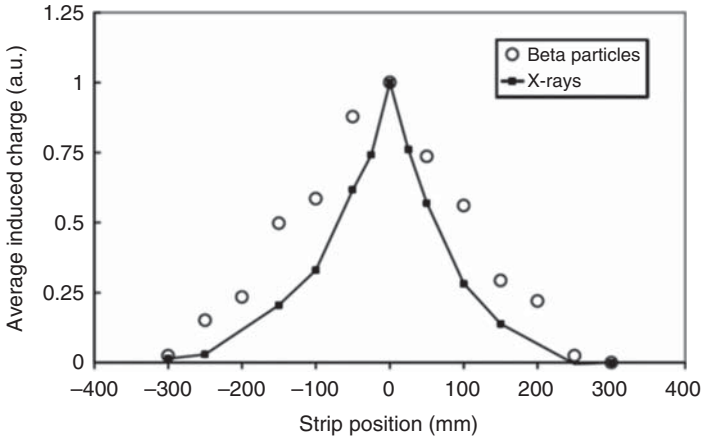

Figure 7.28 Induced charge profile for the detection of collimated X-rays and β-particles. The 0.3-mm gap low-resistivity RPC was filled with a 40% Xe + 40% Kr + 20% CO_2 gas mixture. (Francke *et al*. 2003. Reproduced with permission of Elsevier.)

The induced charge profile obtained with a well-collimated X-ray beam (30 μm width) entering the amplification gap parallel to the cathode and 50 μm far from its surface, and parallel to the anode strips (with 50 μm mean pitch), is shown in Figure 7.28. The profile width is ≈200 μm full width at half maximum (FWHM).

Another feature of avalanche RPCs (or PPACs) operating in pure avalanche mode (where no strong space-charge effect is present) is that the primary electrons, created close to the cathode, gain the maximum amplification, since the avalanche size exponentially depends on their distance from the cathode. For this reason, these detectors are mainly sensitive to the coordinate corresponding to the point where the particles traverse the inner cathode surface.

There is an interesting consequence of this. If an X-ray beam impinges close to the cathode and parallel to it, the detector can record the coordinate of the X-ray photons with an excellent precision (≈50 μm in digital form) even if photons have enough energy to produce long photoelectron tracks.

Some experimental results obtained with ≈30 keV X-rays are presented in Figure 7.29. In these measurements, a 0.3-mm gap high-rate RPC (with a GaAs cathode) with metallic 50 μm anode strips located on the inner surface of the ceramic anode was used. The number of counts from various strips (a digital image) with a collimated X-ray beam is shown in Figure 7.29a; the beam was oriented along anode strip 8, and, as expected, the highest counting rate was recorded from this particular strip. The image of the same slit, but shifted 25 μm in the direction perpendicular to the strips (towards strip 9) is shown in Figure 7.29b, and in this case the counting rates from the two neighboring strips are comparable. This feature was periodically repeated with the beam moving further across the strips. From the image contrast (ratio of counts from neighboring strips), it can be concluded that a position resolution better than 30 μm was achieved, in spite of the fact that the induced region width was much larger. The image of a 7-line pairs/mm phantom is shown in Figure 7.29c; three slits 70 μm apart are easily resolved.

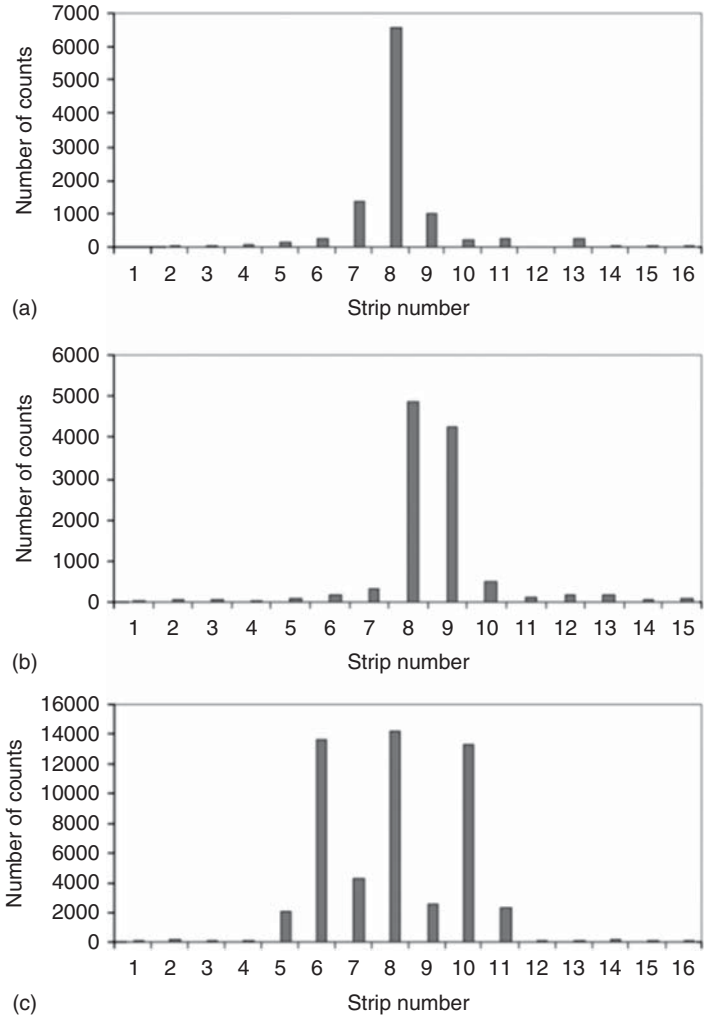

Figure 7.29 Number of counts from various strips in the case when X-rays entered the RPC through a 30 μm slit (a) with the beam oriented along the strip 8 and (b) in between strips 8 and 9, parallel to the cathode and 50 μm far from it. This feature repeats periodically, with the beam moving perpendicularly to the strips. (c) Number of counts for X-ray imaging of a 7-line pairs/mm phantom. (Francke *et al*. 2003. Reproduced with permission of Elsevier.)

High-rate high-position resolution RPCs were also used as sensitive elements for low-dose mammographic scanners, detaily described in Chapter 9 (Francke *et al*., 2001; Maidment *et al*., 2006).

High-rate, high-resolution RPCs were also suggested for high-rate particle tracking (Francke *et al*., 2003). In these prototypes, electrodes made of GaAs (resistivity $\approx 10^8\ \Omega\,\text{cm}$) were used, and 30 or 50 μm readout strips were located inside the gas gap to reduce the induced signals area (in order to allow simultaneous registration of several closely located tracks as earlier explained), as

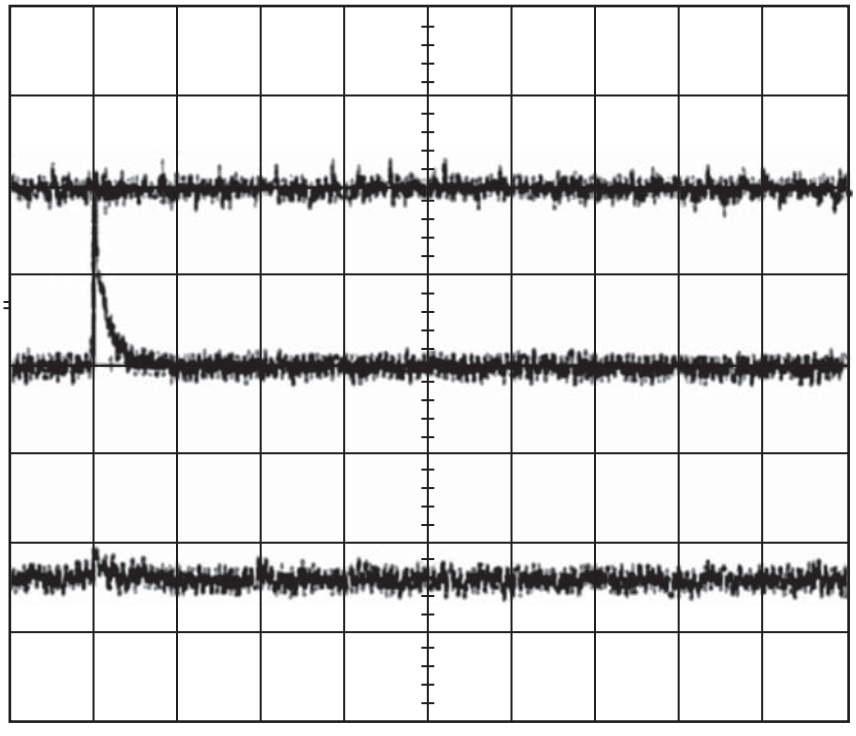

Figure 7.30 Oscillograms from three adjacent strips, acquired when a particle crossed the CsI-coated RPC perpendicularly to its electrode and in the vicinity of the central strip. Horizontal scale 0.5 ms/div; vertical scale 0.5 V/div. It can be seen that the area of the induced signals, in this particular case, is on the order of the strip pitch (see also Figure 4.37). (Francke *et al*. 2003. Reproduced with permission of Elsevier.)

shown in Figure 7.30. Another feature implemented in these prototypes was the use a cathode coated with a CsI layer, which serves as a secondary electron emitter. A porous CsI converter was already described in Chapter 4; it allows increasing RPC efficiency, but has a counting rate limitation due to charging up effect of this emitter. In Iacobaeus *et al*. (2003), a thin (0.5 – 0.6 μm) uniform CsI converter was tested. Although it shows less efficiency compared to the porous one, its rate capability was excellent and no charging up effect was observed up to counting rates of 10^5 Hz/cm^2; the position resolution in digital form was about 50 μm.

7.6 High-Position Resolution Timing RPCs

Another logical step in improving RPC performance is to develop high-position resolution timing RPCs, joining in the same device a sub-millimeter spatial resolution with a 100 picosecond order time resolution.

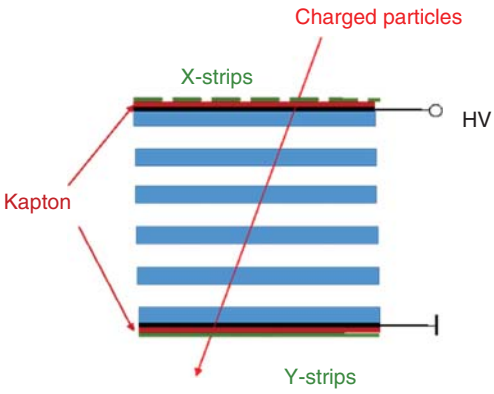

Figure 7.31 Schematic representation of a time of flight multi-gap RPC having a high-position resolution: the outer electrodes were equipped with readout strips connected to timing and charged sensitive circuitry.

The first attempt in this direction is described in Blanco *et al*. (2012); the authors built a telescope composed of timing RPCs, each with five 0.35-mm wide gaps, and whose plates, 0.4-mm thick, were fabricated with soda-lime glass. The high voltage was applied via thin layers of a semiconducting polymer, called SEMITRON, and the RPCs were read out by means of electrodes coupled to both charge-sensitive and timing circuits (see Figure 7.31).

Due to the low counting rate used in these tests (performed with cosmic radiation), there was no need to have readout strips inside the gas gap: for simplicity, they were located onto the outer surface and isolated from the readout electrodes by Kapton foils. The strips on top (X-strips in Figure 7.31) and bottom (Y-strips) were oriented perpendicularly to each other, with a 4-mm pitch. Each X-strip delivered part of the induced charge to a common printed circuit board (PCB) via a 40-pF capacitor and the rest to a charge amplifier via a choke coil (MURATA BLM21BB201SH1) to filter out the common mode noise that can be problematic in differential transmissions. The common PCB was connected to a custom timing amplifier and comparator via two cables of equal length. This arrangement directs the high-frequency signal components toward the timing amplifiers and the low frequencies toward the charge amplifiers. It should be noted that this way it is possible to use the total induced charge for position determination and not just the prompt component. The Y-strips were used for timing purposes only.

The strip signals were fed via the chokes to integrating amplifiers with 10-ms integration time, digitized by 40-MHz streaming analog to digital converters (ADCs) and digitally filtered in the time domain by a trapezoidal filter with 2-ms leading, 1-ms top, and 2-ms falling time constants. The particle passing times were recorded by 100-ps bin time to digital converters (TDCs).

Of course, three (or more) similar detectors can be stacked vertically, forming a multilayer telescope (see Figure 7.32), for improved particle tracking. A tracking system capable of simultaneous accurate measurements of coordinates and times has some advantages. For instance, each particle is measured several times, improving timing accuracy, and there is no need for an external initial time detector, which can sometimes be problematic.

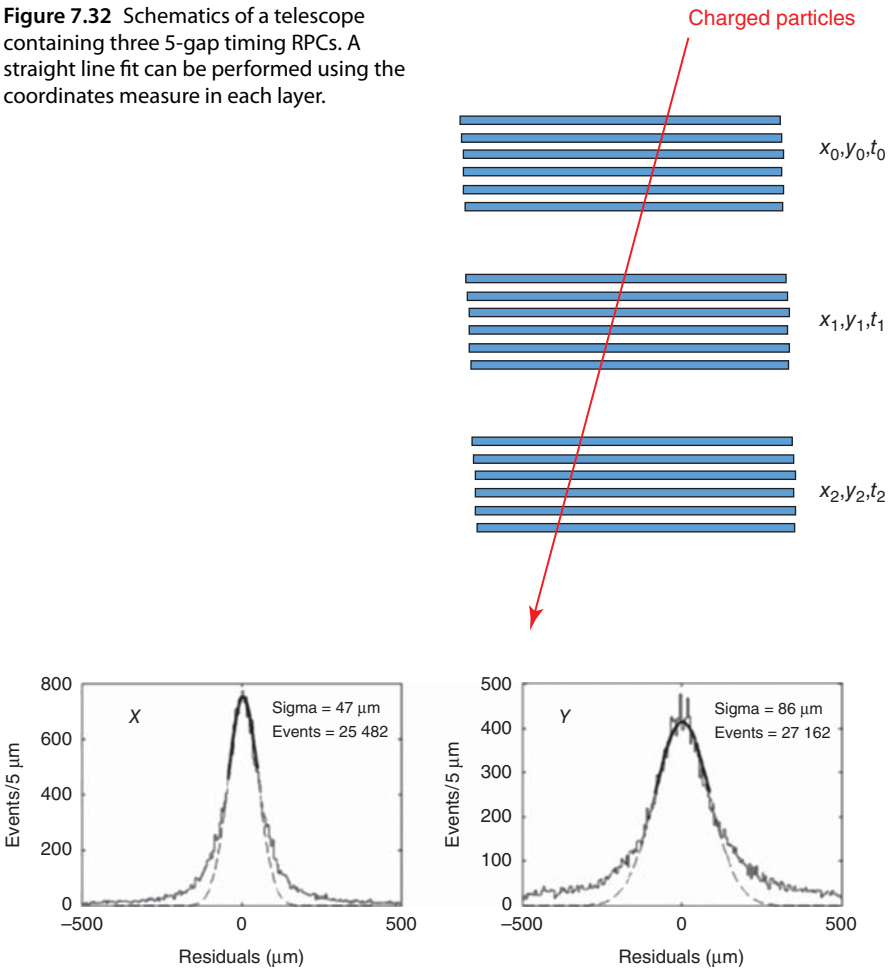

Figure 7.32 Schematics of a telescope containing three 5-gap timing RPCs. A straight line fit can be performed using the coordinates measure in each layer.

Figure 7.33 X and Y residuals to a straight-line fit, measured with the cosmic telescope described in the text; in this case, just tracks crossing the telescope almost perpendicularly were considered. (Blanco *et al*. 2012. http://iopscience.iop.org/article/10.1088/1748-0221/7/11/P11012/meta. Licensed under CC BY 3.0.)

The X and Y distributions measured with a three layer telescope are shown in Figure 7.33; a Gaussian performed within ±1 σ is superimposed. The bulk of the X distribution shows a 47 μm width, while the Y distribution is 86 μm wide. After applying corrections on some systematics, the following results were achieved: X distribution width of 38 μm σ and the Y distribution width of 71 μm σ. The average single-layer resolution was found to be 77 ps and the overall telescope resolution (combination of the three layers) was $77/\sqrt{3} = 44$ ps.

Material presented in these last paragraphs clearly demonstrates that small gap RPCs may combine in one design several unique features: excellent time and spatial resolution together with high-rate capability, opening interesting possibilities for applications in the near future.

References

Abbrescia, M. (2004) The dynamic behaviour of Resistive Plate Chambers. *Nucl. Instrum. Methods Phys. Res., Sect. A*, **533**, 7–10.

Abbrescia, M. (2016) Improving rate capability of Resistive Plate Chambers. *JINST*, **11**, C10001.

Affatigato, M. *et al*. (2015) Measurements of the rate capability of various Resistive Plate Chambers. *JINST*, **10**, P10037.

Agosteo, S. *et al*. (2000) A facility for the test of large area muon chambers at high rates. *Nucl. Instrum. Methods Phys. Res., Sect. A*, **452**, 94–104.

Aielli, G. *et al*. (2002) RPC ageing studies. *Nucl. Instrum. Methods Phys. Res., Sect. A*, **478**, 271.

Arnaldi, R. *et al*. (2000) A low-resistivity RPC for the ALICE dimuon arm. *Nucl. Instrum. Methods Phys. Res., Sect. A*, **451**, 462–473.

ATLAS collaboration (2015) ATLAS Phase-II Upgrade Scoping Document. CERN-LHCC-2015-020, LHCC-G-166, September, 2015.

Bacci, C. *et al*. (1995) Test of a resistive plate chamber operating with low gas amplification at high intensity beams. *Nucl. Instrum. Methods Phys. Res., Sect. A*, **352**, 552.

Bilki, B. *et al*. (2009) Measurement of the rate capability of Resistive Plate Chambers. *JINST*, **4**, P06003.

Biondi, S. (2015) Upgrade of the ATLAS Muon Barrel Trigger for HL-LHC. PoS(EPS-HEP2015), 289.

Blanco, A. *et al*. (2012) TOFtracker: gaseous detector with bidimensional tracking and time-of-flight capabilities. *JINST*, **7**, P11012.

Carboni, G. *et al*. (2003) A model for RPC detectors operating at high rate. *Nucl. Instrum. Methods Phys. Res., Sect. A*, **498**, 135–142.

Cardarelli, R. *et al*. (1988) Progress in resistive plate counters. *Nucl. Instrum. Methods Phys. Res., Sect. A*, **263**, 20–25.

Cardarelli, R. *et al*. (2013) Performance of RPCs and diamond detectors using a new very fast low noise preamplifier. *JINST*, **8**, P01003, 106.

CMS collaboration (2015) Technical proposal for the phase-II upgrade of the Compact Muon Solenoid. CERN, LHCC-2015-10, LHCC-P-008, CMS-TDR-15-02, 1 June 2015. ISBN: 978-92-9083-417-5.

Colucci, A. *et al*. (1999) Measurement of drift velocity and amplification coefficient in C2H2F4–isobutane mixtures for avalanche-operated resistive-plate counters. *Nucl. Instrum. Methods Phys. Res., Sect. A*, **425**, 84.

Crotty, I. *et al*. (1993) Investigation of resistive parallel plate chambers. *Nucl. Instrum. Methods Phys. Res., Sect. A*, **329**, 133–139.

Crotty, I. *et al*. (1994) The non-spark mode and high rate operation of resistive parallel plate chambers. *Nucl. Instrum. Methods Phys. Res., Sect. A*, **337**, 370–381.

Crotty, I. *et al*. (2003) High-rate, high-position resolution microgap RPCs for X-ray imaging applications. *Nucl. Instrum. Methods Phys. Res., Sect. A*, **505**, 203–206.

Dai, T. *et al*. (2014) Low resistance bakelite RPC study for high rate working capability. *JINST*, **9**, C11013.

Fagot, A. *et al*. (2016) R&D towards the CMS RPC Phase-2 upgrade. *JINST*, **11**, C09017.

Fleury, J. *et al*. (2014) Petiroc and Citiroc: front-end ASICs for SiPM read-out and ToF applications. *JINST*, **9**, C01049.
Fonte, P. *et al*. (1991) *Nucl. Instrum. Methods Phys. Res., Sect. A*, **305**, 91.
Fonte, P. *et al*. (1998) Thin gap parallel mesh chamber: a sparkless high-rate detector, arXiv:physics/9803021.
Fonte, P. *et al*. (1999a) Rate and gain limitations of MSGCs and MGCs combined with GEM and other preamplification structures. *Nucl. Instrum. Methods Phys. Res., Sect. A*, **419**, 405–409.
Fonte, P. *et al*. (1999b) The fundamental limitations of high-rate gaseous detectors. *IEEE Trans. Nucl. Sci.*, **46**, 321.
Fonte, P. *et al*. (1999c) A spark-protected high-rate detector. *Nucl. Instrum. Methods Phys. Res., Sect. A*, **431**, 154–159.
Francke, T. *et al*. (2001) Dose reduction in medical x-ray imaging using noise free photon counting. *Nucl. Instrum. Methods Phys. Res., Sect. A*, **471**, 85–87.
Francke, T. *et al*. (2003) Potential of RPCs for tracking. *Nucl. Instrum. Methods Phys. Res., Sect. A*, **508**, 83–87.
Francke, T. *et al*. (2004) High rate (up to 105Hz/cm2), high position resolution (30 μm) photosensitive RPCs. *Nucl. Instrum. Methods Phys. Res., Sect. A*, **533**, 163.
Gonzalez-Diaz, D. (2006) Research and developments on timing RPCs. Application to the ESTRELA detector of the HADES experiment at GSI. PhD thesis. Universidade de Santiago de Compostela.
Gonzalez-Diaz, D. *et al*. (2005) The effect of temperature on the rate capability of glass timing RPCs. *Nucl. Instrum. Methods Phys. Res., Sect. A*, **555**, 72.
Iacobaeus, C. *et al*. (2003) The development and study of high-position resolution (50 μm) RPCs for imaging X-rays and UV photons. *Nucl. Instrum. Methods Phys. Res., Sect. A*, **513**, 244–249.
Ivaniouchenkov, Y. *et al*. (1999) Breakdown limit studies in high-rate gaseous detectors. *Nucl. Instrum. Methods Phys. Res., Sect. A*, **422**, 300–304.
Karabadzhak, G.F. and Peskov, V.D. (1987) Properties of glow discharges at high pressures. *J. Tech. Phys.*, **57**, 891 (in Russian).
Lagarde, F. *et al*. (2016) High rate, fast timing Glass RPC for the high η muon detectors. *JINST*, **11**, C09006.
Lalham, R. (1995) *High Voltage Vacuum Insulation*, Academic Press, New York, pp. 1–663.
Laso Garcia, A. *et al*. (2016) High-rate timing resistive plate chambers with ceramic electrodes. *Nucl. Instrum. Methods Phys. Res., Sect. A*, **818**, 45–50.
Lee, K.S. (2014) Rate-capability study of a four-gap phenolic RPC with a 137Cs source. *JINST*, **9**, C08001.
Lei Xia (2014) Development of High Rate RPCs, https://indico.cern.ch/event/192695/contributions/353406/ (accessed 30 October 2017).
Lopes, L. *et al*. (2004) *Nucl. Instrum. Methods Phys. Res., Sect. A*, **533**, 69.
Lopes, L. *et al*. (2006) *Nucl. Phys. B (Proc. Suppl.)*, **158**, 66–70.
Maidment, A., Ullberg, C., Lindman, K. *et al*. (2006) Evaluation of a photon counting breast tomosynthesis imaging system, in *Proceedings of SPIE International Symposium on Medical Imaging*, SPIE, San Diego, CA, p. 2006.
Naumann, L. *et al*. (2011) High-rate timing RPC with ceramics electrodes. *Nucl. Instrum. Methods Phys. Res., Sect. A*, **635**, S113.

Peskov, V. *et al*. (2009) Research on Discharges in Micropattern and Small Gap Gaseous Detectors, arXiv:0911.0463.

Petrovici, M. *et al*. (2012) High Counting Rate, Differential, Strip Read-Out, Multigap Timing RPC, JINST POS (RPC 2012) 067.

Santonico, R. (2014) RPCs for high radiation environment. presentation given at the 2nd ECFA Workshop on HL-LHC, Aix-les-Bains, October 21–23, 2014.

Santonico, R. and Cardarelli, R. (1981) Development of resistive plate counters. *Nucl. Instrum. Methods Phys. Res.*, **187**, 377.

Vari, R. and On behalf of the ATLAS collaboration (2015) A proposal to upgrade the ATLAS RPC system for the High Luminosity LHC. 13th Pisa Meeting on Advanced Detectors, May 24–30, 2015, La Biodola, Isola d'Elba, https://cds.cern.ch/record/2021484/files/ATL-MUON-SLIDE-2015-301.pdf (accessed 30 October 2017).

Wang, J. *et al*. (2010) Development of multi-gap resistive plate chambers with low-resistive silicate glass electrodes for operation at high particle fluxes and large transported charges. *Nucl. Instrum. Methods Phys. Res., Sect. A*, **621**, 151.

Wang, Y. *et al*. (2008) Study on the performance of high rating MRPC. Nuclear Science Symposium Conference Record, NSS âAZ08, IEEE, pp. 913–916. doi: 10.1109/NSSMIC.2008.4774543

8

New Developments in the Family of Gaseous Detectors: Micropattern Detectors with Resistive Electrodes

8.1 "Classical" Micropattern Detectors with Metallic Electrodes

In this chapter we speak about gaseous micropattern detectors, whose invention constitutes the third breakthrough (after the invention of multiwire proportional chambers (MWPCs) and resistive plate chambers (RPCs)) in the field of gaseous detectors at the end of the past millennium. Micropattern detectors, which have flourished in a plethora of many different forms, have been described in literally hundreds of papers; a nice recent and interesting review is contained in Francke and Peskov (2014).

Micropattern detectors are gas amplification structures with the following features, combined together:

1) Their electrodes have a very small distance between them, typically below 100 μm.
2) They are manufactured using microelectronic technology.
3) Their electrodes often have a segmented micropattern structure.

Classical examples of micropattern detectors are the Micro Strip Gas Chamber (MSGC), the MICRO-MEsh GAseous Structure (usually called MICROMEGAS) and some hole-type devices, like the gas electron multipliers (GEMs) and the microdot gaseous detector.

The schematic drawing of an MSGC, which was invented by Oed (1988), is shown in Figure 8.1. Basically, it consists in an array of metallic strips; they are alternately narrow (anodes) and wide (cathodes), and they are manufactured on a dielectric substrate (see Oed, 1988). When appropriate voltages are applied to the electrodes, electrons released in the drift gap (the region between the drift plane and the detector surface, indicated in Figure 8.1 as "gas volume") by an ionizing particle move toward the strips, and multiply in the region of intense electric field created around the anodes.

A MICROMEGAS is basically a parallel-plate chamber (conceptionally similar to one shown in figure 7.20, but with metallic anode) with a small avalanche gap, typically 50–100 μm wide (Charpak *et al*., 1995). The detector consists in a thin metal grid (the cathode) stretched above a metallic readout electrode (the anode). A relatively low applied voltage across the gap (let us say, around

Resistive Gaseous Detectors: Designs, Performance, and Perspectives, First Edition.
Marcello Abbrescia, Vladimir Peskov, and Paulo Fonte.

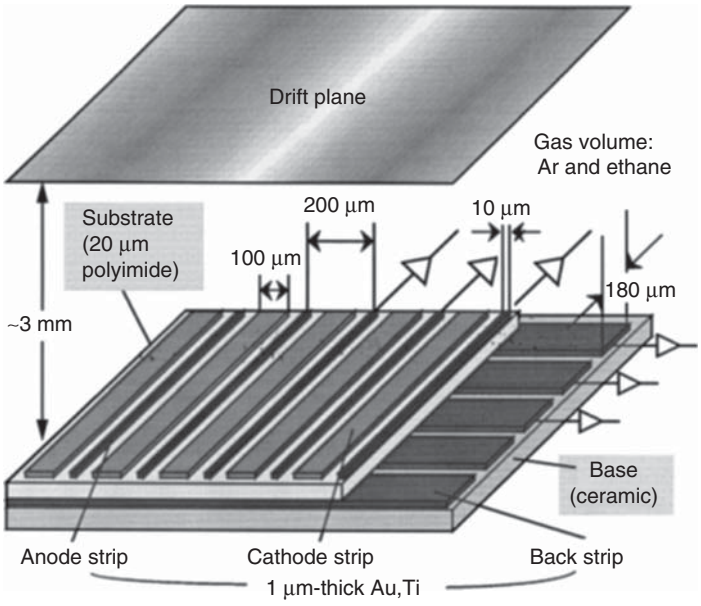

Figure 8.1 Schematic picture of a microstrip gas chamber (MSGC). The main dimensions are shown. (Nishi *et al*. 1998. Reproduced with permission of John Wiley and Sons.)

600–700 V) causes a quite intense electric field to be created in the gap, typically above 30 kV/cm. Electrons released in the upper drift region are drifted through the openings in the mesh, and multiplied in the microgap. To ensure a uniform thickness of the multiplying gap, an array of insulating supports (pillars) are manufactured using microelectronic technology.

A GEM consists in a thin, metal-clad kapton foil, typically 50 μm thick, chemically perforated with a set of holes, with a density on the order of a hundred per millimeter square (see Sauli, 1997). A GEM is inserted between a drift and a collection electrode (see Figure 8.2), which are kept at suitable voltages, in such a way that most electrons released by ionization in the overlaying gas gap migrate into

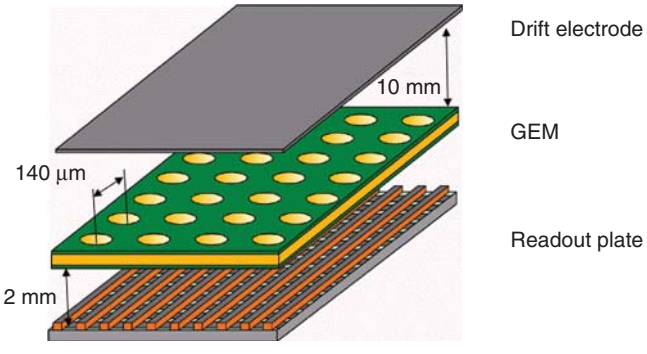

Figure 8.2 A simplified drawing of a GEM detector consisting from a perforated foil, drift electrode, and the readout plate. (CERN Courier 1998. Reprinted with permission of CERN.)

the holes, where, due to the applied electric field, they multiply by the usual charge avalanche processes. Thereafter, part of the electrons generated in the avalanches transfer into the lower region where the readout plate is located.

Microdot/micropin/micro-pixel detectors (all these names are used to refer to detectors based on the same principles) are made from a matrix of individual circular small radius anodes ensuring high enough electric field for charge multiplication, surrounded by circular cathodes. Usually, anodes are interconnected on the backplane to provide one coordinate; the second coordinate can be obtained from orthogonal cathode strips, as shown in Figure 8.3. While suffering, as most other micropattern detectors, with a gain shift after the initial switch on, due to charging-up of the dielectric substrate (shown in Figure 8.3 as the white part), these detectors have been considered for various applications, such as readout of time projection chambers (TPCs) and time-resolved neutron imaging.

In general, the main advantage of micropattern detectors is that they are produced using microelectronic technology, which offers high granularity and, thus, excellent 2D position resolution, even down to 20–40 μm, which is quite difficult to achieve with other classical detectors. Since the distance between the anode and the cathode electrodes is reduced, in some cases even down to 50 μm, the operating voltages needed are significantly lower than in classical detectors. As a consequence, these detectors can strongly compete with alternative devices in many applications. They have also opened paths for new possibilities outside high-energy physics, as described at the end of this book. On the other hand, the thin gap between electrodes and the fine electrodes structures makes them

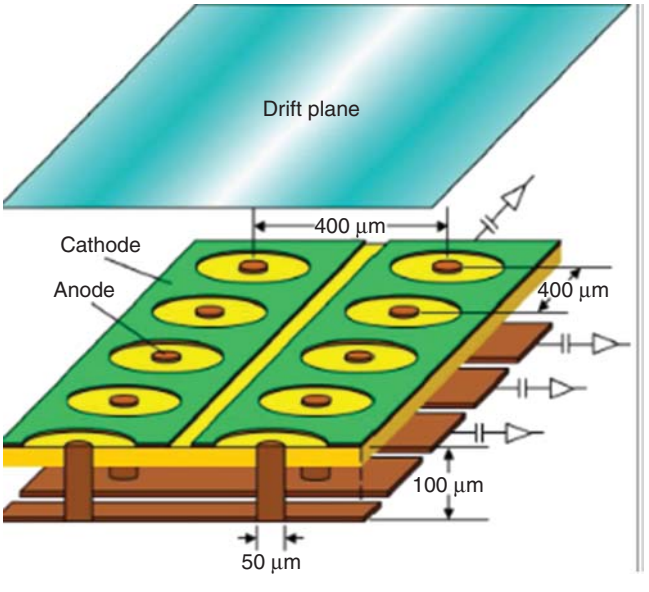

Figure 8.3 Schematics of a micropixel chamber with metallic electrodes and a circular dielectric structure between them. (From Ochi *et al*. (2002). Reproduced with permission of Elsevier.)

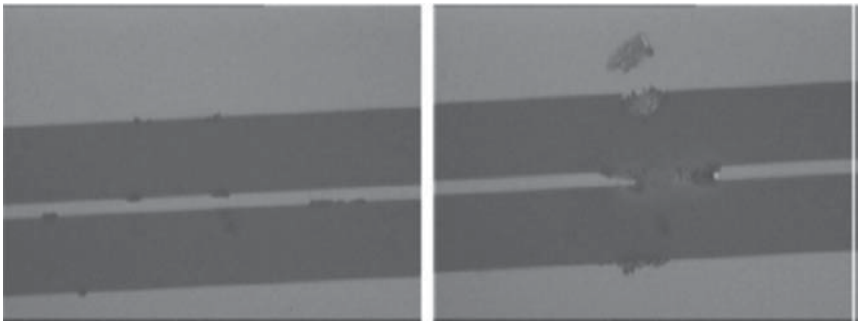

Figure 8.4 (a) Photograph of a damaged, but still operational, MSGC. (b) A severely damaged anode of an MSGC, which caused this detector part to become not operational. (From Visbeck 1996.)

electrically fragile, and in fact they can be easily damaged in occasional breakdowns. As an example, photographs of typical damages in MSGCs are shown in Figure 8.4.

There are several causes of breakdowns in micropattern detectors; among many, we can cite the following:

1) Electrically weak regions, due to some specific detector design (for instance, sharp edges, etc.).
2) Various imperfections in the actual structure, which may appear during the manufacturing processes, during storage or installation (which, of course, are critical for any small gap detector): tips, microparticles (like dust), dirt.
3) If the detector has excellent quality, a discharge may appear in case the total charge in an avalanche exceeds a critical value, which we know is typically around 10^7 electrons (Fonte *et al.*, 1999). This is a actually related to the Raether limit discussed earlier.
4) At high counting rates, avalanches may overlap each other, and thus the Raether limit could be reached even at low gas gain. Due to this effect, in micropattern detectors, the maximum achievable gain drops with rate.
5) At high counting rates, jet emission from the cathode may also trigger breakdown, if the total charge in a jet exceeds the Raether limit.

Several methods have been implemented to protect micropattern detectors from damage caused by discharges: segmentation of cathodes (to reduce the total capacitance involved in the discharge process), protection of the front-end electronics by means of diodes, or connecting several megaohm resistors in series with the electrodes. All these measures were only partially successful, and never offered a complete protection from the damage caused by discharges.

A new momentum to the use of these detectors was therefore given when discharge quenching using resistive electrodes was introduced. These exciting developments are described in the following paragraphs.

8.2 Spark-Proven GEM-like Detectors with Resistive Electrodes

If one follows the chronological order, then a resistive electrode approach was first implemented in the case of a GEM-like detector made out from a printed circuit; this detector configuration is often called "thick" resistive GEM (see Bidault *et al*., 2006). Later on, several prototypes of various kinds were developed and successfully tested (see, e.g., Oliveira *et al*., 2007; Peskov *et al*., 2009, 2012, 2013). Here, we concentrate, in particular, on the most advanced designs of resistive GEM-like detectors.

One of them is shown in Figure 8.5. In this detector, the GEM foils are not coated with metal as in standard GEMs, but the coating is rather made of some resistive material. The best results have been obtained so far with resistive kapton (of type 100XC10E5, 50 μm thick) and with a resistive paste (Encre MINICO), also generally used for transistors in printed circuits. Typically, the manufacturing procedure used is as follows. On both sides of a printed circuit board (PCB) (0.5–1.5 mm thick), a charge collecting copper mesh (see Figure 8.5) is manufactured by photolithographic technology. Then on the top of these inner mesh electrodes, a resistive layer is deposited using screen printing technology. The plate is then treated in an oven at 200 °C, in order to harden it. After this procedure, holes are drilled between the metallic strips by a computer numerical control (CNC) machine. Typically, hole diameter is in the range 0.8–1 mm, and pitch between 1.2 and 1.3 mm.

The difference between the development of a discharge in a standard GEM and in a GEM detector with resistive electrodes can be understood with the

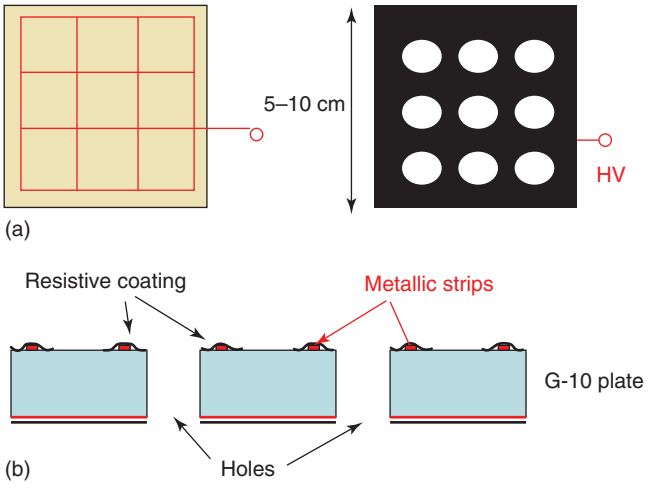

Figure 8.5 (a) Top views of a thick resistive GEM at different stages of manufacturing. (a) Left shows a printed circuit board with metallic strips; (a) right depicts a resistive GEM already coated with its resistive layer and where holes have been drilled. (b) cross section of a thick resistive GEM (Fonte *et al*. 2009. Reproduced with permission of Elsevier.)

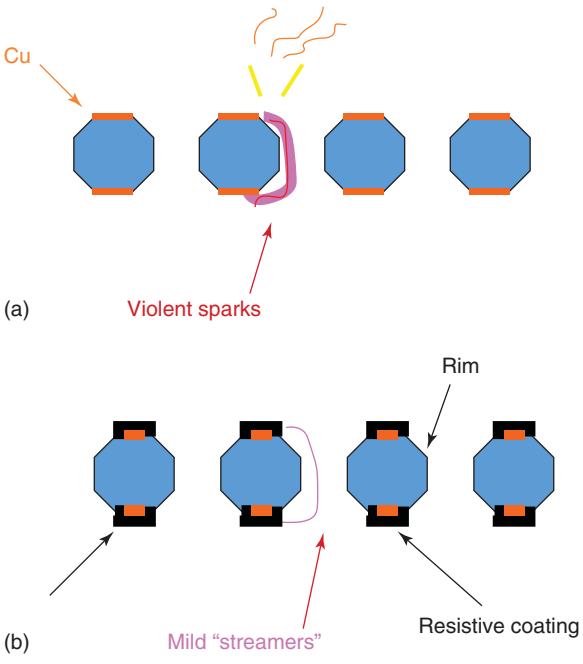

Figure 8.6 Cross section schematics of (a) a GEM and (b) a resistive GEM with inner metallic electrodes (mesh).

help of Figure 8.6. In the former, the whole energy stored in the detector-related capacitances is released in the spark; whereas in the latter the discharge develops in a way similar to RPCs, namely, through its resistive layer, so that the related current is strongly limited.

Moreover, designs employing resistive materials allow the collection of the charge associated to an avalanche onto the inner metallic (see Figure 8.5a) strip closest to the hole where the avalanche occurs, and thus minimizes the current flowing along the electrode surface. This allows building relatively large size detectors, like the one shown in Figure 8.7. In some prototypes, the grid metallic electrodes below the resistive layer are designed in such a way as to offer the possibility of obtaining 2D information about the avalanche position from the signals measured on the metallic strips. Such detectors can operate without a noticeable charging-up effect at a counting rate up to 10^4 Hz/cm^2 (see Figure 8.8).

Resistive electrode technology for micropattern detectors was tested and then further developed by many groups (see, e.g., Razin *et al*., 2009; Akimoto *et al*., 2010; Yu *et al*., 2011). Probably, the most impressive achievements are described in Yoshikawa *et al*. (2017); in this case, the authors used a laser etching technique to manufacture a resistive GEM characterized by a geometry very close to a "classical" GEM, with a 140-μm hole pitch and a 100-μm-thick dielectric layer between the electrodes (see Figure 8.9).

Another type of thick resistive GEM was suggested in the work reported in Di Mauro *et al*. (2006). In this design, the anode of the thick resistive GEM is in direct mechanical contact with the readout plate, so that there is no gap between them (see Figure 8.10). The advantages of this approach are as follows:

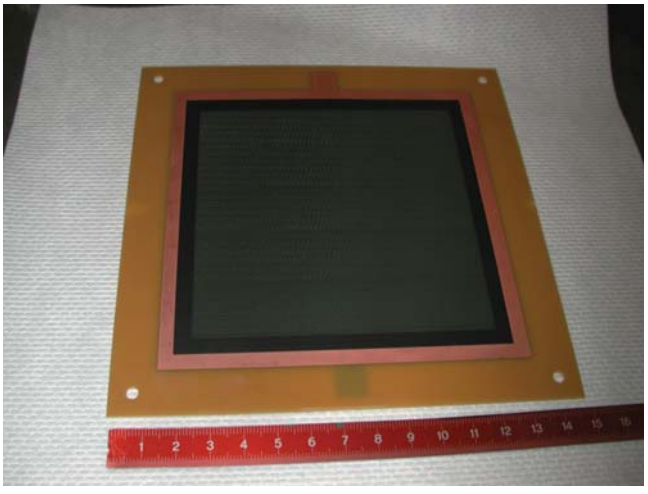

Figure 8.7 Photograph of 10 ×10 cm^2 thick GEM with resistive electrodes and inner metallic mesh.

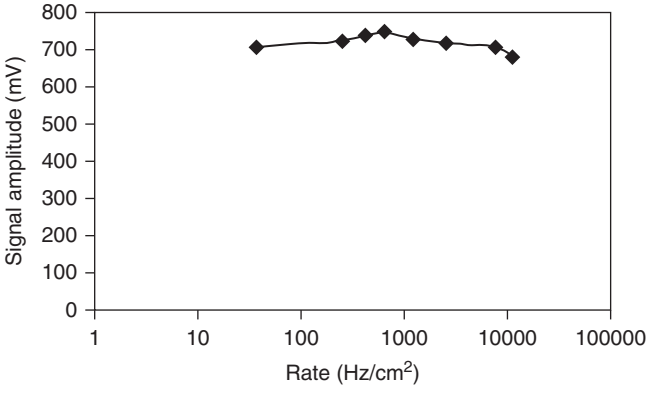

Figure 8.8 Signal amplitude (from a ^{55}Fe source) versus the counting rate for a thick GEM detector made of resistive kapton and operating at a gas gain around 1400. (Oliveira *et al*. 2007. Reproduced with permission of Elsevier.)

1) Compared to ordinary GEMs, this device is characterized by signals almost twice higher for the same voltage across the gap, since there is no loss of avalanche electrons taking place during their extraction from the hole.
2) The possibility of using a much wider variety of resistive materials for the anode plate, since there are more relaxed requirements on the layer thickness and also the demands on its pattern structure are different.

This approach was further developed by several other groups (see, for instance, Rubin *et al*., 2013; Arazi *et al*., 2013 and references therein). These detectors have often different names, but all of them operate on the same principle, and have quite similar designs. As an example, let us mention a large-area device, generally named "resistive microwell" (or "R-microwell"), proposed also for the compact

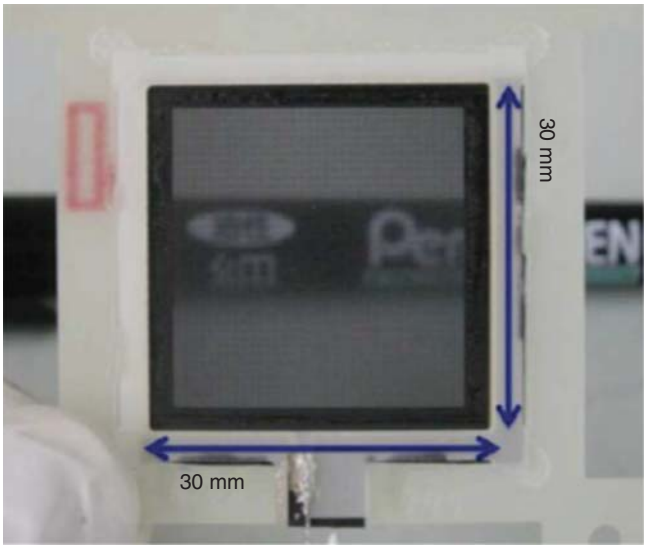

Figure 8.9 Photograph of a resistive GEM manufactured using the laser etching technique. (Yoshikawa *et al*. 2017. Reproduced with permission of IOP Publishing.)

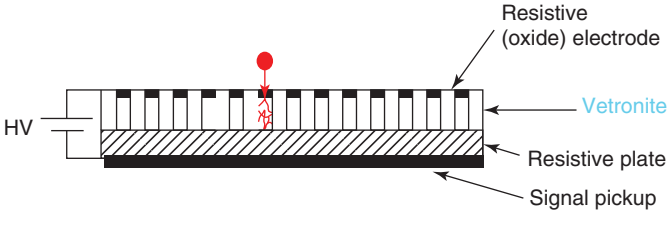

Figure 8.10 Schematics of a thick resistive GEM, whose anode is in direct mechanical contact with the readout plate. (From Di Mauro *et al*. (2006).)

muon solenoid (CMS) phase 2 muon system upgrade. Its schematic drawing is shown in Figure 8.11.

In this case, the detector structure is realized by merging a suitable etched GEM foil with a readout PCB plane, coated with a resistive deposition. Since geometrically this structure resembles an array of wells, it is called a microwell. The copper on the bottom of the GEM foil is patterned in order to create small copper dots corresponding to each well structure. The resistive coating is performed using screen printing technique as in the earlier designs described. In principle, a more sophisticated sputtering technology such as diamond-like carbon (DLC) can be used for precise resistive layer patterning. In this case the matrix of wells is realized on a 50-μm-thick polyimide foil, with conical channels 70 μm in diameter on the top and 50 μm at the bottom of the GEM, with a 140 μm pitch. A cathode electrode, defining the gas conversion/drift gap, completes the detector structure.

A magnified picture of a microwell structure is shown in Figure 8.12, whereas the photograph of a large-area readout board is reported in Figure 8.13.

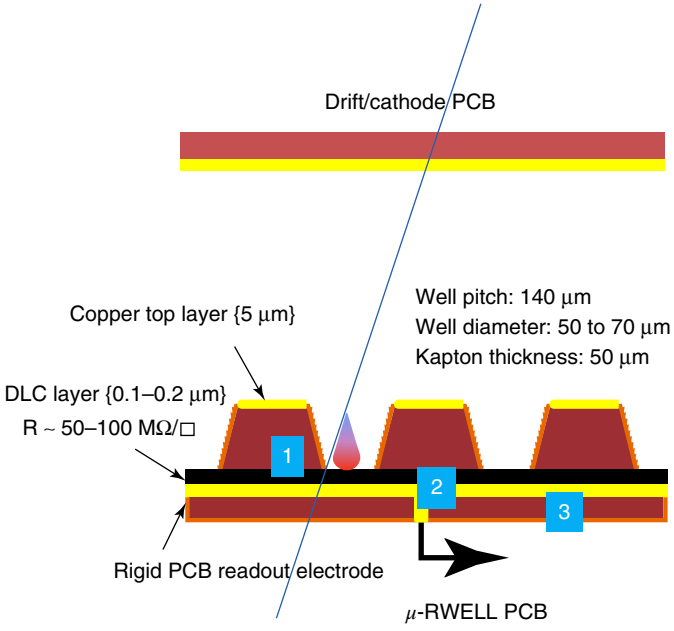

Figure 8.11 Sketch of a microwell detector; the legend is as follows: (1) GEM conical structure (resembling a well), (2) resistive layer, and (3) PCB-based readout electrode. (From Bencivenni *et al*. 2017.)

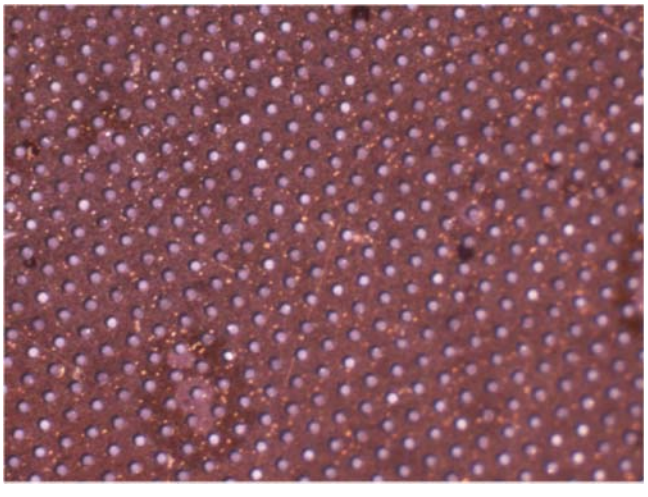

Figure 8.12 Magnified photograph of a microwell structure. (From Bencivenni *et al*. 2015.)

The success achieved with the first prototypes of resistive GEMs triggered further developments and researches in this field (see, for instance, De Araujo, 2016); nowadays the resistive electrode approach is applied practically to all types of micropattern detectors. In the following paragraphs, we review some specific examples.

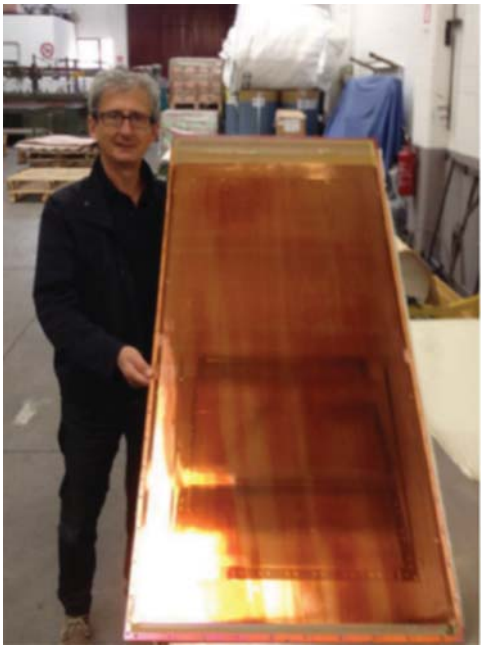

Figure 8.13 Photograph of a large-area readout board, developed for a microwell detector proposed in the framework of the phase 2 upgrade of the muon system of the CMS experiment. (Bencivenni *et al*. 2016. Courtesy of Dr. Giovanni Bencivenni.)

8.3 Resistive Micromesh Detectors

Earlier on in this book, we have cited the parallel-plate avalanche counters (PPACs), that is, parallel-plate detectors operating in avalanche mode. One of its modifications was a detector in which one of the two electrodes was made from a metallic mesh. This detector was used as a pre-amplification structure in the early designs of *R*ing *I*maging *CH*erenkov (RICH) detectors (already mentioned in Chapter 1), with a typical gap between the electrodes around 3–5 mm. A micropattern version of this mesh-type detector is named MICROMEGAS (see paragraph 8.1) having almost 100 times smaller gap allowing to correspondingly reduce the operating voltage and improve the spatial resolution to the sub-micrometer level. Both in PPACs and MICROMEGAS, discharges appear when the total charge in avalanches reaches the Raether limit; but while the Raether limit for PPACs is around 10^8 electrons, in MICROMEGAS, as a consequence of the much smaller gap, this limit is 1 order of magnitude less.

To protect MICROMEGAS and its front-end electronics from the damage due to sparks, the use of a resistive cathode mesh instead of a metallic one was proposed; in one instance, it was manufactured using resistive (carbonated) kapton and employing a laser drilling technique (see, for instance, Oliveira *et al*., 2010).

Alternative designs, developed later and in parallel by various groups, use a resistive anode instead of a resistive mesh (Jeanneau *et al*., 2012); this is schematically shown in Figure 8.14.

The idea is to use a double-layer PCB readout board. The top layer, facing the mesh, is made of a resistive layer or, in some designs, of resistive strips serving

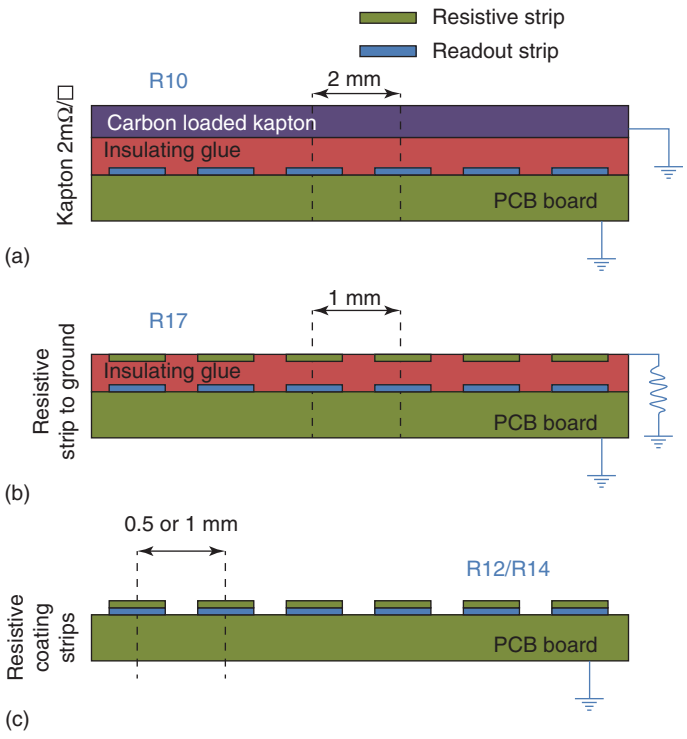

Figure 8.14 Geometry of the different resistive-anode technologies (marked as a,b,c) used for spark-protected MICROMEGAS. The resistivity of the anode strips could be varied, depending on the experimental demands, in the 0.5–100 MΩ/cm range.

simultaneously as charge collection and discharge protection elements. The readout metallic strips are located around 0.12 mm below; their role is to detect the induced signals from the resistive layer or the resistive grid. As an isolator between the resistive and metallic strips, photoimageable Coverlay, typically 60 μm thick, is used. Coverlay consists of a solid sheet of polyimide with a layer of flexible adhesive that is then laminated under heat and pressurized to the circuit surfaces. It is used to encapsulate and protect the external circuitry of flexible circuit boards.

As can be seen, in this design the detector itself and the front-end electronic connected to the readout strips are well protected. The maximum rate characteristics of these detectors are quite similar to ones measured with resistive GEMs: the signal amplitude starts to drop at a counting rate around 10^4 Hz/cm^2 (see Figure 8.15).

Recently a large-area resistive MICROMEGAS (1×2.4 m^2) with an anode plate (shown in Figure 8.16) was manufactured and tested in order to prove the feasibility of constructing a large-size detector of this type (Bianco, 2016).

Large-area resistive MICROMEGAS will be employed for the first time in high-energy physics for the upgrade of the muon spectrometer of the ATLAS experiment at CERN. The forward regions of the muon spectrometer will be equipped with eight layers of resistive MICROMEGAS modules, each covering

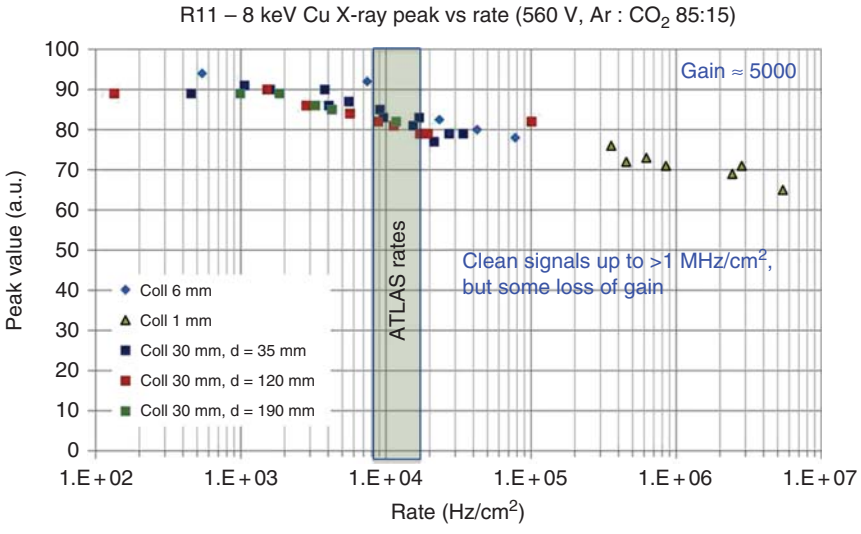

Figure 8.15 The response of a resistive MICROMEGAS to collimated 8 keV photons impinging on the detector, as a function of the rate/cm^2; the data with the 30-mm collimator were taken at different distances *d* between the collimator and the MICROMEGAS. (Alexopoulos *et al*. 2011. Reproduced with permission of Elsevier.)

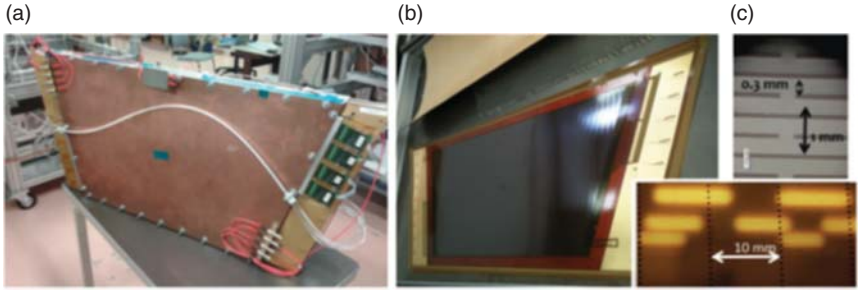

Figure 8.16 Photographs of a resistive MICROMEGAS prototype for the ATLAS small wheels (a), the readout board (b), and magnified views of the resistive strip pattern (c). (Bianco 2016. Reproduced with permission of Elsevier.)

a surface of 2÷3 m^2, for a total active area of around 1200 m^2. Together with small-strip thin-gap chambers, resistive MICROMEGAS compose the two New Small Wheels, which will replace the innermost stations of the ATLAS Endcap Muon tracking system during the 2018/2019 shutdown. Some photographs of one of the MICROMEGAS prototypes for the Small Wheels are shown in Figure 8.16.

Results about spatial resolution measurements with MICROMEGAS having a resistive strip 300 μm wide and with a 415 μm pitch are shown in Figure 8.17. In the case of perpendicular tracks, a good estimate of the position of the crossing point can be obtained from the charge-weighted positions of the clusters of hits in the detector. The spatial resolution for perpendicular tracks can be

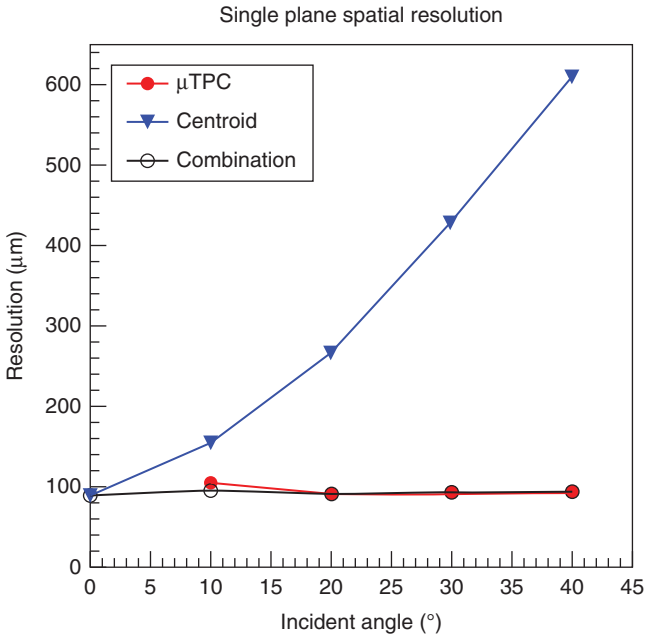

Figure 8.17 Position resolution of a resistive MICROMEGAS, measured using three different methods: the standard charge centroid (triangles), the so-called μTPC method described in the text (full circles) and the combination of the two (open circles), as a function of the particle incident angle. (Bianco 2016. Reproduced with permission of Elsevier.)

estimated from the difference of the cluster centroid measured in pairs of resistive MICROMEGAS chambers. Of course, the standard deviation from the Gaussian fit has to be divided by $\sqrt{2}$, assuming the same resolution for the two chambers. Measurements have shown that a spatial resolution of about 73 mm can be obtained with an average cluster size of 3.2 strips.

However, for impact angles larger than 10° the cluster charge-centroid method cannot guarantee the desired resolution. So an idea was proposed to exploit the timing information from each single strip, by operating the detector in the so-called micro time projection chamber (μTPC) mode, made possible by the fact that the measure of the arrival times of the ionization electrons can be performed with a time resolution of a few nanoseconds (Iodice, 2015). With an Ar/CO_2 93/7 gas mixture and an electric drift field of 600 V/cm (both typical of these devices), the drift velocity results to be around 47 mm/ns; by converting the measured time to the position from which the drift electrons originate, it is possible to reconstruct the segment of the tracks inside the drift gap and thus determine the position of an inclined track (see Figure 8.17).

In principle, the intrinsic time resolution of a MICROMEGAS could potentially be quite good, thanks to the small gap between the electrodes. However, reaching the theoretical limits in practice is not so straightforward, since MICROMEGAS, in contrast with small-gap RPCs, have a drift region. Primary electrons created by the ionization radiation in this region have a considerable jitter in arrival time and

this, as a consequence, imposes a limit in time resolution no better than about a few nanoseconds.

Certainly, much better timing could be achieved if all electrons were to be created at a fixed distance from the anode, for example, from the cathode mesh surface of the drift electrode. But even in this case one can reach good timing only with high-enough number of primary electrons, since for timing measurements, even when current amplifiers are used, the signal amplitude has to be high enough.

8.4 Resistive Microstrip Detectors

For a long time, GEMs and MICROMEGAS were the most popular micropattern detectors. Other types of micropattern detectors were considered to be less reliable for practical applications and, with time, they were almost abandoned. However, after the introduction of the resistive electrode approach, some almost forgotten micropattern designs got a second life.

A relevant example is the MSGCs, already mentioned at the beginning of this chapter. The spark-protected version of this detector is manufactured from a conventional multilayer PCB 0.5 mm thick, whose top surface is coated with a 5-μm-thick Cu layer (see Figure 8.18a).

The two bottom layers of this board consist of 0.1-mm-thick FR-4 sheets, each equipped with parallel metallic readout strips; the width of the readout strips is

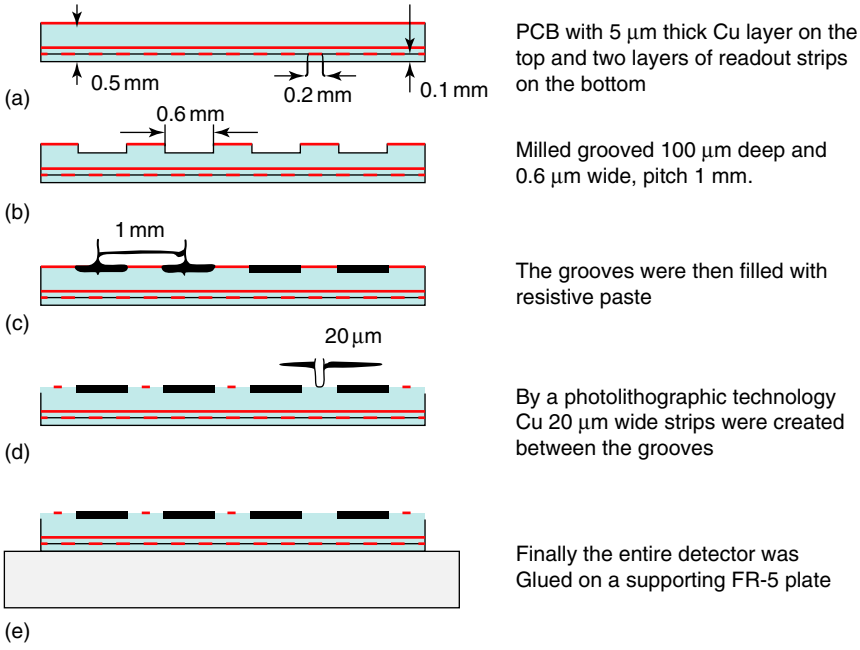

Figure 8.18 Schematic illustration of a resistive MSGC manufacturing process. (Peskov *et al*. 2011. Reproduced with permission of IEEE Transactions.)

200 μm and their pitch 1 mm. The strips of the second layer (counting from the top) are oriented perpendicular to the strips of the third layer. Subsequently, on the top surface of the PCB, parallel grooves are milled, 100 μm deep, 0.6 mm wide, with a pitch of 1 mm. These grooves are oriented parallel to the strips of the third layer (see Figure 8.18b). The grooves are then filled with a resistive paste (ELECTRA Polymers) and the resistive MSGC surface is chemically cleaned (see Figure 8.18c). Finally, using a photolithographic technology, 20 μm wide copper strips are created between the grooves (Figure 8.18d). Then this detector is glued onto a 2-mm-thick FR-5 supporting plate (Figure 8.18e). Both the anode and the cathode strips are covered near their edges by a Coverlay layer to avoid discharges on the surface.

Figures 8.19 shows the gain of a resistive MSGC as a function of the applied voltage. Gas gains in the interval 1–100 were measured with alpha particles. This was done because one can clearly see the signal S_{ich} even at gain one (at low voltages, when the detector operates in ionization mode–see Chapter 1) and this is exploited for further gain calibrations: the gain at higher voltages is simply $A = S_{\text{obs}}\,(V)/S_{\text{ich}}$, where S_{obs} is the signal measured at a given voltage. Due to the Raether limit, at gas gains higher than 100, alpha particles cause breakdown. For this reason, for gas gains higher than 100 the measurements were performed with 6 keV photons from an ^{55}Fe source. In this case, the maximum achievable gain is around 10^4, which is as high as it typically can be reached with ordinary MSGCs manufactured on a glass substrate.

The energy resolution measured is around 25% full width at half maximum (FWHM), which also is close to the typical values measured with MSGCs. The position resolution achieved with this detector is about 200 μm (Peskov *et al.*, 2011) and its rate characteristics very similar to the ones measured with other resistive micropattern detectors (for instance, MICROMEGAS, shown in Figure 8.15), the gain starting to drop at counting rates above 10^5 Hz/cm^2 (see Figure 8.20).

Resistive MSGCs have some advantages with respect to other designs of spark-protected micropattern detectors. For example, compared to MICROMEGAS, they have a simpler design (no cathode mesh), are easier to manufacture, and they are easier to clean from undesirable microparticles. On the contrary, in the

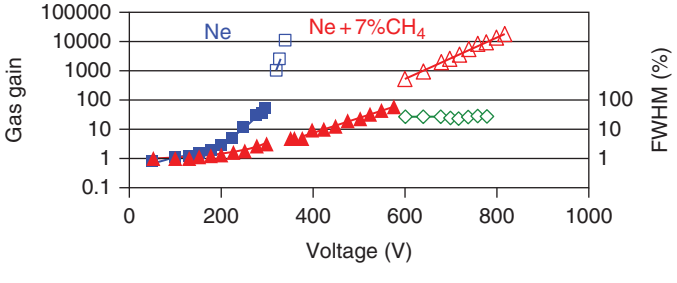

Figure 8.19 Gas gain of a resistive MSGC as a function of the voltage applied, measured in pure Ne and in Ne + 7% CH_4 with alpha particles (filled triangles and squares) and with ^{55}Fe (empty triangles and squares). The curves with open diamonds represent the energy resolution (FWHM at 6 keV) measured in Ne + 7%CH_4.

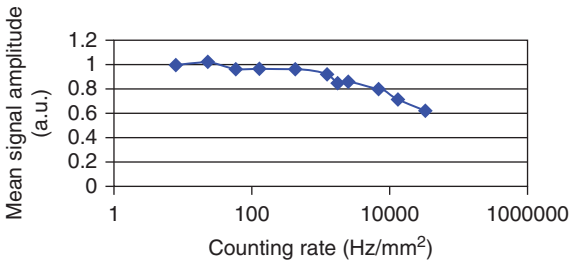

Figure 8.20 Gas gain of a resistive MSGC variations as a function of the counting rate, measured with an X-ray gun in neon-based mixtures initial at a gas gain of 5×10^3.

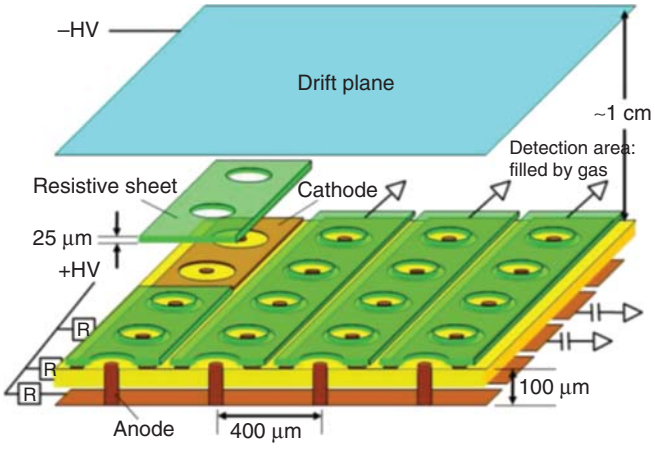

Figure 8.21 Schematic structure of resistive cathode micro-pixel detector. In this case, the anodes are connected to back strips, the cathodes are printed on surface to surround the anode pin and are covered with resistive layers. Two coordinates can be reconstructed by reading the signals from anodes and cathodes. (Ochi *et al*. 2012. http://iopscience.iop.org/article/10.1088/1748-0221/7/05/C05005/meta. Licensed under CC BY 3.0.)

case of resistive MICROMEGAS, the dust particles stacked between the mesh and the anode plate might cause problems.

8.5 Resistive Micro-Pixel Detectors

We now describe another example of resistive micropattern detector, namely, a spark-protected version of the micropixel detector (mentioned earlier, for instance, see Figure 8.3). The original version of this detector has some similarity with the microwell detector; however, in this first case, the diameter of the anode dot is less than the diameter of the cathode holes.

The schematic drawing of a resistive micropixel detector is shown in Figure 8.21, and its cross section in Figure 8.22. Comparing Figures 8.3 and 8.21 one can conclude that at first glance the detectors seem to be almost identical. In fact, there is an essential difference: the cathode electrodes are covered with resistive material (see Figure 8.21 for more details) (Ochi *et al*., 2012).

During typical operation, the static electric field around the anode is almost the same as in conventional micropixel detectors, whose cathodes are made with

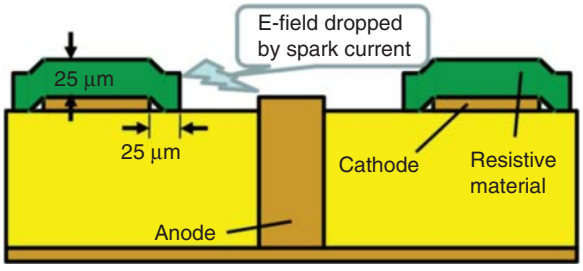

Figure 8.22 Magnified cross section around anode and cathode electrodes of a resistive micro-pixel detector, like the one shown in Figure 8.21. Huge current caused by sparks or large energy deposits will reduce electric field due to higher resistive film on cathodes. (Ochi *et al*. 2012. http://iopscience.iop.org/article/10.1088/1748-0221/7/05/C05005/meta. Licensed under CC BY 3.1.)

metal. The signals can be read out directly from the anodes. The signal from the cathodes will also be the same as in the conventional version because there are metal cathodes under the resistive foil that sense the induced charges. However, if a large amount of energy is deposited or a discharge happens, the electrical potential of the cathode surface on the resistive foil will rise and this will reduce the electric field around the anode and ultimately terminate the discharge. The charge of a spark is limited by the very small (0.1 pF) capacitance of single pixels.

8.6 Resistive Microhole-Microstrip and Microstrip-Microdot Detectors

From the material presented it is clear that the resistive electrode approach is not technologically too complicated and can be applied practically to any design of micropattern detectors. As further examples proving this, resistive microhole-microstrip and microstrip-microdot detectors are hereafter described (see also Fonte *et al*., 2012).

These detectors are, in fact, hybrids between GEMs and microstrip detectors and GEMs and microwell/microdot detectors, respectively; they are especially useful in applications in which ion and photon feedback suppression is important. Relevant applications are with TPCs and various types of gaseous and cryogenic photodetectors (see, for instance, (Lyashenko *et al*., 2009; Peskov *et al*., 2013). The original version of this type of detectors (with metallic electrodes) was introduced in Veloso *et al*. (2000).

Both resistive microhole-microstrip and microstrip-microdot detectors are manufactured from a printed circuit plate, typically 0.4 mm thick. In the case of the microhole-microstrip, the manufacturing procedure is similar to that used in the production of the resistive microstrip detectors (see preceding text) with an additional last step which includes holes drilled by a CNC machine.

The top surface of the PCB board is coated with a copper layer, while the bottom surface has arranged alternatively resistive cathode and metallic

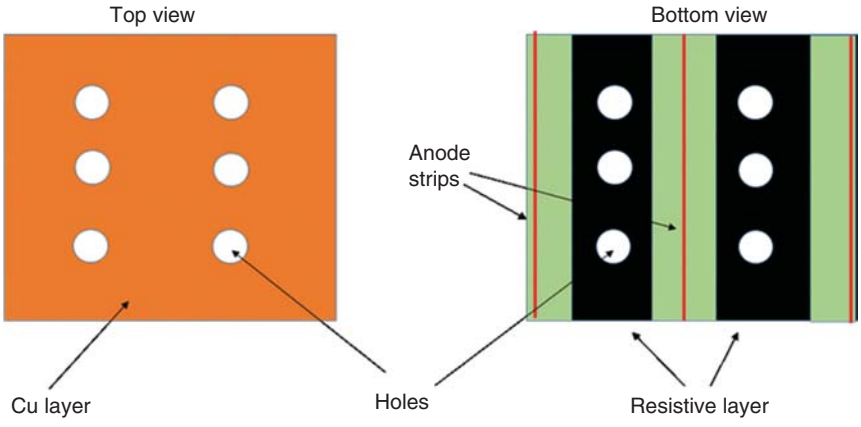

Figure 8.23 Simplified view of a resistive microhole-microstrip detector. Its top surface is coated by a copper layer with a matrix of holes drilled through. The bottom layer has parallel resistive strip cathodes and thin copper anodes.

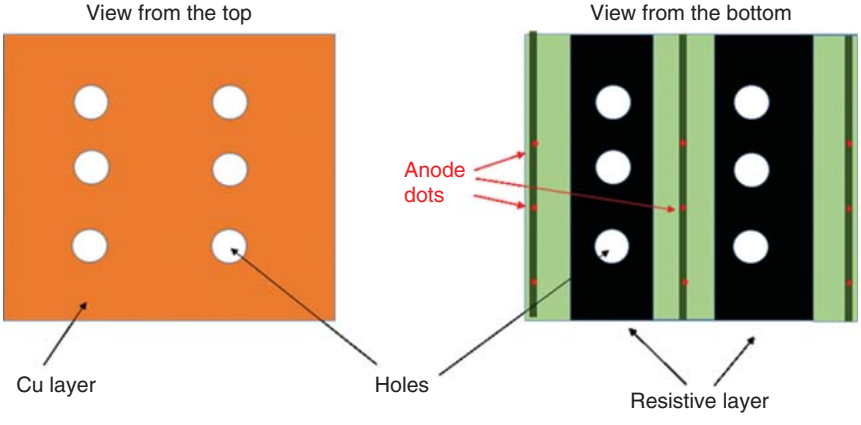

Figure 8.24 Schematic representation of a microstrip-microdot detector.

anode strips. The geometrical characteristics of this detector were anode strip width 20 μm, cathode width 0.6 mm, pitch 1 mm, a hole diameter 0.3 mm, active areas 60×60 mm^2 and 100×100 mm^2 (see Figure 8.23).

Microstrip-microdot detectors have a quite similar design, but the cathode strips are wider and coated with a Coverley layer with periodic circular openings which serve as anode dots (see Figure 8.24).

Figure 8.25 explains in a simplified way why resistive microhole-microstrip and microstrip-microdot detectors allow to effectively suppress photon and ion feedback. As can be seen from this figure, the light emitted by avalanches, is geometrically shielded from the photocathode, so only a small fraction of it, mainly the scattered light inside the detector and the chamber volume, can reach it. Thus, the photon feedback is practically completely eliminated.

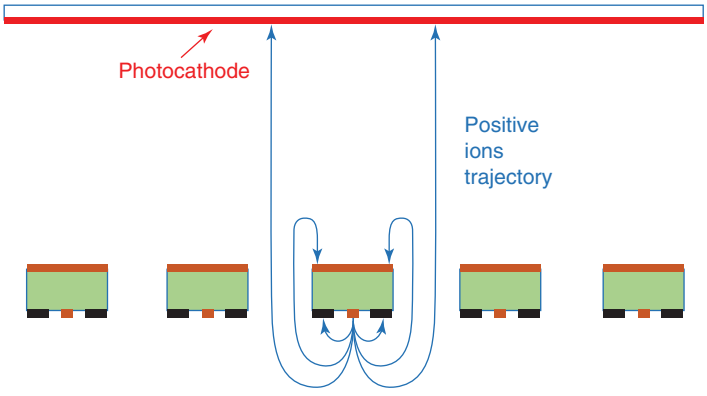

Figure 8.25 Schematic illustration of the photon and ion feedback suppression in resistive microhole-microstrip and microstrip-microdot detectors. All photoelectrons are initiated from the photocathode and create avalanches near anode strops/dots. The trajectories of positive avalanche ions are shown.

After the short avalanche light flash and fast electron collection, the positive ions will still continue their slow motion toward the surrounding electrodes. Some of them will be collected onto the closest resistive cathode strips, while some will be collected on the upper electrode, so that only a fraction of them will reach the photocathode (Figure 8.25). By a careful optimization of the applied several voltages (namely, the voltage across the anode strips/dots and the resistive cathodes; the voltage applied across the holes; the voltage drop between the cathode and the top electrode of the detector), it is possible to suppress the ion back flow by a factor of 10 or even more. In practice, often cascaded hole-type detectors are used, allowing to suppress ion feedback to negligible levels.

Summarizing, several conclusions can be drawn from the developments described:

1) Resistive electrode approach was successfully applied to various designs of micropattern detectors, making them spark protected.
2) All restive micropattern detectors can operate practically without gain reduction up to counting rate of 10^4 Hz/cm^2.
3) As already pointed out in Chapters 6 and 7, electrode resistivity can be optimized, allowing to achieve a better rate characteristic.
4) Applications of resistive micropattern detectors are growing, for example, large-area resistive MICROMEGAS will be installed in ATLAS Small Wheels and large-area microwell detectors are considered for the CMS muon system upgrade.

At the moment, all these development are a premise for an even better future, when the resistivity approach applied to micropattern gaseous detectors will spread more and more (the latest developments are reviewed in (Peskov *et al.*, 2013).

References

Akimoto, R. *et al*. (2010) Measurements of basic features of thick-GEM and resistive GEM. *JINST*, **5**, 1–8. doi: 10.1088/1748-0221/5/03/P03002.

Alexopoulos, T. *et al*. (2011) A spark-resistant bulk-micromegas chamber of high-rate applications. *Nucl. Instrum. Methods Phys. Res., Sect. A*, **640**, 110–118.

Arazi, L. *et al*. (2013) Beam studies of the segmented resistive WELL: a potential thin sampling element for digital hadron calorimetry. *Nucl. Instrum. Methods Phys. Res., Sect. A*, **732**, 199.

Bencivenni, G. *et al*. (2015) The micro-resistive WELL detector: a compact spark-protected single amplification-stage MPGD. *JINST*, **10** (P02008), 1–10.

Bencivenni, G. *et al*. (2016) Status of the R&D on μ-RWELL, https://indico.cern.ch/event/532518/contributions/2184447/attachments/1287085/1915054/Micro-RWELL-status-report-RD51-June-2016.pdf (accessed 24 October 2017).

Bencivenni, G. *et al*. (2017) The RWELL detector. *JINST*, **12** (C06027), 1–8.

Bianco, M. (2016) Micromegas detectors for the muon spectrometer upgrade of the ATLAS experiment. *Nucl. Instrum. Methods Phys. Res., Sect. A*, **824**, 496.

Bidault, J.M. *et al*. (2006) A novel UV photon detector with resistive electrodes. *Nucl. Phys. B, Proc. Suppl.*, **158**, 199–203.

CERN Courier (1998) A GEM of a detector, 27 November 1998.

Charpak, G., Giomataris, Y., Rebourgerad, P. *et al*. (1995) High resolution position detectors for high-flux ionizing particles. Patent WO1996FR01576.

De Araujo, T. (2016) Timing and High Rate Capable (THRAC) Gas Detector, https://kt.cern/technologies/timing-and-high-rate-capable-thrac-gas-detector (accessed 08 November 2017).

Di Mauro, A. *et al*. (2006) A new GEM-like imaging detector with electrodes coated with resistive layers. IEEE Nuclear Science Symposium Conference Record, vol. 6, pp. 3852–3859.

Fonte, P. *et al*. (1999) The fundamental limitations of high-rate gaseous detectors. *IEEE Trans. Nucl. Sci.*, **46**, 321.

Fonte, P. *et al*. (2009) Progress in developing hybrid RPC:GEM-like detectors with resistive electrodes. *Nucl. Instrum. Methods Phys. Res., Sect. A*, **602**, 850.

Fonte, P. *et al*. (2012) Development and preliminary tests of resistive microdot and microstrip detectors. *JINST*, **7**, P12003.

Francke, T. and Peskov, V. (2014) *Innovative Applications and Developments of Micro-Pattern Gaseous Detectors*, IGI Global, Hershey, PA. ISBN-10: 1466660147.

Iodice, M. (2015) Micromegas detectors for the Muon Spectrometer upgrade of the ATLAS experiment. *JINST*, **10**, C02026.

Jeanneau, F. *et al*. (2012) arXiv:1201.1843v1, http://arxiv.org/abs/1201.1843 (accessed 24 October 2017).

Lyashenko, A. *et al*. (2009) Development of high-gain gaseous photomultipliers for the visible spectral range. *JINST*, **4** (07P07005), 1–22. doi: 10.1088/1748-0221/4/07/P07005.

Nishi, Y. *et al*. (1998) X-ray polarimetry with the microstrip gas chamber. *J. Synchrotron Rad.*, **5**, 857.

Ochi, A. *et al*. (2002) Development of micro pixel chamber. *Nucl. Instrum. Methods Phys. Res., Sect. A*, **478**, 196.
Ochi, A. *et al*. (2012) Development of micropixel chamber with resistive electrodes. *JINST*, **7**, C05005.
Oed, A. (1988) Position-sensitive detector with microstrip anode for electron multiplication with gases. *Nucl. Instrum. Methods Phys. Res., Sect. A*, **251**, 35.
Oliveira, R. *et al*. (2007) First test of thick GEM with electrodes made of resistive kapton. *Nucl. Instrum. Methods Phys. Res., Sect. A*, **576**, 362–366.
Oliveira, R. *et al*. (2010) First test of MICROMEGAS and GEM-like detectors made of a resistive mesh. *IEEE Trans. Nucl. Sci.*, **57**, 3744–3752.
Peskov, V., Di Mauro, A., Fonte, P. *et al*. (2013) Development of a new generation of micropattern gaseous detectors for high energy physics, astrophysics and medical applications. *Nucl. Instrum. Methods Phys. Res., Sect. A*, **732**, 255–259.
Peskov, V. *et al*. (2009) Progress in developing of photosensitive GEMs with resistive electrodes manufactured by a screen printing technology. *Nucl. Instrum. Methods Phys. Res., Sect. A*, **610**, 169–173.
Peskov, V. *et al*. (2011) Conference awards. IEEE Nuclear Science Symposium Conference Record, N5–2, p. 80.
Peskov, V. *et al*. (2012) Development of novel spark-protected micropattern gaseous detectors with resistive electrodes. *JINST*, **7**, 1–18.
Razin, V.I. *et al*. (2009) RETGEM with Polyvinylchloride (PVC) Electrodes, ArXiv:0911.4807, pp. 1–5, also in Instruments and Experimental Technique. doi: 10.1134/S002044121104021X.
Rubin, A. *et al*. (2013) First studies with resistive plate WELL gaseous multiplier. *JINST*, **8**, P11004.
Sauli, F. (1997) GEM: a new concept for electron amplification in gas detectors. *Nucl. Instrum. Methods Phys. Res., Sect. A*, **386**, 531–534.
Veloso, F.C.A. *et al*. (2000) A proposed new microstructure for gas radiation detectors: the microhole and strip plate. *Rev. Sci. Instrum.*, **71**, 2371.
Visbeck, S. (1996) Untersuchungen von Prototypen der Mikrostreifen-Gaskammern (MSGC) des inneren Spurkammersystems des HERA-B Experiments. Diploma thesis. Physikalisches Institut der Universität Heidelberg.
Yoshikawa, A. *et al*. (2017) Development of resistive electrode gas electron multiplier (RE-GEM). *JINST*, **7** (C06006), 1–9. doi: 10.1088/1748-0221/7/06/C06006.
Yu, B.X. *et al*. (2011) Performances of RETGEM with resistive elec-trodes made of kapton foils. *Chinese Phys. C*, **35**, 1120–1123. doi: 10.1088/1674-1137/35/12/007.

9

Applications beyond High Energy Physics and Current Trends

In this chapter we mainly focus on some applications of resistive gaseous detectors outside the field of high-energy physics. Of course, there are many other applications that we do not mention, and here we briefly report about just some of the most interesting from the conceptual or technological points of view. This chapter will help the reader grasp how vast and important could be the potential impact of these devices even on our everyday life. Of course alternative technologies with comparable or, in some aspects, even better performances, are presently available or will be in the near future. This is the case, for instance, of Micro Pattern Gaseous Detectors or solid state sensors. The choice on which one to use will have to be done considering the specific application. Of course, the reader is invited to go through the relevant literature on this subject and find even more exciting applications.

9.1 Positron Emission Tomography with RPCs

Positron emission tomography (PET) is a powerful diagnostic technique employed in functional medical imaging, based on the simultaneous detection of the two 511 keV γ-rays produced in the annihilation in the matter of a positron emitted by the β^+ decay of a suitable radionuclide (see Figure 9.1), previously injected in the body of the subject under study.

The concept of using gaseous detectors for the detection of 511 keV γ-rays was first pursued in the 1980s. As all gases at atmospheric pressure are essentially transparent to such gamma rays, this approach requires thin layers of solid materials where the photons will interact, generating energetic electrons that may escape from the material and be detected in the gas volume. Two main approaches were investigated: "converter plates," multiwire proportional chambers (MWPCs, already briefly described in Chapter 2) with cathodes made of thin lead plates (Bateman *et al*., 1981, 1984) and the "High-Density Avalanche Chamber" (Jeavons *et al*., 1983; Missimer *et al*., 2004), essentially a multi-hole drift volume with thin lead walls read out by a single MWPC.

The expected advantages compared with the standard scintillating crystal detection technology are the low cost per unit area (as an electric signal is generated directly forgoing the use of a photodetector and the crystals are costly *per se*) and the, in principle, good localization of the photon interaction point

Resistive Gaseous Detectors: Designs, Performance, and Perspectives, First Edition.
Marcello Abbrescia, Vladimir Peskov, and Paulo Fonte.

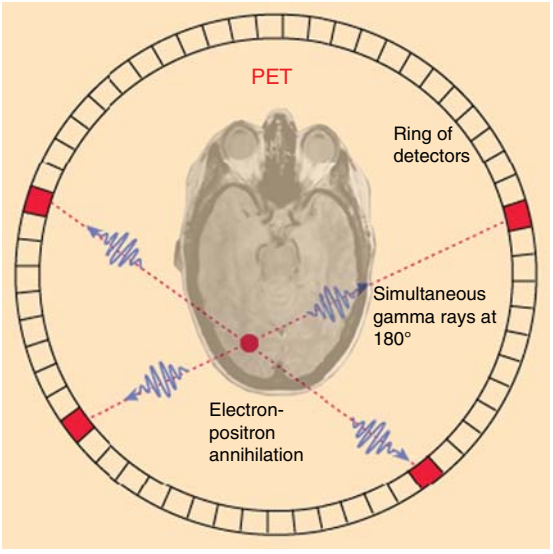

Figure 9.1 Principle of operation of the positron emission tomography (PET); the photons emitted back to back from electron-positron annihilation are detected by means of a ring of detectors placed all around the sample to be investigated.

in three dimensions. This is to be weighted against the much lower detection efficiency, to be partially compensated for by the use of many thin detector layers.

Alternatively it has been suggested that RPCs may offer an advantage over the lead converter plate approach (see Bateman, J.E. *et al.*, 1985) because the naturally layered structure of the multi-gap architecture offers a very economic way to multiply the number of sensitive layers. Moreover timing can be excellent, allowing to consider time of flight-positron emission tomography (TOF-PET) modality (Blanco *et al*., 2004,b, 2013). Two possible application areas were identified: small animal pre-clinical PET, where the position resolution advantage may be decisive, and full-body human PET, where the low cost and good timing may offset the lower efficiency by considering full-body field-of-view scanners instead of thin crystal rings.

Experimental and modeling developments have so far confirmed these expectations. The efficiency was measured to be close to 0.2% per gap with glass plates which are compatible with the simulation results shown in Figure 9.2 (Blanco *et al*., 2009) or more with other materials (Georgiev *et al*., 2013), and the time resolution $\sigma_i \approx 90$ ps for single photons (Lopes *et al*., 2007). Images were demonstrated with a 0.4 mm FWHM resolution (Martins *et al*., 2014) (Figure 9.3), which is roughly half of the best resolution obtained with crystals, and detailed simulations yielded that a full-body field-of-view RPC-PET scanner may yield a sensitivity that is eightfold higher than the best current commercial tomograph (Couceiro *et al*., 2014) (Figure 9.4).

Modeling and prototyping efforts were made also in the direction of applying RPC-PET to the monitorization of oncological hadron therapy treatments (Diblen *et al*. 2012; Watts *et al*. 2013). The efficiency of 0.2% per gap already measured by other authors has been confirmed, but the timing resolution was much lower. Indeed the RPC-PET technology needs some more development to become competitive in this application niche.

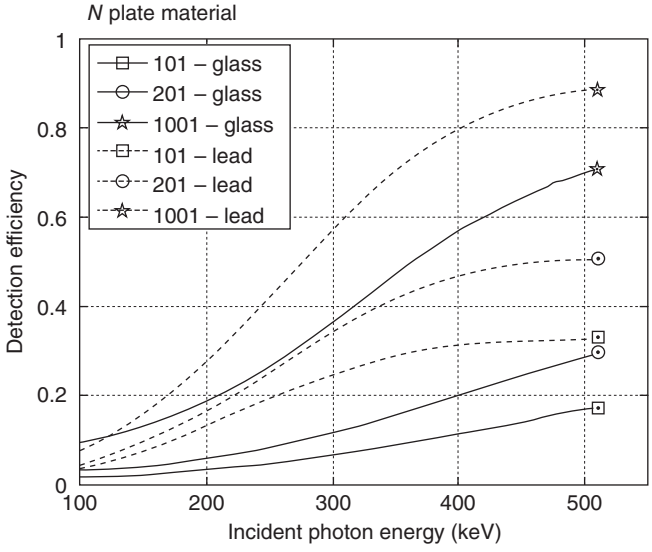

Figure 9.2 Simulated detection efficiency as a function of the incident photon energy for stacks of glass and lead optimum-thickness plates, for an RPC conceived to be used for PET. For comparison, note that efficiency for thick crystals can approach values up to 100%. (Blanco *et al*. 2009. Reproduced with permission of Elsevier.)

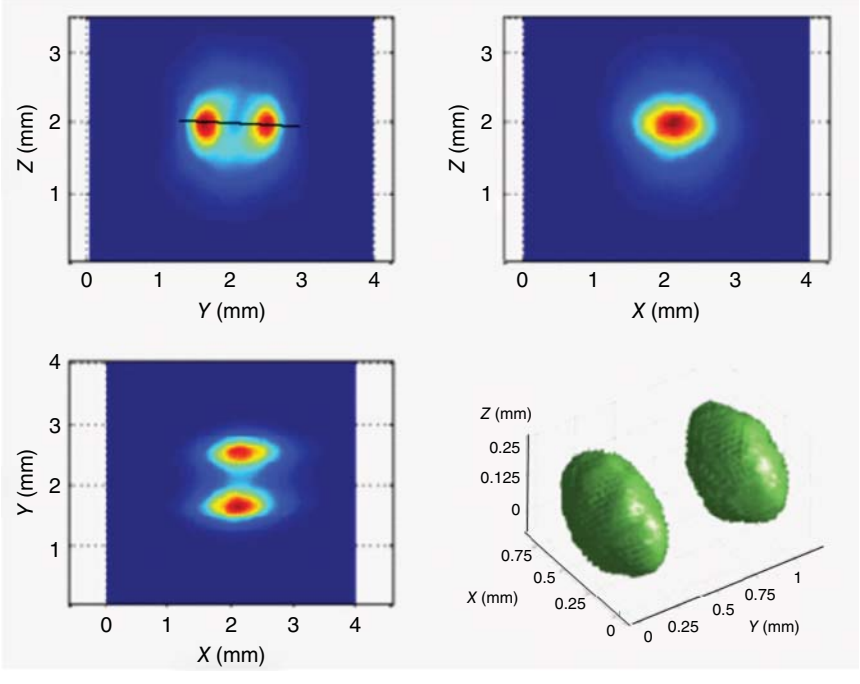

Figure 9.3 Images of a needle-like source placed in two positions physically separated by 1 mm and reconstructed by means of an RPC prototype intended to be used for PET. (Martins *et al*. 2014. Reproduced with permission of IOP Publishing.)

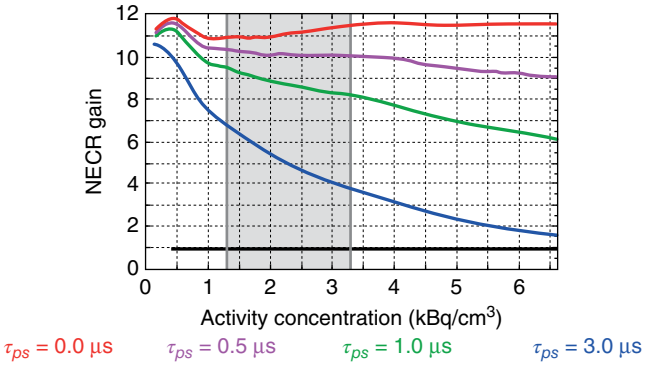

Figure 9.4 Ratio of the noise equivalent count rate (NECR)[1] expected in an RPC-PET whole-body scanner to the best available commercial tomograph (Philips gemini TF, represented with the horizontal line), for several scenarios of the electronics dead time (indicated with T_{ps}). The lowest lines corresponds to the largest T_{ps}. The shaded area corresponds to the generally accepted activity range in clinical examinations. (Couceiro *et al.* 2014. Reproduced with permission of IEEE Transactions.)

The concept of full-body field-of-view scanners with crystalline (Zhang *et al.*, 2014) or polymeric (Moskal *et al.*, 2016) scintillators is being also pursued, so far without conclusive results.

9.2 Thermal Neutron Detection with RPCs

The detection of thermal neutrons by means of gaseous detectors, and RPCs in particular, is especially relevant because of its possible applications also outside the field of high-energy physics. One of them was the DIAMINE (Detection and Imaging of Antipersonnel Land-Mine by Neutron Backscattering) project, which took place in the 2000s and whose target was to develop new detectors suitable for the neutron backscattering technique (NBT), employed to spot small mines made mainly with plastics and with low metal content, which are difficult to detect with the standard methods.

The NBT technique consists in irradiating the soil with a low-activity neutron source, typically ^{252}Cf, which, undergoing fission, emits neutrons with an energy in the 1–4 MeV range. They penetrate the ground and scatter with the nuclei in the layer of terrain overhanging the mine; part of them thermalize and are backscattering, so that they can be detected using a thermal neutron detector placed immediately above the ground. The yield of low-energy backscattered neutrons depends on the quantity of hydrogen contained in the irradiated volume, and therefore the presence of a landmine causes a localized increase of the yield due to the hydrogen content of the explosive and of the plastic case of the mine. The signature of the presence of a small mine will be an augmented

1 The Noise Equivalent Count Rate (NECR) is a quantity used in PET imaging that represents the net count rate of True events that is attained after Random and Scattered events are corrected. See (Dahlbom 2012) for details.

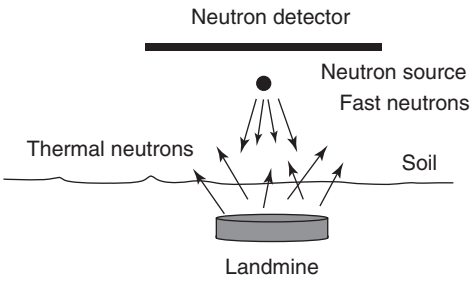

Figure 9.5 The neutron backscattering technique (NBT), proposed to detect small mines with low metal content.

detector counting rate when passing over a well-localized spot on the ground (see Figure 9.5).

In this framework, developing a simple, inexpensive, and easy-to-operate detector for thermal neutrons is of primary relevance. However, since neutrons are not charged particles, they can be detected in a gaseous detector only after an interaction with a suitable material, called converter, which, in turn, generates ionizing particles. One possibility is to use ^{3}He, because of its large reaction cross section and energy released when reacting with thermal neutrons; moreover, ^{3}He can be, in principle, added to the standard mixtures used in a gaseous detector, so that that the ionizing particles are produced directly where drifting and multiplication phenomena take place. The drawback is that ^{3}He is quite rare in nature, and it is difficult to produce artificially. Therefore, alternatives using more common materials are sought for.

Another possibility is using ^{10}B which, when interacting with thermal neutrons, can generate α particles. In addition to ^{10}B, two gadolinium isotopes, namely, ^{157}Gd and ^{155}Gd, have the largest cross section to thermal neutrons (on the order of 10^5 barn) and are therefore natural candidates for this task. Both are solid converters, so that they have to be used in thin layers adjacent to the detectors gas volumes, in such a way that the ionizing secondaries have a large probability to escape the layer and enter the gas.

A popular choice is a layer made of natural Gd, where the fraction of the two abovementioned isotopes is about 30%. As a consequence of the capture process of a thermal neutron, natural Gd produces, in around 60% of the cases, an electron from internal conversion, with a complex spectrum ranging from 30 to more than 200 keV, and a main peak around 70 keV. The range for the produced electrons in Gd starts from about 5 μm up to 20–30 μm.

In fact, when dealing with solid converters, the thickness of the converter layer is an important parameter to be optimized. Secondary particles produced by the interaction with the primary neutrons have to escape the converter layer and enter the gas in order to produce ion–electron pairs that can give rise to a detectable signal. Therefore, increasing the converter thickness improves the probability of neutron interaction, but one has also to consider that some of the secondaries can stop inside the converter if this is too thick.

In an RPC, there are two surfaces facing the gas where, in principle, the converter layer can be deposited, as shown in Figure 9.6. These two possible configurations can be conveniently classified as “forward” or “backward” in relation to

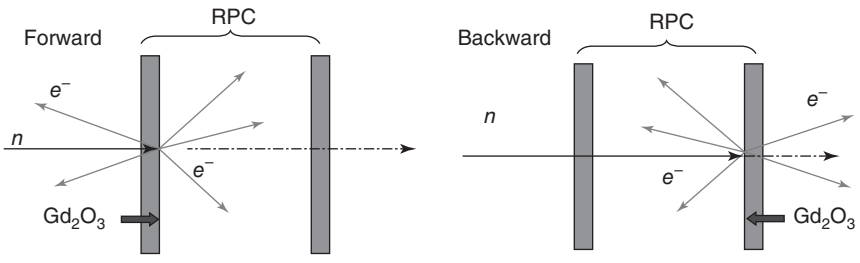

Figure 9.6 Schematics of the "forward" and "backward" configurations. (Abbrescia *et al*. 2004b. Reproduced with permission of Elsevier.)

the direction, with respect to the direction of the incoming neutrons, which the secondary electrons have to move in order to get into the gas.

One has to take into consideration the fact that even if secondary electrons are produced isotropically, neutron flux decreases exponentially inside the converter layer, because of neutron interactions with nuclei. This means that in the "forward" configuration, most conversions take place far from the gas gap, and the converter thickness cannot exceed the electrons' range to let them enter the gap. In the "backward" configuration, converter thickness does not play such a relevant role.

Natural Gd, however, is a metal not stable in air, and therefore not too easy to use in an RPC. This was the reason why one prototype of such a device was built using, as a converter, Gd-oxide (Gd_2O_3, usually called "Gadolina"), which is commercially available as a white inert powder, with granules l–3 μm in diameter, easy to handle and inexpensive. Gd-oxide powder was mixed with the linseed oil normally used to coat the inner surfaces of the electrodes in Bakelite RPCs, and before assembling, sprayed onto them. In this way, the granules of Gd-oxide remain trapped inside the oil once it polymerizes, producing uniform layers, with constant thickness and density, without altering the electric properties of the Bakelite electrodes, in particular their surface resistivity (see, for details, Abbrescia *et al*., 2003).

The prototype, shown in Figure 9.7, was tested in a beam line of the accelerator GELINA (*G*eel *E*lectron *LIN*ear *A*ccelerator), located at Geel, Belgium, where a

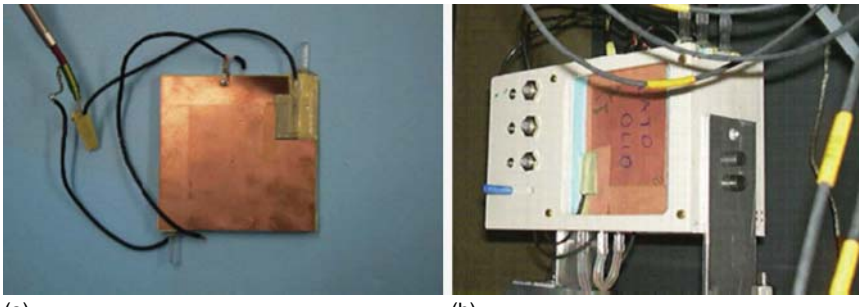

(a) (b)

Figure 9.7 Pictures of the first prototype of RPC coated with a mixture of linseed oil and gadolinium oxide (a) on a workbench. (From Abbrescia *et al*. 2004a.) and (b) mounted at a test beam. (From Abbrescia *et al*. 2004b.)

high-intensity neutron beam is obtained from an electron beam impinging onto a uranium target. The RPC detection efficiency, reported in Figure 9.8, for the region of thermal neutrons, resulted to be in the 10% range, making this one of the most performant detectors for thermal neutrons in absolute. Note that, as shown in Figure 9.8, the efficiency decreases with energy because of the decrease of the neutron cross section, which in this region is typically proportional to the inverse of the neutron velocity.

Similar prototypes of RPCs were built some years later by Korean (Hong *et al*., 2006) and Chinese groups (Qian *et al*., 2009, 2015), obtaining a thermal neutron detection efficiency comparable to the previous results (see Figure 9.9). In China,

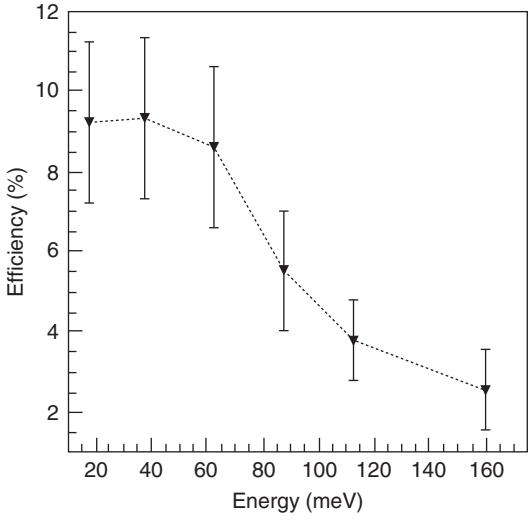

Figure 9.8 Percentage efficiency of the prototype shown in the previous figure as a function of the energy of the impinging neutrons. (Abbrescia *et al*. 2004a. Reproduced with permission of Elsevier.)

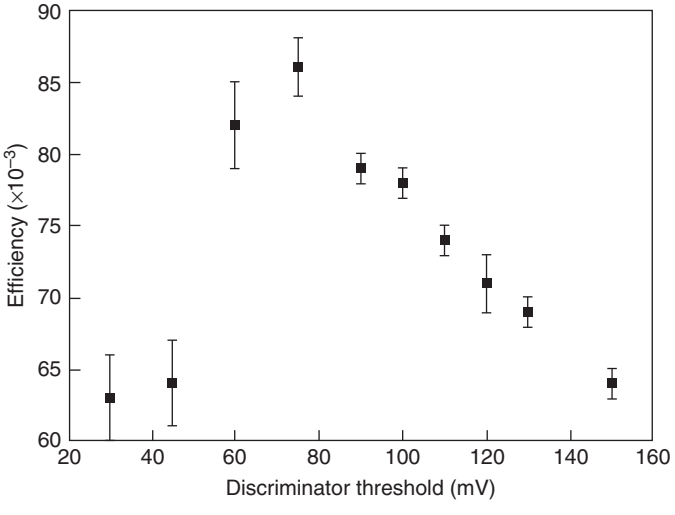

Figure 9.9 Efficiency for thermal neutron detection of an RPC with Gd converter versus the signal discrimination threshold; maximum efficiency is around 8.5%. (Qian *et al*. 2009. Reproduced with permission of IOP Publishing.)

in particular, these devices are studied in connection with the China Spallation Neutron Source (CSNS) Project, which will provide an important center for neutron scientific research, and the studies on the subcritical nuclear piles by the accelerator-driven system (ADS). In general, monitoring the neutron flux on large surfaces is an important issues in all nuclear plants.

RPCs made sensitive to neutrons have also been built using other converters, like LiF, where Li is the active target (see again Hong *et al*., 2006) and B_4C, with an enriched ^{10}B content (see Arnaldi *et al*., 2004, 2006), the latter developed in the framework of the DIAMINE Project already cited. In the two cases, the detectors proved to work, the advantage in these cases being that the secondaries are heavy-ionizing tritons or α particles, in principle, easy to distinguish against background. However, lower efficiencies (around a few percentages) were obtained, reflecting the lower neutron cross sections for Li and ^{10}B with respect to Gd.

More recently, in connection with possible applications for neutron reflectometry at the European Spallation Source (ESS), also thin (350 μm)-gap RPCs have been developed, suitable to be assembled in stacks of many single-gaps or in a multi-gap configuration (see Margato *et al*., 2016). In this case, a 2-μm layer of $^{10}B_4C$ was coated on an 8×8 cm^2 aluminum plate and used as cathode, while the anode was fabricated in glass. The peculiarity was the 2-mm-wide readout strips, which allowed demonstrating the possibility of building neutron detectors with a sub-millimeter spatial resolution. Note that for on field applications some technological issues have to be solved, like operating these chambers with very low or no gas flow at all, and with portable batteries to supply HV.

9.3 Muon Tomography and Applications for Homeland Security

Muon tomography is a technique to perform imaging of objects using cosmic ray muons. Since muons are characterized by a high penetrating capability (higher than X-rays, for instance) they can be used to obtain images of large, thick, and dense objects in a reasonable exposure time. It was invented in the early 1950s and has developed in two main branches, namely, muon transmission radiography and muon scattering tomography (MST).

Muon transmission is a shadow radiographic technique, consisting in comparing the amount of cosmic muons expected to arrive at a detector to how many are in fact incident (which can be obtained from simulation or measured on-site), to determine the amount of material (e.g., rock) they have traversed and reveal the presence, or not, of any voids. Basically, cosmic ray muon radiography is similar to X-ray radiography, except that penetrating muons serve in place of X-rays: the absorption of cosmic muons is a measure of the thickness and density of the material crossed. Moreover, by repeating the measurements from different locations, 3D maps of the matter density distribution can be computed.

It was first used in the1950s by Eric George to measure the depth of a tunnel in Australia, but probably its most famous instance is due to the Nobel Prize

winner Luis Alvarez, who used muon transmission imaging to search for hidden chambers in the Pyramid of Chephren at Giza, although none were found (Alvarez *et al*., 2007).

Various detectors have been, and are currently used, in connection with projects exploiting some form of muon transmission technique. In particular, it is presently applied to study the local density variations in volcanoes, down to a depth of a few hundred meters, where this system should perform better with respect to standard gravimetric techniques. In this case, in order to reconstruct the direction of the incoming muons, at least two layers of detectors, each providing the three coordinates of the muon crossing point, are needed. Moreover, the larger the surface and the acceptance, the less the time needed to get enough statistics to estimate the target profile, and this naturally leads to use inexpensive, large size, and easy-to-operate gaseous detectors, like RPCs.

Glass RPCs have been used for this purpose in the framework of the TOMUVOL experiment, which is a proof of principle for imaging volcanoes with atmospheric muons, the case being the Puy de Dôme volcano, in the French Massif Central (Le Menedeu, 2016). The TOMUVOL detector is made of four layers, each about 1 m^2 in area, made out assembling together six 50×33 cm^2 RPCs, very similar to the ones designed at the Institute for Nuclear Physics in Lyon for the CALICE hadron calorimeter. The 1.2-mm gas gap is filled with 93% of $C_2H_2F_4$, 5.5% of isobutane and 1.5% of SF_6, while glass thickness is 1.1 mm. A very high granularity, essential to obtain the necessary spatial resolution, is assured by reading these detectors via 1 cm^2 pads, for a total of about 40 000 channels. Particular care has to be taken in the readout electronics, based on the HARDROC2 application-specific integrated circuits (ASICs), already mentioned in Chapter 4, which are low power consuming devices; in fact, power budget is important for devices intended to be deployed on volcanoes, where one has to typically rely on batteries.

Different campaigns of data taking have been performed by the TOMUVOL collaboration. A first prototype detector was used in 2011–2012 for some preliminary measurements, which confirmed the possibility of performing imaging on volcanoes using cosmic muons, some of which are displayed in Figures 9.10 and 9.11. It was immediately evident that even with a reduced data taking time and simplified detectors and analysis techniques it was possible to obtain transmission images of the Puy de Dôme. In particular, in Figure 9.11, a structure with lower muon transmission located just beneath the summit can be seen, while, scattered muons (background tracks) appear to come from the base of the volcano simulated a higher transmission.

These results encouraged to perform other campaigns, which were carried out from 2013 up to 2016, at different locations. Of course, one important issue is to keep the detector performance (and, in particular, efficiency) stable against changing environmental conditions, and this is done using the same corrections to the operating voltage as in high-energy experiments, summarized in Equation 3.34. In general, a detailed knowledge of the detector performance is crucial in order to apply the necessary corrections to raw data. An example of the results obtained is shown in Figure 9.12, where the reconstructed muon flux versus azimuth and elevation measured during a 4-month campaign carried out at

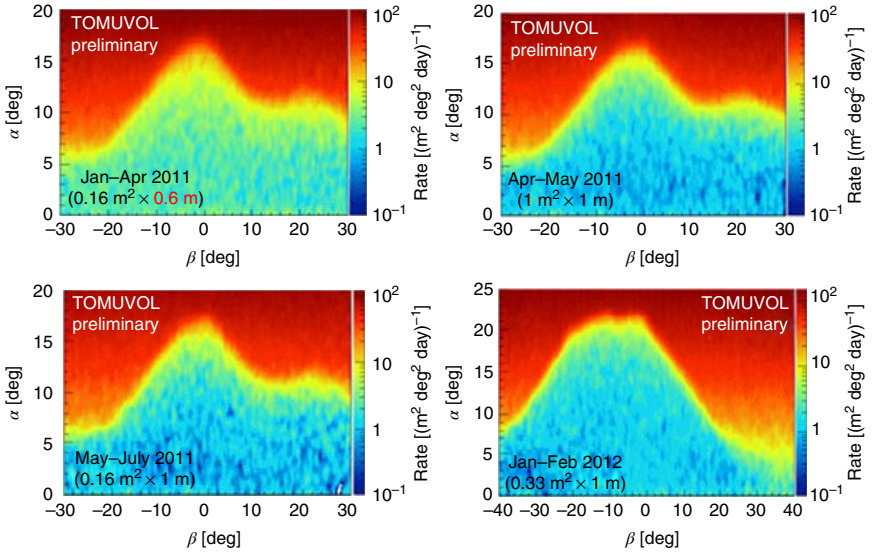

Figure 9.10 Images of the Puy de Dôme volcano obtained using cosmic muons, during the preliminary campaigns performed in 2011–2012 by the TOMUVOL collaboration; the different shapes in one of the images reflect the fact that the detector was placed in a different position. (Cârloganu *et al*. 2013. https://doaj.org/article/28768b5d62344f7ba108ee3fca059158. Licensed under CC BY-SA 4.0.)

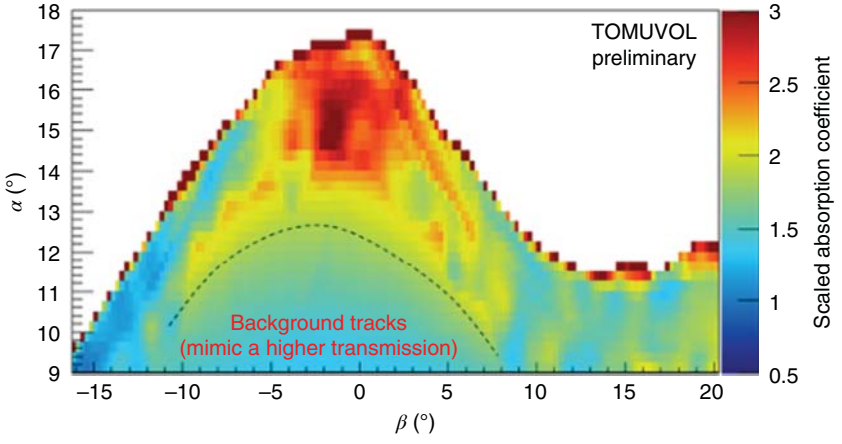

Figure 9.11 Map of the muon scaled transmission coefficient through the Puy de Dôme as measured over 7 months from the Grotte de la Taillerie with a ∼1/6 m^2 detector; a structure just beneath the summit can be noticed. (Cârloganu *et al*. 2013. https://doaj.org/article/28768b5d62344f7ba108ee3fca059158. Licensed under CC BY-SA 4.0.)

Col de Ceyssat is shown. Again, some hints of a structure inside the volcano can be inferred, confirming promising outcomes for this technique. Indeed, muon radiography is more and more regarded as a powerful method for shallow geological surveys, and it has been even considered for studies of extraterrestrial planets (Kedar *et al*., 2013).

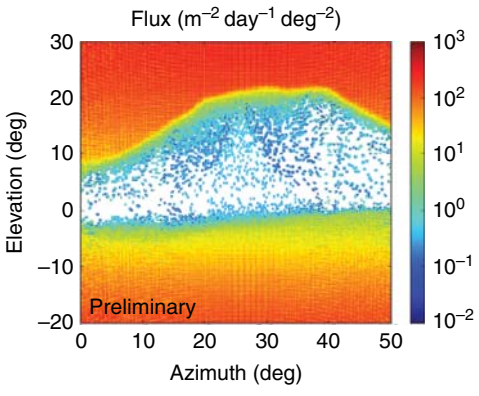

Figure 9.12 Reconstructed cosmic muon flux as a function of azimuth and elevation for the campaign carried out by the TOMUVOL collaboration at Col de Ceyssat from October 2015 to January 2016. Here, negative elevations point to the free sky in the direction opposite from the volcano. (Le Menedeu 2016. Reproduced with permission of IOP Publishing.)

The principle of MST is shown in Figure 9.13. Basically, a cosmic muon is tracked by means of a stack of detectors before and after it passes through an object to be analyzed; the muon undergoes multiple scattering inside the material, the average scattering angle depending on its thickness and atomic number Z, hence the possibility to roughly distinguish among different chemical species. This technique is presently considered as very promising for applications in the field of homeland security, in particular to address the issue of illicit trafficking of radiological or nuclear material hidden in containers or large trucks.

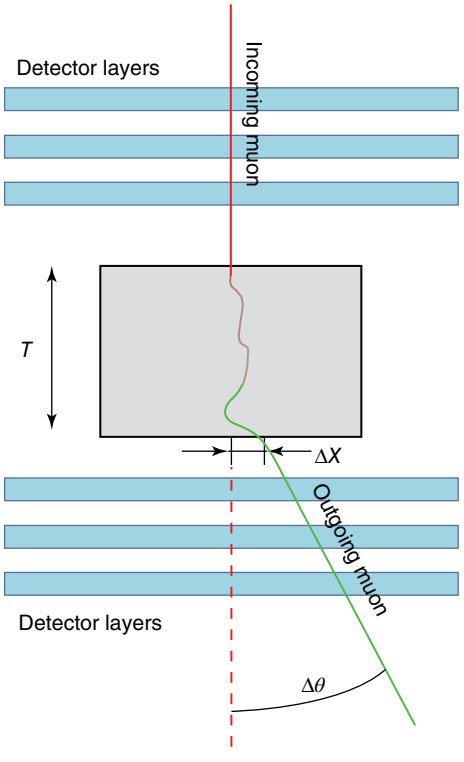

Figure 9.13 Muon scattering tomography principle. The muon passes through the upper detectors, scatters in the target, and leaves via the lower detectors. The measured scatter angle allows for estimation of the target Z. (Thomay *et al*. 2012. http://www.geosci-instrum-method-data-syst.net/1/235/2012/gi-1-235-2012.pdf. Licensed under CC BY 3.0.)

From the practical point of view, it has some important advantages: first, using cosmic muons, it does not require the generation of any artificial dose above background levels. Then, as in muon radiography, due to the highly penetrating nature of muons, images of large objects can be obtained in a reasonable amount of time. On the other side, there are limitations to this technique, one being that that it only distinguishes between low, medium, and high Z materials, so that that legitimate materials such as lead or tungsten might appear the same as uranium or plutonium; another being the fact that the muon energy cannot be tuned and its spectrums extend over several order of magnitudes.

The detector requirements to build an effective tomography system have been the subject of a variety of detailed studies (see, for instance, Cox *et al*., 2008). The muons undergoing multiple scattering in a slab of material emerge with a deviation angle that can be fitted by a Gaussian distribution with mean at zero, whose width σ_θ is given by

$$\sigma_\theta \approx \frac{13.6\,\text{MeV}}{p_m c\beta}\sqrt{\frac{T}{X_0}\left[1 + 0.038\ln\left(\frac{T}{X_0}\right)\right]} \tag{9.1}$$

where p_m is the momentum of the muon, β is its speed divided by the speed of light c, X_0 is the radiation length of the material, and T is the thickness of the material traversed. The radiation length X_0, in turn, can be expressed as

$$X_0 \approx \frac{716.4A_w}{Z(Z+1)\ln\left(\frac{287}{\sqrt{Z}}\right)}(\text{g/cm}^2) \tag{9.2}$$

where A_w is the atomic weight of the medium in g/mol and Z, already introduced, is its atomic number (Cox *et al*., 2008). Equations (9.1) and (9.2) clearly show the dependence of σ_θ on Z. Moreover, σ_θ depends on muon momentum, material geometry, and radiation length (which itself depends on its Z); a given angle can therefore derive from a combination of these (see Figure 9.14), making the problem more complex.

In order to make coincidences, two or more detectors have to be positioned on either side of the item of interest; to effectively distinguish coincidences from independent background counts in each detector, a timing resolution of the nanosecond order is generally needed. Moreover, the spatial resolution is dictated by the need to measure the small angle between the incoming and outgoing muon tracks. To distinguish between medium and high Z materials, this angle typically ranges around 10 mrad and leads to a spatial resolution on the order of centimeters if detectors are positioned around 1 m from the target. In case a sub-millimeter spatial resolution can be reached, detectors can be placed closer to the target, resulting in more compact and, in general, more performing devices. Moreover, if timing resolution under 100 ps can be somehow provided and, TOF techniques can be implemented to give a rough estimate of the energy of muons.

3D imaging is achieved by applying tomographic reconstruction methods to the data; for instance, the location of the scattering event can be determined using

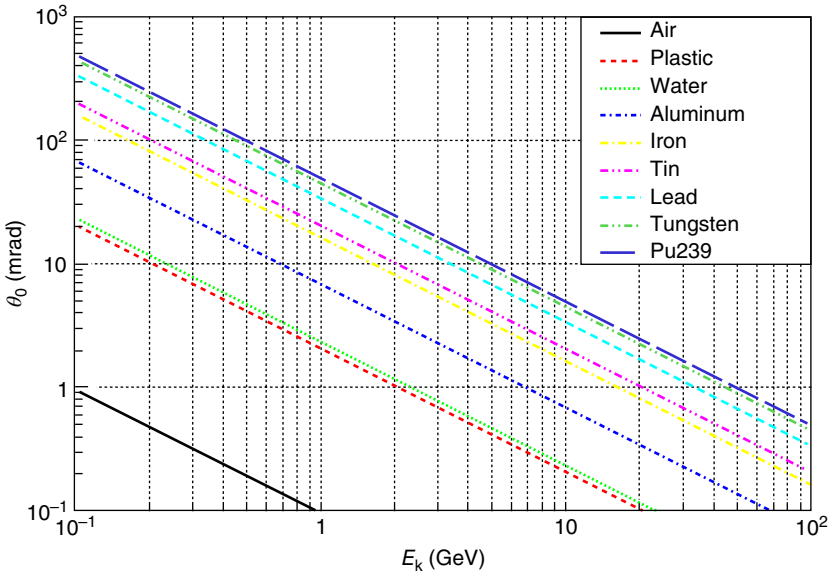

Figure 9.14 σ_θ as defined in Equation (9.1), computed for one radiation length of a selection of materials, as a function of muon kinetic energy. (Adapted from Cox *et al*. 2008.)

a point of closest approach (PoCA) algorithm, backtracking the incident and exit muon trajectories (see Schultz *et al*., 2004 for details).

The effectiveness of this technique has been demonstrated using several detectors, including MWPC (Burns *et al*., 2015; La Rocca *et al*., 2015), and micropattern gaseous detectors like GEMs (see for instance Gnanvo *et al*., 2010), the relative literature is growing steadily. Here, we review just a few of the results obtained, limited to the use of resistive gaseous detectors.

One prototype system has been built at the University of Bristol, and it is shown in Figure 9.15 (Thomay *et al*., 2012; Baesso *et al*., 2014). It uses glass RPCs 58 × 58 cm in dimensions, with a 2-mm gas gap filled with $Ar/C_2H_2F_4/iC_4H_{10}$ 60/30/10 mixture. Each is read out by means of a printed circuit board hosting 330 strips with a 1.5-mm pitch connected to hybrid boards supporting HELIX chips, originally designed for the HERA-B experiment and optimized for silicon microstrip and gaseous detectors; later on also, the MAROC chips were used. The system is made of 12 RPCs in total, hosted in pairs in six aluminum cassettes, three placed above the target and three below.

This device has been collecting data for several years, showing an efficiency between 87% and 95%, and spatial resolution better than 0.5 mm (Baesso *et al*., 2014). An image obtained with this prototype in several hours of data taking, of three small blocks, made in aluminum ($Z = 13$), iron ($Z = 26$), and tungsten ($Z = 74$), is shown in Figure 9.16; the blocks are more and more evident at increasing atomic numbers, giving an idea about the capability of distinguishing among different chemical species with this device.

A similar prototype, named TUMUTY, was built at Tsinghua University using glass MRPCs (see Figure 9.17 for a conceptual layout of the system and a picture).

Figure 9.15 Picture of the system built at Bristol University for muon scattering tomography with RPCs. The six aluminum cassettes contain two RPCs each, providing *X* and *Y* coordinates. High and low voltage cables and data connections are visible. The gas mixers are located at the bottom. (Baesso *et al*. 2014. Reproduced with permission of IOP Publishing.)

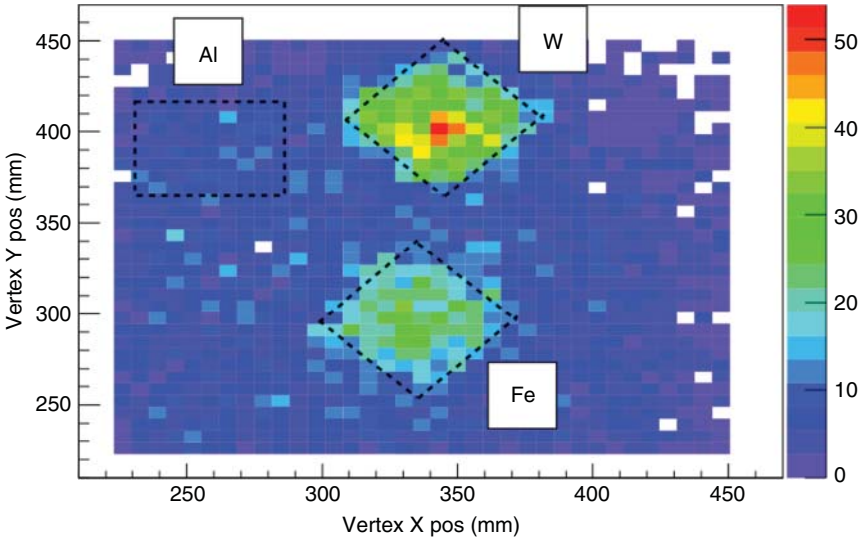

Figure 9.16 Image of $50 \times 50 \times 50$ mm^3 block of aluminum, iron, and tungsten obtained using the detector prototype developed at the University of Bristol, and using the point-of-closest algorithm. The image was obtained with several hours of data taking. (Baesso *et al*. 2014. Reproduced with permission of IOP Publishing.)

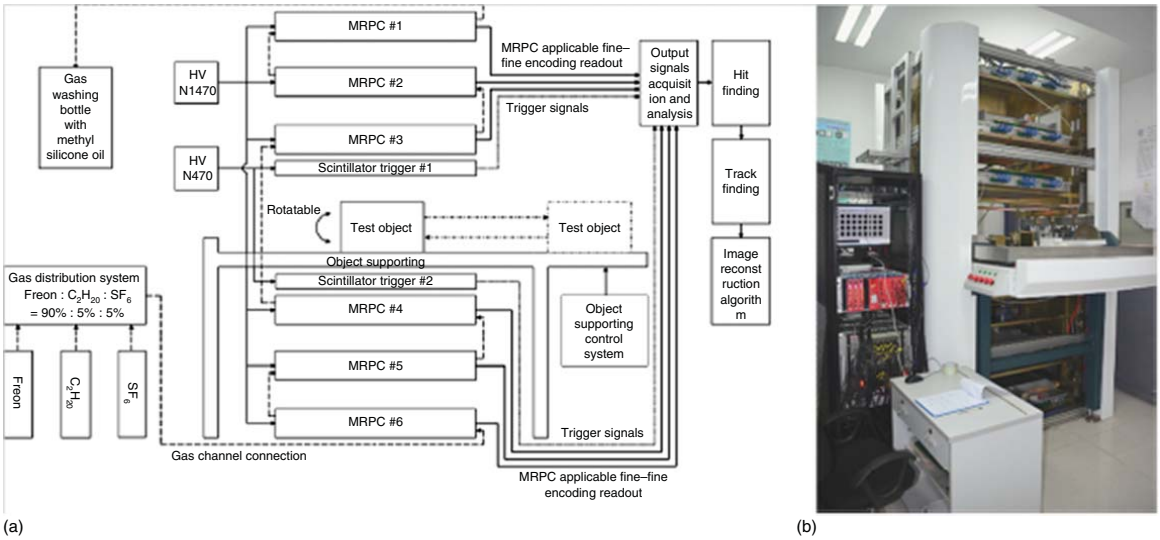

Figure 9.17 Block diagram (a) and picture (b) of the TUMUTY facility at Tsinghua. (Wang *et al*. 2015. Reproduced with permission of Elsevier.)

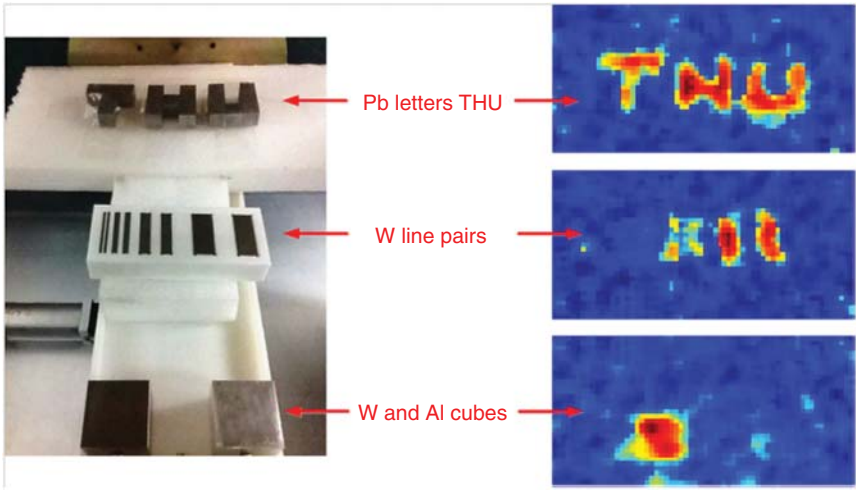

Figure 9.18 (left) Photograph of some test kits and (right) how they are imaged at the TUMUTY facility. (Wang *et al*. 2015. Reproduced with permission of Elsevier.)

In this case, each MRPC is a 2D readout with 224 copper strips per side, so that just six MRPCs are needed, three above and three below the sample, for a total of 2688 channels. Each has six gas gaps 0.25 mm thick, filled with a gas mixture made out of $C_2H_2F_4/i\text{-}C_4H_{10}/SF_6$ 90/5/5 in relative fractions (Wang *et al*., 2015). Images obtained during a 12-day data taking period with the TUMUTY facilities are shown in Figure 9.18, showing that high and low Z materials can be distinguished, and that small (down to around 20 mm) and complex objects can be visualized.

MST is nowadays well established, and some companies have commercialized this technique, constructing and deploying large portal monitors at various locations, capable of screening order of 10-m containers in less than a minute. It is considered also for nuclear treaty verifications and imaging of reactors, an example being the one performed by the Los Alamos Muon Radiography Team on the damaged Fukushima Daiichi reactors (Morris *et al*., n.d.).

9.4 X-Ray Imaging

In most medical X-ray examinations it is very important not only to obtain high-quality images but also to ensure the lowest possible delivered dose to the patient. A compromise between these two requirements can be achieved by using the so-called photon counting technique, where each individual photon is counted by means of a single-photon position sensitive detector. Historically, the first low-dose X-ray scanner was developed by a Novosibirsk group (Baru *et al*., 1985) (Baru *et al*., 1989).

Following this idea, the Swedish company XCounter AB developed and tested in a clinic environment a commercial low-dose mammographic installation based on high-rate narrow-gap RPCs (see, for instance, Francke *et al*., 2001a,b;

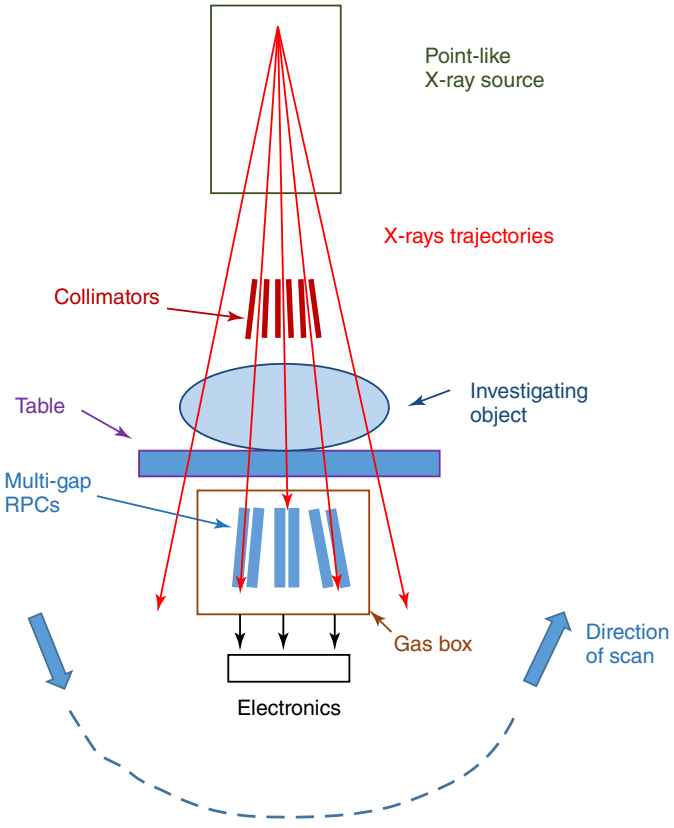

Figure 9.19 Functional scheme of an RPC-based mammographic scanner developed by the Swedish company XCounter. The dashed line represents the circular arc along which the scan is performed.

Martin and Flynn, 2004; Thunberg *et al.*, 2004,b). A schematic drawing of a mammographic scanner using such devices, illustrating its principle of operation, is shown in Figure 9.19; and the photograph of a commercial prototype in Figure 9.20.

The detector is integrated in a standard mammographic installation, containing an almost point-like X-ray source (i.e., a special X-ray tube having an emitting point as small as a few tens of microns) and a table for women's breast compression. Below this table an array of RPCs with a gap thickness $\leq$0.3 mm is located (for details about this RPC configuration, see Chapters 4 and 7). Thanks to the collimators, the X-rays enter each RPC in a position close to its cathode (the distance being less than 50 μm) and in a direction parallel to it (see Figure 9.21). The RPCs are built using ceramic anodic plates and silicon cathodes, with metallic strips on the inner surfaces, pointing toward the X-ray micro focus, and therefore aligned with the photons trajectories. Each strip is connected to its ASIC.

Detectors are filled with a 40% Xe + 40% Kr + CO_2 gas mixture, at a pressure, depending on the specific configuration, between 1 and 3 atm. Position resolution

Figure 9.20 Photograph of a clinic prototype of a mammographic scanner developed by the Swedish company XCounter.

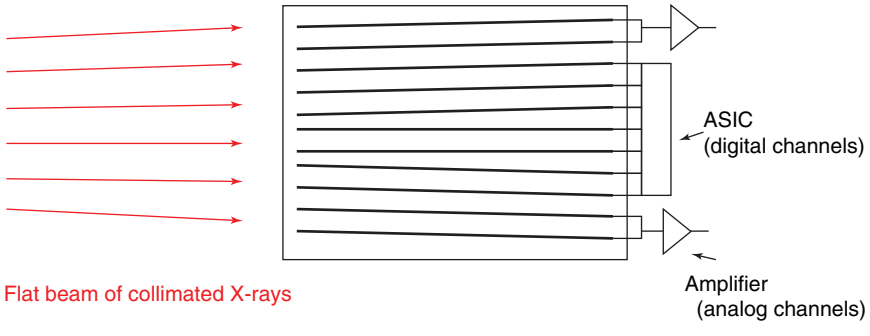

Figure 9.21 Schematics of the anode plates used for the X-ray photon imaging RPCs described in the text and used for mammographic purposes. Average strip pitch is 50 μm, while distance from the X-ray focus is 78 cm.

of these devices results to be around 50 μm in digital mode (dictated by the strip pitch, and worsened by misalignment and other instrumental effects); counting rates up to 10^5 Hz per strip can be reached.

The XCounter mammographic system comprises 48 photon counting RPCs; the X-ray source and the detectors are scanned across the patient; each linear detector collecting a digital image at a distinct angle. To solve the dead zones problem (due to RPC electrodes and space between RPCs) the gas vessel containing the RPCs performs short movements during the image taking, of a few seconds' duration, along a circular arc (shown in Figure 9.19 as a dashed line). XCounter scanners deliver high-quality mammographic images fulfilling medical standard requirements, while delivering an X-ray dose around five times less with respect to conventional devices.

As a next step, a novel tomosynthesis system was developed and tested in a clinical environment; see Figure 9.22 and references (ADA *et al*., 2005, 2006; Thunberg *et al*., 2002, 2004,b). Tomosynthesis is a special mammographic technique that produces a 3D image of the breast using several low-dose X-rays delivered at different angles. In this case, the breast is positioned and compressed in the same way as for a usual mammogram, but the X-ray tube moves in a circular

Figure 9.22 Photograph of an XCounter imaging system, capable of both projection mammography and tomosynthesis. The system is larger than the installation shown in Figure 9.19 to accommodate the scanning detector and the X-ray source. (Maidment 2006. Reprinted with permission of Springer Nature.)

arc around the breast (see Figure 9.19). The information is then treated by a computer, which produces a 3D image of the breast that is very useful for medical diagnostics. Breast tomosynthesis is an advanced technique not yet available at all facilities for medical imaging.

The collected images have a very high quality, due to several specific characteristics of this detector technology:

1) The RPCs are practically insensitive to scattered radiation; the collimators and the detector geometry ensure that only primary photons emanating from the focal spot of the X-ray source elicit a response from the detector.
2) The detector itself does not contribute to any electronic noise: the high gaseous amplification of each photon allows simply to apply a sufficiently high threshold to exclude electronic noise from being counted and included in the final image reconstruction.
3) The image pixels are very small (around 60 μm), avoiding motion blurring from scanning times of each sub-image.

Note that this detector technology does not produce any residual or ghost image, which may confuse doctors. Information appropriate for tomosynthesis is acquired over a region 24×30 cm^2 within 15 s.

Clinical tests proved that the image quality achieved by this device satisfies all the requirements needed for medical applications. In general, more calcifications were identified with the tomosynthesis images than in the screen-film mammograms. Moreover, the calcifications in the tomosynthesis images had sharper margins and higher contrast than in screen-film images.

As an example, breast tomosynthesis images are shown in Figure 9.23; all details of breast anatomy, like the glandular and adipose tissues, Cooper's ligaments, blood vessels, lymph nodes, and other structures, are quite well distinguishable. The effectiveness of this device was demonstrated during the first evaluation test, where 1 patient with cancer out of 20 women was quite obviously identified using tomosynthesis, while the illness was only marginally visible in the screen-film image.

For the moment, the use of RPC-based X-ray scanners is limited, and the future will show if they will be able to withstand a growing competition from other solid-sate and scintillation photon counting devices.

9.5 Cost-Efficient Radon Detectors Based on Resistive GEMs

Another potential field of application for gaseous detectors with resistive electrodes is alpha particle counting in ambient air. This is related to the fact that, in the past decade, some studies have shown the possibility of correlating increased concentrations, in soil or in ground water, of Radon (Rn), a noble radioactive gas, to the early prediction of earthquakes (e.g., see Richon *et al.*, 1994; Yasuoka and Shinogi, 1997; Wakida *et al.*, 1995; Dobrovsky *et al.*, 1978; Fleischer *et al.*, 1981; Magro-Campero, 1980; Segovia *et al.*, 1986; Khan *et al.*, 1990; Igarashi *et al.*, 1995).

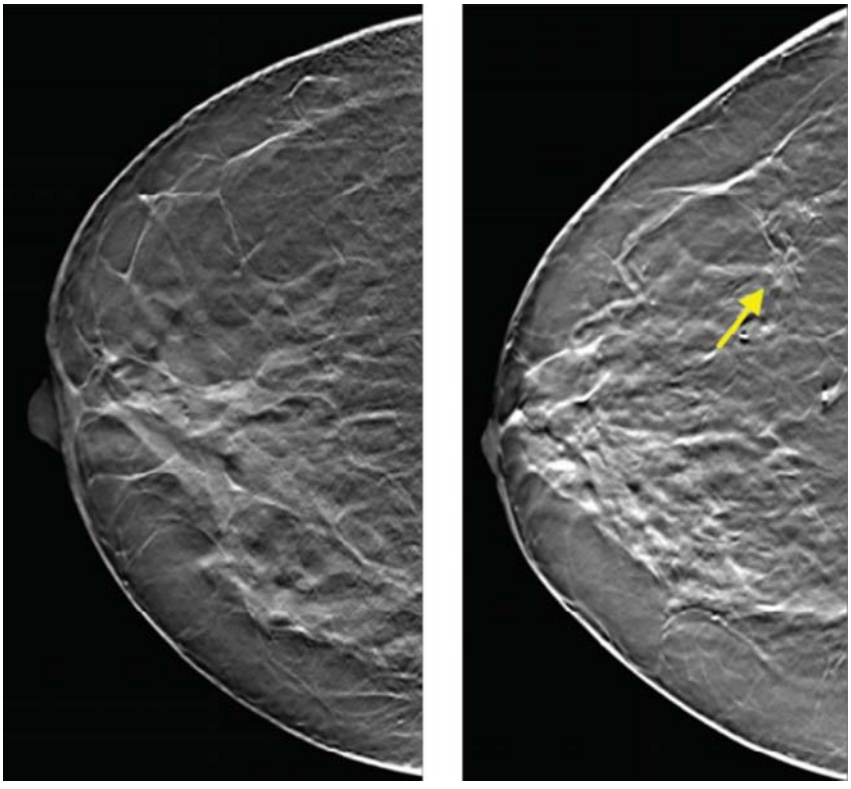

Figure 9.23 Examples of images of features interesting from the medical point of view, obtained with a mammographic scanner implemented with RPCs. The patient on (a) has numerous calcifications that can be identified by a specialist. The patient on (b) has a suspicious mass., which later on was identified via a biopsy as a ductal carcinoma. (Maidment 2006. Reprinted with permission of Springer Nature.)

Probably one of the most impressive observations was the one taken from a satellite, showing an increased infrared radiation several days before the M9 Tohoku Earthquake in Japan (see Figure 9.24). This was explained by the appearance of Radon, which was released due to the small movements of the crust occurring before an earthquake takes place (Ouzounov *et al*., 2011). Radon is an α emitter, which are highly ionizing particles. The mentioned research, in particular, suggests that Radon creates ionized particles in the air which, in turn, cause water molecules to condense out of their vapor state. This condensation process releases energy, causing the nearby atmosphere to increase its temperature, and hence the increased infrared radiation.

In order to verify such observations on more solid statistical grounds, and, in general, the correlation between increased Radon concentrations and an upcoming earthquake, a large network of inexpensive, compact, and high-sensitivity Radon detectors would be needed; these are to be deployed in key points where earthquakes may potentially occur. The existing excellent commercial detectors,

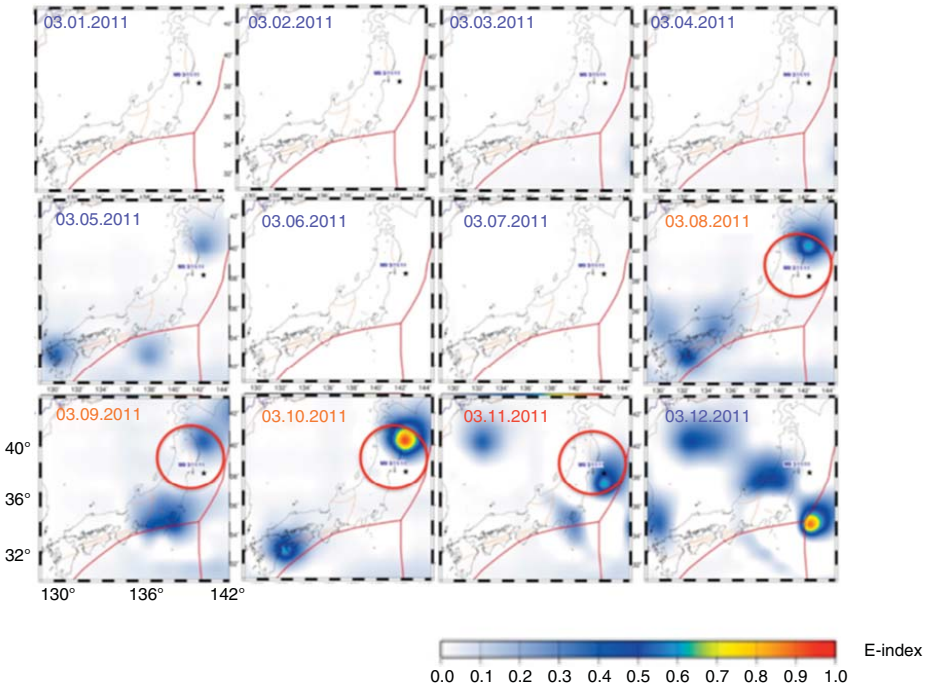

Figure 9.24 Time series of daytime anomalous infrared (10–13 μm) radiation observed from a satellite during March 1 to March 12, 2011. Circles show the spatial location of infrared anomalies in the vicinity of the M9.0 Tohoku earthquake. All frames have the same scale indicated on the left lower picture. (Ouzounov *et al*. 2011. Reproduced with permission of Springer.)

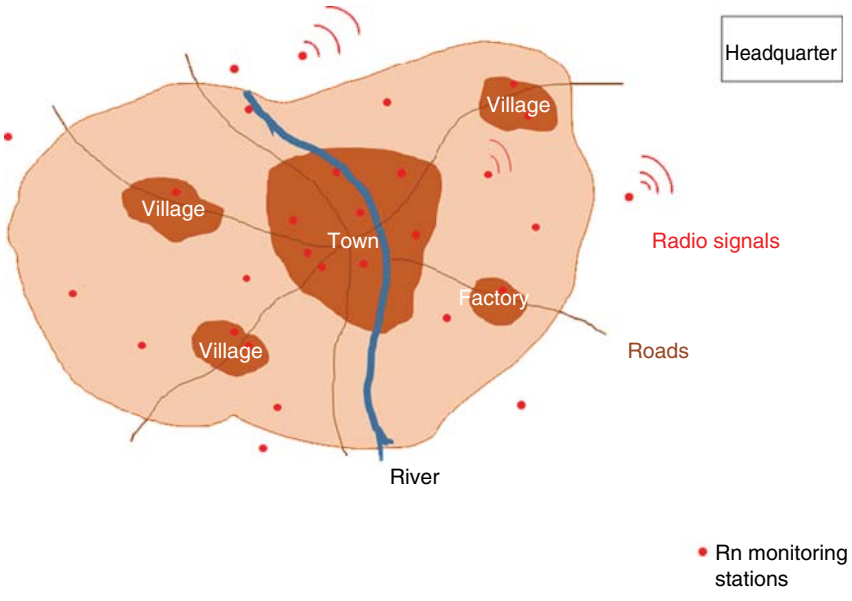

Figure 9.25 Schematics of a possible network of Radon monitoring stations in a seismic region; each station is equipped with radio transmitters sending signals to a headquarter, where data are collected and analyzed in real time.

for example, ATMOS 12dpx (Radon Analytics Inc., 2014) or RADIM3 (Plch M. Eng.-SMM, 2015), costing on the order of tens of thousands of Euros, are too expensive to be employed on a large scale. Their high cost is justified by their excellent performance, for instance, in terms of spectroscopic response. However, for the purpose of measuring Rn concentration at several locations and determining the correlation between different measurements, such a good energy resolution is not always required. In most cases it is sufficient to simultaneously record signals above a given threshold, in order to provide reliable information about the Rn appearance and accumulation (see Figures 9.25 and 9.26).

The key points for the implementation of this approach are low-cost, low power consuming sensors. The detector network must be equipped with radio transmitters, in order to broadcast signals to a headquarter, where the data are stored and analyzed. In order to extend the battery lifetime, it is possible to perform the measurement for a few minutes each hour. This approach has already been successfully tested on several battery-operated devices, for example, by DT Linc. Inc., Geneva, Switzerland.

One of the possible options to build such devices is to use gaseous detectors. Their main advantages are low cost and the unique possibility to operate in avalanche mode in ambient air, which offers a high signal-to-noise ratio and, as a consequence, high detection efficiency. Of course, detectors with resistive electrode are especially interesting, due to their robustness and spark protection (Charpak *et al*., 2008a).

The difficulties, however, are that these detectors should be capable of operating under harsh conditions, for example, in 100% humid air. For this reason,

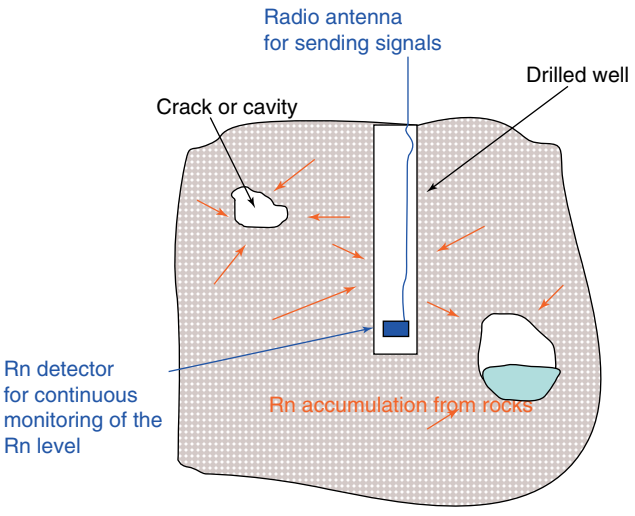

Figure 9.26 Possible arrangement of a Radon monitoring station, installed either in a specifically drilled well, or in a house basement.

experiments were also conducted with traditional single-wire detectors and MWPCs, but having a specially shaped dielectric interface between the anode wires and the cathode, preventing leakage current from appearing (Charpak *et al*., 2010).

Anyhow, for mass. production of inexpensive Radon sensors, micropattern detectors with resistive electrodes produced by industrial microelectronic technology could be, in principle, much more attractive, since they can be easily produced at an industrial scale. Following this idea, a special GEM-like detector capable of operating in 100% humid air was recently developed (see Figures 9.27 and 9.28 and Peskov *et al*., 2013). This detector consists of two resistive plates

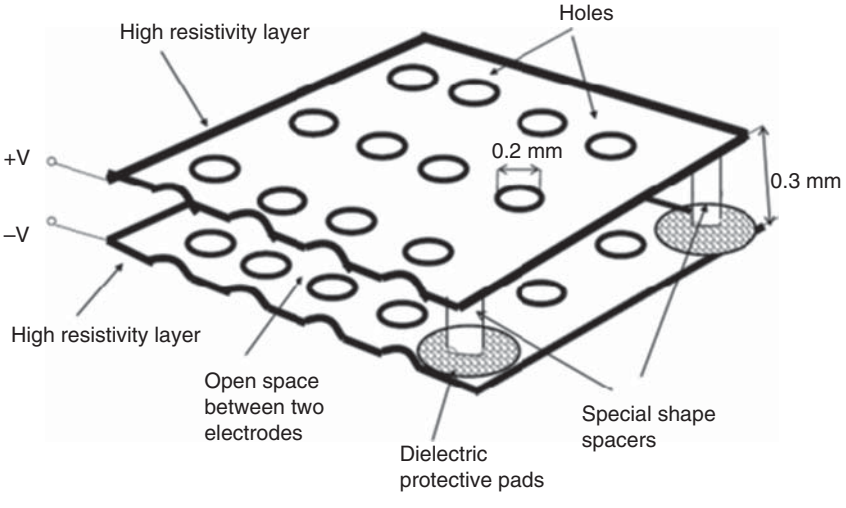

Figure 9.27 Schematic drawing of a "wall-less GEM" detector with resistive electrodes. (Peskov *et al*. 2013. Reproduced with permission of Elsevier.)

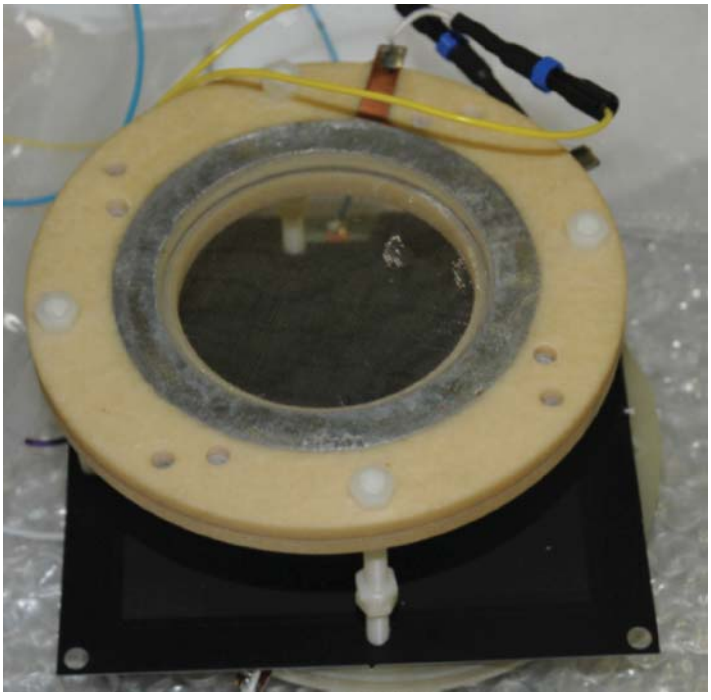

Figure 9.28 Photograph of a Radon detector prototype, consisting of a drift mesh and a restive GEM with a 10×10 cm^2 active area. (Peskov *et al*. 2013. Reproduced with permission of Elsevier.)

drilled with holes, supported by a few specially shaped spacers located in positions far away from the holes (a so-called wall-less GEM). The holes are carefully aligned, allowing the formation of an electric field very similar to the one present in a standard GEM. Such a structure has been operated without spurious pulses at gas gains up to 10^3 in 100% humid air and it detects Rn with a sensitivity close to the best commercially available Rn sensors, whereas the estimated cost of this detector is at least 10 times lower than commercially available detectors. Moreover, the main advantage of this detector is its ability to detect variations in Radon concentration 10 times faster than commercial detectors. This, in particular, was achieved by the fast removal (with the help of a special replaceable drift electrode) of Rn progeny from the detector fiducial volume.

9.6 Resistive GEMs for UV Photon Detection

Cascaded GEMs are excellent detectors for single electrons: thanks to their geometry, they can operate at very high gains in many gases, including pure noble gases, without strong ion or photon feedback. Moreover, if equipped with a proper photocathode converting impinging photons to electrons, they can also serve as gaseous photomultipliers. Work in this direction was performed by several groups, and all necessary information can be found, together with an exhaustive list of references in the recent book (Francke *et al*., 2016). Since

GEMs are position sensitive, if combined with optical systems they can provide also imaging capabilities, which is another quite unique feature. Such imaging gaseous photomultipliers can compete with other detectors for several applications, such as *R*ing *I*maging *CH*erenkov (RICH, whose principle of operation is briefly described in the following), or ultraviolet visualization under daylight conditions, or flames and sparks detection.

However, it must be noted that, at the high gains ($>10^4$) necessary for the detection of single photoelectrons at an around 100% efficiency, occasional breakdowns are practically unavoidable. This is due to the well-known Raether limit, governing the maximum a*c*hievable total charge in an avalanche before breakdowns appears. Experiments show that in cascaded GEMs, depending on the particular geometry and gas chosen, the maximum total charge in an avalanche typically ranges between 10^6 and 10^7 electrons (Francke *et al*., 2014) and thus the maximum achievable gain in the best case is

$$A_{\max} \sim 10^7(\text{electrons})/n_0 \tag{9.3}$$

where n_0 is the number of primary electrons created by the ionizing radiation.

It is reasonable to assume that at an operational gain around 10^4 one should have a safety factor at least about 10 with respect to the maximum achievable gain. Since under standard conditions, operating in presence of cosmics and/or natural radioactivity, the number of primary electrons created by this background ranges around 100, $A_{\max}$ cannot be set to be higher than 10^5 in order to avoid breakdown. Hence, spark-protected resistive GEMs offer a practical option which can overcome this problem.

There are two main designs of imaging photomultipliers based on resistive thick GEMs:

1) GEMs combined with a CsI photocathode
2) GEMs filled with some kind of photosensitive vapors, for instance, Tetrakis dimethylamine ethylene (often called simply TMAE).

Here, we describe the first option, which offers a better position resolution.

9.6.1 CsI-Based Resistive GEMs for RICH

When a charged particle traverses a dielectric medium with a velocity larger than the speed of light in this medium, $v = c/n_r$ (where n_r is the refractive index of the medium), it produces an electromagnetic radiation called Cherenkov light. The unique feature of this radiation is that the emission takes place at a specific angle θ with respect to the particle trajectory given by:

$$\cos\theta = 1/\beta n_r \tag{9.4}$$

and is mainly in the visible and ultraviolet regions of the spectrum, for which $n_r > 1$. Since the aperture of the cone of light depends on the particle velocity, one can combine this information with a particle momentum measurement (performed using other techniques), in such a way to identify the particle. An essential element of devices exploiting this technique, like it is done in RICH,

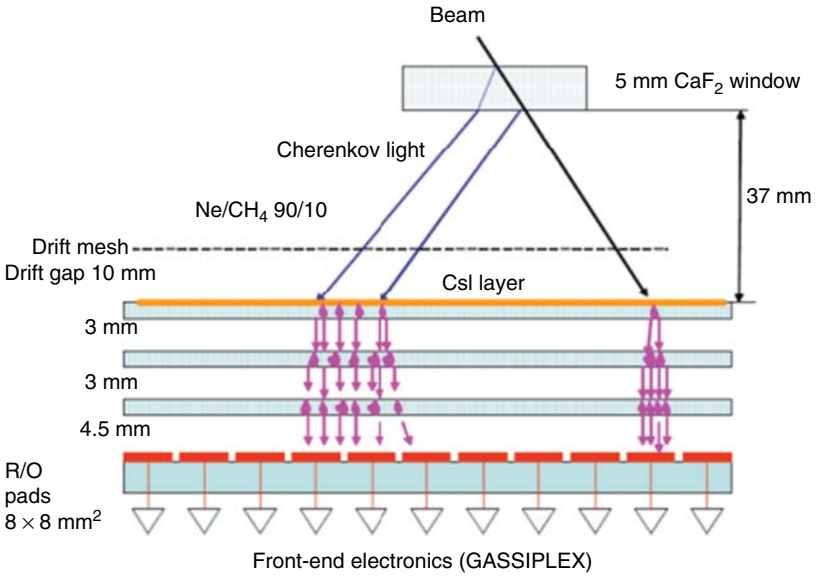

Figure 9.29 Layout of a RICH prototype, equipped with a CaF_2 radiator and a triple resistive GEM combined with a CsI photocathode. (Martinengo *et al*. 2011. Reproduced with permission of Elsevier.)

is a position-sensitive detector capable of detecting single photons with high efficiency.

Cascaded resistive GEMs represent one of the attractive options. Some preliminary tests of a RICH prototype employing CsI-coated thick resistive GEMs are described in (Martinengo *et al*., n.d.); the corresponding setup is presented in Figure 9.29, and its photograph in Figure 9.30.

It consists of a CaF_2 Cherenkov radiator, coupled to a triple-resistive GEM detector, whose top GEM is coated with CsI, flushed with either $Ne + 10\%CH_4$ or $Ne + 10\%CF_4$ at 1 atm pressure. Each resistive GEM has a 10×10 cm^2 active area, 0.45 mm thickness, 0.4 mm hole diameter, and 0.8 mm pitch. Below the GEM, a pad readout plane is placed. In this device, a UV photon can extract an electron from the CsI photocathode that is deposited on top of the first GEM upper surface. The electron is led by the electric field action to the nearest hole, where it experiences the first amplification; then the avalanche electrons undergo a second amplification in the following GEM (and more, depending on the number of GEM foils) and they finally induce a signal on the pad-type readout plate. Combined with a proper electronics this detector allows visualization the Cherenkov radiation.

Some results are presented in Figure 9.31a–d. In the plots (a) and (c), images of events integrated during some tests of this RICH prototype, when oriented at angles $\approx 20°$ and $\approx 37°$ with respect to a ~ 6 GeV/c π^- beam, are shown. During this particular run, a triple-resistive GEM operated with a reversed drift electric field (around 200 V), to enhance the photoelectron extraction efficiency from the

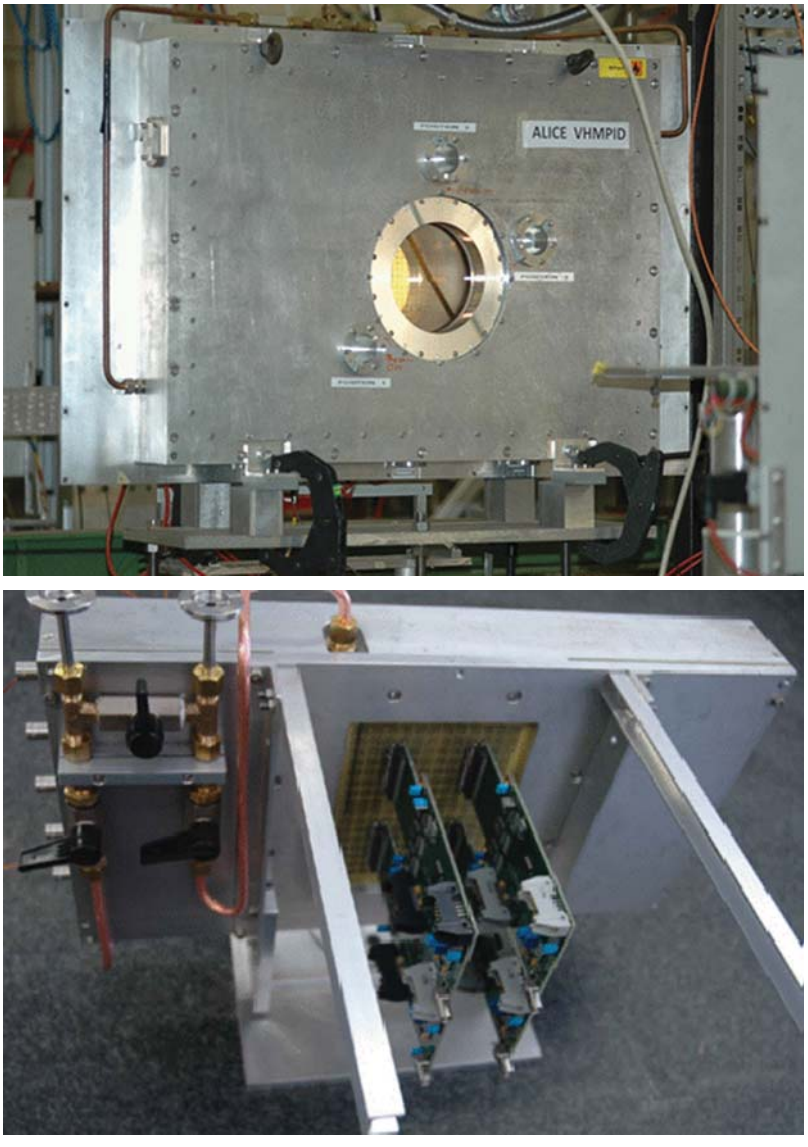

Figure 9.30 (a) Photographs of the front view of a small RICH detector, employing triple-resistive GEMs, with the top electrode coated with CsI, built and tested by the ALICE RICH group. A CaF_2 radiator can be clearly seen in the center of the front flange, facing the particle beam, as well as three windows for radioactive sources used for preliminary tests. (b) Back view of the detectors, showing the front-end electronic connected to the readout pad plane.

CsI cathode at an overall gain of $\sim 10^5$ was used (Azevedo *et al.*, 2010). The spot at the top of each figure is the image of the particle beam, while the horizontal band in the middle corresponds to the detected Cherenkov photons. The histograms (b) and (d) show the projections of the recorded events along the x and y axes of the corresponding upper images.

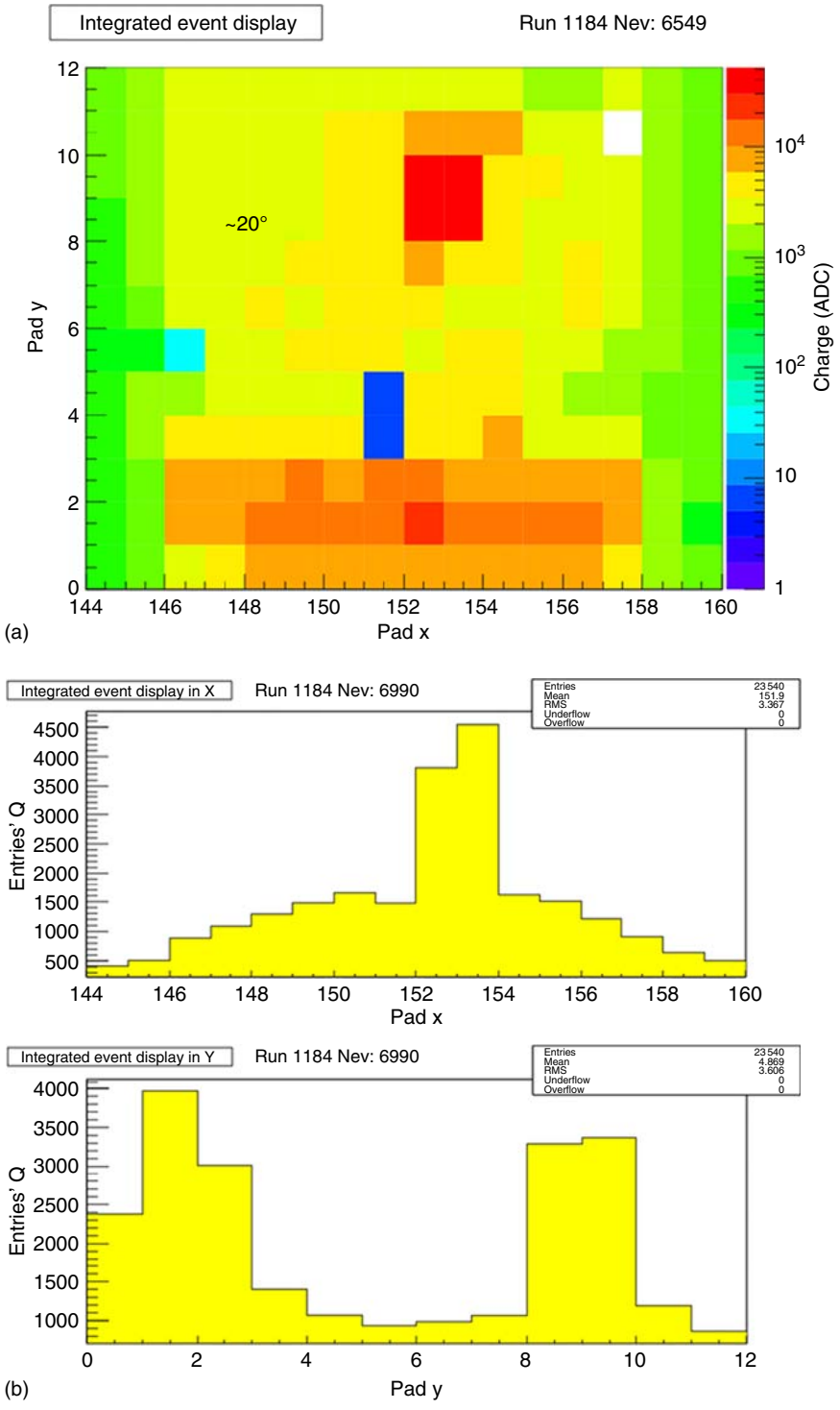

Figure 9.31 (a) Events recorded by a CsI-coated triple-resistive GEM during a test with a ~6 GeV/c π^- beam when oriented at an angle of ≈20°; (b) projections of top plots onto *x* axis; (bottom) projections of top plots onto *y* axis; (c,d) the same measurements performed at the angle of ≈37° with respect to the ~6 GeV/c π^- beam.

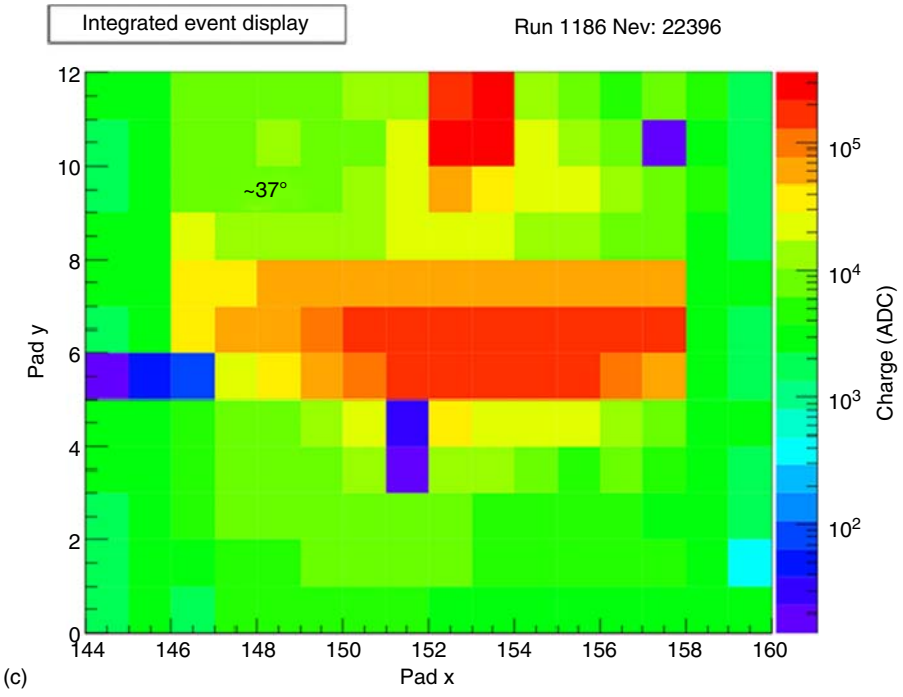

(c)

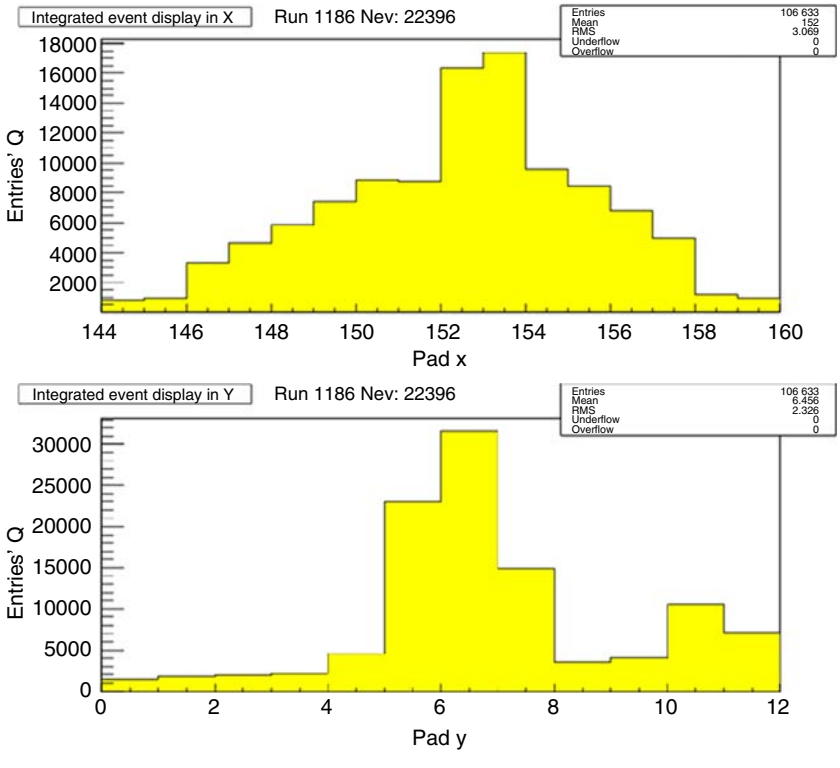

(d)

Figure 9.31 (*Continued*)

9.6.2 Flame and Spark Detection and Visualization with Resistive GEMs

Practically the same detectors, as described earlier, but operating in a gas-sealed vessel, can be used for indoor and outdoor fire detection systems, allowing not only to record the appearance of open flames and sparks but also accurate localization of fire hazards. The schematics of this design, recently developed by one of the authors of this book (Vladimir Peskov), with the support of the ALICE team and the CERN Technology Transfer Project, is shown in Figure 9.32. This was a modified version of earlier prototypes (see Bidault *et al*., 2006, 2007; Di Mauro *et al*., 2007; Charpak *et al*., 2008b, 2009), where examples of some digital images of flames are presented).

Some narrow band filter (shown in Figure 9.32) selects the wavelength to be in the 185–220-nm interval, in which all the flames in air emit quite strongly, whereas the sunlight is blocked by the ozone in the upper layer of the atmosphere. Then the photoelectrons extracted from the CsI diode are multiplied in the cascaded GEMs and finally produce a signal on the readout electrodes.

Preliminary measurements show that such a device can reach a sensitivity and a time resolution 100 times better than the best commercial flame detectors, which, in addition, do not have any imaging capability. Moreover, provided

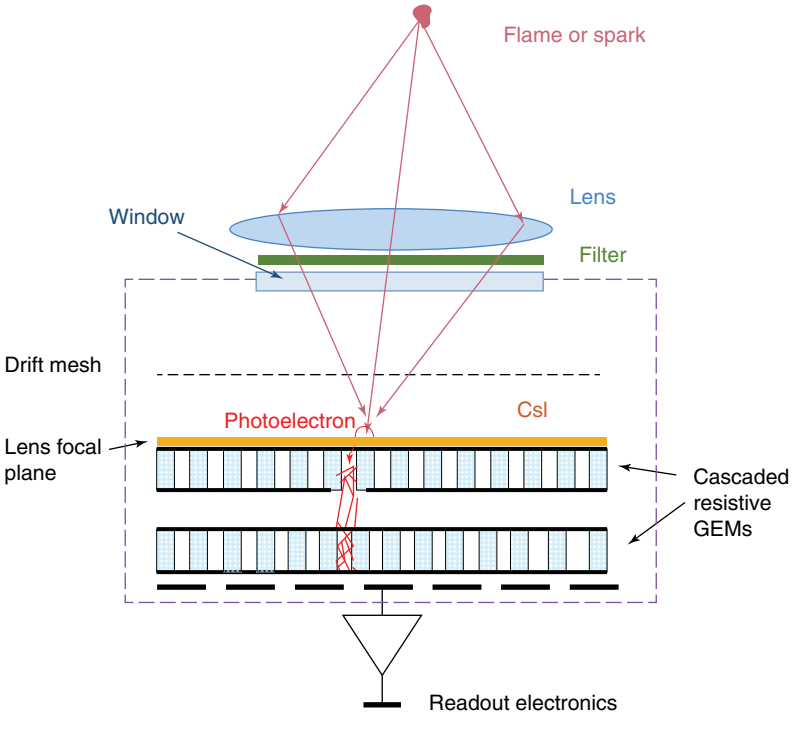

Figure 9.32 Working principle of a cascaded resistive GEM combined with a CsI photocathode; the optical system is also shown.

with an appropriate algorithm for pattern recognition, this detector could achieve a high rejection of false signals, making this flame-detection system very robust.

9.7 Cryogenic Detectors with resistive electrodes

In some dark matter search experiments, dual-phase noble liquid time projection chambers (TPCs) are used (see, for instance, Chepel *et al*., 2013). As can be seen from Figure 9.33, their principle of operation is based on primary electrons extraction from a suitable liquid, followed by secondary scintillation in a uniform electric field present in the abovementioned gas volume. The primary electrons can be produced by various mechanisms, for example, thanks to the elastic interactions (recoils) of weakly interacting massive particles (WIMPs), which are sometimes the subject of the search. Part of the electrons experience recombination and this produces a prompt signal S_1 which is recorded by an array of photomultiplier tubes (PMTs) surrounding the liquid volume of the TPC. Electrons, which escape recombination, drift away from the interaction point toward the top of the TPC, under the action of an applied uniform electric field. On the border between liquid and gas, a stronger electric field is applied, which extracts the electrons into the gap between two parallel meshes. Here, the electrons produce an intense secondary scintillation signal S_2, which is directly proportional to the amount of electrons extracted from the liquid. The 3D position of the interaction point is obtained by combining the time difference between the prompt and

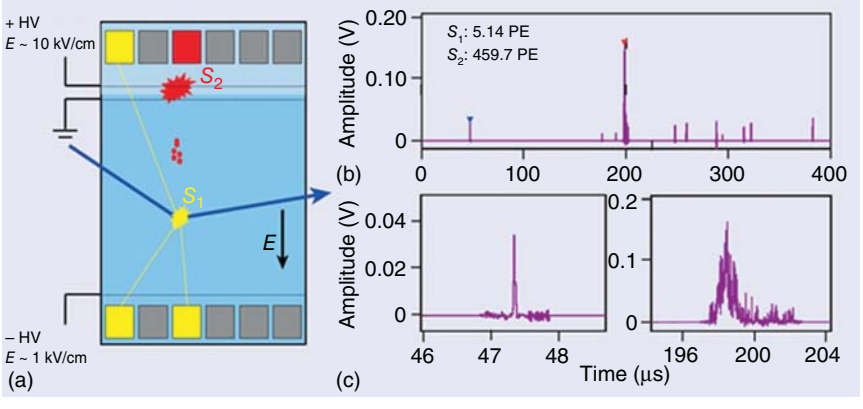

Figure 9.33 Illustration of the operation principle of a double-phase electroluminescence detector. (a) The scintillation light S_1, produced by the interaction in liquid (dark grey) is identified thanks to the coincidence from several PMTs (marked in yellow in the figure). The strong secondary scintillation light S_2 in the gas (light blue) produces a large-amplitude signal on the nearest top PMT (marked in red). (b) Oscillograms of the PMT signals S_1 and S_2 from a noble liquid TPC. (c) Signals S_1 and S_2 in expanded scales. (Schumann 2013. Reprinted with permission of CERN.)

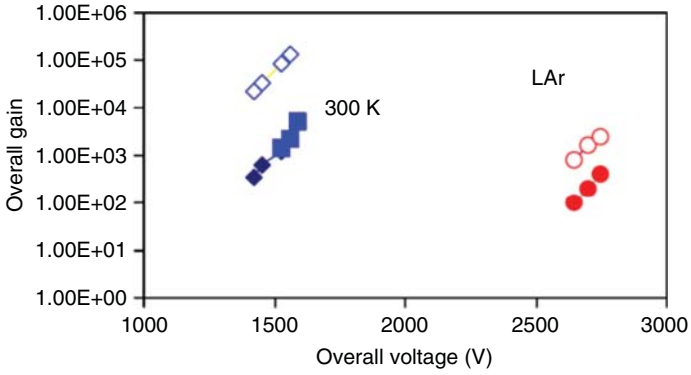

Figure 9.34 Gain versus voltage measured with a 1-mm-thick resistive GEM with CrO electrodes, coated with a 0.4-nm-thick CsI layer and operated in argon, at room temperature and 1 cm above the argon liquid level of a dual-phase TPC. In the plot, closed symbols refer to a single-resistive GEM, open symbols to double-resistive GEM. (Di Mauro *et al*. 2007. Reproduced with permission of IEEE.)

the secondary scintillation signals with the hit pattern of the secondary signals localized onto the array of the PMTs positioned at the top of the device.

There are encouraging tests indicating that CsI-coated resistive GEMs might represent an alternative to PMTs for these applications. Indeed, it was shown in Periale *et al*. (2004, 2005) that a *C*sI cathode retains sufficiently high quantum efficiency even when cooled down to the temperature of liquid argon. Moreover, some detectors with resistive electrodes, for example, resistive thick GEMs (Di Mauro *et al*., 2007, 2009) or resistive microhole-microstrip detectors (see Chapter 8 and Peskov *et al*., 2013) can still operate at low temperatures, although their maximum achievable gain drops in dense gases, as well as their counting rate capability, due the sharp increase of the electrode resistivity (see, for instance, Figure 9.34).

With a view to possible applications in noble liquid TPCs, two main functional schemes have been investigated: detectors located in sealed chambers equipped with UV transparent windows (Figure 9.35) and windowless electron multipliers, for example, hole types, placed in the gas just above the liquid surface (Figure 9.36).

Each option, of course, has its advantages and disadvantages. For instance, windowless detectors offer simplicity and high sensitivity for far UV photons, which is essential in the case of liquid argon TPC, while microhole-microstrip chambers, due to their capability to strongly suppress photon feedback (see Chapter 8), open a possibility to operation in a combination with a CsI photocathode immersed in the liquid (Peskov *et al.*, 2013).

An alternative approach, which is currently under study, is to use a glass capillary plate or thick GEMs (e.g., see Periale *et al*., 2004, 2005, 2006; Breskin *et al*., 2011; Badertscher *et al*., 2011; Erdal *et al*., 2017). However, resistive detectors certainly are superior due to their spark protection feature.

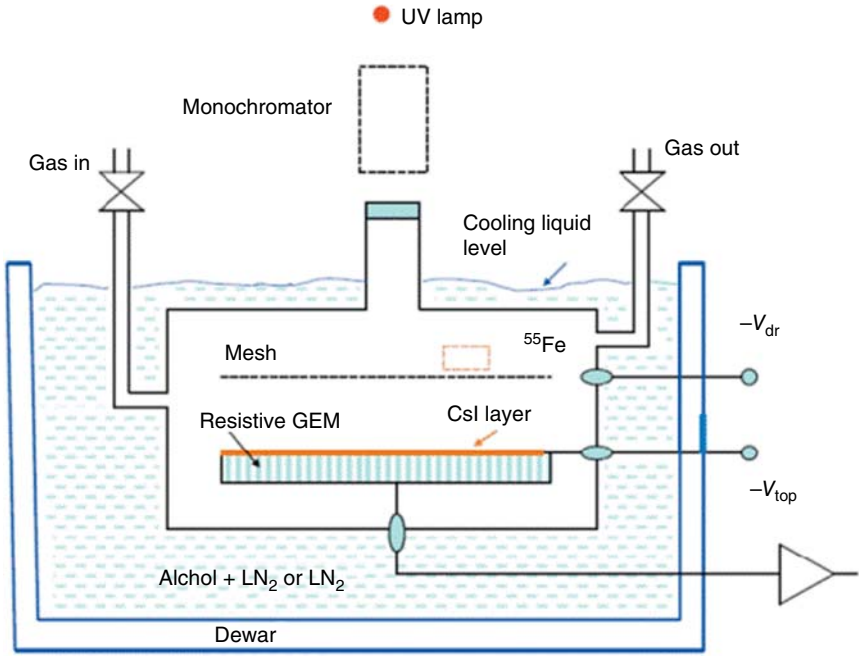

Figure 9.35 Schematic drawing of the experimental setup used for studies on a CsI-coated resistive GEM operated in sealed mode at cryogenic temperatures. (Martinengo *et al*. 2009. Reproduced with permission of Elsevier.)

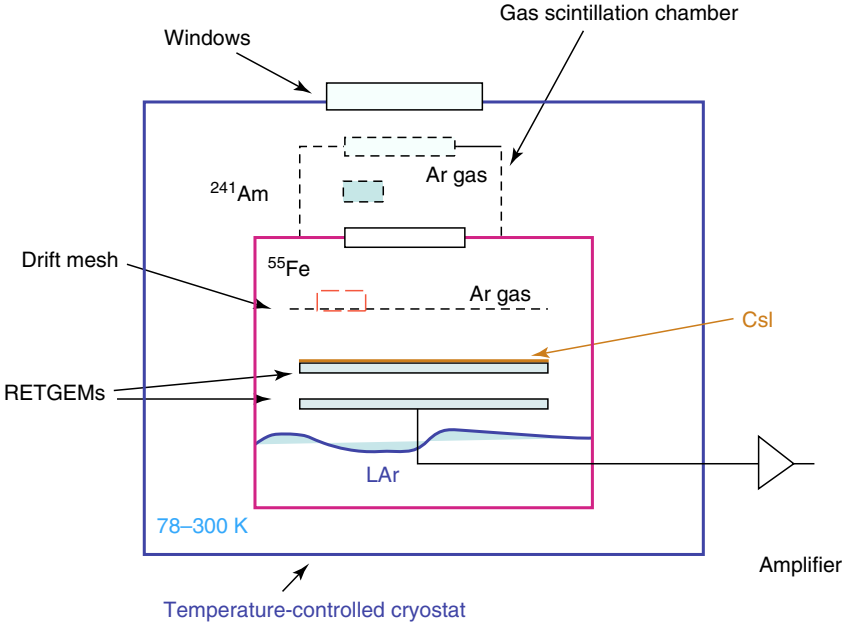

Figure 9.36 Schematic of a setup used for measurements with a windowless resistive GEM at cryogenic temperatures. (Peskov *et al*. 2007. Reproduced with permission of IEEE.) The term "RETGEMs" here stands for resistive thick GEMs.

9.8 Digital Calorimetry with RPCs

The Calorimenter for Linear Collider Experiment (CALICE) Collaboration is an R&D group of around 280 physicists and engineers from around the world, working together to develop new high-performance detectors for high energy e^+e^- experiments. In the field of hadron calorimetry it aims at the application of particle flow algorithms (PFAs, see Brient *et al.*, 2002), requiring calorimeters with extremely fine segmentation of the readout (usually called digital sampling calorimetry), on the order of 1 cm^2 laterally and layer-by-layer longitudinally.

Among several approaches, the collaboration developed two calorimeter prototypes based on RPCs, named, for convenience, Digital Hadron Calorimeter (DHCAL) (Adams *et al.*, 2016) and Semi-Digital Hadronic Calorimeter (SDHCAL) (The CALICE collaboration, 2016).

Both prototypes are composed of layers of 1.15–1.2-mm single-gap soda-lime glass RPCs interleaved with heavy material absorbers. The readout is made by 1×1 cm^2 pads placed on the anode side. The glass thickness was kept as thin as considered practical, around 0.8 mm minimum. The gap width was defined by the rim frames (PVC or fiberglass) and PVC sleeves or ceramic spheres along the active area. High voltage was applied by resistive coatings with surface resistivity around 1–5 MΩ/□ in the case of DHCAL. The number of layers/prototype was on the order of 50, composing an active volume (including absorbers) close to 1 m^3. Images of these impressive prototypes can be seen in Figures 9.37 and 9.38.

As high granularity is the hallmark of this calorimetric approach, the number of readout channels was over 400 000. Specialized ASICs were developed for each prototype and were discussed in Section 4.7. The SDHCAL version allowed a

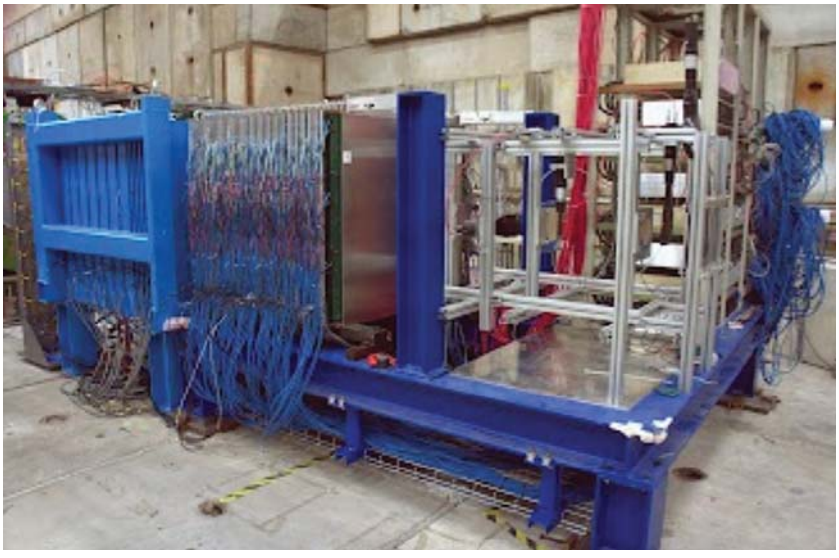

Figure 9.37 Photograph of the DHCAL setup at CERN showing the main stack with tungsten plates followed by the TCMT (tail catcher/muon tracker) with steel plates. (Adams *et al*. 2016. Reproduced with permission of IOP Publishing.)

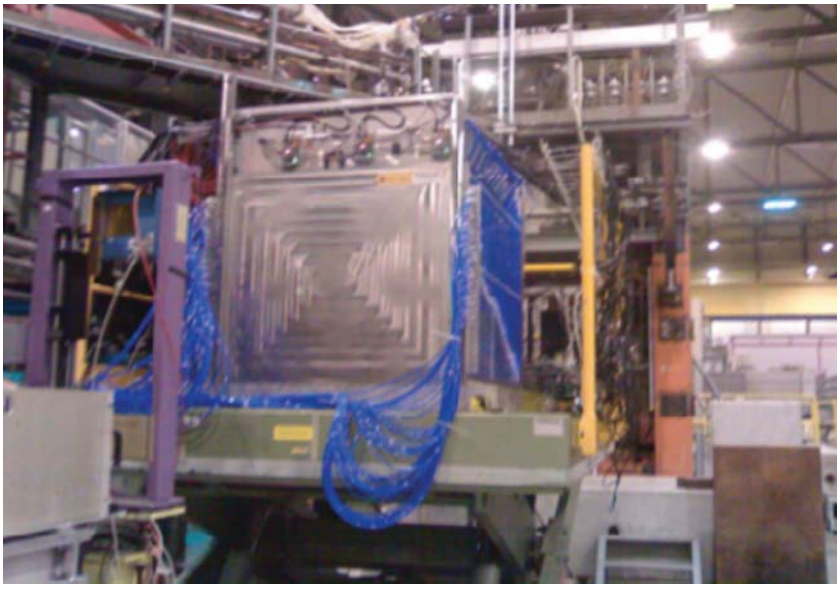

Figure 9.38 The SDHCAL prototype at the SPS test beam area. (The CALICE collaboration 2016. Reproduced with permission of IOP Publishing.)

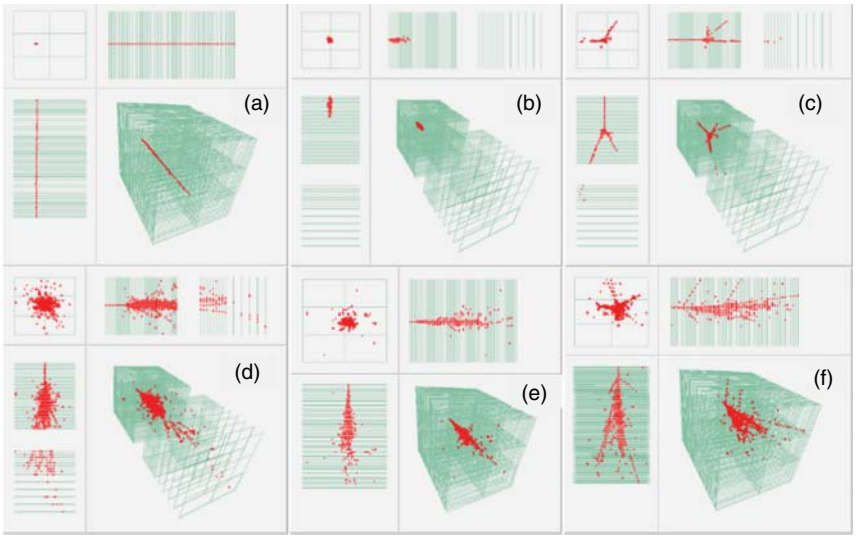

Figure 9.39 Event displays showing different views: in each figure (a) Muon track in the absorber stack, (b) 8 GeV positron in the DHCAL, (c) 8 GeV pion in the DHCAL and TCMT, (d) 120 GeV proton in the DHCAL and TCMT, (e) 10 GeV positron in the absorber stack, and (f) 10 GeV pion in the absorber stack. (Adams *et al*. 2016. Reproduced with permission of IOP Publishing.)

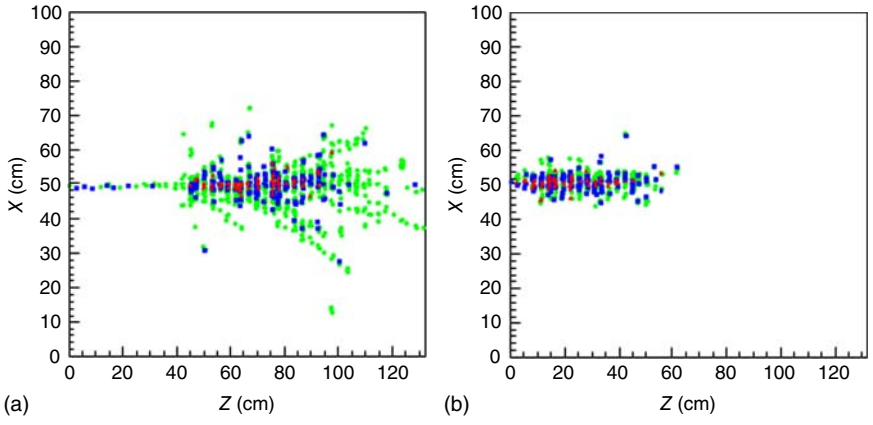

Figure 9.40 Events from SDHCAL. (a) 70 GeV pion event display with dark pixels indicating highest threshold fired pads, light grey pixels indicating the lowest ones. (b) 70 GeV electron event display with the same coding. (The CALICE collaboration 2016. Reproduced with permission of IOP Publishing.)

rough measure of the pad occupancy. For this aim the amplified signals from each pad were sensed by comparators with three different thresholds.

The prototypes were extensively tested at Fermilab and at CERN and performed according to expectations. A sample of event displays, shown in Figures 9.39 and 9.40, demonstrates the unique imaging and particle identification capabilities of the devices.

The energy resolution reaches 7.7% at 80 GeV (Figure 9.41) with an energy response with a 4–5% deviation from linearity when applied to the raw data over a wide energy range (5–80 GeV) (The CALICE collaboration, 2016).

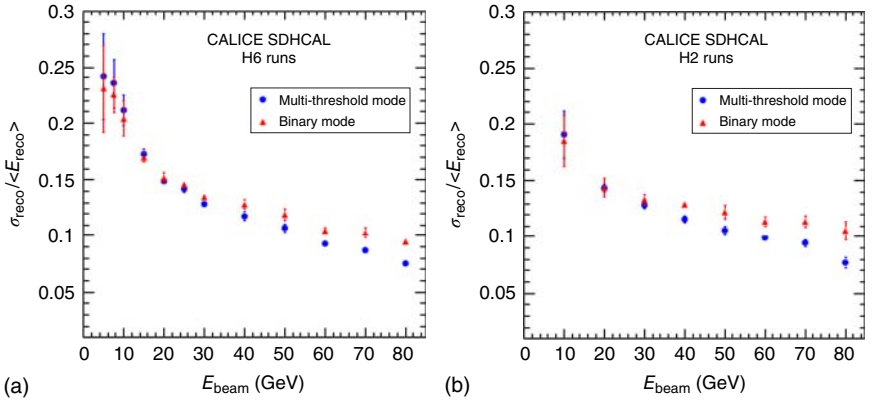

Figure 9.41 Relative energy resolution of the reconstructed hadron energy as a function of the beam energy of the 2012 H6 (a) and the 2012 H2 (b) data. For the triangles graph, the reconstructed energy is computed using only the total number of hits (binary mode). For the circles graph, the reconstructed energy is computed using the three-threshold information (indicated in the original figures as multi-threshold mode). For both modes, the energy is reconstructed using quadratic functions of the total number of hits. (The CALICE collaboration 2016. Reproduced with permission of IOP Publishing.)

References

Abbrescia, M. *et al*. (2003) Resistive plate chambers as thermal neutron detectors. *Nuclear Physics B (Proc. Suppl.)*, **125**, 4347.

Abbrescia, M. *et al*. (2004a) Resistive plate chambers as detectors for thermal neutrons. *Nucl. Instrum. Methods Phys. Res., Sect. A*, **518**, 440–442.

Abbrescia, M. *et al*. (2004b) Resistive plate chambers with Gd-coated electrodes as thermal neutron detectors. *Nucl. Instrum. Methods Phys. Res., Sect. A*, **533**, 149–153.

Adams, C. *et al*. (2016) Design, construction and commissioning of the Digital Hadron Calorimeter—DHCAL. *JINST*, **11**, P07007.

Alvarez, L.W. *et al*. (2007) Search for hidden chambers in the pyramids using cosmic rays. *Science*, **832** (New series), 167.

Arnaldi, R. *et al*. (2004) Resistive plate chamber for thermal neutron detection. *Nucl. Instrum. Methods Phys. Res., Sect. B*, **213**, 284–288.

Arnaldi, R. *et al*. (2006) RPC for thermal neutron detection. *J. Phys. Conf. Ser.*, **41**, 384–390.

Azevedo, C.D.R. *et al*. (2010) Towards THGEM UV-photon detectors for RICH: on single-photon detection efficiency in ne/CH4 and ne/CF_4. *JINST*, **5**, P01002.

Badertscher, A. *et al*. (2011) First operation of a double phase LAr Large Electron Multiplier Time Projection Chamber with a two-dimensional projective readout anode. *Nucl. Instrum. Methods Phys. Res., Sect. A*, **641**, 48.

Baesso, P. *et al*. (2014) Toward a RPC-based muon tomography system for cargo containers. *JINST*, **9**, C10041.

Baru, S.E. *et al*. Digital x-ray imaging installation for medical diagnostics. *Nucl. Instrum. Methods Phys. Res., Sect. A*, **238** (1985), 165.

Baru, S.E. *et al*. Multiwire proportional chamber for a digital radiographic installation. *Nucl. Instrum. Methods Phys. Res., Sect. A*, **283** (1989), 431.

Bateman, J.E. *et al*. (1981) X-ray and gamma imaging with multiwire proportional counters. *Nucl. Instrum. Methods*, **221**, 131.

Bateman, J.E. *et al*. (1984) The Rutherford Appleton laboratory's mark I multiwire proportional counter positron camera. *Nucl. Instrum. Methods Phys. Res.*, **225**, 209.

Bidault, J.M. *et al*. (2006) A novel UV photon detector with resistive electrodes. *Nucl. Phys. B (Proc. Suppl.)*, **158**, 199.

Bidault, J.M. *et al*. (2007) The first applications of newly developed gaseous detectors with resistive electrodes for UV imaging in daylight conditions. *Nucl. Instrum. Methods Phys. Res., Sect. A*, **580**, 1036.

Blanco, A., Carolino, N., Correia, C.M.B.A., Ferreira Marques, R., Fonte, P., González-Díaz, D., Lindote, A., Lopes, M.I., Macedo, M.P., and Policarpo, A. (2004) An RPC-PET prototype with high spatial resolution. *Nucl. Instrum. Methods Phys. Res., Sect. A*, **533**, 139–143.

Blanco, A., Chepel, V., Ferreira-Marques, R., Fonte, P., Lopes, M.I., Peskov, V., and Policarpo, A. (2013) Perspectives for positron emission tomography with RPCs. *Nucl. Instrum. Methods Phys. Res., Sect. A*, **508**, 88–93.

Blanco, A., Couceiro, M., Crespo, P., Ferreira, N.C., Ferreira Marques, R., Fonte, P., Lopes, L., and Neves, J.A. (2009) Efficiency of RPC detectors for whole-body human TOF PET. *Nucl. Instrum. Methods Phys. Res., Sect. A*, **602**, 780–783.

Blanco, A. *et al*. (2004) Progress in timing resistive plate chambers. *Nucl. Instrum. Methods Phys. Res., Sect. A*, **535**, 272–276.

Breskin, A. *et al*. (2011) CsI-THGEM gaseous photomultipliers for RICH and noble-liquid detectors. *Nucl. Instrum. Methods Phys. Res., Sect. A*, **639**, 117.

Brient, J.C. *et al.* (2002) The calorimetry at a future e^+e^- linear collider, arXiv:hep-ex/0202004v1.

Burns, J. *et al*. (2015) A drift chamber tracking system for muon scattering tomography applications. *JINST*, **10**, 10041.

Cârloganu, C. *et al*. (2013) Towards a muon radiography of the Puy de Dôme. *Geosci. Instrum. Methods Data Syst.*, **2**, 55–60.

Charpak, G. *et al*. (2008a) Detectors for alpha particles and X-rays operating in ambient air in pulse counting mode or/and with gas amplification. *JINST*, **3**, P02006.

Charpak, G. *et al*. (2008b) Development of new hole-type avalanche detectors and the first results of their applications. *IEEE Trans, Nucl. Sci.*, **55**, 1657.

Charpak, G. *et al*. (2009) Progress in the development of a S-RETGEM-based detector for an early forest fire warning system. *JINST*, **4**, P12007.

Charpak, G. *et al*. (2010) arXiv:1002.4732v2.

Chepel, V. *et al*. (2013) Liquid noble gas detectors for low energy particle physics. *JINST*, **8**, R04001.

Couceiro, M. *et al*. (2014) Scatter fraction, count rates, and noise equivalent count rate of a single bed position RPC TOF PET system assessed by simulations following the NEMA NU2 2001 standards. *IEEE Trans. Nucl. Sci.*, **61**, 1153–1163.

Cox, L. *et al*. (2008) Detector requirements for a cosmic ray muon scattering tomography system. Nuclear Science Symposium Conference Record, pp. 706–710.

Dahlbom M. (2012) "PET Imaging: Basics and New Trends". *In Handbook of Particle Detection and Imaging*, Ch. 38, pp. 935-71 (eds Grupen C., & Buvat I.), Springer-Verlag, Germany, ISBN: 978-3-642-13270-4.

Di Mauro, A. *et al*. (2007) Development of innovative micro-pattern gaseous detectors with resistive electrodes and first results of their applications. *Nucl. Instrum. Methods Phys. Res., Sect. A*, **581**, 225.

Di Mauro, A. *et al*. (2009) GEMs with double layered micropattern electrodes and their applications. *IEEE Trans. Nucl. Sci.*, **56**, 1550.

Diblen, F. *et al*. (2012) Comparison study of RPC and crystal based PET systems for hadron therapy monitoring. IEEE Nuclear Science Symposium and Medical Imaging Conference (NSS/MIC). doi: 10.1109/NSSMIC.2012.6551504.

Dobrovsky, I.P. *et al*. (1978) Estimation of the size of earthquake preparation zones. *Pure Appl. Geophys.*, **117**, 1025.

Erdal, E. *et al*. (2017) First demonstration of VUV-photon detection in liquid xenon with THGEM and GEM-based Liquid Hole Multipliers. *Nucl. Instrum. Methods Phys. Res., Sect. A*, **845**, 218.

Fleischer, R.L. *et al*. (1981) Dislocation model for radon response to distant earthquakes. *Geophs. Res. Lett.*, **8**, 477.

Francke, T. *et al*. (2001a) Dose reduction in medical X-ray imaging using noise free photon counting. *Nucl. Instrum. Methods Phys. Res., Sect. A*, **471** (1–2), 85–87.

Francke, T. *et al*. (2001b) High contrast and position resolution using photon counting digital-ray imaging. Proceedings of ASNT Digital Imaging Conference, Mashantucket, CT, USA, August 2001.

Francke, T. *et al*. (2014) *Innovative Applications and Developments of Micro-Pattern Detectors*, IGI Global, USA.

Francke, T. *et al*. (2016) *Position-Sensitive Gaseous Photomultipliers: Research and Applications*, IGI Global, USA.

Georgiev, G., Ilieva, N., Kozhuharov, V., Lessigiarska, I., Litov, L., Pavlov, B., and Petkov, P. (2013) Multigap RPC for PET: development and optimisation of the detector design. *JINST*, **8**, P01011. doi: 10.1088/1748-0221/8/01/P01011.

Gnanvo, K. *et al*. (2010) Detection and imaging of high-Z materials with a muon tomography station using GEM detectors. Nuclear Science Symposium Conference Record (NSS/MIC), IEEE. doi: 10.1109/NSSMIC.2010.5873822.

Gnanvo, K. *et al*. (2011) Imaging of high-Z material for nuclear contraband detection with a minimal prototype of a muon tomography station based on GEM detectors. *Nucl. Instrum. Methods Phys. Res., Sect. A*, **652**, 16–20.

Hong, B. *et al*. (2006) Sensitivity of hybrid resistive plate chambers to low-energy neutrons. *Nucl. Phys. B (Proc. Suppl.)*, **158**, 161–165.

Igarashi, G. (1995) Ground-water radon anomaly before the Kobe earthquake in Japan. *Science*, **269** (5220), 60–61. doi: 10.1126/science.269.5220.60.

Jeavons, A., Parkman, C., Donath, A., Frey, P., Herlin, G., Hood, K., Magnanini, R., and Townsend, D. (1983) The high-density avalanche chamber for positron emission tomography. *IEEE Trans. Nucl. Sci.*, **NS-30**, 640–645.

Kedar, S. *et al*. (2013) Muon radiography for exploration of Mars geology. *Geosci. Instrum. Methods Data Syst.*, **2**, 157–164.

Khan, H.-A. *et al*. (1990) *J. Islamic Acad. Sci.*, **3** (3), 229; (1997) *Access to Energy News Lett. Arch.*, **24**, (9).

La Rocca, P. *et al*. (2015) Fabrication, characterization and testing of silicon photomultipliers for the Muon portal project. *Nucl. Instrum. Methods Phys. Res., Sect. A*, **787**, 236–239.

Le Menedeu, E. (2016) For the TOMUVOL collaboration, RPC application in muography and specific developments. *JINST*, **11**, C06009.

Lopes, L., Pereira, A., Fonte, P., and Ferreira Marques, R. (2007) Accurate timing of gamma rays with high-rate resistive plate chambers. *Nucl. Instrum. Methods Phys. Res., Sect. A*, **573**, 4–7.

Magro-Campero, A. (1980) *J. Geophys. Res.*, **85**, 3053.

Maidment, A.D.A. (2006) Clinical evaluation of a photon-counting tomosynthesis mammography system, in *Digital Mammography. IWDM 2006*, Lecture Notes in Computer Science, vol. **4046** (eds S.M. Astley, M. Brady, C. Rose, and R. Zwiggelaar), Springer-Verlag, Berlin, Heidelberg.

Maidment, A.D.A., Adelow, L., Blom, O. *et al*. (2006) Evaluation of a photon-counting breast tomosynthesis imaging system, in *Physics of Medical Imaging, Proceedings of SPIE*, vol. **6142** (ed. M.J. Flynn), SPIE.

Maidment, A.D.A., Albert, M., Thunberg, S. *et al*. (2005) Evaluation of a photon-counting breast tomosynthesis imaging system, in *SPIE Medical Imaging* (ed. M.J. Flynn), pp. 572–582.

Margato, L. *et al*. (2016) Boron-10 based thin-gap hybrid RPCs for sub-millimeter resolution thermal neutron detectors. Presentation Given at RPC 2016 – The XIII Workshop on Resistive Plate Chambers and Related Detectors, Gent February 2016.

Martinengo, P. *et al*. (2009) A new generation of GEM detectors and their applications. *Nucl. Instrum. Methods Phys. Res., Sect. A*, **604**, 8–10.

Martinengo, P. *et al*. (2011) *Nucl. Instrum. Methods Phys. Res., Sect. A*, (126), 639.

Martins, P. *et al*. (2014) Towards very high resolution RPC-PET for small animals. *JINST*, **9**, C10012.

Missimer, J. *et al*. (2004) Performance evaluation of the 16-module quad-HIDAC small animal PET camera. *Phys. Med. Biol.*, **49**, 2069.

Morris, C.L. *et al*. Analysis of muon radiography of the Toshiba nuclear critical assembly reactor. *Appl. Phys. Lett.*, **106** (2). doi: 10.1063/1.4862475.

Moskal, P. *et al*. (2016) Time resolution of the plastic scintillator strips with matrix photomultiplier readout for J-PET tomography. *Phys. Med. Biol.*, **61**, 2025.

Ouzounov, D. *et al*. (2011) arXiv:geoph/1105.2841v1, https://arxiv.org/ftp/arxiv/papers/1105/1105.2841.pdf (accessed 31 October 2017).

Periale, L. *et al*. (2004) The development of gaseous detectors with solid photocathodes for low-temperature applications. *Nucl. Instrum. Methods Phys. Res., Sect. A*, **535**, 517.

Periale, L. *et al*. (2005) The successful operation of hole-type gaseous detectors at cryogenic temperatures. *IEEE Trans. Nucl. Sci.*, **52**, 927.

Periale, L. *et al*. (2006) *Nucl. Instrum. Methods Phys. Res., Sect. A*, **567**, 381.

Peskov, V. *et al*. (2007) Development and first tests of GEM-like detectors with resistive electrodes. *IEEE Trans. Nucl. Sci.*, **54**, 1784.

Peskov, V. *et al*. (2013) Development of a new generation of micropattern gaseous detectors for high energy physics, astrophysics and environmental applications. *Nucl. Instrum. Methods Phys. Res., Sect. A*, **732**, 255.

Plch M. Eng.-SMM (2015) https://www.irsm.cas.cz/materialy/pristroje/Radim3A_manual_EN.pdf (accessed 31 October 2017).

Qian, S. *et al*. (2009) Study of the RPC-Gd as thermal neutron detector. *Chin. Phys. C*, **33** (9), 769–773.

Qian, S. *et al*. (2015) The study and design of the large area neutron monitor with RPC-Gd. *JINST*, **10**, C02014.

Radon Analytics Inc. (2014) http://www.radon-analytics.com and http://www.radon-analytics.com/index.php?show=atmos12dpx.

Richon, P. *et al*. (1994) Radon anomaly in the soil of Taal volcano, the Philippines: a likely precursor of the M 7.1 Mindoro earthquake (1994). *Geophys. Res. Lett.*, **30**, **34** (9).

Schultz, L.J. *et al*. (2004) Image reconstruction and material Z discrimination via cosmic ray muon radiography. *Nucl. Instrum. Methods Phys. Res., Sect. A*, **519**, 687–694.

Schumann, M. (2013) http://cerncourier.com/cws/article/cern/54673 (accessed 31 October 2017).

Segovia, N. *et al*. (1986) Radon variations in active volcanoes and in regions with high seismicity: internal and external factors. *Nucl. Track*, **12**, 871.

The CALICE collaboration (2016) First results of the CALICE SDHCAL technological prototype. *JINST*, **11**, P04001.

Thomay, G. *et al*. (2012) Resistive plate chambers for tomography and radiography. *Geosci. Instrum. Methods Data Syst.*, **1**, 235–238.

Thunberg, S.J., Maidment, A.D.A. *et al*. (2004) Tomosynthesis with a multi-line photon counting camera. 7th International Workshop on Digital Mammography (ed. E. Pisano), pp. 459–465.

Thunberg, S.J. *et al*. (2002) Evaluation of a photon-counting mammography system. *Proc. SPIE*, **4682**, 202–208.

Thunberg, S.J. *et al*. (2004) Dose reduction in mammography with photon counting imaging. *Proc. SPIE*, **5368**, 457–465.

Wang, X. *et al*. (2015) The cosmic ray muon tomography facility based on large scale MRPC detectors. *Nucl. Instrum. Methods Phys. Res., Sect. A*, **784**, 390–393.

Watts, D., Borghi, G., Sauli, F., and Amaldi, U. (2013) The use of multi-gap resistive plate chambers for in-beam PET in proton and carbon ion therapy. *J. Radiat. Res.*, **54** (Suppl. 1), i136–i142. doi: 10.1093/jrr/rrt042.

Yasuoka, Y. and Shinogi, M. (1997) Anomaly in atmospheric radon concentration. *Health Phys.*, **72**, 759.

Zhang, X. *et al*. (2014) Feasibility study of micro-dose total-body dynamic PET imaging using the EXPLORER scanner. *J. Nucl. Med.*, **55**, 269.

Conclusions and Perspectives

The end of the gaseous detectors era has been predicted several times. Likewise, as many times, this prediction has been proved wrong. After more than a hundred years from their invention, gaseous detectors still play a key role in all major experiments, both at accelerators and with cosmic rays, and they are steadily gaining more and more space in applied physics.

The future seems even more brilliant, as the R&D in this field is flourishing again, and the major upgrades of the big experiments in operation foresee the use of some kind of gaseous detector. Moreover, new gigantic experiments are starting to be designed for possible future linear and/or circular accelerators, most of them including the use of gaseous detectors, many of them equal or derived by the ones described here.

We hope that in this book we made it clear how this was made possible: major breakthroughs took place in the second half of the twentieth century, which periodically brought new life to this branch of detector physics. Among them, the idea of using resistive materials in gaseous detectors is probably one of the most successful ones, and this was the leitmotif of this book.

The question naturally arises: is the story finished? Is there anything else in the near future to further develop in this field? Well, the answer is that there is much that we can envisage right now, and most probably much more that we cannot imagine.

For instance, it has been pointed out that one comprehensive simulation model of resistive plate chambers (RPCs) still does not exist, and that the understanding of the many aspects of its operation is in a very different status. Exemplifying, an evolved theory of avalanche development and signal induction exists, which provides reliable predictions, while the dynamics of avalanche-to-streamer transition or the physicochemical interactions in the gas or between gas and electrodes is still rudimentary. It would be particularly interesting to bring together the scattered models in existence for different parts of the full problem into an open common framework, serving as a reference for RPC physical simulation and evolving as the knowledge progresses. This would promote the comparison between model and experiment, as experimentalists would tend to compare their data with the reference model, testing it in a much more intense and organized way that it is possible together. There is an entire continent to be explored here!

Resistive Gaseous Detectors: Designs, Performance, and Perspectives, First Edition.
Marcello Abbrescia, Vladimir Peskov, and Paulo Fonte.

There are less far-reaching tasks to tackle in the near future, but essential as well. One of them is finding a replacement for tetrafluoroethane and sulfur hexafluoride, the main components of the gas mixtures used in RPCs. They are not only rather expensive but are also greenhouse gases and therefore have been banned in the European Community. Even if some time can be gained thanks to the fact that scientific applications are exempt from this ban and damage can be limited by recirculating the gas and fixing any leaks, some long-term solution must be found. This implies finding a new gas mixture, whose behavior has to be understood anew, in particular for what concerns aging. This is not an easy task at all; gas is the "core" of a gaseous detector.

Aging in RPCs is one open space to be filled with knowledge. Some has been gained at the cost of hard lessons thought by experience on the field, but much more would be needed. A deeper understanding of the complex chemical processes taking place in the gas and how it does interact with the electrode surfaces would shed new light on which are the key factors for aging and how it can be slowed down.

All this is correlated with the searches for new materials suitable for devices conceived to be used background and rate conditions orders of magnitude higher than present, typical of the next generation accelerators. Interesting new materials have been produced, typically in small samples, but high-quality large-area sheets, due to various kinds of technical problems, were not manufactured yet. Of course we are going in the direction of larger and larger experiments, and this implies that rate capability – as well as other important characteristics – have to be achieved uniformly over large areas, which in turn calls for improved manufacturing techniques and stringent quality assurance protocols.

Or maybe the present materials could be enough? Maybe once we have learnt to carefully tune their resistivity and how rate capability depends on detector configuration we could be ready for the next-generation experiments? This is a concrete possibility to consider and, as a matter of fact, this is the direction big collaborations are moving toward; considerable effort is put here.

However, even in this field not everything is understood. To have an idea of the work to do let us consider that we do not even know the details of the conduction of electric current in Bakelite or glass, and these materials have been used since almost 30 years. The search for new materials as well as improving and using better the ones presently employed in RPCs will be another challenge. And, of course, electronics will continue to play an important role in all this, as it already was in the past, so this is another factor to be considered.

We also expect in the near future an expansion of resistive micropattern detectors technology, because of their excellent position resolution, approaching in some designs the one of solid-state detectors. Introducing the use of resistive materials in these devices was a breakthrough that has made them intrinsically spark protected, overcoming one of the problems encountered at the early stages. Now, for the first time, they are being used over hundreds of square meter areas in big experiments, and this will be a crucial test to demonstrate full maturity.

So, anybody willing to approach this field will be spoilt for choice! There are plenty of questions in need for an answer here.

As a final consideration, let us point out that an approach, which could effectively tackle all these issues in a reasonable lapse of time, has a chance to be successful only if it will rely on the combined efforts of the many groups that are presently active in this field. If an appropriate framework is established, coordinating the work done in so many laboratories spread across the world would greatly profit, the competences of the various groups would complete each other and a broader vision of the problems could be much more rapidly achieved.

In exchanging information and comparing results, an important role is played by the bi-annual workshops on RPCs and related detectors which, for already more than 20 years, act as a point of reference for the community active in this field. In this forum, very interesting discussions, sometimes animated – which is a sign of vitality – often take place. However, probabaly more could be done. A promising strategy could be to replicate what was done establishing RD51, a collaboration counting around 500 authors and 75 institutions born with the specific goal to develop micropattern gaseous detector technologies, for applications in basic and applied research. Indeed, this approach proved to be quite effective, and relevant progresses were made thanks to the cooperation that was established in this fertile environment. This probably is the way to go, and these authors would be glad to promote this endevour.

"We have become eager. We want everything in one single detector." This was the opening statement of the wrap-up talk during the last RPC workshop. The dream is to have a device, completely understood from the theoretical point of view, characterized at the same time by a several tens of kHz/cm^2 high-rate capability, sub-millimeter spatial and better than a hundred nanosecond time resolutions, which in addition is easy to build, inexpensive, and reliable in operation for many years. We are moving in that direction.

A

Some Guidelines for RPC Fabrication

In the previous chapters of this book we have tried to provide exhaustive information about the theory of resistive plate chamber (RPC) operation, and an overview of the present applications of these devices as well as of the new promising developments in this field.

This Appendix is dedicated to practical issues: in particular, we discuss how Bakelite and glass RPCs are assembled in laboratory. We believe that this section will be especially interesting for newcomers to this field who might be interested in building these devices in their laboratories.

The main steps for the construction of a Bakelite RPC are described in the first part of the Appendix; here we used photographs and comments from Biswas (2010) with the kind permission from the author. The second part deals with the assembling of glass RPCs, with pictures taken from Loterman (2014) and Repond (2009). The third part is devoted the assembling of multi-gap timing RPCs. In this part we used material from the EEE collaboration; the photos illustrating the procedure, in particular, are from La Rocca *et al*. (2017), with the kind permission of the authors, and were taken in the CERN Laboratory, led by C. Williams, where these chambers are assembled. We warmly acknowledge them all.

A.1 Assembling of Bakelite RPCs

A sketch of the RPC whose construction procedure is described here is shown in Figure A.1. In this particular case, 2-mm Bakelite planes and a 2-mm gas gap thickness were used but, of course, the procedure can be followed also with other parameter values. Uniform distance between the electrodes is ensured by button-like spacers (usually 1 button for a 10×10 cm^2 RPC, 5 buttons for a 30×30 cm^2 RPC, 49 buttons for a 100×100 cm^2 are used), 1 cm in diameter. Gas tightness is obtained by means of a perimetral seal, sometimes also called edge frame, 8 mm thick. Both buttons and the edge frame are made of polycarbonate.

Two nozzles as gas inlet and outlet, also made of polycarbonate, are placed as part of the edge frame, close to two opposite corners of the detector; in the case of larger dimension RPCs, four of such nozzles are generally used. All these components (gas nozzles, edge spacers, and button spacers) are glued to the Bakelite

Resistive Gaseous Detectors: Designs, Performance, and Perspectives, First Edition.
Marcello Abbrescia, Vladimir Peskov, and Paulo Fonte.

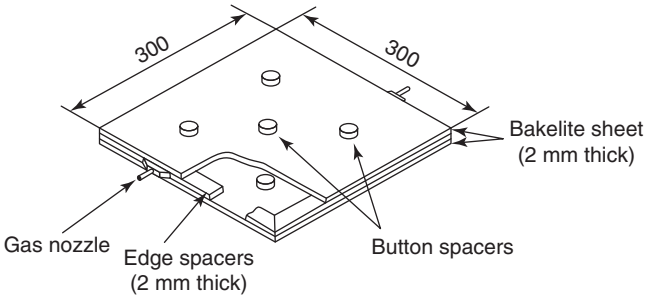

Figure A.1 Simplified sketch of a resistive plate chamber, whose construction process is described here. (From Biswas, 2010.)

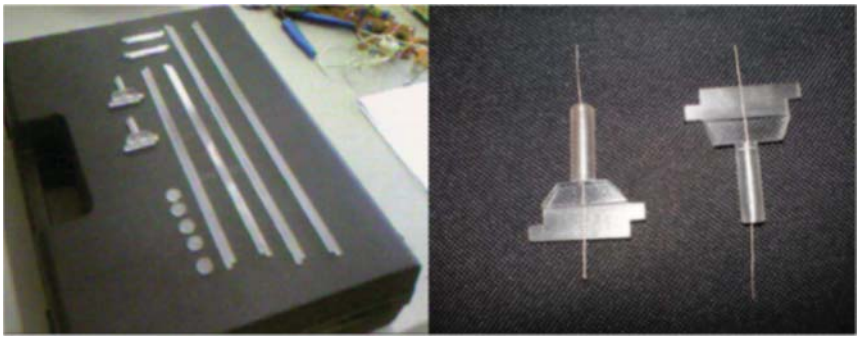

Figure A.2 Polycarbonate button spacers, edge spacers and gas nozzles. (From Biswas, 2010.)

using Araldite epoxy adhesive; some of them are shown in Figure A.2. The edges of the Bakelite sheets are sealed by applying a layer of the epoxy adhesive to prevent any gas leakage.

It is important that gas tightness is checked before operation, and this can be done by filling the RPC with argon or helium and using sniffer probes. An alternative way consists in inflating air (or some gas) inside the chamber while keeping the gas outlet closed, in order to create a few millibar overpressure inside; gas tightness is verified checking that the pressure remains stable in time.

The main steps for assembling the RPC are shown in Figures A.3–A.5. In particular, gluing of the spacers and gas nozzles on the Bakelite plate is shown in Figure A.3. After proper cleaning, the outer surfaces of the Bakelite electrodes have to be coated with a thin graphite layer (surface resistivity $\approx 1\ \mathrm{M\Omega/\square}$), using a spray gun, in order that the high voltage (HV) can be uniformly distributed over the entire RPC. Note, that if the resistivity of the coating is too low, the induced charge will fire multiple strips, thus worsening spatial resolution. On the contrary, if the resistivity is too high, the electric field might not be uniform enough, or the electrodes will not be rapidly recharged after a discharge. Therefore, the optimal value must be found, sometimes by means of empirical tests.

A 1-cm gap is left between the Bakelite edges and the graphite layer, in order to avoid discharges. Then two small ($20\ \mathrm{mm} \times 10\ \mathrm{mm}$) copper foils, thick $\approx 20\ \mu\mathrm{m}$,

Figure A.3 Gluing of spacers and gas nozzles on a 30×30 cm^2 Bakelite plates (From Biswas, 2010.)

Figure A.4 Photograph of a 30×30 cm^2 RPC module, complete with gas tubes and high voltage connections. (From Biswas, 2010.)

are pasted using kapton tapes on both the outer surfaces; the HV connectors are soldered on these copper strips (see Figure A.4).

In order to collect the induced signals, pickup strips are placed above the graphite-coated surfaces, separated by an insulator (Figure A.5). The pickup strips are made of copper (20 μm thick), pasted on one side on a 10-mm-thick foam used as dielectric and also to give rigidity to the structure. Strips are 300 mm $\times$ 30 mm in dimension, with a 2-mm separation between two adjacent strips. The ground plane, made of aluminum, is pasted on another foam placed on the opposite side of the device.

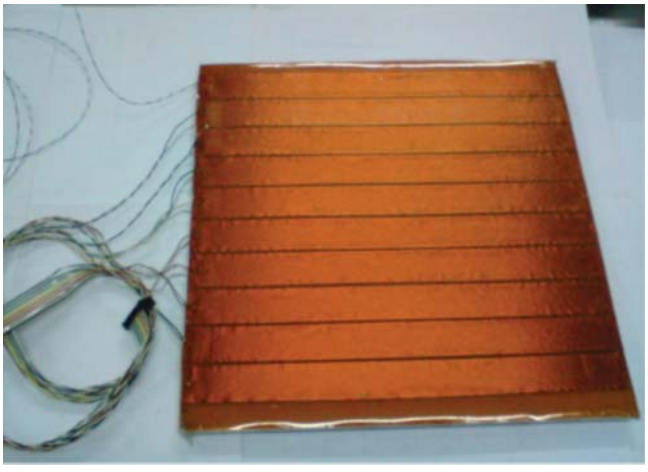

Figure A.5 Photograph of an assembled RPC with, in evidence, the 30-cm-long pickup strips connected to a ribbon cable. (From Biswas, 2010.)

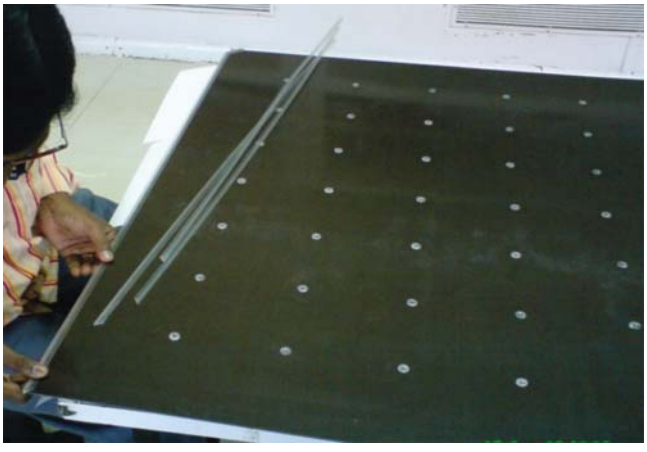

Figure A.6 Photograph of the spacers assembling process on a 1×1 m^2 Bakelite electrode. (From Biswas, 2010.)

Obviously, fabrication of larger RPCs is more complicated, but the main technological steps remain the same. As an example, phases of the assembling of a 100×100 cm^2 RPC are shown in Figures A.6 and A.7, while a complete RPC module of the same dimensions is shown in Figure A.8.

A.2 Assembling of Glass RPCs

The steps needed for the construction of glass RPCs depend, of course, on what purpose the RPC is designed for and its size; in this particular case, we make reference to the construction procedure described in Loterman (2014). The design

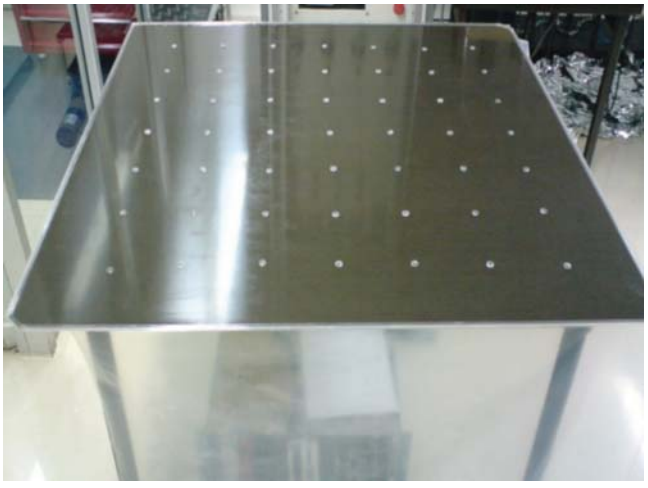

Figure A.7 Photograph of a 1×1 m^2 Bakelite electrode, complete with glued spacers, and ready to be assembled with another electrode. (From Biswas, 2010.)

Figure A.8 Photograph of a fully assembled RPC, wrapped in a shielding foil. (From Biswas, 2010.)

under consideration, a double-gap RPC where the two anodes are facing each other and are read out by the same copper strips, is shown in Figure A.9.

Glass cleaning is utterly important during construction of RPC made out of this material; therefore glass plates are thoroughly polished with appropriate chemical products then, on one surface, a resistive layer is deposited, using a spray gun. In order to keep the edge spacers and gas adapters out of the active region, tape is applied on the glass sheets.

The next step is to assemble the RPC gas gap. In this particular case, uniformity of the gap is ensured by adding nine ball spacers in between the plates; the

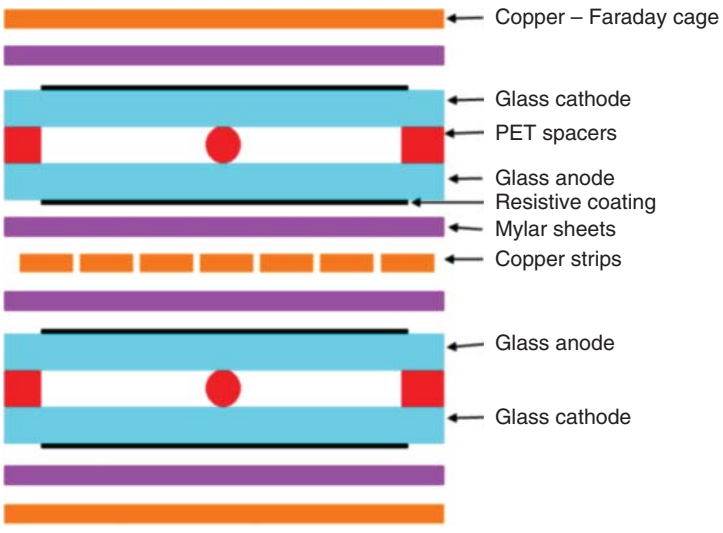

Figure A.9 Cross-sectional view of a double-gap glass RPC prototype. (From Loterman, 2014.)

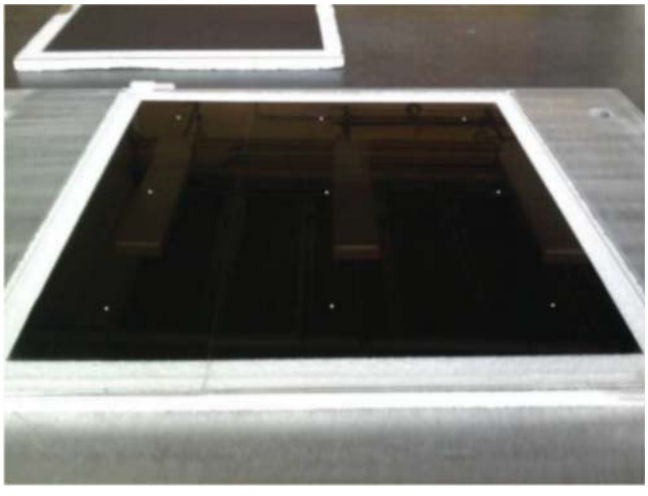

Figure A.10 Construction of the RPC glass gas gap: the white dots are the ceramic ball spacers, while on the edges the polyethylene terephthalate (PET) seal can be seen. In the top left corner, one of the gas inlet adapters is spotted. (From Loterman, 2014.)

balls are 1 mm in diameter and made of ceramic (Figure A.10). The outer seal is typically made of polyethylene terephthalate (PET), which is a hard, stiff, strong, dimensionally stable material that absorbs very little water.

Once all the spacers are glued, the second glass sheet is put on the top. During the curing of the glue, some weight (i.e., metal bars) is added on top of the plate to apply an appropriate pressure. Thereafter, high-voltage cables are connected to the resistive coating. First, a small sheet of copper is glued on the resistive coating using a silver-filled epoxy. The high-voltage cables are soldered on top

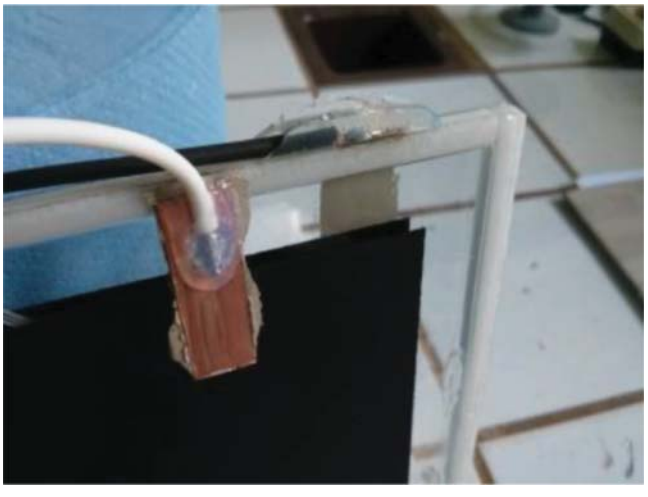

Figure A.11 High-voltage connections: The white cable is the high-voltage cable, while the black one is the ground cable, connected to the opposite side of the RPC. (From Loterman, 2014.)

of the copper sheet (Figure A.11). Insulation is assured using a silicone glue and then a dielectric tape on top of it.

Sixteen copper readout strips (with a thin layer of tin on top of them), 15-mm wide and 1.5-mm spaced, fabricated out of copper tape are then applied on a Mylar sheet that acts as an insulation foil (Figure A.12). Finally, the gaps, with the readout strips in between, are wrapped into a copper foil to minimize the external noise that may be picked up by the strips.

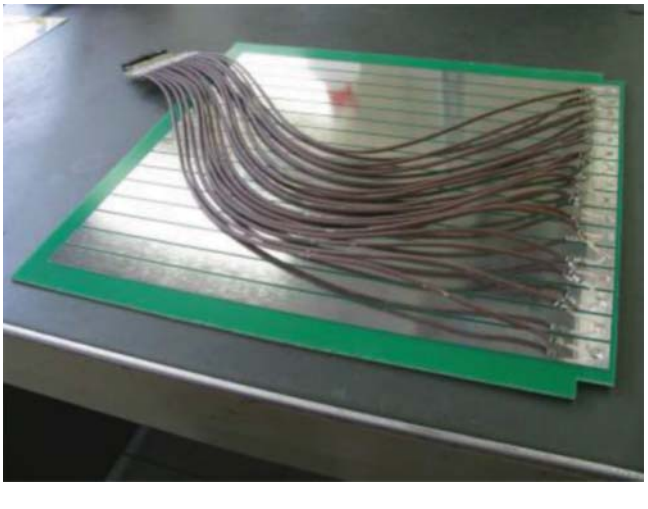

Figure A.12 Photograph of a glass RPC equipped with readout strips connected to the readout wires. (From Loterman, 2014.)

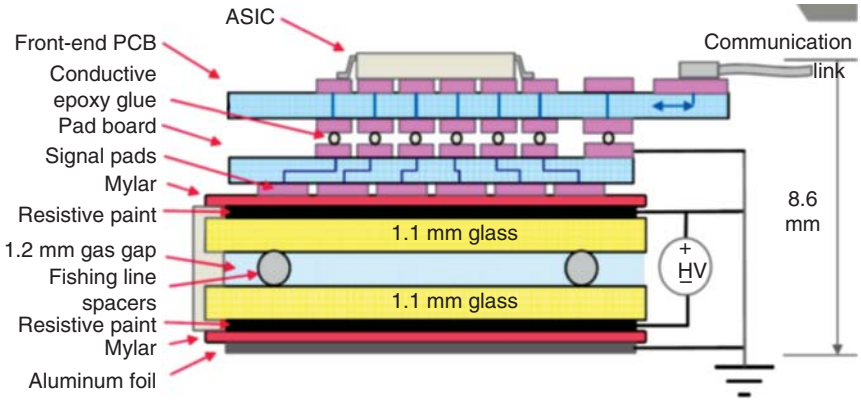

Figure A.13 Schematic layout of an glass RPC with a pad readout board connected via conductive epoxy to the front-end electronics; in this particular case, nylon fishing lines (see next paragraph for more details), partially clad in PVC sleeves, were used as spacers. (From Repond, 2009.)

(a)

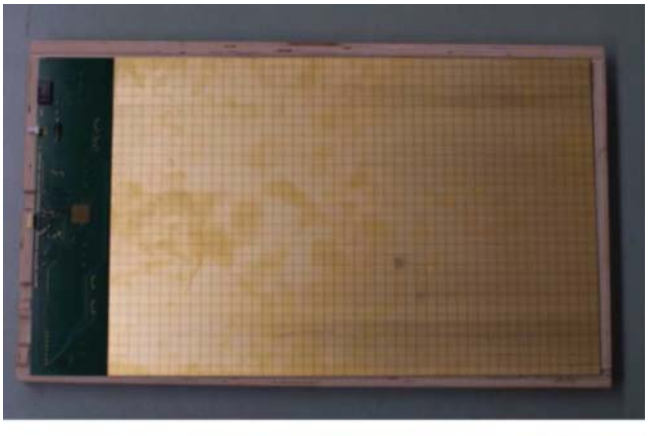

(b)

Figure A.14 Photographs of (a) the front and (b) backside of a pad readout board; front-end chips can be clearly seen. (From Repond, 2009.)

There are interesting variations to the readout schema. For instance, if pads are used, 2D signal readout can be performed using special circuit printed boards (PCB, see Figures A.13 and A.14).

A.3 Assembling of Glass MRPCs

Let us now move to the description of the construction procedure of a multi-gap RPC; as already pointed out, we make particular reference to the ones produced in the framework of the EEE experiment, whose assembling procedure has been put in place and refined by C. Williams and his team at CERN. Stratigraphy of one of such chambers is shown in Figure A.15. The materials used are quite common, namely, plastic, glass, fishing line, adhesive copper tape; the construction procedure basically consists in building the stack reported in Figure A.15 step by step, starting from the bottom and moving upwards.

At first the readout electrodes are manufactured; these are realized by applying adhesive copper tape onto a vetronite panel, where lines are usually drawn as a guide during the application of the strips. Then the tape is cut in such a way that it sticks out from the panel edges for about 2 cm and folded on the other side of the panel, so that this part can be, later on, used to solder the wires connecting the strip to the front-end electronics (see Figure A.16).

Then the vetronite plane is put on a honeycomb panel and holes are drilled along the edges; these panels are used to contain the inner planes of the chamber and to give rigidity to the entire structure. The vetronite is then removed and the holes in the vetronite are widened and threaded so that they can accommodate for 1.5 cm nylon screws (see Figure A.17). Then the vetronite and honeycomb panels

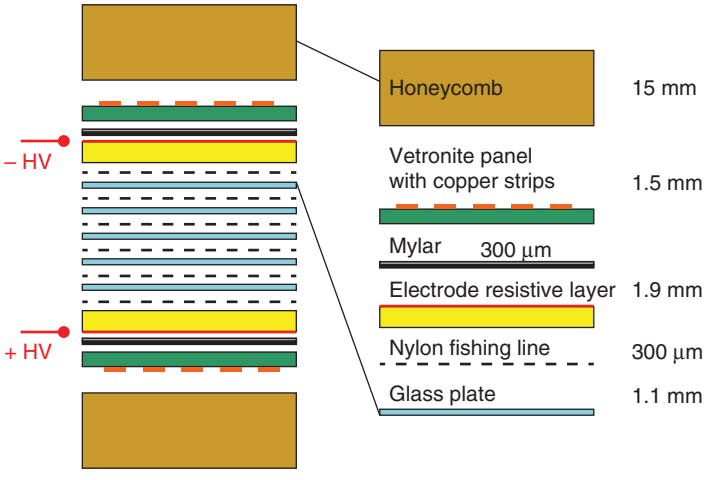

Figure A.15 Stratigraphy on a multi-gap RPC used for the EEE experiment. (From Garritano *et al.*, 2015.)

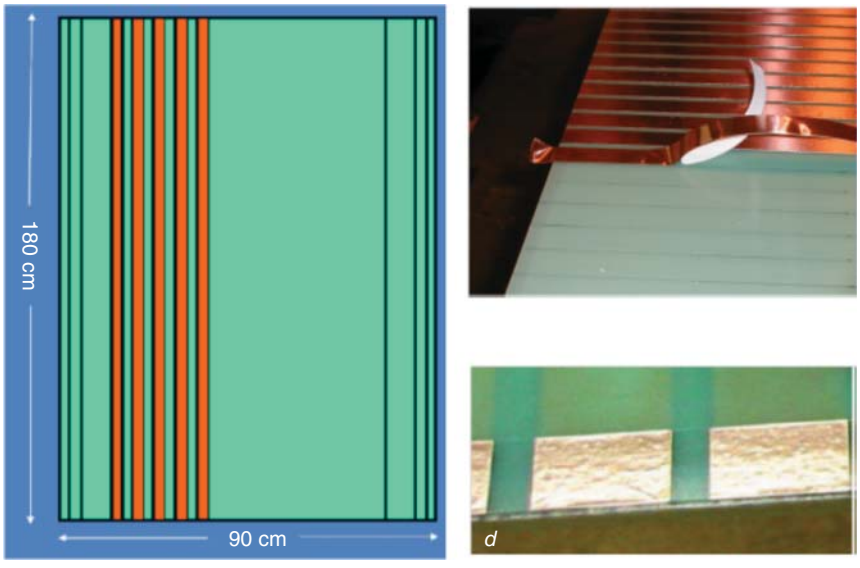

Figure A.16 Various steps of manufacturing the readout strips. (From La Rocca *et al*., 2017.)

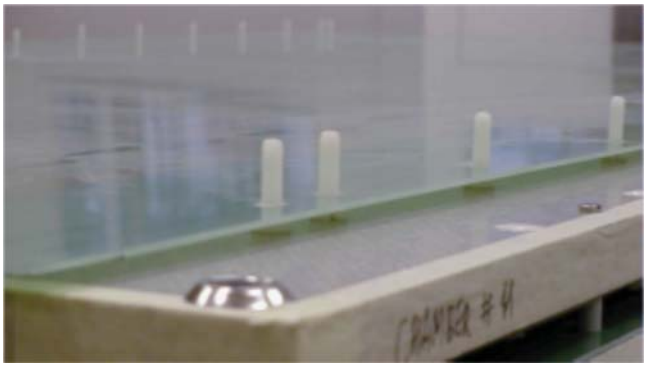

Figure A.17 Detail of the nylon screws along the edges of a vetronite panel used for MRPC construction. (From La Rocca *et al*., 2017.)

are assembled together again, attaching them by means of bi-adhesive tape and using the screws as guides.

On top of the vetronite plane a Mylar foil, 175 μm thick, is placed. On the foil a HV contact pad is realized, made in copper, with a piece of bi-adhesive tape on top. When the protective layer on the tape is removed, it will establish an electrical contact with the first glass plate (see Figure A.18).

The two outer glass electrodes are made of common float glass, $164 \times 85 \times 0.19$ cm^3 in dimension. To assure optimum results, glass surfaces are at first polished with alcohol and water (which is a procedure applied to all glass sheets used in the construction, since they generally arrive from factory covered with a

Figure A.18 High-voltage connection on an MRPC of the EEE experiment. (From La Rocca *et al*., 2017.)

thin layer of paraffin). Since the HV must be applied on one surface of each outer glass electrodes, a resistive paint (Licron) was applied using a spray can. This operation is repeated few times in order to obtain a layer with a resistivity as uniform as possible. After that the Licron paint gets dry, which typically takes about half a day, an additional protective layer of urethane is also sprayed.

Now chamber assembly can begin. The glass coated with the Licron paint is moved down on the honeycomb/vetronite plane previously prepared. The glass plate is cleaned, by means of an electrostatic gun, which uses a small jet of ionized argon; this operation has to be repeated each time a new glass plate is positioned.

Then the fishing line is wrapped around the nylon screws like in Figure A.19; it can be 250 or 300 in diameter (or others), determining the gap size between two successive glass plates. Another glass plate is positioned on top, and the fishing line is wrapped on top of this, then another glass plate is positioned, until five or six gaps are realized. As shown in Figure A.15, the inner glass plates are 1.1 cm thick, while the last glass plate – identical to the first – is 1.9 cm thick, with the upward surface coated with Licron paint.

On both panels, 20-cm long wires are soldered to the high-voltage contacts previously manufactured. The second vetronite-honeycomb is placed on top of the structure, taking care to position 1.5 cm rubber spacers at the four corners. To join together the two panels, 1 cm from the edges, holes are drilled, and screws are inserted. A vacuum cleaner is used to prevent dust getting inside the chamber. Then readout wires are connected to the strips, soldering them as shown in Figure A.20.

Then the MRPC is inserted into an aluminum box previously prepared, which contains the glass stack and ensures gas tightness; this has to be equipped with

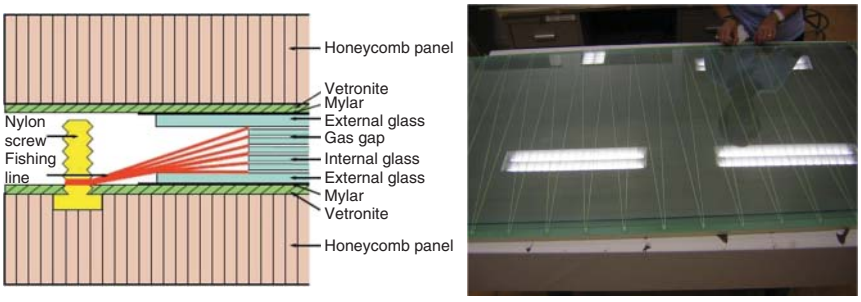

Figure A.19 (a) Schematics of the fishing lines wrapped around the nylon screws. (From Abbrescia *et al*., 2008.) (b) Actual photograph of fishing lines, keeping the glass plates at the right distance in an MRPC of the EEE experiment. (From La Rocca *et al*., 2017.)

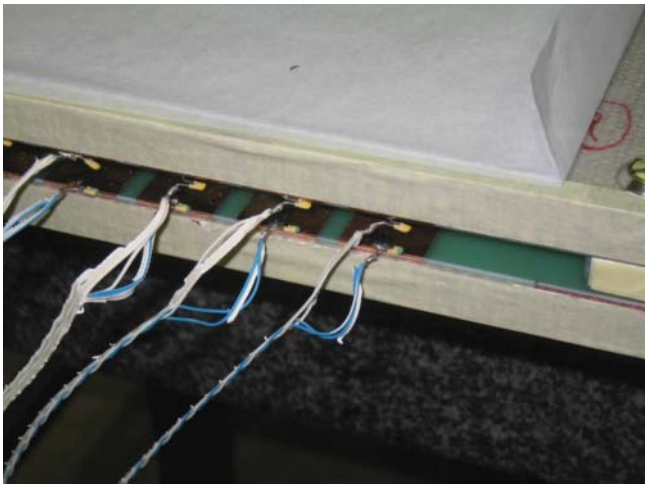

Figure A.20 Photograph showing the readout wire soldered to the strip in an EEE MRPC. (From La Rocca *et al*., 2017.)

suitable connectors joining the strip wires to front-end electronics and the high-voltage cables to the power supply, and with gas connectors as well. Then, the honeycomb/vetronite/glass sandwich is raised and positioned inside the box, positioning suitable spacers along the chamber sides to provide mechanical stability (Figure A.21). Finally signal and high-voltage cables are soldered to the relative connectors inside the box and the box is closed.

Of course, for more details about the construction procedures described, both for Bakelite and glass and multi-gap RPCs, the reader is invited to consult the original documents cited here.

Figure A.21 The vetronite/glass stack of one of the MRPCs of the EEE experiment while it is positioned inside the relative metallic box. (From La Rocca *et al*., 2017.)

References

Abbrescia, M. *et al*. (2008) Performance of a six gap MRPC built for large area coverage. *Nucl. Instrum. Methods Phys. Res., Sect. A*, **593**, 263–268.

Biswas, S. (2010) Development of high resolution gas filled detectors for high energy physics experiments. PhD thesis. University of Calcutta, http://www.ino.tifr.res.in/ino/theses/Saikat.Biswas-thesis.pdf (accessed 30 October 2017).

Garritano, L. *et al*. (2015) An educational activity: building a MRPC. *World J. Chem. Educ.*, **3** (6), 150–159.

La Rocca, P., Riggi, F., and (for the EEE collaboration) (2017) Aspetti operativi e legati alla sicurezza durante le procedure di costruzione e assemblaggio delle camere MRPC, EEE Internal note 2017/01.

Loterman, D. (2014) *Development of a Glass Resistive Plate Chamber for the Phase-2 Upgrade of the CMS Detector at the Large Hadron Collider*, University of Gent, http://lib.ugent.be/fulltxt/RUG01/002/163/596/RUG01-002163596_2014_0001_AC.pdf (accessed 30 October 2017).

Repond, J. (2009) *A Calorimeter with Resistive Plate Chambers*, Seminar at University of Virginia, Charlottesville, VA, http://www.phys.virginia.edu/Files/fetch.asp?EXT=Seminars:1873:SlideShow (accessed 30 October 2017).

Glossary

Anode streamer When the streamer/"Kanal process" occurs in the enhanced field region ahead of the electron cloud, moving toward the anode.

Attachment coefficient The probability (per unit of projected path length) that an electron drifting through a gas under the influence of an electric field will undergo electron attachment.

Attachment The process where an electron drifting in a gas under the influence of an electric field is captured by an atom or molecule in the gas forming a negative ion. It reduces the amount of free electrons in an avalanche.

Avalanche mode In RPC terminology, when most incoming particles will not cause a streamer, remaining mostly in the proportional or saturated avalanche stages.

Avalanche The process of electron multiplication (in gases, liquids or solids) by successive ionization of the medium by free (non-attached) electrons that gain energy from an applied electric field.

Background counting rate - (also called dark count rate) of a detector: the rate of self-generated signals in absence of external radiation.

Bubble chamber A detector of charged particles using superheated liquid (e.g. liquid hydrogen). The liquid is contained in a vessel, and effect a piston to rapidly decrease the pressure in the vessel when a charged particle crosses it. As a result, the liquid transits into the superheated phase causing bubble formation around the ions, allowing to visualize the particle track.

Cathode streamer When the streamer/"Kanal process" occurs in the enhanced field region in the back of the ion cloud, moving toward the cathode. When the gas gain in a gaseous detector is increased (by increasing the applied field), the cathode streamer appears before the anode streamer; therefore, it has more practical relevance than the latter. A typical feature of the cathode streamer at the onset of the process is a discernible time delay between the initial avalanche and the streamer current pulses. The initial avalanche is then called "the precursor."

Centroid of charges It is a geometric point evaluated from the measured charges on the readout strips. It is analogous to the center of mass of a mass distribution. In measurements with charged particles, one determines the statistical distribution of centroids and a sigma or a FWHM of this distribution represents an estimate for position resolution of the detector under test.

Resistive Gaseous Detectors: Designs, Performance, and Perspectives, First Edition.
Marcello Abbrescia, Vladimir Peskov, and Paulo Fonte.

Cloud chamber (another common name is Wilson chamber) A gas chamber filled with supersaturated vapors of water (or alcohol). When passing through the chamber, a charged particle ionizes the gas and vapors condense around the ions forming a visible mist along the particle track.

Cluster size Number of adjacent strips, or, in general, readout channels, fired at the same time at the passage of a particle. It is also sometimes referred to as strip multiplicity. Ideally, just the strip crossed by the particle should be fired, but cross-talk or other phenomena (for instance the occurrence of streamers in the presence of a sensible front-end electronics) increase this number of fired strips. High cluster size increases occupancy and may spoil the detector spatial resolution.

Delta electrons Electrons created by a high-energy particle passing through a medium (in our case, typically, a gas) and having energies much larger than the ionization potential of the gas. Delta electrons have short curved tracks and create clusters of secondary electrons.

Discharge The complex processes that occurs after the positive column is established. Depending on the amount of charge available, the conductive channel may go through several stages eventually culminating in a spark. In metallic gaseous detectors, typically the spark stage is reached, with full discharge of the anode–cathode capacitance. In resistive detectors, the process is quenched (see "Streamer quenching").

Effective first Townsend coefficient The difference between the first Townsend coefficient and the attachment coefficient. This is the quantity actually relevant to describe avalanche growth.

Efficiency The probability of a particle crossing a detector to be revealed by giving rise to a detectable signal of some kind.

Electron tunneling A quantum mechanical effect where electron/electron wave tunnels through an energy barrier.

Electronegative gas A gas where the attachment processes are relevant and the attachment coefficient is not negligible. For electronegative gases, the difference between the first Townsend coefficient and the effective first Townsend coefficient is significant.

Fermi level The energy level above which the probability of finding an electron is zero at zero absolute temperature. As the temperature rises, electrons can be found above the Fermi level. The Fermi level plays an important role in the band theory of solid-state physics.

First Townsend coefficient The probability (per unit projected path length) that an electron drifting through a gas under the influence of an electric field will produce another free electron after interaction with the molecules or atoms of the gas.

FWHM Full width at half maximum – a parameter often used to describe the width of a "bump" on a curve or a function. It is defined by the distance between points on the curve at which the function reaches half its maximum value. In the case of the Gaussian distribution FWHM $\approx 2.355\sigma$.

Gas gain The average electron multiplication factor arising from avalanches in a certain stable situation. Typically, the avalanche process stops when the electron cloud reaches the anode, determining the gas gain.

Gas number density The number of molecules or atoms of a gas per unit volume; usually expressed in inverse cubic meters.

Glow discharge It is a type of discharge with specific current-voltage characteristics formed by passing a current, typically below one ampere, through a gas at voltage drop from several hundred volts to several kilovolts. The glow discharge has a well-defined structure, for example, a bright cathode spot when the current density is constant over its surface and a positive column, where the drop voltage is relatively low.

Hopping conductivity In the context of this book it is a conductivity via quantum-mechanical tunneling of charge carriers, for example, electrons, between localization sites. This mechanism is made possible by crystal vibrations that emit or absorb the energy difference between the initial and final electronic states.

Ion and photon feedback Secondary avalanches created in the gaseous detector by photon emission from the primary avalanche and/or by the avalanche positive ions recombination on the cathode. This process may cause either a short or a quite long (in time) sequence of secondary avalanches.

Jet emission (another name is "explosive field emission") – emission of electrons from thin dielectrics on the cathode, charged by positive ions from the avalanches. However, occurring not in the form of single electrons as in classical Malter effect but rather as bursts/jets of electrons: a huge number of electrons emitted within a short period of time.

Kanal process or Kanalaufbau, see streamer/Kanal.

Limited proportionality mode In the context of cylindrical gaseous detectors, when most avalanches are saturated (due to the space charge effect). Normally, this happens at large gas gains.

Malter effect It is originated when ions are deposited on thin insulating layers on cathodes, creating a double layer of charges where the electric field is locally enhanced to high values. This gives rise to secondary electrons from the surface by field emission.

Ocupancy On a given event, the fraction of readout channels of a detector that have non-zero signal.

Positive column In the context of this book, a conductive column (at the anodic potential) created between anode and cathode by streamers.

Precursor In the context of this book, an initial avalanche in a cathode streamer process.

Proportional avalanche When the progression of the avalanche is not influenced by the number of electrons in it. In this case, after a certain development in time the average number of electrons in a statistical collection of identically started avalanches is proportional to the initial number of electrons. Sometimes also called a Townsend avalanche.

Quenching gas A gas where discharge quenching effects are relevant, usually because of high UV absorption coefficients, which suppresses photon feedback.

Rate capability The maximum flux of impinging particles that can be revealed by an RPC without significant efficiency degradation; the usual request is that

efficiency should be >95%. RPCs operated in "streamer" mode can have rate capability of several tens (sometimes few hundreds) of hertz per square centimeter; RPCs operated in avalanche mode are characterized by rate capabilities larger by more than 1 order of magnitude.

RPC conditioning The operation consisting in keeping RPCs switched on for some time (from days to weeks, depending on the specific case) to allow for a significant decrease in current and background counting rate after these devices have been switched on for the first time after construction.

Saturated avalanche When the progression of the avalanche is influenced by the number of electrons in it via the space charge effect. If the streamer process is not dominant, this causes a reduction of the effective gas gain of the avalanche.

Self quenched streamer (SQS) mode A streamer formed in some geometries having radial electric field, for example, in the case of a cylindrical detectors with thick anode wires. The streamer develops toward the cathode, but stops its development in the region of weak electric field, does not reach the cathode and does not create a conductive bridge (Kanal) between the electrodes.

Sensitivity In the context of this book, the probability for neutral particles to interact inside or immediately around a detector giving rise to charged secondaries that are revealed. It is a relevant factor to be taken into account, for instance, when detectors operate immersed in intense backgrounds of neutrons or photons.

Space charge effect In the region between the electron and ion clouds the space charge field is contrary to the applied field, while ahead of the electron cloud and in the back of the ion cloud it reinforces the applied field. Sideways to the avalanche these effects are also present, but to a smaller magnitude. The effect becomes discernible when the space-charge field becomes comparable to the externally applied field. From the lower and higher gain regions arise two different phenomena (see saturated avalanche and streamer)

Space-charge field The electric field created by the drifting avalanche charges, electrons ahead and ions lagging behind. The field actually depends on the charge densities present.

Streamer mode In RPC terminology, when most incoming particles will cause a streamer and subsequent discharge. The signals generated are quite large, on the order of nanocoulombs.

Streamer probability Fraction of events in an RPC characterized by a "large" amplitude of the induced signals, usually sufficient to fire channels of the readout electronics neighboring to the one corresponding to the impinging particle. RPCs operating in streamer mode should keep the streamer probability sufficiently low (typically <10%) while keeping the overall efficiency still acceptable (>95%).

Streamer quenching In resistive detectors, the impossibility of large currents to flow through the resistive electrodes limits (quenches) the discharge sequence toward a full spark. This has very important practical implications in the safety of operation of such detectors but also limits its rate capability.

Streamer/Kanal If free electrons appear in the regions where the space-charge effect created an enhanced electric field, much stronger multiplication will take place there. If the supply of free electrons is sustained by some physical process, the situation becomes self-sustainable and it is called a streamer (the process is also called Kanalaufbau, after the original papers in German). Typically, in a streamer the region of larger charge production (most active region) moves in space much faster than the drifting velocity of the participating particles. See cathode streamer and anode streamer.

Strip multiplicity Typically used as synonymous of cluster size.

Time resolution The precision by which the crossing time of a particle can be measured by a particle detector.

Time-of-flight (TOF) An experimental technique to measure the velocity of a particle by measuring the time it takes to travel across a known distance. For relativistic particles this technique is limited to particles with energy not exceeding by much of its rest mass-energy.

Tomosynthesis A 3D picture of an object, for example, a woman's breast, using X-rays. In this case, the breast is positioned the same way it is in a conventional mammogram, but only a little pressure is applied, just to keep the breast in a stable position. The X-ray tube moves in an arc around the breast while around 10 images are taken during a few seconds of examination. The obtained information is sent to a computer, for tomographic image reconstruction.

Townsend avalanche The avalanche process in gases, which was initially investigated by John Sealy Townsend in the late nineteenth century.

Trigger In high energy physics, a trigger can be defined as a system that uses criteria to rapidly decide which events in a particle detector to select and to further process.

Useful plateau The region in the efficiency curve of an RPC versus applied voltage characterized by a sufficiently high efficiency (typically >95%) for detecting particles and at the same time low (typically <10%) fraction of "streamers" (also called streamer probability).

Vacuum ultraviolet (VUV) photons Ultraviolet photons strongly absorbed by the air. Typically, it is a radiation with wavelength between ≈50 and 300 nm.

Wilson Camera (see Cloud chamber).

Index

Resistive Gaseous Detectors: Designs, Performance, and Perspectives, First Edition.
Marcello Abbrescia, Vladimir Peskov, and Paulo Fonte.